DEVELOPING IMAGING TECHNIQUES FOR STUDYING BRACHYURAN CRAB ZOEAE AND ADULT MORPHOLOGY OF GONOPODS WITH AN EMPHASIS ON THE INVASIVE CHINESE MITTEN CRAB, *ERIOCHEIR SINENSIS*

A thesis submitted to the University of London for the degree of

Doctor of Philosophy

By

Seyit Ali Kamanli

School of Biological Sciences

Royal Holloway, University of London

September 2017

DECLARATION

I, Seyit Ali Kamanli, hereby declare that this thesis and the work presented in it is entirely my own. Where I have consulted the work of others, this is always clearly stated.

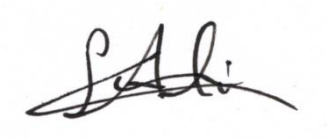

Seyit Ali Kamanli

September 2017

ABSTRACT

In the present study, the zoeal stages of the Chinese mitten crab, *Eriocheir sinensis* H. Milne Edwards, 1853, which is now well established in the Thames catchment and other watersheds around the UK, were examined as a case study. Traditional illustration techniques such as line drawings were rejected, instead zoeal images were visualised using a modern-day technique; namely Confocal Laser Scanning Microscopy. A protocol was established to re-describe the zoeal stages of this invasive species. A number of steps were considered and trialled including pre-processing of zoea comprising cleaning, staining, digesting, dissecting and mounting; the scanning of zoeal mouthpart etc. using a Nikon A1-Si confocal laser microscope and the post-processing of data by applying open-source, freeware programs ImageJ and Drishti to visualise the larval appendages. This study also investigated the brood potential of ovigerous mitten crabs collected from the Thames Estuary and held in the laboratory for observation. And lastly, the various techniques used to study the zoeal stages were applied in an investigation to scan the first male gonopod of a number of brachyuran crab species. The male gonopod is a species diagnostic character, the distal morphology of which can be extremely complex and difficult to draw. The results of this work confirmed that a second species of mitten crab, not *Eriocheir sinensis*, is present on the European mainland, it verified the existence of an undescribed species of *Libystes* A. Milne Edwards, 1867 from the Red Sea and proved the true identity of *Monomia argentata* A. Milne-Edwards, 1861 from an old specimen held in the dried collections of the Natural History Museum, London.

ACKNOWLEDGMENTS

First and foremost, I would like to thank the Ministry of National Education, Republic of Turkey, for without their generous financial support, this work could not have been achieved.

I would like to express my sincere gratitude and thanks to my supervisors: Dr David Morritt, Royal Holloway University of London and Dr Paul Clark and Dr Alex Ball both Natural History Museum, London, for their continuous support, encouragement and guidance throughout my PhD study. I have learned a great deal from them.

I would like to thank the following from the Imaging and Analysis Centre, Natural History Museum, London; Dr Tomasz Goral teaching me confocal microscopy and his many helpful comments; Dr Farah Ahmed, Dr Amin Garbout, Dan Sykes and Rebecca Summerfield, for training on the use of Drishti and other software programmes as well as obtaining micro-CT images.

I am grateful to Dr Terue Kihara, German Centre for Marine Biodiversity Research, Senckenberg am Meer, Wilhelmshaven, Germany, for her most helpful advice with regard to confocal microcroscopy.

I would like to extend my sincerest gratitude to all post-doctoral researchers, especially to Dr Argun A. Özak, Prof Edson A. Adriano, Dr Ashlie Hartigan, Dr Juliana Naldoni, Dr Paolo Ruggeri and Dr Tara Thrupp for their support and helpful discussions during writing my thesis. I would also like to thank Dr Deniz İnnal, Prof Naime Arslan, Prof Güler Çolak, Dr Özgür Emiroğlu, Prof Sibel Atasagun, Prof Süphan Karaytuğ and Dr Hakan Şentürk for their suggestions.

Furthermore, I would like to thank Dr Eileen Cox, Prof Geoff Boxshall, Prof Beth Okamura, Prof Ronny Huys, Dr Anouk Gouvras, Dr Chris Jones and all staff of Department of Life Sciences, Natural History Museum, London.

I wish to express my thanks to Dr Tony Stead, PhD Advisor, Tracey Jeffries Departmental PA and Neil Morley Research Technician, all School of Biological Sciences Royal Holloway University of London.

I would also like to thank my dear friends Muhammed Kürşad Özekin, Pınar Akgül, Mehmood Khan, Fiza Elahi, Mevlüt Yurtseven, Christopher Mills, Martin Richardson, Mehmet Hüsnüoglu, Emre Çolak, Salih Ersoyoglu, Toygun Kılıçoğlu, Zeynel Karakaş, Ali Salman, Cem Özkan, Düzgün Dalgıç, Emrah Yıldız, Onur Temel, Derya Arslan, Nagihan Tuna, Hilal Yıldız, Funda Kutlu, Gizem Bedir and Nagehan Küçükşahin for their sincerity and support. They gave me reliance, peace and strength with their true friendship.

Last but not least, I would like to thank my family for their endless support during my studies in London. I could not have completed my PhD without them. I would like to express my feelings in Turkish:

"Sevgili annem İnci Kamanlı ve babam Mezzin Kamanlı' ya: siz olmadan asla başaramazdım. Bu kitabin içinde yazılanlar belki sizin icin çok anlamlı olmayacak, fakat sizin varlığınız ve bitmeyen desteğiniz ile, bu kitapta benden çok emeğiniz var. Sizin kadar mükemmel bir aileye sahip olduğum icin çok şanslıyım. O yüzden sizlere, beni yıllarca sabırla desteklediğiniz ve beklediğiniz için sonsuz teşekkür ederim. Ayrıca çalışmalarım boyunca bitmeyen destekleriyle beni hiçbir zaman yalnız bırakmayan kız kardeşlerim Semra ve Derya; yiğenlerim Berke, Efe ve ailelerine de çok teşekkür ederim. Son olarak, amcam Nazım Kamanlı ve amcam Kadir Gürel'e de desteklerinden dolayı teşekkür ederim. Hepiniz iyi ki varsınız".

CONTENTS

LIST OF FIGURES

microscope. (b) Demonstrating these areas using SEM. Scale bars: (a) = 500 μm; (b) = 100 μm.

Figure 2.5: (a) Slides embedded in polyvinyl lactophenol. (b) Gluing reinforcement rings.

Figure 2.6: Schematic illustration of the mounting method. (a) Self-adhesive reinforcement rings are glued on the slide; (b) A few drops of the mixture of diluted glycerine are dropped into the rings; (c) Appendage of the specimen is placed inside the mounting media using the fine needles; (d) Cover slip is placed on the rings carefully to avoid air bubble formations.

Figure 2.7: The Nikon graphical user interface showing the schematic light path through the instrument with the various selected settings. Represented colours as channels in specific nm levels. Ch1 = blue channel at the wavelength of 403 nm; Ch2 = green channel at wavelength of 487 nm; Ch3 = orange channel at the wavelength of 561 nm; Ch4 = red channel at the wavelength of 638 nm.

Figure 2.8: File formats of the different confocal microscopes. Leica uses ***.lif files. Nikon uses ***.nd2 files. Olympus uses ***.oib files. Zeiss uses ***. Czi files (Kamanli *et al.*, 2017).

Figure 2.9: Schematic illustration of the designed platform used to hold the male gonopod firmly during 10−12 hours of confocal scanning (CLSM): (1) Two groups of 7 microscope slides were glued each other using polyvinyl lactophenol and these merged microscope slides were glued on each side of the glass/plastic platform; (2) Two sides of the new platform was sealed using Blu Tack®. The level of the Blu Tack® and microscope slides were levelled by using a cylindrical metal holder; (3) The male gonopod was placed and arranged inside the slide channel; (4) The gonopod was covered using Blu Tack® to immobilise it during long duration scanning; (5) The

channel was filled with 100% glycerine until it reached the highest level of the adjacent slides; (6) The channel was covered with a long coverslip (avoiding the inclusion of air).

Figure 2.10: A general view of designed platform to scan large appendages using CLSM. The G1 pictured was removed from an *Eriocheir* (specimen captured in Hollands Diep, Netherlands).

Figure 2.11: Compensating images having noisy background after increasing the offset.

Figure 2.12: Illustration of channels according to wavelengths. c1 represents blue channel (405 nm), c2 represents green channel (488 nm), c3 represents orange channel (561 nm) and c4 represents red channel (640 nm).

Figure 2.13: Container designed to hold samples during micro-CT scanning.

Figure 2.14: Resulting scanning dry specimen, *Monomia argentata*, using a Nikon Metrology HMX ST 225 micro-CT scanner and processing with Drishti. (a) Dorsal side of the sample. (b) Ventral side of the sample. (c) Viewing the G1 by clipping and carving the image using Drishti. (d) Making the gonopods visible without destroying the old, fragile dry crab.

Figure 2.15: Scanning a large G1 using high resolution micro-CT. The G1 was placed inside a micro-centrifuge tube filled with 70% ethanol.

Figure 3.1: An ovigerous Chinese mitten crab from the River Thames, London showing a mass of eggs attached to the pleon. Photo credit: http://www.nhm.ac.uk/our-science/our-work/biodiversity/report-your-invasive-crab-sightings.html.

Figure 3.2: The female crab genital organs showing the reproductive organs (after Becker *et al.*, 2011).

Figure 4.4: Advantages of digesting appendages. *Eriocheir sinensis*, zoea I, images of second maxilliped using CLSM. (a) Confocal image of non-digested appendage showing basial musculature. (b) Drishti image based on this data. c) Confocal image after digestion of the basial muscles. (d) Drishti image from this data (tiny structures are circled). All 40× oil immersion objective, applying "large images" option, scan area of 1×2 fields for image stitching. (e) Enlargement of (b). (f) Enlargement of (d). Scale bars = 100 μm.

Figure 4.5: Advantages of staining. *Eriocheir sinensis*, zoea I, scanned images of the maxilla using CLSM. (a) Stained using only Congo red, 60× oil immersion objective. (b) Stained using the mixture of Congo red and acid fuchsin, 40× oil immersion objectives. Scale bars a = 50 μm; b = 100 μm.

Figure 4.6: *Eriocheir sinensis*, zoea I, scanned images of first maxilliped using CLSM. (a) Non-digested and unstained appendage. (b) Stained using Congo red. (c) Non-digested and stained using the mixture of Congo red and acid fuschin. (d) Digested and stained using the mixture of Congo red and acid fuschin. Scale bars = 100 μm.

Figure 4.7: *Eriocheir sinensis*, zoea I, scanned appendages using CLSM and processed using Drishti. (a) Non-digested and unstained first maxilliped. (b) Non-digested and stained dorsal view of telson. (c) Digested and stained first maxilliped. (d) Digested and stained ventral view of telson. Scale bars = 100 μm.

Figure 4.8: Disadvantages of using polyvinyl lactophenol with stained *Eriocheir sinensis* zoeal appendages. Debris from dissection adhered to the exoskeleton. (a) ZII, confocal image of endopod using CLSM, 60× oil immersion objective. (b) ZII, Drishti image of endopod. (c) ZII, attempt at debris removal using Drishti and Photoshop was not always successful, see circled areas (d) Mounted Congo red stained appendages stained blue, see arrowed areas. Scale bars a-c = 100 μm.

Figure 4.9: Disadvantages of using diluted glycerine for mounting the samples. (a) Blurred images because the specimen had moved, (arrowed area). (b) Creation of air bubbles and disruption of the image, (arrowed areas). Scale bars a = 100 μm; b = 1000 μm.

Figure 4.10: Compensating for background colour using confocal software and Drishti. (a) MIP after increasing the offset. (b) MIP with a black background. (c) Drishti processed image from the same dataset.

Figure 4.11: "Tiling" appendages when scanning at higher magnification. *Eriocheir sinensis*, zoea V, image of maxilla using CLSM. (a) Confocal image showing tiled areas. (b) Drishti image. 40× oil immersion objective, scan area of 2×3 fields. Scale bars a = 100 μm; b = 200 μm.

Figure 4.12: Merging Drishti images using additional software programmes. *Eriocheir sinensis* zoeal appendages using CLSM. (a) ZII, maxilla image merged using Adobe Photoshop. (b) ZIV, maxilla image merged using VGStudio Max. Merged areas are circled. Scale bars a = 200 μm; b = 100 μm.

Figure 4.13: Applying large images option to visualise fine detail on bigger appendages using CLSM. *Eriocheir sinensis*. (a) ZI, visualisation of fine setae on pleon, 40× oil immersion objective, scan area of 2×6 fields (Fine setae arrowed). (b) Visualisation of adult male gonopod applying large images option with the order of "Z series (Lambda (Large images))", 10× objective, scan area of 5×5 fields (Displaced tiles are arrowed). Scale bars a = 200 μm; b = 1000 μm.

Figure 4.14: Scanned brachyuran crab larvae using different brands of CLSM processed in Drishti. *Eriocheir sinensis*, zoea I, first maxilliped. (a) Basis, Nikon A1-Si CLSM. (b) Endopod, Olympus Fluoview FV1000 IX8. (c) Antenna, Zeiss LSM 880 airy scan. All

40× oil immersion objective. (d) *Sesarma curacaoense*, ZII, lateral view of pleon, Leica TCS SP5, 10× dry objective. Scale bars a-b = 100 μm; c = 50 μm; d =500 μm.

Figure 4.15: Post-processing in Dristhi applying different methods. (a) All confocal channel data was merged using ImageJ and processed using Drishti. (b) One single channel imported using confocal software and processed using Drishti. (c) Separate channels imported using confocal software and were loaded together in Drishti which created an over statured image. Scale bars = 100 μm.

Figure 4.16: Digital dissection. *Eriocheir sinensis*, zoea I, image of maxillule using Nikon A1-Si CLSM and processed using Drishti. (a) Unwanted tissue arrowed. (b) Repositioning of appendage to allow the removal of unwanted tissue (arrowed). (c) After digital dissection of tissue (compare a with c). 40× oil immersion objective. Scale bars = 100 μm.

Figure 4.17: Drishti images of *Sesarma curacaoense*, zoea I appendages using Leica TCS SP5. First maxilliped. (a) Coxa and basis. (b) Endopod. (c) Coxa and basis of second maxilliped. (d) Maxillule. All 40× oil immersion objective. Scale bars a-b = 50 μm; c-d = 100 μm.

Figure 4.18: Drishti images of *Armases miersii*, zoea III appendages using Leica TCS SP5. (a) Coxa and basis of first maxilliped. (b) Endopod of second maxilliped. Both using 40× oil immersion objective. (c) Antenna. (d) Maxillule. Both using 20× dry objective. Scale bars a, d = 200 μm; b-c = 100 μm.

Figure 4.19: Application of 3D rendering programmes to the appendages obtained using CLSM. (a) Appendages processed using Drishti. (b) Appendages processed using Avizo.

Figure 4.20: Comparing bright field, confocal and Drishti images. *Eriocheir sinensis* zoea, images of second maxilliped using CLSM. (a) ZI, DIC image of exopod, 20× dry objective. (b) ZIV, confocal image of exopod, 20× dry objective applying "large images" option, scan area of 1×2 fields for image stitching. (c) Drishti image of b. Scale bars a = 50 μm; b, c = 100 μm.

Figure 4.21: Application of an AZ-C1 macro confocal to the larger appendages of *Eriocheir sinensis*. (a) ZIV, complete pleon, 5× dry objective. (b) ZV, complete antennule 5× dry objective by zooming. (c) ZV, complete second maxilliped, 5× dry objective by zooming. Scale bars a, c = 500 μm; b = 100 μm.

Figure 4.22: Application of other microscopes to investigate the bigger samples of *Eriocheir sinensis*, in this case Zeiss Axio zoom V16 stereo zoom microscope for large fields. (a) ZVI stage. (b) Megalopa stage. (c) Ventral side of crab I stage. (d) Dorsal side of crab I. Scale bars a, c, d = 500 μm; b = 200 μm.

Figure 5.1: *Eriocheir sinensis*, ZI, carapace, Zeiss Ultra Plus Field Emission SEM. (a) Lateral view. (b) Anterior view. Scale bars = 100 μm.

Figure 5.2: *Eriocheir sinensis*, ZI, carapace, Zeiss Ultra Plus Field Emission SEM. (a) One pair of posterodorsal setae present (arrowed). (b) Anterodorsal setae absent. (c) Ventral carapace margin with 8−9 serrations and small spines on lateral spine (arrowed). (d) Dorsoposterior carapace margin (arrowed) without setae. Scale bars a = 20 μm; b-c = 10 μm; d = 100 μm.

Figure 5.3: *Eriocheir sinensis*, ZI, Nikon A1-Si CLSM with Drishti processing. (a) Antennule, 2 aesthetascs and 3 setae arrowed. (b) Antenna, two setae arrowed. Objective: = 60× oil immersion. Scale bars = 50 μm.

Figure 5.4: *Eriocheir sinensis*, ZI, Nikon A1-Si CLSM with Drishti processing. (a) Mandible, incisive teeth arrowed. (b) Maxillule. Objectives: = 40× oil immersion. Scale bars = 50 µm.

Figure 5.5: *Eriocheir sinensis*, ZI, maxilla, Nikon A1-Si CLSM with Drishti processing. (a) Maxilla. (b) Coxal endite. (c) Basial endite and endopod. Objective: 40× oil immersion. Scale bars = 50 µm.

Figure 5.6: *Eriocheir sinensis*, ZI, first maxilliped, Nikon A1-Si CLSM with Drishti processing. (a) Whole appendage. (b) Coxa and basis. (c) Coxa and basis rotated to reveal reverse angle of image a. (d) Endopod. (e) Exopod with 4 natatory setae. Objective: a, b, d = 40× oil immersion; c, e = 20× dry. Scale bars a, b, d = 100 µm; c, e = 200 µm. See video 1 for 3D representation of the first maxilliped.

Figure 5.7: *Eriocheir sinensis*, ZI, second maxilliped, Nikon A1-Si CLSM with Drishti processing. (a) Whole appendage. (b) Coxa, basis and endopod, applying "large images" option, scan area of 1×2 fields for image stitching. (c) Distal endopod segment. Objective: a = 20× dry; b = 40× oil immersion; c = 60× oil immersion. Scale bars a-b = 100 µm; c = 50 µm. See video 2 for 3D representation of the second maxilliped.

Figure 5.8: *Eriocheir sinensis*, ZI, pleon, Nikon A1-Si CLSM with Drishti processing. (a) Dorsal view, one pair of posterodorsal setae on somite 3 presented in detail (arrowed), applying "large images" option, scan area of 2×6 fields for image stitching. (b) Lateral view, image merged using Adobe Photoshop. Zeiss Ultra Plus Field Emission SEM. (c) One pair of posterodorsal setae on somite 4 presented in detail (arrowed). Objective: a = 40× oil immersion; b = 20× dry. Scale bars a = 200 µm; b = 300 µm; c = 100 µm.

Figure 5.9: *Eriocheir sinensis*, ZI, telson, Nikon A1-Si CLSM with Drishti processing. (a) Dorsal view of telson showing posterior margin with 3 pairs of stout spinulate

spines. (b) Ventral view of telson showing anal operculum. Both applying “large images” option, scan area of 2×2 fields for image stitching. Nikon A1-Si CLSM (c) Telson fork. (d) Double row of denticules on inner margin of fork. Objective: a-b = 40× oil immersion; c = 60× oil immersion. Scale bars a-b = 100 µm; c = 50 µm.

Figure 5.10: *Eriocheir sinensis*, ZII, carapace, Zeiss Ultra Plus Field Emission SEM. (a) Anterior view, anterodorsal setae arrowed. (b) Enlargement of paired anterodorsal setae and orbital margin setae. Scale bars a = 100 µm; b = 20 µm.

Figure 5.11: *Eriocheir sinensis*, ZII, carapace, Zeiss Ultra Plus Field Emission SEM. (a) Setae absent on dorsoposterior carapace margin. (b) 2 anterior plumose setae and 2 posterior setae on ventral carapace margin. Scale bars a = 100 µm; b = 10 µm.

Figure 5.12: *Eriocheir sinensis*, ZII, Nikon A1-Si CLSM with Drishti processing. (a) Antennule, image merged using Adobe Photoshop. (b) Antenna with two exopodal setae. (c) Maxillule. Objective: 40× oil immersion. Scale bars a, b = 50 µm; c = 100 µm.

Figure 5.13: *Eriocheir sinensis*, ZII, maxilla, Nikon A1-Si CLSM with Drishti processing. (a) Maxilla, image merged using Adobe Photoshop. (b) Maxilla rotated to reveal reverse angle of image a, and the setation of the coxal and basial endites. Objective: 40× oil immersion. Scale bars = 100 µm.

Figure 5.14: *Eriocheir sinensis*, ZII, first maxilliped, Nikon A1-Si CLSM with Drishti processing. (a) Whole appendage, applying “large images” option, scan area of 1×2 fields for image stitching. (b) Endopod. (c) Basis. (d) Exopod with 6 natatory setae, applying “large images” option, scan area of 1×2 fields for image stitching. Objective: a, d = 20× dry; b-c = 40× oil immersion. Scale bars a, d = 200 µm; b, c = 100 µm.

Figure 5.15: *Eriocheir sinensis*, ZII, second maxilliped, Nikon A1-Si CLSM with Drishti processing. (a) Whole appendage, 20× dry objective, applying “large images”

option, scan area of 1×2 fields for image stitching. (b) Basis. (c) Endopod. Objective: a = 20× dry; b-c = 40× oil immersion. Scale bars a = 200 µm; b-c = 100 µm.

Figure 5.16: *Eriocheir sinensis*, ZII, pleon and telson, Nikon A1-Si CLSM with Drishti processing. (a) Dorsal view of pleon, image merged using Adobe Photoshop. (b) Lateral view of pleon and telson, applying "large images" option with a scanned area of 1×2 fields for image stitching. (c) Somite 1 with a small dorsal medial seta. (d) Dorsal view of telson. Objective: a, c = 40× oil immersion; b, d = 20× dry. Scale bars = 200 µm. (a) Dorsal view of pleon and telson, applying "large images" option, scan area of 1×3 fields for image stitching. (b) Dorsal view of pleon, image merged using Adobe Photoshop. (c) Somite 1 with a small dorsal medial seta and somite 2 in detail. Zeiss Ultra Plus Field Emission SEM. (d) Somite 1 and 2. Objective: a = 20× dry; b-c = 40× oil immersion. Scale bars a = 200 µm; b-c = 100 µm; d = 20 µm.

Figure 5.17: *Eriocheir sinensis*, ZIII, carapace, Zeiss Ultra Plus Field Emission SEM. (a) Anterior view showing anterodorsal setae. (b) One pair of setae on orbital margin. Scale bars a = 20 µm; b = 10 µm.

Figure 5.18: *Eriocheir sinensis*, ZIII, carapace, Zeiss Ultra Plus Field Emission SEM. (a) Setae absent on dorsoposterior carapace margin. (b) 2 anterior plumose setae and 4 posterior setae on ventral carapace margin. Scale bars a = 100 µm; b = 30 µm.

Figure 5.19: *Eriocheir sinensis*, ZIII, Nikon A1-Si CLSM with Drishti processing. (a) Antennule. (b) Antenna. (c) Antenna rotated to reveal reverse angle of image b and developing endopod bud. (d) Maxillule, applying "large images" option, scan area of 1×2 fields for image stitching. Objective: 40× oil immersion. Scale bars = 100 µm.

Figure 5.20: *Eriocheir sinensis*, ZIII, maxilla, Nikon A1-Si CLSM with Drishti processing. (a) Whole appendage, image merged using VGStudio MAX. (b) Maxilla

rotated to reveal reverse angle of image a, and the setation of the coxal and basial endites. Objective: 40× oil immersion. Scale bars = 100 µm.

Figure 5.21: *Eriocheir sinensis*, ZIII, first maxilliped, Nikon A1-Si CLSM with Drishti processing. (a) Coxa and basis, image merged using VGStudio MAX. (b) Exopod with 8 natatory setae, applying "large images" option, scan area of 1×2 fields for image stitching. (c) Endopod, image merged using VGStudio MAX. Objective: a, c = 40× oil immersion; b = 20× dry. Scale bars a, c = 100 µm; b = 200 µm.

Figure 5.22: *Eriocheir sinensis*, ZIII, second maxilliped, Nikon A1-Si CLSM with Drishti processing. (a) Whole appendage, applying "large images" option, scan area of 1×2 fields for image stitching. (b) Endopod. (c) Basis. (d) Basis rotated to reveal reverse angle of image c. Both images merged using VGStudio MAX. Objective: a = 20× dry; b = 60× oil immersion; c-d = 40× oil immersion. Scale bars a = 200 µm; b-d = 100 µm.

Figure 5.23: *Eriocheir sinensis*, ZIII, pleon and telson, Nikon A1-Si CLSM with Drishti processing. (a) Dorsal view of pleon and telson, image merged using Adobe Photoshop. (b) Lateral view of pleon. (c) Somite 1 with a dorsal medial seta. (d) Dorsal view of telson. Objective: a, d = 20× dry; b = 10× dry; c = 40× oil immersion. Scale bars a, b, d = 200 µm; c = 100 µm.

Figure 5.24: *Eriocheir sinensis*, ZIV, dorsal carapace spine, Zeiss Ultra Plus Field Emission SEM. (a) Anterior view of carapace. (b) 3 pairs of setae on dorsal spine (arrowed). Scale bars a = 200 µm; b = 10 µm.

Figure 5.25: *Eriocheir sinensis*, ZIV, anterior carapace setation, Zeiss Ultra Plus Field Emission SEM. (a) 4 pairs of anterodorsal setae. (b) 1 pair of anterodorsal setae on orbital margin. Scale bars a = 20 µm; b = 10 µm.

Figure 5.26: *Eriocheir sinensis*, ZIV, carapace, Zeiss Ultra Plus Field Emission SEM. (a) 3 pairs of setae on dorsoposterior carapace margin. (b) 4 anterior plumose setae and 7−8 posterior setae on ventral carapace margin. Scale bars = 20 µm.

Figure 5.27: *Eriocheir sinensis*, ZIV, Nikon A1-Si CLSM with Drishti processing. ((a) Antennule. (b) Antenna with a more developed endopod and two exopodal setae arrowed. Both applying "large images" option with a scanned area of 2×3 fields for image stitching. Objective: 40× oil immersion. Scale bars a = 100 µm; b = 200 µm.

Figure 5.28: *Eriocheir sinensis*, ZIV, Nikon A1-Si CLSM with Drishti processing. (a) Mandibles. (b) Maxillule, image merged using Adobe Photoshop. (c) Maxillule rotated to reveal reverse angle of image b, and the setation of the coxal and basial endites. Objective: 40× oil immersion. Scale bars = 200 µm.

Figure 5.29: *Eriocheir sinensis*, ZIV, maxilla, Nikon A1-Si CLSM with Drishti processing. (a) Whole appendage, applying "large images" option, scan area of 2×3 fields for image stitching. (b) Maxilla rotated to show reverse angle of image a, and the setation of the coxal and basial endites. Objective: 40× oil immersion. Scale bars = 200 µm. See video 3 for 3D representation of the maxilla.

Figure 5.30: *Eriocheir sinensis*, ZIV, first maxilliped, Nikon A1-Si CLSM with Drishti processing. (a) Whole appendage, applying "large images" option, scan area of 2×2 fields for image stitching. (b) Endopod with 2,2,2,6 setae. (c) Endopod with 2,3,2,2,6 setae. (d) Exopod with 10 natatory setae. Objective: 20× dry. Scale bars a, d = 500 µm; b, c = 200 µm.

Figure 5.31: *Eriocheir sinensis*, ZIV, second maxilliped, Nikon A1-Si CLSM with Drishti processing. (a) Basis and endopod, applying "large images" option, scan area of 1×2 fields for image stitching. (b) Endopod. (c) Exopod with 10 natatory setae, applying

“large images” option, scan area of 1×2 fields for image stitching. Objective: 20× dry. Scale bars a, c = 500 µm; b = 100 µm.

Figure 5.32: *Eriocheir sinensis*, ZIV, Nikon A1-Si CLSM with Drishti processing. (a) Third maxilliped. (b) Pereiopods. Objective: 40× oil immersion. Scale bars = 100 µm.

Figure 5.33: *Eriocheir sinensis*, ZIV, pleon and telson, Nikon A1-Si CLSM with Drishti processing. (a) Lateral view of pleon and telson, image merged using Adobe Photoshop. (b) Somite 1 with 5 medial setae. (c) Ventral margin of telson with 1 additional pair of unequal setae. Objective: 20× dry. Scale bars = 500 µm.

Figure 5.34: *Eriocheir sinensis*, ZV, dorsal carapace spine, FEI Quanta FEG SEM. (a) Anterior view. (b) 3 pairs of setae on dorsal spine (arrowed). Scale bars a = 500 µm; b = 50 µm.

Figure 5.35: *Eriocheir sinensis*, ZV, anterodorsal carapace setae, FEI Quanta FEG SEM. 7 pairs of anterodorsal setae (arrowed). Scale bar = 200 µm.

Figure 5.36: *Eriocheir sinensis*, ZV, carapace, FEI Quanta FEG SEM. (a) 6−7 anterior plumose setae (arrowed) and 10 posterior setae on ventral carapace margin. (b) Inner side of ventral carapace margin. (c) Dorsoposterior carapace margin. Scale bars a = 200 µm; b-c = 100 µm.

Figure 5.37: *Eriocheir sinensis*, ZV, Nikon A1-Si CLSM with Drishti processing. (a) Antennule with developing accessory flagellum. (b) Antennule, primary flagellum showing two rows of subterminal aesthetascs. (c) Antenna with developing endopod. All applying “large images” option, scan area of 2×3 fields for image stitching. Objective: 40× oil immersion. Scale bars a, c = 200 µm; b = 100 µm. See video 4 for 3D representation of the antennule primary flagellum.

Figure 5.38: *Eriocheir sinensis*, ZV, Nikon A1-Si CLSM with Drishti processing. (a) Mandible. (b) Maxillule, applying "large images" option, scan area of 2×3 fields for image stitching. (c) Coxal endite of (b). (d) Basial endite of (b). Objective: 40× oil immersion. Scale bars = 200 µm.

Figure 5.39: *Eriocheir sinensis*, ZV, maxilla, Nikon A1-Si CLSM with Drishti processing. (a) Whole appendage, applying "large images" option, scan area of 3×3 fields for image stitching. (b) Coxal endite. (c) Basial endite. Objective: 40× oil immersion. Scale bars a = 200 µm; b-c = 100 µm.

Figure 5.40: *Eriocheir sinensis*, ZV, first maxilliped, Nikon A1-Si CLSM with Drishti processing. (a) Coxa with 3 setae and basis with 10 setae. (b) Coxa with 3 setae and 1 smaller seta, basis with 12 setae. (c) Endopod with 1,3,2,2,6 setae. (d) Endopod with 2,3,2,2,6 setae. (e) Exopod with 12 natatory setae. (f) Exopod with 13 natatory setae. All applying "large images" option, scan area of 1×2 fields for image stitching. Objective: 20× dry. Scale bars = 500 µm.

Figure 5.41: *Eriocheir sinensis*, ZV, second maxilliped, Nikon A1-Si CLSM with Drishti processing. (a) Basis and endopod, applying "large images" option, scan area of 1×2 fields for image stitching (reverse angle of endopod arrowed). (b) Endopod with 0+1+7 setae. (c) Exopod with 12 natatory setae. (d) Exopod with 13 natatory setae. Objective: 20× dry. Scale bars a, c, d = 500 µm; b = 200 µm.

Figure 5.42: *Eriocheir sinensis*, ZV, Nikon A1-Si CLSM with Drishti processing. (a) Third maxilliped, applying "large images" option, scan area of 1×2 fields for image stitching. (b) Pereiopods. (c) Fifth pleopod with endopod and uropod without endopod. Applying "large images" option, scan area of 2×2 fields for image stitching. Objective: 20× dry. Scale bars a = 100 µm; b, c = 500 µm.

Figure 5.43: *Eriocheir sinensis*, ZV, pleon and telson, Nikon A1-Si CLSM with Drishti processing. (a) Lateral view of pleon and telson, applying "large images" option, scan area of 3×3 fields for image stitching. (b) Somite 1 with 9 medial setae. Zeiss Ultra Plus Field Emission SEM. (c) Somite 1 with 8 medial setae. (d) Ventral margin of telson with 5 pairs of setae. Objective: a = 10× dry; b = 20× dry. Scale bars a = 500 µm; b = 200 µm; c = 20 µm; d = 100 µm.

Figure 5.44: *Eriocheir sinensis*, ZVI, dorsal carapace spine, FEI Quanta FEG SEM. (a) Anterior view. (b) 4 pairs of setae on dorsal spine (arrowed). Scale bars a = 500 µm; b = 50 µm.

Figure 5.45: *Eriocheir sinensis*, ZV, anterior view of carapace, FEI Quanta FEG SEM. 9 pairs of anterodorsal setae circled and arrowed. Scale bar = 500 µm.

Figure 5.46: *Eriocheir sinensis*, ZVI, carapace, FEI Quanta FEG SEM. (a) 4−5 pairs of setae on dorsoposterior carapace margin. (b) 6−7 anterior plumose setae (arrowed) and 10 posterior setae on ventral carapace margin. Scale bars = 20 µm.

Figure 5.47: *Eriocheir sinensis*, ZVI, antennule, Nikon A1-Si CLSM with Drishti processing. (a) Whole appendage showing small proximal seta, applying "large images" option, scan area of 1×2 fields for image stitching. (b) Antennule rotated to show reverse angle of image a, and the developing accessory bud, image merged using Adobe Photoshop. Objective: a = 20× dry; b = 40× oil immersion. Scale bars = 200 µm. See video 5 for 3D representation of the antennule primary flagellum.

Figure 5.48: *Eriocheir sinensis*, ZVI, antenna, Nikon A1-Si CLSM with Drishti processing. (a) Whole appendage with 2 segmented endopod distal protuberances almost equal to length of protopod, applying "large images" option, scan area of 1×2 fields for image stitching. (b) Whole appendage with endopod slightly shorter than

length of protopod, image merged using Adobe Photoshop. Objective: a = 20× dry; b = 40× oil immersion. Scale bars = 200 µm.

Figure 5.49: *Eriocheir sinensis*, ZVI, Nikon A1-Si CLSM with Drishti processing. a) Mandible. (b) Maxillule, applying "large images" option, scan area of 2×3 fields for image stitching. (c) Maxillule rotated to show from reverse angle of image b, and the setation of the coxal and basial endites. Objective: 40× oil immersion. Scale bars a = 200 µm; b, c = 500 µm. See video 6 for 3D representation of the maxillule.

Figure 5.50: *Eriocheir sinensis*, ZVI, maxilla, Nikon A1-Si CLSM with Drishti processing. (a) Whole appendage, applying "large images" option, scan area of 3×3 fields for image stitching, 1 seta on exopod circled and arrowed. (b) Maxilla rotated to show from reverse angle of image a, and the setation of the coxal and basial endites. Objective: 40× oil immersion. Scale bars = 200 µm. See video 7 for 3D representation of the maxilla.

Figure 5.51: *Eriocheir sinensis*, ZVI, first maxilliped, Nikon A1-Si CLSM with Drishti processing. (a) Coxa with 4 +1 setae and basis with 12 setae (b) Endopod. (c) Exopod with 14 natatory setae. All applying "large images" option, scan area of 1×2 fields for image stitching. Objective: 20× dry. Scale bars = 500 µm.

Figure 5.52: *Eriocheir sinensis*, ZVI, second maxilliped, Nikon A1-Si CLSM with Drishti processing. (a) Coxa, basis and endopod, applying "large images" option, scan area of 1×2 fields for image stitching. (b) Endopod with 0+1+7 setae. (c) Exopod with 13 natatory setae. Objective: 20× dry. Scale bars a, c = 500 µm; b = 100 µm.

Figure 5.53: *Eriocheir sinensis*, ZVI, Nikon A1-Si CLSM with Drishti processing. (a) Maxilliped three, applying "large images" option, scan area of 1×2 fields for image stitching. (b) Pereiopods. (c) Uropod. Applying "large images" option, scan area of 2×2 fields for image stitching. Objective: 20× dry. Scale bars a = 200 µm; b, c = 500 µm.

Figure 5.54: *Eriocheir sinensis*, ZVI, pleon and telson, FEI Quanta FEG SEM. (a) Lateral view of pleon and telson. (b) Somite 1 with 10 medial setae. Scale bars a = 100 µm; b = 20 µm.

Figure 5.55: An example measurement of dorsal, lateral and rostral spines using a ZI stage of *Cancer magister* (adapted from Shirley *et al.*, 1987).

Figure 5.56: Confocal images of *Eriocheir sinensis* zoeal stages. (a) ZI, 10× dry objective. (b) ZII, 10× dry objective applying 'large images' option, scan area of 2×1 fields for image stitching. (c) ZIII, 10× dry objective applying 'large images' option, scan area of 2×2 fields for image stitching. (d) ZIV, 10×dry objective applying 'large images' option, scan area of 3×2 fields for image stitching. (e) ZV, 10×dry objective applying 'large images' option, scan area of 4×3 fields for image stitching. (f) ZVI, 10× dry objective applying 'large images' option, scan area of 4×4 fields for image stitching. Scale bars = 500 µm. CLSM, confocal laser scanning microscopy.

Figure 5.57: *Eriocheir sinensis*, maxillule, setae appearing after moult are coloured. Scale bars zoea I = 50 µm; zoea II = 100 µm.

Figure 5.58: *Eriocheir sinensis*, maxillule, setae appearing after moult are coloured. Scale bars zoea III = 100 µm; zoea IV = 200 µm.

Figure 5.59: *Eriocheir sinensis*, maxillule, setae appearing after moult are coloured. Scale bars = 200 µm.

Figure 5.60: *Eriocheir sinensis*, maxilla, setae appearing after moult are coloured. Scale bars zoea I = 50 µm; zoea II = 100 µm.

Figure 5.61: *Eriocheir sinensis*, maxilla, setae appearing after moult are coloured. Scale bars zoea III = 100 µm; zoea IV = 200 µm.

Figure 5.62: *Eriocheir sinensis*, maxilla, setae appearing after moult are coloured. Scale bars = 100 μm.

Figure 6.1: An illustration of thoracic sternum of male and female crabs showing the relationship between the pleon and the first (G1) and second (G2) gonopods of adult male crabs (after Ng, 1998; Tavares, 2002).

Figure 6.2: Examples of detailed drawings of male G1. (a) Dorsal view of *Ashtoret maculata* Miers, 1877. (b) Ventral view of *A. maculata*. NHM reg. number 1847.21. (c) Dorsal view of *Ashtoret miersii* Henderson, 1887. (d) Ventral view of *A. miersii*. NHM reg. number 1892.7.15.347−356. Scale bar = 1 mm (after Galil & Clark, 1994).

Figure 6.3: The line drawings of adult male gonopods of *Eriocheir* species. (a) First male gonopods of three mitten crab species (Guo *et al.*, 1997). (b) The image of the distal tip, with setae removed, of the first gonopod of *E. hepuensis* from Kuwait photographed by Michael Apel under a light microscope (after Naser *et al.*, 2012) and all viewed in dorsal aspect.

Figure 6.4: The line drawings of the distal tip of adult male gonopods (G1) of *Eriocheir* species from Sakai (2013). (a) Mesial* view of *Paraeriocheir sinensis*. (b) Lateral view of *P. sinensis*. (c) Mesial* view of *P. hepuensis*. (d) Lateral view of *P. hepuensis*. (e) Mesial* view of *E. japonica* from Hokkaido, Japan. (f) Mesial* view of *E. japonica* from Taipei, Taiwan. (after Sakai, 2013). *The term "mesial" used by Sakai (2013) refers "distal dorsal view" in the present study.

Figure 6.5: CLSM images of three species of *Eriocheir*. Distal dorsal view of: (a) *E. sinensis* from the Thames. (b) *E. hepuensis* from Shatt Al-Basrah Canal, Iraq. (c) *E. japonica* Tsushima, Japan. Images were scanned using 10× dry objective applying 'large images' option, scan area of 4×4 (a) and 4×5 (b, c) fields for image stitching. See Chapter 2 for details. Scale bars = 1000 μm.

Figure 6.6: Drishti images of three species of *Eriocheir*. Distal dorsal view of: *E. sinensis* from the Thames. (b) *E. hepuensis* from Shatt Al-Basrah Canal, Iraq. (c) *E. japonica* Tsushima, Japan. Scale bars = 1000 μm.

Figure 6.7: Micro-CT image of *E. sinensis*. Image rotated 90° degrees from a to d respectively. (a) Distal dorsal view. (b) Lateral view of left side. (c) Distal ventral view. (d) Lateral view of right side. Scale bars = 1000 μm. See video 8 for detailed view.

Figure 6.8: Micro-CT image of *E. hepuensis*. Image rotated 90° degrees from a to d respectively. (a) Distal dorsal view. (b) Lateral view of left side. c) Distal ventral view. (d) Lateral view of right side. Scale bars = 500 μm. See video 9 for detailed view.

Figure 6.9: Micro-CT image of *E. japonica*. Image rotated 90° degrees from a to d respectively. (a) Distal dorsal view. (b) Lateral view of left side. (c) Distal ventral view. (d) Lateral view of right side. Scale bars = 500 μm. See video 10 for detailed view.

Figure 6.10: The micro-CT image of the male genital pore and tube of *Eriocheir* species from different angles. (a) *E. sinensis*. (b) *E. hepuensis*. (c) *E. japonica*. Scale bars = 500 μm.

Figure 6.11: Molecular analysis using COI gene only showing evolutionary relationships of European *Eriocheir* taxa. The arrows show the haplotypes of Thames and Dutch *E. sinensis* populations with > 70% support (after Palero *et al.*, 2016).

Figure 6.12: CLSM images of three species of *Eriocheir*. Distal dorsal view of: (a) *E. sinensis* from the Thames. (b) Unknown species from Den Oever. (c) Unknown species from Hollands Diep. Images were scanned using 10× dry objective applying 'large images' option, scan area of 4×4 (a) and 5×5 (b, c) fields for image stitching. Scale bars = 1000 μm.

Figure 6.13: Micro-CT image of unknown *Eriocheir* from Den Oever, Holland. Image rotated 90° degrees from a to d respectively. (a) Distal dorsal view. (b) Lateral view of left side. c) Distal ventral view. (d) Lateral view of right side. Scale bars= 500 μm. See video 11 for detailed view.

Figure 6.14: Micro-CT image of unknown *Eriocheir* from Hollands Diep, Holland. Image rotated 90° degrees from a to d respectively. (a) Distal dorsal view. (b) Lateral view of left side. (c) Distal ventral view. (d) Lateral view of right side. Scale bars= 500 μm. See video 12 for detailed view.

Figure 6.15: The micro-CT image of the genital pore and tube of *Eriocheir* species from different angles. (a) *E. sinensis* from the Thames. (b) Unknown *Eriocheir* from Den Oever, Holland. (c) Unknown *Eriocheir* from Hollands Diep, Holland. Scale bars = 500 μm.

Figure 6.16: Confocal images of the gonopods of European pea crabs. (a) G1 of *Nepinnotheres pinnotheres* Linnaeus, 1758. (b) G1 of *Pinnotheres pisum* Linnaeus, 1767. (c) G1 of *Pinnotheres pectunculi* Hesse, 1872. (d) and (e) G2 of *P. pisum*. Scale bars a-c = 300; d-e = 100 μm (after Becker *et al.*, 2012).

Figure 6.17: The line drawings of the G1 of *Libystes nitidus* A. Milne Edwards, 1867 from different studies and localities. (a) Sample from the Maldives described by Crosnier (1962). (b) Sample from male 5×3 mm by Serène (1966). (c) Sample from male 7×4 mm by Serène (1966). (d) Sample from male 11.5×7 mm by Serène (1966). *L.* aff. *nitidus* (e) Sample from the Arabian Gulf described by Apel & Spiridonov (1998). (Images after Crosnier, 1962; Serène, 1966; Apel & Spiridonov, 1998).

Figure 6.18: Drishti images of G1 of *Libystes nitidus* from different localities. Sudanese Red Sea (a) Whole G1. (b) The tip of the G1 in high resolution. Maldives. (c) Whole G1

(d) The tip of the G1 in high resolution. Scale bars a = 1000 μm; b-c = 500 μm; d = 100 μm.

Figure 6.19: Drishti images of *Libystes nitidus* G2 from different localities. Sudanese Red Sea. (a) Whole G2. (b) The tip of G2 in high resolution. Maldives. (c) Whole G1. (d) The tip of G2 in high resolution. Scale bars a, c = 500 μm; b, d = 100 μm.

Figure 6.20: Drawings of *Monomia argentata* as *Portunus argentatus* by Dai & Yang (1991).

Figure 6.21: Micro-Ct images of *Monomia argentata* A Milne-Edwards, 1861 (NHM reg. number: 1847.21). (a) Dorsal view of whole specimen. (b) Ventral view of the first male gonopods. Scale bars a = 5000 μm; b = 2000 μm. See video 13 for 3D animation of whole specimen.

Figure 7.1: Illustrations of ZI stage first maxilliped exopods. (a) Confocal image of muscle bands (arrowed) of *Eriocheir sinensis*; the specimen prepared as undigested and stained with Congo red and acid fuschin. Scale bar = 50 μm. (b) Bi-segmented exopod (arrowed) of *Hyas coarctatus* Leach, 1816 by Christiansen (1973, Fig. 10b). (c) Bi-segmented exopod (arrowed) of *Hyas coarctatus alutaceus* Brandt, 1851 (now Hyas alutaceus J.F. Brandt in Middendorf, 1851) by Pohle (1991, Fig. 3k). (d) Unsegmented exopod of *Clypeasterophilus stebbingi* (Rathbun, 1918) by Marques & Pohle (1996, Fig. 1j).

Figure App. 8.1: Diagrammatic illustration of designed apparatus to sharpen tungsten wire needles electrolytically. Two side of output terminal of the flexible wires were plugged to transformer (12 V power supply) with the connection in parallel. One tip of the wire was attached to brass block and the other tip was plugged to cooper needle and inserted in the brass block using the small hole on the surface (Clark, 2007).

Figure App. 8.2: Application of sharpening tungsten wire needles electrolytically with a 10 V power source.

Figure App. 8.3: Preparation of tungsten wire needles. (a) The length of the aluminium metal holder according the type of the needles; (b) Type of the needles used; (b1) very fine needle to dissect zoeal appendages dissection; (b2) fine needle to hold the larvae/main body during the dissection; (b3) the needle with hook was used to transfer zoeal appendages or whole specimens after dissection, staining, cleaning etc.; (b4) Thick needle to move the cover slip slightly and arrange in the correct position.

Figure App. 8.4: Graphical User Interface (GUI) showing the settings applied in the present study.

Figure App. 8.5: General settings applied in the present study. (a) Adjusting channel settings with a focus on "HV" and "offset". (b) A1 scan area window to zoom, and rotate. (c) Applying Z- intensity correction function (d) "Order of the experiment" for the "large images" option of confocal microscopy software.

Figure App. 8.6: Viewing the confocal data using confocal software, in this case Nikon software, NIS- Elements (version 4.20) was used. (a) Dragging and dropping the confocal data into the software. (b) An alternative way to open the confocal data by going to File>open> your nd2 file.

Figure App. 8.7: Exporting ***.nd2 files as TIFF images using confocal software. (a) Create a new folder for the exported TIFF images. (b) Go to File>Export ND document and click.

Figure App. 8.8: Options of exporting the confocal data as TIFF images. (a) Select the option of "Mono image of each channel". (b) Select "Scale 12 bit to 16 bit". (c) Click "Browse" to locate images (in our example, it is 4 channels). (d) Click "Export".

Figure App. 8.9: Example of using single channel to import. (a) Creating folder for single channels, in the example "Orange channel" was used. (b) Representation of orange channel's TIFF images.

Figure App. 8.10: Viewing image properties. (a) Right click on image using NIS Element viewer. (b) Click "Image Fields" to view x and y calibrations. (c) Click "Experiment Data" to view z-step value.

Figure App. 8.11: The menu bar for ImageJ.

Figure App. 8.12: Opening stack data in ImageJ, e.g. Nikon_MaxillipedII_basis_ZII.nd2 has been selected.

Figure App. 8.13: Import options for stack data.

Figure App. 8.14: Record image properties (voxel size) for later use, e.g. x = 0.31, y = 0.31 and z = 0.7 microns.

Figure App. 8.15: Click on ► to check image quality for each channel.

Figure App. 8.16: Merging selected channels in ImageJ.

Figure App. 8.17 Selecting channels to be merged.

Figure App. 8.18: Image J instructions for exporting confocal data. (a) Go to Image> Color> Channels Tool…. (b) Convert to RGB.

Figure App. 8.19: Image J instructions for exporting confocal data. (a) Click OK for the following processes. (b) Changing image from RGB color to 8-bit in ImageJ.

Figure App. 8.20: Following ImageJ instructions. (a) Save merged channel image stacks as image sequence. (b) Save merged channel image stacks to TIFF format; click OK.

Figure App. 8.21: Save merged image stacks to new folder, e.g. ImageJ_Nikon_Maxilliped II_basis.

Figure App. 8.22: Shortcut icon for “drishtiimport”.

Figure App. 8.23: Importing processed data into Drishtiimport. (a) Importing single channel data processed using confocal data. (b) Importing multi-channel processed using ImageJ.

Figure App. 8.24: Following instructions for importing the data to Drishti.

Figure App. 8.25: Save to ***.pvl.nc file which are referred to as volumes in Drishti.

Figure App. 8.26: Following save, a series of 5 windows will open; for each click OK.

Figure App. 8.27: Entering “image properties” (voxel size); x, y and z values.

Figure App. 8.28: Saving the data for the use of Drishti.

Figure App. 8.29: Shortcut icon for “Drishti”.

Figure App. 8.30: Loading ***.pvl.nc file, e.g. “MaxillipedII_basis_Drishti_import.pvl.nc” into Drishti.

Figure App. 8.31: Viewing 3D representation of the volumes and cropping the initial scanned volume.

Figure App. 8.32: Getting high resolution images and some useful tools for Drishti.

Figure App. 8.33: Adding a scale bar in Drishti.

Figure App. 8.34: Saving the image and selecting image size.

Figure App. 8.35: Naming image and saving in ***.jpg format.

Figure App. 8.36: Taking a snapshot by selecting Mono Image and saving image.

Figure App. 8.37: Segmentation: selecting mop update off for 3D data using Drishti.

Figure App. 8.38: Rotating and removal of unwanted fragments in 3D images using Drishti.

Figure App. 8.39: Adjusting opacity and colour of the image by manipulating interface.

LIST OF TABLES

Table 4.1. List of reviewed papers that used CLSM in the study of macro-invertebrates with information on studied material, stain, mounting medium, confocal microscope, visualisation and performance observed.

Table 4.2: Combination of methods applied to determine the optimum visualisation technique using CLSM to examine dissected zoeal stages of brachyuran crabs.

Table 5.1: A comparison between the zoea I stage of *Eriocheir sinensis* described by Schnakenbeck (1926) and the present study.

Table 5.2: A comparison between the zoea I stage of *Eriocheir sinensis* described by Schnakenbeck (1933) and the present study.

Table 5.3: A comparison between the zoea V stage of *Eriocheir sinensis* described by Hinrichs & Grell (1937) and the present study.

Table 5.4: A comparison between the zoea I stage of *Eriocheir sinensis* described by Panning (1939) and the present study.

Table 5.5: A comparison between the zoea II stage of *Eriocheir sinensis* described by Panning (1939) and the present study.

Table 5.6: A comparison between the zoea III stage of *Eriocheir sinensis* described by Panning (1939) and the present study.

Table 5.7: A comparison between the zoea IV stage of *Eriocheir sinensis* described by Panning (1939) and the present study.

Table 5.8: A comparison between the zoea I stage of *Eriocheir sinensis* described by Liang *et al*. (1974) and the present study.

Table 5.9: A comparison between the zoea II stage of *Eriocheir sinensis* described by Liang *et al*. (1974) and the present study.

Table 5.10: A comparison between the zoea III stage of *Eriocheir sinensis* described by Liang *et al*. (1974) and the present study.

Table 5.11: A comparison between the zoea IV stage of *Eriocheir sinensis* described by Liang *et al*. (1974) and the present study.

Table 5.12: A comparison between the zoea V stage of *Eriocheir sinensis* described by Liang *et al*. (1974) and the present study.

Table 5.13: A comparison between the zoea I stage of *Eriocheir sinensis* described by Ingle (1991) and the present study.

Table 5.14: A comparison between the zoea II stage of *Eriocheir sinensis* described by Ingle (1991) and the present study.

Table 5.15: A comparison between the zoea III stage of *Eriocheir sinensis* described by Ingle (1991) and the present study.

Table 5.16: A comparison between the zoea IV stage of *Eriocheir sinensis* described by Ingle (1991) and the present study.

Table 5.17: A comparison between the zoea V stage of *Eriocheir sinensis* described by Ingle (1991) and the present study.

Table 5.18: A comparison between the zoea I stage of *Eriocheir sinensis* described by Kim & Hwang (1995) and the present study.

Table 5.19: A comparison between the zoea II stage of *Eriocheir sinensis* described by Kim & Hwang (1995) and the present study.

Table 5.20: A comparison between the zoea III stage of *Eriocheir sinensis* described by Kim & Hwang (1995) and the present study.

CHAPTER 1

INTRODUCTION

The present thesis is primarily concerned with developing imaging techniques for brachyuran crab zoeae, with an emphasis on the invasive Chinese mitten crab, *Eriocheir sinensis* H. Milne Edwards, 1853. It also investigates the adult morphology of the gonopods of various brachyuran crab species using Confocal Laser Scanning Microscopy (CLSM) and Micro-Computed Tomography (micro-CT). In the present study, imaging techniques were used to examine zoeal appendages in detail by providing a workflow of imaging techniques using CLSM, Scanning Electron Microscopy (SEM) and micro-CT scans. These were compared in terms of their suitability for specimens/material of different sizes. A summary description of the Chinese mitten crab, their zoeal development and the need for developing imaging techniques to investigate them is provided in the introductory chapter. Information about the fecundity of adult females, the development of imaging techniques to examine the zoeal development of brachyuran species, the re-description of Chinese mitten crab zoeal development, visualisation of adult gonopod morphology and the comparison of different techniques are provided in detail in the subsequent chapters.

1.1 General introduction

The Chinese mitten crab, *Eriocheir sinensis*, is officially listed as one of the world's 100 worst invasive species (Lowe *et al*., 2000). The spread of many aquatic invasive species has intensified (Carlton, 2003) with the global increase of transoceanic shipping (Dittel & Epifanio, 2009). These introductions mainly involve the transportation of adults or their larvae via the ballast water of ships (Carlton, 1996; Herborg *et al*., 2003) or hull fouling (Yeo *et al.*, 2010; Cuesta *et al*., 2016). Another major factor resulting in

the spread of invasive species is deliberate/intentional release (Herborg *et al*., 2005). Cohen & Carlton (1997) considered ten theoretical reasons for the dispersal of brachyuran species outside their native range; two of these are natural, whereas eight are based on human activities (Table 1.1). However, active transport of the mitten crabs as a food source and the spread of the species via ballast water were reported as two main reasons for the dispersal of mitten crabs outside their normal distribution.

Table 1.1: Theoretical reasons of the dispersal of brachyuran species (adapted from Cohen & Carlton, 1997).

Natural reasons	**Dispersal of larvae by currents** **Dispersal of adults or juveniles on floating material**
Human activities	Transport of adults or juveniles in ship fouling Transport of adults or juveniles in cargo Transport of adults or juveniles on semisubmersible drilling platforms and other long distance, slow-moving vessels ***Transport of larvae or juveniles in ballast water**** Transport of adults or juveniles in fisheries product Transport of larvae in water with shipment of live fish Escape or release from research, public, or private aquaria ***Intentional planting to establish a food resource****

*Items in italics and bold identify the most likely pathways for the Chinese mitten crab.

The Chinese mitten crab is one of the species which has been introduced into both marine and fresh water systems, largely because *E. sinensis* is genuinely euryhaline and capable of highly effective osmoregulation (e.g. Cieluch *et al.*, 2007). This is closely associated with the catadromous life history (Veldhuzien, 2001; Dittel & Epifanio, 2009; Bentley, 2011; Low *et al*., 2013). In addition, it is considered to be one of the first recorded crab species which was transported via ballast water (Carlton, 1985).

1.2 Taxonomy and phylogeny

Brachyuran crabs belong to the Decapoda, crustaceans processing 10 thoracic appendages. Brachyuran crabs are called “true crabs” as they have four pairs of well-

developed legs compared to the false crabs (Anomura) which have three visible pairs of walking legs and a much smaller fourth pair (Ng, 1998). *Eriocheir* De Haan, 1835 is assigned to the Grapsoidea, family Varunidae, subfamily Varuninae (Ng *et al*., 2008). The grapsoid crabs are adapted to semi-terrestrial, marine and freshwater environments worldwide (Dittel & Epifanio, 2009).

Eriocheir comprises four species (Tang *et al*., 2003): *E. japonica* (De Haan, 1835), *E. sinensis* H. Milne Edwards, 1853, *E. hepuensis* Dai, 1991, and *E. ogasawaraensis* Komai, Yamasaki, Kobayashi, Yamamoto and Watanabe, 2006 (Ng *et al.*, 2008). However, there has been controversy regarding the systematics of mitten crabs in general (Dai, 1991; Li *et al*., 1993; Chan *et al*., 1995; Guo *et al*., 1997; Du, 1998; Ng *et al*., 1999; Li and Zou, 1999; Tang *et al*., 2003). Five species were assigned to three genera i.e. *Eriocheir* (*E. hepuensis*, *E. sinensis*, and *E. japonica*), *Neoeriocheir* Sakai, 1983 and *Platyeriocheir* N.K. Ng, Guo & Ng, 1999 by Ng *et al*. (1999); whereas five species were included in one genus, *Eriocheir*, by Chu *et al.* (2003). They stated that *E. hepuensis* and *E. japonica* are genetically and morphologically close to *E. sinensis*. Tang *et al*. (2003) remarked that three species (*E. hepuensis*, *E. sinensis*, and *E. japonica*) are "conspecific". They suggested that these three species should be subspecies of *E. japonica* and referred as *E. j. hepuensis*, *E. j. sinensis*, and *E. j. japonica*, while two species (*E. formosa* and *E. leptognathus*) are morphologically more distant. These conflicts in mitten crab systematics require further investigation both genetically and morphologically to clarify the status of *E. sinensis* (Veilleux & de Lafontaine, 2007).

In general, mitten crabs are considered to be restricted to East Asian waters. *Eriocheir japonica* is widely distributed in the Far East and is dominant in Southern China, and especially Japan (Chan *et al*., 1995). *Eriocheir sinensis* is more restricted in distribution, being recorded from North Korea southwards to the coastal waters of Central China.

While these two species have similar characteristics (Kobayashi, 2003), *E. japonica* has only been found once outside is natural range and was recorded in the Columbia River approximately 3 km west of Astoria Megler Bridge, Astoria, Oregon, USA in 1997 (see Jensen & Armstrong, 2004). In contrast, *E. sinensis* first invaded Europe in the early 1900s and North America (Cohen & Carlton, 1997) and was first recorded in the Detroit River in 1965 and subsequently in Lake Erie in 1973 (Nepszy & Leach, 1973).

1.3 Classification

Chinese mitten crab classification was suggested by many workers (Martin & Davis, 2001; Clark, 2006; Ng *et al*., 2008) and stated that *Eriocheir* belongs to the Varunidae instead of Grapsidae. As a result, it was classified by the Integrated Taxonomic Information System (2007) as shown in Table 1.2.

Table 1.2: Classification of the Chinese mitten crab (WoRMS, 2017).

Kingdom	Animalia
Phylum	Arthropoda
Subphylum	Crustacea
Superclass	Multicrustacea
Class	Malacostraca
Order	Decapoda
Superfamily	Grapsoidea
Family	Varunidae
Genus	*Eriocheir* (De Haan, 1835)
Species	*Eriocheir sinensis* (H. Milne Edwards, 1853)
Common (vernacular) names	Chinese mitten crab Chinese freshwater edible crab Shanghai hairy crab Chinese river crab Moon crab The hand warmer

1.4 General identification of adult Chinese mitten crab

The adult Chinese mitten crab has dense brown setae known as “mittens” on its claws which covers the white- tipped chelae (Veldhuzien, 2001; Fig. 1.1). Although female crabs have also mittens on the claws, Robbins *et al*. (2003) and Veldhuzien (2001) provided data to support the hypothesis that the dense of setae is an indication of male dominance. Another distinctive feature is that there are four spines on the antero-lateral margin of the carapace and four broad spines on the frontal margin between the eyes. Large adult crabs, especially males, can exceed a carapace width of 8 cm (Robbins *et al*., 2006; www.mittencrabs.org.uk) and pereiopod length is typically almost twice the carapace width (Santos, 2014). The species is dimorphic with the sexes being easily separated (Solovyeva & Bailey, 2017). Males have a narrow V-shaped pleon (Fig. 1.1a), whereas females have a broad U-shaped pleon (Fig. 1.1b; Rudnick *et al*., 2000; Gollasch & Nehring, 2006; Škraba *et al*., 2013).

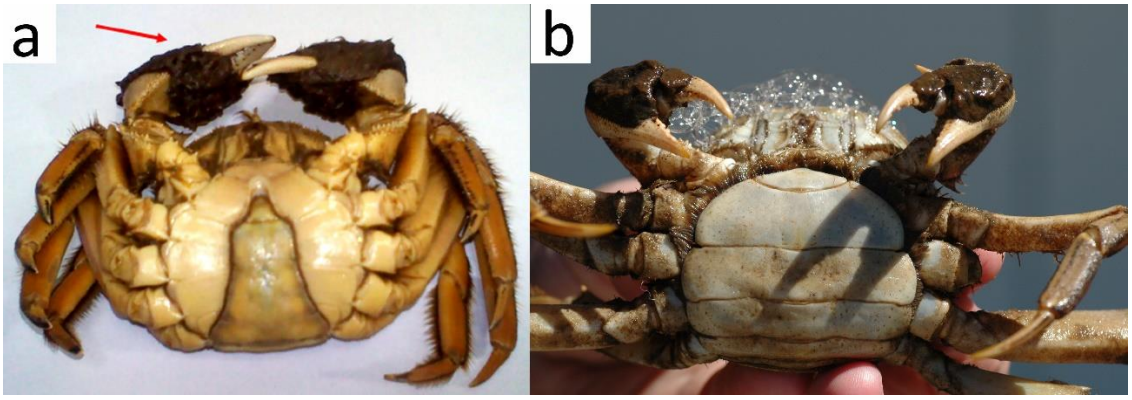

Figure 1.1: Adult Chinese mitten crab. (a) Male crab, arrowed areas show the dense setae on the claws (b) Female crab, the setae on the female claws are not as distinct as male claws. Photo credits: Christian Fischer (http://mittencrab.nisbase.org/page/ident) and Škraba *et al*. (2013) respectively.

1.5 Distribution

The Chinese mitten crab, *Eriocheir sinensis*, is native to the Far East (Hymanson *et al*., 1999; Wang *et al*., 2008; Naser *et al*., 2012; Fig. 1.2), however, they have invaded many countries (Herborg *et al*., 2007; Fig. 1.2). The species was first introduced into northern Germany in 1912 and they spread rapidly throughout NW Europe (Dittel & Epifanio, 2009; Gollasch, 2011). The species has also been reported along the North and Baltic Sea coastlines, southern France, the Spanish and Portuguese Atlantic coast (Cuesta *et al*., 2004), the Estonian and Lithuanian Baltic coastlines, North America (Rudnick *et al*. 2003), and Russia. Other recent reports include different areas in western Asia in Northern Iran (Robbins *et al*., 2006). But two previous reports of *Eriocheir sinensis* from the Shatt Al Basrah Canal (Clark *et al*., 2006) and Shatt Al-Arab River in Iraq (Hashim, 2010) were re-identified as *E. hepuensis* in the study of Naser *et al*. (2012).

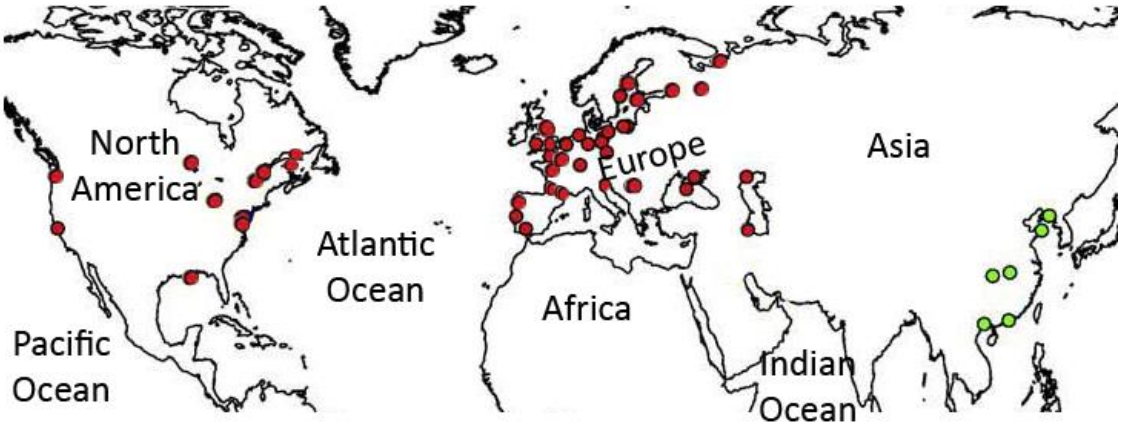

Figure 1.2: The worldwide distribution of the Chinese mitten crab, *Eriocheir sinensis*. Green dots show native range; red dots show non- native range (adapted and updated from Dittel & Epifanio, 2009).

The invasive Chinese mitten crab is also well established in the River Thames and tributaries (Clark *et al*., 1998a) and is still spreading throughout mainland Britain (www.mittencrabs.org.uk; Fig. 1.3). It was first recorded in the River Thames in 1935

and it is believed that they reached the region via ship ballast water (Panning, 1938). Although the River Thames population had remained low until the 1970s, recent evidence suggests that mitten crab numbers increased and continued to do so dramatically in the mid-1980s and 1990s (Clark *et al*., 1998a). Their ability to disperse extensively means that many UK water bodies are at risk of invasion from this species i.e. now colonised in Nene and Ouse washes (APEM, 2010).

Figure 1.3: Current distribution (8th June 2017) of the Chinese mitten crab in the UK (www.mittencrabs.org.uk). Red dots indicate authenticated records.

1.6 Impacts

Mitten crabs are highly invasive and can affect human health as well as cause ecological damage which can potentially lead to substantial economic cost (Clark, 2011; Webster

et al., 2015). Invasive Chinese mitten crab populations threaten native species (Webster *et al.*, 2015; Mills *et al.*, 2016) and their habitats (Rudnick *et al*., 2005) causing bank erosion by weakening stream and river banks due to their burrowing activities (Panning 1938; Dutton & Conroy, 1998; Zucco, 1999; Rudnick *et al*., 2000; Rudnick *et al.*, 2005; Gilbey *et al.*, 2008). Additionally, especially during their downstream migration, large numbers of mitten crabs can cause blockages of grills associated with water abstraction infrastructure (e.g. Morritt *et al.*, 2013 for the River Thames). During this adult migration, mitten crabs can also cause problems in fish and shrimp nets by damaging catch and nets (Veldhuizen & Stranish, 1999) and consume bait in traps/pots (Panning, 1938). Furthermore, mitten crabs are reported to prey on the native white clawed crayfish, *Austropotamobius pallipes* (Lereboullet, 1858), in the UK (Kelly & Maguire, 2009) as well as salmonids in the USA (Veldhuizen & Stranish, 1999). Having said this, the actual economic impact of the Chinese mitten crab can be difficult to assess (Sewell, 2016), but there are estimates that the economic cost has been around 80 million Euros in Germany since 1912 (Gollach, 2006). White *et al*. (2000) estimate millions of dollars of damage as a result of their impact in California.

With regard to human health, as mitten crabs are a delicacy in the Far East there are some issues associated with their consumption by humans. During the autumnal migration, mitten crabs are trapped and their developing ovaries are consumed. At least one species, *E. sinensis*, is an intermediate host for the Oriental lung fluke, *Paragonimus westermanii*, (Cohen & Carlton,1995; Clark *et al*., 1998a, Gollasch, 2011) and disease has been reported in humans that had ingested inadequately cooked mitten crabs (Gollasch & Rosenthal, 2006) causing chronic and acute symptoms such as diarrhoea, urticaria, fever, chest pain and hemoptysis (see Chung *et al.*, 1981). There are no reports of lung fluke in River Thames mitten crab populations as the conditions are

not suitable for this parasite as the first intermediate host is reported to be freshwater snail species which is not present in NE Europe (Stentiford, 2005).

1.7 Life cycle

Eriocheir sinensis is a euryhaline species (Veilleux & de Lafontaine, 2007) characterized by a catadromous life cycle (Solovyeva & Bailey, 2017). The Chinese mitten crab was defined as "practically a freshwater animal" by Panning (1938) as they spend most of their lives in fresh or brackish waters (Veilleux & de Lafontaine, 2007). Panning (1938) stated that mitten crabs reached their sexual maturity in 3−5 years, however, some studies showed that they reach their maturity within 2−3 years in laboratory conditions (Anger, 1991; Rudnick *et al*., 2005). In addition, Dittel & Epifanio (2009) highlighted that the lifespan and duration can vary significantly. The life stages, the estimated duration and the habitat are given in Table 1.3.

Table 1.3: Duration and habitat of the life history stages of the mitten crab *Eriocheir sinensis* (adapted from Dittel & Epifanio, 2009).

Stage	**Duration**	**Habitat**
Zoea larva (5 stages) *	2−8 weeks	Estuarine/ marine
Megalopa (one stage)	3−6 weeks	Estuarine/ marine
Early juvenile	6−12 months	Brackish waters
Late juvenile	12−24 months	Lakes, levees, rivers, streams
Adult (non-productive stage)	2−4 years	Lakes, levees, rivers, streams
Adult (reproductive stage)	4−10 months	Brackish open waters

*Five zoeal stages were reported by Dittel & Epifanio (2009), whereas Anger (1990), Montú *et al*. (1996) and the present study, described an additional 6th zoeal stage.

Mature adults migrate long distances from the inland waters to estuarine habitats to breed (Panning, 1938; Dan *et al*., 1984; Rudnick *et al*., 2000; Cohen & Weinstein, 2001; Herborg *et al*., 2003). The longest distance was reported as 1,500 km (ca. 932 miles) in native China (NNSS, www.nonnativespecies.org). The crabs reach sexual maturity in their fourth or fifth year (Rainbow *et al*., 2003). Mitten crabs have a semelparous life cycle; they make only one re-productive migration (Kobayashi & Matsuura, 1995) and die after the breeding season before the start of the following summer (Veilleux & de Lafontaine, 2007; Naser *et al*., 2012; Solovyeva & Bailey, 2017).

Mitten crabs migrate downstream during the autumn to breed in higher salinity waters (Panning, 1938). During this migration, the reproductive organs develop and the crabs become sexually mature. Typically, the female broods the eggs through to hatching and after, the zoeae remain in more saline environment (Rudnick *et al*., 2000) for about two months (Anger, 1991; Dittel & Epifanio, 2009). Zoeae undergo five (Liang *et al.*, 1974; Kim & Hwang, 1995) or six zoeal stages under laboratory conditions depending on the salinity (Anger, 1991; Montú *et al*., 1996) and one megalopal stage. This is related to their ontogenetic migration from saline waters back into freshwater in their life cycle (Cieluch *et al.*, 2007). They stated that first zoea stage has a high capacity of osmoregulation that make hatching possible in estuaries. Following zoeal stages have moderate "hyper-osmoregulation" ability that allows tolerate low salinities (Cieluch *et al.*, 2007). Kim & Hwang (1995) stated that 15 days are required to reach the megalopal stage. The optimum conditions for this was given by Anger (1991) as with the salinity of 25 ‰ at 12−15 °C or 32 ‰S at 18 °C.

It is the megalopal stage that initially starts to migrate back upstream (Zhao, 1999). Megalopa then moult and metamorphose into juvenile crabs during the summer (Anger, 1991). Young crabs continue to migrate upstream into the upper reaches of rivers in

order to commence the freshwater stage of their life cycle (Veilleux & de Lafontaine, 2007; Fig. 1.4).

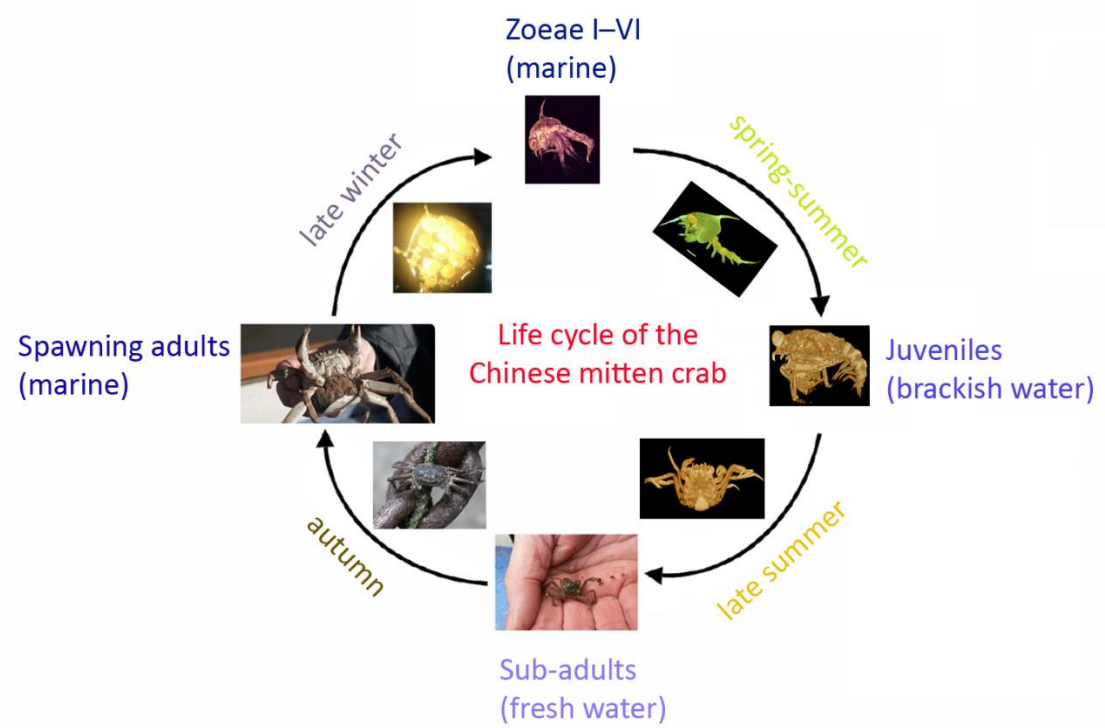

Figure 1.4: Life cycle of the Chinese mitten crab. (adapted from Rudnick *et al*., 2000). * Five zoeal stages were given by Rudnick *et al*. (2000), whereas Anger (1990); Montú *et al*. (1996) and the present study, consider that there is an optional, additional 6th stage, in determine conditions.

1.8 Fecundity of the Chinese mitten crab

The Chinese mitten crab was defined as a "clearly marine species that requires brackish or marine waters for successful larval development" by Anger (1991) who carried out an extensive research on the effect of the salinity and temperature on the larval development of the species. According to him, the larvae can tolerate salinity between 10−30‰ (Anger, 1991).

It is reported that mating occurs in the brackish waters (Panning, 1938), during late-autumn and winter, the exact timing being variable and depending on geographic regions. It mostly occurs between November-March (Zhang *et al*., 2001) in their native environment (China), between October and January in Germany (Panning, 1938) and October-February in the United Kingdom (Herborg *et al*., 2006). Mating of the Chinese mitten crab reaches a peak during new or full moon periods in November in the River Thames (Herborg *et al*., 2006). It was highlighted that ovigerous females stay in deeper water when the eggs are developing (Robbins *et al*., 2007).

After spawning, the eggs are attached to the pleopods (pleonal appendages) of the female with a cement-like substance (Panning, 1938). Another reason why mating occurs in the brackish water was explained by Veilleux & de Lafontaine (2007) that the cement-like substance hardens in brackish waters with salinities of 15‰ or more.

Fecundity is the term used to define the number of eggs generated by a single female. Female mitten crabs are reported to produce between 100,000 and 1 million eggs (Panning,1938; Cohen & Carlton, 1995; 1997; Rudnick *et al*., 2000) with the eggs being held between the ventral surface of the carapace and broad female pleon in ovigerous females. Investigating the fecundity of the species is important in order to understand the population dynamics of the crab and their potential ecological and economic effects within habitats into which they dispersed (Przemyslaw & Marcello, 2013). The fecundity of female crabs varries depending on the age, water body and ecological conditions (Hines, 1982; Turra & Leite, 2001; Tallack, 2007). Herborg *et al.* (2006) stated that the influence of semi lunar cycle was important for the reproduction of some crabs such as *Uca pugilator* Bosc, 1801. They emphasized that mating seemed to be synchronized with the new or full moon and this increased larval retention within in the river mouth or estuaries. Veilleux & de Lafontaine (2007) too presumed that hatching

during the full moon has the advantage of increased larval retention within esturary during the "neap- spring" tidal cycle instead of exportation to the sea.

Research on the relationship between the size, morphology and fecundity of mitten crabs requires more consideration (Przemyslaw & Marcello, 2013) because it is directly related to brachyurans developmental mode, juvenile settlement and adult size (Hines, 1982, 1986). The fecundity of *E. japonicus* was studied by Kobayashi & Matsuura (1995) and Kobayashi (2001) in detail while similar studies on *E. sinensis* are limited. Przemyslaw & Marcello (2013) studied the fecundity of the first brood size of mitten crab populations in the Odra River Estuary, Poland by investigating the relationship with some morphometric characters and found a positive relationship between fecundity and large female crabs. In the present study, a similar approach was conducted in order to have a better understanding of the fecundity and biology of Chinese mitten crab populations in the River Thames.

More than one brood

It has been reported that some male brachyuran crabs in some taxa have the ability to deposit sperm in the seminal receptacles of the females (Epifanio, 2007; Dittel & Epifanio, 2009) and this can result in the fertilisation of more than one batch of eggs during a single reproduction season. A laboratory experiment using *E. japonica* was conducted by Kobayashi (2001) showing that the species had up to three broods in one reproduction season. According to Panning (1938) and Dittel & Epifanio (2009) *E. sinensis* can generate several broods in a single reproduction season. However, the occurrence of this situation in the UK waters is still uncertain (APEM, 2010). Furthermore, it is not clear whether more than one brood of eggs can be fertilised after a single mating. In order to understand the potential of having more than one brood,

without further mating in a single reproductive season of Chinese mitten crabs in the River Thames, the present study conducted a series of experiments to examine this possibility.

1.9 Description of zoeal development

Unlike adults, the identification of decapod larvae from planktonic samples is a complex and formidable task (Ingle, 1991; González-Gordillo *et al*., 2001). Larval development constitutes an important part of the decapod life cycle and such data is beneficial to evaluate species in a particular environment (Kornienko & Korn, 2009). Most decapod larval descriptions have been derived from the laboratory reared samples (Ingle, 1991) as well as those collected from the field (Rice & Tsukimura, 2007).

Investigating larval forms is an important aspect of the study of invasive species which have been introduced to new regions via ballast water (Kornienko & Korn, 2009). Furthermore, the description of larval characters can contribute to the study of crustacean systematics and phylogenetic relationships (Martin & Davis, 2001). In some cases, describing larval characters and stages have been shown to provide additional information in analysis of phylogenetic relationships (Clark & Webber, 1991; Maas & Waloszek, 2001; Marques & Pohl, 2003, Santana *et al*., 2006). It has been shown that larval characters can help resolve existing problems in brachyuran identification. Furthermore, a detailed description and/or DNA barcoding, enables zoeae from the plankton to be correctly identified (Santana *et al*., 2006, Al-Haj & Al-Aidaroos, 2014).

The first description of a decapod larva, *Cancer pagurus* (as *Cancer germanus*), was by Linnaeus (1767; Ingle, 1991; González-Gordillo *et al*., 2001). Many developmental studies have been reported since the beginning of nineteenth century (Gurney, 1939; Ingle, 1992; González-Gordillo *et al*., 2001). Since then, more detailed and specific

descriptions of decapod larvae have been completed (González-Gordillo *et al*., 2001) for the family Xathidae (Martin, 1984), the New Zealand fauna (Wear, 1985), the Mediterranean larvae (Pessani & Robotti, 1992) and in general brachyuran larvae (Rice, 1980; Soltanpour- Gargari *et al*. 1989; Ingle, 1991).

Several identification guides of brachyuran larvae have been produced according to oceanic regions such as North-eastern Atlantic region (Ingle, 1992); Atlantic coast of Europe (Paula, 1996); Northern Chile (Báez, 1997); the Mediterranean (Peassani *et al*, 1998); the Black Sea (Anosov, 2000); the Pacific Northwest (Puls, 2001); South-Western Europe (Santos & González-Gordillo, 2004) and San Francisco Bay (Rice & Tsukimura, 2007).

The identification of Chinese mitten crab zoeal stages has been studied by many researchers since the beginning of the twentieth century including Schnakenbeck (1926; 1933), Hinrichs & Grell (1937), Buhk (1938), Panning (1939), Andrea (1947), Liang *et al*. (1974), Kim & Hwang (1995) and Montú *et al*. (1996). In order to confirm the identity of mitten crab larvae, it is important to easily access clear illustrations and consistent descriptions (Clark *et al.*, 1998a; González-Gordillo *et al*., 2001; Martin & Davis, 2001). The quality of the early descriptions and illustrations of the Chinese mitten crab zoeae, however, were poor and many characters were overlooked and the later studies were not consistent. Therefore, one of the aims of the present study was to re-describe the zoeal development of the Chinese mitten crab. For example, Rice & Tsukimura (2007) used the description of *E. sinensis* by Montú *et al*. (1996), however, the illustration of mitten crabs taken from some old descriptions can cause problems when comparing each larval stage. Another study by Dittel & Epifanio (2009) used the illustration of *E. sinensis* appendages to compare them with *E. japonica* in their review, however, these comparisons do not correspond to the results of the present study.

1.10 Developing imaging techniques for studying brachyuran crab zoeae

The description of development of brachyuran crab zoea is typically based on line drawings to illustrate the defining characters. These include the morphology of the carapace, dorsal, rostral and lateral spines, antennule, antenna, mandible, maxillule, maxilla, maxillipeds (I−III), pereiopods, dorsolateral projections, and posterolateral spines on the pleon, telson, and pleopods in the later zoea stages (Clark *et al*, 1998b; Korn *et al*, 2010; Clark & Cuesta 2015; Fig. 1.5).

Distinguishing species at the zoeal level is a complex task (Ingle, 1991) and requires meticulous work. Morphological characters of brachyuran crab zoeae look incredibly similar at first glance. However, identification of morphological characters by accurately describing the setation of appendages provides many distinguishing features.

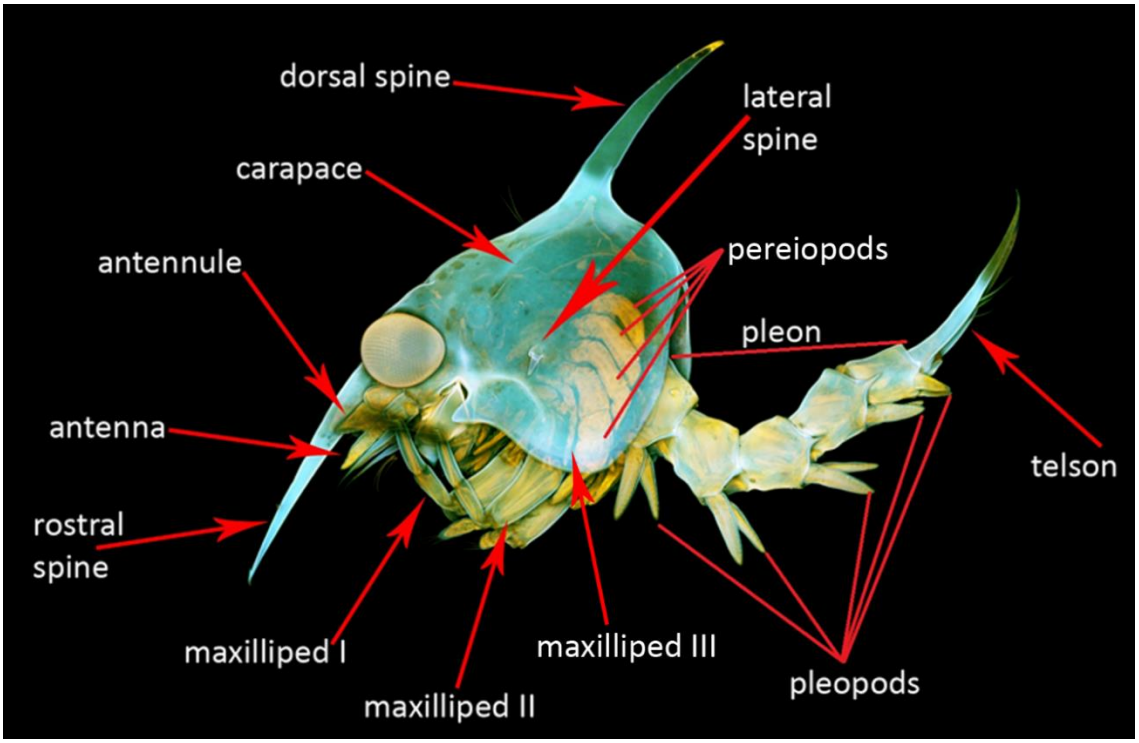

Figure 1.5: Main characters used to identify the brachyuran zoea (adapted from Korn *et al*., 2010). *The mandible, maxilla and maxillule are not visible in this image.

Line drawings to illustrate written taxonomic descriptions are time-consuming to produce (Coleman, 2006). These figures are usually drawn using a *camera lucida* attached to a light microscope. After dissection, however, viewing all the setae on the appendages in one horizon can be difficult as they may be located in different focal planes. This requires refocusing the microscope constantly. During this procedure, some features can be overlooked. In addition, some setae are very difficult to view using light microscopy. This is another reason for the requirement to re-describe the zoeal stages, especially with reference to older mitten crab larval studies.

Therefore, another aim of the present study is to trial the use of confocal microscopy to record zoeal development. This scanning technique has become more popular in marine biology with the declining costs of confocal microscopes (Chandler & Volz, 2004). Furthermore, confocal microscopy provides 3D data which can provide a better understanding of the complex morphological structures.

Specimen preparation techniques for confocal microscopy, however, differ from species to species depending on the focus of the study. Thus, another aim of the present study was to develop optimum imaging techniques which would be suitable for brachyuran crab zoeae. A number of different combinations of preparation techniques and confocal settings were applied in order to obtain satisfactory images of appendages during the present study. As confocal microscope software programmes were not found to be adequate, additional post-processing techniques (3D visualisation) were also trialled.

A workflow diagram including pre-processing, confocal microscopy and post-processing procedure was produced as well as adapted traditional SEM techniques for carapace setation. The steps of the technical development and trialled combinations are detailed in separate chapters of the present thesis. The techniques developed were also

confocal microscopes from different manufacturers in order to assess the overall utility of the procedure.

1.11 Describing male gonopods using CLSM and micro-CT techniques

The morphology of the male gonopod is a species diagnostic character. They can be extremely difficult to illustrate by traditional penned line drawings especially when distinguishing closely related species (see Crosnier, 1962; Serène,1966; Guo *et al*., 1997; Ng *et al*., 1999), SEM pictures (see Apel & Spiridonov, 19980 or basic photography (see Naser *et al*., 2012). Another aim of the present study was to visualise more details of gonopod morphology using confocal microscopy by processing the data using 3D data processing software as an alternative to traditional methods. Also trialled was the visualisation, by micro-computed tomography (micro-CT), of the gonopod of valuable old dry museum crab specimens without causing any damage to the material.

1.12 Research objectives

This thesis comprises seven chapters. Chapter 1 includes a general description of the biology of the invasive Chinese mitten crab, *Eriocheir sinensis*, which is now well established in the Thames, its tributaries and at other sites around the UK and other regions globally. The current taxonomy, distribution, life cycle and zoeal development are also considered. The second chapter is the Material and Methods section which explains the techniques applied for understanding brooding, fecundity, hatching of zoeae and the preparation of zoeal mitten crab stages for examination using confocal scanning laser microscopy. In addition, there is a description of the software programmes used to visualise *E. sinensis* zoeal development. This chapter also describes other approaches such as macro confocal, SEM and micro-CT techniques. The

third chapter determines fecundity and the possibility of producing more than one brood from a single mating of Chinese mitten crabs from the River Thames, London. Chapter four is concerned with developing imaging techniques to investigate the zoeal development of brachyuran species in the case of *E. sinensis* using confocal microscopy and 3D imaging techniques. The fifth chapter is a re-description of zoeal stages of the Chinese mitten crab based on novel information obtained from the confocal studies described in the previous chapters. The sixth chapter is concerned with CLSM and CT scanning of the male gonopods of a number of crab species. The results from applied CLSM and micro-CT techniques are illustrated in this chapter. The last chapter provides concluding remarks and a wider discussion of the implications of the work by discussing the advantages or disadvantages of the modern-day standards to describe the early and adult stages of the brachyuran species. It mainly focuses on comparing light microscopy, confocal microscopy, SEM and micro-CT techniques for the purpose of producing zoeal descriptions.

CHAPTER 2

MATERIAL & METHODS

2.1 Materials

2.1.1 Specimens used to conduct the present study

Unless otherwise specified, specimens were obtained from the School of Biological Sciences, Royal Holloway University of London and the Department of Life Sciences, Natural History Museum, London. For further details see Table App. 8.1 in Appendix 1.

All *E. sinensis* specimens were collected at Tilbury, River Thames, England, unless otherwise stated. Collector names and details of the collection events are given in Table App. 8.1 in Appendix 1. Post-collection, the crabs were held in the marine aquarium at Royal Holloway and eggs and first zoeal stage larvae were collected, preserved and incorporated in the research collections at the Natural History Museum, London. This study thus drew from both collections material and freshly collected specimens.

2.1.2 Fecundity in the River Thames

Estimation of the fecundity of the Chinese mitten crab in the River Thames was based upon examination of 30 freshly-collected ovigerous females.

2.1.3 Observations on multiple brood productions without mating

12 ovigerous females were used for observation of multiple brood productions in the Chinese mitten crab without mating based on freshly-collected specimens.

2.1.4 Species used for general material & methods and developing of imaging techniques for the study of brachyuran larvae

Larval specimens used for the development of imaging methodologies were drawn from both NHM collections (registration number 2002.791; see Table App. 8.1 in Appendix 1) and material collected fresh or hatched from adult females collected between 2013 and 2015 (Table App. 8.1 in Appendix 1).

Numerous larvae at different zoeal stages of *Sesarma curacaoense* De Man, 1892 and *Armases miersii* (Rathbun, 1897) were also used in this study (see Table App. 8.1 in Appendix 1).

2.1.5 Specimens used for re-description of zoeal development

Specimens used for re-description of zoeal development were obtained from NHM collections (registration number 2002.791; see Table App. 8.1 in Appendix 1) collected by Roni Robbins, 16 March 1999; hatched 14−16 April 1999; reared London by Roni Robbins and Paul F. Clark in 25‰ seawater.10 larvae for each zoeal stages were used to describe each zoeal stage (ZI−VI).

2.1.6 Specimens used for examination of the gonopods of adult crabs using CLSM and micro-CT

Eriocheir sinensis: One adult male from the Bam Elms reservoir, Barnes, London (NHM registration number 1992.361; Table App. 8.1 in Appendix 1).

Eriocheir sinensis? Undescribed species: One adult male from Den Oever, Holland (Table App. 8.1 in Appendix 1).

Eriocheir sinensis? Undescribed species: One adult male from Hollands Diep, Holland (Table App. 8.1 in Appendix 1).

Eriocheir japonica De Haan, 1835: One adult male; from a stream at Sasuna near tsol of Tsushima, Japan (NHM reg. number: 1907: 12.9.1; Table App. 8.1 in Appendix 1).

Eriocheir hepuensis Dai, 1991: One adult male; Shatt Al-Basrah Canal, Iraq (NHM reg. number: 2011.8035−8037; Table App. 8.1 in Appendix 1).

Libystes nitidus A. Milne Edwards, 1867: One adult male from South of Maldives in open ocean (NHM reg. number: 1991: 156.1; Table App. 8.1 in Appendix 1).

Libystes nitidus? Undescribed species: One adult male; Sudanese Red Sea (NHM reg. number: 1934: 117.114; Table App. 8.1 in Appendix 1).

Monomia argentata A. Milne Edwards, 1861: One adult male, mouth of Lundu River Borneo (NHM reg. number: 1847.21; Table App. 8.1 in Appendix 1).

2.1.7 Laboratory instruments

Unless otherwise specified, all laboratory instruments were provided by the School of Biological Sciences, Royal Holloway University of London or Departments of Life Sciences and Core Research Laboratories at the Natural History Museum, London. General laboratory reagents were purchased from Sigma-Aldrich Chemical Company and Fisher Scientific UK Ltd. (see Appendix 2 and Appendix 3 for the list of instruments and microscopes used to conduct present study).

2.2 Methods

2.2.1 Egg count in broods of Chinese mitten crab

The aim of this study was to establish more information on the reproductive biology of the Chinese mitten crab in the Thames catchment especially in terms of female fecundity.

Crab collection and maintenance

Thirty ovigerous female crabs were collected and temporarily stored in cooler boxes containing ice in order to keep the crabs chilled during the transportation to RHUL. After being transferred to the laboratory, crabs were maintained in aerated holding tanks at a 12 hour light, 12 hour dark regime (Herborg *et al*., 2006) at approximately 12 °C in the freshwater aquarium until being examined.

Crabs used for multiple brood observations were established in artificial seawater aquaria. According to Anger (1991), the optimum salinity for the Chinese mitten crab is between 15‰ and 25‰. Dittel & Epifiano (2009) stated that first zoea stage of Chinese mitten crab can tolerate salinity between 10‰ and 30‰. This statement, however, was narrowed down to between 20‰ and 25‰ by Anger (1991) for mitten crab zoea stages. Therefore, crabs were established in separate water tanks with the salinity of between 20‰ and 25‰ for each term. (see Appendix 4 for the preparation of artificial sea water).

Brood experiments

Ovigerous crabs were individually removed from the aquarium using a net with a gloved hand. All crabs were washed with tap water to eliminate particles/foreign

material on the crabs that could possibly contaminate the sea water during investigations. The crabs were then numbered. The collection date, colour of eggs, carapace width (C.W.), freezing duration of each crab (to anaesthetise it prior to manipulation) were recorded for each sample. In addition to these values, the density of eggs attached the pleon, (in terms of brood volume, mean diameter of the eggs, volume of one egg and number of eggs) were recorded.

Carapace width (C.W.) was measured between the small 4th pair of lateral spines (Fig. 2.1) to ± 0.1 mm using a Vernier slide caliper following the technique described by Dittel & Epifanio (2009) and Webster *et al*. (2015). Different species of crab have different standards of measuring the carapace width (Xiao & Kumar, 2004; Hall *et al*., 2006; Tuset *et al*., 2011; Verísimo *et al*., 2011; Severino-Rodrigues *et al*., 2013). The relationship between the number of eggs and the size of the female crabs was also assessed by examining the fecundity. This relationship was modelled applying linear regression data using PAST-UiO freeware software programme (Hammer *et al*., 2001).

Removing brood from ovigerous Chinese mitten crabs

Individual crabs were placed in separate plastic bags and then transferred to a freezer (ca. -18 °C) for approximately 20 to 90 minutes depending on the size and responsiveness of the crabs. Crabs were checked after 20 minutes. If the crab was "lethargic" and relatively unresponsive, it was removed from the freezer and examined. If it still appeared to be reasonably "active" (this may be size-dependent), it was returned to the freezer for a longer time before being checked again. Relatively large crabs needed to be retained in the freezer for a longer time.

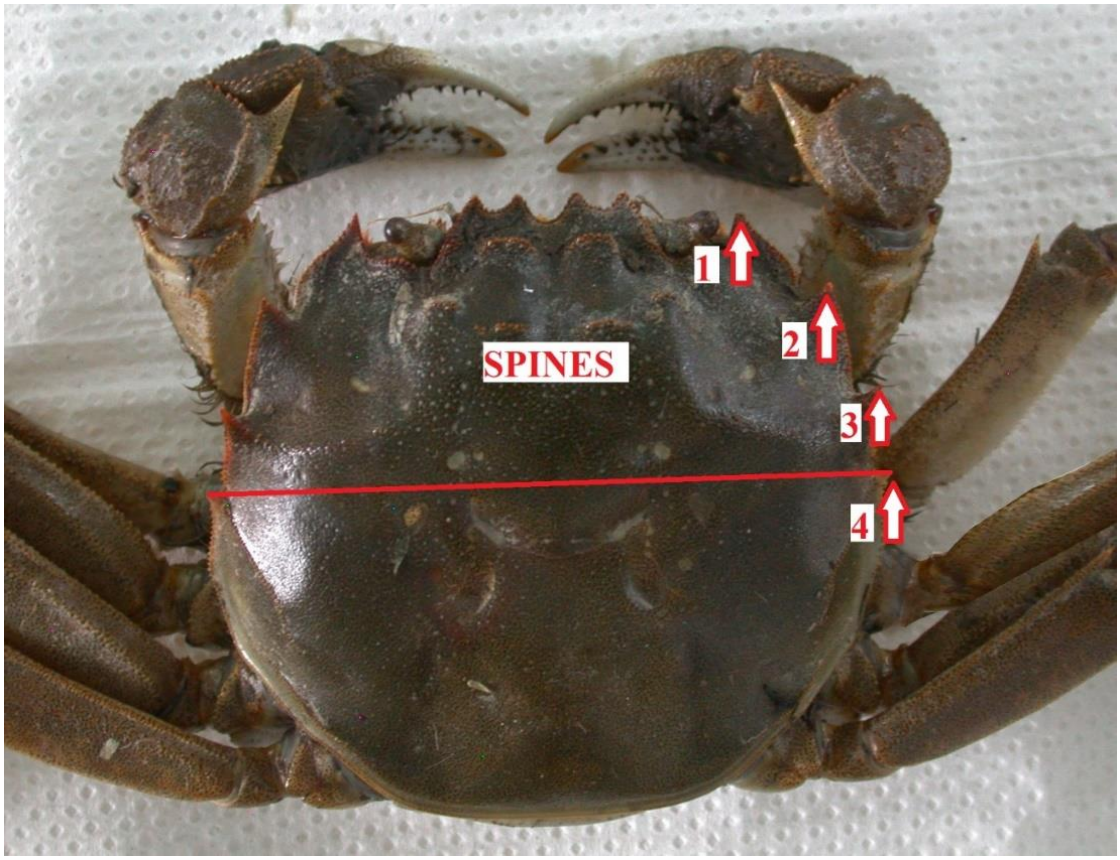

Figure 2.1: Measurement of the carapace width (C.W.) of an adult Chinese mitten crab (*Eriocheir sinensis*). The measurement was taken from between the 4th pair of lateral spines using a Vernier slide caliper (± 0.1 mm).

Suitably chilled crabs were then restrained by placing elastic bands over their chelipeds to keep the claws closed and allow access to the pleon. The eggs were removed from the pleopods using forceps following the technique by Okazaki & Wehrtmann (2014). These crabs were then referred to as de-brooded and numbered D1−D30. After de-brooding, the crabs were then returned to the freezer and subsequently disposed of in the appropriate biological waste receptacle. All eggs were stored in 70% ethanol in a labelled plastic vials containing 70% ethanol (see Figure 2.2 for the calculation).

Estimating/calculating brood numbers

Using a Gilson pipette 5 ml of artificial seawater was transferred into a 10 ml measuring cylinder. Stripped eggs were then placed into the cylinder. Following the egg transfer, 1 ml and 200 µl Gilson pipettes were used to add/remove seawater into the measuring cylinder until the water level reached a clearly distinguishable mark (whole number) on the cylinder. The volume of water used and the size of the measuring cylinder was adjusted dependent on the size of the egg mass.

An example how to calculate the volume of the brood is given below:

E.g. Initial volume of artificial seawater = 5 ml. Add eggs (after carefully removing excess water from the egg mass). For example, if the volume in the cylinder increased to a volume slightly over 7 ml – in this case remove water from the cylinder so that the water level was exactly 7 ml – record the volume of liquid withdrawn to achieve this level.

The brood volume can then be calculated as the final volume (7 ml) – 5 ml (initial volume) + the volume removed to adjust the level.

For example: for an Initial Volume of 5ml and a Final Volume of 7 ml, if 250 µl were removed to adjust the level, then the Brood Volume would be 2 ml + 250 µl = 2250 µl or 2.25 ml.

In order to measure the egg diameter, several eggs were randomly selected. For example, ca. 15−20 eggs measured (to the nearest 0.01 mm) using a Carl Zeiss, BL 2612 microscope equipped with an eye piece graticule, (calibrated against the relevant stage graticule) 20× magnification. The mean volume of eggs was calculated using the standard for calculating the volume of a sphere Since the eggs of *E. sinensis* are almost spherical throughout the development. (see formula below).

$$V = \frac{4}{3}\pi r^3 \text{ or } \frac{4}{3}\pi\left(\frac{MD}{2}\right)^3$$

The total number of eggs in each brood was estimated by calculating the average volume of each egg in the brood and dividing the total volume of the brood by the volume of individual eggs (see Fig. 2.2 for an example calculation).

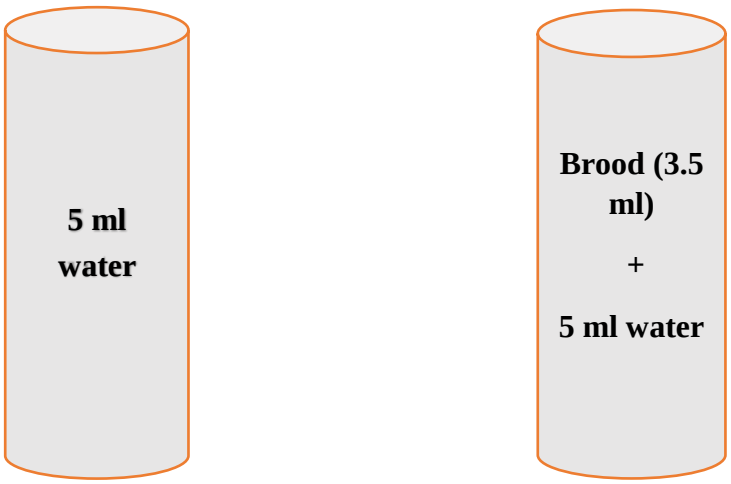

Brood volume = 8500 µl – 5000 µl = 3500 µl.

Mean diameter (MD) of the eggs = 410 µm.

One egg volume = $4/3 \times \pi \times (0.41/2)^3 = 0.03606$ mm^3.

Total number of eggs = Brood volume / one egg volume.

Total number of eggs = 3500 / 0.03606 = 97,060 eggs.

Figure 2.2: Calculation of brood volume, volume of one egg and calculation of total number of eggs.

2.2.2 Investigation of multiple broods

The aim of these observations was to establish more information on the reproductive biology of mitten crabs by observing the possibility of producing more than one brood after one mating event.

In order to investigate the production of multiple broods after one mating event, a total of 12 ovigerous mitten crabs were observed over the following periods between the breeding seasons of 2013−2014, 2014−2015 and 2015−2016. Five ovigerous crabs were established in the aquarium on 5th of November 2013 and another five were established on the 21st of November. In the following years, one ovigerous female was collected in November 2014 and another in November 2015.

In all cases, crabs were established in individual, aerated water tanks in either a constant temperature (CT) room or an incubator at 18 °C and 12-hour day/night cycle. The crabs were numbered O1−O12 respectively. Recorded data included a condition index to categorise the health of each crab, the carapace width (C.W.), colour of eggs when the crabs were initially collected, colour of eggs during the observation of the first brood, mean diameter of eggs of first brood, first larval release observation date, date of observation of second brood, colour of eggs in second brood, mean diameter of eggs in the second brood, and second larval release observation date by each crab. The date of death of any of the crabs was also recorded.

First brood

After collection, all crabs were washed, and after recording the required condition index, transferred to numbered holding tanks. The artificial seawater in the tanks was changed on a weekly basis in order to prevent contamination. The crabs in CT room and incubators were not fed whilst carrying their first brood in order to prevent

contamination of the water and reduce the potential for infection of the eggs. The aim was to maintain females under these conditions until each crab had completely released their eggs so that the capacity to produce multiple broods without mating could then be examined.

When the crabs started to release their first brood, the date was recorded and eggs were examined for colour and mean diameter was recorded. Eggs that had settled on the bottom of the tanks were collected using a plastic pipette and preserved in 70% ethanol. These eggs were stored at RHUL. Any hatched, swimming first stage zoeae were attracted to one side of the water tank using a bright light. The zoeae were then transferred into a glass laboratory dish using a plastic pipette. All first stage zoeae were preserved in 70% ethanol.

As pipetted larvae and eggs included salt water, this was gradually removed using a thin glass pipette, and replaced with 70% ethanol. This procedure was repeated several times (5−6 times) until no salt water remained and only 70% ethanol was present. Fixed larvae were then taken to the NHM for further investigation.

After removing eggs and larvae, the holding tanks were cleaned carefully using tap water. The females were then put back into the tanks with freshly prepared artificial seawater and returned to the incubator/CT room. This process was repeated several times during the observation of first brood.

Once the crabs had released all their eggs/first stage zoeae, the females were then fed. The aim was to provide energy reserves to allow crabs to survive a longer period in the laboratory.

Feeding

Crabs were fed with squid or salmon once or twice a week. Defrosted squid/ salmon were cut into small pieces and left in each tank overnight (12−14 hours). After feeding, the water in the tanks was changed using freshly prepared seawater to prevent contamination of the water and infection of the crabs. This process was repeated until observation of the second brood in some crabs was observed on the pleon or the crab died.

Second brood

Not all the females survived after releasing the first brood of eggs. However, those that survived went on to spawn a second brood of eggs. Feeding was then stopped. After recording the date of the second brood, colour of eggs observed, mean diameter of the eggs and any second larval observation dates were also recorded. Successfully hatched zoeae were preserved in 70% ethanol and taken to the NHM for further investigation.

Third brood

After observing the second brood/larvae, the surviving crabs were then fed with squid until a possible observation of a third brood or the females died.

2.2.3 Developing a visualisation workflow using different preparation techniques for Confocal Scanning Electron Microscopy (CLSM) for brachyuran crab larvae

Different combinations of preparation methods, CLSM scanning and 3D imaging methods were applied to create an optimum workflow for the visualisation of mitten crab zoeal development. The successful workflow (Fig. 2.3) has been applied in the present study.

Protocol

A number of protocols were applied to larval specimens during the preparation of slides: cleaning, staining, protein digestion and mounting. Specimens were scanned using a Nikon A1-Si confocal microscope (Nikon Corporation, Tokyo, Japan) fitted to a Nikon Eclipse upright microscope. Some data processing was carried out using ImageJ (http://imagej.nih.gov/ij/; Schneider *et al.*, 2012) prior to the generation of the 3D images using the open source software program Drishti (version 2.6.1; http://sf.anu.edu.au/Vizlab/drishti/; Limaye, 2012). Other brands of confocal microscopes including an Olympus Fluoview FV1000 IX81 inverted microscope (Olympus Corporation, Tokyo, Japan), Zeiss LSM 880 airy scan upright confocal microscope (Carl Zeiss, Jena, Germany) and Leica TCSSP5 (Leica Microsystems, Wetzlar, Germany) equipped with a Leica DM5000 B (upright microscope) were also tested using this protocol with the aim of finding a consistent workflow which would work with any microscope, thus ensuring a broad uptake of the successful methodology.

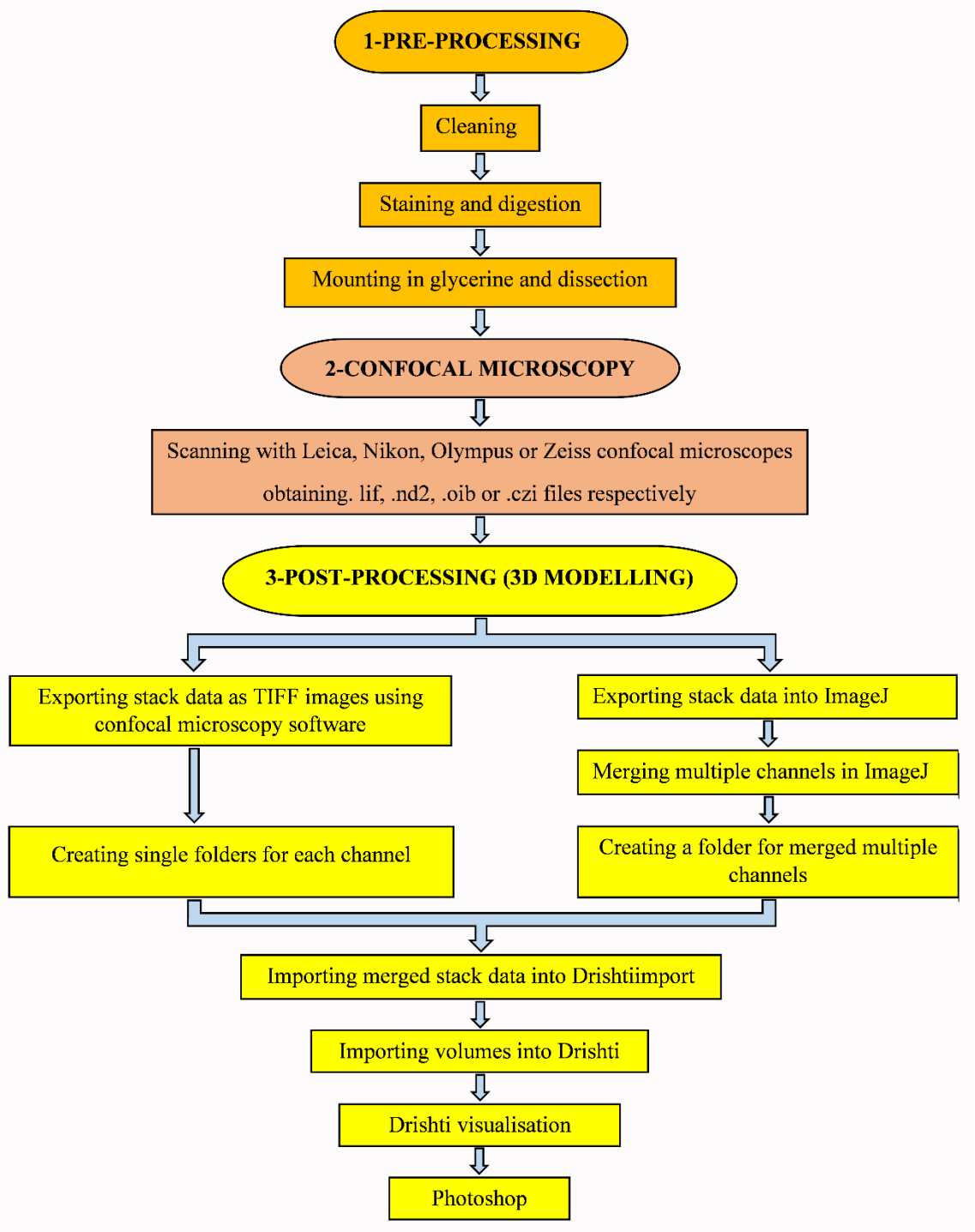

Figure 2.3: A flowchart for visualisation and 3D imaging of brachyuran crab larvae.

2.2.3.1 Pre-processing

Cleaning

Laboratory hatched zoeal stages of *E. sinensis* as well as other brachyuran crabs such as *Sesarma curacaoense* and *Armases miersii* previously fixed in 70% ethanol and deposited in the crustacean collections of the NHM, were often found to be contaminated with debris that had adhered to the exoskeleton (Fig. 2.4). These specimens needed to be cleaned before preparation for microscopic examination.

Contaminated zoeae were cleaned using Decon 90 (Decon Ltd., England). Two or three drops of Decon 90 (see Sewell & Cannon, 1995; McAllen & Taylor, 2001) were added to 100 ml of 70% ethanol. Specimens were left in this solution for 3–4 h. The solution was gently agitated periodically by hand during the cleaning process. The sonication methodology and use of a tumbler to remove particles as proposed by Felgenhauer (1987) were also trialled, but found to be unsuccessful. After cleaning, the specimens were pipetted into deionised water for five minutes and washed thoroughly (three changes of deionised water lasting five minutes each).

Staining

The larvae in deionised water were stained using a 1:1 mixture of Congo red (Fisher Scientific Ltd., Loughborough, England) and acid fuchsin (Sigma-Aldrich Co. Ltd., Irvine, England). These stains were available in powdered form and were each made into a stock solution by dissolving 0.5 mg of stain in 100 ml of deionised water. Stock solutions were filtered (Filtropur 0.2 µm) to remove unwanted particles. The stains were stored in a cupboard at room temperature (ca. 20 °C) in dark glass vials covered with

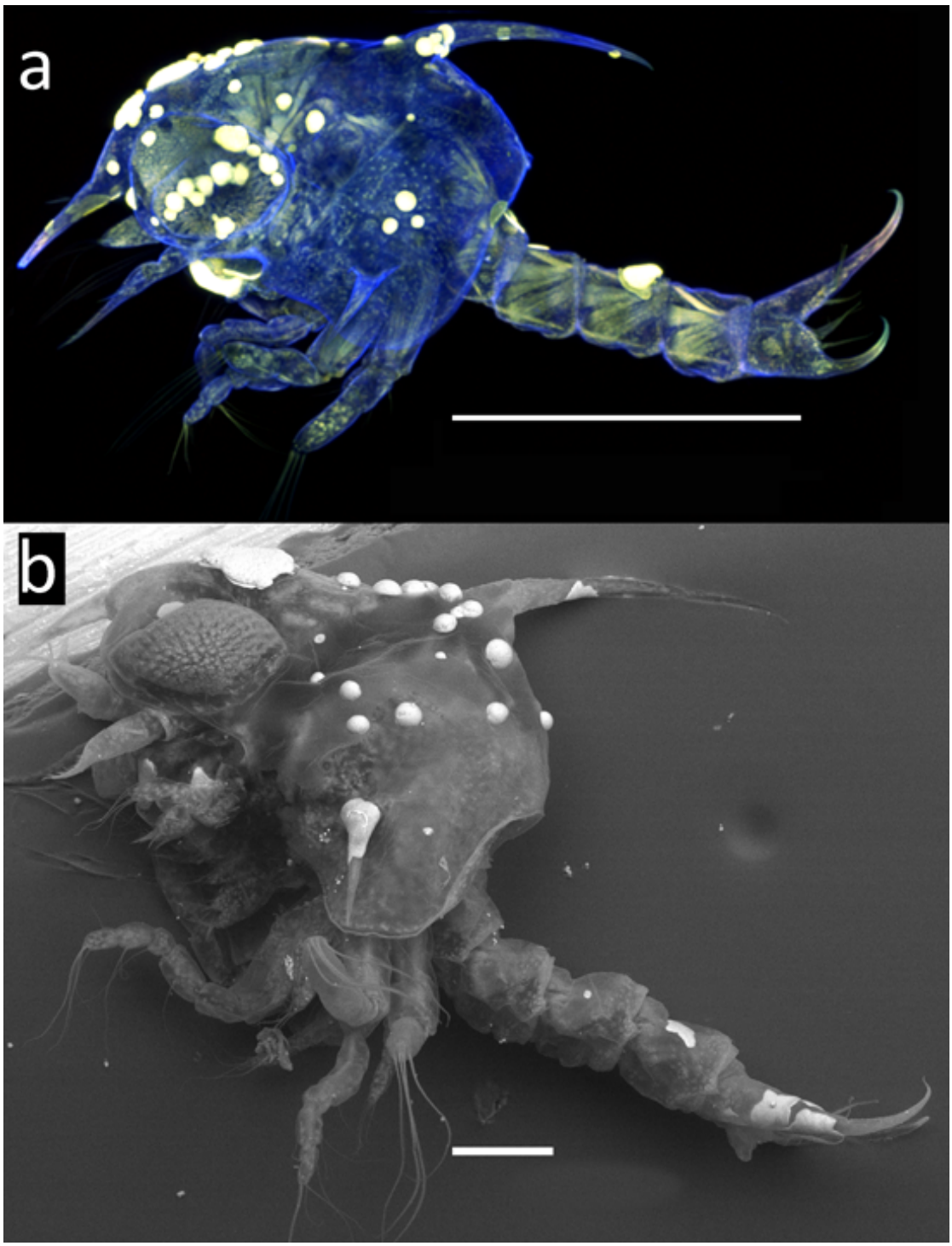

Figure 2.4: *Eriocheir sinensis*, ZI, contaminated zoeae with debris adhered to the exoskeleton. (a) Showing the contaminated areas using a Nikon A1-Si confocal microscope. (b) Demonstrating these areas using SEM. Scale bars: (a) = 500 μm; (b) = 100 μm.

aluminium foil to exclude light which causes bleaching of the solution. Before staining the specimens, Congo red and acid fuchsin stock solutions were mixed 1:1 in a glass dish using separate plastic pipettes for each stain. Using mounted needles, the larvae were carefully lifted into the mixed stain, covered with a glass lid to prevent evaporation and left in a covered box for 24 hours at room temperature.

Digestion

The larvae were next transferred into a freshly-made mixture of SDS (sodium dodecyl sulphate) and DTT (1,4-dithio-DL-threitol) to be digested (Fischer & Ahlrichs, 2011) – see preparation details below. After preparing the solution, a few drops of the SDS + DTT solution (depending of the size and number of specimens) were pipetted into the well of a cavity slide. The stained specimen was placed into the solution and left until the muscles within the larvae were digested. Staining the samples before digestion gave the advantage to detect the specimens easily in the watch glass which become exteremely transparent after digestion. For zoea I (ZI) larvae this was achieved in 75 minutes. As the size increased in subsequent zoeal stages (ZII–ZVI), the duration of immersion in the SDS + DTT solution was increased depending on the stage of development, e.g. ZII = 2−3 hours, ZIII = 4−5 hours, ZIV = 6−8 hours, ZV = 10 hours, ZVI = more than 10 hours (see comparison of size of the larvae in Fig. 5.56 in Chapter 5). When digestion was complete, the larvae were rinsed three times in deionised water. Each rinse lasted ca. 5 minutes. Digested specimens were then transferred back into the mixture of Congo red and acid fuchsin where they remained for a further 24 hours in a box, at room temperature, for final staining.

Preparation of SDS & DTT and application to larvae

A stock solution of SDS was prepared by adding 5.2 g (0.18 M) SDS (sodium dodecyl sulphate) and 0.24 g (0.03 M) NH_4HCO_3 (ammonium hydrogen carbonate) to 100 ml deionised water in an Erlenmeyer flask (pH 8.3). The reducing agent, 0.1 g DTT (1,4-dithio-DL-threitol) was added to a 5-ml stock solution of SDS in a glass vial using a micropipette before each digestion process. The mixture of SDS + DTT was then shaken vigorously. The stock solution of SDS can be safely stored in a fridge for up to 6 months. Once SDS is mixed with DTT, the mixture should be used within a week as the solution should be fresh.

Mounting and dissection

The use of a suitable mounting medium was essential in order for the CLSM to deliver optimum images for 3D reconstruction purposes. Therefore, in the present study, two different mounting media were trialled based upon information from literature. Several permanent and non-permanent mounting mediums were suggested by previous studies. Thus, one permanent and one non-permanent mounting media in different concentrations were tested in the present study. The first one was polyvinyl lactophenol which is a permanent mounting medium. The latter was glycerine (a non-permeant mounting medium). The aim was to find the most suitable mounting medium for the species in the present study and accordingly determine its suitability for other brachyuran crab larvae.

Polyvinyl lactophenol and dissection

The crab larvae needed to be mounted in a way that the cover slip is raised to avoid crushing or flattening the sample. This was achieved using self-adhesive reinforcing rings commonly available through stationary suppliers (e.g. Ryman Ltd., England) to reinforce punched papers. Typically, the reinforcement ring was divided into four pieces and pressed onto plain slides (standard 25 × 75mm microscope slide) to form a wider circle (Fig. 2.5a; Kihara & Falavigna da Rocha, 2009).

Two drops of polyvinyl lactophenol (diluted using 70% ethanol to avoid shrinkage of the material) were pipetted onto the plain slide, then the pre-stained larva was transferred to the mounting media using tungsten needles.

The specimens were dissected under a Leica MZ 16 stereomicroscope (Leica Microsystems, Wetzlar, Germany) using tungsten wire needles (Clark & Cuesta, 2015). After arranging the position of the appendages using fine needles, the slide was left to harden under ambient conditions. After the mounting media had hardened for approximately 2−3 hours, 2 further drops of diluted polyvinyl lactophenol were added and the preparation was covered using 0.17 mm thick coverslips (No 1.5). Cover slips were sealed with clear nail- varnish as described in Clark *et al*. (1998b) to prevent air bubbles from creeping into the sample as the mountant dried. Prepared slides were left in microscope slide boxes at room temperature for 24 h to allow them to harden prior to CLSM imaging.

Glycerine and dissection

Stained zoeae (ZI and ZII) were removed from the stain and transferred into a well slide containing a solution of 10% glycerine and 90% deionised water. This solution

prevented shrinkage when transferring the larvae from the stain to glycerine for dissection, but this solution concentration was varied according to the stage and size of the larvae, for example, 25% glycerine and 75% deionised water was used for ZIII and ZIV, and 50% glycerine and 50% deionised water was used for ZV and ZVI. Before dissection, glass slides were prepared using self-adhesive reinforcement rings (Fig. 2.5b).

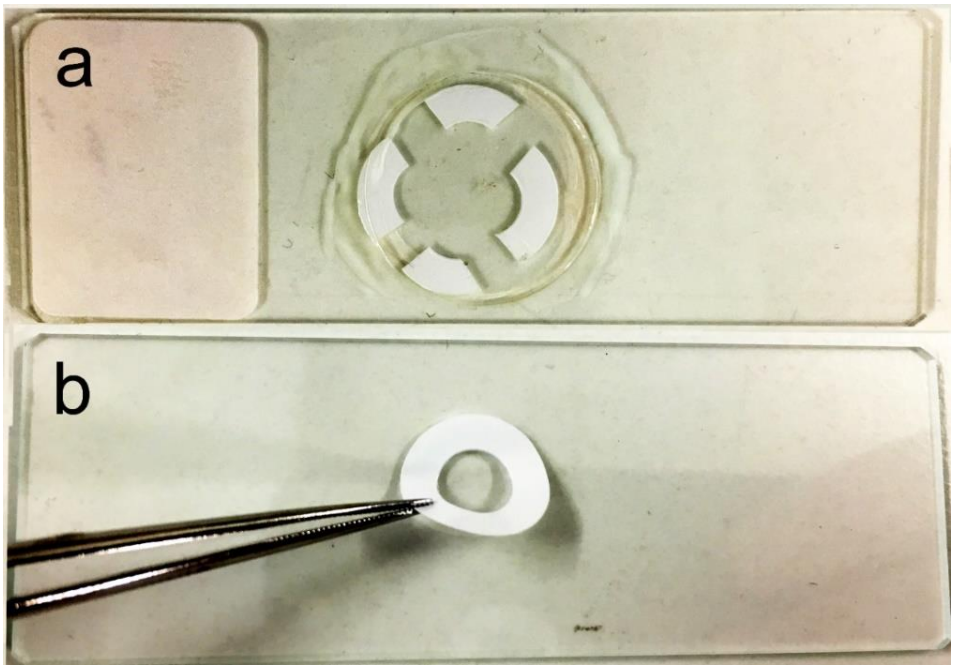

Figure 2.5: (a) Slides embedded in polyvinyl lactophenol. (b) Gluing reinforcement rings.

Cavity wells were constructed from reinforcement rings (as described above). Two to three droplets of glycerine solution were pipetted into the well. The larvae were then dissected. After dissection, the mouthparts (antennule, antenna, maxillule, maxilla and maxillipeds) were individually transferred into the prepared cavities of the glass slides (Fig. 2.6). This ensured that the slide had a clean, debris-free background for confocal microscopy scanning. Depending on the size of the specimens and appendages, the number of rings could be increased (Michels & Büntzow, 2010). For example, 2 self-

adhesive reinforcement rings were used to embed the mouthparts of the zoea IV−VI stages of larvae. 4 rings were used to scan whole zoea I crab larvae. For pleon, depending on the zoeal stage, between 4−8 reinforcement rings were used. After the appendages had been placed into the cavities, they were carefully covered using a cover slip (Fig. 2.6). After dissection and mounting, slides were kept in the dark at room temperature prior to scanning since Congo red and acid fuchsin are affected by light.

Using tungsten wire needles

Tungsten wire needles are widely used in dissection of small specimens such as brachyuran crab zoea (Clark & Cuesta, 2015), entomology material (Brady, 1965) and embryology (Packard *et al*., 2000). Sharpened tungsten wire provides an extremely fine and sufficiently strong needle for dissection that does not bend easily and can cut precisely. Tungsten wire can be sharpened electrolytically in aqueous KOH (potassium hydroxide) by applying low voltage across two terminals (Clark *et al*., 1998b). The needles are then fitted to handles for use. The finest needles were mostly needed to dissect the smallest zoea stage (zoea I or zoea II) of brachyuran larvae (see Appendix 5 for details).

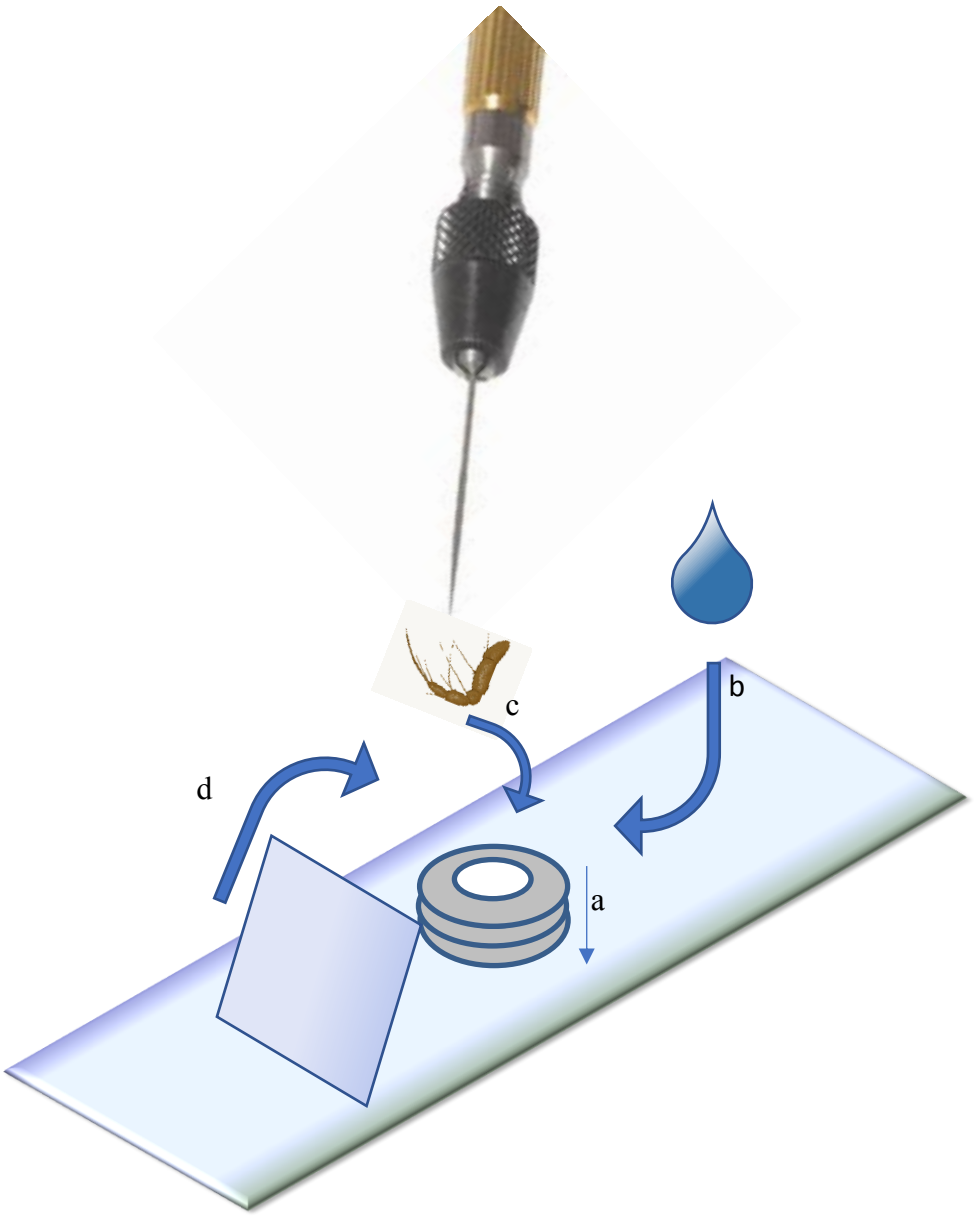

Figure 2.6: Schematic illustration of the mounting method. (a) Self-adhesive reinforcement rings are glued on the slide; (b) A few drops of the mixture of diluted glycerine are dropped into the rings; (c) Appendage of the specimen is placed inside the mounting media using the fine needles; (d) Cover slip is placed on the rings carefully to avoid air bubble formations.

2.2.3.2 Confocal laser scanning microscopy

Larval appendages were mainly scanned using a Nikon A1-Si confocal laser scanning microscopy (CLSM). Other brands of confocal microscope including Olympus, Zeiss and Leica were used to ensure that the tested workflow was universally applicable to data from any CLSM. There are many books, handbooks or publications available which describe the working principle of confocal microscopes.

Confocal microscopy working principle (Ball et al., 2017a)

"*The confocal microscope scans a laser spot across the sample to excite fluorescence from the sample. The emitted fluorescent light passes from the specimen back through the optical train (i.e., the optical and mechanical components of the microscope) and through a pinhole, sized to allow only focused light rays to reach the detector. As a result, each image frame represents a single focal plane. By moving the stage in the Z plane, additional focal planes are collected, with the end-result being a stack of slices forming a registered 3-D dataset that can subsequently be reconstructed and rendered for visualization from different orientations.*

The output format from a confocal microscope is a stack of aligned image frames. Each frame reflects a single optical plane and image channel (i.e., representing a portion of the emitted signal within a specific wavelength range), and the dataset is typically grouped by channel and image plane. Thus, a stack of 50 slices in three channels would be packaged as 150 frames in three groups of 50.

A typical confocal microscope has several lasers of different wavelengths. For example, at ~400 nm for near-UV excitation, in the range 450–500 nm for blue light, 500–550 nm

for green light, 550–570 nm for yellow light, 600–630 nm for orange, and >640 nm for red light excitation, a typical, four-laser setup might include 405, 488, 561, and 640 nm.

The theoretical resolution of a confocal microscope is defined by: 1) the numerical aperture of the lens (i.e., a measure of its ability to gather light and resolve fine-specimen detail at a fixed object distance); 2) the wavelength of the excitatory light (i.e., the wavelength generated by the laser used for fluorescence excitation); and 3) the refractive index of the medium under examination, measured as the change in the speed of light as it passes from a vacuum (or air as an approximation) into that medium. This normally equates to a spatial resolution in the X/Y plane of approximately half the illumination wavelength (i.e., for green excitatory light of ~550 nm, the resolution would be expected to be in the range of 200–300 nm). However, in the Z plane, the resolution is considerably reduced, and therefore is typically two to three times worse than the lateral resolution. Confocal datasets thus have nonisotropic voxels. This has implications for 3-D reconstruction and for morphometric analysis. In practical terms, the greatest factors in the ability to resolve features of interest are the topography of the specimen (which can prevent the use of high-resolution, high numerical- aperture lenses), the strength of the emitted fluorescent signal (balancing the signal-to-noise ratio), and the opacity of the specimen medium (which can scatter the laser and reduce signal strength)".

The present study used all available lasers at the excitation wavelengths of 405 nm, 488 nm, 561 nm and 640 nm (Fig. 2.7).

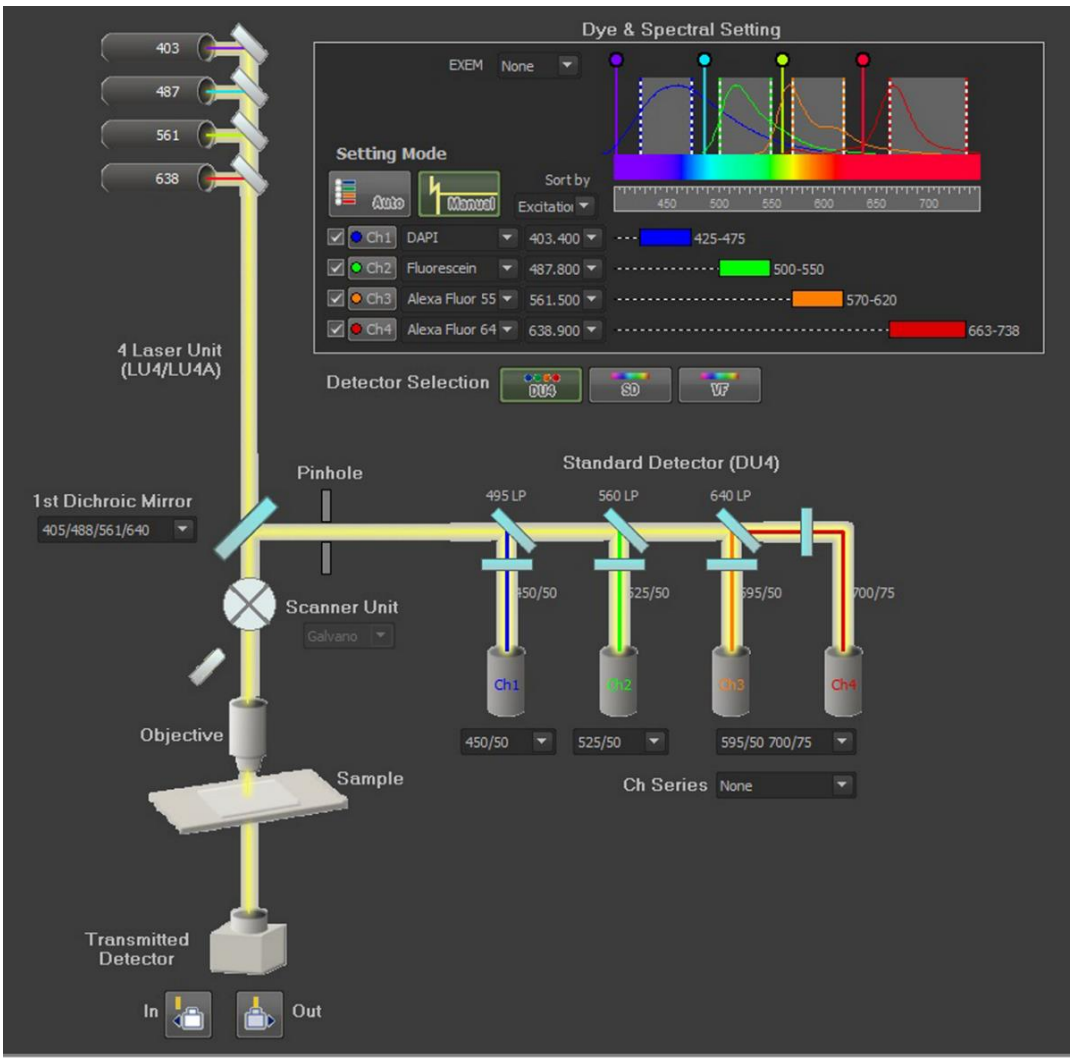

Figure 2.7: The Nikon graphical user interface showing the schematic light path through the instrument with the various selected settings. Represented colours as channels in specific nm levels. Ch1 = blue channel at the wavelength of 403 nm; Ch2 = green channel at wavelength of 487 nm; Ch3 = orange channel at the wavelength of 561 nm; Ch4 = red channel at the wavelength of 638 nm.

In addition to this information, CLSM manufacturers provide guidelines specific to their own brands. This information can be found on their websites: Zeiss Microscopy Online Campus, http://zeiss-campus.magnet.fsu.edu/index.html; Nikon Microscopy, http://www.microscopyu.com/; Leica Science Lab, https://www.leica-

microsystems.com/science-lab/; Olympus Microscopy Resource Centre, http://www.olympusmicro.com/.

The applications, workflows or final data format of each brand differ, but the major applications of the confocal settings will be explained for the Nikon A1-Si as this was the instrument used at the Natural History Museum, London. The processing of data obtained using other brands of CLSM data will be explained in the post-processing section as a common workflow has been developed for all microscopes.

Confocal microscopy workflow

After placing the slide on the mechanical microscope stage, the specimen was focussed and positioned ready for scanning. This made use of the standard optical microscope in the confocal system and could employ additional contrast methods (DIC, phase contrast), however, since the specimens were already stained, in practice these were not required.

Obtaining confocal images

The format of all image tiles captured was 1024×1024 pixels. This produced the optimum resolution images for 3D software programmes to process. 512 × 512 pixel images were insufficient for the present samples and use of the 2048 × 2048 pixel images was found to be undesirable since it quadruples the scanning duration and can cause bleaching of the stained specimen.

Acquisition times were manually adjusted to deliver an acceptable background noise level and slides were typically scanned with 2× frame averaging (see Appendix 6: *Obtaining confocal images*). Averaging time was used to improve signal noise ratio.

"Pinhole" which eliminates out of focus light and increases the resolution of the images was set to 1.2 AU (airy unit) for each sample in the present study (see Appendix 6: *Obtaining confocal images*). This gave a good balance between signal level and z-slice resolution.

Channel settings and Image acquisitions

Although an excitation wavelength of 561 nm was recommended by Michels & Büntzow (2010) to match the optimal fluorescence of Congo red, a wavelength of 638 nm was found to be effective. As the zoeae also exhibit autofluorescence when illuminated at excitation wavelengths of 403 and 487 nm, during scanning, all available wavelengths were used so that no data were missed.

For each preparation, the most appropriate objectives were chosen to match the size of the appendages. For larger appendages, such as the pleon, a 20× dry objective with a numerical aperture (N.A.) of 0.75 was used to obtain a general image before scanning at a higher magnification. Oil immersion objectives were used to increase resolving power of the microscope for scanning at 40× with N.A. of 1.30 and 60× with N.A. of 1.4 to produce higher resolution images of smaller larval appendages (see Appendix 6: *Channel settings and Image acquisitions*).

The instrument's signal brightness and contrast (gain and offset) were set to give a black background and appropriate signal strength (avoiding over saturation) for each specimen and image stack collection task.

For image setting, the Z-intensity correction function was used to avoid producing oversaturated images. This function provided an opportunity to make adjustments

between oversaturated or under saturated layers (see Appendix 6: *Channel settings and Image acquisitions*).

Two options were applied to scan large appendages at higher magnification using CLSM. The first method used a software option of the microscope called "large images" which scans the sample in discrete areas known as tiles. The large images software option automatically stitches the tile together after scanning. Whilst it was found to be challenging to set the gain and offset settings correctly, by applying these settings to all tiles at the same time, it gave precise results for larger specimens using higher magnification objectives.

However, using the "large images" option results in extended scan times and the resulting data sets can be extremely large. Manipulating such data sets may present problems during post-processing unless a powerful computer is available. A second option was to scan the sample in sections (i.e. basis and endopod separately) and after applying ImageJ and Drishti, to each section individually, then merging them using Adobe Photoshop. In this case, the datasets are smaller and easier to process.

Confocal datasets were saved in the native Nikon ND2 format which saves all of the experimental metadata and allows it to be restored so that experiments can be repeated using exactly the same microscope conditions. Other confocal microscopes use a similar "packaged" file format: Leica use a format ***.lif; Olympus's file format is ***.oib files and Zeiss microscope use ***.czi files (Fig. 2.8). Each manufacturer provides its own software package to manipulate the data. FV10−ASW 4.2 software was developed by Olympus for the Fluoview FV1000 IX81 inverted microscope; ZEN lite imaging software for the Zeiss LSM 880 airy scan upright confocal microscope; LAS AF 2.2.1 software was used by Leica for the TCS SP5 equipped with a Leica DM5000 B and NIS-Elements viewer (version 4.20) by Nikon. A demo version of the NIS-Elements

viewer software (version 4.20) is freely available from the Nikon website: https://www.nikoninstruments.com/en_GB/Products/Software/NIS-Elements Advanced-Research/NIS-Elements-Viewer.

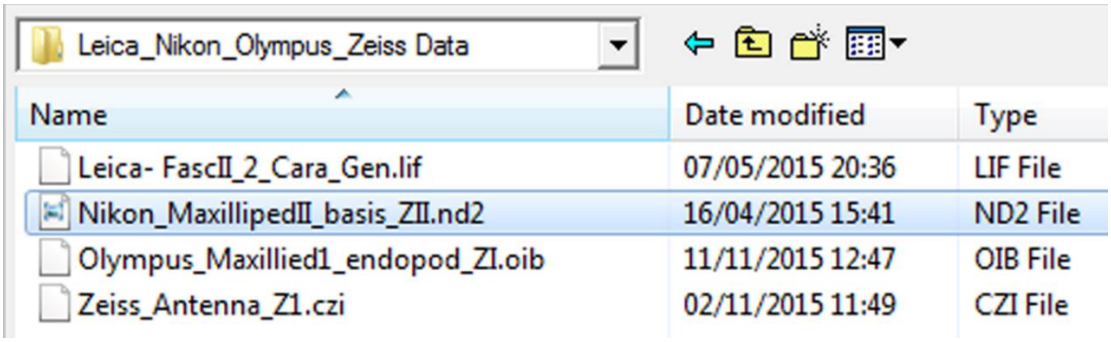

Figure 2.8: File formats of the different confocal microscopes. Leica uses ***.lif files. Nikon uses ***.nd2 files. Olympus uses ***.oib files. Zeiss uses ***. Czi files (Kamanli *et al.*, 2017).

However, these proprietary formats are not easily processed by other software, so data must be exported in the form of image stacks or single images, typically as "Maximum Intensity Projections (MIP)". An MIP image is composed of the brightest pixel along the Z axis at any X/Y position. An alternative would be the Average Intensity Projection (AIP) which uses the average value for each pixel (Ball *et al.*, 2017a).

Using CLSM for scanning gonopods

The left gonopods (G1) were dissected away from the adult male *Eriocheir* crabs of (see Table App. 8.1 in appendix 1) and placed in a petri dish. The distal ends of the gonopods were carefully cleaned using a fine paint brush to remove all unwanted particles. Then, the gonopods were stained with a mixture of Congo red and acid fuchsin for 24 hours. After staining, they were washed using deionised water. The

gonopod of adult Chinese mitten crab from the River Thames was too large (ca. 2.2 cm) to embed on a normal glass slide with coverslip. Other samples including gonopod (G1) of *E. hepuensis* and *E. japonica* gonopods, were also too large for the standard cavity slide. Therefore, a new platform was designed for scanning using CLSM.

The embedding platform comprised a glass gutter formed from 2 groups of 7 slacked microscope slides glued to each other using polyvinyl lactophenol. These were then fixed to a larger piece of glass to form a deep gutter which was dammed at end by Blu Tack® (Bostik Ltd., England). The gonopod was placed in the gutter ventral side up and firmly held using more Blu Tack® in order to keep it completely immobilised during the proposed 12 hour scan. The gutter was then filled using 100% glycerine until reaching the highest level of the stacked slides and then examined for any signs of air bubbles. If present, these were carefully removed using a fine tungsten wire needle. A rectangular coverslip (No. 1.5) was used to seal off the pleopods avoiding any additional inclusion of air bubbles. Avoidance of air bubbles was considered critical as they would expand during the 12h session due to the heat from the lasers and prevent a sharp image (Fig. 2.9).

After preparing the platform and embedding the G1 inside the channel, tape was fitted around the microscope slide to secure the platform and prevent leaking of glycerine. Then, the platform was carefully placed on the mechanical stage of the confocal microscope. In order to hold the large platform (Fig. 2.10) stable for long acquisition time, the edges of the platform were secured using Blu Tack® before scanning. This prevented the movement of the platform when the “large images” option was applied and when changing the position of the platform to scan each tile. Between 16−25 tiles were required to scan the tip of the gonopods.

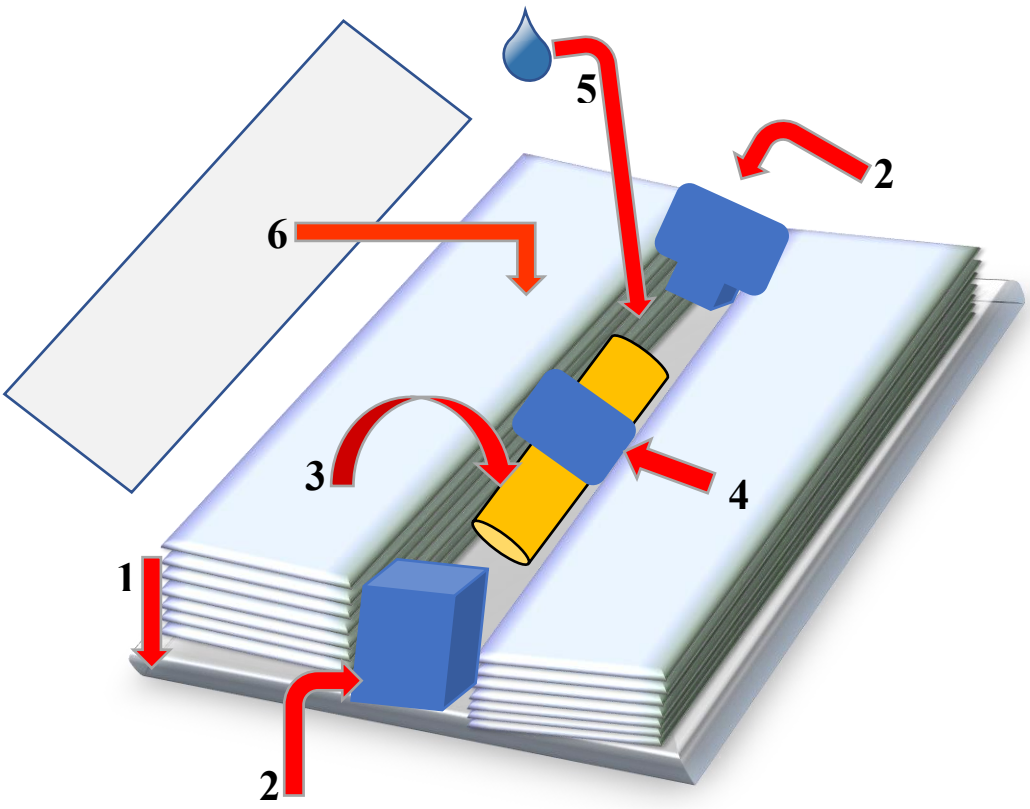

Figure 2.9: Schematic illustration of the designed platform used to hold the male gonopod firmly during 10−12 hours of confocal scanning (CLSM): (1) Two groups of 7 microscope slides were glued each other using polyvinyl lactophenol and these merged microscope slides were glued on each side of the glass/plastic platform; (2) Two sides of the new platform was sealed using Blu Tack®. The level of the Blu Tack® and microscope slides were levelled by using a cylindrical metal holder; (3) The male gonopod was placed and arranged inside the slide channel; (4) The gonopod was covered using Blu Tack® to immobilise it during long duration scanning; (5) The channel was filled with 100% glycerine until it reached the highest level of the adjacent slides; (6) The channel was covered with a long coverslip (avoiding the inclusion of air).

10× dry objective with N.A. of 0.3 was used to scan the surface of the gonopod in conjunction with the “large images” option of the confocal software. Four lasers at wavelengths of 405 nm, 488 nm, 561 nm and 640 nm were used to produce this maximum intensity projection. The Nikon software (NIS-Elements viewer version 4.20) was used for image stitching to combine tiled areas. Adobe Photoshop was applied to final image to adjust brightness/contrast, to remove a few unwanted particles and to provide a black background.

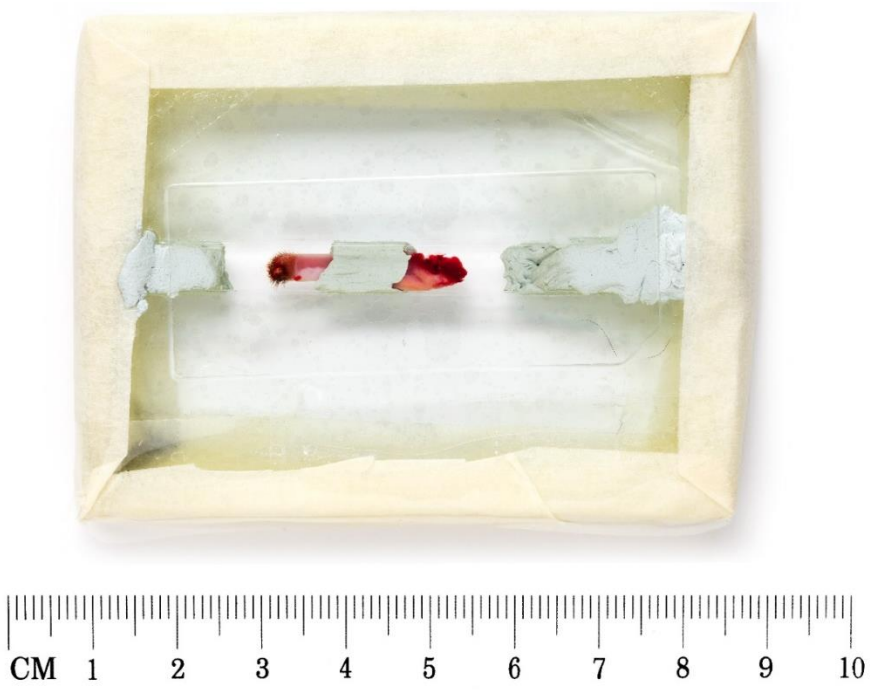

Figure 2.10: A general view of designed platform to scan large appendages using CLSM. The G1 pictured was removed from an *Eriocheir* (specimen captured in Hollands Diep, Netherlands).

Image data processing

The Nikon confocal microscope software includes basic data and image manipulation tools which can be used to generate projection images, carry out simple image maths

(background subtraction for example), basic data analysis and create simple movies. However, it has limited functionality and different confocal manufacturer's software packages also differ in capability. As a single example, in the present study, setules of the appendages (fine structures with a relatively low signal level), proved challenging to scan. To specifically visualise the setules, the offset was increased in order to make them apparent; this would also apply to any similar fine arthropod feature (fine setae, scales etc.).

Increasing the offset resulted in a noisy background. This could be compensated for in the Nikon software by subtracting the image background by selecting a square area in the noisy background. The software then subtracts the background around the specimen. This would apply a clean background when viewing the image using confocal software (Figure 2.11). However, the results were not entirely effective (see Fig. 4.10 in Chapter 4). It is clear from this single example that more capable software programmes are required, but the commercial software packages available are: 1) very expensive and 2) designed to process data for fluorescent anti-body labelled data, usually for cell biology and are thus not entirely suited for rendering surface information. A key aim of this study was to develop universally applicable workflows which could be applied to confocal data from any source instrument. This requires access to the raw data from the microscope. In a confocal microscope, each emission channel (the signal data emitted from the sample and collected by the detector) is split into individual channels. Each channel corresponding to an individual detector setting. For example, a single laser line with one excitation wavelength could be examined with a number of different detectors, leading to more than one detected channel. All confocal microscopes give the option to either merge the data channels into a single merged image stack, or to export individual channels as a series of numbered image stacks (channel 1, 2 3 etc.). Experiments were

carried out to determine if merged data, or individual channel data yielded the best results for subsequent data processing steps.

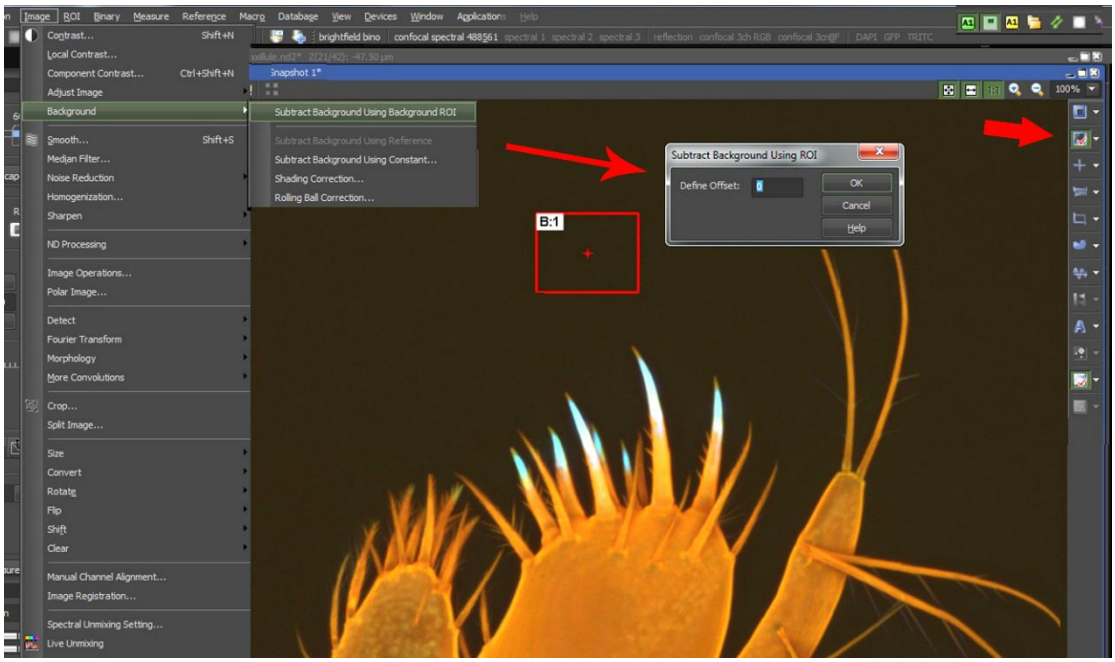

Figure 2.11: Compensating images having noisy background after increasing the offset.

2.2.3.3 Post-processing confocal data using ImageJ and Drishti

Post-processing, using 3D surface rendering, is an essential way to view the confocal data. Although, most confocal microscope companies offer their own basic 3D visualisation software programmes, their functionality and capacity can be limited (Ball *et al*., 2017a). In addition, CLSM software is mostly optimised for generating transparent and fluorescent images (Kamanli *et al*., 2017). Furthermore, commercial software programmes capable of producing this type of visualisation tend to be expensive (Kamanli *et al*., 2017). Therefore, the present study created its own method to produce 3D images using open source software programmes which are available for free. Other commercial software programmes, such as Avizo, VGStudio Max (version

2.2) were also trialled. However, no considerable difference was found in the final images. Additionally, using ImageJ followed by Drishti was found to be more effective in terms of availability and the quality of the pictures and functions offered.

As shown in the workflow developed (Fig. 2.3), after obtaining the confocal data, there are two possible ways to process it using Drishti. The first method required using the confocal manufacturer's software programmes, to pre-process the data prior to importing it into Drishti whilst the second method required using ImageJ to carry out the pre-processing.

Data pre-processing is a two-step process of exporting the data as a staff of TIFF images and then combining the image channels to produce a single image stack.

Exporting stack data as TIFF images using Nikon confocal microscopy software

Image stacks were exported as 16-bit TIFF images from the experimental data using Nikon NIS-Elements (version 4.20). This generates a single folder containing a number of image stacks (dependent on the number of active channels in the experiment). Each folder contains a series of TIFF images (the "tiff stack") numbered sequentially representing the different focal planes (z positions) for the data (Figure 2.12). If the experiment is making use of autofluorescence in a single channel, then it is only necessary to export the relevant channel into the reconstruction software. If the experiment uses multi-channel fluorescence, then each channel needs to be exported separately. Typically, only a single channel was selected for 3D modelling. For Congo red and acid fuchsin stained materials, the signal corresponding to excitation from the 561nm (orange) laser (emission wavelengths between 561 and 620 nm) was found to be optimal.

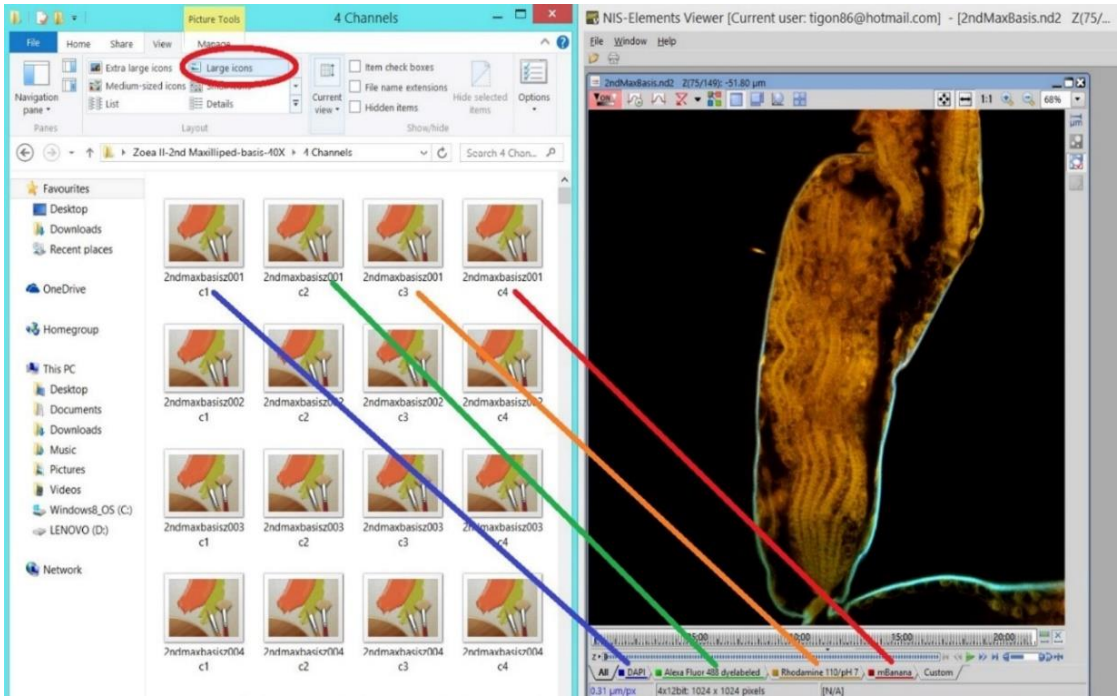

Figure 2.12: Illustration of channels according to wavelengths. c1 represents blue channel (405 nm), c2 represents green channel (488 nm), c3 represents orange channel (561 nm) and c4 represents red channel (640 nm).

Before importing the data into Drishti, the datasets X, Y and Z values were noted from the image properties and experimental data. This gives the value for pixel size in the X/Y dimensions and the Z interval (step-size). These properties are required for accurate 3D reconstruction using Drishti (see Appendix 6: *Exporting stack data as TIFF images using Nikon confocal microscopy software*).

Exporting stack data using ImageJ

The second method for importing image stacks into Drishti involved the use of ImageJ. Instead of using the confocal software, the image stacks were opened directly into ImageJ which splits the stack data into channels which can be viewed independently. At this point, the "image properties" (X/Y pixel size and Z slice interval) were noted (from

ImageJ) in order to produce a scale bar later in Drishti. Any channels considered to be of insufficient quality could be ignored and the remaining channels merged. The advantage of using ImageJ is that merged channels can be converted to 8-bit greyscale composite images creating one common workflow for data from any confocal microscope. The merged images can then be exported into Drishti via its Drishtiimport programme. This process is described in detail in Appendix 6: *Exporting stack data using ImageJ*.

Single and multi-channel data can be easily manipulated by Drishti and produce images of much greater resolution. Whichever workflow was chosen, the new folder was then imported into Drishtiimport which standardises the data and creates a volume file. The user has the option to individually import all the channels into Drishtiimport to be saved as volumes. Although Drishti does provide an option to load more than one volume, the size of the files can be extremely large and may prevent the programme from operating. Furthermore, there was a tendency for resulting images to be over saturated. Therefore, merging the channels using ImageJ prior to import into Drishti was found to be the preferred method (see Appendix 6: *Exporting stack data using ImageJ*).

Visualisation of data using Drishti (3D Visualisation)

The volume files (***.pvl.nc) created using Drishtiimport were imported into Drishti for processing and visualisation in 3D. Before visualising the volumes in high resolution, the images were cropped in 3D to exclude any data that was outside of the area of interest on the appendages. Adjusting the lighting option helped to visualise the setae on the appendages (see Appendix 6: *Application of Drishti*).

As well as visualising the surface characters on the appendages in detail, Drishti allowed the 3D specimen dataset to be reoriented and images of the virtual specimen to

be taken from different angles. Consequently, the exact number of setae and other details could be accurately determined. Since Drishti includes advanced lighting models, adjusting the lighting option helped to visualise the setae on the appendages. Drishti includes advanced data manipulation functions including the possibility to edit 3D volumes. One of the most helpful options of the programme was the ability to use this function to remove debris or unwanted tissues on the images in 3D.

Adding a scale bar and increasing the image quality was also possible using the programme. Finally, complex videos could be produced from the 3D datasets, including the option to "virtually" dissect specimens within the movie.

After acquiring the required viewpoints in Drishti and exporting them as images, final adjustments to brightness and contrast (through use of the "levels" function) were made using Adobe Photoshop. Photoshop was also used for general image editing including cropping images, adding text and arrows, scale bars etc. as required for publication (see Appendix 6: *Visualisation of data using Drishti (3D Visualisation*).

Digital dissection (segmentation) instructions

Unprocessed CLSM datasets frequently contained fragments of dissected debris and additional tissue which appeared to "float" in the 3D volume or which were attached to appendages. This unwanted data can be removed (cleaned) using Adobe Photoshop, but such editing may pose ethical issues with regards to alteration of the image since areas "behind" the fragment would also be removed and need to be "cloned" back into the image.

A much better option was to remove the unwanted scanned fragments directly from the 3D volume using Drishti to rotate the specimen. From examination of the rotated

specimen, the viewer can determine whether the fragment was a part of the specimen. If not, it can be removed to allow for an improved visualisation of the specimen. 3D volume manipulation therefore allowed for the specimen to be digitally dissected in post-processing and this was considered to be a much more powerful technique than simple 2D image manipulation (see Appendix 6: *Digital dissection (segmentation) instructions*). After the 3D manipulation process, a 2D image was saved and edited in Photoshop.

The confocal data can also be used for creating short videos using Drishti (see Appendix 6: *Preparing videos using Drishti*).

2.2.4 Macro confocal scanning

A disadvantage of conventional confocal microscopes is their reliance on conventional microscopes and optics. This means that to obtain overview images of larger specimens requires extensive scanning in X/Y and Z to build up the area and 3D data required. Using lower power objectives still required X/Y scanning and with relatively poor numerical apertures, data acquired from these lenses was not suitable for 3D reconstruction and did not show fine surface detail (setae, setules).

Macro confocal systems are available which use optics derived from stereo microscopes. These offer a larger field of view and relatively better numerical aperture. For example, the Nikon AZ100 offers a 5× objective with a numerical aperture of 0.5 compared to the lowest magnification objective fitted to the NHM's Nikon A1 (10× N.A. 0.3). During this study, A Nikon AZ100-C1 high definition macro confocal system was tested with a view to have better images of the larger appendages or late zoeal stage larvae of the Chinese mitten crab. The same preparation method created for CLSM in the present study was followed for the use of macro confocal. All appendages/larvae

were embedded in glycerine using reinforcement rings to form wells. Other similar systems are available from Zeiss (as a structured light microscope) in the form of the Axio Zoom.V16 with ApoTome.2 and from Leica (TSC LSI) as well as add-on structured light or spinning disk confocal fluorescence systems which can be added to zoom microscopes (e.g. Andor Revolution DSD).

2.2.5 SEM preparation

SEM uses electron beams that pass thorough electron lenses of the specimens examined (Oatley *et al.*, 1965). It produces the images by simply scanning the surface of the samples. SEM has the high capacity of producing surface images even for details less than 1 nm (Hafner, 2007). However, obtaining the high-resolution images requires extensive sample preparation such as cleaning, dehydration, embedding and coating. Cleaning is required to get rid of artefacts (Oatley *et al.*, 1965; Felgenhauer, 1987), whereas coating the samples is required in order to avoid the build-up surface electrical surface charge (Hafner, 2007; Ball *et al.*,2017b). Furthermore, Ball *et al.* (2017b) stated that coated samples help to accelerate acquisition times as well as preventing "noisy" images.

In the present study, laboratory hatched mitten crab zoeae previously fixed in 70% ethanol and deposited in the crustacean reference collections of the NHM, were used for SEM examination. Zoea (I−VI) larvae contaminated with debris were cleaned using Decon 90. The specimens were then pipetted into deionised water for 5 minutes and washed thoroughly including three changes of 5 minutes each. Next, the specimens were transferred to 30% ethanol from distilled water as the first step of the dehydration process. This was left for 30 minutes and later refilled with 30% ethanol for another 30

minutes. Then this step was applied to each concentration of the following until 100% dried ethanol.

50% ethanol (2 × 30 min)

70% ethanol (2 × 30 min)

80% ethanol (2 × 30 min)

90% ethanol (2 × 30 min)

95% ethanol (2 × 30 min)

100% dried ethanol (2 × 30 min)

The specimens were then critical point dried (Balzer CPD20) prior to mounting and coating with 20 nm of gold-palladium (Cressington HR208 coater) for SEM observation.

Coated specimens were examined at an accelerating voltage of 5 kV using a Zeiss Ultra Plus Field Emission SEM and FEI Quanta 650 FEG SEM, whereas uncoated samples were examined in variable pressure mode at 20 Pa at an accelerating voltage of 20 kV using a LEO 1455 VP SEM using an Oxford XMax 80 EDX detector with Oxford Inca software to carry out spot analysis for qualitative EDX (X-ray spectroscopy) analysis.

2.2.6 Using micro-CT techniques and other microscopes for larger samples

One of the disadvantages of confocal microscope is their limited ability to scan larger specimens. The lasers penetration ability is also restricted. In such cases, micro-CT can be a great alternative in terms of being both a non-destructive method and providing 3D datasets for detailed examinations. This non-destructive technique uses x-rays to produce cross-sections of the samples (Ball *et al.*, 2017b). The emitted x-rays from the

x-ray generator are recorded to create 3D volumes. This method has been successfully used in many areas as well as the arthropods. In the present study, it has been applied to visualise larger specimens/appendages where CLSM was found to be limited.

Fixed specimens

Specimens fixed with 70% ethanol were stained (using iodine) to improve the X-ray contrast and to reveal soft tissue. The megalopa and crab I stage of the Chinese mitten crab were individually transferred into a glass jar containing 1% iodine in 70% ethanol using a needle and left in iodine solution for a week. Then the samples were transferred into a cut-down plastic pipette in order to hold them steady during the Micro-CT scan. The narrow part of the plastic pipette was put in a length of drinking straw and glued using epoxy adhesive. The end point of the pipette was blocked using epoxy and a section of toothpick to prevent ethanol leaking out. A piece of the plastic cut from the pipette bulb was put inside the container to hold the sample off the bottom of the receptacle. The container was filled with 70% ethanol to prevent the sample from drying out. Finally, the container was covered using Parafilm M® (Fig. 2.13) to avoid evaporation during the scan.

The samples were scanned using a Nikon Metrology HMX ST 225 micro-CT scanner. The final data were processed using Drishti software programme by converting the data into a TIFF stack using VGStudio Max.

Figure 2.13: Container designed to hold samples during micro-CT scanning.

Dry specimens

An extremely old dry fragile specimen of *Monomia argentata* A. Milne-Edwards, 1861, was scanned at 120 kV using a Zeiss Versa 520 Micro-CT system. 3142 X-ray projections were taken over 360° rotation in order to create this image. In order to confirm the species identity of the dry specimen, the morphology of the gonopod (G1) needed to be visualised without destroying/dissecting the crab. After CT scanning, the data was processed using Drishti (Fig. 2.14a-b). In order to view the G1, the image was digitally dissected to generate virtual clipping planes (Fig. 2.14c). Clipping planes were used to produce a digital cross section of the image. After re-arranging the colour interface, the G1 became visible (Fig. 2.14d).

As surface features such as the exoskeleton of the crab blocked the view of the internal G1, the image needed to be edited. These unwanted regions were systematically removed in software. After clearing the external components from around the G1, the appendage became visible. After rotating the image into suitable position, the G1 could

be visualised in ventral aspect. As a final step, Adobe Photoshop (CS3) was used to clean the remaining parts of the external components.

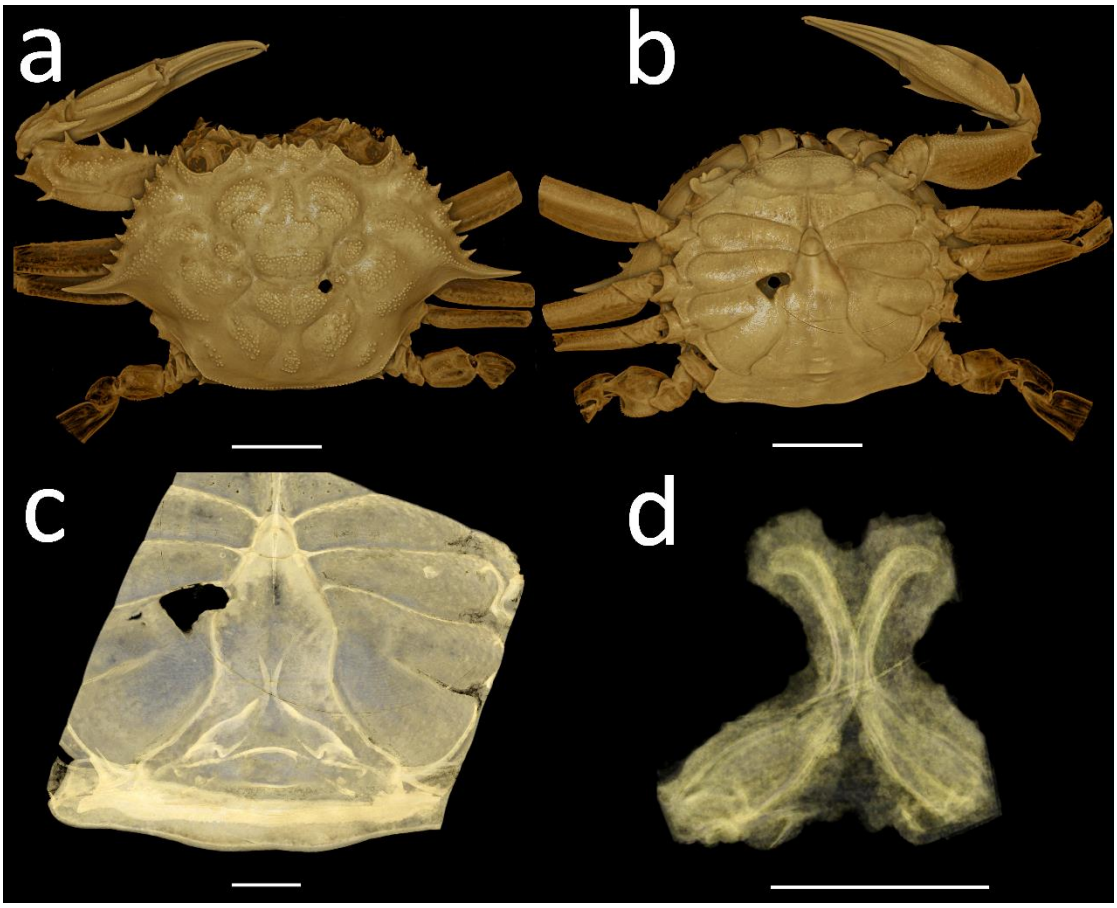

Figure 2.14: Resulting scanning dry specimen, *Monomia argentata*, using a Nikon Metrology HMX ST 225 micro-CT scanner and processing with Drishti. (a) Dorsal side of the sample. (b) Ventral side of the sample. (c) Viewing the G1 by clipping and carving the image using Drishti. (d) Making the gonopods visible without destroying the old, fragile dry crab.

Scanning large gonopods using Micro-CT

Gonopods were also scanned using a micro-CT. The G1 was placed inside a micro centrifuge tube. The base of the micro-centrifuge tube was filled using Blu tack® to hold the G1 firmly and then the tube was filled with 70% ethanol (Fig. 2.15).

Figure 2.15: Scanning a large G1 using high resolution micro-CT. The G1 was placed inside a micro-centrifuge tube filled with 70% ethanol.

After closing the lid, the tip of the tube was wrapped using Parafilm M® to prevent the alcohol from evaporating and G1 from drying out. Next, the tube was placed onto the sample holder in the CT scanner and the gonopods were scanned at 50kV using a Metris X-Tek HMX ST 225 (Nikon) micro-CT system. Between 940986 X-ray projections were taken over 360° rotation in order to create the images. Data was processed using Drishti and Adobe Photoshop for the final corrections.

Light microscopy

A Zeiss Axio zoom V16 stereo zoom microscope was also used to visualise the megalopa and first crab stage of the Chinese mitten crab. All samples were fixed in 70% ethanol in a watch glass prior to data capture.

2.2.7 Other post-processing software packages

VGStudio Max (version 2.2) was trialled to visualise confocal and micro-CT data. For micro-CT data, it was initially used to view the samples immediately after the scanning and to convert the data into TIFF stack formats. It was also used to stitch the confocal datasets from large area scanning experiments.

Amira Avizo 3D, a commercial programme, was also trialled for editing confocal data. It was used as an alternative method to Drishti.

Zeiss XM 3D viewer (version 1.2.8) was used to visualise x-ray microtomography data derived from the Zeiss Versa 520 and converting it to TIFF images for processing in Drishti.

Zeiss' ZEN lite (version 2.1) imaging software was used to view larger image data (i.e. megalopa and crab I stage) from the Zeiss Axio zoom V16 stereo zoom microscope.

All images and some videos captured in the present study are available at full resolution on the enclosed DVD.

CHAPTER 3

FECUNDITY AND BROOD POTENTIAL OF THE CHINESE MITTEN CRAB IN THE RIVER THAMES

This chapter investigates the fecundity of ovigerous female mitten crabs which were caught in the River Thames and examines their potential for producing more than one brood of eggs from a single mating.

3.1 Reproduction of the Chinese mitten crab

Crustacean reproduction is an important area of research for aquaculture and other purposes (Sarda, 1991). The reproductive strategies of brachyuran crabs differ between closely related species (Erdman *et al.*, 1991) and within same species because of the environmental conditions such as ecological niches and latitude (Krouse, 1980). Therefore, acquiring more information on the reproductive strategy of different species or indeed the same species which are dispersed over different geographic areas is essential (Sudha & Anilkumar, 1996). In order to estimate the reproductive output of crustaceans, the egg biomass spawned within one reproductive season is considered (Stella *et al.*, 1996). Brachyuran crabs show a wide range of reproductive strategies but the subject requires further attention (Erdman *et al.*, 1991; Sudha & Anilkumar, 1996; Przemyslaw & Marcello, 2013). This can be explained with respect to invasive brachyuran species such as the Chinese mitten crab by investigating their reproduction outside the native range to aid our understanding of the colonisation of new catchments, especially considering that they have the capacity of producing millions of larvae (APEM, 2010).

Fecundity between and within brachyuran species varies because of different factors such as ecological effects, regional differences, morphology and feeding habit

(Przemyslaw & Marcello, 2013). Studying fecundity of a brachyuran crab species in one specific region can provide an insight to population dynamics, life cycle as well as biology. The term fecundity was referred as "*the number of offspring produced by a female in a determined time period*" by Llodra (2002) stating that this should be defined specifically for each study. Some studies in marine biology specified the term fecundity according the specific studies such as "*potential fecundity*", "*realised fecundity*" "*actual fecundity*" and "*effective fecundity*" (Corey, 1987; Stechey & Somers, 1995; Swetha *et al*., 2015). García-Guerrero & Hendrickx (2004) defined this term with regards to the crabs as "*average number of eggs in ovigerous females and positively correlated with the size of the egg-bearing females*".

Hines (1988) discussed the relationship between body size and brood mass of female brachyuran crabs as well as their fecundity. He emphasised that body size is an important determinant of reproductive output (brood mass), that brood weight is about 10% of female body weight and egg size, which is another reproductive variable, was related to brood mass that results in variation in the fecundity of the female brachyurans (Hines, 1982). Anger (1995) also stated that adult female size is naturally related to egg size.

The fecundity of brachyuran crabs has been examined by many workers focusing on different regions and conditions (Hines, 1988; Elner & Beninger, 1995; Huang & Hsueh, 1998; Litulo, 2004; García-Guerrero & Hendrickx, 2004). These studies showed that there is a positive correlation between fecundity and the carapace width (Matsuura *et al.*, 1972; Carsen *et al.*, 1996; Turra & Leite, 2001; Kobayashi, 2001; Doi *et al.*, 2007).

It is known that, in Europe, the Chinese mitten crab spends 4−6 years freshwater before they migrate to higher salinity waters to reproduce (Anger, 1991). Some reports have

shown that they reach maturity much earlier in their native habitat (Hymanson, 1999; Jin *et al.*, 2002). Since the first report of a Chinese mitten crab at Lots Road Power station, Chelsea, in 1935, this invasive is now well established in the UK (see Herborg *et al.*, 2005; Fig. 1.3). Due to their extensive dispersal, they are now abundant in the River Thames and its tributaries spreading a further 150 km upstream and westwards of Staines to Didcot Power Station, just south of Oxford, in October 2010 (Clark *et al.*, 1998a; www.mittencrabs.org.uk). Studying their reproductive potential in the River Thames is therefore essential in understanding their breeding cycle in the lower estuary (Clark *et al.*, 1998a).

The maximum fecundity values for *E. sinensis* migrating to higher salinity/brackish waters to breed in the Thames Estuary are currently unknown. In invaded locations, female mitten crabs have generally been found to carry between 100,000 and one million eggs (Panning, 1938; Cohen & Carlton, 1995; Dittel & Epifaino, 2009; Fig. 3.1). In Polish waters, this value was found to be 140,000 and 680,000 (Przemyslaw & Marcello, 2013). The egg diameter of the Chinese mitten crab has been previously reported as 350 to 380 μm (Jin *et al*., 2002) or 361−375 μm (Przemyslaw & Marcello, 2013).

Considering the extensive reproductive potential of the Chinese mitten crab in the River Thames, the present study investigated the fecundity of these Thames crabs by estimating brood size relative to carapace size. The present study has used a limited number of ovigerous crabs from the Thames. This restricted preliminary study, however, can provide an insight for the equivalent for the potential future fecundity studies in the Thames. In addition, this can be taken as a reference study for comparative fecundity studies of the Chinese mitten crab in different geographic regions in the world.

Figure 3.1: An ovigerous Chinese mitten crab from the River Thames, London showing a mass of eggs attached to the pleon. Photo credit: http://www.nhm.ac.uk/our-science/our-work/biodiversity/report-your-invasive-crab-sightings.html.

3.2 Potential for multiple broods

The reproductive tract of female crabs has been previously detailed by many workers (see Harttnoll, 1986; Becker *et al.*, 2011; Vehof *et al.*, 2016) showing the sexual anatomy of the vulva, vagina, oviduct, spermatheca, oocytes and ovary (Fig. 3.2). They stated that sperm is transported as spermatophores to the vagina of the female via the gonopores of the male crabs during copulation. Copulation occurs after the female has moulted or after the carapace has hardened in brachyuran crabs (Epifanio, 2007). This situation was described by Hartnoll (1968) and reported that during the mid-intermoult, the vulva decalcifies for a short time which causes to have a "mobile operculum" before it re-calcifies in the water at a temperature of 24−25 ºC and becoming "immobile". This temporary decalcification is assumed to occur in all species which has an "immobile opercula" (Hartnoll, 1968; Becker *et al.*, 2011; Vehof *et al.*, 2016). It was also

emphasised that calcified opercula can be “mobile” due during intermoult as a result of local decalcification in some species (Vernet-Cornubert, 1958; Hartnoll, 1969; Becker *et al.*, 2011).

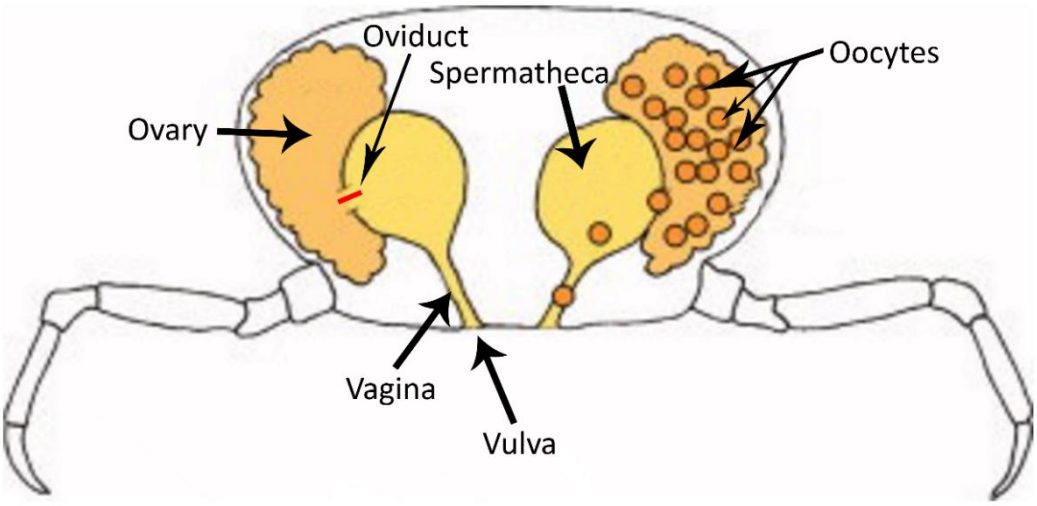

Figure 3.2: The female crab genital organs showing the reproductive organs (after Becker *et al.*, 2011).

In the case of Chinese mitten crabs, it has been reported that mating occurs when females and males are both in the intermoult stage and this is referred to as so-called “hard-shell mating” (Peters, 1938; Otto, 2012). This situation was observed in the closely related species *E. japonica*, by Kobayashi & Matsuura (1999). It is believed that the male deposits sperm in the seminal receptacles (spermatheca) of the female crab and, through storage, they then have the potential to produce more than one brood following a single mating event (Cohen & Carlton, 1995, 1997; Rudnick *et al*., 2000; Dittel & Epifanio, 2009).

Brooding duration ranges from a few days to several months in crabs (Dittel & Epifanio, 2009). The production of more than one brood following a single mating event has been reported in many brachyuran species. It has been suggested that *E.*

sinensis has the potential to produce more than one brood, but clear evidence for such a strategy has not been published (Panning, 1938; Dittel & Epifanio, 2009), although Kobayashi (2001) recorded three broods in the closely related *E. japonica* in one breeding season in its native habitat. The occurrence of this strategy in the UK waters, however, is still uncertain (APEM, 2010) and there are no data available for the duration of sperm storage of the Chinese mitten crab in the River Thames.

3.3 Aims

The overall aim of the present study is to provide more information on the fecundity of the mitten crab in the River Thames by examining brood volume, mean diameter of the eggs, volume of one egg for each crab and the total number of eggs on caught ovigerous crabs. Furthermore, the opportunity was taken to carry out observation in the laboratory to provide evidence for the capacity to produce more than one brood from a single mating.

3.4 Results

3.4.1 Brood experiment results

The egg colour of the crabs which were transported to RHUL marine aquarium in late November and early December 2013 was recorded before they were de-brooded. The colour of eggs of the crabs was found as brown, light brown, dark brown, purple and yellow. Of the 30 crabs, 24 had brown or brown tones to their eggs (Table 3.1); 5 crabs (D4, D6, D8, D9, D14) had purple eggs; 3 crabs (D26, D28 and D29) had both brown and yellow eggs and only one crab (D13) had all yellow eggs. Most of the crabs were too responsive for the de-brooding procedure to be completed in an acceptable manner, therefore, they were placed in freezer for ca. 15−45 minutes. This was found to be a

suitable time to ensure most of the crabs were less responsive and allowed debrooding to be performed effectively and without unnecessary damage to the animal. Larger and more active crabs such as D2 and D12 were left in freezer for longer time (60−90 minutes). D20 was not that responsive and revive from the freezer before de-brooding (Table 3.1). Mean freezing duration was found to be 34 minutes. A summary of the data for each variable is provided in Table 3.1.

Table 3.1: The condition index of 30 ovigerous female *Eriocheir sinensis* including colour of eggs when captured, carapace width (C.W.) and freezing duration to make the crabs "lethargic" for removal of eggs from the pleopods for brood experiments. De-brooded crabs were referred as D1, D2… D30.

Crab #	Collection date	Colour of eggs	C.W. (mm)	Freezing time (mins)
D1	21.11.2013	Brown	53	30
D2	21.11.2013	Brown	64	90
D3	21.11.2013	Dark brown	55	30
D4	21.11.2013	Purple	46.6	60
D5	21.11.2013	Brown	57.5	30
D6	21.11.2013	Purple	45.7	40
D7	21.11.2013	Brown	60	40
D8	21.11.2013	Purple	48.1	30
D9	21.11.2013	Purple	49	30
D10	21.11.2013	Brown	40	35
D11	21.11.2013	Dark brown	48.3	40
D12	21.11.2013	Dark brown	54.5	60
D13	21.11.2013	Yellow	53.1	45
D14	21.11.2013	Purple	43.8	25
D15	05.12.2013	Dark brown	62.4	45
D16	05.12.2013	Brown	65	30
D17	05.12.2013	Brown	48.8	40
D18	05.12.2013	Dark brown	57	20
D19	05.12.2013	Dark brown	49.2	30
D20	05.12.2013	Brown	41.5	0

Table 3.1: Continued.

Crab #	Collection date	Colour of eggs	C.W. (mm)	Freezing time (mins)
D21	05.12.2013	Brown	48.3	45
D22	05.12.2013	Light brown	49.5	30
D23	05.12.2013	Brown	43.6	35
D24	05.12.2013	Light brown	49.2	35
D25	05.12.2013	Light brown	46	30
D26	05.12.2013	Brown & yellow	45.6	20
D27	05.12.2013	Brown	45.4	15
D28	05.12.2013	Brown & yellow	45.9	20
D29	05.12.2013	Brown & yellow	41	20
D30	05.12.2013	Brown	40	20

Carapace width of each crab was measured and the largest crab was recorded with a 65 mm carapace width (D16) and the smallest crab with 40 mm C.W. (D10, D30). Mean carapace width of 30 ovigerous crab was 49.9 mm (Table 3.1). In the literature, there is little reported/published data on the minimum and the maximum size of ovigerous mitten crabs in the River Thames, however, Clark *et al*. (2013) reported C.W. sizes for 9 egg bearing females between 45 mm and 59 mm.The measured parameters of eggs are shown in Table 3.2. Only a few eggs were found on D13 with almost 100 eggs. The pleon of D13 was almost empty and the egg colour was yellow. Consequently, brood calculation was not done for this crab.

Table 3.2: Brood volume (mm^3), mean diameter of eggs (µm), volume of one egg (mm^3) and total number of eggs of 30 ovigerous female *Eriocheir sinensis* captured from the River Thames.

Crab #	Brood volume (mm^3)	Mean diameter of eggs (µm)	Volume of one egg (mm^3)	Estimated total number of eggs
D1	7,800	400	0.03349	232,905

Table 3.2: Continued.

Crab #	Brood volume (mm^3)	Mean diameter of eggs (µm)	Volume of one egg (mm^3)	Estimated total number of eggs
D2	12,200	420	0.03877	314,676
D3	3,500	410	0.03606	97,060
D4	3,000	380	0.02871	104,493
D5	8,000	370	0.0265	301,886
D6	3,300	380	0.02871	114,942
D7	9,200	403	0.03425	268,613
D8	7,500	385	0.02986	251,172
D9	3,700	343	0.02111	175,272
D10	4,600	377	0.02804	164,051
D11	5,500	384	0.02963	185,622
D12	3300	377	0.02804	117,689
D13	0	380	***	~100
D14	3,000	342	0.020934	143,307
D15	15,000	377	0.028041	534,950
D16	14,700	396	0.03215	457,231
D17	3,300	382	0.028989	113,871
D18	1,000	344	0.02130364	46,948
D19	4,000	372	0.0269406	148,478
D20	1,600	372	0.0269406	59,389
D21	4,500	382	0.02917215	154,256
D22	5,400	384	0.02963276	182,230
D23	2,300	366	0.02578433	89,201
D24	3,500	365	0.02549005	137,308
D25	2,600	328	0.01846715	140,790
D26	2,000	358	0.024113289	82,874
D27	3,100	394	0.03200863	96,848
D28	5,500	349	0.02228441	246,809
D29	300	349	0.0222841	13,462
D30	600	356	0.02361176	25,411

The data with anticipated linear regression plotting brood volume against carapace width is represented in Figure 3.3. Despite a few obvious outliers, there is a positive linear relationship between brood volume and carapace width ($r = 0.75$, $P < 0.001$).

The brood volume of the 30 ovigerous crabs ranged between 300 to 15,000 mm^3 (see Fig. 3.3). The highest brood volume was found in D15 and it was the third largest crab

with a 62.4 mm C.W. The brood volume of the largest crab (D16) was calculated at 14,700 mm^3. The second largest crab (D2) had the third greatest brood volume with 12,200 mm^3. The lowest brood volume was found in D29 which was one of the smallest carapace width measurements with C.W. 41 mm. D13 had only almost 100 eggs.

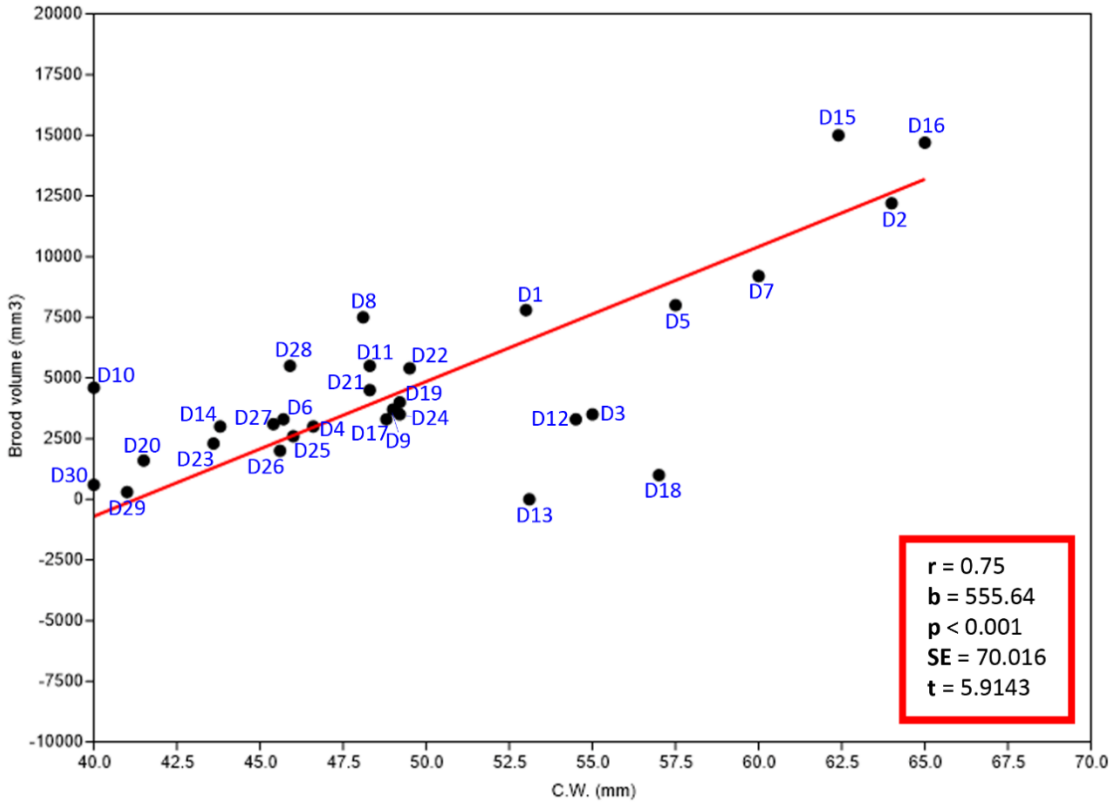

Figure 3.3: The relationship between carapace width (C.W.) and the brood volume of 30 female Chinese mitten crabs.

D30 which was one of smallest crab with 40 mm C.W. and had a brood volume of 600 mm^3. The other crab (D10) with a 40 mm C.W. had a brood volume of 4600 mm^3 (see Fig. 3.3). Therefore, this situation can be explained as "brood loss" because some crabs had already lost their brood before being transferred to the laboratory and this explains some of the outlier points shown in Figure 3.3. The mean brood volume of 30 ovigerous crabs was 4,800 mm^3.

In general, the mean diameter of the Chinese mitten crab eggs has been previously calculated at between 350 to 380 µm (Du *et al*., 1995; Jin *et al*., 2002; Dittel & Epifanio, 2009). The mean diameter for mitten crab eggs from the Odra river estuary in the study of Przemyslaw & Marcello (2013) was found to be between 361 to 375 µm. In the present study, the diameter of eggs ranged from 328 to 420 µm. The mean egg diameter is plotted against carapace width in Fig. 3.4 and demonstrates that there is a positive correlation ($r = 0.51$, $P < 0.01$).

The largest diameter egg was found in D2, the second largest crab examined in the present study with a 64 mm C.W. The diameter of eggs of the largest crab (D16 with 65 mm C.W.) was 396 µm and the smallest D10 and D30, were 377 µm and 356 µm respectively (Fig. 3.4).

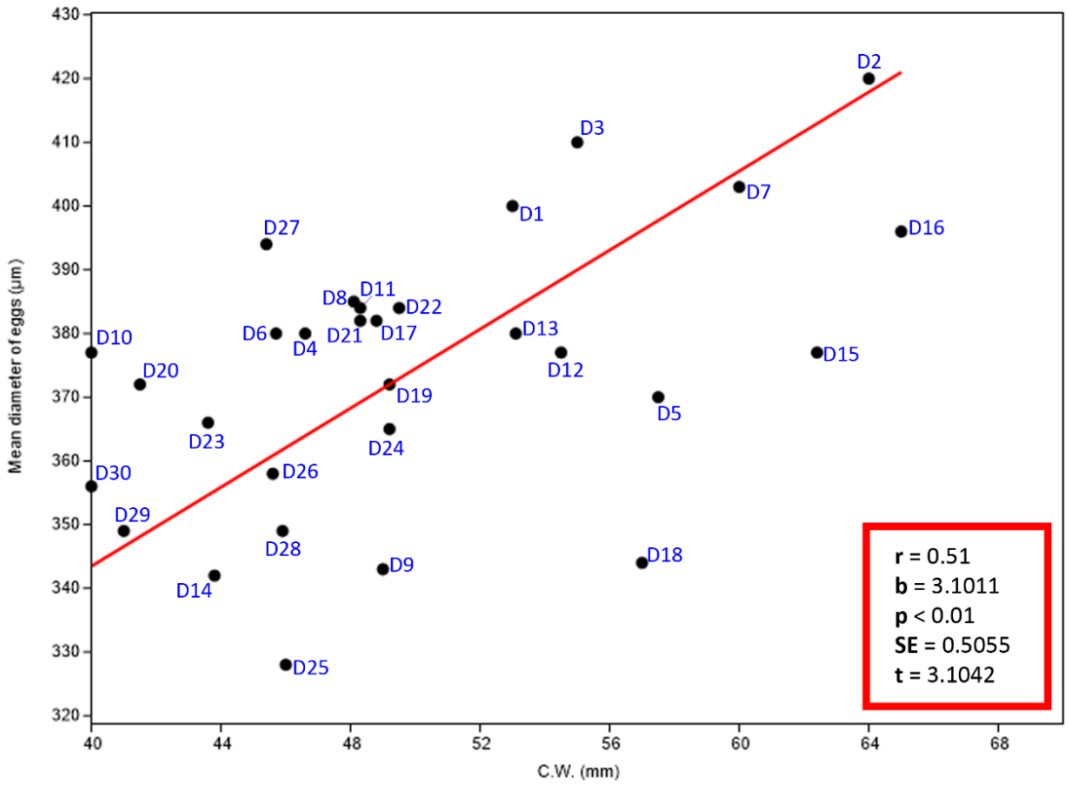

Figure 3.4: The relationship between carapace width (C.W.) and the mean diameter of eggs in 30 female Chinese mitten crabs.

The smallest diameter of eggs was found in D25 which had a 46 mm C.W. The mean egg size of the Chinese mitten crab in the Odra river estuary (Poland) were calculated as 371 µm in study of Przemyslaw & Marcello (2013), whereas it was found as 374 µm in the present Thames study.

In Figure 3.5, plots of data between C.W. and total number of eggs in each female are demonstrated. The linear relationship between these data is found to be positive ($r = 0.68$, $P < 0.001$).

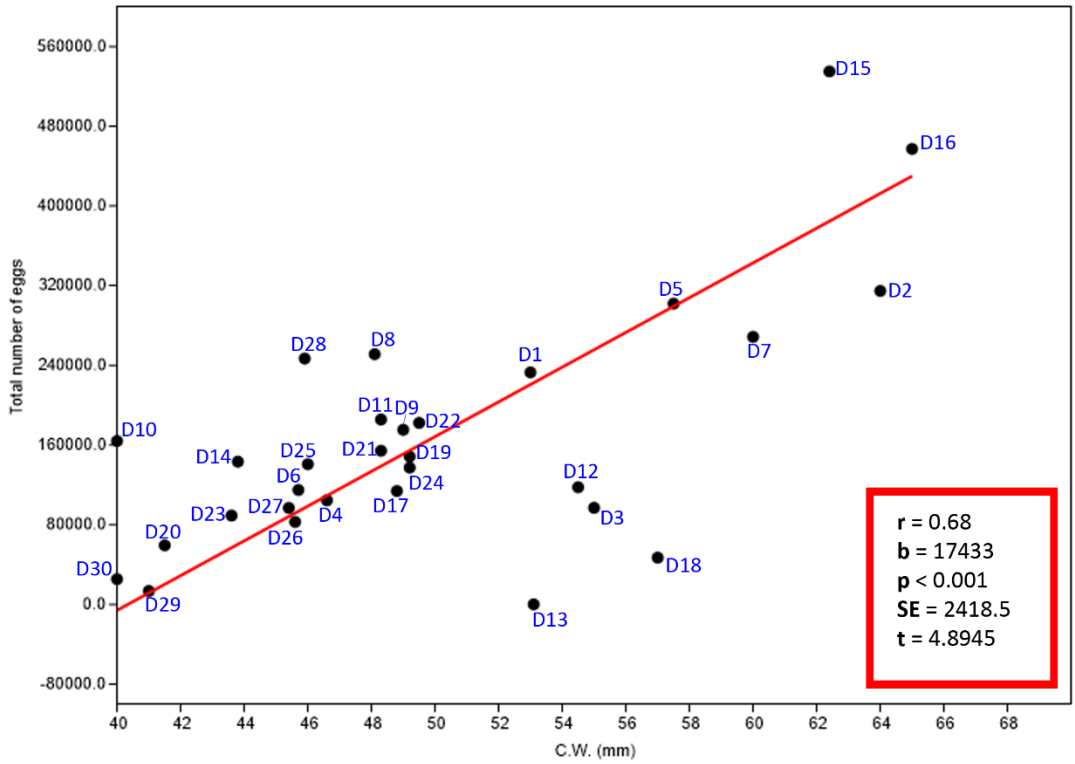

Figure 3.5: The relationship between carapace width (C.W.) and the total number of eggs in 30 female Chinese mitten crabs.

The total number of eggs found on 30 ovigerous crabs ranged from 13,462 to 534,950. The largest crab (D16) with 65 mm C.W. had 457,231 eggs, the next largest (D2) with 64 mm C.W. had 314,676 eggs and the third (D15) with 62.4 mm C.W. had the highest

number of eggs with 534,950 (see Fig. 3.5). D13 only had an empty pleon with almost 100 yellow eggs. Apart from D13, the lowest number of eggs was found in D29 which had 41 mm C.W. with 13,462 eggs. One of the smallest crabs, D30 with 40 mm C.W., had almost 25,411 eggs, whereas the next smallest crab, D10 with 40 mm C.W., had 164,051. This, again, can be explained as "brood loss". The mean total number of eggs in 30 ovigerous crabs was calculated as 166,728.

3.4.2 Capacity to produce multiple broods

A total of 12 ovigerous crabs were examined in a three year-period on an opportunistic basis, being heavily constrained by availability of good quality specimens. In the first year, 10 ovigerous females were trialled (2013−2014), whereas one each crab was investigated in the terms of 2014−2015 and 2015−2016. Ovigerous crabs were labelled O1, O2, O3 … O12. The collection date, description of the crabs in terms of damaged appendages, C.W., and the colour of eggs were recorded for each crab (see Table 3.3). While choosing the crabs for the more than one brood trial, the level of injury, the number of eggs and C.W. were considered. Crabs which were badly damaged were not included in this study. In addition, only the crabs which had what appeared to be a full brood were chosen. The largest crabs were given the positive correlation between fecundity and C.W. The largest crab was O6 with 57.1 mm C.W., whereas the smallest was O9 with 42.8 mm C.W (Table 3.3).

A colour change was observed in the eggs between time of initial collection until hatching. Nine out of the 12 crabs had either completely purple or brown and purple eggs, whereas the remainder had shades of brown (see Table 3.3). These colours were observed in November during the three year-period (2013, 2014 and 2015), but when

hatching was observed (December or early January), the purple colours changed to brown, dark and light brown or sometimes yellow colours (see Table 3.4).

In the 2013−2014 period, 10 ovigerous crabs released their first brood as either zoeae or dropped eggs by 12th of January 2014 (for detail see Table 3.4). During the following trials, all the ovigerous crabs completely released their first brood in late December of 2014 and 2015 (see Table 3.4).

Table 3.3: Collection date of ovigerous female *Eriocheir sinensis*, condition index to categorise the level of injury by each crab, carapace width (C.W.) and the colour of eggs in the pleon for brood studies.

Crab #	**Collection date**	**Description**	**C.W. (mm)**	**Colour of eggs**
O1	05.11.2013	Missing left leg 5	57	Brown
O2	05.11.2013	No missing appendages	48.3	Brown & purple
O3	05.11.2013	Missing right legs 3 & 4	47.9	Purple
O4	05.11.2013	Missing left leg 3 & right leg 5	44.9	Brown
O5	05.11.2013	No missing appendages	43.9	Brown & purple
O6	21.11.2013	No missing appendages	57.1	Purple
O7	21.11.2013	No missing appendages	48.5	Purple
O8	21.11.2013	Missing left leg 3	56.1	Purple
O9	21.11.2013	No missing appendages	42.8	Brown
O10	21.11.2013	Missing left leg 5	54.5	Purple
O11	18.11.2014	No missing appendages	52.5	Purple
O12	12.11.2015	No missing appendages	49.8	Purple

The mean diameter of the eggs of all ovigerous crabs was calculated before the zoeal release (see Table 3.4). Hatching was observed in 10 out of 12 crabs, but not observed for O2 and O4 which had brown & yellow colour of eggs when they were first transferred to the laboratory. Crabs O1, O3, O5, O7, O9, O10, O11 and O12 hatched all

their eggs in one batch, where the largest crab with 57.1 mm C.W., O6, released its first stage zoeae in two separate sessions. Three batches of zoeal release were observed from O8 which was the third largest crab in the experiment with 56.1 mm C.W. (see Table 3.4).

Table 3.4: Brood data, including colour of first brood eggs, mean diameter of first brood eggs (mm), date of zoeal release and the date of death for 12 ovigerous mitten crabs over a three-year period. Ovigerous crabs for brood experiment were referred to as O1, O2… O12.

Crab #	Colour of eggs in first brood	Mean diameter of eggs of first brood (µm)	Date of first larval release	Date of death
O1	Dark brown	431	02.12.13	20.12.2013
O2	Brown & yellow	341	No larval release	05.01.2014
O3	Dark brown	350	02.12.13	22.01.2014
O4	Yellow & brown	354	No larval release	22.01.2014
O5	Brown	364	04.12.2013	27.03.2014
O6	Dark brown	417	20.12.2013 & 10.01.2014	05.04.2014
O7	Purple & brown	381	20.12.2013	15.04.2014
O8	Yellow & light brown	412	21.12.2013, 27.12.2013, 12.01.2014	25.03.2014
O9	Yellow & light brown	324	21.12.2013	27.04.2014
O10	Brown	417	12.01.2014	12.03.2014
O11	Brown	405	22.12.2014	06.05.2015
O12	Brown	385	20.12.2015	28.04.2016

Two females died before the feeding procedure commenced. Crab O1 died 18 days after zoeal release, whereas O2, which did not release any zoeae, died in early January (see Table 3.4 for details). After all crabs had completely released their first batch, the feeding procedure started. Two more crabs, O3 and O4, died during the feeding

procedure. This was possibly due to feeding these crabs with salmon which probably contaminated the water relatively quickly. Therefore, the diet of the remaining crabs was changed and they were fed only squid for the rest of the experiment (see Table 3.4). The previous studies demonstrated that the diet of the Chinese mitten crab consists of a wide range of small specimens of amphipods, molluscs, snails and shrimps (Hymanson *et al*., 1999; Mills *et al*., 2016). All zoeae obtained from the experiments were preserved and transferred to the NHM as explained in Chapter 2.

The mean diameter of the eggs ranged between 324 to 431 μm and mean egg size was calculated as 381.8 ± S.D. μm in 12 crabs. The largest eggs were found in O1 which was the second largest crab with 57 mm C.W. in the present experiment. The smallest eggs were found in O9 which was the smallest crab in the experiment with 42.8 mm carapace width (Table 3.4).

The release of eggs, which were mainly yellow, was found in O5, O6, O8, O9, O10 and O12. Egg numbers, however, were limited ranging from 10 to 62 eggs (see Table 3.5). The release of these eggs occurred in following February after the first brood hatched. The eggs were found on different parts of the pleopods (see Figure 3.6a). The mean diameter of the second brood ranged between 385 to 431 μm (Table 3.5). The average mean size of these eggs was 404.6 ± S.D. μm. O8, the third largest female with a carapace width of 56.1 mm had the largest eggs.

No hatching of zoeae were observed except for crab O11. There was however, a massive spawning of purple eggs by crab O11, and these turned brown with time (see Figure 3.6b). This spawning was observed at the beginning of February 2015 (see Table 3.5) and zoeal release occurred after 38 days from spawning (8th March 2015). Eight ZI were removed from the tank and preserved for larval description. In the meantime, O11

shed all its eggs without further hatching of zoeae. After zoeal release or shedding of eggs, all crabs were fed prior to the possible spawning of a third brood.

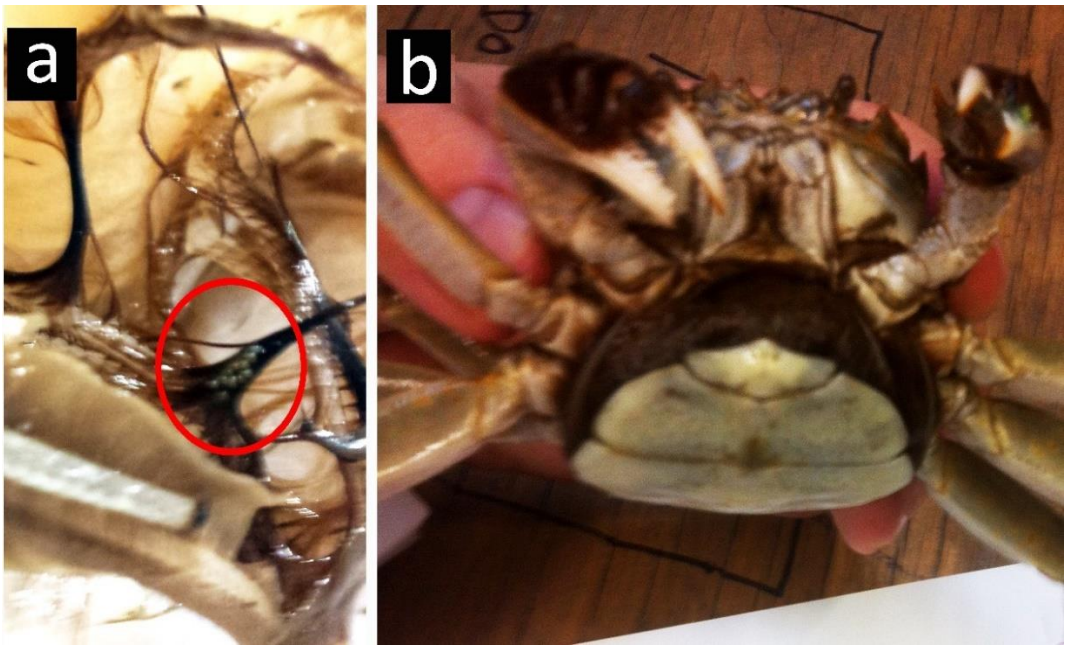

Figure 3.6: The formation of second brood in the Chinese mitten crab. (a) The formation of yellow eggs in crabs, O5, O6, O8, O9, O10 and O12. (b) The massive spawning of eggs for the female O11.

A third brood, however, was not recorded during the current study although has been previously observed in the laboratory (D. Morritt, unpub. obs.; Table 3.5). After the second spawning event, the crabs gradually died in late March, April and May. This was expected because the majority of adult Chinese mitten crabs are known to die after their semelparous breeding event.

Table 3.5: Second brood data: date of spawning, colour of eggs, mean diameter of eggs (mm), number of eggs and second date of hatching, date of survival of ovigerous mitten crabs.

Crab #	Date of second brood	Colour of eggs at spawning in second brood	Mean diameter of eggs in the second brood (µm)	Number of eggs found in second brood	Hatching date
O5	20.02.2014	Yellow	404	10 eggs on different parts of pleopods	No larval release
O6	20.02.2014	Yellow	402	62 eggs on different parts of pleopods	No larval release
O7	No second brood	None	None	None	No larval release
O8	20.04.2014	Yellow &light brown	431	16 eggs on different parts of pleopods	No larval release
O9	No second brood	None	None	None	No larval release
O10	24.02.2014	Yellow	400	39 eggs on different parts of pleopods	No larval release
O11	01.02.2015	Purple	406	Massive spawning of eggs	8 ZI were found on 08.03.2015
O12	29.02.2016	Yellow	385	25 eggs on different parts of pleopods	No larval release

3.5 Discussion

3.5.1 Brood experiments

The interaction of the endogenous and exogenous factors such as salinity, temperature, lunar cycle that affects tides, food availability and photoperiod influence the reproduction characteristics of crabs (Rabalais & Cameron, 1985; Thurman, 1985). The most limiting exogenous factor for the effective reproduction of Chinese mitten crabs is considered to be salinity (Panning 1938; Anger, 1991; Otto & Brandis 2011). According

to Panning (1938), after spawning, the mitten crab eggs adhered to the pleopods with a "cement-like" substance. This substance is thought to be hardened in the saline waters over 15‰ and explains their successful egg release in brackish or salinity environments (Veilleux & de Lafontaine, 2007). Buhk (1938) stated that 23‰ salinity is required for hatching of *E. sinensis* zoeae, while Anger (1991) considered the optimal salinity range to be between 20−25‰. It has been reported that egg-carrying setae do not harden in the Chinese mitten crab at a salinity lower than 14−15‰ (Veilleux & de Lafontaine, 2007; Wójcik & Normant, 2014). In addition, if the cement-like substance does not harden, the females shed their eggs in the salinities of under 14‰ (Wójcik & Normant, 2014). However, in terms of reproduction more generally, some laboratory and aquaculture experiments conducted by other workers (Peters, 1938; Hymanson, 1999) suggested that for *E. sinensis* the developing gonads can be harvested either in low salinity or even freshwater. Peters (1938) recorded this at salinities of 6.5‰ (Wójcik & Normant, 2014) and Hymanson (1999) reported that gonad development occurred in freshwater environments using cultured crabs in their native range, China (Rudnick *et al.*, 2000). Wójcik & Normant (2014), however, claimed that this situation was only observed in the laboratory conditions and has not been proven in the natural environment.

According to Anger (1991) water temperature has an effect on salinity tolerance. He observed that the mortality rate was less at the water temperatures between 12−18 °C than the temperature between 6−9 °C at any salinity. After their downstream migration into the estuary in Europe Chinese mitten crabs, copulate in late autumn or early winter (Panning, 1938). Cold temperature itself also can be a problem for the larval development. Anger (1991) stated that cold winters negatively affect recruitment as low temperatures damage embryos causing loss of larvae. The optimum water temperature for hatching was stated as 15–25 °C (Ingle, 1986).

The Thames becomes more brackish between Battersea and Gravesend (see Fig. 3.7) and this permits more catadromous species to undertake their life cycle (http://www.the-river-thames.co.uk/thames.htm). After Gravesend, the Thames water becomes completely marine. Since their first record in the UK, the population of the Chinese mitten crab has been increasing in the Thames. Herborg *et al.* (2005) linked this increase to the drought conditions in 1989−1990 which lowered flows and increased the salinity of the river (Attrill & Thomas, 1996). This has been proposed as being a key factor for the dispersal of catadromous species (Paula, 1998) and may have caused the increase of larval retention of *E. sinensis* in the Thames. Another factor which increase the salinity and thereby the mitten crab population could be the irregular tides of the Thames between Teddington (Fig. 3.7) and the sea (http://www.the-river-thames.co.uk/thames.htm). However, mitten crabs have already spread into the non-tidal Thames beyond Staines (http://www.the-river-thames.co.uk/wildlife.htm#twenty) which is 65km away from Tilbury (Fig. 3.7; Clark *et al.*, 1998a).

Figure 3.7: A map of River Thames (Adapted from http://www.the-river-thames.co.uk/thames.htm).

Other than the exogenous factors, life history traits (egg size, life span, reproductive effort and age at maturity) are directly related to fecundity (Llodra, 2002). Female body size (carapace width, C.W.) is considered to be the main factor contributing to the fecundity of brachyuran crabs (Hines, 1982). It was observed that larger crabs generally

produce a greater brood mass within and between species (Hines, 1988). The reason for this is the limitation of the space within the cephalothorax of the females (Hines, 1982) with respect to the developing gonads and this was considered to be the case for the mitten crabs (Wójcik & Normant, 2014). A similar relationship was reported by Przemyslaw & Marcello (2013) who found between around 140,000 to 680,000 eggs in their study on *E. sinensis* from the Odra Estuary. They stated that larger crabs produced more eggs than smaller crabs. High female fecundity in mitten crab was found to be the key to a successful invasion as they die after the breeding season (Wójcik & Normant, 2014). The present data also supports this statement as the females died after a few months of releasing their brood.

Anger (1995) stated that female size shows a natural relationship with number of eggs spawned. Fecundity shows a positive correlation with the number of eggs (Hines, 1988), whereas it shows negative correlation with the egg size (Hines, 1986). He specified that the mean egg size of the brackish and marine water species ranged from 250 to 450 μm, whereas the egg size of *Armases miersii* and *Sesarma curacaoense*, which are semi terrestrial species and have relatively low fecundity, was between 600−700 μm. These two species have less zoeal stages (three and two respectively) than *E. sinensis* and hatch in advanced condition.

The mean number of eggs was found to be around 460,000 eggs per female in the study of Przemyslaw & Marcello (2013). In the present study, however, which the mean number of eggs was calculated to be 166,728 per female. The highest number of eggs was found in the study of Przemyslaw & Marcello (2013) was around 686,000 whereas it was 534,950 for the present study. The lowest number of eggs found in their study was 141,000, while it was 13,462 eggs (D29) in the current examination.

These differences between two studies can be explained, but involved a number of factors. First of all, the investigated crabs in their study mated under laboratory conditions and it allowed them to calculate the full amount of brood. Whereas, the present study investigated ovigerous crabs which previously mated in the River Thames and then transferred to the laboratory examination. The main reason could be "brood loss" as well as other abiotic and biotic factors (Torres *et al.*, 2009). The main abiotic factors are the temperature (Anger 1991; Pinheiro & Fransozo, 2002), photoperiod (Giese & Kanatani, 1987), food availability (Flores & Negreiros-Fransozo, 1998), salinity (Anger, 1991), intertidal zonation, lunar periodicity (Emmerson, 1994), rainfall (Litulo, 2004) and pollution (Kuris, 1991). The differing conditions in the natural environment compared to that of the laboratory could also be responsible for some of the observed differences.

In the current study, 9 out of 30 ovigerous crabs had less than 100,000 eggs; D13 had only ca. 100 eggs. As the colour of the eggs of D13 was yellow, it could be the case that this crab had already hatched zoeae before being transferred to the laboratory.

In addition, the carapace width, which is mainly related to fecundity, was a significant factor when comparing the two studies. In the present study, the size of the crabs was relatively smaller than the crabs used in the examination of Przemyslaw & Marcello (2013). The size of the females used for their study ranged from between 46.68−80.44 mm (mean 68.17 mm), whereas this was between 40−65 mm (mean 49.9 mm) in the present analysis. As the current study used smaller average sized females, the number of eggs was also found to be lower than the average.

Hines (1986) stated that the mean egg size shows negative correlation with the brood size. This can be another reason for having this low fecundity in the present study as highest number of eggs were obtained from the crabs having relatively smaller eggs (see

Table 3.2). The mean diameter of the eggs found in the present study was larger than the previously published reports. The average mean diameter of the eggs in the current examination was 373.96 μm, whereas it was 371.4 μm and 365 μm in studies of Przemyslaw & Marcello (2013) and Jin *et al.* (2002) respectively. Broadly speaking these values are comparable.

3.5.2 Capacity to produce multiple broods

The number of broods per year of the brachyuran crabs ranges between 1 to 10 and has been listed in detail by Hines (1982). Although various ecological data were provided for *E. sinensis*, there is no information about the possibility of producing more than one brood in a single season without additional mating. Furthermore, the survival rate of mitten crabs after hatching was also recorded in the present study. It was reported that *E. sinensis* can generate several broods, however, it was not clear if this occurred with or without mating (Panning, 1938; Dittel & Epifanio, 2009). In fact, this situation was referred as "*not certain for the UK*" (APEM, 2010).

Kobayashi (2001) investigated the fecundity of *E. japonica* and reported that the species is highly fecund and can produce three broods during the marine phase in one reproductive season. It was stated that after the first brood, the ovaries of *E. japonica* re-develop and oviposition occurs again (Kobayashi, 1999). It is well known that brachyuran crabs can store the sperm for fertilisation of subsequent broods, however, the existence of spermatophores and longevity in the spermatheca is still poorly understood (Otto, 2012). Klaus *et al*. (2009) stated that decapod crustaceans have simple spermatophores consisting of chitinous material. Indeed, they emphasised that the spermatophores of some brachyurans are assumed to dissolve after copulation. There are two suggested types of spermatophores for brachyurans. The first type, which

dissolves after copulation, whereas the second type remains and is stored in the spermatheca (Moriyasu & Benhalima, 1998). The report by Hou *et al.* (2010) showed that *E. sinensis* has the rapid dissolving type. Otto (2012) who investigated the reproduction biology of *E. sinensis* in Baltic Sea reported that secondary copulation occurs just after females hatch their eggs, however details were not provided.

Successful copulation in the mitten crabs only occurs when the ovary is mature (Kobayashi & Matsuura 1995; Kobayashi 1999). On the contrary, Otto (2012) claimed in the Baltic Sea juvenile Chinese mitten crabs, with immature gonads, were also able to copulate. The occurrence of injured crabs (loss of walking legs) increases after reproduction season as the walking legs only regenerate after moulting (Kobayashi & Matsuura, 1997). Kobayashi *et al*. (1997) reported that most of the exhausted individuals cannot produce three broods or die after the first brood. This situation was also reported for *E. sinensis* (Hymanson *et al.*, 1999; Jin *et al.*, 2002; Rudnick *et al.*, 2003). Kobayashi (2001) observed that some specimens of *E. japonica*, which produced three broods, lived for up to a further five months. Otto (2012) also reported that *E. sinensis* do not die immediately after reproduction. There is also anecdotal evidence that some adult mitten crabs survive in the Thames estuary following the autumn breeding migration as evidenced by capture of animals in the spring which had barnacles attached to the carapace (P. Clark & D. Morritt pers. obs.).

The present study also showed that not all females die immediately after the reproduction. All ovigerous crabs were brought to the laboratory for the current experiment in November of 2013, 2014 and 2015. Only two individuals died a short time after releasing their first brood. A further two crabs died in the middle of January, however, it was probably due to feeding contamination and thus not directly related their production. The rest of the crabs lived longer, clearly demonstrating a capacity to

survive, and potentially produce subsequent broods, following the release of the first brood.

A second brood, albeit limited in terms of number of eggs, was observed in five crabs. In addition to the very low egg number, the colour of their eggs was predominantly yellow. The one exception, crab O11, had produced a substantial second brood and zoeal release occurred, these zoeae being fully functional, component individuals. A third brood, however, was not observed in the present study although has been reported from the laboratory on previous occasions. Thus, the present study has demonstrated that the species can indeed produce at least one brood, leading to fully functional offspring without the female needing to copulate a second time.

Although some marine grapsoid crabs are reported to moult and oviposit about 5 or 6 times a year and more than ten times in total in their life time ca. three years period (Fukui, 1988), moulting was not observed in *E. japonica* after producing three broods (Kobayashi & Matsuura, 1995). This was also observed in the present study, no moulting occurred between broods.

Fecundity of *E. japonica* decreased in the second and third brood (Kobayashi, 2001). This was also observed for six out of seven crabs in the present study and in many cases the second brood was extremely small. Although the optimum salinity and the temperature for the Chinese mitten crabs were used in the current experiment, most the ovigerous crabs were continuously shedding their eggs during the experiment period. In addition, not all crabs hatched zoeae. This may be related to their stress level under laboratory conditions and therefore these results should be viewed with a degree of caution.

3.6 Conclusions

Female mitten crabs in the River Thames were highly fecund, however, some of the crabs were found carrying smaller broods compared to previous reports (Dittel & Epifaino, 2009; Przemyslaw & Marcello, 2013). In the present study, between 13,000−535,000 eggs were found in the first brood of the crabs. The main reason is clearly that the mean carapace width of the crabs observed in the present study was smaller than these previous reports. Positive relationships were found between brood volume (and also egg number) and carapace width as well as between mean egg diameter and carapace width. It is worth noting that samples used in the present study used only crabs caught in the field. Therefore, there was a high possibility that the crabs could have lost eggs before or during transport to the laboratory.

The present study showed that *E. sinensis* can produce more than one brood without further mating. It demonstrates that when the optimum conditions (temperature, salinity and food availability) are available, the Chinese mitten crab in the River Thames can be highly productive and during one reproductive season has the potential to produce more than one brood as a result of a single copulatory event. This aspect of their reproductive biology further explains their success as an invasive species globally and the documented spread throughout the Thames and its tributaries.

CHAPTER 4

DEVELOPING IMAGING TECHNIQUES USING CLSM FOR THE STUDY OF BRACHYURAN CRAB LARVAE: A CASE STUDY OF THE CHINESE MITTEN CRAB ZOEAL STAGES

4.1 Introduction

Confocal laser scanning microscopy (CLSM) offers an excellent option for non-destructive imaging of brachyuran crab larvae and other macro-invertebrates (Butler *et al*., 2010). The images obtained are comparable in quality to scanning electron microscopy (SEM) at the same magnifications and the technique offers a 3D data set. In addition, CLSM presents a simplified sample preparation routine compared to SEM. Applying SEM protocols to individual larval appendages, which may be only a few hundred microns in length and tens of microns in diameter, can be difficult (Wolf, 2010) and often results in them being damaged (Michels, 2007) or even lost during the preparation steps (e.g. fixation, dehydration, critical point drying or coating) due to the fact that they are so small. Finding a suitable SEM dehydration protocol which does not result in distortion of the cuticle, particularly in larval specimens, has proven to be extremely challenging (Meyer & Melzer, 2004; Meyer *et al.*, 2006; Wolf, 2010; Meyer *et al.*, 2014), whereas samples are examined in a hydrated state for CLSM. This allows the appendages to be manipulated within the mounting medium to offer views of the specimen from multiple angles which can be problematical to achieve using SEM since some viewpoints may be inaccessible due to the way that the specimen is mounted and the tilt limitations in the SEM (e.g. Fig. 4.1a). Since CLSM is an optical technique, the transparency of the sample allows the origins of spines/setae and internal anatomy (musculature, digestive or nervous system) to be viewed/recorded. In addition, specimens held in historical slide collections can be examined and then compared with recently collected material. CLSM illustrations can include much finer details than the traditional line drawings (e.g. Fig. 4.1b, c) for morphological descriptions. Indeed, line

drawings are incredibly time consuming (Coleman, 2006) to prepare and figuring dense concentrations of setae can be challenging. Furthermore, CSLM samples can be recovered after imaging and used for DNA extractions or returned to museum collections.

Previous studies have described a number of different techniques for applying CLSM to macro-invertebrates including the use of a variety of stains, mounting media, and cleaning protocols (Table 4.1). However, one issue with CLSM visualisation is that the software is optimized for generating images of transparent, fluorescent volumes rather than for rendering and lighting surfaces. Commercial software capable of producing this type of visualisation tends to be expensive. Workflows can be developed to allow the use of the open-source freeware programme "Drishti" (Limaye, 2012) to visualise CLSM data (e.g. Fig. 4.1d).

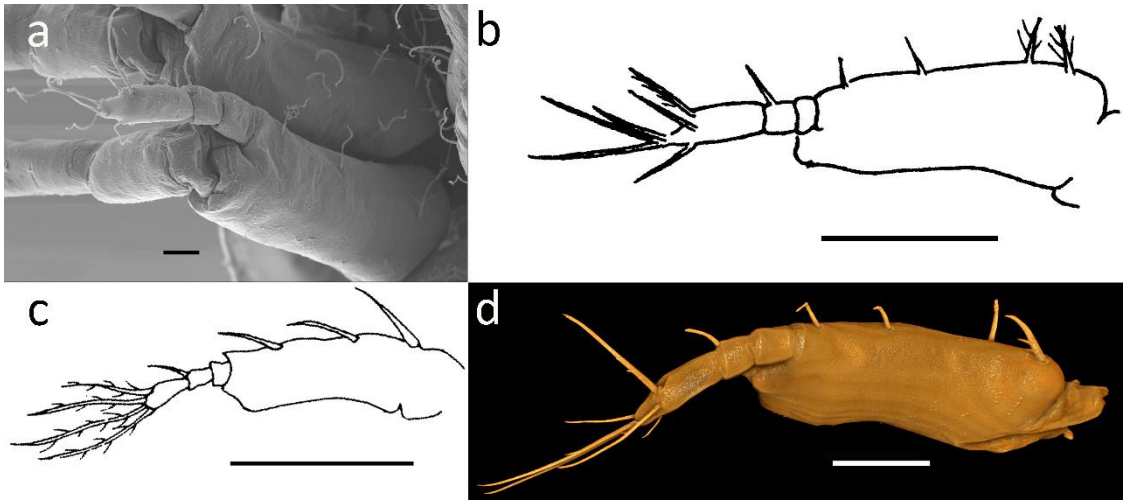

Figure 4.1: *Eriocheir sinensis*, zoea I, second maxilliped. A comparison of (a) SEM image obtained using Zeiss Ultra Plus Field Emission. (b) Line drawing from Kim & Hwang (1995). (c) Line drawing from Montú *et al*. (1996). (d) Image obtained using a Nikon A1-Si CLSM and processed using Drishti. Scale bars a = 20 μm; b-d = 100 μm.

CLSM has been a useful tool for researchers studying arthropods/macro- invertebrates as well as other taxa. Technological developments in visualisation techniques, including sample preparation and the quality of images have improved since trial studies began ca. 2000. In the literature, many different preparation methods such as mounting, staining and digesting have been suggested for the use of CLSM or applied to different types of macro-invertebrate specimens. In addition to preparation techniques, many different scanning settings of the confocal microscope have been recommended. These settings mostly show the similarities between the different brands of confocal microscope such as Leica, Nikon, Olympus and Zeiss. The post-processing procedures, such as advanced image processing techniques applied to these data, however, can be differentiated from each other. 3D visualisation techniques were applied to arthropods using a variety of software. Although some of these studies applied 3D techniques using different confocal data, they did not explain in detail how their results were obtained. In addition, applications to create 3D images varied according to the brand of microscope used, consequently, there was no common method between different studies.

The following studies used a variety of techniques and methods to produce CLSM images.

4.2 Literature review

One of the earliest studies in the field of macro-invertebrates using CLSM was conducted by Bundy and Paffenhofer (1993). They used CLSM in order to understand the morphology and physiology of the sensory structures of copepods (*Labidocera aestival*, *Calanopia elliptica*, *Centropages velificatus*, *Temora stylifera* and *Eucalanus pileatus*). The species used in their research were larger than the currently examined species, larvae of *Eriocheir sinensis*. Therefore, only a few appendages such as the

antenna and the sensilla were examined, due to the size limitation of the confocal microscope they used. They used DiL (dioctadecyl-tetramethylene carbocyanine perchlorate), to stain the neurons of the sensilla, a mixture of seawater and deionised water as the mounting medium and 'Voxelview' software to visualise, animate and rotate the optical cross-sections of their specimens. They did, however, encounter a problem with bleaching of the stained appendages during the scanning procedure. In addition, the final images of the antenna cuticle were partly oversaturated. Bundy and Paffenhofer (1993) considered that a bleaching problem occurred because of the mounting medium and the long duration of the scan. Furthermore, the confocal images lost their resolution while transforming the data into film unless the confocal signals were not initially converted to a digital format. Their study concluded that CLSM had a great advantage over conventional light microscopy because of the ability to eliminate any interference from the structure which can obscure the image. Another advantage of CLSM was that the digitally stored images provided an opportunity for continued investigation. Bundy *et al.* (1998) used a similar method to examine the first antenna of *Diaptomus sicilis* (Copepoda) and identify the anterio-dorsal direction of the sensory setae. In another study, Bundy *et al*. (2002) examined the feeding appendages of *Skistodiaptomus oregonensis* (Copepoda) using CLSM without dissecting the material. Therefore, some of their images were oversaturated.

The application of CLSM was initially widely used by researchers to observe the morphology of the copepods. Williams-Howze (1996) applied a number of different visualisation tools (SEM, TEM, light microscopy and CLSM) for the study of the marine harpacticoid copepod, *Heteropsyllus nunni* Coull. In her study, CLSM was specifically applied to visualise the dorsal and ventral views of the lower urosome and caudal rami. Although she obtained images, the scanning details were not described. Morphological analysis of *Pseudectinosoma kunzi* (Copepoda) was conducted by

Galassi (1997) using CLSM to corroborate the morphology of the tegument and he used the permanent mounting medium, polyvinyl lactophenol to mount whole and dissected specimens prior to their examination. In a similar study conducted by Galassi & De Laurentiis (1997), line drawings of *Pseudectinosoma reductum* were supplemented by CLSM produced images. Their method was initially applied to assess the integumental morphology in their subsequent research (Galassi *et al*., 1998). In the above-mentioned studies, however, the only descriptions of the applied methods referred to polyvinyl lactophenol as the mounting medium as used in Galassi (1997). In these studies, CSLM was mainly utilised to corroborate the morphology of selected appendages. A detailed description of the complete naupliar stage of *Temora stylifera* (Copepoda) using CLSM was conducted by Caretenuto (1999). The naupliar stage was visualised by staining the material with DiL, mounting the specimens in seawater and scanning at different magnifications. Caretenuto (1999) obtained clear images of the appendages without any need for dissecting. The number of the setae could be counted, and even the tiny setules were visible. When considering the recent technological developments in the field of microscopy, however, the images obtained in the early studies were not actually comparable to those present in the studies of today, mainly because CLSM were only used as a supportive tool for their main studies.

Only a few studies were specifically performed on decapods using CLSM and were mostly concerned with the examination of the internal anatomy. In their CLSM study, Haond *et al*. (1998) used a specific dye, dimethylaminostyrylmethylpyridiniumiodine (DASPMI, Bereiter-Hahn, 1976), to label the mitochondria of the gill filaments, the epipodites and the branchiostegite tissue of a dissected adult lobster, *Homarus gammarus*. Another study was conducted on the larval development of *Hippoolyte inermis* by Zupo & Buttino (2001). They scanned the dorsal and ventral views of the zoeal stages and described the functional internal anatomy of the shrimp using CLSM as

a non-destructive method. The specimens were scanned whole and as separate appendages. DiL was used to stain the internal structures and the development of the gills, heart and midgut were examined for different zoeal stages. The images were only taken at an excitation wavelength of 543 nm and the internal structure was visualised using 'Metaview'. *Penaeus* (*Litopenaeus*) *vanamei* (decapod) was investigated by Hertzler (2005). The eggs and embryos of the shrimp were stained with Sytoz Green. As the aim of the research was to visualise the internal anatomy, serial sections of some of the Z-planes were saved as multi-TIFF files. These were then post-processed using Adobe Photoshop and saved at an image size of 1024×1024 pixels as previously described in Hertlez (2002). Buttino *et al*. (2003) examined the developmental biology of marine decapods and copepods so as to visualise both external and internal structures of their material. They concluded that using bright field microscopy was time consuming, however, CLSM was an effective method for visualising the morphology of marine crustaceans. Belanger *et al*. (2008) conducted their study on the major chelae of *Orconectes rusticus* (crayfish). The external structure of the setae was visualised using SEM, whereas the sensory setae and their nerve fibres located in the sections of the major chela were visualised using CLSM.

CLSM was used by Buttino *et al*. (2004) for detecting the embryo viability of *Calanus helgolandicus* (Copepoda) and successful images were obtained. CLSM was also applied in the field of marine ecotoxicology to understand their effects on embryo quality of harpacticoid copepods (Chandler & Volz, 2004). Caretenuto *et al*. (2006) examined algal autofluorescence in naupliar stages of copepods' stomach. Leasi *et al*. (2006) preferred CLSM for the visualisation of the muscular system of gastrotrichs to overcome the limitations of the conventional epifluorescence microscopy such as photobleaching and low resolution. Liposomes of some copepod species were identified by visualising their ingestion (Buttino *et al*., 2006). Central nervous systems of

copepods were also examined with CLSM (Sousa *et al*., 2008) while Uttieri *et al*. (2008) used SEM, TEM and line drawings to examine the morphology of antennular sensors of copepods. These studies took advantage of CLSM by means of using the optical sections of scanned data to demonstrate fluorescent aesthetascs and simple setae. CLSM was also effectively used to identify the bacteria on small aquatic species such as benthic copepods (Beckman *et al*., 2008). In addition, CLSM was applied in the study of Leasi & Todaro (2009) to detect the morphological characteristics of the sibling species of *Xenotrichula intermedia* (Gastrotricha). They considered that the preparation of the samples was easier than for SEM and fewer specimens were required for confocal visualisation.

Confocal microscopy techniques have become very popular in marine biological research as well as other scientific disciplines due to recent developments in the technology and declining costs (Chandler & Volz, 2004). During the last decade, confocal imaging has improved to provide greater definition of structures and features (Haug *et al*., 2011). Improving a range of CLSM techniques depends on many factors including the staining, mounting, microscope settings and analysing data after scanning. Consideration to all these steps is vital if confocal images are to improve. In addition, a need for using high-tech data to post-process these images using cheap methods was required.

Many recent studies were conducted to examine the external structures of small arthropods/ crustaceans and these have experimented with different preparation and processing methods. Using cuticular autofluorescence for small crustaceans is now common (Zill *et al*., 2000). One of the earliest studies using cuticular autofluorescence with CLSM was the examination of a cockroach leg without staining (Zill *et al*., 2000). They greatly benefited from the thickness and autofluorescence of the exoskeleton of their specimen. Only two objectives (4× and 10×) were used but they were sufficient to

visualise surface features, sense organs and the deep surface of the appendages by scanning at the excitation wavelength of 568 nm during their examination. Commercially available software, Voxblast, was used for reconstruction purposes by reducing the confocal image sizes from 2048 × 1024 to 512 × 256 pixels. This, however, may have caused a loss of image quality. Zill *et al*. (2000) stated that the images taken using 4× magnification did not provide sufficient resolution for 3D purposes. Therefore, only the images obtained from the 10× objectives provided enough resolution for the construction of 3D images. Yet, the 10× objective was not enough to scan the entire length of the leg segment in one session. Therefore, they used montage techniques to assemble one appendage using several scanned images. Another limitation to their study was the exoskeleton thickness of their samples. The penetration of the laser beam was limited. Pawley (1995) considered this to only be around 100 µm.

A successful application of cuticular autofluorescence using CLSM was applied to *Drosophila melanogaster* and *Culex tarsalis* by Klaus *et al*. (2003) and they described the morphology in detail. No staining method was used in their study as natural cuticular autofluorescence of the samples produced adequate excitation level at a wavelength of 560 nm. Two commonly used mounting media were trialled to embed the dissected and whole specimens, euparal and glycerine jelly. Klaus *et al*. (2003) applied the "flipping technique" to prepare the slides. The dissected appendages were placed between two cover slips so that both sides could be scanned by the "slide". It was noted that one of the main problems were artefacts which caused signal loss and blurred images when using 20× objectives, whereas a 40× oil objective was more appropriate for their study. Klaus *et al*. (2003) concluded that glycerine jelly was more effective than euparal since glycerine provided high background signal. In addition, it was effective when visualising the images using MIPs (maximum intensity projection), which is freely available in the software packages supplied by the confocal microscope

manufacturers. Klaus *et al*. (2003), however, suggested that commercially available software programmes such as volume and iso-surface rendering programmes were much more effective than MIP images. Maximum intensity projection images were also found to be ambiguous in the study of Klaus *et al*. (2003) as well as the present thesis as background signal issue was problematic as previously stated by Schroeder *et al*. (1998). It was emphasised that using post-processing software was important to have a better understanding of CLSM images. The disadvantage of using dry objective lenses and the penetration ability of confocal microscope onto the thicker samples were discussed in detail in their study. It was concluded that using oil immersion with higher magnification provided better data for processing 3D images.

Schawaroch *et al*. (2005) discussed the use of traditional light microscopes such as stereomicroscopy and compound microscopy for the study of insect morphology. They criticised both systems in terms of difficulty of illumination, the depth of field, penetration and low resolution. SEM, a routinely used tool for studying insect morphology, was also found to be limited. Whilst SEM provided good images of the surface, the structure of the insects may not always be flat to view comfortably. This statement was also valid for all the crustaceans as their surfaces consist of folds and obscuring layers etc. Furthermore, SEM specimen preparation was found to be destructive for some species. Schawaroch *et al*. (2005) emphasised the importance of using CLSM for the re-examination of material as it allows setae, spines and appendages to be imaged separately with the high potential of discovering new morphological details. They slightly modified the method of Klaus *et al*. (2003) for their examinations as specimens were scanned using 20× dry objectives at the excitation level of 543 nm and they visualised collected data using MIPs instead of applying 3D rendering programmes. In addition, Schawaroch *et al*. (2005) used Adobe Photoshop to enhance their final MIPs. The images obtained were superior to SEM because they are

completely in focus (i.e. CLSM has a greater depth of field). Additionally, it provided data for obtaining 3D versions of the objects. One problem was emphasised in their study that the expense of purchasing a CLSM could be a problem.

A few studies used cuticular autofluorescence to study the internal anatomy of *Drosophila*. Epithelial tubes in the *Drosophila* trachea were examined using CLSM (Toning *et al*., 2005). Early chitin deposition in trachea was also visualised by labelling embryos with Congo red. According to Cohen (1993), this stain penetrates into the chitin chain. Toning *et al*. (2005) used a mixture of 50% glycerol and 50% deionised water to mount embryos for analysis by CLSM. Congo red helped them highlight the cuticular lining of their samples. Similarly, Moussian *et al*. (2006) also observed cuticle differentiation in the developing *Drosophila* trachea using CLSM.

Klaus & Schawaroch (2006) brought a new and novel perspective for the visualisation strategy of data collection from small arthropod structures. Using the miniscule structures of *Drosophila melanogaster* and *Culex tarsalis*, the mounting and imaging procedures were described in detail. Non-permanent glycerine jelly and permanent euparal mediums were utilised to mount their material. They considered the thickness of exoskeleton, and applied the "flipping method". An inverted CLSM was used to scan their samples and the freeware package "Zeiss Image Browser" was employed to obtain final MIPs. Furthermore, Klaus & Schawaroch (2006) also used a commercial software package, Imaris, for the surface re-construction. They stated that although obtaining MIPs are quicker than applying 3D visualisation software, MIP images are not comparable to those processed using rendering software programmes. Klaus & Schawaroch (2006) found the commercial software for 3D visualisation to be extremely expensive. They concluded that CLSM has a great advantage for morphological studies of minute arthropod structures compared to the hand illustrated methods and other

microscopy techniques such as light microscopy and SEM as also stated by Coleman (2006).

The strategy of using CSLM for high resolution morphological images were discussed by Michels (2007). They supplied more details on CLSM laser power and the effects of different mounting mediums for small crustaceans. A few species of copepods were selected as model organisms for the application of CLSM preparations. Some species were scanned as an entire specimen while others were dissected in glycerine. Dissected and entire specimens were then mounted using either 100% percent euparal or glycerine jelly. This analysis demonstrated the importance of using a suitable excitation wavelength for copepods based on autofluorescence only. Michels (2007) used four lasers to obtain the best suitable excitation wavelength for his copepods. The most effective wavelength was found to be krypton- argon and argon lasers at the excitation wavelength of 488 nm. This suggested that the assumption of excitation level for some crustaceans was important in terms of using all lasers. This situation, however, could differ from species to species in terms of size, structure and specific morphology of appendages. Another important point from his study was the use of specific mounting media for CLSM. Euparal was found to be a favourable medium at an excitation level of 488 nm or less. However, the red autofluorescence of euparal caused a loss of information at these wavelengths. This problem was not discussed in previous studies as euparal was found to be an acceptable mounting medium at an excitation level of 543 nm or above. In contrast, Michels (2007) found glycerine jelly to be an extremely favourable embedding medium. The effectiveness of glycerine, in terms of providing a clearer background and displaying even the smallest structures such as setae on appendages, was described in detail. A similar comment to previous researchers was made in terms of the limitation of CLSM for larger specimens. Apart from the thickness of the specimens, the working distance was also considered important by Michels

(2007) to obtain images with high resolution. In his study, the largest *Alteutha potter* structure illustrated had a total length of 1.3 mm and was scanned using only 10× objective. In conclusion, it was suggested that the use of CLSM had great potential for morphological descriptions but required specific methodology for each species/taxon.

Schawaroch & Li (2007) examined the genitalia of *Drosphila melanogaster* and according to them the use of suitable mounting media, appropriate excitation levels and choice of specimens for CLSM studies is essential. They were concerned with eliminating the background noise using CLSM and the software for processing 3D images. Their study was an exploration of using different ratios of water and glycerine, and glycerine jelly and euparal for the preparation of non-permanent mediums. They considered that glycerine jelly displayed a higher level of background noise than euparal. In addition, background noise levels increased when data was re-constructed for 3D images using thicker specimens. They considered that the ideal mounting medium should be viscous enough to prevent the samples from moving during scanning and provide sufficient autofluorescence. If too much deionised water was added to the glycerine jelly mixture then the samples would move during long (3 hours) image acquisition processes. Schawaroch & Li (2007) also found that using agarose mixture with glycerine jelly decreases the background noise and was also an effective way in increasing the depth of field for thicker specimens. In addition, Schawaroch & Li (2007) further suggested that the low level of background noise could be eliminated by using the imaging software such as ImageJ, Imaris and Adobe Photoshop. These processes, however, were found to be time-consuming with an additional risk of losing information while editing the images, especially if the operator was not familiar with the specimens and taxon.

The importance of using modern technology for re-description of the species was stated by Brooker *et al*. (2007). They emphasised that there is a great need for re-examining

some species which were described many years ago. They implied that misidentification was possible using the traditional methods. In their study, they re-examined the parasitic copepod, *Lernaeocera branchialis*, which has a two-host life-cycle and a mature stage and was previously described by Kabata (1979) and later Boxshall (1990). Brooker *et al*. (2012a) re-examined this species using bright field and confocal microscopy. They fixed their specimens in 2.5% glutaraldehyde to enhance autofluorescence and then rinsed them in distilled water before staining with Blankophor or Gomori's trichrome separately. The specimens were covered with distilled water and scanned using two lasers at the excitation levels of 405 nm and 488 nm. After obtaining the images as MIPs, the images were extracted to drawings using Adobe Photoshop CS3. CLSM was effectively used for the generation of specimen drawings. As setation is a diagnostic character in copepods, the specimens/appendages were scanned by Brooker *et al*. (2012a) focusing on autofluorescence of the setae. Oversaturated confocal images were not a problem in their study as they extracted only the segmental boundaries of the appendages as line drawings. Extracting the images as line drawings, however, can limit the 3D construction of the features. Mapping the exact location of setae is as important as describing the number of setae. But some of the setal features were obscured by other appendages. To overcome this problem, Brooker *et al*. (2012b) viewed the obstructed features from different angles by rotating the CLSM data and extracting final images as line drawings. This could, however, be more time-consuming than reorienting and capturing more than one snapshot of the same appendages from different angles using 3D software packages.

The first application of CLSM in water mite taxonomy was conducted by Valdecasas (2008). Line drawings, analogue photography, bright field or other light microscopy systems, and SEM were used in the previous studies of water mites. Valdecasas (2008) cited a number of reasons including time and expense for adopting CLSM to describe a

new genus of water mite. He stated that line drawing requires too much time and skill while light microscopy techniques cause loss of spatial relationships. In addition, he found SEM unable to portray subepidermal structures of the examined samples. Therefore, he used CLSM to capture clean images as previously described by Klaus *et al*. (2003) and Conchello & Littman (2005). Dissected parts in their examination were mounted in glycerine and scanned using 20× objectives with a numerical aperture (N.A.) of 0.40 and 40× with N.A. of 1.25. They overcame the problem of the limitation of a small pinhole for larger appendages by scanning the whole sample (ventral and dorsal shield) sequentially. Then, all the images were processed using the freeware software programme, ImageJ. He emphasised that CLSM provided realistic images and captured perfect resolution as well as giving the opportunity for renewing the studies, especially of type specimens of museum collections.

Staining material is crucial when there is no adequate autofluorescence provided by the sample. Lee *et al*. (2009) applied a combination of stains to a new species of *Carpatolechia* (Lepidoptera). The stains were applied to the dissected genitalia. Although the sclerotized structure of the genitalia provided a high level of autofluorescence, the level of autofluorescence in dissected genitalia was too low to generate decent images with high resolution using CLSM. In their study, Lee *et al*. (2009) applied seven treatments (including unstained samples as a control group) and samples stained with merbromin, safranine O, orange-G, eosin Y, chlorazol black E and eosin Y + chlorazol black E. They compared the fluorescence from different stains. Samples were cleaned in 10% KOH, washed with distilled water, stained accordingly, then cleaned in 70% ethanol and dehydrated in 100% ethanol. Samples were mounted in euparal and scanned at low resolution (512-pixel frame size) with 5× objectives to obtain the results quickly. This study showed that the application of different stains provided better fluorescence from the specimens. In their study, the most effective

results were obtained using eosin Y, safranine and mercurochrome respectively. Lee *et al*. (2009) considered that using 70% ethanol and dehydrating the specimens with 100% ethanol could be problematic for smaller arthropod species as this application can cause serious shrinkage problems and distortion of the samples.

Recently, many different combinations of preparation techniques have been applied to a wide range of arthropod species in preparation for CLSM applications. Maruzzo *et al*. (2009) used CLSM, as well as SEM and light microscopy to examine the external morphology of nauplii stages of *Artemia* sp.(Branchiopoda). They described the segmental features of the exopod of antennas. Instead of taking advantage of the autofluorescence of the cuticle (Valdecasas, 2008; Michels, 2007; Schawaroch & Li, 2007; Klaus and Schawaroch, 2006; Schawaroch *et al*., 2005; Klaus et al., 2003; Zill et al., 2000 and so on), they applied a stain. After digesting their materials overnight using KOH, the samples were stained with Evans blue for about 10 minutes. This generates a bright red autofluorescence using CLSM. The samples were embedded in glycerol and scanned at the excitation level of 543 and 570 nm. Successfully scanned samples were visualised using Maximum Intensity Projections (MIPs). Maruzzo *et al*. (2009) found that Evans blue was a more effective method than the natural autofluorescence of the specimens and that duration of digestion changed depending on the thickness and the size of the material. Use of 100% glycerol, however, did not seem to affect their samples in terms of shrinkage.

Another different study was conducted by Butler *et al*. (2010) with the aim of resolving the phylogenetic position of *Ballonema gracilipes* (Chilopoda) and was based on historical museum material preserved in ethanol. The reason for applying CLSM was that this technique is a non-destructive imaging method compared to SEM. In order to obtain maximum fluorescence at any excitation wavelength, they used Canada balsam as a mounting medium to embed the dissected legs, gonopods and mouth parts. In

addition, using the confocal software, their image stacks were recompiled using Average Intensity Projection (AIP) as well as MIP.

An extensive study using a wide range of small crustaceans was carried out by Michels & Büntzow (2010). The main aim of their examination was to prove the effectiveness of Congo red staining as a fluorescence marker for cuticular structures. They addressed a few problems from previous studies which were conducted without staining and considered that the autofluorescence of a considerable number of crustaceans was not sufficiently intensive to obtain a satisfactory visualisation of external structures. They criticised Maruzzo *et al*. (2009) for using a non-specific dye, Evans blue, and DiL (dioctadecyl-tetramethylene carbocyanine perchlorate) which did not stain the exoskeletons efficiently. In addition, they found that DiL tended to bleach rapidly. Therefore, Congo red, which was proved as an effective dye for chitin, (Toning *et al*., 2005; Matsuoka *et al*., 1995; Cohen, 1993) was trialled on several species (Copepoda, Decapoda and Phyllopoda) in terms of efficiency and intensity. After staining their material with filtered Congo red for 24 hours, they used reinforcement rings as described by Kihara & Falavigna da Rocha (2009) as a spacer between the cover slip and glass slide. This was a different approach to the "sandwich flipping" method which was applied in the previous studies (Schawaroch & Li, 2007; Klaus & Schawaroch, 2006; Klaus *et al*., 2003). As the specimens were not dissected, several reinforcement rings were required to mount their samples without crushing them. Relatively thinner and smaller specimens compared to previous crustaceans were used for their study. They suggested the mounting medium should be diluted depending on the size of specimens. After experimenting with the excitation level of wavelengths, they found that the best excitation level for samples stained with Congo red were between 543 nm and 561 nm. Whole specimens were scanned with 10× or 20× dry objectives and visualised as MIPs. Most of the stained samples were successfully visualised using

CLSM. They pointed out that one of the advantages of Congo red was that long scan times from almost two to six hours did not cause bleaching. More importantly, Congo red has a capability of staining different types of chitin, such as α-chitin in the case of the exoskeleton of crustaceans (Ifuku *et al*., 2009) and β-chitin for polychaetes (Fan *et al*., 2008). One disadvantage of Congo red was that when it was applied to museum species, the red colour was hard to remove, even after several washing applications of ethanol. Furthermore, they also studied the external structure of a stained decapod larva applying CLSM. In this instance, they found that the autofluorescence of exoskeleton in the larva was relatively weak compared to other crustaceans and their staining technique would have to be developed in order to visualise the specimen. Michels & Büntzow (2010) tried adjusting the detector gain of the CLSM, but the results were not satisfactory and the tiny structures of the larvae were not sufficiently visualised. Moreover, when the detector gain was increased, it led to much more background noise. Therefore, a combination of autofluorescence at the excitation level of 488 nm and Congo red fluorescence at the excitation level of 561 nm was used for this decapod larva. Lee *et al*. (2009) applied a mixture of the stains to obtain a strong fluorescence from decapod larva that could be an effective method as shown in the current study.

Using the Congo red methodology of Michels & Büntzow (2010), Wolf (2010) examined larval stages of endoparasitic copepod, *Ismaila belciki*. He considered that SEM protocols can be difficult and destructive causing distortion of the cuticle particularly in larval specimens, consequently he preferred CLSM. The larval stages were stained with Congo red dissolved in 100% ethanol but some parts of the specimen were more stained that others. For example, Congo red was more effective on mouthparts which are cephalic features, the dorsal surface of first pleonal somite and later copepodid stages. These, it was explained, were heavily fortified with chitin. Furthermore, the appendages which contained more chitin were stained brightly with

Congo red and caused the images to be oversaturated in these areas. This problem could be compensated via digesting the chitin layer using chemicals or using additional stain to balance the acquisition settings of the CLSM. Preparing Congo red with 100% ethanol may not however, be useful for the specimens with thinner exoskeletons such as in the larvae of Grapsidae and Varunidae (brachyuran crabs) as it can cause shrinkage problems while being transferred from the stain to mounting medium. Menzel (2011) applied the same method of Michels & Büntzow (2010) in order to visualise the adult female copepod, *Mesocletodes elmari*. Kihara & Arbizu (2012) applied a similar methodology to their new copepod species. Three lasers were used to scan the whole and dissected appendages at 10× objective with an N.A. of 0.4. Staining the different structures apart from chitin also became common. Michels & Gorb (2012) stained their species, (Copepoda and Insecta) with Congo red to obtain 3D images of resilin, an elastomeric protein, in the exoskeleton. The reason for staining with Congo red was that the natural fluorescence of resilin was not strong enough to be visualised using CLSM. The autofluorescence of resilin was found to be at the excitation levels of between 320 nm and 415nm (Andersen, 1963). Therefore, most modern CLSMs were unable to visualise them as they are mostly equipped with the lasers at the excitation levels of between 405 nm and 643 nm. Perfect images of the structures were visualised in the study of Michels & Gorb (2012) because they followed the protocol of Michels & Büntzow (2010). In a similar study, (Michels *et al*., 2012), the chitinous appendages of copepods were stained with Congo red. After washing the stained samples with distilled water, they were subsequently stained with fluorescein isothiocyanate to view the silica within the structures. All four available lasers at the excitation levels of 405 nm, 488 nm, 555 nm and 639 nm were applied with the 40× objective selected. The resulting image was visualised using microscope software and Adobe Photoshop.

A different procedure for the preparation of CLSM specimens was applied by Valdecasas & Abad (2011). After discovering that water mites have a strong autofluorescence signal (Valdecasas, 2008), Valdecasas & Abad (2011) aimed to compare the morphological conditions of the chitinised exoskeleton in different water mite species. The dorsal and ventral views of the mites were scanned before and after the extraction of proteinase K. The enzyme, proteinase K, was found to be effective in digesting the body content without affecting the external morphological structure of the samples (Roy *et al*., 2009). The specimens extracted using proteinase K, were found to be easier to dissect. This treatment also helped to enhance the natural fluorescence of the material and ultimately helped visualise the structures in more detail.

As well as the application of molecular extraction methods such as digestion and DNA extraction, Böhm *et al.* (2011), evaluated different mounting mediums and compared unstained and Congo red stained materials by imaging the exoskeleton and endoskeleton of Protura using CLSM. They considered that it was difficult to study minute arthropods without performing clearing and appropriate mounting methods before scanning. Their study highlighted the importance of the application of non-destructive DNA extraction methods. Böhm *et al.* (2011) modified a specific DNA digestion buffer from Pfeiffer *et al*. (2004) and Gilbert *et al*. (2007), comprising of 3mM $CaCl_2$, 2% sodium dodecyl sulphate (SDS) 40 mM dithiotreitol (DTT), 250 µg proteinase K, 100 mM Tris buffer and 100 mm NaCl. This buffer is used widely in molecular analysis. A similar digestion buffer containing SDS and DTT was previously applied by Kleinow *et al*. (1990) and Fischer & Aldrichs (2011) to *Cephalodella* species (Rotifera) prior to SEM analysis. The digestion contents and their immersion durations can differ according to the material being processed. For instance, Böhm *et al.* (2011) digested their specimens for about 2 hours at 55 °C whereas Gilbert *et al*., (2007) digested the beetles for about 16−20 hours with overnight incubation and Kleinow *et al.*

(1990) applied their digestion to dog hairs for about 2−5 hours during their forensic studies. A modified version of the Kleinow *et al*. (1990) digestion mixture was then applied to rotifers by Fischer & Aldrichs (2011). Apart from applying different non-destructive DNA extraction methods, Böhm *et al.* (2011) also examined unstained and stained the appendages from samples. Although an unstained head showed good autofluorescence, other appendages required staining with Congo red. They also trialled two different types of permanent mounting medium, polyvinyl lactophenol and euparal. Polyvinyl lactophenol was used for the unstained samples/appendages whereas euparal was only used for specimens stained with Congo red for about 1.5 days. The reason polyvinyl lactophenol was used for only unstained samples was that it changed the colour of Congo red stained material. As this mounting medium is also a pH indicator, it turned stained specimens blue. Böhm *et al.* (2011) emphasised that Congo red was not effective in staining the tarsal sensilla of their samples. Additionally, using the two different embedding media required changing the CLSM settings of the excitation levels between scans. Moreover, the low autofluorescence of unsclerotised cuticle also required making significant changes in microscope settings. As previously emphasised by Schawaroch & Li (2007), the study of Böhm *et al.* (2011) also highlighted that the application of 3D volume rendering should be used by experts who are familiar with the species. Furthermore, they considered that the artificial thickness of the images was a problem when volume rendering programmes were applied. The main problem was to measure length of the z-axis in CLSM image stacks because of the weak signal intensity. This could cause misinterpretation. Therefore, they applied "*non-blind deconvolution algorithms which utilise a measured point spread function obtained by confocal image stacks*" (Difato *et al*., 2004) to compensate for this problem. 3D software programmes were applied to solve the similar problem in the study of Ball *et al.* (2017a).

Hess & Bauer (2002) stained testes and pleopods of the adult hermit crab, *Clibanarius vittatus*, with acid fuchsin in order to make the appendages clearer for drawing under light microscopy. Acid fuchsin was also used for the histological studies of *Hippolyte inermis* (Decapoda) by Manjón-Cabeza *et al*. (2009). Light green + orange G+ acid fuchsin and other mixtures of stains were used for their study. The application of acid fuchsin to stain the cuticular structure of the crustaceans being prepared for CLSM was conducted by Kottman *et al*. (2013). A whole specimen of *Wellsopsyllus antarcticus* (Copepoda) was stained with aqueous acid fuchsin, scanned using three lasers and visualised with MIP and Adobe Photoshop. In their study, acid fuchsin proved to be an effective dye for external morphology. Acid fuchsin stain with water solution was also used to scan the holotypes of *Emertonia clause* and *Emertonia ingridae* (Copepoda) prior to using CLSM. Good resolution was obtained using MIPs and Adobe Photoshop (Pointner *et al*., 2013). In the study of Brix *et al*. (2014) adult specimens of *Chelator aequabilis* (Isopoda) were stained with Congo red, whereas an adult specimen of *Parvochelus russus* (Isopoda) was stained with acid fuchsin for their observations using CLSM. Brandt *et al*. (2014) studied undissected and dissected males and females of *Atlantoserolis vemae* (Isopoda). Their specimens were stained with a mixture of Congo red and acid fuchsin, embedded in glycerine and scanned using 3 lasers at excitation levels of 488 nm. Brandt *et al*. (2014) applied MIPs and Adobe Photoshop to their scan data and their results demonstrated that using this mixture of two stains proved to be an effective method for the study of external morphology. Recently, this effective mixture was also used in the study of Vakati *et al*. (2016) for observations of *Nanopus* (Copepoda) prior to CLSM.

In the latest studies, glycerine was the favoured mounting medium for arthropods. Dreszer *et al*. (2015) used glycerine as a mounting medium for their examination of *Cyphophthalmus solentiensis* (Arachnida) using CLSM. In addition, Wilkommen *et al*.

(2015) applied a similar method to visualise *Ischnura elegans* (Insecta) using confocal microscope software and they obtained successful results. Recently, the different structures of the arthropods were examined by Michels *et al*. (2016). The mixture of autofluorescence and Congo red stained arthropods were visualised using different excitation levels. See Table 4.1 as a summary of previous CLSM studies.

Table 4.1: List of reviewed papers that used CLSM in the study of macro-invertebrates with information on studied material, stain, mounting medium, confocal microscope, visualisation and performance observed.

References	Species	Stain	Mounting medium	CLSM	Visualisation*	Performance
Bundy and Paffenhöfer (1993)	*Labidocera aestival*, *Eucalanus pileatus*, *Centropages velificatus* (Copepoda)	DiI (Dioctadecyl-tetramethylindocarbocyanine perchlorate)	Seawater	Biorad MRC600	VoxelView	Optical cross-sections of the specimens can be animated and rotated in 3D.
Galassi *et al*. (1998)	*Moraria poppei*, *Parastenocaris vicesimal* (Copepoda)	Autofluorescence	Polyvinyl lactophenol	Sarastro 2000	Maximum intensity projection (MIP)	CLSM provides better understanding of 3D structure of copepods.
Carotenuto (1999)	*Temora stylifera* (Copepoda)	Autofluorescence	Seawater	Zeiss 410	MIP	A non-destructive and fast method to distinguish transparent copepod stages.
Buttino *et al*. (2003)	*Calanus helgolandicus* (Copepoda, Calanoida), *Hippolyte inermis* (Decapoda)	DiI (Dioctadecyl-tetramethylindocarbocyanine perchlorate)	Seawater	Zeiss 410	Zeiss and Crisel instruments software packages MetaVue	Using bright-field microscopy is time consuming, however, CLSM is an effective method for visualising copepod morphology.

Table 4.1: Continued.

References	Species	Stain	Mounting medium	CLSM	Visualisation*	Performance
Klaus *et al*. (2003)	*Culex tarsalis*, *Drosophila melanogaster* (Insecta)	Autofluorescence	Euparal, Glycerine jelly	Zeiss 510	MIP, volume rendering and isosurface rendering	MIP images can be ambiguous. Volume rendered models enhance surface features.
Klaus & Schawaroch (2006)	*Drosophila melanogaster, Culex tarsalis*, *Cladochaeta inversa* (Insecta)	Autofluorescence	Euparal, Glycerine jelly	Zeiss 510	Zeiss LSM image browser for MIP and Imaris	Using spacer between coverslips protects 3D structure of the specimens. MIP images are good, but Imaris provides more satisfactory visualisation.
Michels (2007)	*Acanthocyclops mirnyi*, *Heterorhabdus* sp., *Alteutha potter* (Copepoda)	Autofluorescence	Euparal, Glycerine jelly	Leica TCS SP5	Amira 3D software	Euparal produces red autofluorescence at excitation wavelength of 488nm or less. Glycerine jelly is a favourable embedding medium to visualise tiny structures of crustaceans.
Schawaroch & Li (2007)	*Drosophila melanogaster* (Insecta)	Autofluorescence	Glycerine jelly (mixture of mountants)	Zeiss 510	Zeiss LSM image browser for MIP and Imaris	Using agarose with glycerine jelly decreases background noise. Using 3D image re-construction removes low level of background noise.

Table 4.1: Continued.

References	Species	Stain	Mounting medium	CLSM	Visualisation*	Performance
Valdecasas (2008)	Water mites; *Vagabundia sci* (Axonopsinae (Acari, Parasitengona, Hydrachnidia)	Autofluorescence	Glycerine jelly	Leica TCS SP2	ImageJ	CLSM provides more efficient results than bright field microscope results.
Lee *et al*. (2009)	*Carpatolechia* (Insecta)	Autofluorescence, Mercurochrome, Safranine, Chlorazol black E, Eosin Y, Eosin Y + Chlorazol black E, Orange G	Euparal	Zeiss LSM 510	MIP	Autofluorescence level of chitin was low. The best results were obtained using eosin Y, safranine and mercurochrome respectively. Poor images were obtained using orange-G and eosin Y + chlorazol black E.
Maruzzo *et al*. (2009)	*Artemia* (Crustacea, Branchiopoda, Anostraca)	Evans Blue	Glycerol	Nikon Eclipse E600	MIP	Specimens digested in KOH and stained with Evans Blue provided better results.
Butler *et al*. (2010)	*Ballonema gracilipes* (Chilopoda)	Autofluorescence	Canada balsam	Leica TCS SP1	MIP	Non-destructive imaging for historical museum material. Resolution is comparable to SEM. Canada balsam makes specimens more fluorescent for CLSM visualisation.

Table 4.1: Continued.

References	Species	Stain	Mounting medium	CLSM	Visualisation*	Performance
Michels & Büntzow (2010)	Small crustaceans and polychaetes	Autofluorescence, Congo red	Glycerine	Leica TCS SP5	Leica LAS software for MIPs	Congo red stains exoskeleton effectively, but internal tissues and proteins were not stained so successfully.
Böhm *et al.* (2011)	*Ionescuellum carpaticum* (Protura, Entognatha Artrophoda)	Autofluorescence Congo red	Polyvinyl lactophenol (unstained), Euparal (Congo red)	Leica TCS SP 2	MIP, Fiji, OsiriX	Congo red fades in polyvinyl lactophenol, any mountant such as Euparal can be used so long as it is not strongly autofluorescent. Autofluorescence of unsclerotised cuticle is low. Stained regions with Congo red was effective.
Menzel (2011)	*Mesocletodes elmari* sp. (Copepoda, Harpacticoida, Argestidae)	Congo red	Glycerol	Leica TCS SP5	MIP	Successful visualisation.
Valdecasas & Abad (2011)	Aquatic mites (Acari, Hydrachnidia)	Autofluorescence	Glycerine jelly	Leica SPE	ImageJ to obtain MIPs, Gamma correction with Photoshop CS3	Using proteinase K does not affect the external morphology of mites.

Table 4.1: Continued.

References	Species	Stain	Mounting medium	CLSM	Visualisation*	Performance
Brooker *et al*. (2012)	*Lernaeocera branchialis* (Copepoda)	Blankophor, Gomori's trichrome	Distilled water	Leica TCS SP2	Leica Confocal Software (MIP), Photoshop CS3	Successful visualisation.
Brooker *et al*. (2012)	*Lernaeocera branchialis* (Copepoda)	Blankophor, Gomori's trichrome	Distilled water	Leica TCS SP2	LCSM composite images in Photoshop CS3	Using 3D CLSM stack data to draw specimens digitally provides accurate data.
Kihara & Martinez Arbizu (2012)	*Cerviniella danae*, sp. nov., *Cerviniella arctica* sp. nov., *Cerviniella hitoshii* sp. nov. (Copepoda, Harpacticoida)	Congo red	Glycerine	Leica TCS SP5	LAS AF 2.2.1. for MIPs and CLSM illustrations, Adobe Photoshop CS4	For the taxonomic study of new species, CLSM is used to visualise the details of the appendages of the specimens.
Michels & Gorb (2012)	*Locustamigratoria*, *Sympetrum striolatum*, *Eristalis tenax* and so on (Insecta), *Temora longicornis* (Copepoda)	Autofluorescence, Congo red	Glycerine	Zeiss LSM 700	ZEN software	CLSM is a good tool to visualise resilin in arthropods. It is also effective to detect the differences in the material composition.
Michels *et al*. (2012)	*Centropages hamatus* (Copepoda)	Congo red, Fluorescein isothiocyanate	Glycerine	Zeiss LSM 700	Nikon Capture NX 2, Adobe Photoshop CS4	Successful visualisation.

Table 4.1: Continued.

References	Species	Stain	Mounting medium	CLSM	Visualisation*	Performance
Brandt *et al*. (2014)	*Atlantoserolis vemae* (Isopoda: Serolidae)	Congo red and acid fuchsin	Glycerine	Leica TCS SPV	LAS AF 2.2.1. for MIPs and CLSM illustrations, Adobe Photoshop CS4	Stained whole specimen and the dissected parts (e.g. mouthparts and legs) were visualised using CLSM.
Kaji *et al*. (2014)	Clam shrimp (Crustacea, Branchiopoda)	Rhodamine, Phalloidin	Vectashield	Leica TCS SP5 II	Imaris	The cuticle surface is smooth and fine setae are present using Imaris.
Dreszer *et al*. (2015)	*Cyphophthalmus solentiensis* sp. nov. (Arachnida)	Autofluorescence	Glycerine	Zeiss Elyra	Carl Zeiss Zen software	Successful visualisation by taking advantage of the autofluorescence of the arthropod cuticle.
Wilkommen *et al*. (2015)	*Ischnura elegans* (Insecta)	Autofluorescence	Glycerine	Zeiss LSM 700	ZEN 2009 for MIPs	Successful visualisation.
Michels *et al*. (2016)	*Locusta migratoria* (Insecta) *Temora longicornis* (Copepoda)	Autofluorescence, Congo red	Glycerine	Zeiss LSM 700	ZEN software	Successful visualisation.

*Papers did not provide detailed information on visualisation.

4.3 Aims

For the present study, consideration was given to the application of specimen cleaning agents, mounting medium, stains, digesting methods, confocal settings during scanning and the use of 3D visualisation techniques. Other studies only used methods that were considered applicable to the specific specimen being examined. The reason for this is that the researchers' specimens/material were of different sizes and they aimed to undertake scanning of either whole animals or only dissected appendages. The size, structure and morphology of these specimens from these investigations were completely different from each other. The closest study comparable to this present work was conducted by Michels & Büntzow (2010) who examined a decapod larva (Grapsidae) that was not named in his research. They stained whole specimens of a crab larva with Congo red prior to scanning. This present study was based on developing this technique further and adapted its application to dissected larval appendages. Michels & Büntzow (2010) acknowledged that brachyuran crab larvae were challenging, especially setae, in particular provided an extremely weak signal. Consequently, the present study required different techniques in cleaning specimens, mounting, staining, scanning and 3D visualisation packages.

Therefore, a new workflow was established to apply not just to Chinese mitten crab larvae but also to other brachyuran species such as *Armases miersii* and *Sesarme curacaoense*. The purpose of this present study was to trial different combinations of preparation, scanning and post-processing techniques specifically for small brachyuran specimens and to demonstrate a workflow for the 3D imaging of this material using a combination of ImageJ and Drishti (both free and open-source software packages) to process the resulting CLSM data.

4.4 Different applied methods

The procedures for preparing specimens for CLSM and subsequent visualisation differ greatly depending on the material. The best approach for this current study was to modify techniques in line with the requirements of the larval material to be examined. Therefore, the present study trialled two types of microscope slides, two cleaning reagents, four mounting media, three staining methods, different CLSM settings, and two rendering programmes to observe the best combination for developing an optimum technique to visualise zoeal development.

4.4.1 Specimen preparation

Cleaning and digesting agents

Decon 90 diluted using 70% ethanol (as explained in detail in Chapter 2) was applied to the contaminated specimens only. The SDS + DTT solution was applied to all zoeal stages of the Chinese mitten crab larvae for different durations until all the muscles were completely digested.

Microscope slides

Cavity and plain slides were trialled for dissected first stage zoea of *Eriocheir sinensis*. Appendages were either directly embedded into a cavity slide or reinforcement rings were glued onto the plain slides to create wells.

Mounting media

Normal strength polyvinyl lactophenol, polyvinyl lactophenol diluted with 70% ethanol, glycerine and glycerine diluted at different concentrations using deionised water were tested.

Application of the stains

Solutions of Congo red using both 70% ethanol and deionised water, and a mixture of Congo red and acid fuschin using deionised water (as explained in detail in Chapter 2) were prepared and trialled.

Combinations applied for the specimen preparation

The combinations applied are listed chronologically and in detail, see Table 4.2.

Table 4.2: Combination of methods applied to determine the optimum visualisation technique using CLSM to examine dissected zoeal stages of brachyuran crabs.

Combinations applied #	Microscope slide	Mounting medium	Cleaning	Digesting	Staining	CLSM	Visualisation/ Post-processing
1	Plain slide	PVLP	☒	☒	Autofluorescence	☑	MIP + APS
2	Plain slide with pieces of coverslip	PVLP	☒	☒	Autofluorescence	☑	MIP + APS
3	Cavity slide	PVLP	☒	☒	Autofluorescence	☑	MIP +APS
4	Cavity slide	Diluted PVLP with 70% ethanol	☒	☒	Autofluorescence	☑	MIP + APS
5	Plain slide with divided RR	Diluted PVLP using 70% ethanol	☑	☒	CR prepared using 70% ethanol	☑	Processed exporting one channel using confocal software+ Drishti + APS
6	Plain slide with RR	Glycerine	☑	☑	CR prepared using 70% ethanol	☑	Processed exporting one channel using confocal software + Drishti +APS
7	Plain slide with RR	Glycerine/ DI water 50/50	☑	☑	CR prepared using 70% ethanol	☑	Processed exporting one channel using confocal software + Drishti +APS
8	Plain slide with RR	Glycerine/ DI water 50/50; 25/75;10/90	☑	☑	CR prepared using 70% ethanol	☑	Processed exporting one channel using confocal software + Drishti +APS

Table 4.2: Continued.

Combinations applied #	Microscope slide	Mounting medium	Cleaning	Digesting	Staining	CLSM	Visualisation/ Post-processing
9	Plain slide with RR	Glycerine/ DI water 50/50; 25/75;10/90	☑	☑	CR prepared using DI water	☑	Processed exporting two channels using confocal software + Drishti +APS
10	Plain slide with RR	Glycerine/ DI water 50/50; 25/75;10/90	☑	☑	CR prepared using DI water	☑	ImageJ + Drishti +APS
11	Plain slide with RR	Glycerine/ DI water 50/50; 25/75;10/90	☑	☑	CR prepared using DI water	☑	Avizo + APS
12	Plain slide with RR	Glycerine/ DI water 50/50; 25/75;10/90	☑	☑	Mixture of CR and AC prepared using DI water	☑	ImageJ + Drishti +APS

Note: PVLP = polyvinyl lactophenol; RR= reinforcement ring; CR = Congo red; AF = acid fuschin; MIP = maximum intensity projection; DI = deionised water; APS = Adobe Photoshop.

4.4.2 CLSM settings

Prepared slides were scanned applying different CLSM settings. “Pinhole size” was mostly set to 1.2 AU (airy unit). Pinhole diameter is adjusted according to the objective used. This is used to detect the thickness of the sections (The W.M. Keck Microscopy Center, 2017). The calculation of the width of 1 Airy unit is given as “Airy disk diameter × magnification of lens = 1 Airy unit = resolution of lens × magnification of lens × 2” by Thorn (2017). Settings were applied using 512 × 512 pixel size for “faster live scanning”. All materials were scanned applying 1024 × 1024 pixel size. 2048 × 2048 pixel size was rarely utilised. All averaging settings, 16×, 8×, 4×, 2× (which are applied to reduce noise) were trialled depending on the noise level of the preparations. “Ch Series” was turned “on” in the early experiments (see combinations applied # 1−7 in Table 4.2). Then, “Ch Series” was turned “off” for the rest of the experiments. Ch series is to decide whether to operate all lasers together or one laser after another. All appendages, according to their size, were scanned at different magnifications including 10×, 20× dry objectives or 40× and 60× oil immersion objectives. Gain (HV) was set for each sample separately. “Offset” was decreased to negative values in some experiments (see combinations applied # 1−7 in Table 4.2). Then, the “Offset” was increased to positive values to obtain more signal from weak areas such as setules (see combinations applied # 8−12 in Table 4.2). Gain/offset settings are used for adjusting background and sensitivity of the detectors and subsequently brightness of produced images.

4.4.3 Post-processing

Two types of projection can be created automatically by the confocal software: Maximum Intensity Projection (MIP) uses the brightest pixel at any X/Y position within the Z-stack, whereas the Average Intensity Projection (AIP) uses the average of all

pixels in the Z-stack at each X/Y position (Ball *et al.*, 2017a). Early results, in the present thesis, were visualised as maximum intensity projections using the confocal microscope software (see combinations applied # 1−4 in Table 4.2). The samples where the offset was increased were processed using the confocal software to apply a black background to the image; as described in Chapter 2. Maximum intensity projections were then processed using Adobe Photoshop to adjust the levels – to give the best combination of brightness and contrast.

As the confocal software was found insufficient for 3D reconstruction in the present study, all confocal data were processed using the 3D rendering programme, "Drishti" by converting the confocal data into TIFF stacks by using either the confocal software or standardising confocal data using ImageJ. The commercial software programmes "Avizo" and "VGStudio Max" were also tested to compare effectiveness of the 3D techniques and merge images in 3D respectively. All images were then finalised by applying Adobe Photoshop as explained in Chapter 2.

4.4.4 SEM

SEM, in the present study, was used for two purposes. First, to visualise the setation on the carapace as well as to visualise the other larger material such as the pleon. These appendages were too thick to visualise fine setae using CLSM. Second, it was used to chemically analyse to help to devise an improved cleaning strategy for the structure of the debris found on the exoskeleton of the contaminated larvae.

4.5 Results and discussion

Microscope slide and mounting methods

Initially, a zoea was transferred into a few drops of polyvinyl lactophenol (PVLP) placed on a glass slide (see applied combination # 1 in Table 4.2). The zoea was dissected and the appendages were arranged within the PVLP. A cover slip was then carefully placed on the mountant and left to settle. There were a number of problems with this technique that resulted from the weight of the cover slip including appendages were crushed/flattened, the appendages moved around in the media from their original positions and the appendages could be squeezed out from under the cover slip into the surplus PVLP. To prevent the crushing of appendages, broken glass shards of cover slips were place around the PVLP in which the zoea was to be dissected (see applied combination # 2 in Table 4.2). The cover slip was then carefully laid across the glass shards. Although the appendages were not flattened, they still moved about while the cover slip was settling down. Furthermore, while the PVLP was hardening, it shrank and air bubbles eventually formed under the cover slip, spoiling the position or engulfing the appendage.

PVLP in glass cavity slides were also trialled, however, the appendages still moved when the cover slip was applied (see combinations applied # 3−4 in Table 4.2). Consequently, some appendages settled on against the slope of the cavity instead of resting flat. When diagonally positioned appendages were scanned, the duration time increased because of the depth of focus and the number of z-stacks required to provide an image compared to if the sample was horizontal.

In order to produce a well, that stopped the cover slip from crushing the specimen, self-adhesive, plastic reinforcement rings were trialled. These were dived into quarters (see applied combination # 5 in Table 4.2). The reinforcement rings remained stationary but

the issues regarding the movement of dissected appendages and the formation of air bubbles remained.

The PVLP mountant was changed to glycerine which was more viscous, however, in order to retain a well the reinforcement rings were kept whole (see applied combination # 6 in Table 4.2). In order to prevent shrinkage, in the rest of the trials, glycerine was diluted with different concentrations using deionised water and a whole reinforcement ring (see combinations applied # 7−12 in Table 4.2).

Cleaning

Specimens were predominantly cleaned with Decon 90 (see combinations applied # 5−12 in Table 4.2) as detailed in Chapter 2. The results of the SEM-EDX analysis showed that debris found on limbs was composed of calcium carbonate (Fig. 4.2a). These items of debris were effectively removed using the surface-active cleaning agent, Decon 90 (4.2b). The sonication methodology proposed by Felgenhauer (1987) for cleaning aquatic arthropods, proved ineffective as it often resulted in the natatory setae of the maxillipeds of the zoeae becoming tangled. A similar problem was encountered when using a tumbler.

Digestion

Muscle digestion within specimens was accomplished by using a mixture of SDS + DTT (Fischer & Ahlrichs, 2011). This was an effective method of clearing the appendages, making them more transparent and fluorescent for CLSM imaging (see combinations applied # 6−12 in Table 4.2). The clearing of internal tissue also helped the visualisation of setae on the distal side of the appendage that were otherwise masked

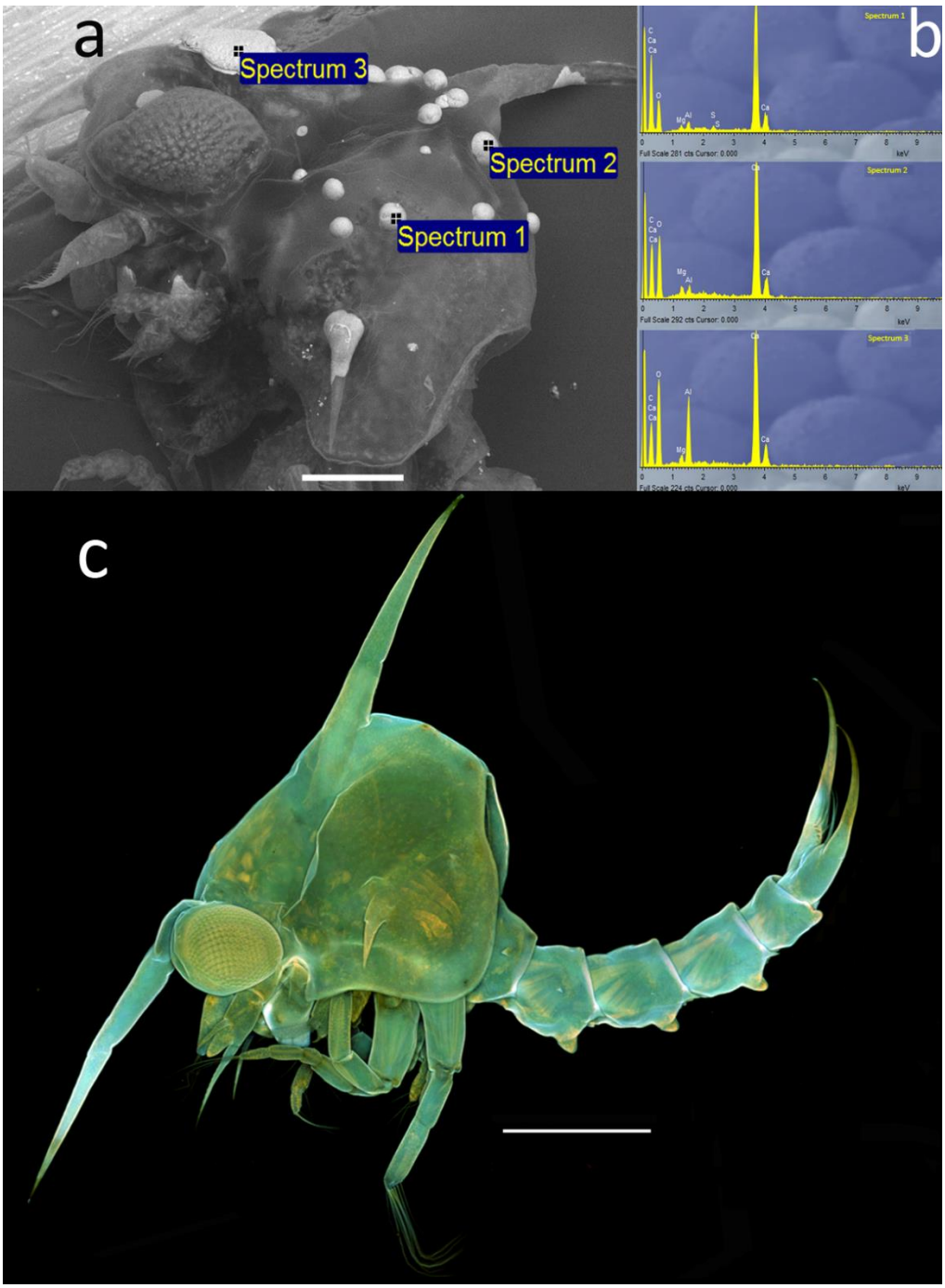

Figure 4.2: Cleaning *Eriocheir sinensis* using Decon 90. (a) SEM image of ZI showing debris and EDX testing locations. (b) Example of EDX spectra showing that the debris is rich in Calcium, Carbon and Oxygen indicating that it is composed of calcium carbonate. (c) CLSM image of ZIV, after cleaning the samples using Decon 90. Scale bars a = 300 µm; b = 500 µm.

behind the muscle blocks. Furthermore, dissection of zoeae became much easier after the specimen had been placed in the digesting solution. Another advantage of using the digestion mixture was to balance the acquisition settings of the confocal microscope to avoid having over/under saturated images. As the setae provided a weaker signal than the main part of the exoskeleton, the settings needed to be increased to visualise these smaller structures. If the settings were increased, however, the main exoskeleton had a tendency to become over saturated because it yielded a stronger signal (compare Fig. 4.3a and Fig. 4.3b).

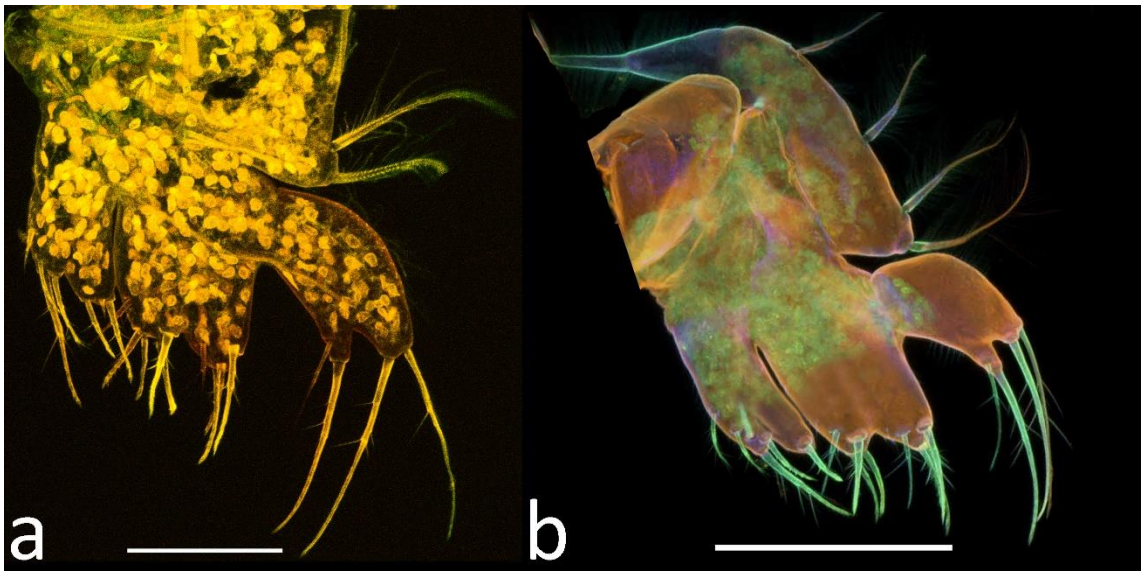

Figure 4.3 Advantages of digesting appendages. *Eriocheir sinensis*, zoea I, scanned images of the maxilla using CLSM. (a) Undigested, 60× oil immersion objective. (b) Digested, 40× oil immersion objective. Scale bars a = 50 μm; b = 100 μm.

If the appendage was not digested, however, some of the minute exoskeletal structures were "masked" (Fig. 4.4a) by the signal from basial musculature of the second maxilliped and could not be visualised using ImageJ and Drishti to manipulate the confocal stack data (Fig. 4.4b). After digestion of the basial muscles (Fig. 4.4c), these tiny structures could be visualised when fully processed (Fig. 4.4d).

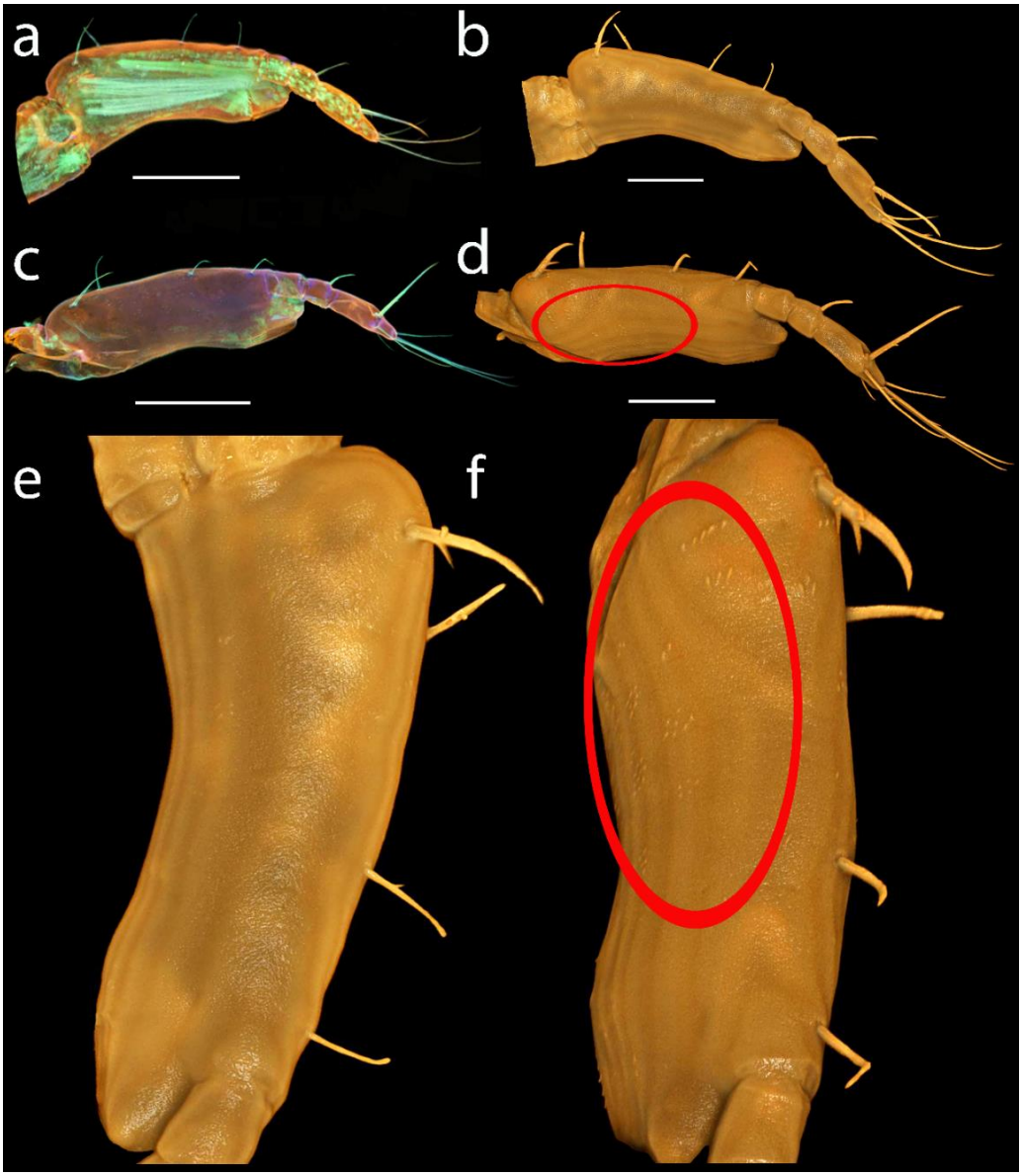

Figure 4.4: Advantages of digesting appendages. *Eriocheir sinensis*, zoea I, images of second maxilliped using CLSM. (a) Confocal image of non-digested appendage showing basial musculature. (b) Drishti image based on this data. c) Confocal image after digestion of the basial muscles. (d) Drishti image from this data (tiny structures are circled). All 40× oil immersion objective, applying "large images" option, scan area of 1×2 fields for image stitching. (e) Enlargement of (b). (f) Enlargement of (d). Scale bars = 100 μm.

Comparing methods to eliminate oversaturation after staining

Congo red has been commonly used as an external stain for crustaceans and polychaetes (Michels & Büntzow, 2010; Michels & Gorb, 2012) for CLSM. Although the present study demonstrated good results using Congo red alone (see combinations applied # 5−11 in Table 4.2), some appendages were not completely saturated by the stain (Fig. 4.5a). This problem of patchy staining was mentioned by Michels & Büntzow (2010) and Böhm *et al.* (2011) who were attempting to stain small crustaceans, the cuticle of polychaetes and the tarsal sensilla of Protura. Michels & Büntzow (2010) clarified that Congo red stained the exoskeleton effectively, but was not so successful for internal tissues and proteins. Böhm *et al.* (2011) attributed this to the embedding medium and compensated for this by changing acquisition settings during CLSM imaging. In order to overcome this problem in the present study, Congo red was mixed with acid fuchsin, which is another effective stain of arthropod exoskeletons. The combination of Congo red and acid fuchsin (see applied combination # 12 in Table 4.2) greatly improved the overall saturation of staining and proved a more effective way to balance the acquisition settings compared to using Congo red alone (Fig. 4.5b).

In addition, Michels & Büntzow (2010) suggested that after staining, specimens should be washed several times until the Congo red was no longer present prior to dissection. This was not found to be an issue in the present study because the specimens were removed from the stain and placed in a solution of diluted glycerine and then the appendages were dissected. The dissected appendages were then individually transferred to slides containing a fresh solution of dilute glycerine to be scanned; the specimens were thus effectively isolated from any excess Congo red.

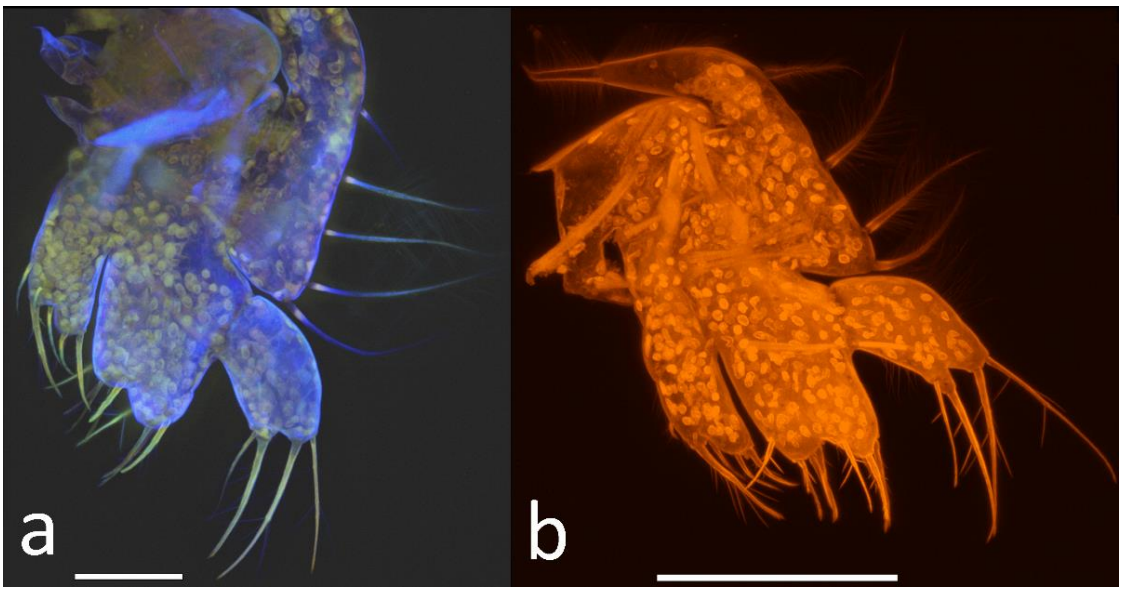

Figure 4.5: Advantages of staining. *Eriocheir sinensis*, zoea I, scanned images of the maxilla using CLSM. (a) Stained using only Congo red, 60× oil immersion objective. (b) Stained using the mixture of Congo red and acid fuchsin, 40× oil immersion objectives. Scale bars a = 50 μm; b = 100 μm.

In the present study, the shrinkage of specimens posed a real problem. One of the factors that cause shrinkage was the preparation of the stains. If the Congo red and acid fuschin powders were mixed using deionised water, then shrinkage did not occur (see combinations applied # 9−12 in Table 4.2). Congo red and acid fuschin powders prepared with 70% ethanol cause shrinkage as the present study required a long staining duration (see combinations applied # 5−8 in Table 4.2).

Advantages of digesting and staining in CLSM and post-processing

Digesting and staining greatly improved the confocal images and help to avoid them being oversaturated. In order to visualise fine setae on appendages, the signal gain level needed to be increased during confocal scanning. If set low, setae are scanned weakly (Fig. 4.6a). When appendages are stained using only Congo red, the chance of obtaining

a better signal from setae increased, however, this resulted in an oversaturated image (Fig. 4.6b). The reason for this was the stain dyed the whole appendage including the internal muscle (Fig. 4.6c). This was not required as only the external morphology needed to be visualised for the present study. In digestion treated appendages, the internal muscles were completely dissolved and the subsequent staining with Congo red and acid fuschin meant that the signal was only emitted from the exoskeleton (Fig. 4.6d).

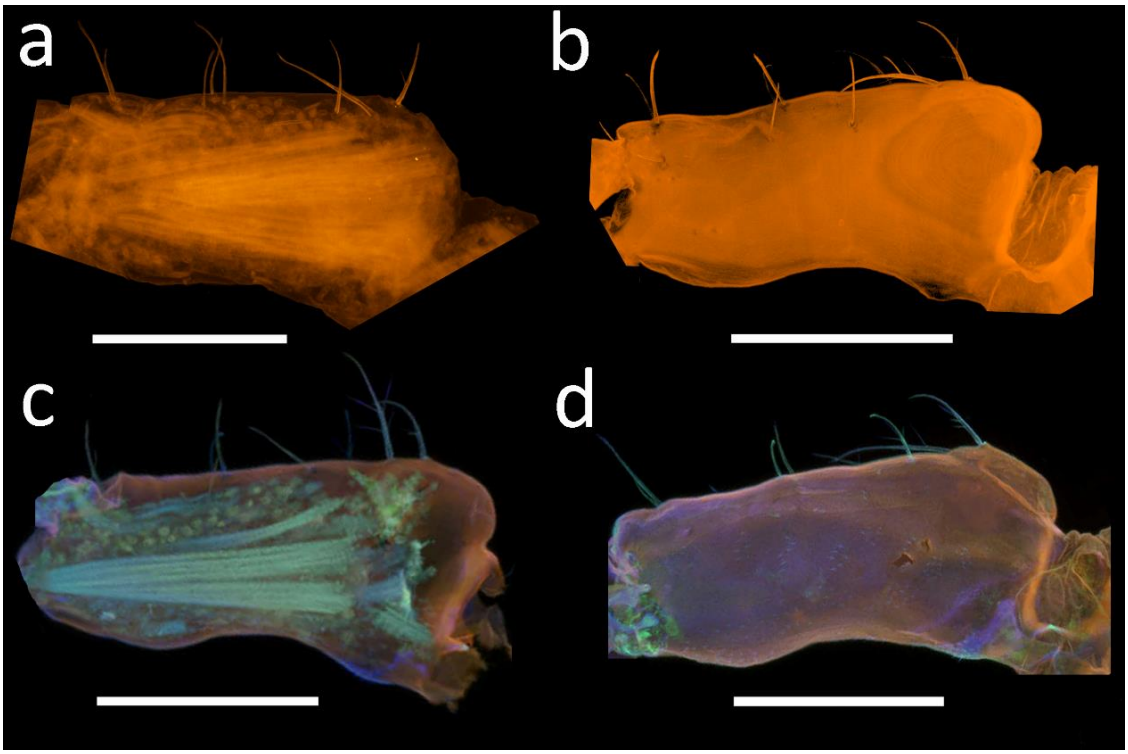

Figure 4.6: *Eriocheir sinensis*, zoea I, scanned images of first maxilliped using CLSM. (a) Non-digested and unstained appendage. (b) Stained using Congo red. (c) Non-digested and stained using the mixture of Congo red and acid fuschin. (d) Digested and stained using the mixture of Congo red and acid fuschin. Scale bars = 100 µm.

Avoiding problems of over/under saturation while scanning samples was also important for post-processing of the acquired data using Drishti. When the sample was non-digested and unstained properly, it reflected the final Drishti image (see combinations

applied # 6−12 in Table 4.2; Fig. 4.7a), this resulted in poor, low resolution images after processing. This was due to the weak CLSM signal. Chromatophores and other internal structures (i.e. muscles) disrupted the final image (Fig. 4.7b). When material was digested and stained, the final Drishti images were detailed and with high resolution (Figs. 4.7c, d). Therefore, early experiments in the present study failed to supply adequate data to visualise appendages properly.

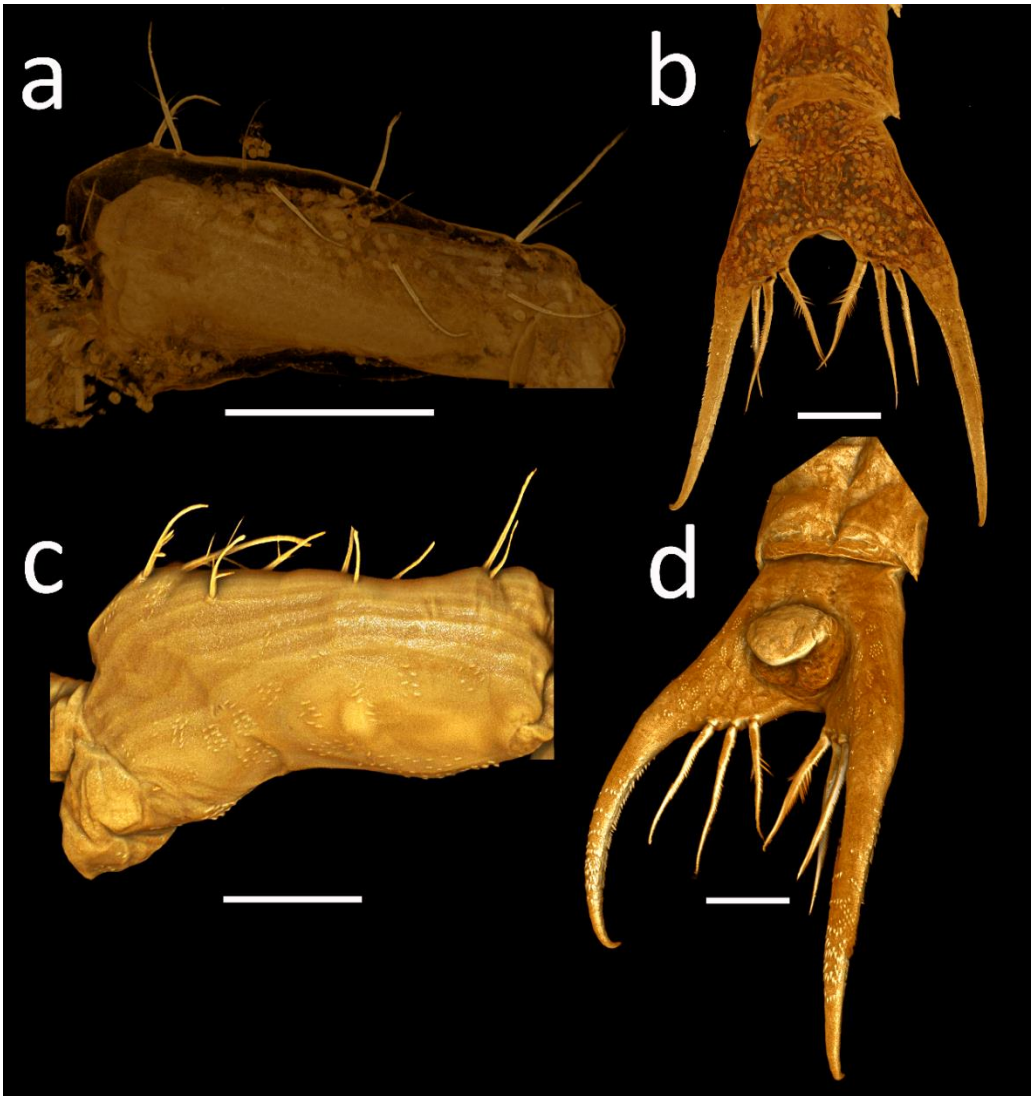

Figure 4.7: *Eriocheir sinensis*, zoea I, scanned appendages using CLSM and processed using Drishti. (a) Non-digested and unstained first maxilliped. (b) Non-digested and stained dorsal view of telson. (c) Digested and stained first maxilliped. (d) Digested and stained ventral view of telson. Scale bars = 100 μm.

Comparison of mounting media

Two types of mounting medium were trialled; polyvinyl lactophenol (permanent) and glycerine (non-permanent). Clark *et al*. (1998b) suggested that polyvinyl lactophenol (PVLP) was a good mounting media for examining brachyuran crab larvae as it cleared appendages, did not inhibit transmitted light and resulted in a permanent slide. Therefore, PVLP was initially trialled and proved to be extremely viscous and hard when set. An advantage of a hard setting mountant was that during scanning the heat caused by the laser did not change the position of the specimen. But there are a number of disadvantages to a hard setting mountant including that the manipulation of appendages into an improved position for CLSM was almost impossible, recovery of the specimen to use it for DNA analysis after scanning was difficult, if PVLP was used and during dissection, much debris was produced and these fragments adhered to the appendages (Fig. 4.8a-b) causing background noise during scanning. Indeed, removing the debris from the appendage or background using Drishti or Adobe Photoshop proved extremely time-consuming and was not always successful (see circled areas, Fig. 4.8c). The background noise could be compensated for by increasing averaging times. But this would increase the duration of scanning. For example, scan time doubled with 2 times averaging, quadrupled with 4 times averaging and increased by a factor of 8 with 8 times averaging. Consequently, a clean background reduced the duration of scanning and helped to avoid bleaching of the stain. Another issue with PVLP was that it caused immediate shrinkage of the specimens that were transferred to the medium. The mountant could be diluted with alcohol to avoid specimen shrinkage, but, both polyvinyl lactophenol and alcohol, individually and together, did in time bleach stained material. Another disadvantage of using PVLP was that Congo red stained appendages turned blue (see arrowed areas, Fig. 4.8d) as the mountant is a pH indicator (Böhm *et al.*, 2011).

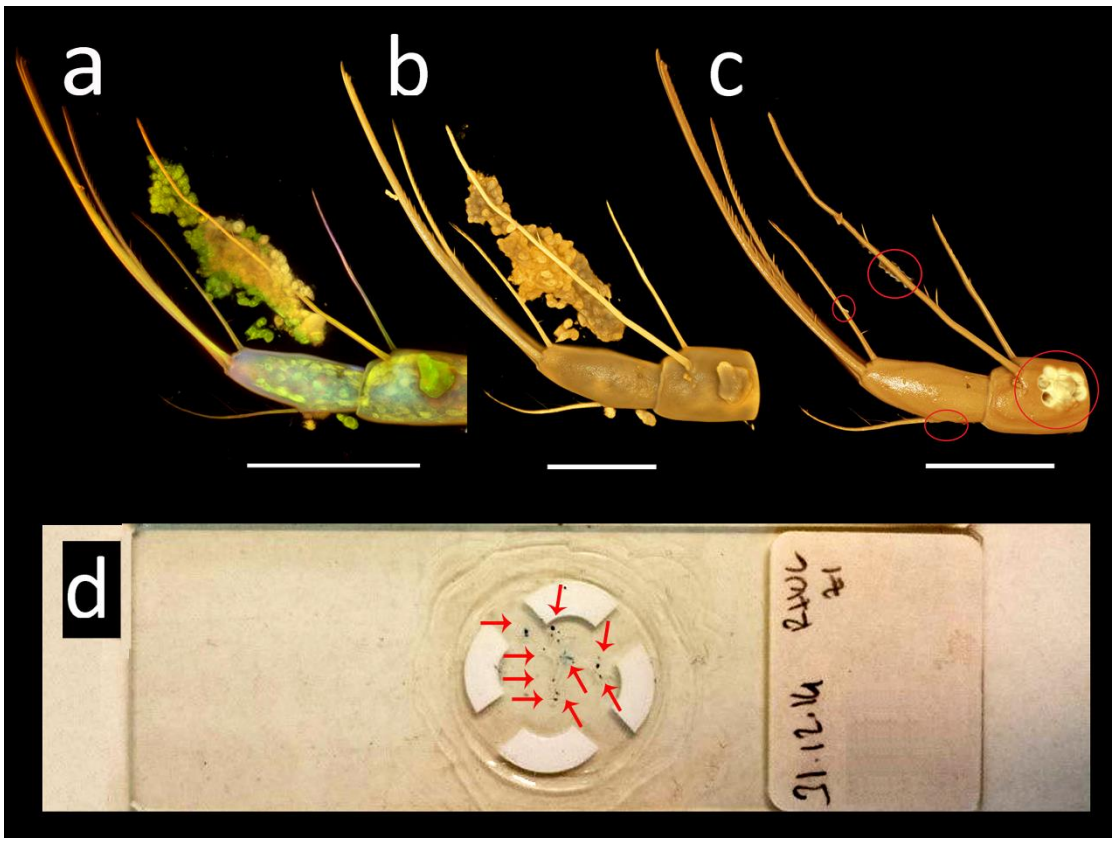

Figure 4.8: Disadvantages of using polyvinyl lactophenol with stained *Eriocheir sinensis* zoeal appendages. Debris from dissection adhered to the exoskeleton. (a) ZII, confocal image of endopod using CLSM, 60× oil immersion objective. (b) ZII, Drishti image of endopod. (c) ZII, attempt at debris removal using Drishti and Photoshop was not always successful, see circled areas (d) Mounted Congo red stained appendages stained blue, see arrowed areas. Scale bars a-c = 100 μm.

Glycerine proved to have a number of advantages over PVLP and was therefore the preferred mounting medium for CLSM studies. Shrinking specimens placed in diluted glycerine could be recovered with the addition of more deionised water and, furthermore, could be easily manipulated for re-positioning. A disadvantage of this medium, especially when diluted, was that it could be heated by the lasers during scanning. There was a tendency for this mountant to liquefy which caused movement of the specimen. Another problem was the formation of air bubbles. Their expansion

during scanning caused the specimen to move and the production of a blurred final image (Fig. 4.9a). Air bubbles also tended to form over time and appeared overnight between mounting the specimen and scanning (Fig. 4.9b). This was possibly because the initial volume of fluid was insufficient or evaporation had taken place. It was therefore better to scan directly after the sample had been mounted. Furthermore, samples could also lose their stain if allowed to remain in glycerine over long periods of time.

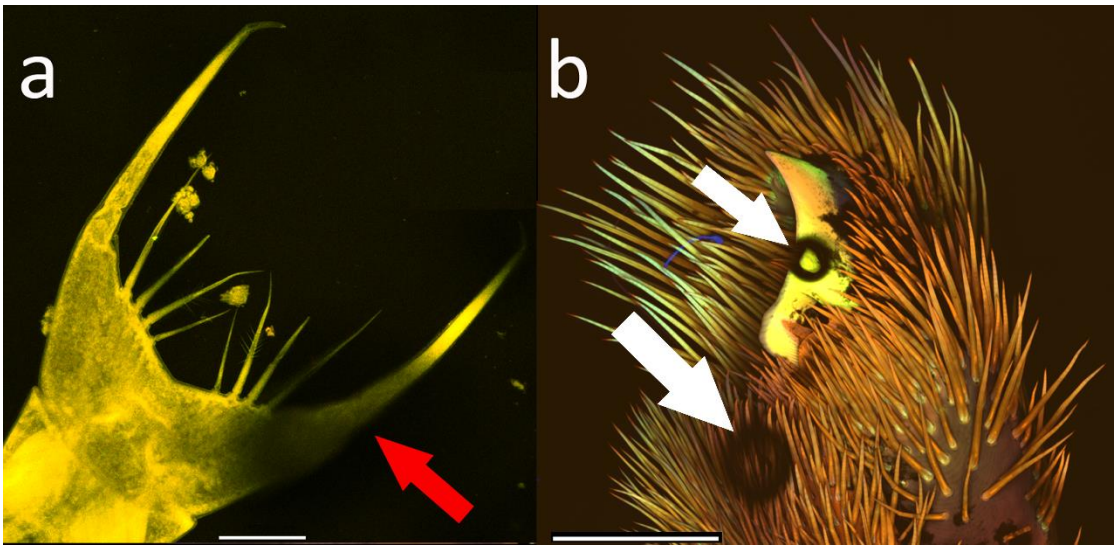

Figure 4.9: Disadvantages of using diluted glycerine for mounting the samples. (a) Blurred images because the specimen had moved, (arrowed area). (b) Creation of air bubbles and disruption of the image, (arrowed areas). Scale bars a = 100 μm; b = 1000 μm.

Scanning procedures

Using cavity slides was not found to be effective in the present study. Another disadvantage of the cavity slide was that a longer scanning duration for the appendages was required when they were not positioned horizontally. Vertically positioned

appendages increased the number of the z-stacks to be scanned and thereby lengthened the scanning duration as well as caused loss of resolution.

The use of plastic reinforced rings, stacked on plain glass slides, proved extremely effective. This created an adequate space (well) under the coverslip and prevented the samples from being crushed and distorted. Once the sample was correctly positioned, the confocal microscope was able to obtain extremely high-quality image data. As the setae and body part of the appendages have different signal levels, applying z-intensity correction during scanning proved to be an effective method to avoid over/under saturated images. "Z-intensity correction" option helped to adjust and optimise the signal levels of the scanned specimen along the Z plane while scanning.

Scanning samples using channels at different excitation levels was a more effective method than only using one channel. Scanning the samples at 1024 ×1024 pixel size was found sufficient for the present study considering that the data was to be processed using a 3D rendering programme. Therefore, 2048 × 2048 pixel size was not applied most of the samples as this quadrupled the scanning duration.

For the present study, 16×, 8×, 4× and 2× averaging times depending on the samples, were initially applied to decrease the background noise. When individual appendages were mounted in clean, fragment free, diluted glycerine, then the scanning duration could be decreased to 2× averaging times. This greatly reduced the chance of movement, dehydration, bubbles and photo bleaching.

Another effective improvement in lowering the scanning time involved the "Ch series" option. When Ch series was on, the microscope scanned each sample 4 times using only one laser channel in each round. These scans were then merged at the end of the scanning process with "Ch series" disabled, the microscope scanned all channels simultaneously. For the present study, there appeared to be no real difference between

the samples scanned using “Ch series” enabled compared to when “Ch series” was switched off. Therefore, “Ch series” was not applied for the rest of the scans. Another time saving improvement was the use of fragment free samples and mounting media. This allowed samples to be scanned by applying faster settings. These applications greatly decreased the scanning duration from 2−3 hours for only one appendage to 20−30 minutes when applying the 40× oil immersion objective. When applying lower power objectives such as 10× and 20× the scanning duration decreased considerably i.e. to 6−15 minutes as less frame time was needed.

Decreasing the scanning duration prevented the lasers from bleaching the stain from the specimens, and also allowed more appendages to be examined in one CLSM session. The latter was more cost effective considering the expense of running a CLSM as well as saving time and accelerating the process of examining specimens in detail.

Scanning large specimens is also extremely time-consuming, especially at high resolution, because the material does not completely fit in the field of view. Therefore, to produce a complete image, the specimen must be scanned part by part separately and the data later merged using either Adobe Photoshop or VGStudio max. Both these merging processes are extremely time-consuming. There is another method, however, using the “large images” option. This alternative method scans the specimen in sections known as tiles and a whole extended field of view is automatically produced by the confocal software package. The main advantage in using the “large images” option is that the process of merging the tiles is automatic and completed without the use of Adobe Photoshop or VGStudio max.

The signal from setules of the setae was improved by increasing the “offset”, but the final MIP (Maximum intensity projection) did not have a distinct black background (Fig. 4.10a). There is an option to compensate for this using the confocal software

programme to create the MIP image (Fig. 4.10b) with a black background, however the details of the setules was degraded. If, instead of using the confocal software programme to create the MIP image, Drishti was applied then resulting TIFF has a black background and the details of the setules were clearly visible (Fig. 4.10c).

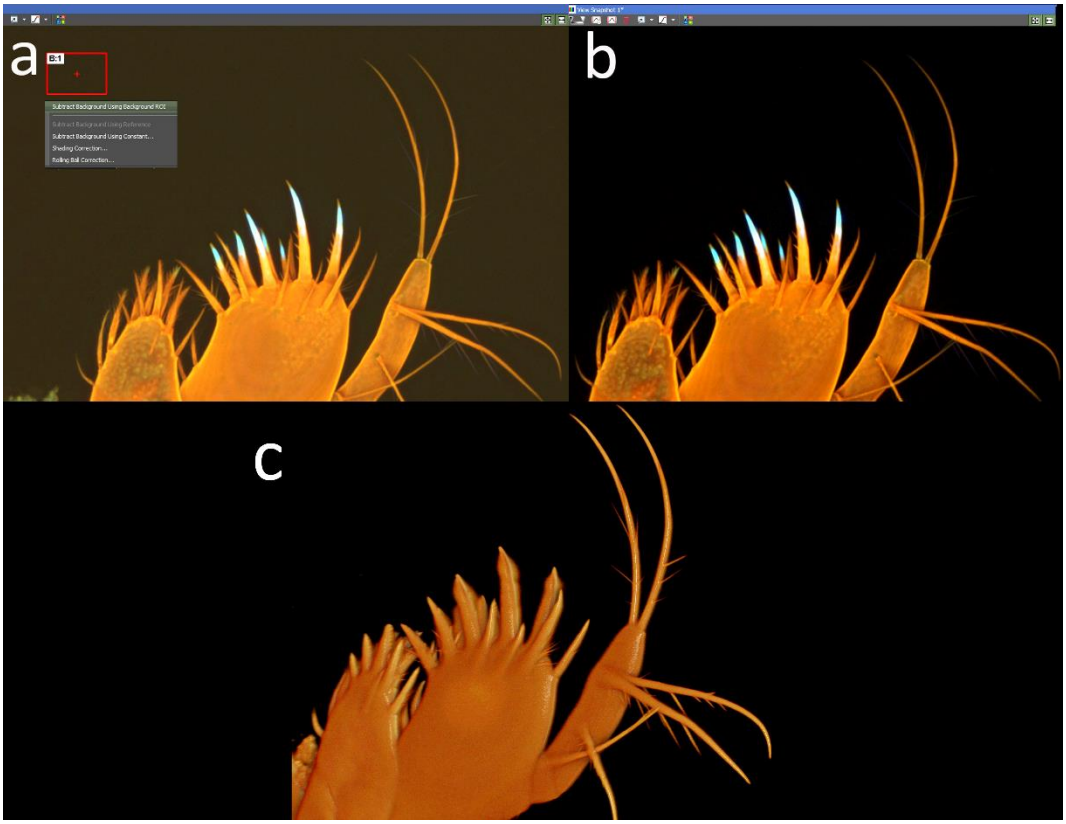

Figure 4.10: Compensating for background colour using confocal software and Drishti. (a) MIP after increasing the offset. (b) MIP with a black background. (c) Drishti processed image from the same dataset.

There were additional problems with larger specimens and the use of tiled data since long acquisition times increased the risk of movement (Fig. 4.11a). Furthermore, the resulting data files were exceptionally large and processing these data using Drishti required an extremely powerful computer (Fig. 4.11b). For example, the computer used

in the present study had an “Intel(R) Core(TM) i7-3770K CPU @ 3.50GHz with 16 GB installed memory (RAM) and NVIDIA GeForce GTX 670 graphics card.

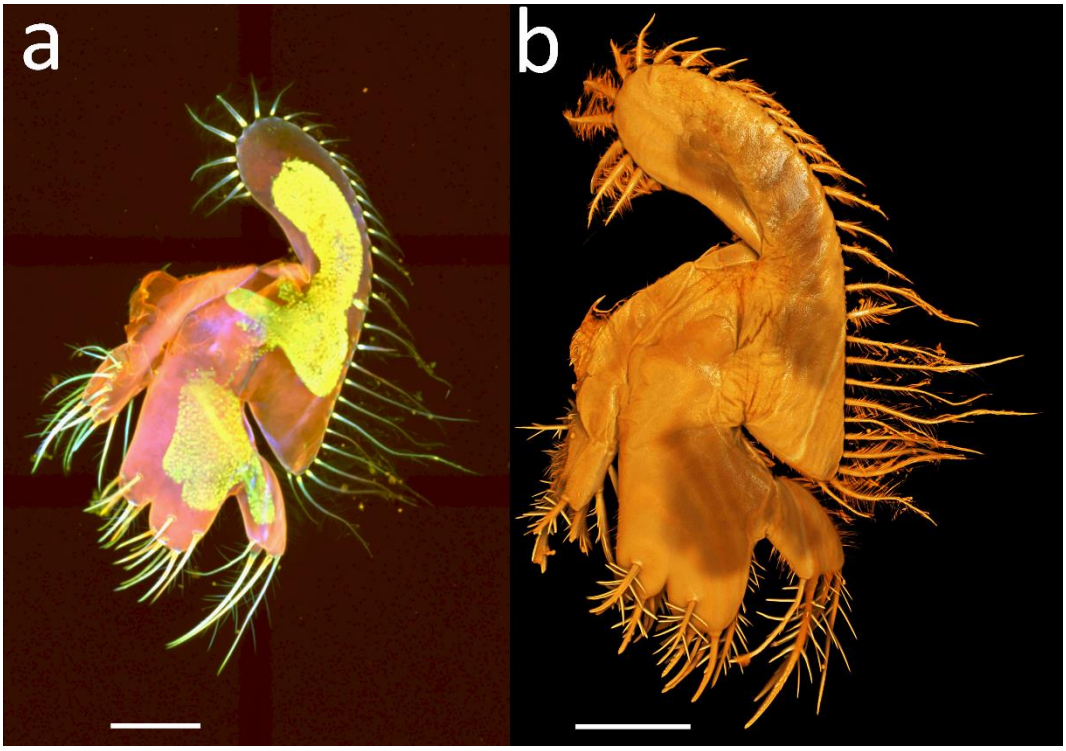

Figure 4.11: “Tiling” appendages when scanning at higher magnification. *Eriocheir sinensis*, zoea V, image of maxilla using CLSM. (a) Confocal image showing tiled areas. (b) Drishti image. 40× oil immersion objective, scan area of 2×3 fields. Scale bars a = 100 μm; b = 200 μm.

If a powerful computer was not available, then the appendage could be scanned in separate sections and merged using Adobe Photoshop (Fig. 4.12a) or VGStudio Max (Fig. 4.12b). However, Adobe Photoshop only allows data to be merged in 2D, whereas finding the exact X, Y and Z planes to merge two images in 3D using VGStudio Max was found to be challenging and time-consuming.

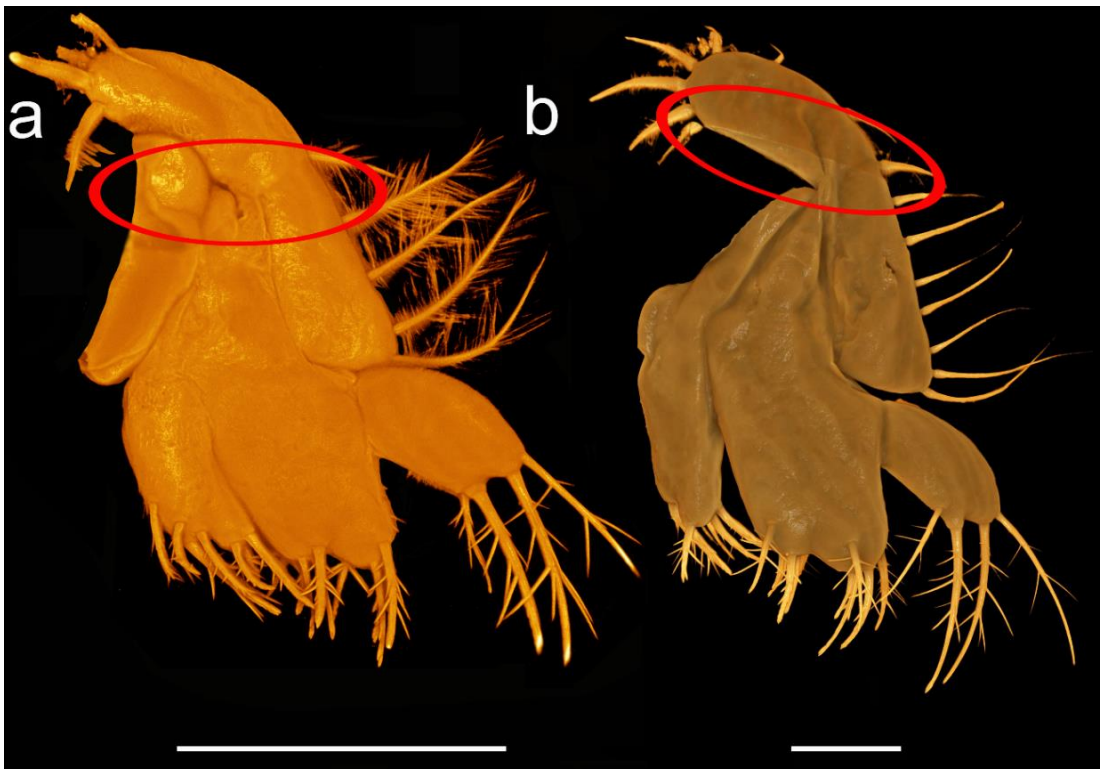

Figure 4.12: Merging Drishti images using additional software programmes. *Eriocheir sinensis* zoeal appendages using CLSM. (a) ZII, maxilla image merged using Adobe Photoshop. (b) ZIV, maxilla image merged using VGStudio Max. Merged areas are circled. Scale bars a = 200 μm; b = 100 μm.

For smaller larval appendages, 40× and 60× oil immersion objective lenses were used to produce higher resolution images. Applying a lower magnification objective lens to obtain a larger field of view was ineffective since these did not provide adequate resolution to resolve fine setae such as the dorsal setae on the somite of the zoeal pleon (Fig. 4.13a).

Obtaining large numbers of Z slices, especially during "large image tiling", means that confocal microscope data acquisition was relatively slow, could take several hours and there is a requirement to optimise the stability of the slide. Therefore, when selecting "large images" by tiling, it was important to carefully consider the "order of the

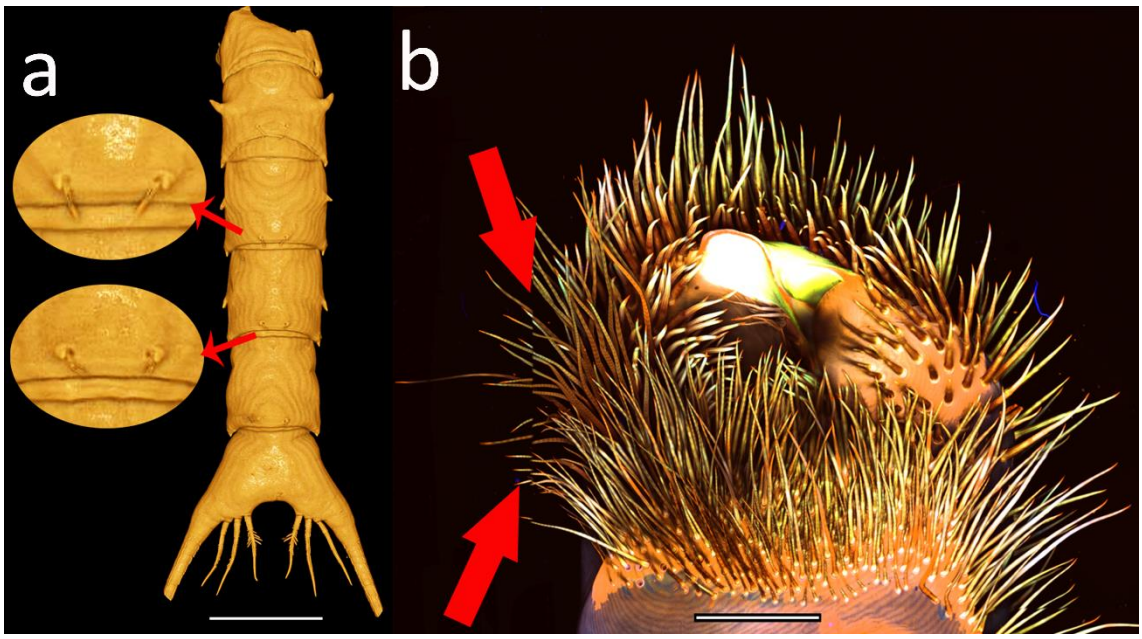

Figure 4.13: Applying large images option to visualise fine detail on bigger appendages using CLSM. *Eriocheir sinensis*. (a) ZI, visualisation of fine setae on pleon, 40× oil immersion objective, scan area of 2×6 fields (Fine setae arrowed). (b) Visualisation of adult male gonopod applying large images option with the order of "Z series (Lambda (Large images))", 10× objective, scan area of 5×5 fields (Displaced tiles are arrowed). Scale bars a = 200 μm; b = 1000 μm.

experiment" option to produce the minimal amount of disturbance to the slide. Should the Z-stacks in these tiles be scanned vertically or horizontally? For example, consider a specimen covered by an area of four tiles with 50 Z-stacks in each tile to be scanned. When the option for the order of the experiment is "Z series (Lambda (Large images))", the CLSM starts scanning the top Z-stack of every tile first, and the second Z-stack for every tile and so on until reaching the bottom of all the tiles. In this case, the mechanical slide carriage moves quickly by zigzagging so that the objective ranges over all the tiles. In this example, as there are four tiles with 50 Z-stacks in each to be scanned, the slide carriage moves horizontally 200 times increasing the odds for the mechanical adjustment to drift. This option was avoided as resulting tiles could be displaced (Fig.

4.13b). Therefore, the order of the experiment “Large images (Lambda (Z series))” was the preferred setting because each tile was scanned vertically by starting the procedure from top of the specimen to bottom, then repeating the same procedure for the next tile and so on. In this procedure, if there are four tiles with 50 Z-stacks in each to be scanned, the mechanical slide carriage stage only moves horizontally 4 times. Consequently, the risk of image misalignment was greatly reduced (Fig. 4.11a).

ImageJ, Drishti and Avizo

The methodology and data processing workflow (Fig. 2.3) described in Chapter 2 (Material & Methods) was successfully tested on confocal microscopes manufactured by Olympus, Zeiss, Nikon and Leica. The method for handling the data was the same and the ImageJ and Drishti import process was identical for each file format (Fig. 4.14).

Channel merging

The final quality of merged channel images combining ImageJ and Drishti appeared (see applied combination # 10−12 in Table 4.2) to be an improvement compared to importing a single channel into Drishti (using the manufacturers’ own programmes to extract each channel; Fig. 4.15a). When extracting several channels using confocal software programmes, each volume of data had to be processed (loaded) individually using Drishti (see combinations applied # 5−9 in Table 4.2). The resulting image was one of poor quality (Fig. 4.15b) as a single channel did not provide sufficient data.

When two volumes were individually processed using the confocal software programme and loaded into Drishti as separate volumes, the resulting image was oversaturated (Fig.

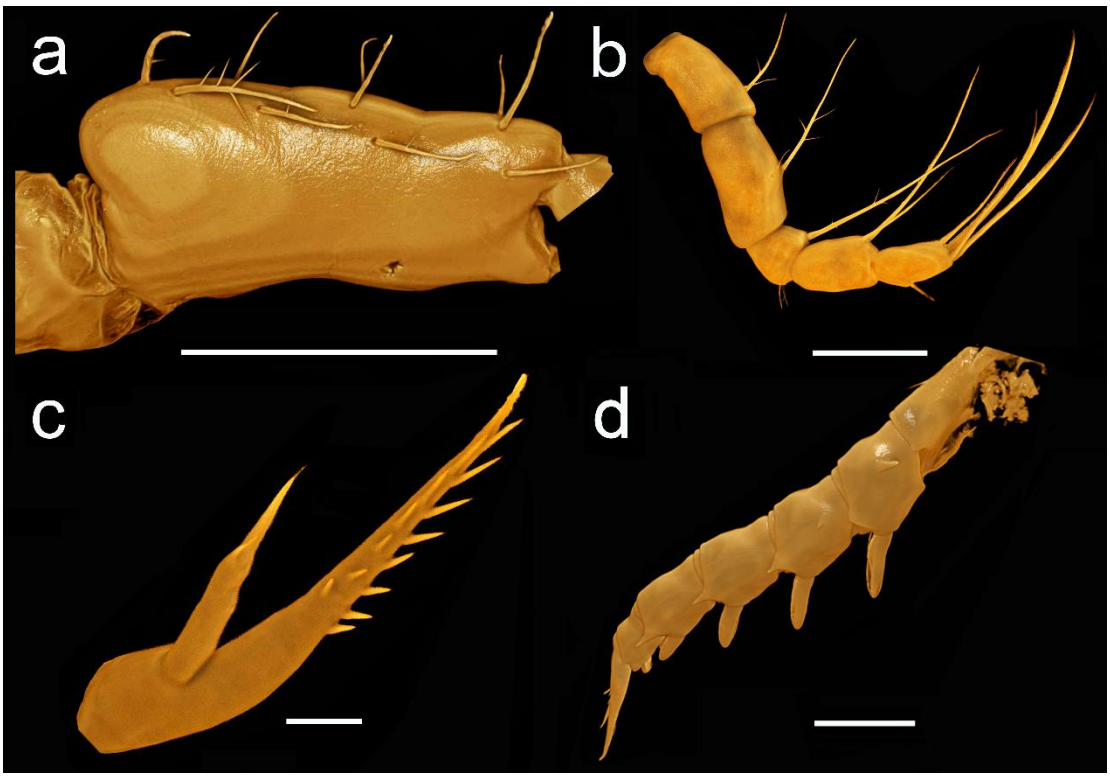

Figure 4.14: Scanned brachyuran crab larvae using different brands of CLSM processed in Drishti. *Eriocheir sinensis*, zoea I, first maxilliped. (a) Basis, Nikon A1-Si CLSM. (b) Endopod, Olympus Fluoview FV1000 IX8. (c) Antenna, Zeiss LSM 880 airy scan. All 40× oil immersion objective. (d) *Sesarma curacaoense*, ZII, lateral view of pleon, Leica TCS SP5, 10× dry objective. Scale bars a-b = 100 μm; c = 50 μm; d =500 μm.

4.15c). This even caused the software to "hang" and stop operating when attempting to merge more than two channels. The reason for this was that there were too many z-stacks and the total file size was excessive.

For example, the confocal data which was shown as an example in Chapter 2 (Fig. 2.14) had a z-stack complied from 149 slices. This number was only for one channel. If 4 channels are loaded separately, the number of slices would increase four folds (e.g. 596 slices). Moreover, this data was obtained using 1024 × 1024-pixel size. The total file size would be quadrupled if 2048 × 2048-pixel size were applied. This total file size

calculation was calculated by Bourke (2011) as “Total file size = number of slices × horizontal pixels × vertical pixels × number of bytes per pixel”. In the present data, more z-stacks were required and the resulting 4 channel data could not be processed by converting as TIFF stacks via confocal software and merging using Drishti. 2 Channel data was successfully processed using this method, however, this caused the resulting image to be oversaturated (Fig. 4.15c). Whereas merging channels using ImageJ and applying Drishti afterwards provided more information, especially with regard to the visualisation of setae.

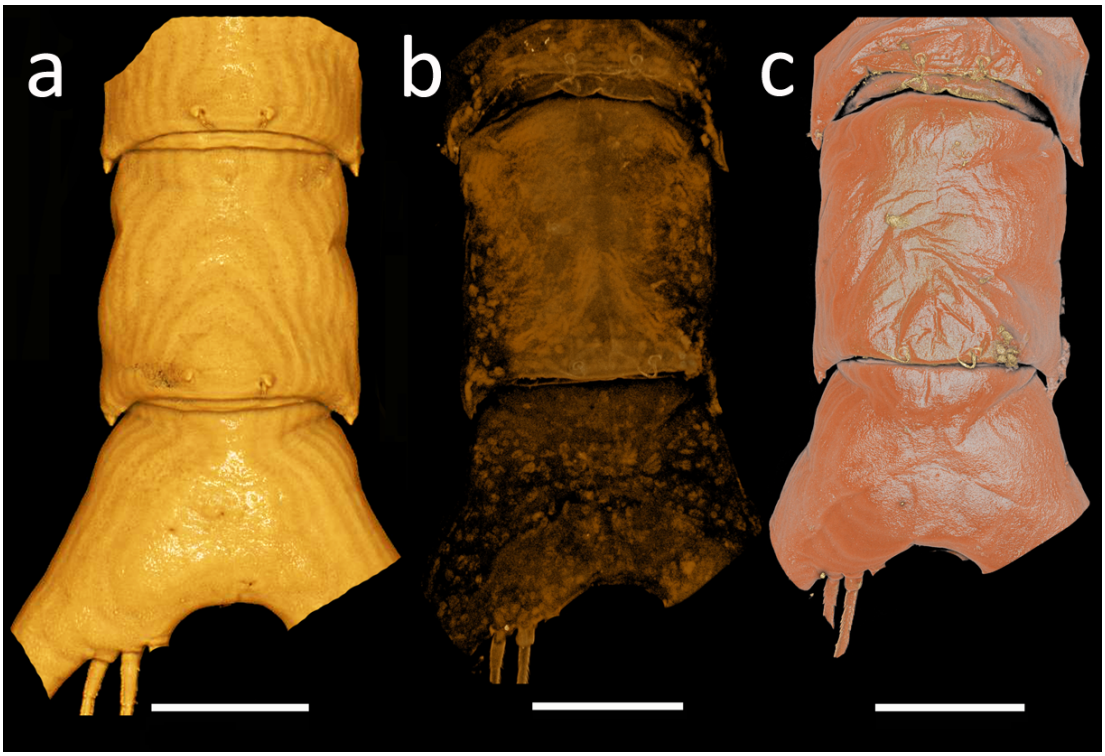

Figure 4.15: Post-processing in Dristhi applying different methods. (a) All confocal channel data was merged using ImageJ and processed using Drishti. (b) One single channel imported using confocal software and processed using Drishti. (c) Separate channels imported using confocal software and were loaded together in Drishti which created an over statured image. Scale bars = 100 µm.

Once 3D datasets were acquired, Drishti proved to be a powerful tool in reconstructing the specimen from different viewpoints (Fig. 4.16) and also offered the advantage of allowing the operator to remove parts of the specimen from the foreground to reveal features which would otherwise be obscured (a useful form of digital dissection; Fig. 4.16c).

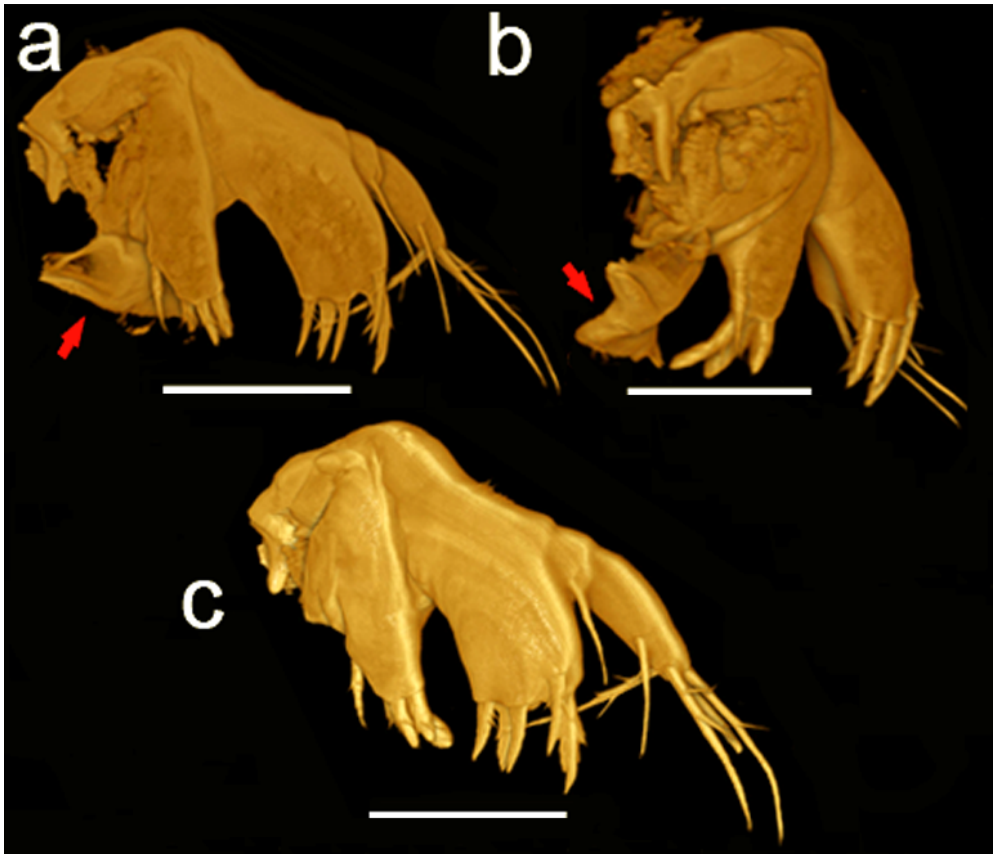

Figure 4.16: Digital dissection. *Eriocheir sinensis*, zoea I, image of maxillule using Nikon A1-Si CLSM and processed using Drishti. (a) Unwanted tissue arrowed. (b) Repositioning of appendage to allow the removal of unwanted tissue (arrowed). (c) After digital dissection of tissue (compare a with c). 40× oil immersion objective. Scale bars = 100 μm.

Besides *Eriocheir sinensis*, various images of other brachyuran crab larvae, *Sesarma curacaoense*, *Armases miersii*, were also tested by applying the same methods described here using other confocal microscopes (see Figs. 4.17−4.18).

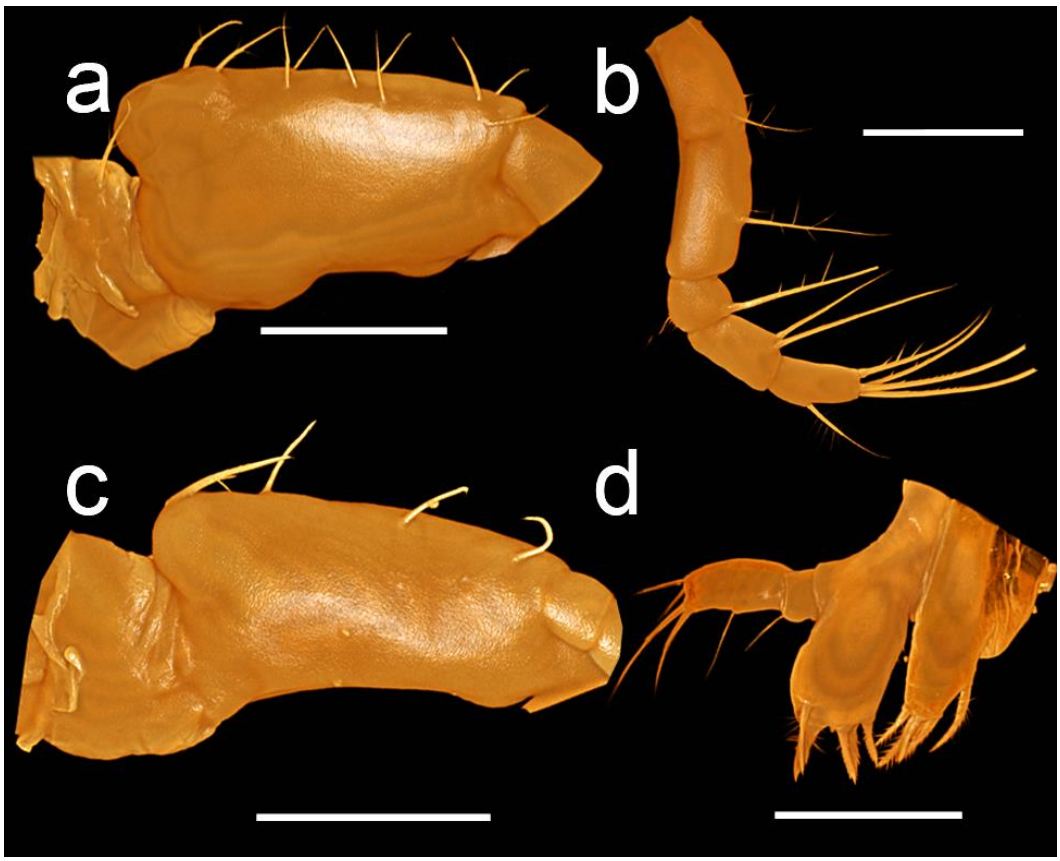

Figure 4.17: Drishti images of *Sesarma curacaoense*, zoea I appendages using Leica TCS SP5. First maxilliped. (a) Coxa and basis. (b) Endopod. (c) Coxa and basis of second maxilliped. (d) Maxillule. All 40× oil immersion objective. Scale bars a-b = 50 μm; c-d = 100 μm.

The application of this successful method was also applied to different species in different studies. It was applied to *Clausidium* copepods (*Clausidium sarii* sp. and *Clausidium makranensis* sp.) by Sepahvand *et al*. (2017) and other copepods (*Remaneicaris siankaan* sp.) by Corgosinho *et al*. (2017). This post-processing procedure also provided a high-resolution image of a wasp head (Ball *et al*., 2017a).

Drishti is a freeware software programme while other comparable surface rendering packages are extremely expensive. The visualisation packages produced by Nikon, Leica, Olympus and Zeiss are limited and not cross compatible, whereas ImageJ and

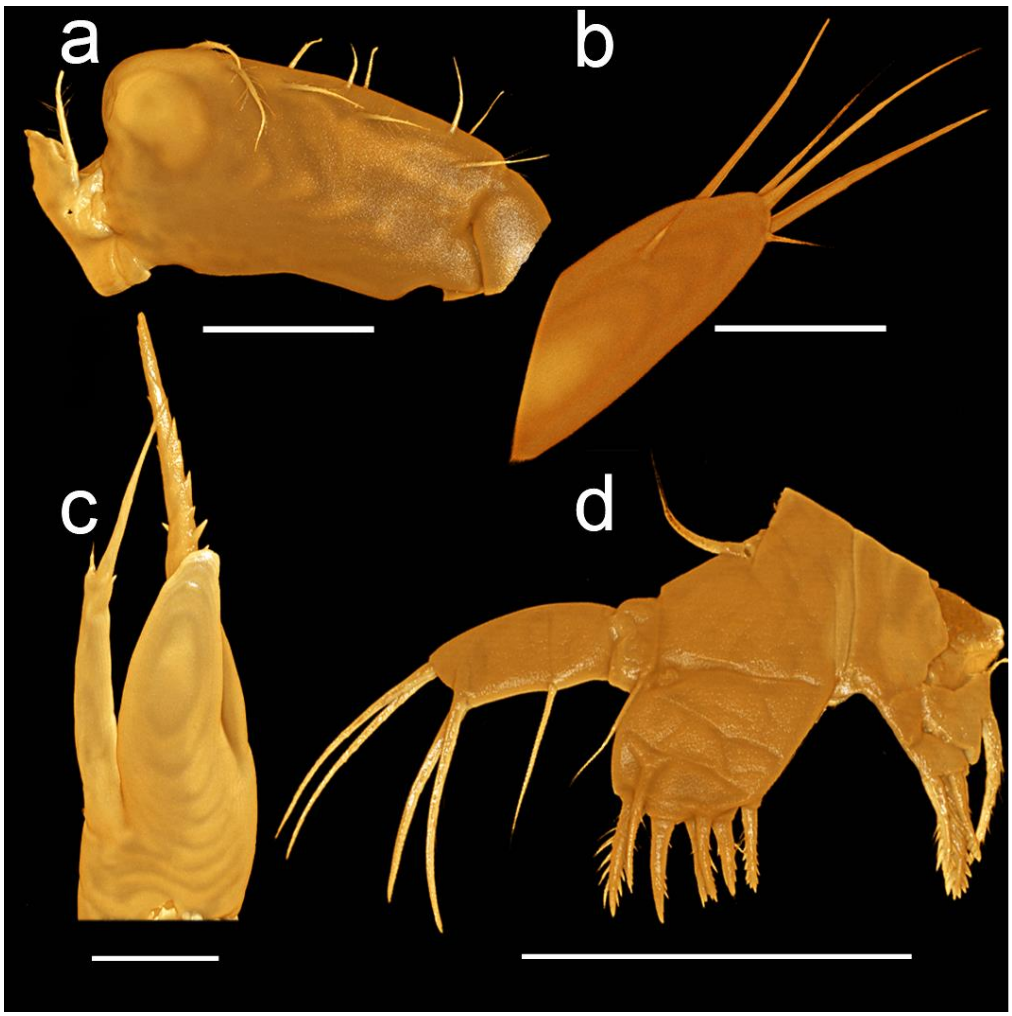

Figure 4.18: Drishti images of *Armases miersii*, zoea III appendages using Leica TCS SP5. (a) Coxa and basis of first maxilliped. (b) Endopod of second maxilliped. Both using 40× oil immersion objective. (c) Antenna. (d) Maxillule. Both using 20× dry objective. Scale bars a, d = 200 µm; b-c = 100 µm.

Drishti are universal for all brands and comparable in quality of results with the commercial software programmes. Avizo (version 2.2), which is a commercially available 3D rendering programme, was also applied to the final datasets (see applied combination # 11 in Table 4.2). However, Drishti (see applied combination # 12 in Table 4.2) was found to be more suitable for the present study (Fig. 4.19).

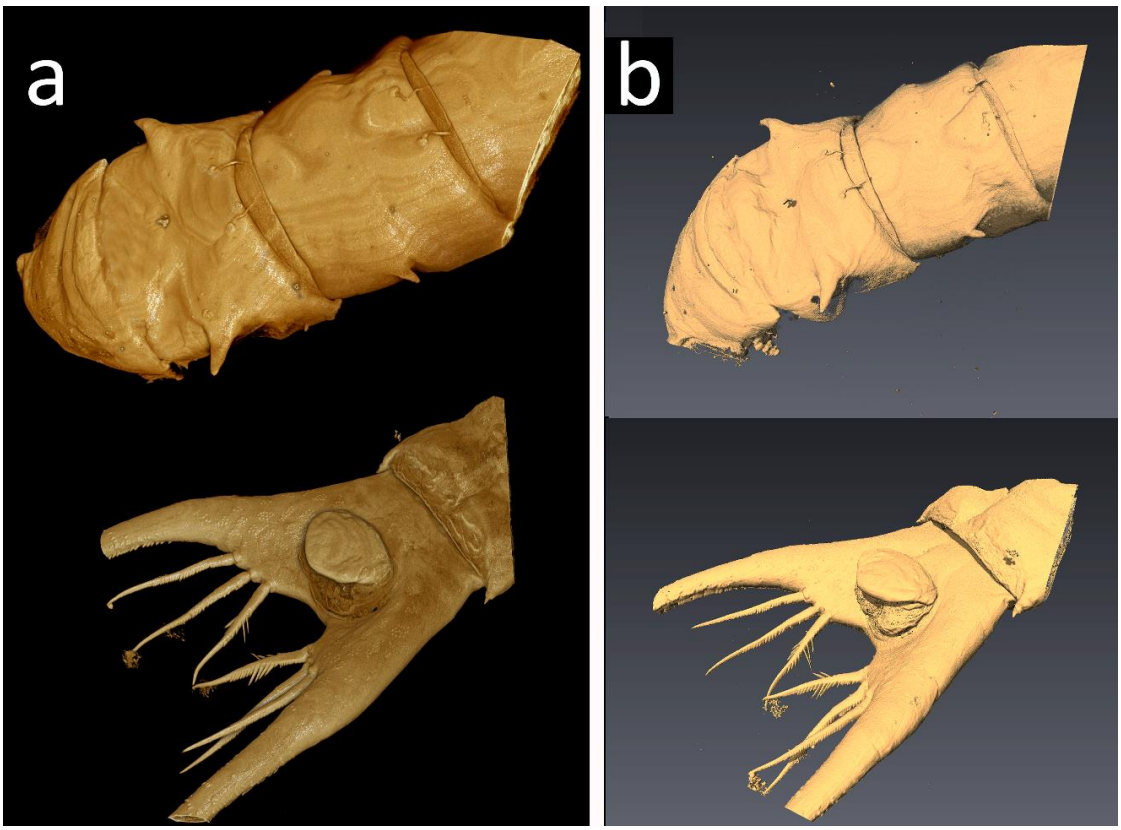

Figure 4.19: Application of 3D rendering programmes to the appendages obtained using CLSM. (a) Appendages processed using Drishti. (b) Appendages processed using Avizo.

4.6 Conclusions

Conventional observation of fine features, as seen in brachyuran larvae, normally rely on light microscopy often using techniques such as DIC (differential interference contrast) or phase contrast (Fig. 4.20a).

Furthermore, dissected appendages are challenging to mount as they can continually move whilst trying to fix them in an appropriate position. The narrow focal depth of compound microscopes may also make some direct observations difficult. As a result, features can be overlooked. Consequently, many line drawings tend to simplify and codify the essential features for diagnostic illustrations. For specimens with complex topography and setation, however, this approach can be subjective and makes

comparison difficult. In addition, traditional 2D photography, even with the addition of focal stacking, may not accurately record the 3D complexity of limbs and larval appendages or the position of setae. In comparison, high quality CLSM image data can be further enhanced by the use of Drishti (Fig. 4.20b, c).

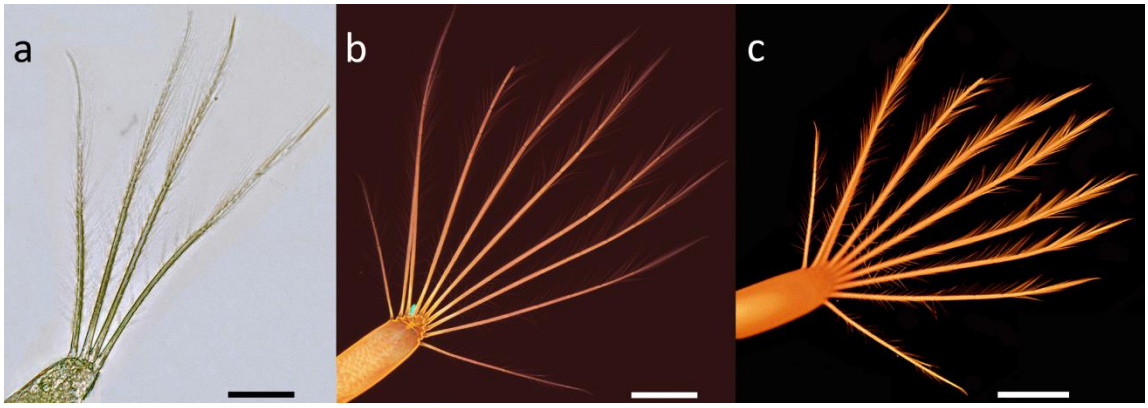

Figure 4.20: Comparing bright field, confocal and Drishti images. *Eriocheir sinensis* zoea, images of second maxilliped using CLSM. (a) ZI, DIC image of exopod, 20× dry objective. (b) ZIV, confocal image of exopod, 20× dry objective applying "large images" option, scan area of 1×2 fields for image stitching. (c) Drishti image of b. Scale bars a = 50 µm; b, c = 100 µm.

In previous studies, the number of setae on the basis of the first maxilliped especially in the small early zoea stages, such as ZI and ZII (for correct setation see Chapter 5) and the fine second seta on the first and second segments of the first maxilliped endopod were overlooked (for correct setation see Chapter 5). In addition, one seta can mask another if it lies along the same image path, but on a different focal plane. The masked setae can be visualised by rotating the appendage using Drishti. Another advantage of Drishti is the application of digital dissection and the removal of unwanted fragments.

The methodologies described here, including the combination of improved cleaning, digestion and preparation methods, allowing for reduced transfer of contaminants into the final slide mounts, the confocal data processing protocols and the possibility of post-acquisition removal of artefacts using free software have been shown to overcome all of the previous limitations in the use of confocal microscopy for the examination of small arthropods. Furthermore, the methodologies described for the use of Drishti to post-process samples have also been successfully applied to other confocal datasets and can even be used for the production of 3D prints from the data.

The main limitation of the present study was the speed of the confocal microscope and its ability to handle and image larger specimens. “Macro confocal microscopes” have been assessed, but found to have inadequate resolution for this application. Even though macro confocal provided a decent general image of the larger appendages such as the pleon (Fig. 4.21a), the resolution was not found sufficient to visualise the fine setae on other appendages (Figs. 4.21b, c). Therefore, it was not a preferable method to apply in the present study.

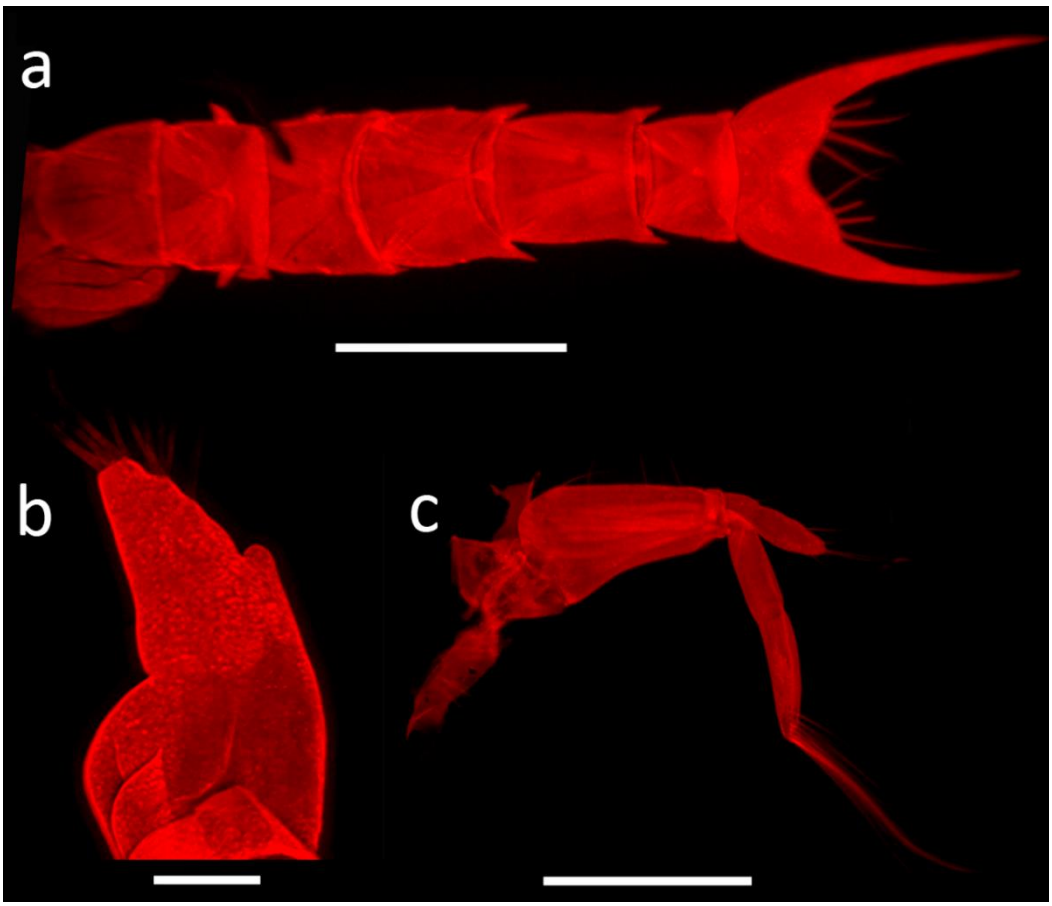

Figure 4.21: Application of an AZ-C1 macro confocal to the larger appendages of *Eriocheir sinensis*. (a) ZIV, complete pleon, 5× dry objective. (b) ZV, complete antennule 5× dry objective by zooming. (c) ZV, complete second maxilliped, 5× dry objective by zooming. Scale bars a, c = 500 μm; b = 100 μm.

For large material, such as ZVI, megalopa and crab I stage of *Eriocheir sinensis*, the use of a Zeiss Axio zoom V16 light microscope did not provide adequate resolution when trialled in the present study (Fig. 4.22).

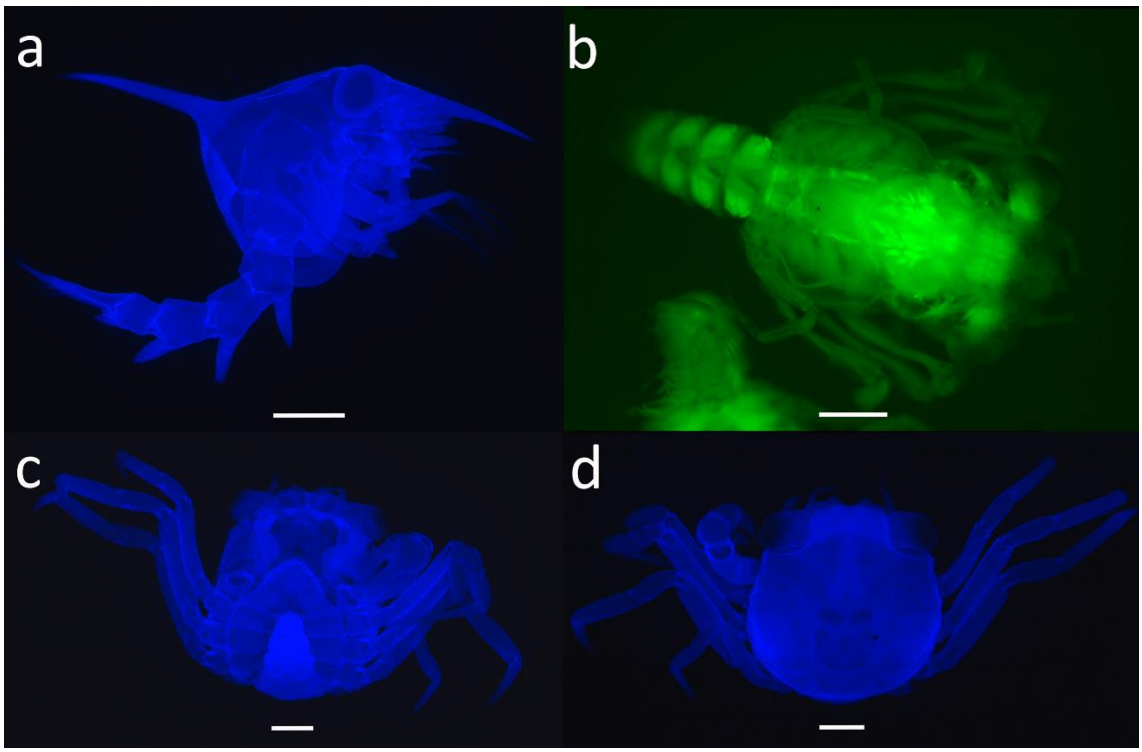

Figure 4.22: Application of other microscopes to investigate the bigger samples of *Eriocheir sinensis*, in this case Zeiss Axio zoom V16 stereo zoom microscope for large fields. (a) ZVI stage. (b) Megalopa stage. (c) Ventral side of crab I stage. (d) Dorsal side of crab I. Scale bars a, c, d = 500 μm; b = 200 μm.

The use of high resolution micro-CT was also investigated as a complementary technique to provide further contextual 3D information on macro-invertebrates. Its application to large samples is detailed in Chapter 6.

CHAPTER 5

RE-DESCRIPTION OF THE ZOEAL DEVELOPMENT OF THE CHINESE MITTEN CRAB *ERIOCHEIR SINENSIS* H. MILNE EDWARDS, 1853

5.1 Introduction

Although the zoeal development of the Chinese mitten crab, *Eriocheir sinensis* H. Milne Edwards, 1853, has been investigated by many researchers, the early descriptions of Schnakenbeck (1926; 1933), Hinrichs & Grell (1937), Buhk (1938), Panning (1939) and André (1947) were too brief, and often incomplete. These larval descriptions which are frequently difficult to find in digital form to view online or download from scientific journals, were defined as "grey" literature by Vela & Gonzalez-Gordillo (2016). Once accessed this old literature can cause difficulties when comparing with modern larval descriptions (see Clark *et al*., 1998b). This situation was recognised by many workers (Wear, 1985; Soltanpour-Gargari *et al*., 1989; Gonzalez-Gordillo *et al*., 2001; Vela & Gonzalez-Gordillo, 2016). Gonzalez-Gordillo *et al*. (2001) who considered that early decapod crustacean larval descriptions were limited due to the brief definitions and lack of illustrations/figures. It was emphasised (Clark *et al.*, 1998b; Clark & Cuesta, 2015; Vela & Gonzalez-Gordillo, 2016) that such studies should be readily accessible and illustrated with good figures.

The later larval descriptions of *E. sinensis* by Liang *et al*. (1974), Ingle (1991), Kim & Hwang (1995) and Montú *et al*. (1996) were, however, not consistent in terms of the description of the characters, and clarity of illustrations. Although these studies provided more information than the earlier zoeal descriptions of *E. sinensis*, they collectively contained a number of contradictions, inconsistences in terms of setal formulae and these were confusing. Furthermore, they are now more than 20 years old and subsequently many *Eriocheir* species have been re-named or re-classified during

this period of time (Vela & Gonzalez-Gordillo, 2016). Mitten crabs were re-classified (Ng *et al*., 2008) as a result of molecular, larval and morphological studies conducted by Cuesta & Schubart (1999), Schubart *et al*. (2000; 2002), Spivak & Cuesta (2000), and Sternberg & Cumberlidge, (2000), grapsoid subfamilies were raised to family level based on ecological and morphological differences (Martin & Davis, 2001; Clark, 2006). Additionally, the authority date of *E. sinensis* was confused according to Clark (2006); 1853 or 1854?

According to Rice (1979), larval characters are either quantitative or qualitative. The quantitative characters are described numerically such as the lengths of the spines/proportions of appendages/segments and their setal formulae. Whereas the qualitative methods focus on the shape of the characters or the arrangements of the setae/appendages. Therefore, it is important to define the characters precisely by describing them correctly as well as providing reliable illustrations. Indeed, providing consistent illustrations and the text descriptions are important for the classification of crab species (Rice, 1979). Furthermore, Clark *et al*. (1998b) emphasised the importance of using suitable characters for the descriptions and stated that many have been overlooked or ignored. They also provided a model and standardised terminology for the brachyuran larvae (see Clark *et al*., 1998b). These issues were again raised in the latest study of Clark & Cuesta (2015). These studies emphasised the importance of accurate descriptions.

Most of the early zoeal descriptions of *E. sinensis* larvae are not consistent in terms of the text, figures and comparisons within and between studies. For example, the first zoeal description of *E. sinensis* examined by Schnakenbeck (1926) was incomplete and with only a simple illustration of the first zoeal stage. His second description (Schnakenbeck, 1933) was also inadequate and not complete. Later André (1947) used the figures of Schnakenbeck's (1933) to illustrate mitten crab zoea, while Hinrichs &

Grell (1937) described only the fifth zoeal stage of the Chinese mitten crab and Buhk (1938) just re-cycled the illustration of Hinrichs & Grell (1937). Panning (1939), however, suggested that the mitten crab zoeal phase comprised a pre-zoea and four zoeal stages. This has subsequently been found to be in error as *E. sinensis* passes through more than four zoeal stages.

More importantly, however, is the fact that some researches (Pohle & Telford, 1981; Williamson, 1982; Clark *et al*. 1998b; Clark & Cuesta, 2015) do not regard pre-zoea as an actual stage. In fact, pre-zoea do not appear to have completely formed setae and are not functional, e.g. swim with great difficulty (Clark & Cuesta, 2015). Therefore, descriptions of pre-zoea stage were not conducted in the present study as they have little value for the identification and they have undeveloped setae.

The first detailed description of the zoeal development of the Chinese mitten crab was accomplished by Liang *et al*. (1974) and they defined five zoeal stages for *E. sinensis*. Their description of some appendages, however, lacked reference to the setation of the carapace; numbers of setae on the antennule, maxillule and maxilla in some zoeal stage; reference to the coxa of the maxillipeds, and the description of the telson in the first zoea stage. A detailed larval description was conducted by Kim & Hwang (1995) and they defined the number of zoeal stages as five. Although, their description was more precise than previous studies, there were important differences between their work and the present study in terms of the number of the setae on some appendages. More importantly, however, possible variations in the last zoeal stages were not highlighted in their study. The most recent description of *E. sinensis* was conducted by Montú *et al*. (1996). They stated that depending on the salinity in which the larvae were reared (Anger, 1991), the Chinese mitten crab zoea can have an additional stage after the fifth zoea. Describing the sixth zoeal stage provided an insight into the variations that occur especially in the later zoeal stages. Meanwhile, the early zoeal stages such as the first

three stages were poorly described in the study of Montú *et al*. (1996). In addition, their text descriptions and illustrations were not always consistent. All of these reasons suggested a requirement for the re-description of zoeal stages of *E. sinensis*.

5.2 Aims

Previous studies provided incompatible descriptions of the Chinese mitten crabs larvae in terms of the appendage setation and the number of the zoea stages. Furthermore, the old studies utilised only light microscope and the traditional line drawing techniques to make descriptions. Thus, there was a possibility in these studies that the tiny appendage structures could be overlooked. There was a considered necessity to access the zoeae of *E. sinensis* and develop a new technique, confocal scanning for describing larvae and illustrations of characters. For the present study, the well accepted standard (Mantelatto *et al*., 2014; Marco-Herrero *et al*., 2014; Calado & Leal, 2015; Rebolledo *et al*., 2015; Vela & Gonzalez-Gordillo, 2016; Tamura *et al*., 2017) to describe brachyuran larvae as proposed by Clark *et al.* (1998b) was adopted.

5.3 Methodology

The description method of Clark *et al*. (1998b) was followed; the zoeae were described from anterior to posterior starting from the cephalic appendages (antennule, antenna, mandible, maxillule, maxilla), thoracic appendages (first, second and third maxillipeds, pereiopods) and pleonal somites to telson respectively. In the present study, "pleon" was used to refer "abdomen" as updated in the study of Clark & Cuesta (2015). Each appendage was described from the proximal to distal segments, endopod to the exopod. Setal formulae follow Clark *et al*. (1998b) such as 10 setae arranged as 2+2+3+3 for the basis and 3,2,1,2,5 (1 subterminal + 4 terminal) for five-segmented endopod of the first

maxilliped. In the present study, first zoeal stage is completely described, whereas only the changes are described in the subsequent zoeal stages.

Carapace description included the setation of the dorsal spine, posterodorsal and anterodorsal setae, ventral carapace margin setae and posterior marginal setae. The rostral spine remained devoid of setae throughout zoeal development. Boxshall (2004) suggested that the antennule is not a biramous structure. "Primary flagellum" was preferred to exopod, whereas "accessory flagellum" (secondary flagellum) was used instead of endopod (Boxshall, 2004; Clark & Cuesta, 2015). The antenna description included the protopod, endopod development, and exopod morphology. The maxillule description included the appearance of the epipod and exopod setae, and the setation of the coxal and basial endites and the endopod respectively. Similarly, the setation of the maxilla included a description of the coxal and basial endites, the endopod and exopod (scaphognathite). While the setation of the first and second maxillipeds was described for the coxa, basis, endopod and exopod, only the development of the third maxilliped and pereiopods was defined. Then the pleon was described and this included the number of somites, the dorsolateral processes, posterodorsal processes, the medial setae on somite one, and the pleopods. Finally, the posterior marginal setae and the denticules of the inner margin of each fork were used to form the description of telson. For the description of setal types, Ingle (1991) and Kim & Hwang (1995) are followed.

According to Clark & Cuesta (2015), the illustrations play a crucial role in complementing the descriptions as they remain universally informative. They suggested that the drawings should be as large as possible, however, the present research did not use line drawings. Instead of traditional techniques, the high-resolution images were obtained using SEM, CLSM and Drishti software programme. SEM images were mainly used for the description of the fine setae on the carapace. Images of the

appendages were obtained using CLSM and Drishti software as explained in Chapter 2. All digital images and videos are provided on a CD.

The final images were arranged in the most suitable size on the page so as to demonstrate the fine details of each appendage. Where necessary, the magnification of setae was increased to illustrate the setation in more detail, e.g. the coxal and basial endites of the maxillule and the maxilla in the later zoeal stages (Z-IV, V and VI). Furthermore, a few videos are provided in order to view rotating images of certain appendages. Some setal variations occurred in the later zoeal stages (ZIV-VI), the different setal formulae were displayed.

General size measurements for each zoeal stage were not provided as the present study claims that such information was not found to be realistic. For example, a measurement from the dorsal tip rostral spine to the end of the dorsal spine sometimes differs from specimen to specimen because the tips may be damaged or the spines grow at slightly different rates (see Figs 5.55−5.56). For this reason, a general picture of each zoea (ZI-VI) was provided as an estimation of their size.

5.4 Description of zoeal phase

Systematics

Phylum: Arthropoda von Siebold, 1848

Subphylum: Crustacea Brünnich, 1772

Class: Malacostraca Latreille, 1802

Subclass: Eumalacostraca Grobben, 1892

Superorder: Eucarida Calman, 1904

Order: Decapoda Latreille, 1802

Infraorder: Brachyura Latreille, 1802

Section: Eubrachyura de Saint Laurent, 1980

Subsection: Thoracotremata Guinot, 1977

Superfamily: Grapsoidea MacLeay, 1838

Family: Varunidae H. Milne Edwards, 1853

Subfamily: Varuninae H. Milne Edwards, 1853

Genus: *Eriocheir* De Haan, 1835

Species: *Eriocheir sinensis* H. Milne Edwards, 1853

Figures 5.1−5.56

Eriocheir sinensis: Schnakenbeck, 1926: 352, Fig. (zoea I), 1933: 157, Figs 46−66 (pre-zoea, zoea I); Hinrichs & Grell, 1937: 217, Abb. 1−3 (zoea V); Buhk, 1938: 776, Abb. 3−5 (zoea I−V); Panning, 1939: 273, Abb. 1−11 (zoea I−IV), 1939a: 361, Fig. 2 (zoea I); André, 1947: 35, Figs 2−5 (zoea I,); Liang *et al*., 1974: 67, Figs 1−63 (zoea I−V); Ingle, 1986: 101, Fig. 1 (zoea I), 1991: 248−250, Figs 1.10n; 1.14d; 1.18f; 1.22g; 1.23e; 1.29f; 1.32g; 1.35c; 1.36k; 1.38g; 2.37d-j; 2.38, (zoea I-V); Kim & Hwang, 1995: Figs 1−7 and tables III-IV (zoea I-V); Montú *et al.*, 1996: 50, Figs 1−16 (pre-zoea, zoea I−VI).

Descriptions:

Zoea I (Figs 5.1−5.9)

Carapace (Figs 5.1−5.2): Globose; dorsal spine present, gently curved, longer than rostral and lateral spines; rostral spine present and shorter than dorsal spine and with small spinules; lateral spines present with small spines on surface; anterodorsal setae absent; one pair of posterodorsal simple setae present; ventral margin with 8−9 serrations, setae absent; dorsoposterior margin without setae; eyes sessile.

Antennule (Fig. 5.3a): Uniramous; primary flagellum with 4 terminal aesthetascs (2 broad, 2 slender) and 1 small simple seta; accessory flagellum absent.

Antenna (Fig. 5.3b): Uniramous; protopod distally bilaterally spinulate; endopod absent; exopod short, ca. 30% of protopod, with 2 unequal (1 short, 1 minute) medial spines.

Mandible (Fig. 5.4a): Palp absent, incisive teeth distinct.

Maxillule (Fig. 5.4b): Uniramous; epipod seta absent; coxa with 5 plumodenticulate setae, basial endite with 5 armed processes (4 cuspidate setae, 1 long thin plumodenticulate seta); endopod 2-segmented, proximal segment with 1 plumodenticulate seta, distal segment with 5 (1 subterminal, 4 terminal) plumodenticulate setae; exopod seta absent but with microtrichia.

Maxilla (Fig. 5.5): Biramous; coxal endite bilobed with 4 +3 (2 plumodenticulate, 1 spine-like seta) plumodenticulate setae ; basial endite bilobed with 5+4 sparsely plumodenticulate setae; endopod bilobed with 2+2 plumodenticulate setae; exopod (scaphognathite) margin with 4 plumose + 1 long distal stout process.

First Maxilliped (Fig. 5.6): Biramous; coxa without seta; basis with 10 plumodenticulate setae arranged 2+2+3+3; endopod 5-segmented with

2,2,1+microtrichia,2,5 (1 subterminal (dorsal), 4 terminal) setae; exopod 2-segmented, distal segment with 4 long terminal plumose natatory setae.

Second Maxilliped (Fig. 5.7): Biramous; coxa without seta; basis with 4 plumodenticulate setae arranged 1+1+1+1; endopod 3-segmented with 0,1,6 (3 subterminal (1 dorsal, 2 ventral), 3 terminal) sparsely plumose setae; exopod 2-segmented, distal segment with 4 terminal plumose natatory setae.

Third Maxilliped: Absent.

Pereiopods: Absent.

Pleon (Fig. 5.8): Five somites, somite 2 with 1 pair of dorsolateral processes directed anteriorly; somites 3 and 4 with a small pair of dorsolateral processes directed ventrally, somite 1 with rounded posterolateral process; somites 2−4 with short dorsolateral process; somite 1 without medial setae; somites 2−5 with a pair of simple posterodorsal setae; pleopods absent.

Telson (Fig. 5.9): Bifurcated; each fork long curved distally with an inner row of paired spinules; lateral and dorsomedial spines absent; posterior margin with 3 pairs of stout spinulate setae, inner pair with a couple of long spinules medially on inner margin; anal operculum ventrally.

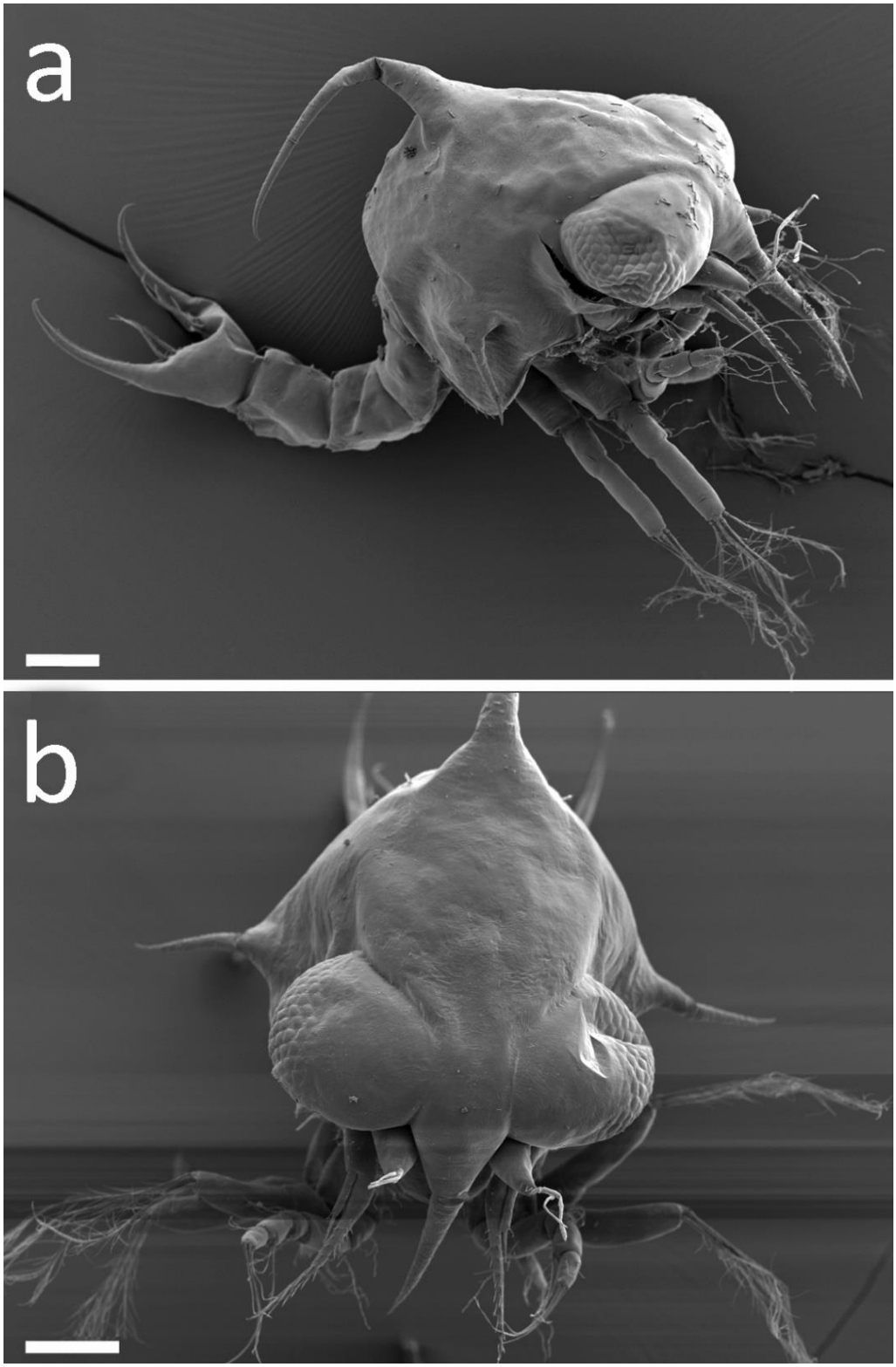

Figure 5.1: *Eriocheir sinensis*, ZI, carapace, Zeiss Ultra Plus Field Emission SEM. (a) Lateral view. (b) Anterior view. Scale bars = 100 µm.

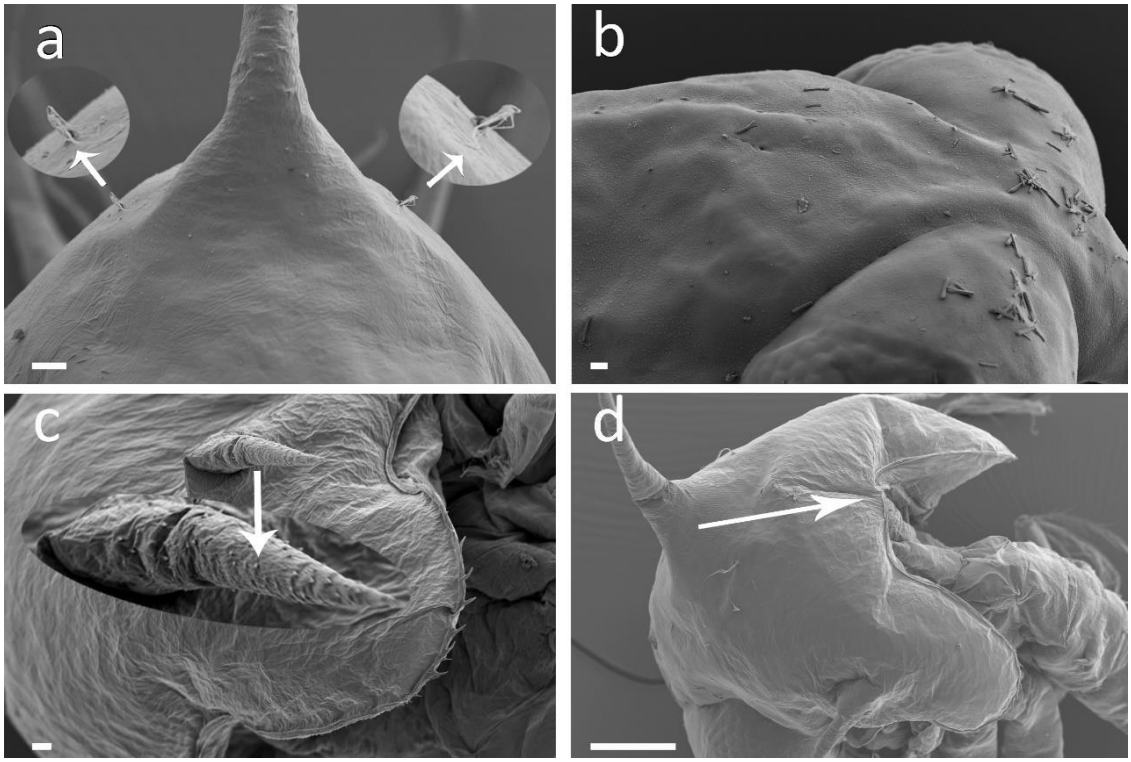

Figure 5.2: *Eriocheir sinensis*, ZI, carapace, Zeiss Ultra Plus Field Emission SEM. (a) One pair of posterodorsal setae present (arrowed). (b) Anterodorsal setae absent. (c) Ventral carapace margin with 8−9 serrations and small spines on lateral spine (arrowed). (d) Dorsoposterior carapace margin (arrowed) without setae. Scale bars a = 20 µm; b-c = 10 µm; d = 100 µm.

Figure 5.3: *Eriocheir sinensis*, ZI, Nikon A1-Si CLSM with Drishti processing. (a) Antennule, 2 aesthetascs and 3 setae arrowed. (b) Antenna, two setae arrowed. Objective: = 60× oil immersion. Scale bars = 50 µm.

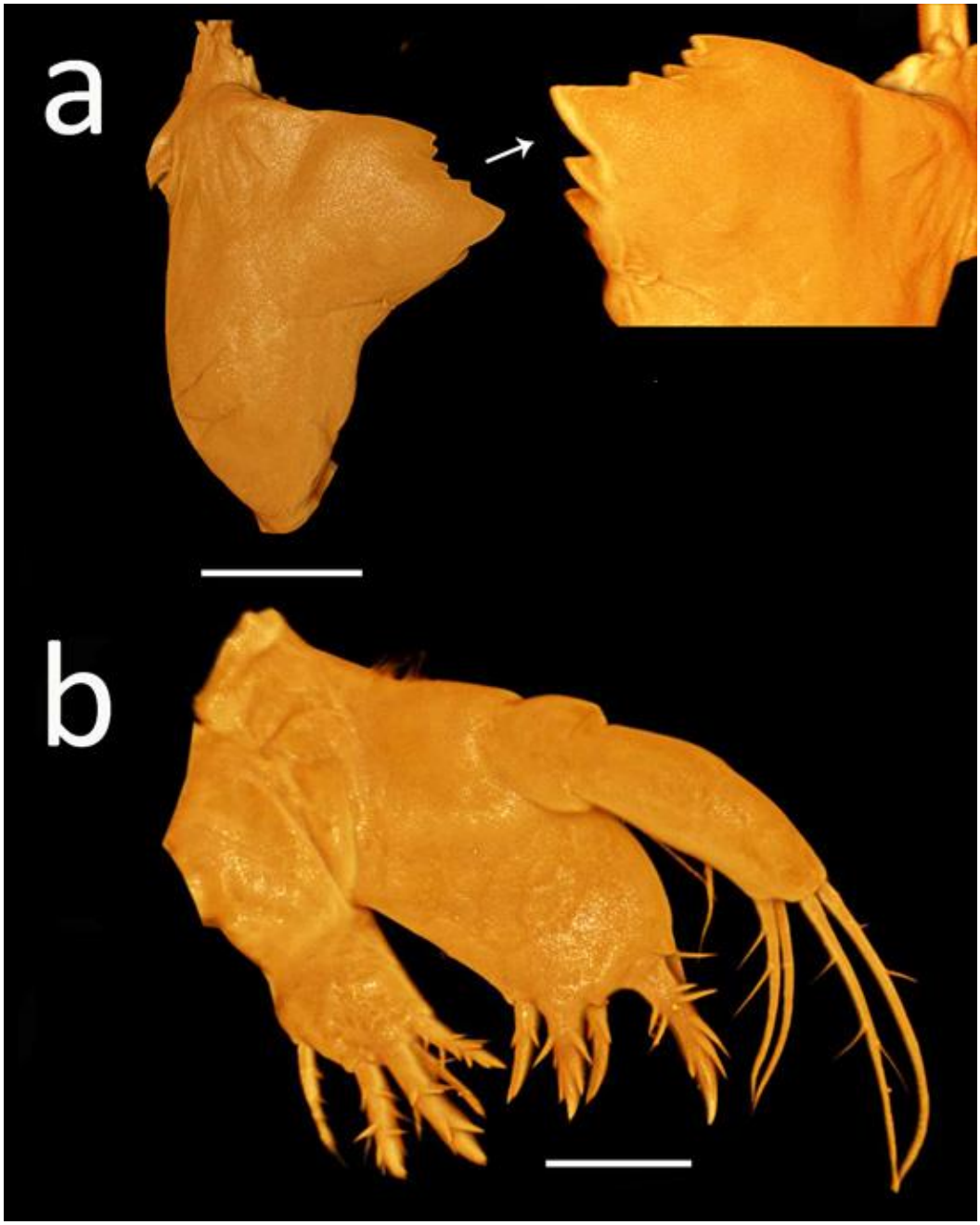

Figure 5.4: *Eriocheir sinensis*, ZI, Nikon A1-Si CLSM with Drishti processing. (a) Mandible, incisive teeth arrowed. (b) Maxillule. Objectives: = 40× oil immersion. Scale bars = 50 µm.

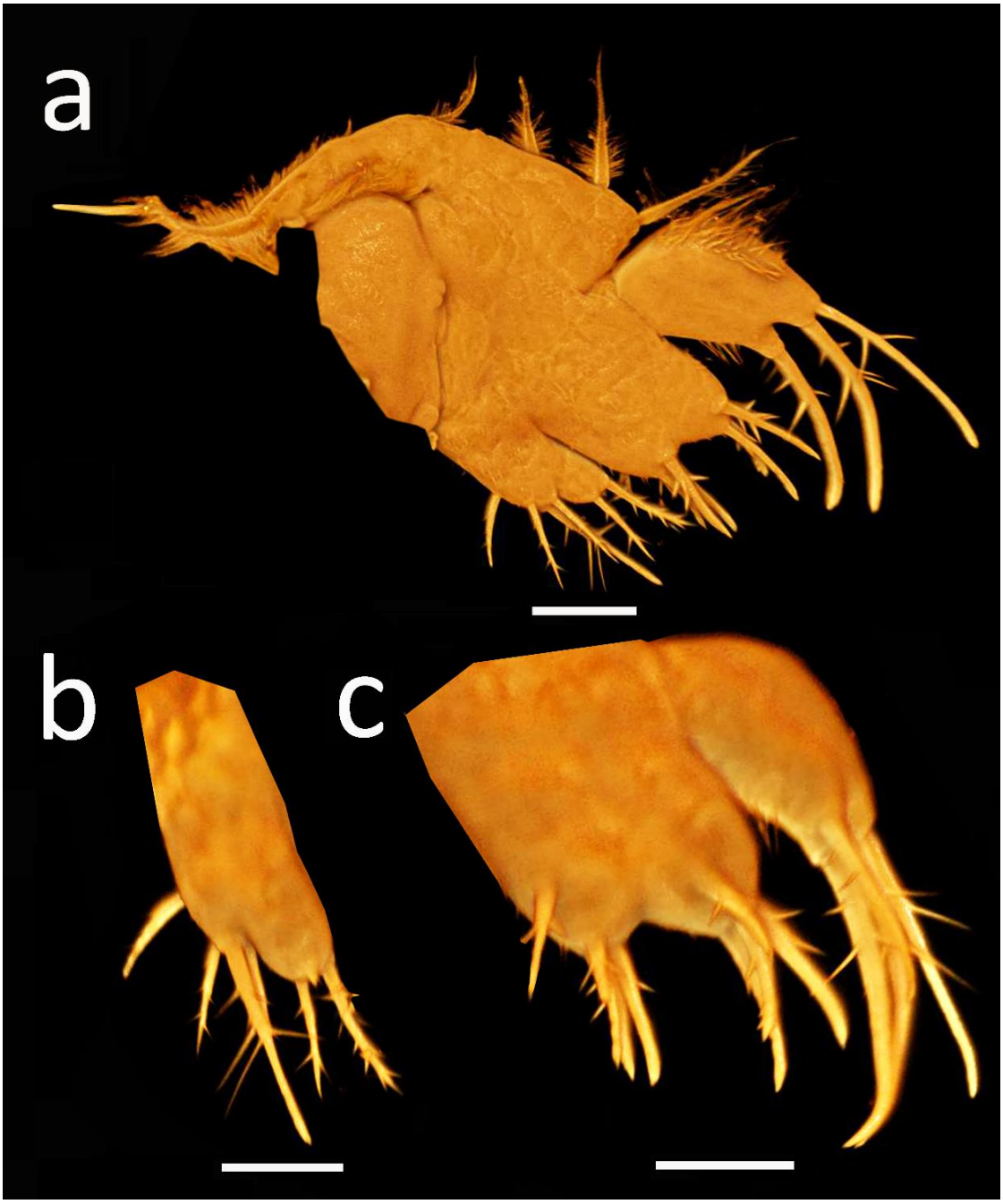

Figure 5.5: *Eriocheir sinensis*, ZI, maxilla, Nikon A1-Si CLSM with Drishti processing. (a) Maxilla. (b) Coxal endite. (c) Basial endite and endopod. Objective: 40× oil immersion. Scale bars = 50 µm.

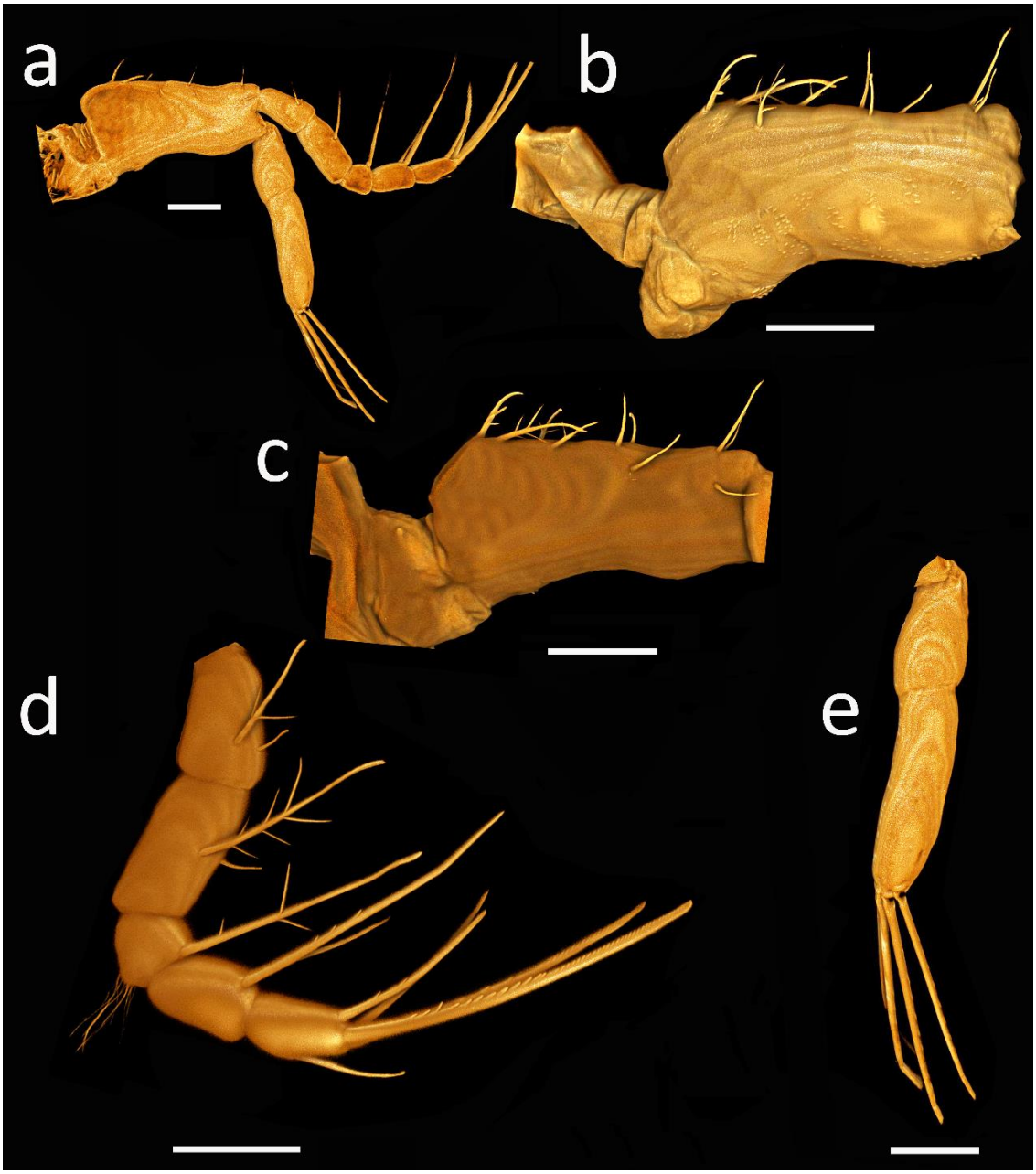

Figure 5.6: *Eriocheir sinensis*, ZI, first maxilliped, Nikon A1-Si CLSM with Drishti processing. (a) Whole appendage. (b) Coxa and basis. (c) Coxa and basis rotated to reveal reverse angle of image a. (d) Endopod. (e) Exopod with 4 natatory setae. Objective: a, b, d = 40× oil immersion; c, e = 20× dry. Scale bars a, b, d = 100 µm; c, e = 200 µm. See video 1 for 3D representation of the first maxilliped.

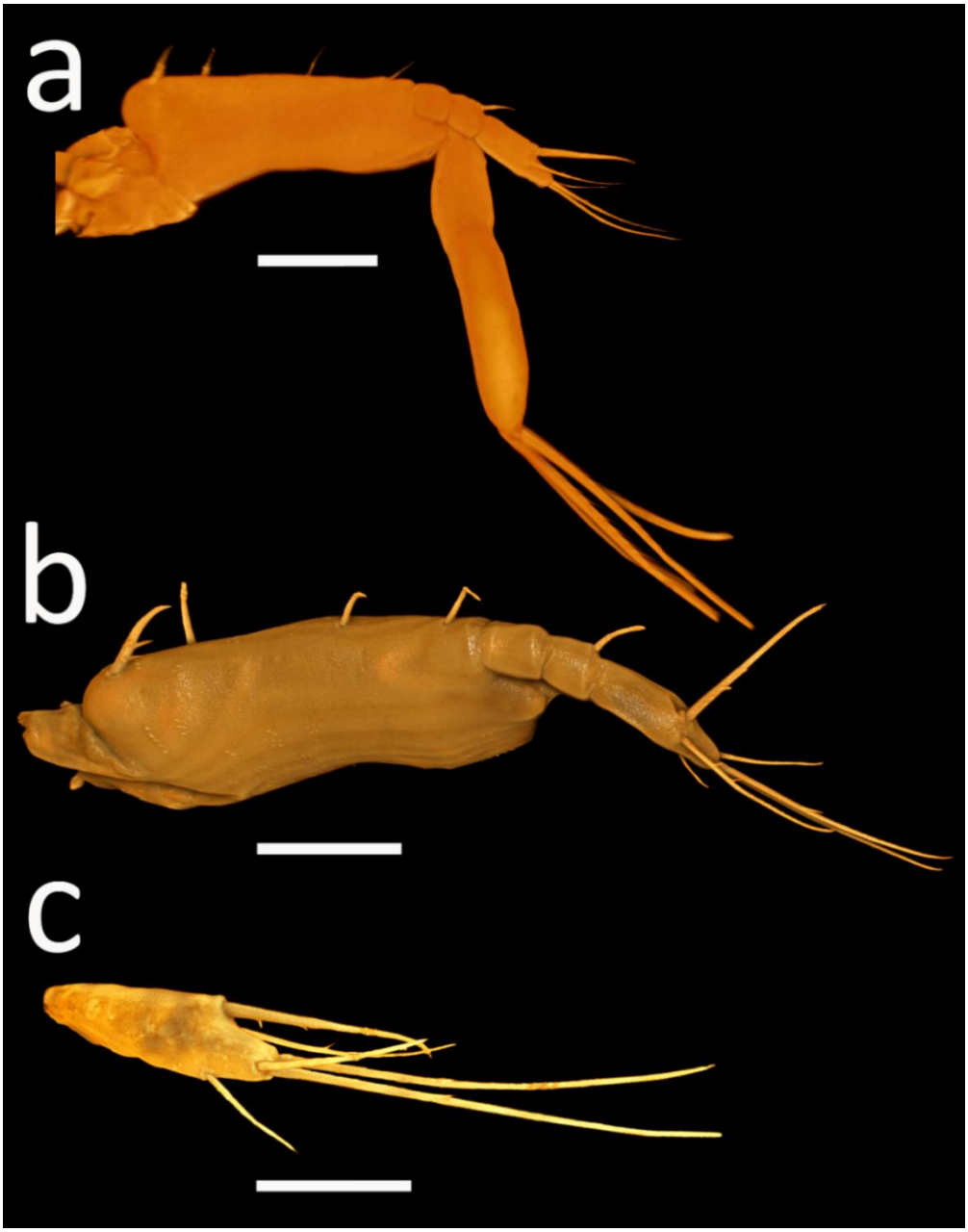

Figure 5.7: *Eriocheir sinensis*, ZI, second maxilliped, Nikon A1-Si CLSM with Drishti processing. (a) Whole appendage. (b) Coxa, basis and endopod, applying "large images" option, scan area of 1×2 fields for image stitching. (c) Distal endopod segment. Objective: a = 20× dry; b = 40× oil immersion; c = 60× oil immersion. Scale bars a-b = 100 µm; c = 50 µm. See video 2 for 3D representation of the second maxilliped.

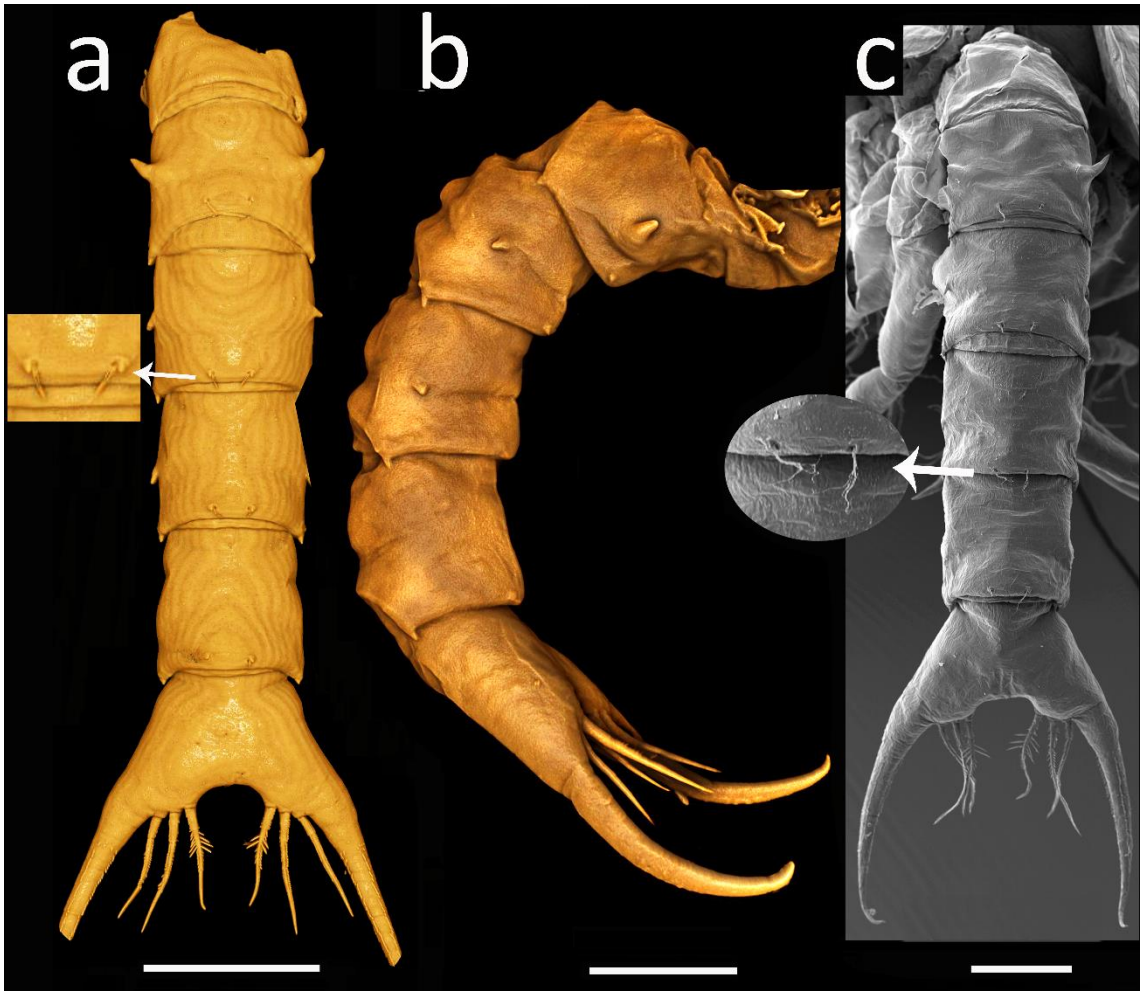

Figure 5.8: *Eriocheir sinensis*, ZI, pleon, Nikon A1-Si CLSM with Drishti processing. (a) Dorsal view, one pair of posterodorsal setae on somite 3 presented in detail (arrowed), applying "large images" option, scan area of 2×6 fields for image stitching. (b) Lateral view, image merged using Adobe Photoshop. Zeiss Ultra Plus Field Emission SEM. (c) One pair of posterodorsal setae on somite 4 presented in detail (arrowed). Objective: a = 40× oil immersion; b = 20× dry. Scale bars a = 200 µm; b = 300 µm; c = 100 µm.

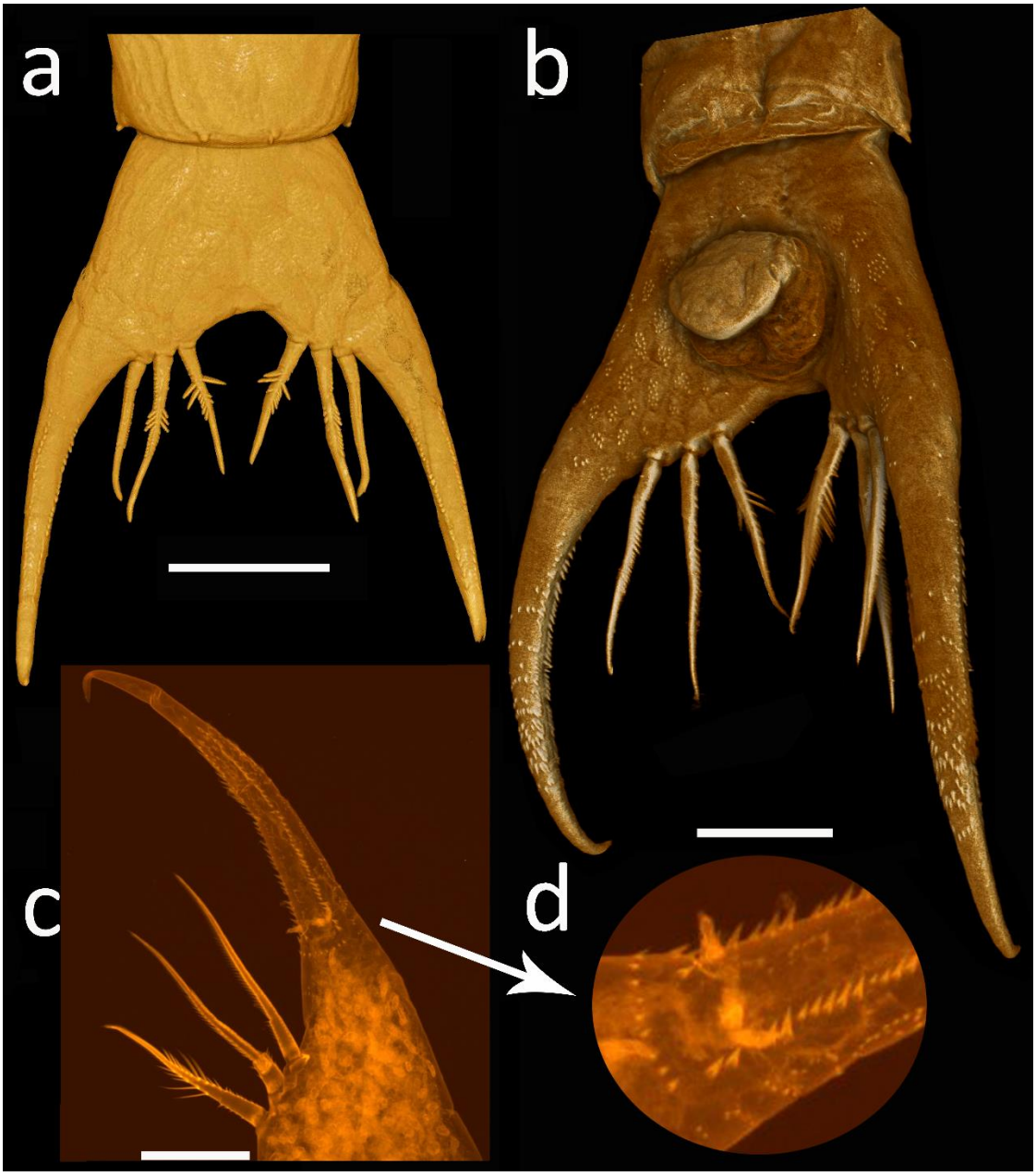

Figure 5.9: *Eriocheir sinensis*, ZI, telson, Nikon A1-Si CLSM with Drishti processing. (a) Dorsal view of telson showing posterior margin with 3 pairs of stout spinulate spines. (b) Ventral view of telson showing anal operculum. Both applying "large images" option, scan area of 2×2 fields for image stitching. Nikon A1-Si CLSM (c) Telson fork. (d) Double row of denticules on inner margin of fork. Objective: a-b = 40× oil immersion; c = 60× oil immersion. Scale bars a-b = 100 µm; c = 50 µm.

Zoea II (Figs 5.10−5.16)

Carapace (Figs 5.10−5.11): Two pairs of anterodorsal (one pair on orbital margin); ventral margin with 2 anterior highly plumose setae and 2 posterior sparsely plumose setae with additional serrations; eyes stalked.

Antennule (Fig. 5.12a): Primary flagellum with 4 broad aesthetascs and 2 equal short simple setae.

Antenna (Fig. 5.12b): Exopod more developed, ca. 35% of protopod.

Mandible: Unchanged.

Maxillule (Fig. 5.12c): Biramous; basial endite with 7 armed processes (6 cuspidate setae, 1 plumodenticulate seta); exopod, plumose seta present.

Maxilla (Fig. 5.12): Exopod (scaphognathite) margin with 5+3 plumose setae; long distal stout process reduced in size.

First Maxilliped (Fig. 5.14): Exopod, distal segment with 6 long terminal plumose natatory setae.

Second Maxilliped (Fig. 5.15): Exopod, distal segment with 6 long terminal plumose natatory setae.

Third Maxilliped: Absent.

Pereiopods: Absent.

Pleon (Fig. 5.16): Somite 1 now with 1 small dorsal medial seta.

Telson (Fig. 5.16a): Unchanged.

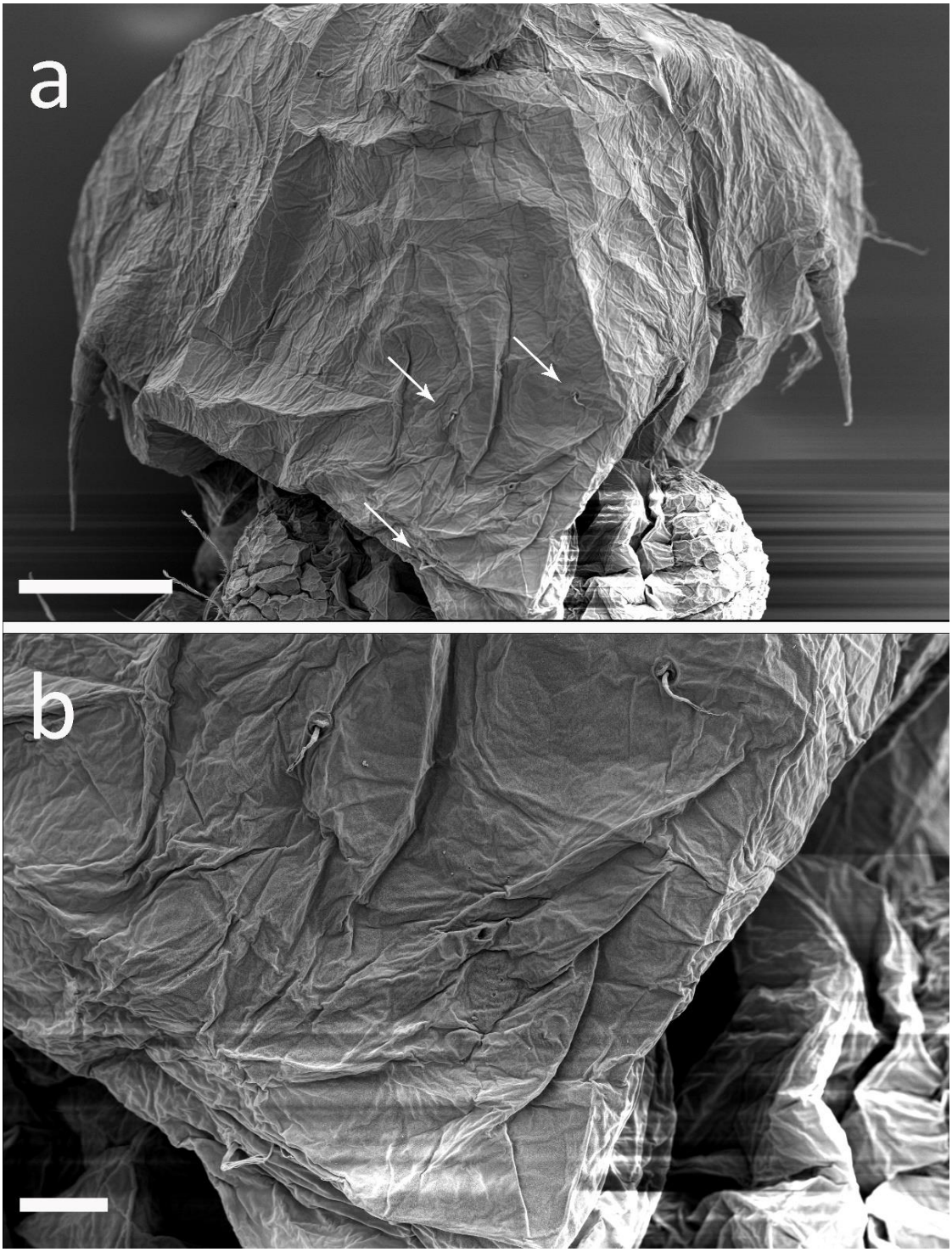

Figure 5.10: *Eriocheir sinensis,* ZII, carapace, Zeiss Ultra Plus Field Emission SEM. (a) Anterior view, anterodorsal setae arrowed. (b) Enlargement of paired anterodorsal setae and orbital margin setae. Scale bars a = 100 µm; b = 20 µm.

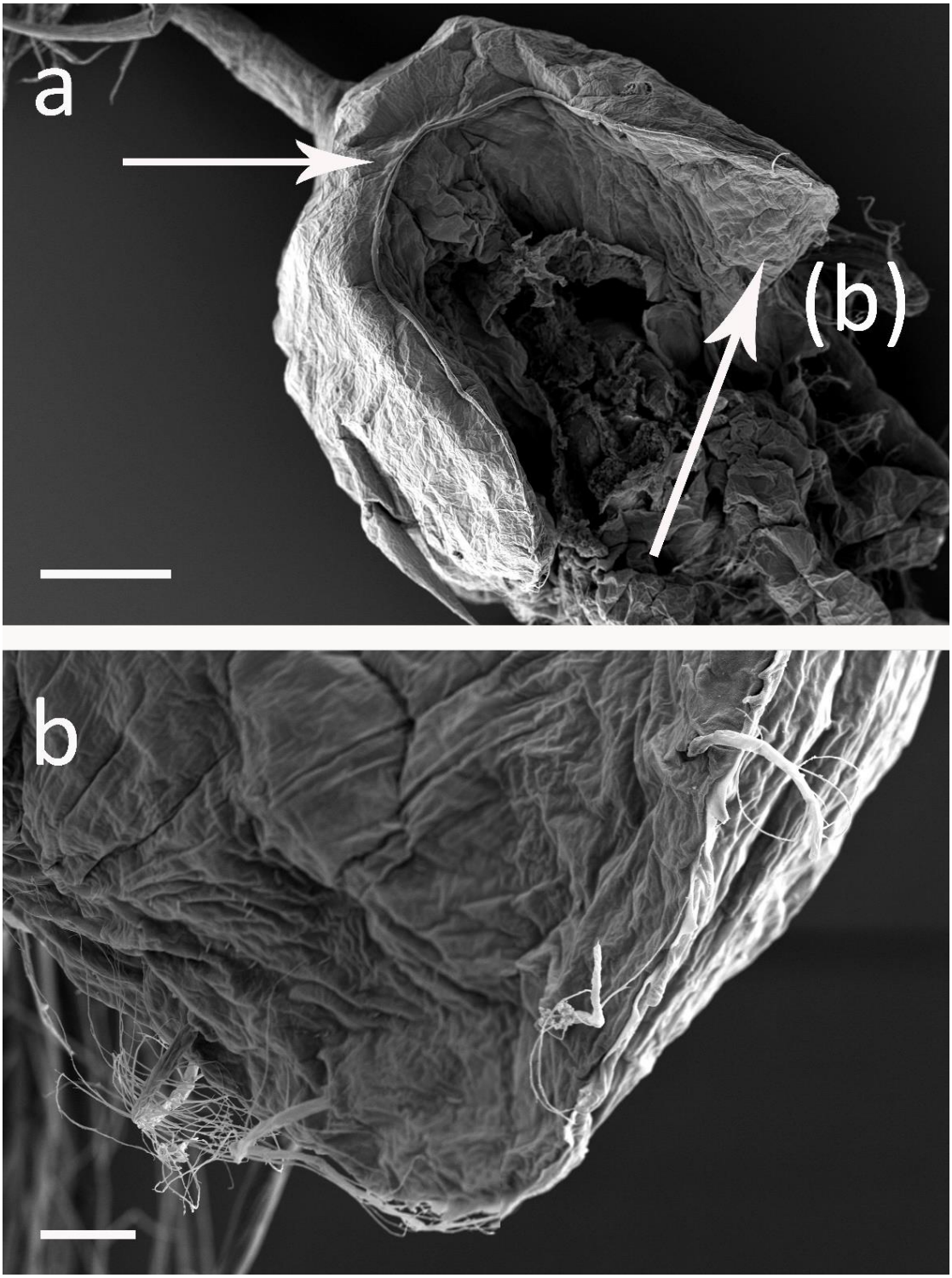

Figure 5.11: *Eriocheir sinensis*, ZII, carapace, Zeiss Ultra Plus Field Emission SEM. (a) Setae absent on dorsoposterior carapace margin. (b) 2 anterior plumose setae and 2 posterior setae on ventral carapace margin. Scale bars a = 100 µm; b = 10 µm.

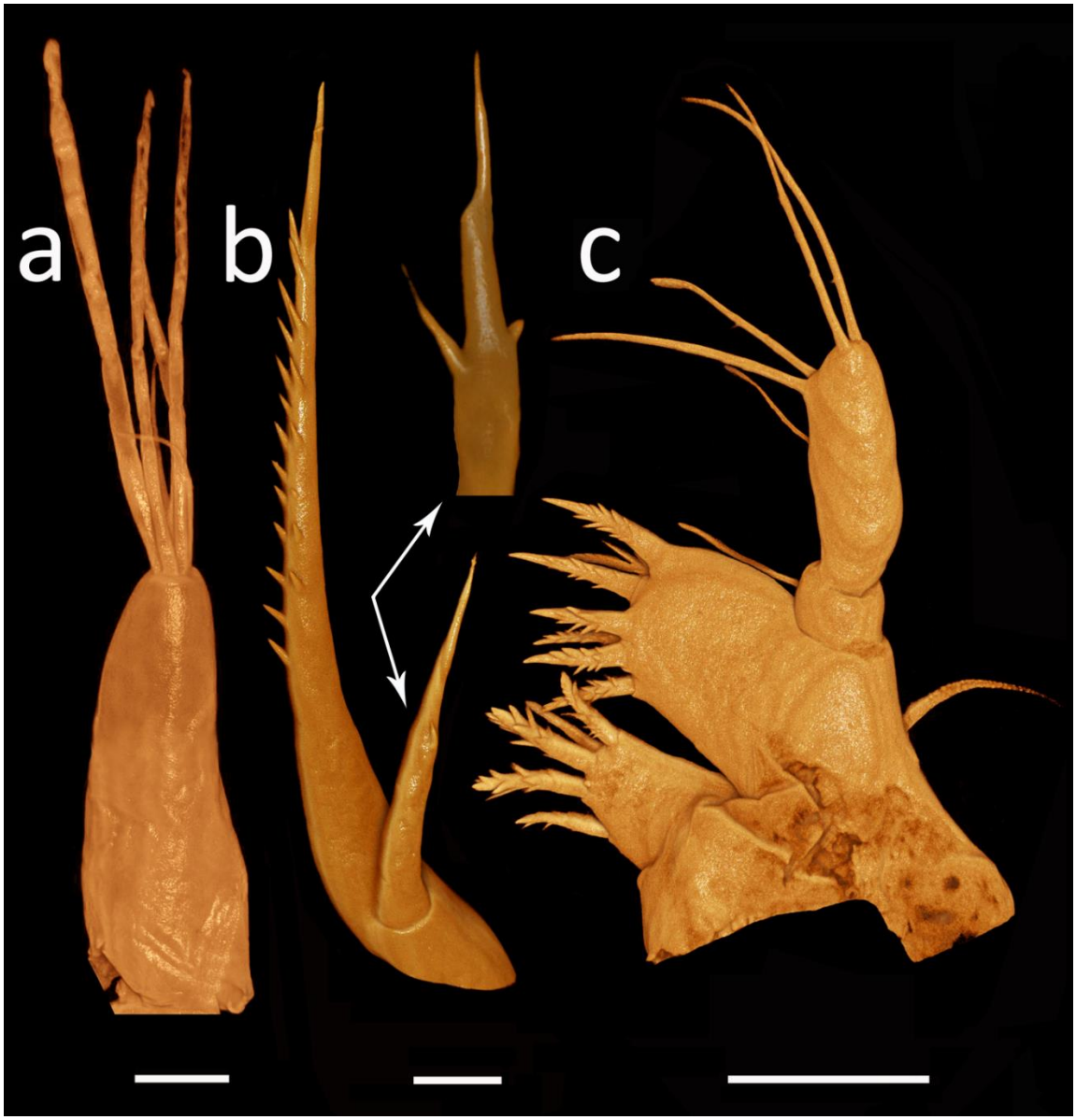

Figure 5.12: *Eriocheir sinensis*, ZII, Nikon A1-Si CLSM with Drishti processing. (a) Antennule, image merged using Adobe Photoshop. (b) Antenna with two exopodal setae. (c) Maxillule. Objective: 40× oil immersion. Scale bars a, b = 50 µm; c = 100 µm.

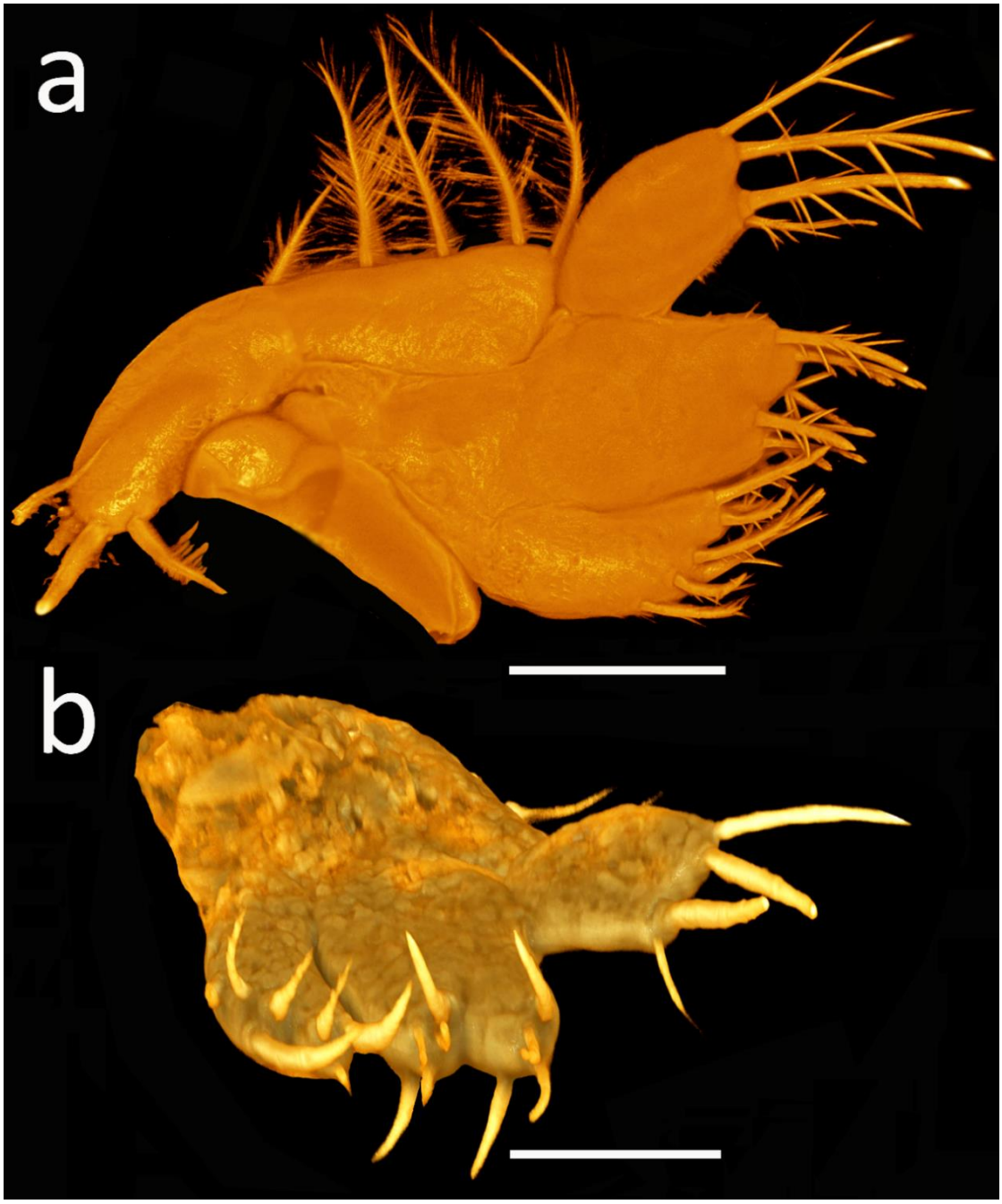

Figure 5.13: *Eriocheir sinensis*, ZII, maxilla, Nikon A1-Si CLSM with Drishti processing. (a) Maxilla, image merged using Adobe Photoshop. (b) Maxilla rotated to reveal reverse angle of image a, and the setation of the coxal and basial endites. Objective: 40× oil immersion. Scale bars = 100 µm.

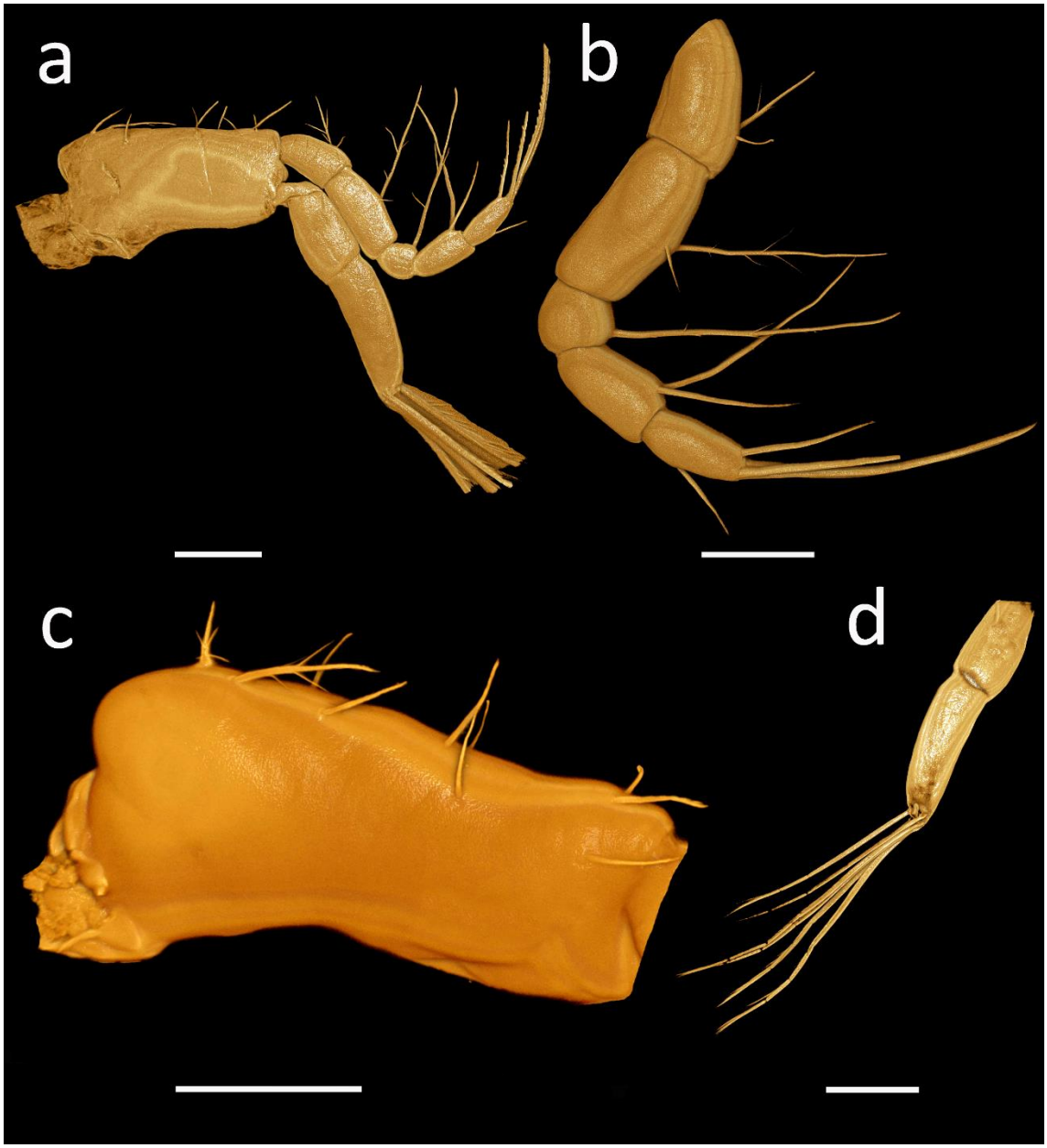

Figure 5.14: *Eriocheir sinensis*, ZII, first maxilliped, Nikon A1-Si CLSM with Drishti processing. (a) Whole appendage, applying "large images" option, scan area of 1×2 fields for image stitching. (b) Endopod. (c) Basis. (d) Exopod with 6 natatory setae, applying "large images" option, scan area of 1×2 fields for image stitching. Objective: a, d = 20× dry; b-c = 40× oil immersion. Scale bars a, d = 200 µm; b, c = 100 µm.

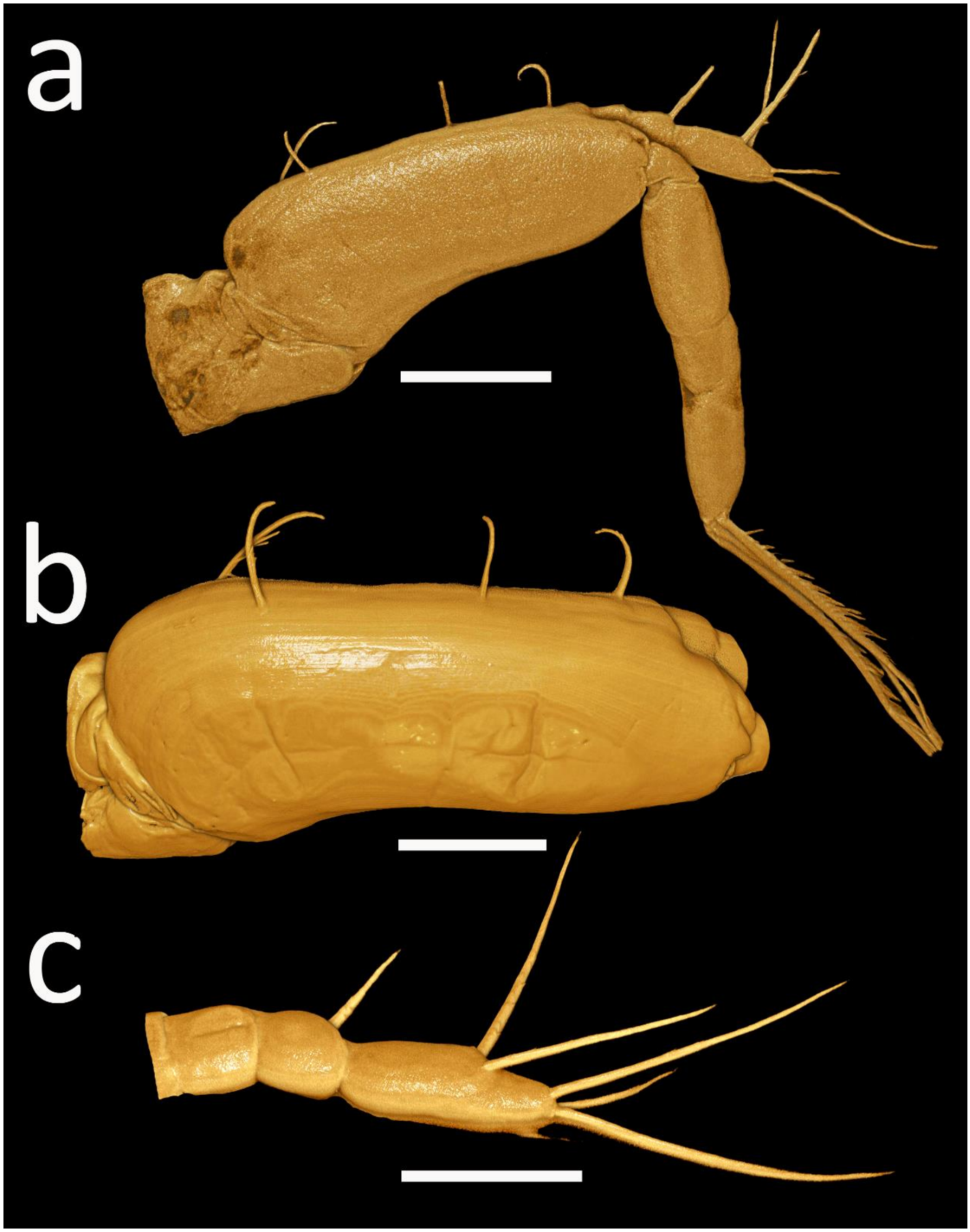

Figure 5.15: *Eriocheir sinensis*, ZII, second maxilliped, Nikon A1-Si CLSM with Drishti processing. (a) Whole appendage, 20× dry objective, applying "large images" option, scan area of 1×2 fields for image stitching. (b) Basis. (c) Endopod. Objective: a = 20× dry; b-c = 40× oil immersion. Scale bars a = 200 µm; b-c = 100 µm.

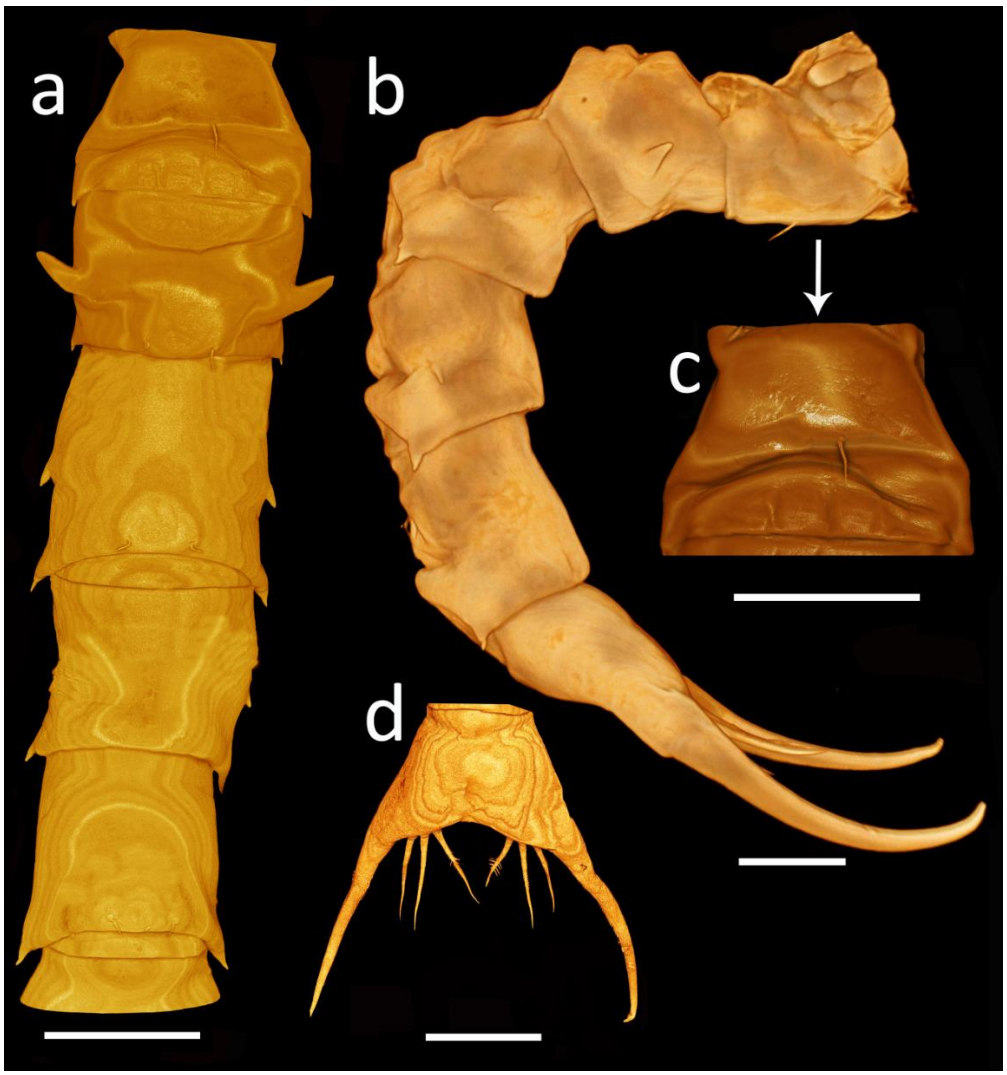

Figure 5.16: *Eriocheir sinensis*, ZII, pleon and telson, Nikon A1-Si CLSM with Drishti processing. (a) Dorsal view of pleon, image merged using Adobe Photoshop. (b) Lateral view of pleon and telson, applying "large images" option with a scanned area of 1×2 fields for image stitching. (c) Somite 1 with a small dorsal medial seta. (d) Dorsal view of telson. Objective: a, c = 40× oil immersion; b, d = 20× dry. Scale bars = 200 µm. (a) Dorsal view of pleon and telson, applying "large images" option, scan area of 1×3 fields for image stitching. (b) Dorsal view of pleon, image merged using Adobe Photoshop. (c) Somite 1 with a small dorsal medial seta and somite 2 in detail. Zeiss Ultra Plus Field Emission SEM. (d) Somite 1 and 2. Objective: a = 20× dry; b-c = 40× oil immersion. Scale bars a = 200 µm; b-c = 100 µm; d = 20 µm.

Zoea III (Figs 5.17−5.23)

Carapace (Figs 5.17−5.18): Now with four pairs of anterodorsal setae; ventral margin 2 anterior highly plumose setae and 4 posterior sparsely plumose setae and with additional serrations.

Antennule (Fig. 5.19a): Unchanged.

Antenna (Figs 5.19b-c): Biramous; endopod present as small bud (ca. 20% of whole appendage); exopod more developed, ca. 40% of protopod.

Mandible: Unchanged.

Maxillule (Fig. 5.19d): Simple epipod seta present.

Maxilla (Fig. 5.20): Coxal endite now with 5+3 plumodenticulate setae; basial endite with 6+5 sparsely plumodenticulate setae; exopod (scaphognathite) margin now with 9+6 plumose setae.

First Maxilliped (Fig. 5.21): Endopod 5-segmented arranged 2,2,2 (now with a dorsal seta),2,5 (1 subterminal, four terminal) setae; exopod, distal segment now with 8 long terminal plumose natatory setae.

Second Maxilliped (Fig. 5.22): Exopod, distal segment now with 8 terminal plumose natatory setae.

Third Maxilliped: Absent.

Pereiopods: Absent.

Pleon (Fig. 5.23): Somite 6 now differentiated.

Telson (Fig. 5.23): Posterior margin with an additional inner pair of small simple setae.

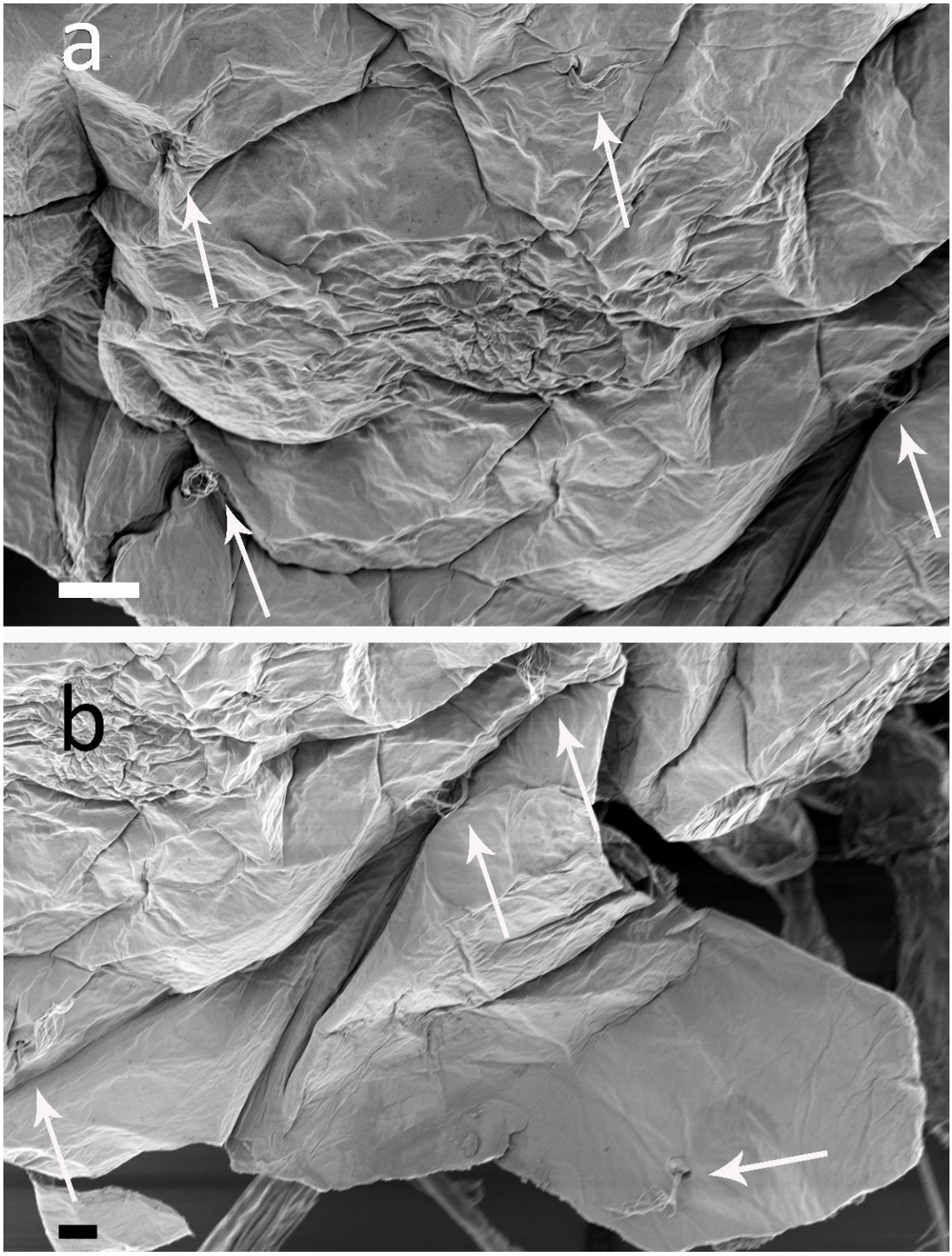

Figure 5.17: *Eriocheir sinensis*, ZIII, carapace, Zeiss Ultra Plus Field Emission SEM. (a) Anterior view showing anterodorsal setae. (b) One pair of setae on orbital margin. Scale bars a = 20 µm; b = 10 µm.

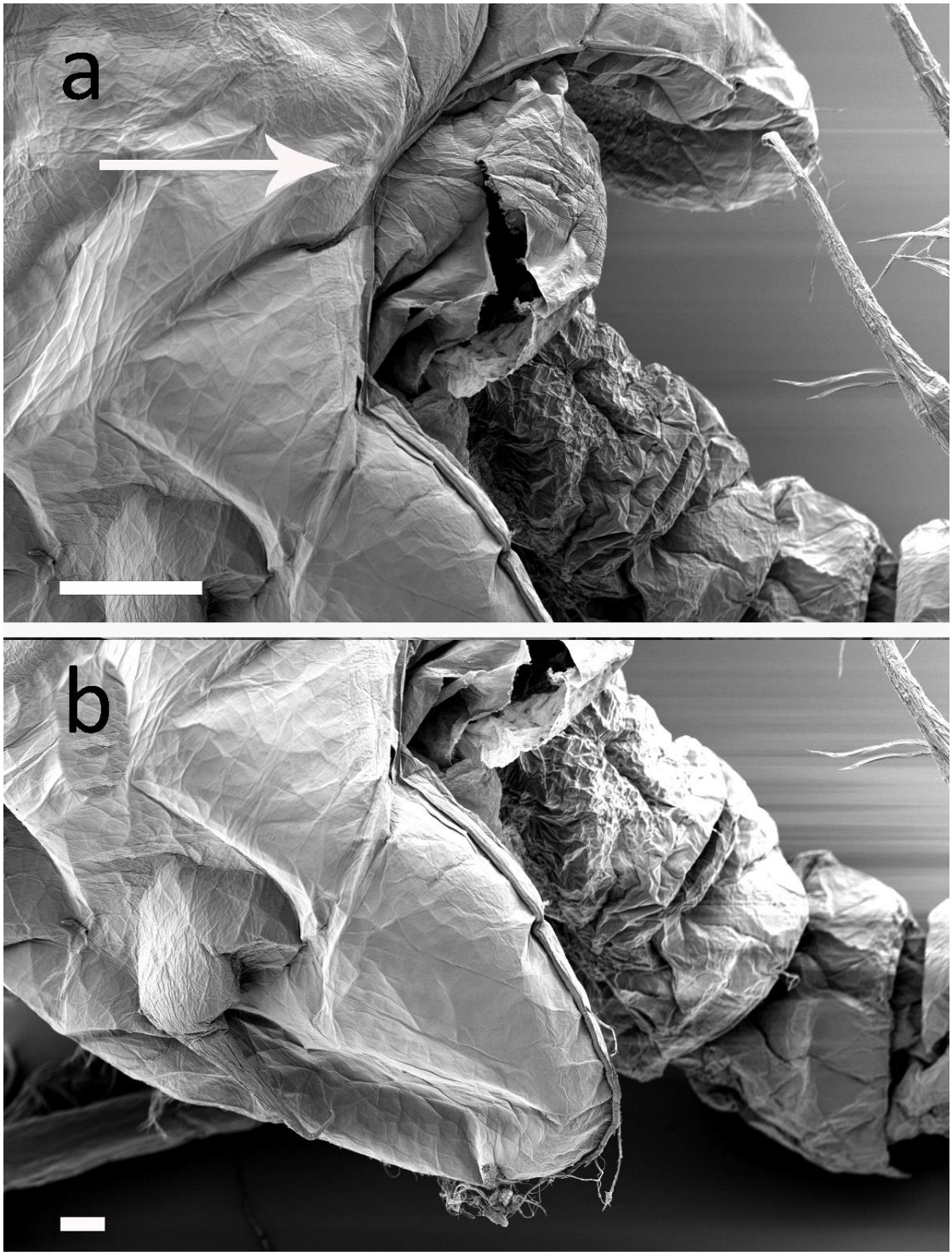

Figure 5.18: *Eriocheir sinensis*, ZIII, carapace, Zeiss Ultra Plus Field Emission SEM. (a) Setae absent on dorsoposterior carapace margin. (b) 2 anterior plumose setae and 4 posterior setae on ventral carapace margin. Scale bars a = 100 µm; b = 30 µm.

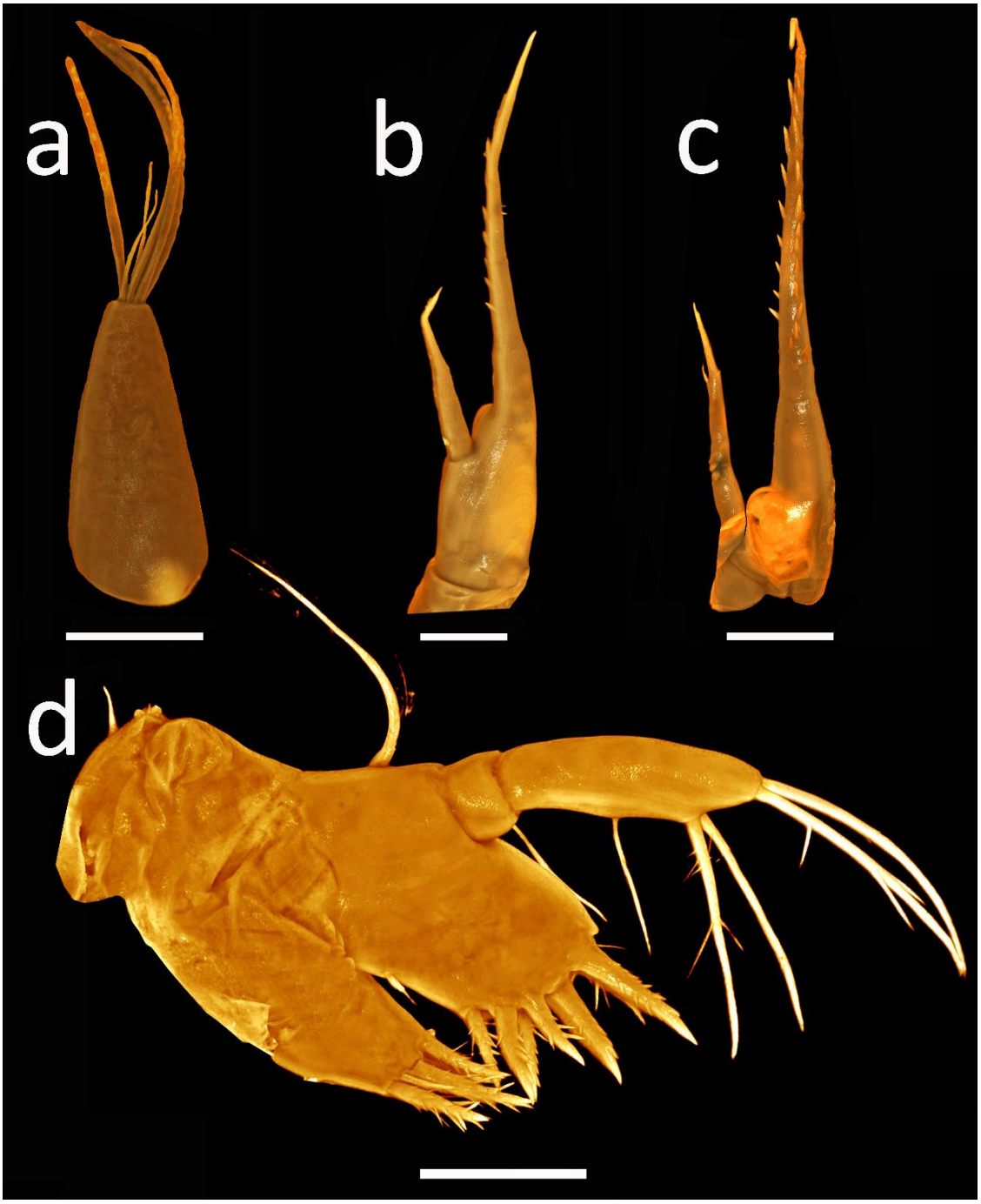

Figure 5.19: *Eriocheir sinensis*, ZIII, Nikon A1-Si CLSM with Drishti processing. (a) Antennule. (b) Antenna. (c) Antenna rotated to reveal reverse angle of image b and developing endopod bud. (d) Maxillule, applying "large images" option, scan area of 1×2 fields for image stitching. Objective: 40× oil immersion. Scale bars = 100 µm.

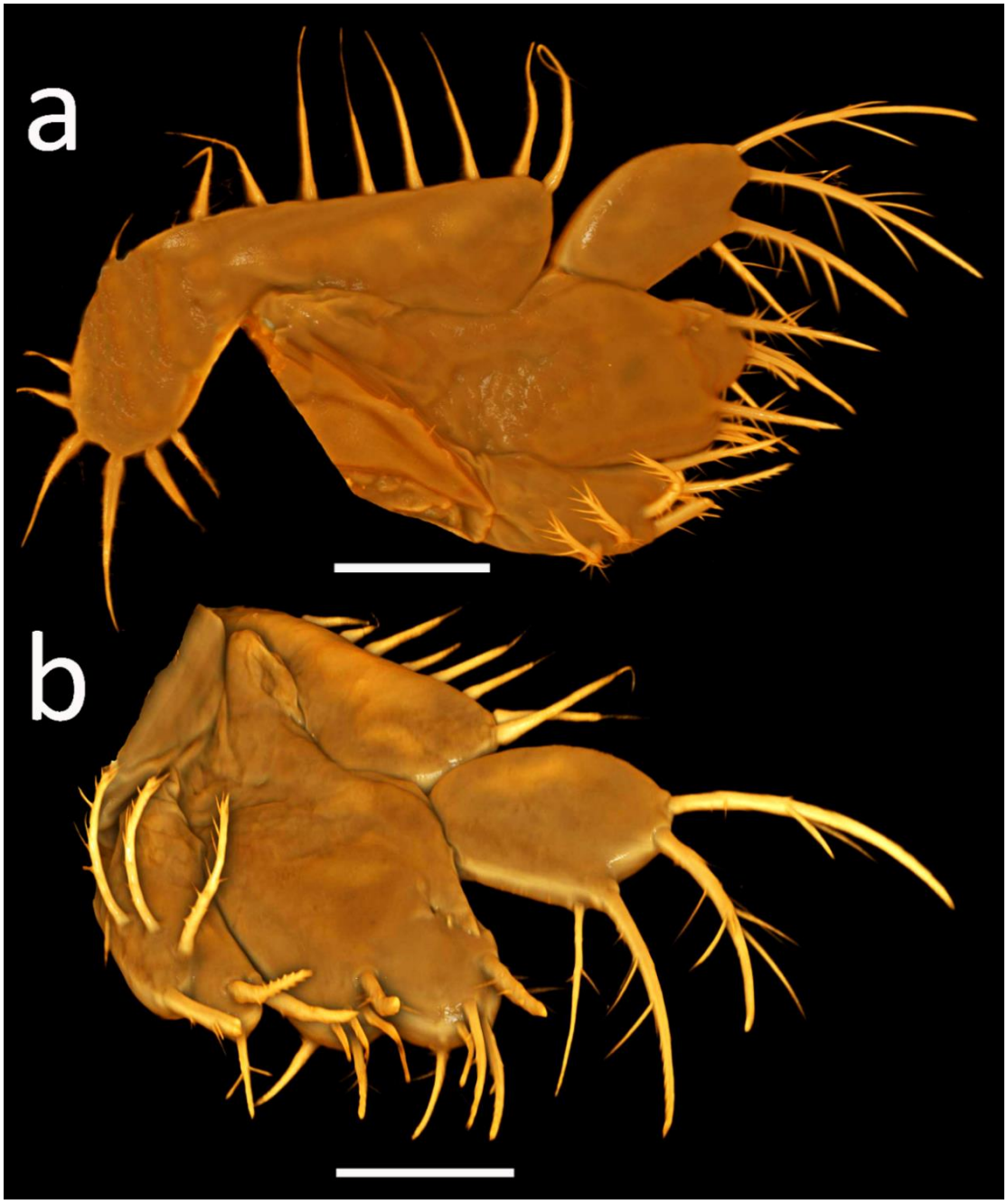

Figure 5.20: *Eriocheir sinensis*, ZIII, maxilla, Nikon A1-Si CLSM with Drishti processing. (a) Whole appendage, image merged using VGStudio MAX. (b) Maxilla rotated to reveal reverse angle of image a, and the setation of the coxal and basial endites. Objective: 40× oil immersion. Scale bars = 100 µm.

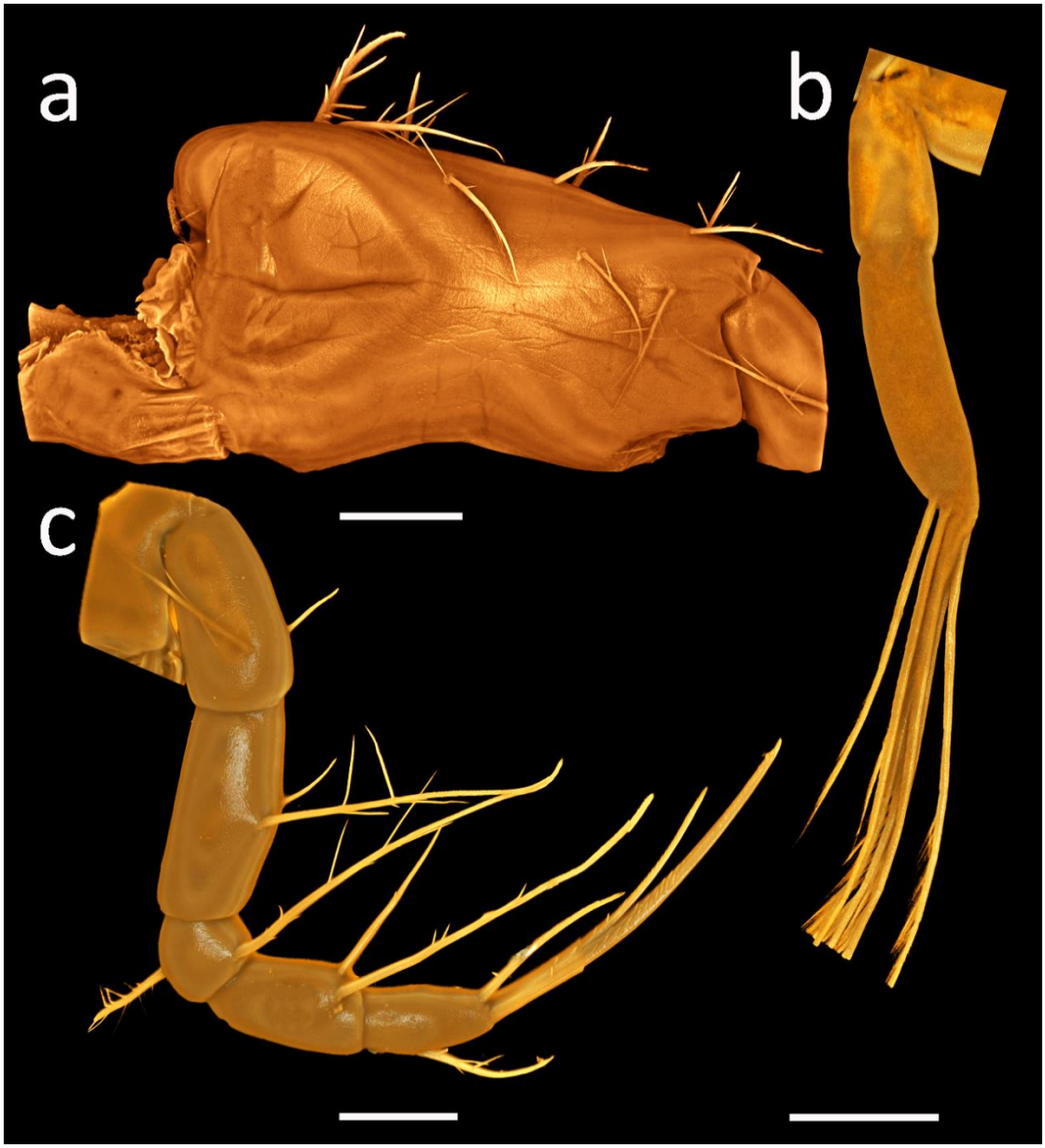

Figure 5.21: *Eriocheir sinensis*, ZIII, first maxilliped, Nikon A1-Si CLSM with Drishti processing. (a) Coxa and basis, image merged using VGStudio MAX. (b) Exopod with 8 natatory setae, applying "large images" option, scan area of 1×2 fields for image stitching. (c) Endopod, image merged using VGStudio MAX. Objective: a, c = 40× oil immersion; b = 20× dry. Scale bars a, c = 100 µm; b = 200 µm.

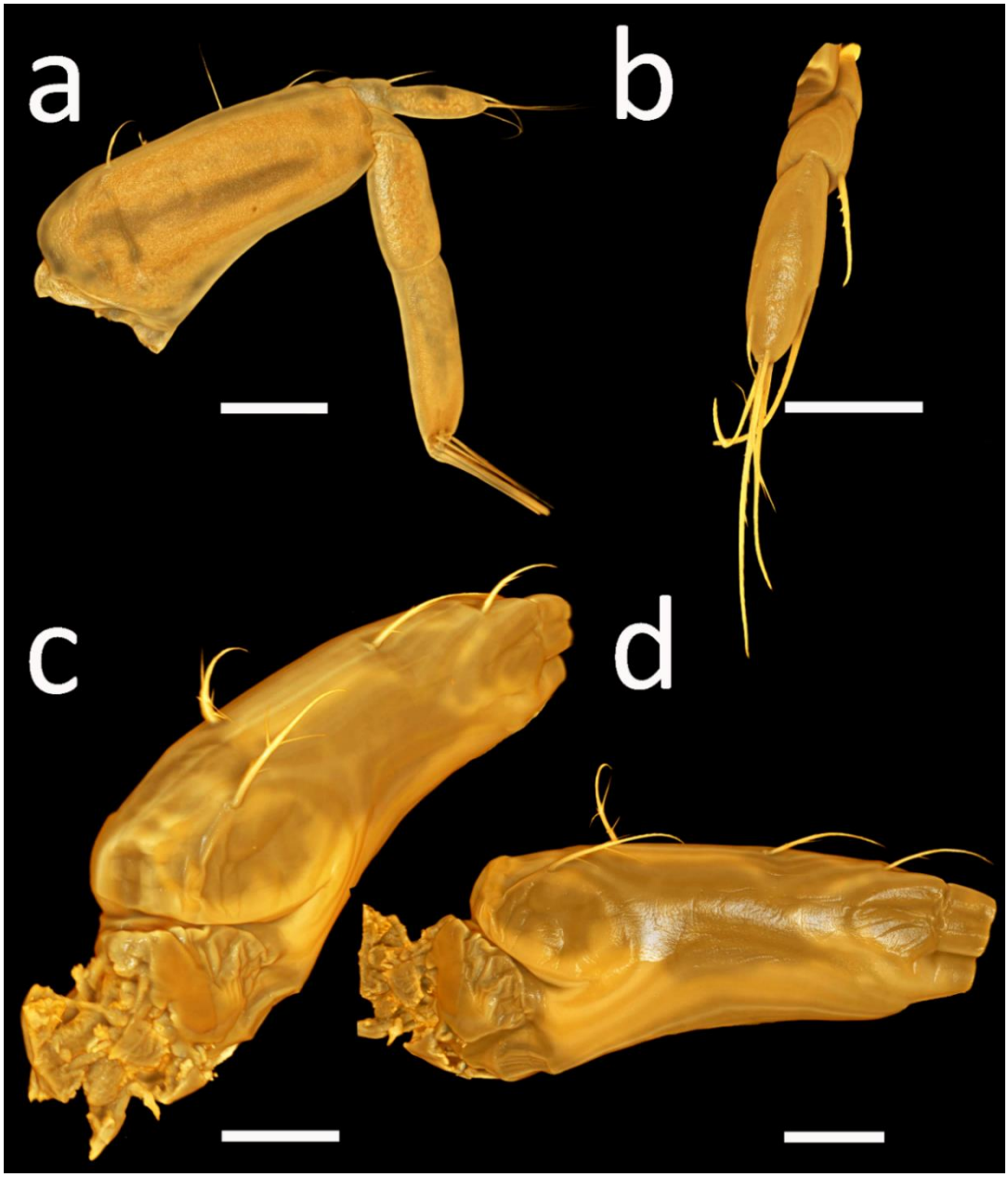

Figure 5.22: *Eriocheir sinensis*, ZIII, second maxilliped, Nikon A1-Si CLSM with Drishti processing. (a) Whole appendage, applying "large images" option, scan area of 1×2 fields for image stitching. (b) Endopod. (c) Basis. (d) Basis rotated to reveal reverse angle of image c. Both images merged using VGStudio MAX. Objective: a = 20× dry; b = 60× oil immersion; c-d = 40× oil immersion. Scale bars a = 200 µm; b-d = 100 µm.

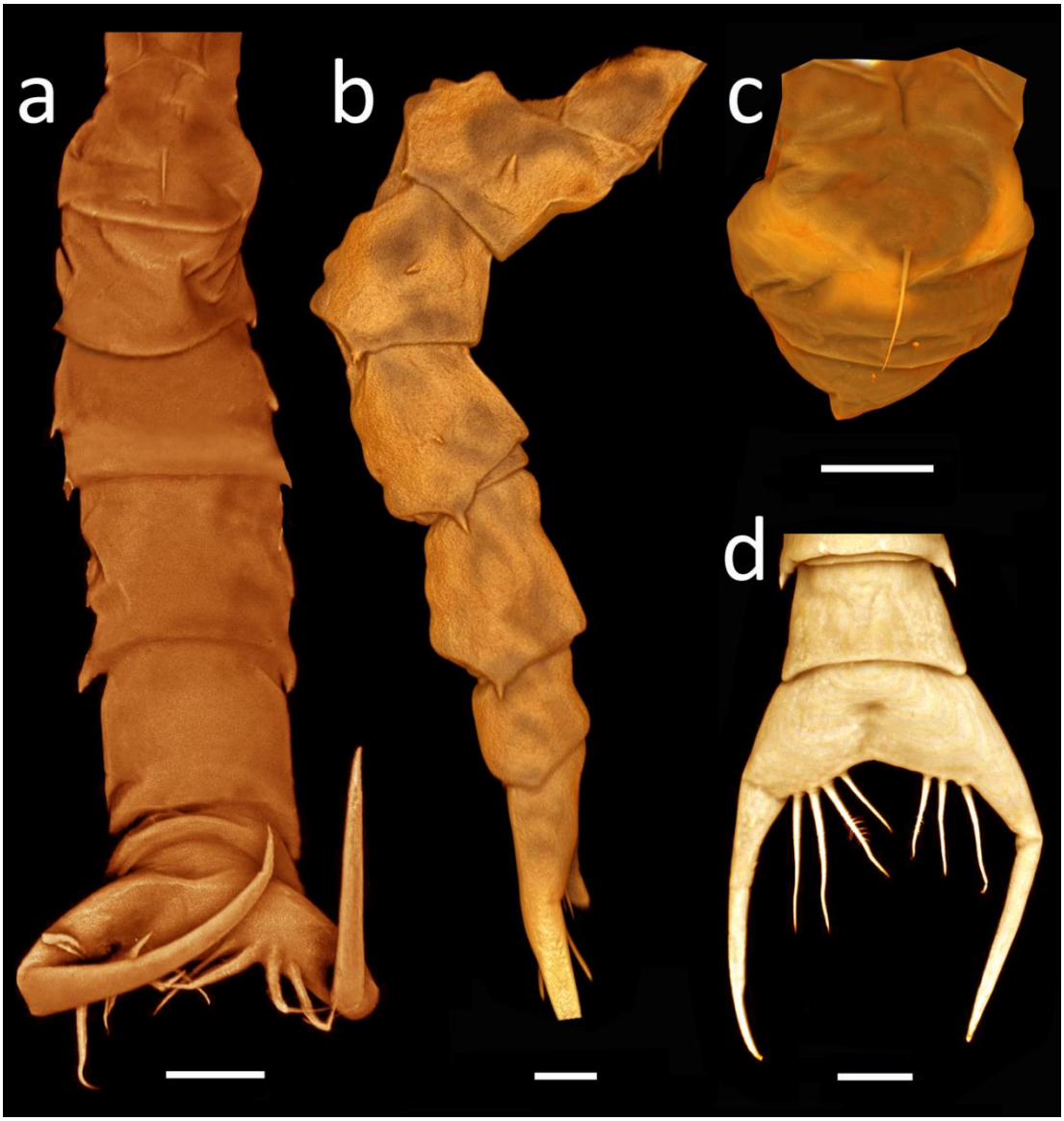

Figure 5.23: *Eriocheir sinensis*, ZIII, pleon and telson, Nikon A1-Si CLSM with Drishti processing. (a) Dorsal view of pleon and telson, image merged using Adobe Photoshop. (b) Lateral view of pleon. (c) Somite 1 with a dorsal medial seta. (d) Dorsal view of telson. Objective: a, d = 20× dry; b = 10× dry; c = 40× oil immersion. Scale bars a, b, d = 200 µm; c = 100 µm.

Zoea IV (Figs 5.24−5.33)

Carapace (Figs 5.24−5.26): Dorsal spine now with 3 pairs of simple setae; now with 5 pairs of anterodorsal simple setae; 4 anterior highly plumose setae and 7−8 posterior sparsely plumose setae on ventral margin with additional serrations on each side; 3 pairs of sparsely plumose setae on dorsoposterior margin.

Antennule (Fig. 5.27a): Primary flagellum with 2-tiers of subterminal aesthetascs; 1 proximal subterminal aesthetasc on 1-tier; 1 subterminal aesthetasc on 2-tier; 3 long terminal aesthetascs and 1 short simple terminal seta.

Antenna (Fig. 5.27b): Endopod now more developed (ca. 30% of whole appendage); exopod now more developed, ca. 40−50%.

Mandible (Fig. 5.28a): Well developed, palp absent.

Maxillule (Fig. 5.28b-c): Coxa now with 7 plumodenticulate and 1 simple setae, basial endite now with 11 armed processes (cuspidate, marginal), 1 plumose and now 1 short simple setae on inner margin of basal endite.

Maxilla (Fig. 5.29): Coxal endite bilobed now with 7+3 plumodenticulate setae and 1 distal simple seta; basial endite now with 8+8 unequal plumodenticulate setae; exopod (scaphognathite) margin now with 18+7 highly plumose setae of various length.

First Maxilliped (Fig. 5.30): Coxa now with a seta; endopod now arranged either 2,2 (1 dorsal, 1 ventral seta),2,2,6 (2 subterminal (now with 1 ventral seta, 4 terminal) or 2,3 (1 dorsal, 2 ventral setae),2,2,6 setae; exopod, distal segment now with 10 long terminal plumose natatory setae.

Second Maxilliped (Fig. 5.31): Exopod, distal segment now with 10 terminal plumose natatory setae.

Third Maxilliped (Fig. 32a): Present; biramous; epipod present; endopod longer than exopod.

Pereiopods (Fig. 32b): Present; bilobed cheliped; walking legs with some segmentation.

Pleon (Figs 5.33a-b): Somite one now with medial 5 simple setae; pleopods present on somites 2−6, endopods absent.

Telson (Fig. 5.33c): Additional pair of minute setae on posterior margin.

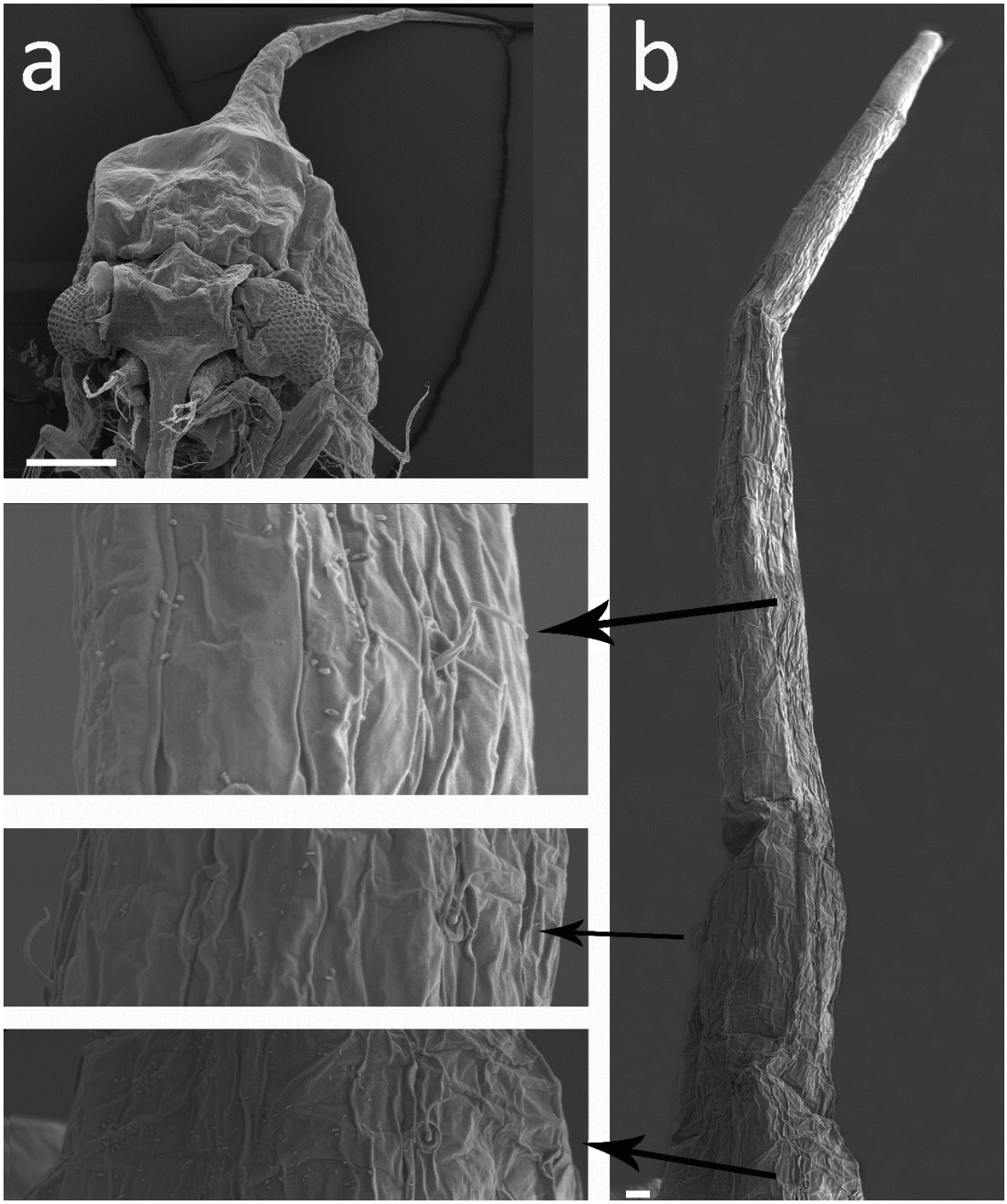

Figure 5.24: *Eriocheir sinensis*, ZIV, dorsal carapace spine, Zeiss Ultra Plus Field Emission SEM. (a) Anterior view of carapace. (b) 3 pairs of setae on dorsal spine (arrowed). Scale bars a = 200 µm; b = 10 µm.

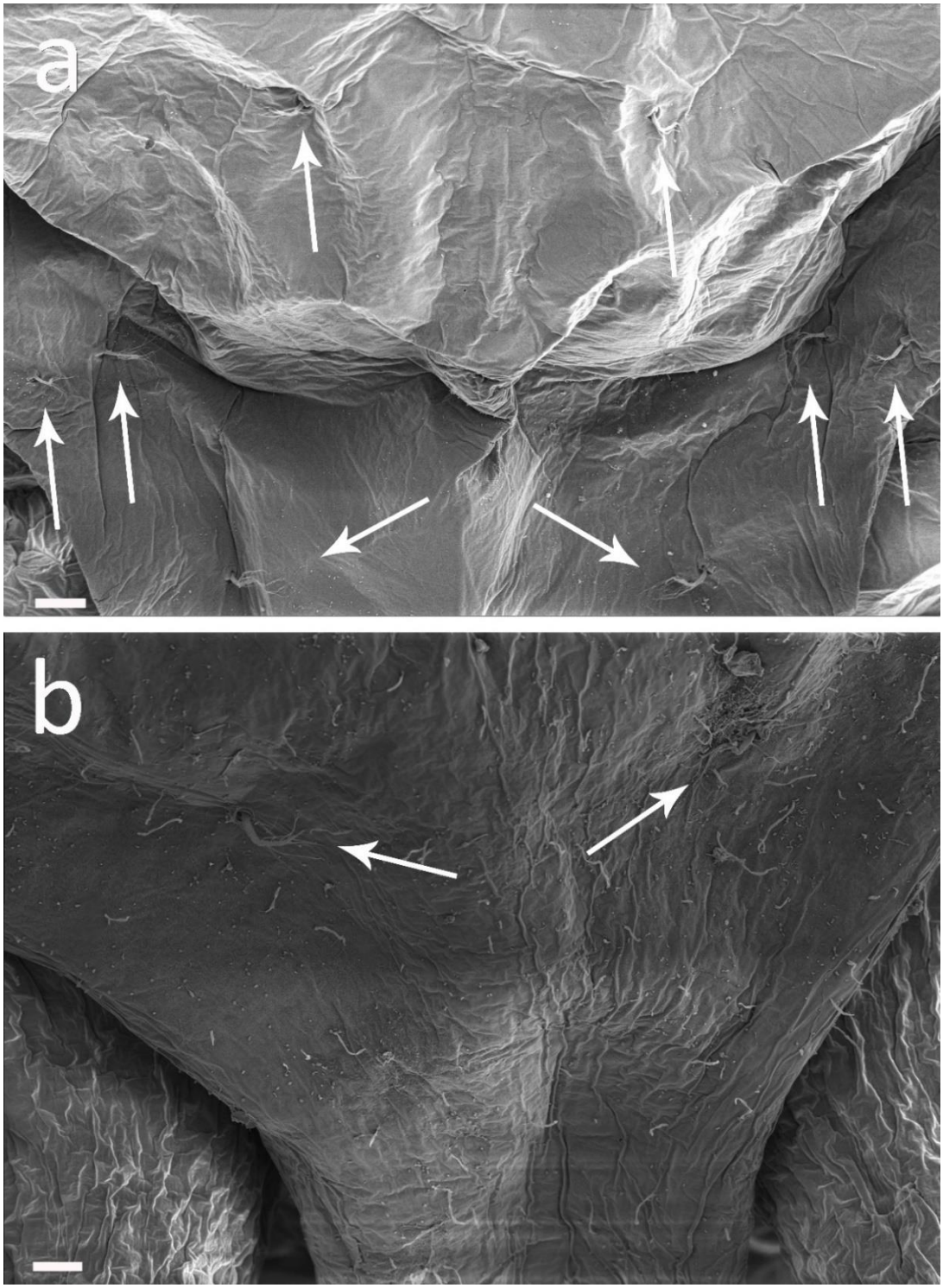

Figure 5.25: *Eriocheir sinensis*, ZIV, anterior carapace setation, Zeiss Ultra Plus Field Emission SEM. (a) 4 pairs of anterodorsal setae. (b) 1 pair of anterodorsal setae on orbital margin. Scale bars a = 20 µm; b = 10 µm.

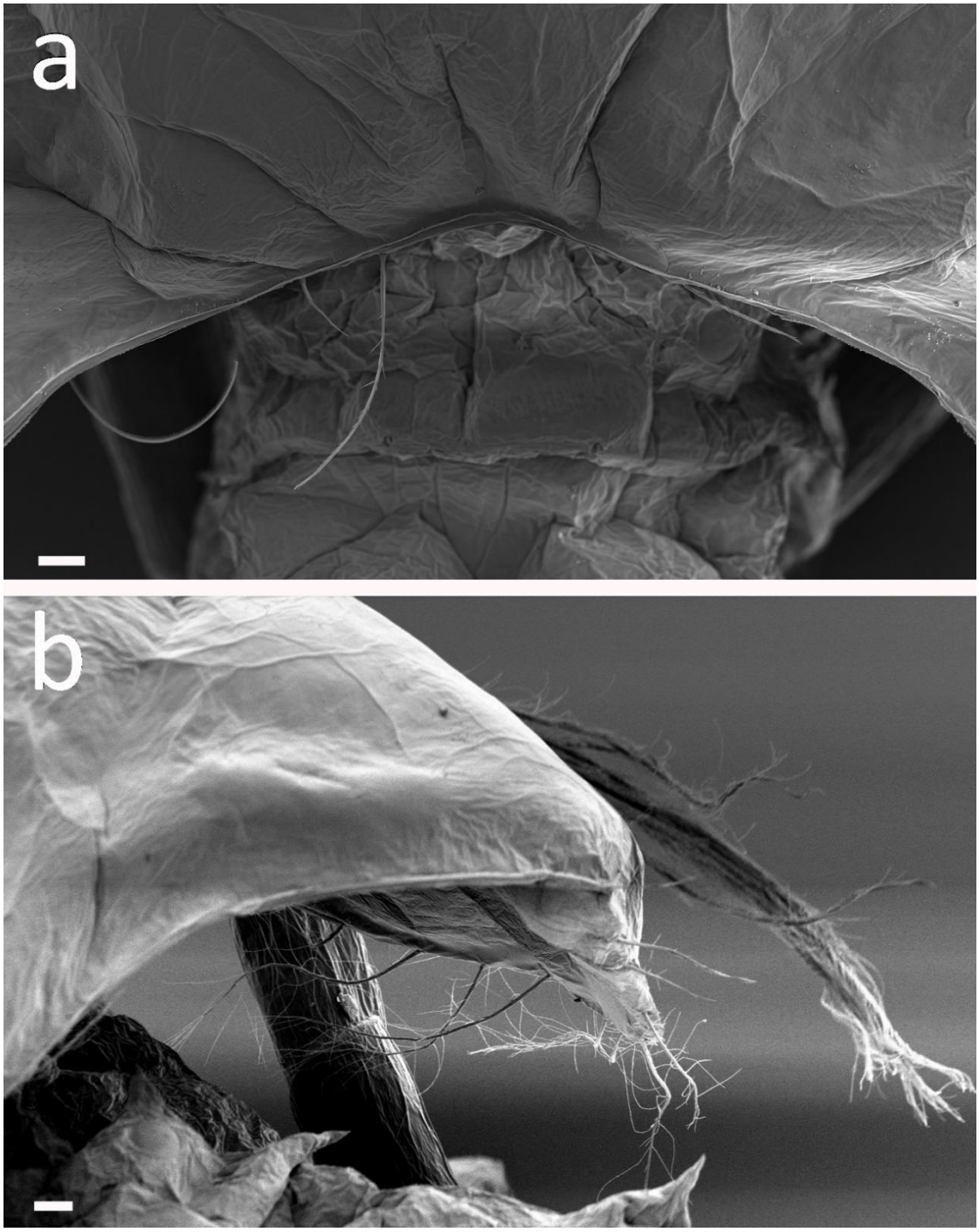

Figure 5.26: *Eriocheir sinensis*, ZIV, carapace, Zeiss Ultra Plus Field Emission SEM. (a) 3 pairs of setae on dorsoposterior carapace margin. (b) 4 anterior plumose setae and 7−8 posterior setae on ventral carapace margin. Scale bars = 20 μm.

Figure 5.27: *Eriocheir sinensis*, ZIV, Nikon A1-Si CLSM with Drishti processing. ((a) Antennule. (b) Antenna with a more developed endopod and two exopodal setae arrowed. Both applying "large images" option with a scanned area of 2×3 fields for image stitching. Objective: 40× oil immersion. Scale bars a = 100 µm; b = 200 µm.

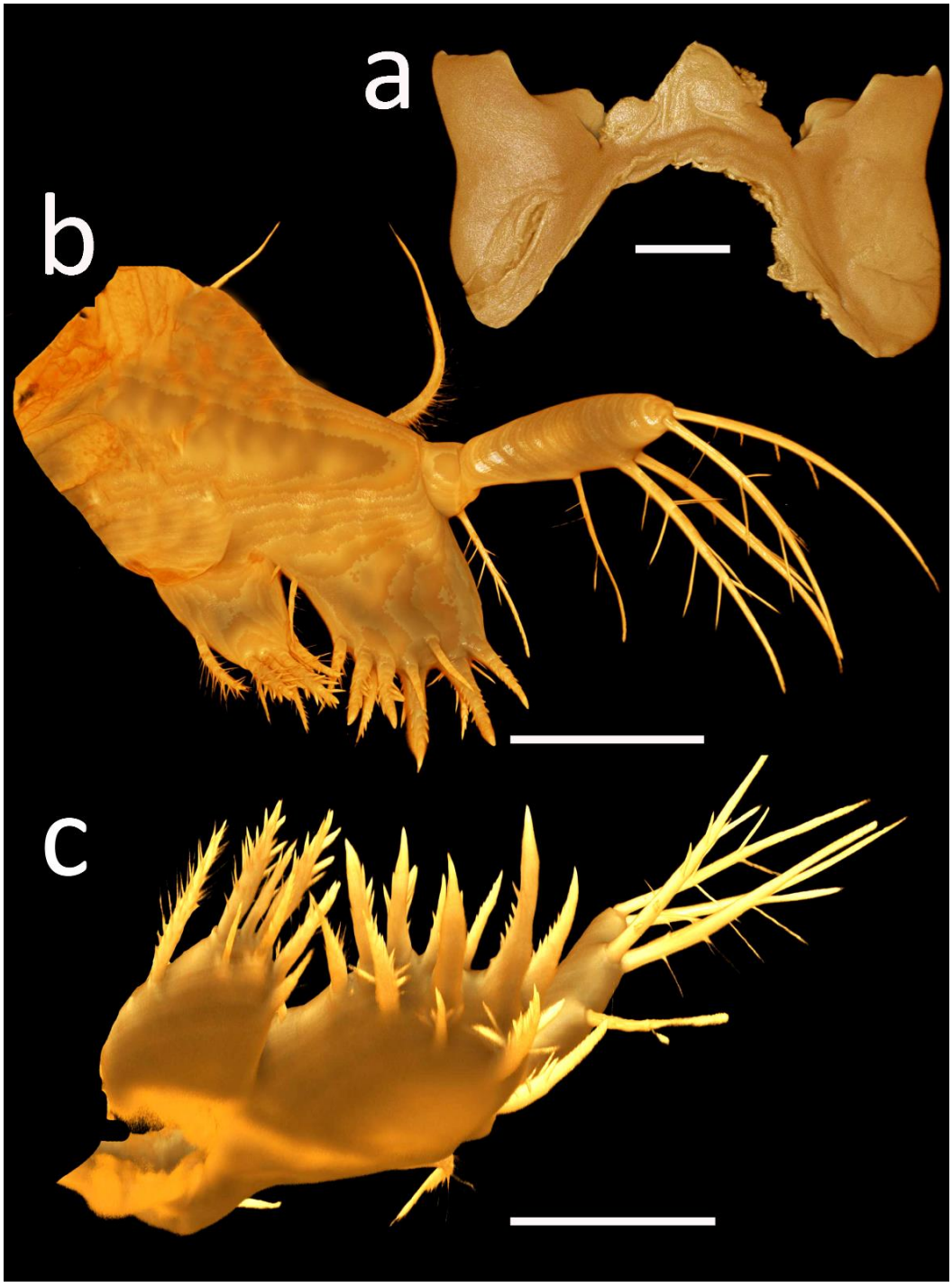

Figure 5.28: *Eriocheir sinensis*, ZIV, Nikon A1-Si CLSM with Drishti processing. (a) Mandibles. (b) Maxillule, image merged using Adobe Photoshop. (c) Maxillule rotated to reveal reverse angle of image b, and the setation of the coxal and basial endites. Objective: 40× oil immersion. Scale bars = 200 µm.

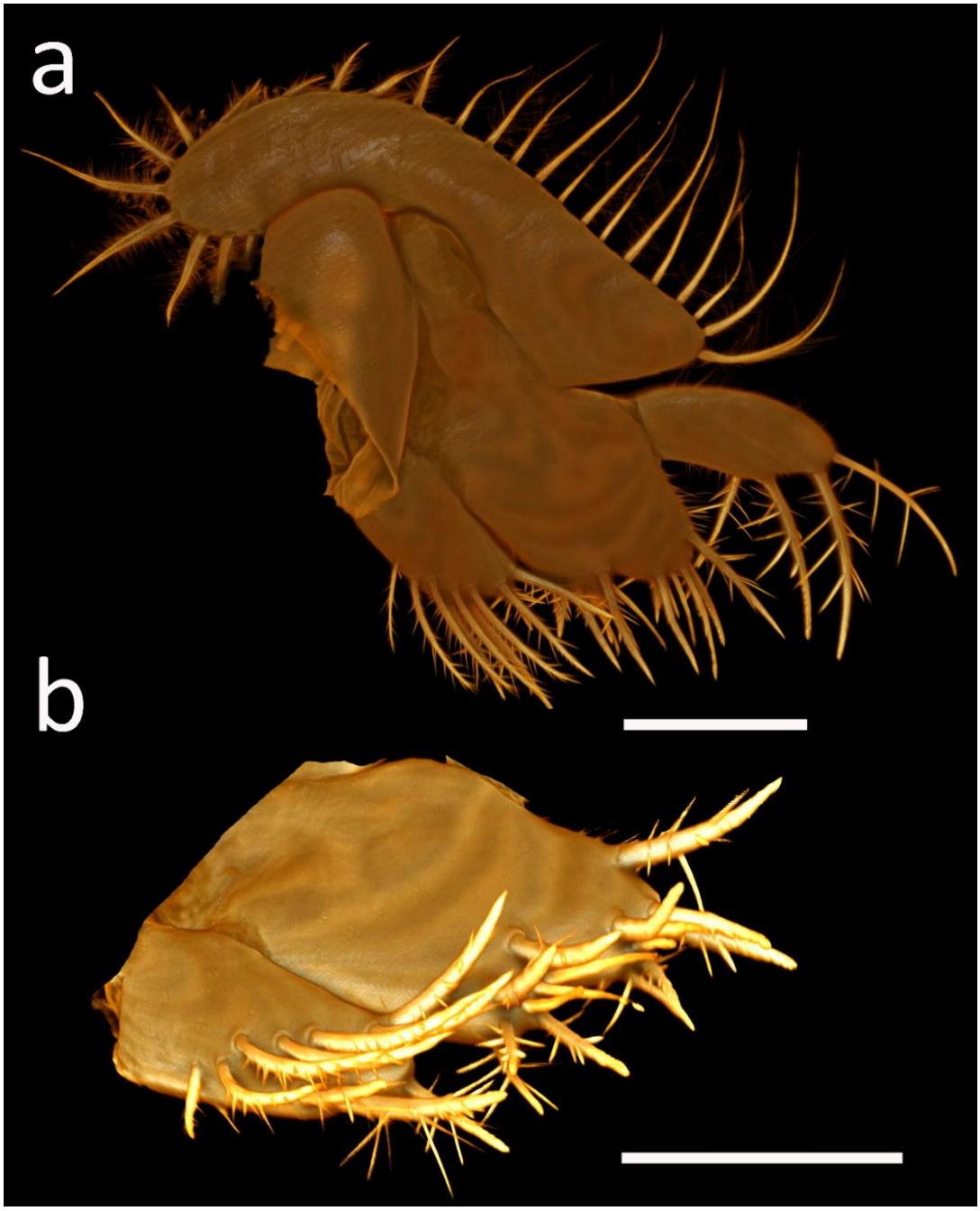

Figure 5.29: *Eriocheir sinensis,* ZIV, maxilla, Nikon A1-Si CLSM with Drishti processing. (a) Whole appendage, applying "large images" option, scan area of 2×3 fields for image stitching. (b) Maxilla rotated to show reverse angle of image a, and the setation of the coxal and basial endites. Objective: 40× oil immersion. Scale bars = 200 µm. See video 3 for 3D representation of the maxilla.

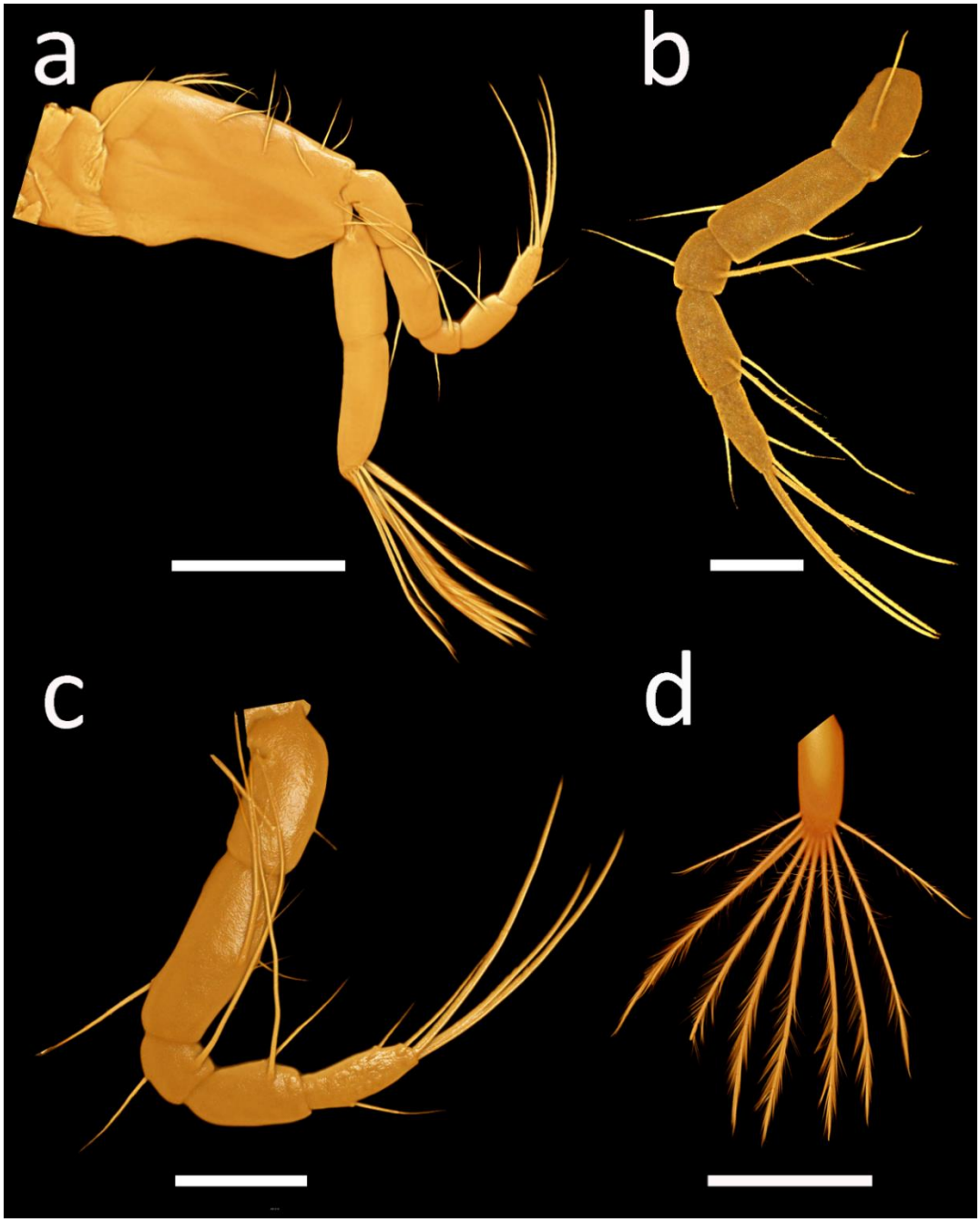

Figure 5.30: *Eriocheir sinensis*, ZIV, first maxilliped, Nikon A1-Si CLSM with Drishti processing. (a) Whole appendage, applying “large images” option, scan area of 2×2 fields for image stitching. (b) Endopod with 2,2,2,6 setae. (c) Endopod with 2,3,2,2,6 setae. (d) Exopod with 10 natatory setae. Objective: 20× dry. Scale bars a, d = 500 µm; b, c = 200 µm.

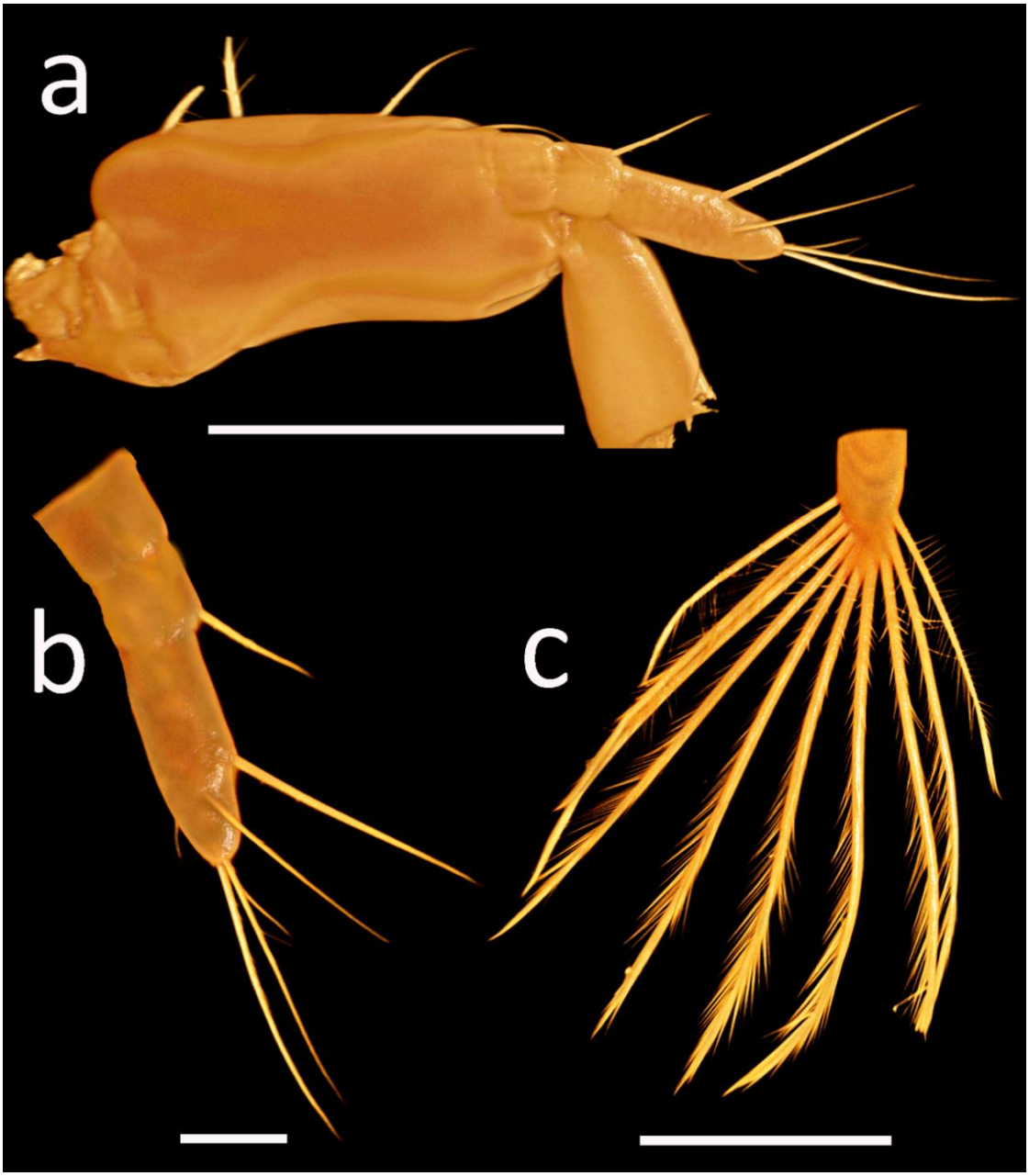

Figure 5.31: *Eriocheir sinensis*, ZIV, second maxilliped, Nikon A1-Si CLSM with Drishti processing. (a) Basis and endopod, applying “large images” option, scan area of 1×2 fields for image stitching. (b) Endopod. (c) Exopod with 10 natatory setae, applying “large images” option, scan area of 1×2 fields for image stitching. Objective: 20× dry. Scale bars a, c = 500 µm; b = 100 µm.

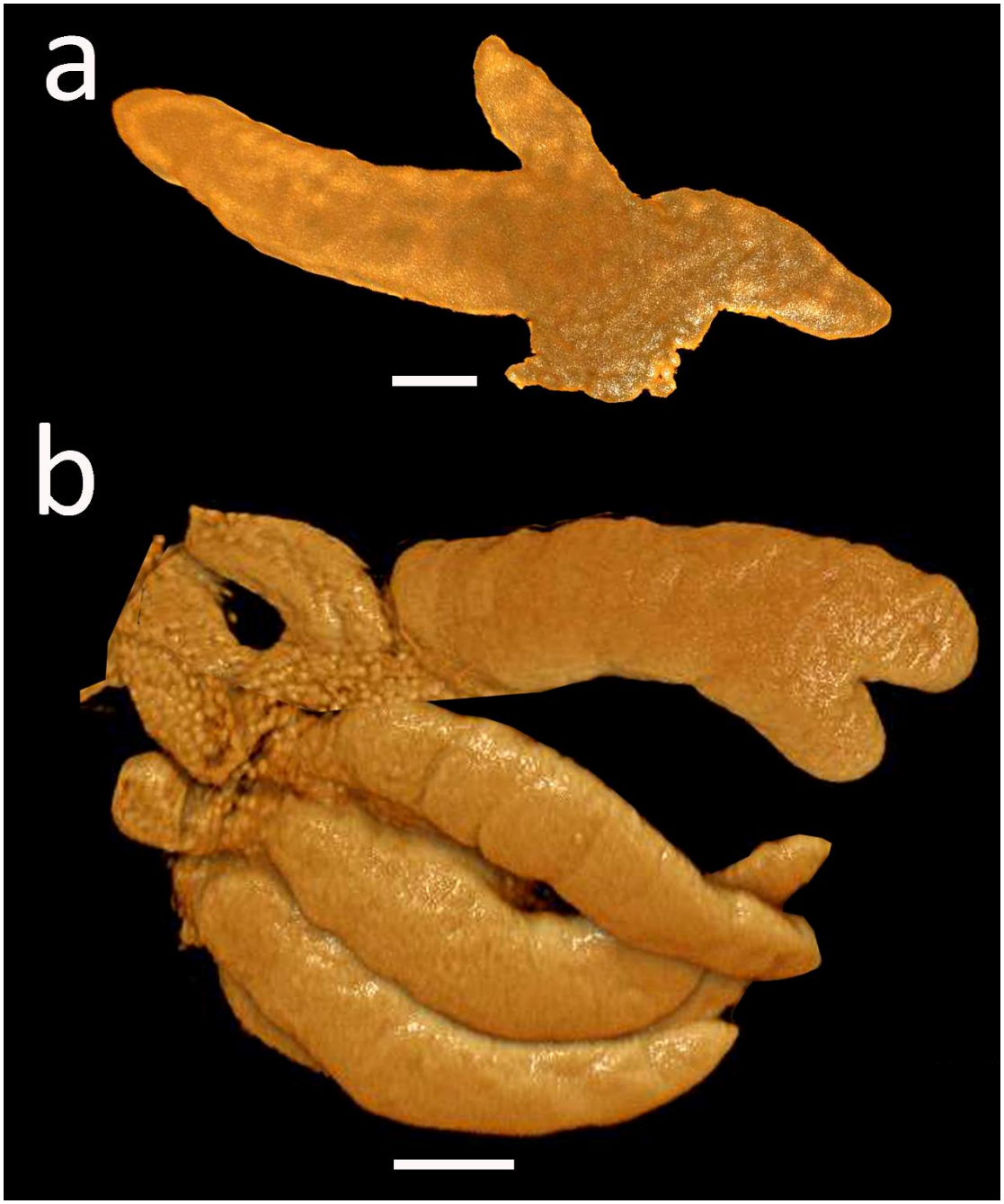

Figure 5.32: *Eriocheir sinensis*, ZIV, Nikon A1-Si CLSM with Drishti processing. (a) Third maxilliped. (b) Pereiopods. Objective: 40× oil immersion. Scale bars = 100 µm.

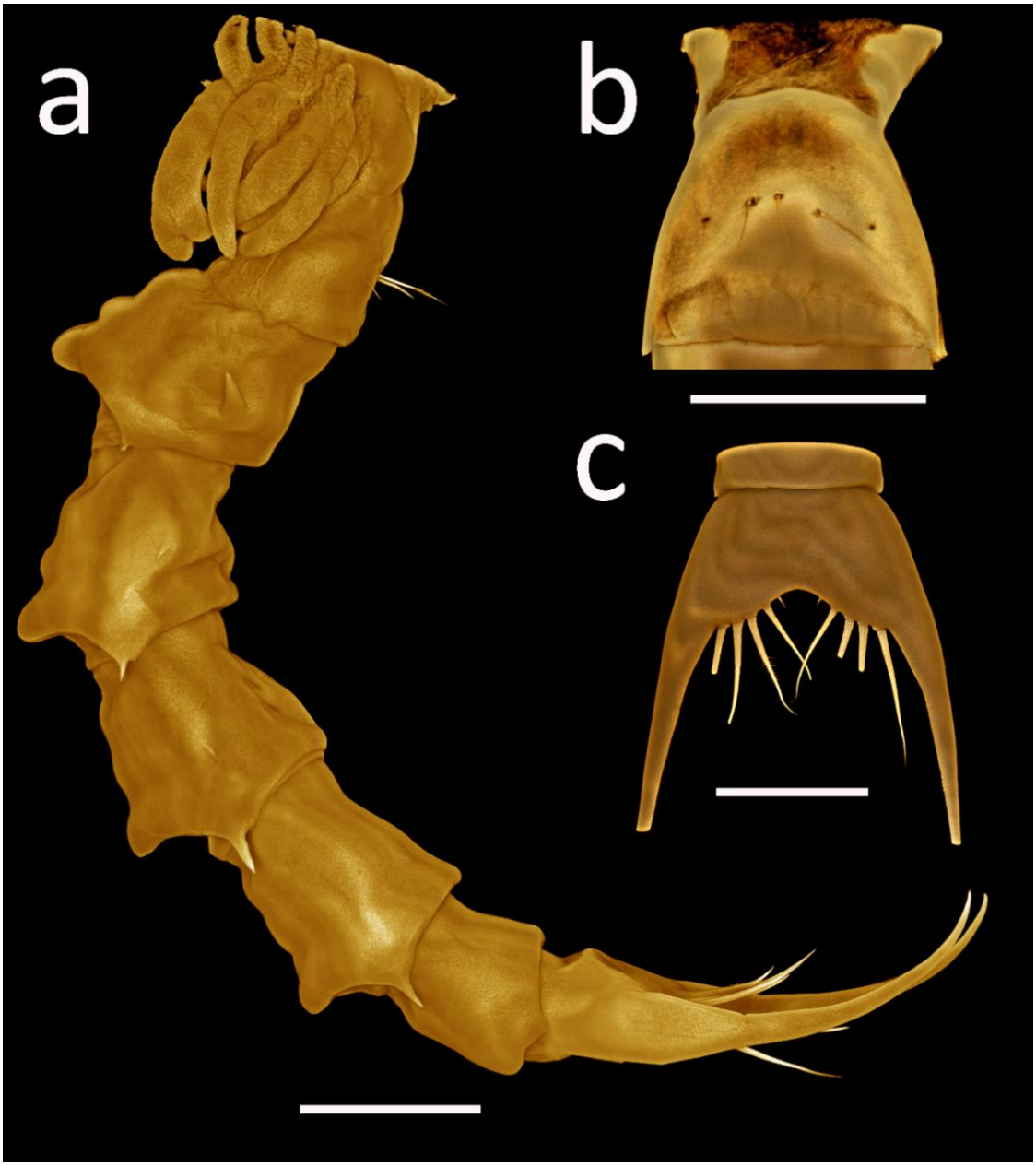

Figure 5.33: *Eriocheir sinensis*, ZIV, pleon and telson, Nikon A1-Si CLSM with Drishti processing. (a) Lateral view of pleon and telson, image merged using Adobe Photoshop. (b) Somite 1 with 5 medial setae. (c) Ventral margin of telson with 1 additional pair of unequal setae. Objective: 20× dry. Scale bars = 500 µm.

Zoea V (Figs 5.34−5.43)

Carapace (Figs 5.34−5.36): Now with 7 pairs of anterodorsal simple setae; 16−17 highly plumose posterior setae on ventral margin with additional spines on each side.

Antennule (Figs 5.37a-b): Basal region shaped as convex with two simple setae; primary flagellum with 2-tiers now with 4 subterminal long aesthetascs on 1-tier; 5 long aesthetascs on 2-tier; 5+1 terminal (5 long aesthetascs, 1 simple seta) setae; accessory flagellum present as small bud.

Antenna (Fig. 5.37c): Protopod distally bilaterally spinulate; endopod now clearly discrete (ca. 60% of whole appendage), exopod more developed now with only 1 simple seta.

Mandible (Fig. 5.38a): Palp present, with more distinct incisor teeth.

Maxillule (Fig. 5.38b-d): 2 epipod long simple setae; coxa now with 3-tiers, 9 armed processes (plumodenticulate, marginal) setae + 4 plumodenticulate setae + 3 simple setae respectively; basial endite now with 16 armed processes (cuspidate, marginal) and 4 simple setae on inner margin.

Maxilla (Fig. 5.39): Coxal endite now with 11+4 plumodenticulate setae; basial endite now with 10+11 unequal plumodenticulate setae; endopod unsegmented and bilobed with 2+2 highly plumose setae; exopod (scaphognathite) margin now with 32−33 highly plumose setae of various length.

First Maxilliped (Fig. 5.40): Coxa now with epipod lobe with either 3 simple setae or 3simple setae and 1 small simple seta; basis now with 10–12 setae arranged either 2+2+3+3 or 2+3+4+3; exopod, distal segment now with 12–13 long terminal plumose natatory setae.

Second Maxilliped (Fig. 5.41): Endopod now with either 0,1,6 (2 subterminal (1 dorsal, 1 ventral)), 4 terminal or 0,1,7 (3 subterminal (1 dorsal, 2 ventral)), 4 terminal sparsely plumose setae; exopod now with 12–13 terminal plumose natatory setae.

Third Maxilliped (Fig. 5.42a): Epipod with segmentation; two gills present (podobranch and arthrobranch).

Pereiopods (Fig. 5.42b): Cheliped more distinct; some segmentation; 3 developed gill buds (artrobranchs?).

Pleon (Figs 5.42c−5.43a-c): Somite one now with 8−9 medial simple setae of variable lengths; pleopods on somites 2−5 much more developed, and with endopod buds, pleopod (uropod) on somite 6 much smaller than on somites 2−5 and endopod bud absent.

Telson (Fig. 5.43d): Now with 5 pairs (4 long, 1 small) plumodenticulate setae.

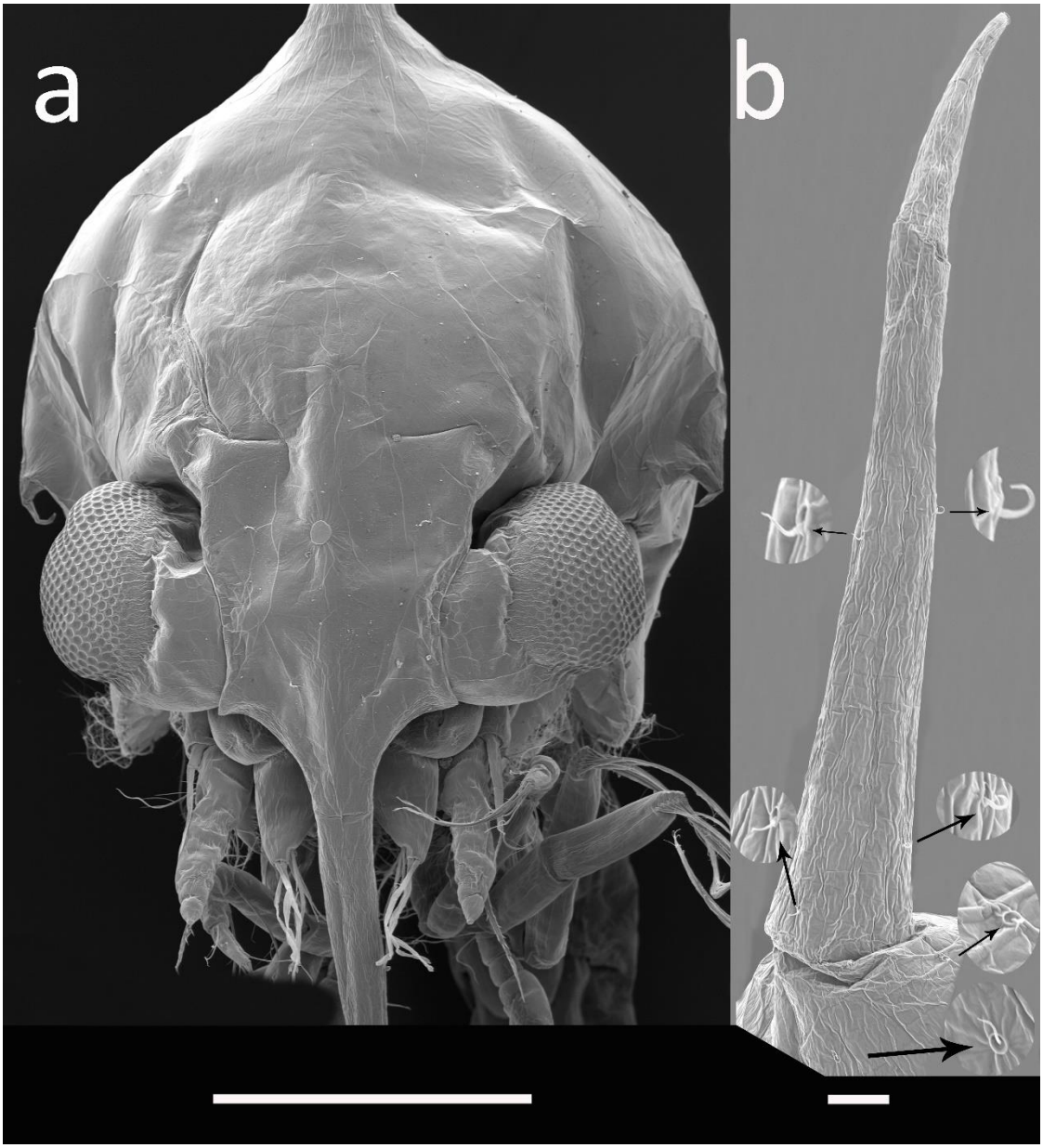

Figure 5.34: *Eriocheir sinensis*, ZV, dorsal carapace spine, FEI Quanta FEG SEM. (a) Anterior view. (b) 3 pairs of setae on dorsal spine (arrowed). Scale bars a = 500 µm; b = 50 µm.

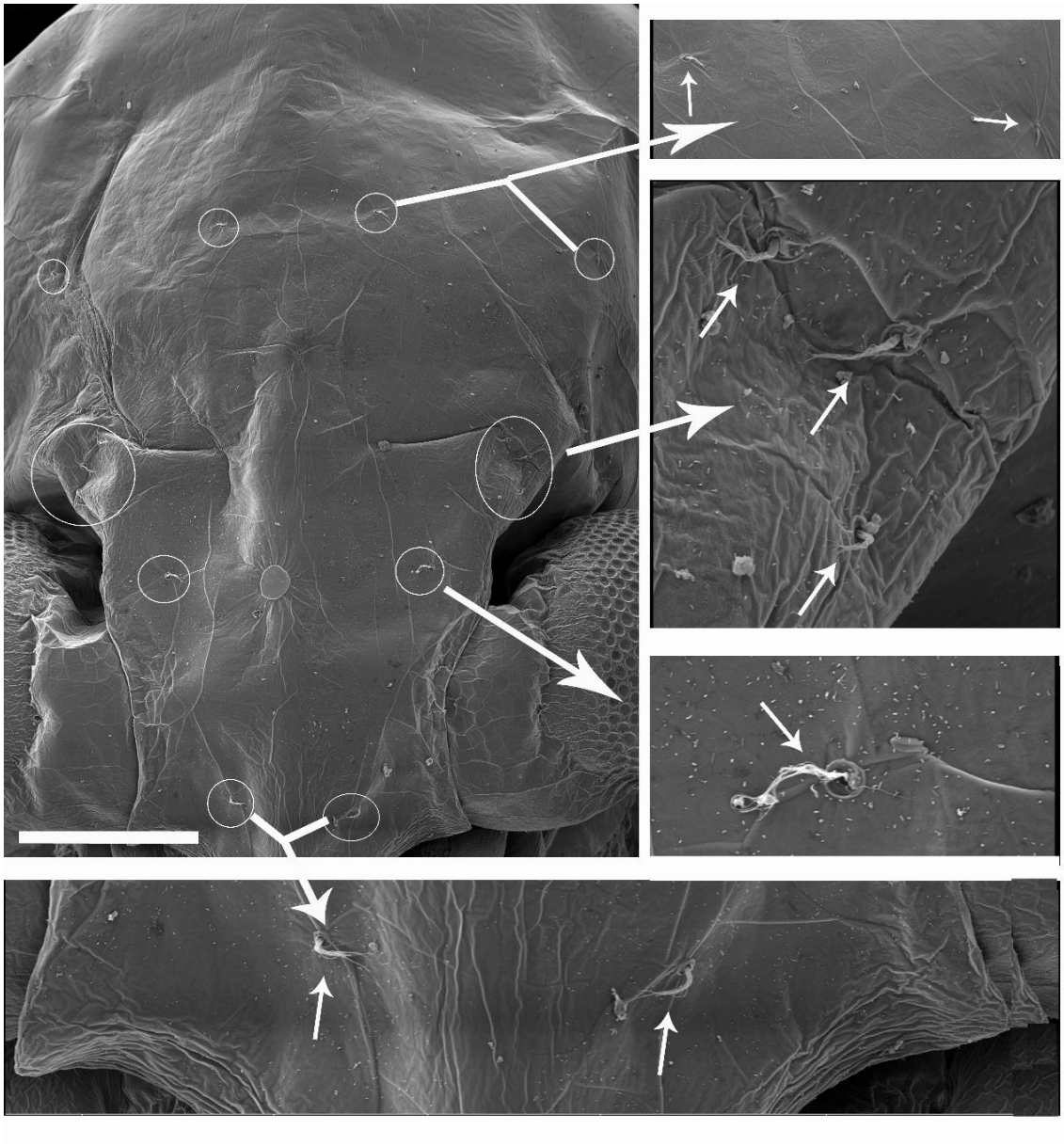

Figure 5.35: *Eriocheir sinensis*, ZV, anterodorsal carapace setae, FEI Quanta FEG SEM. 7 pairs of anterodorsal setae (arrowed). Scale bar = 200 µm.

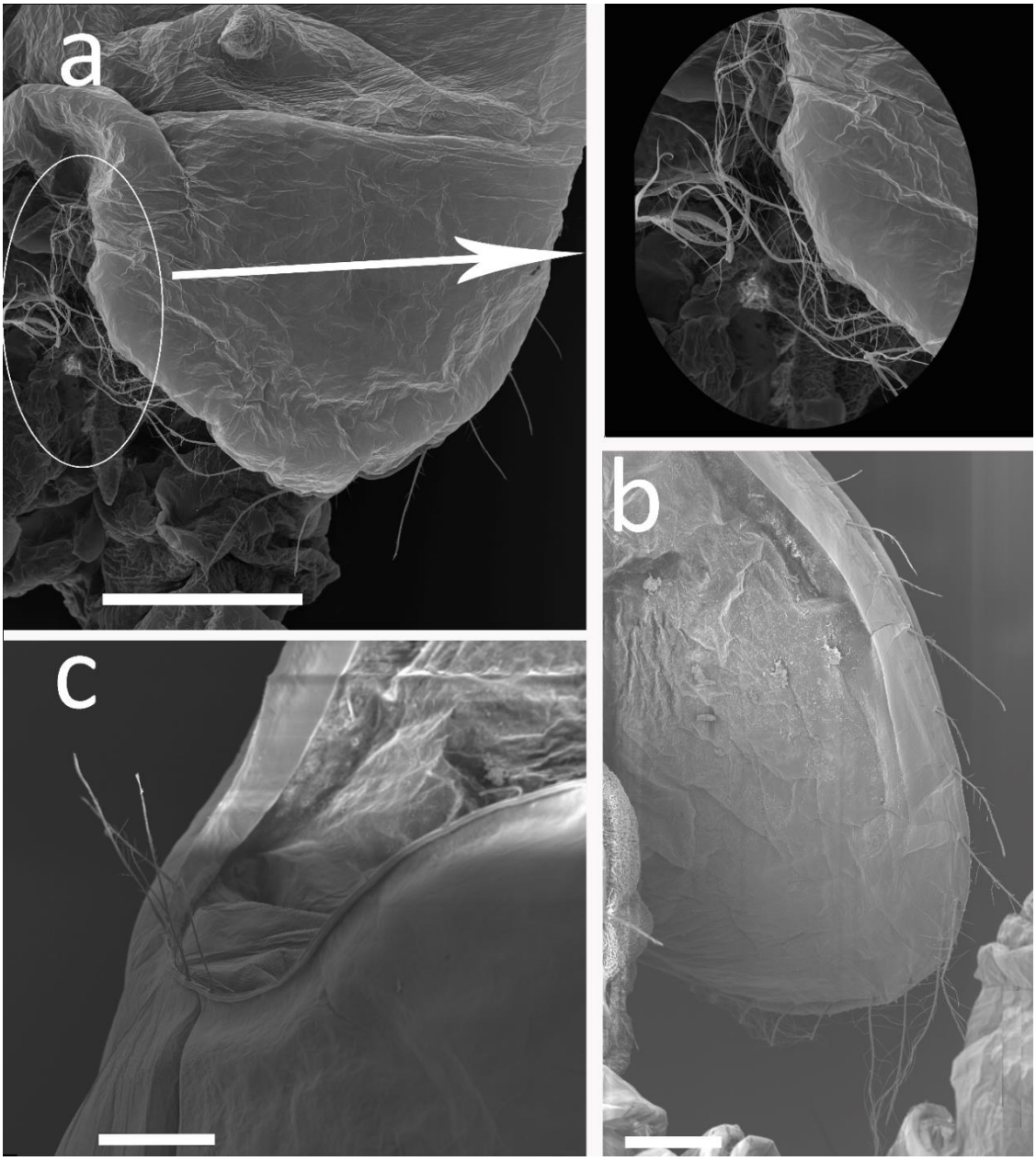

Figure 5.36: *Eriocheir sinensis*, ZV, carapace, FEI Quanta FEG SEM. (a) 6−7 anterior plumose setae (arrowed) and 10 posterior setae on ventral carapace margin. (b) Inner side of ventral carapace margin. (c) Dorsoposterior carapace margin. Scale bars a = 200 µm; b-c = 100 µm.

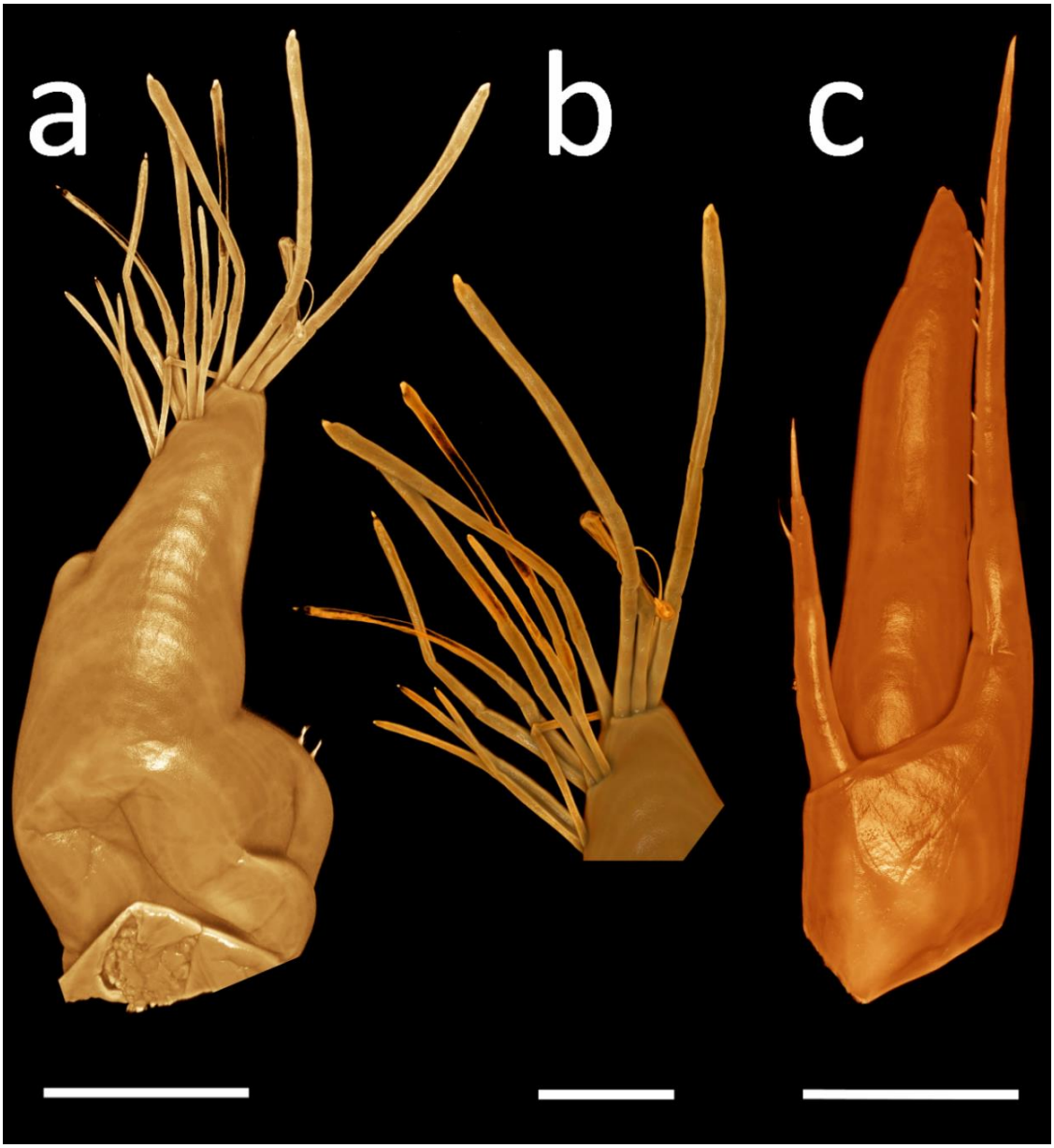

Figure 5.37: *Eriocheir sinensis*, ZV, Nikon A1-Si CLSM with Drishti processing. (a) Antennule with developing accessory flagellum. (b) Antennule, primary flagellum showing two rows of subterminal aesthetascs. (c) Antenna with developing endopod. All applying "large images" option, scan area of 2×3 fields for image stitching. Objective: 40× oil immersion. Scale bars a, c = 200 µm; b = 100 µm. See video 4 for 3D representation of the antennule primary flagellum.

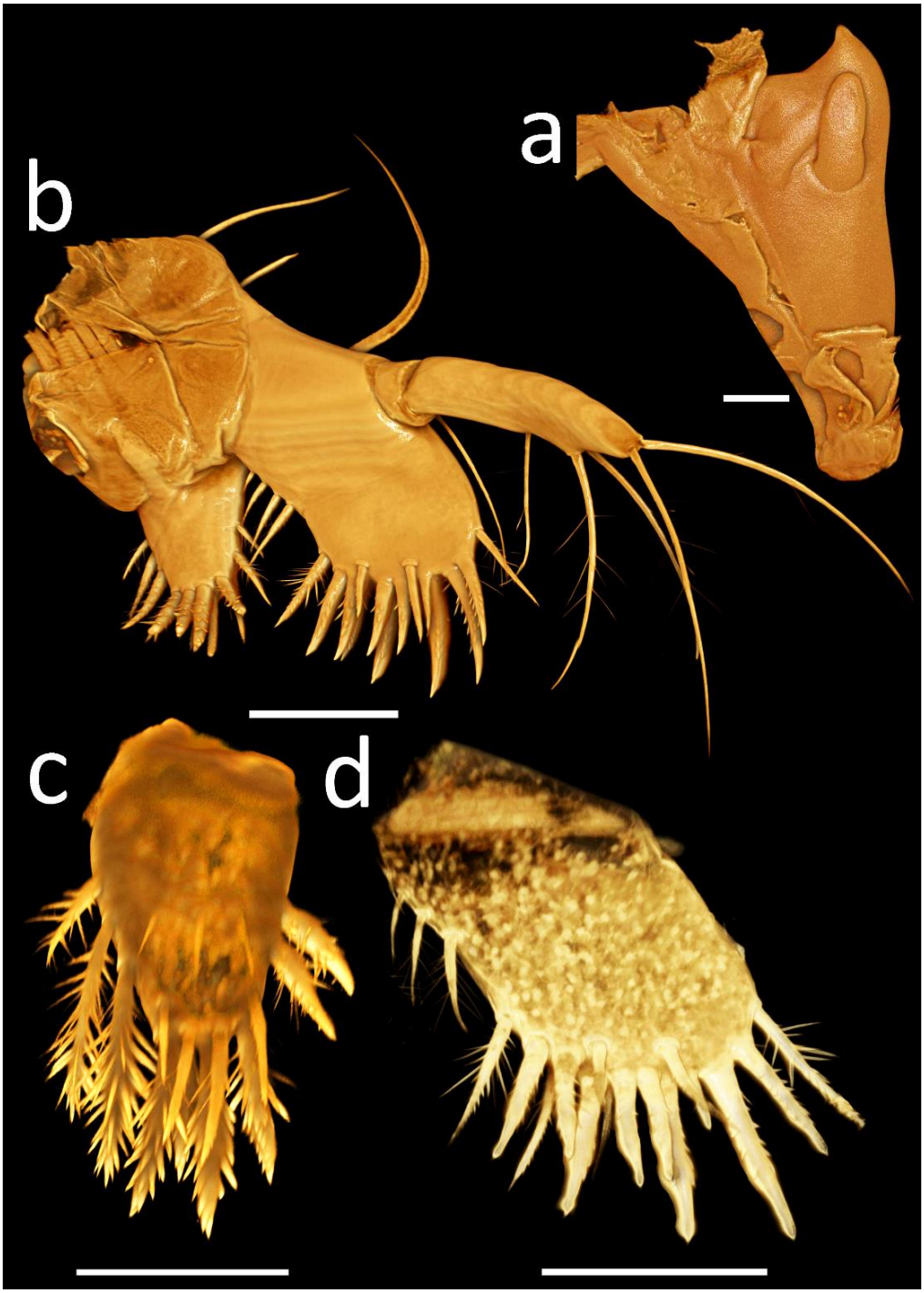

Figure 5.38: *Eriocheir sinensis*, ZV, Nikon A1-Si CLSM with Drishti processing. (a) Mandible. (b) Maxillule, applying "large images" option, scan area of 2×3 fields for image stitching. (c) Coxal endite of (b). (d) Basial endite of (b). Objective: 40× oil immersion. Scale bars = 200 µm.

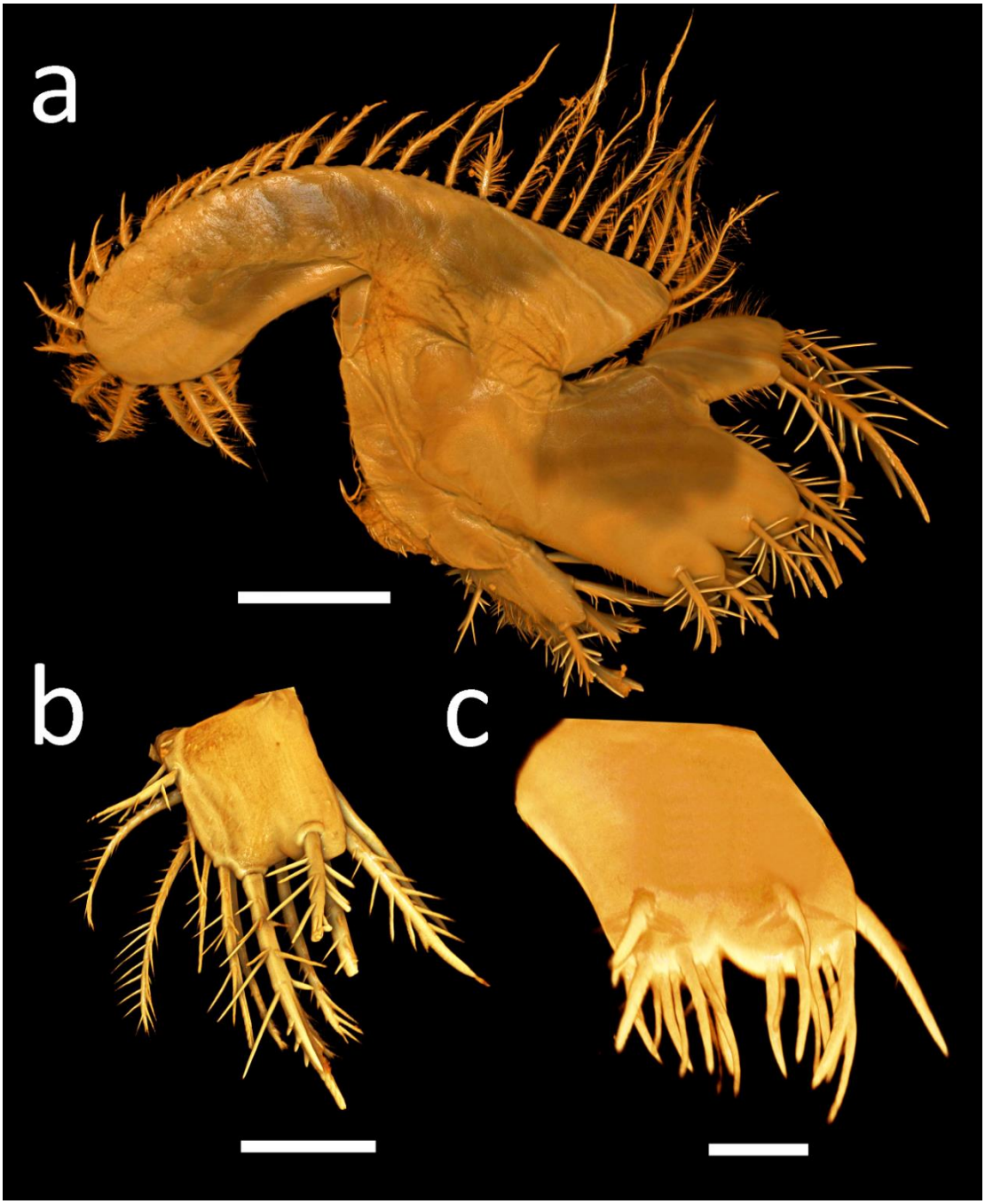

Figure 5.39: *Eriocheir sinensis*, ZV, maxilla, Nikon A1-Si CLSM with Drishti processing. (a) Whole appendage, applying "large images" option, scan area of 3×3 fields for image stitching. (b) Coxal endite. (c) Basial endite. Objective: 40× oil immersion. Scale bars a = 200 µm; b-c = 100 µm.

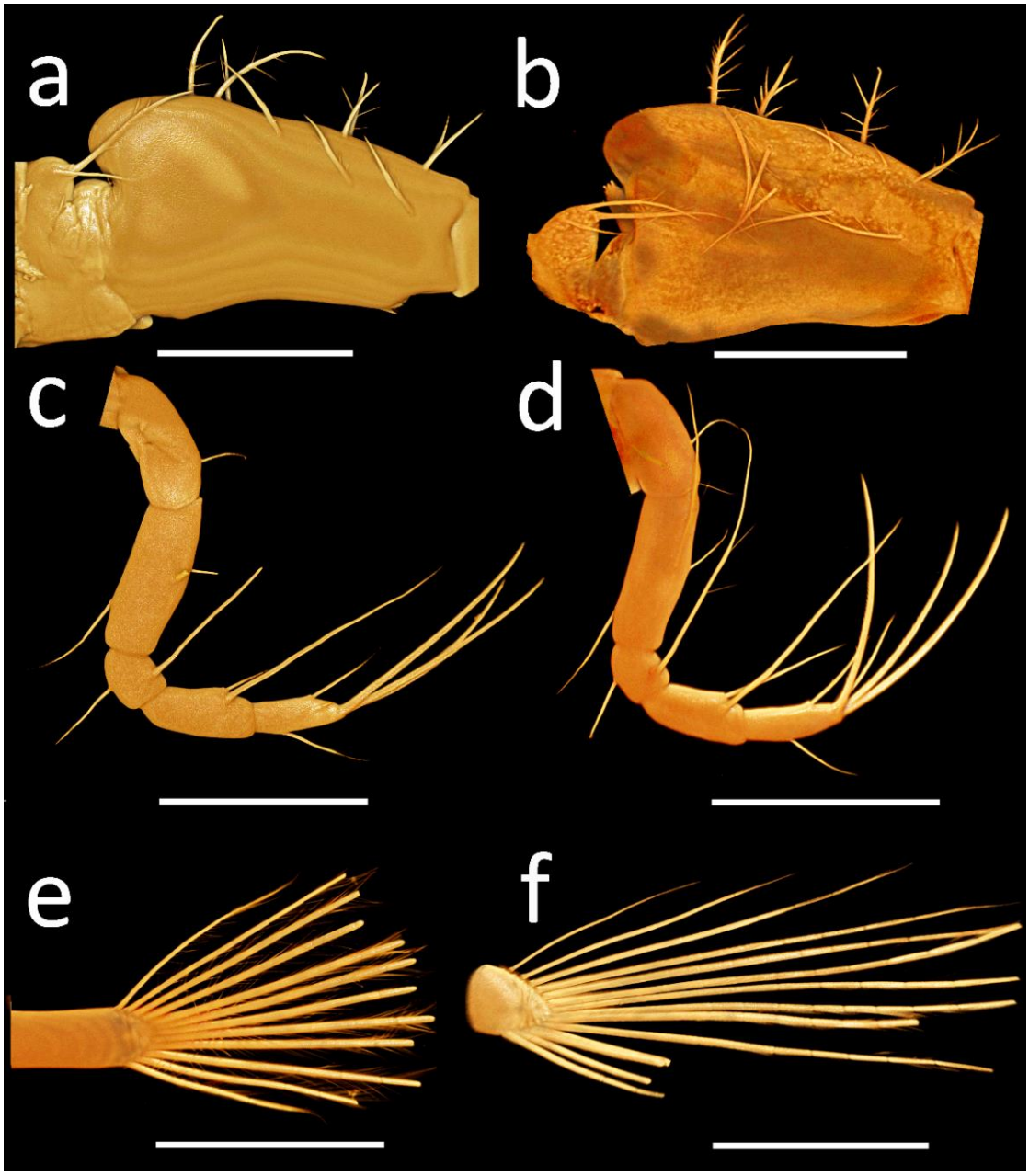

Figure 5.40: *Eriocheir sinensis*, ZV, first maxilliped, Nikon A1-Si CLSM with Drishti processing. (a) Coxa with 3 setae and basis with 10 setae. (b) Coxa with 3 setae and 1 smaller seta, basis with 12 setae. (c) Endopod with 1,3,2,2,6 setae. (d) Endopod with 2,3,2,2,6 setae. (e) Exopod with 12 natatory setae. (f) Exopod with 13 natatory setae. All applying "large images" option, scan area of 1×2 fields for image stitching. Objective: 20× dry. Scale bars = 500 µm.

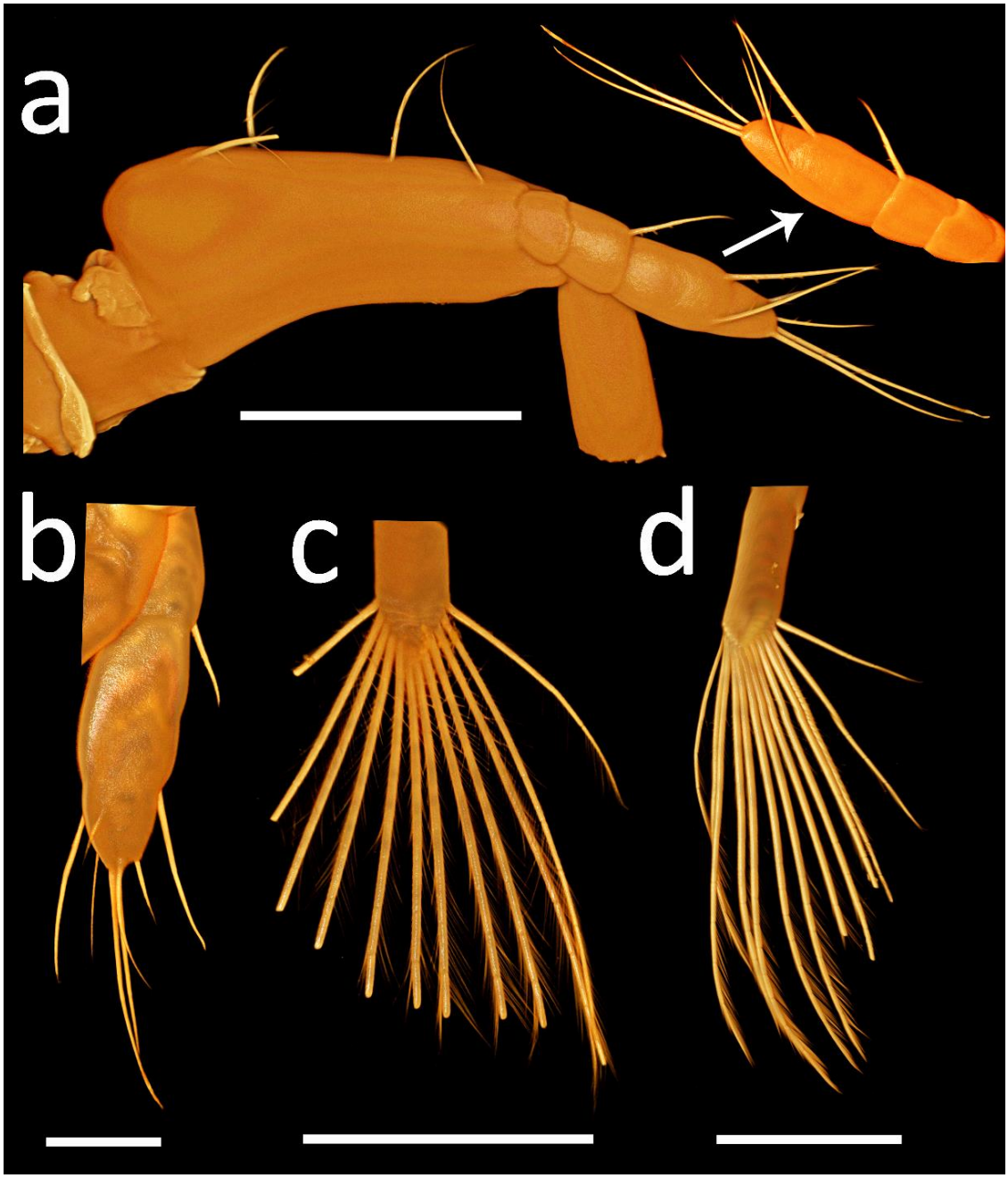

Figure 5.41: *Eriocheir sinensis*, ZV, second maxilliped, Nikon A1-Si CLSM with Drishti processing. (a) Basis and endopod, applying "large images" option, scan area of 1×2 fields for image stitching (reverse angle of endopod arrowed). (b) Endopod with 0+1+7 setae. (c) Exopod with 12 natatory setae. (d) Exopod with 13 natatory setae. Objective: 20× dry. Scale bars a, c, d = 500 µm; b = 200 µm.

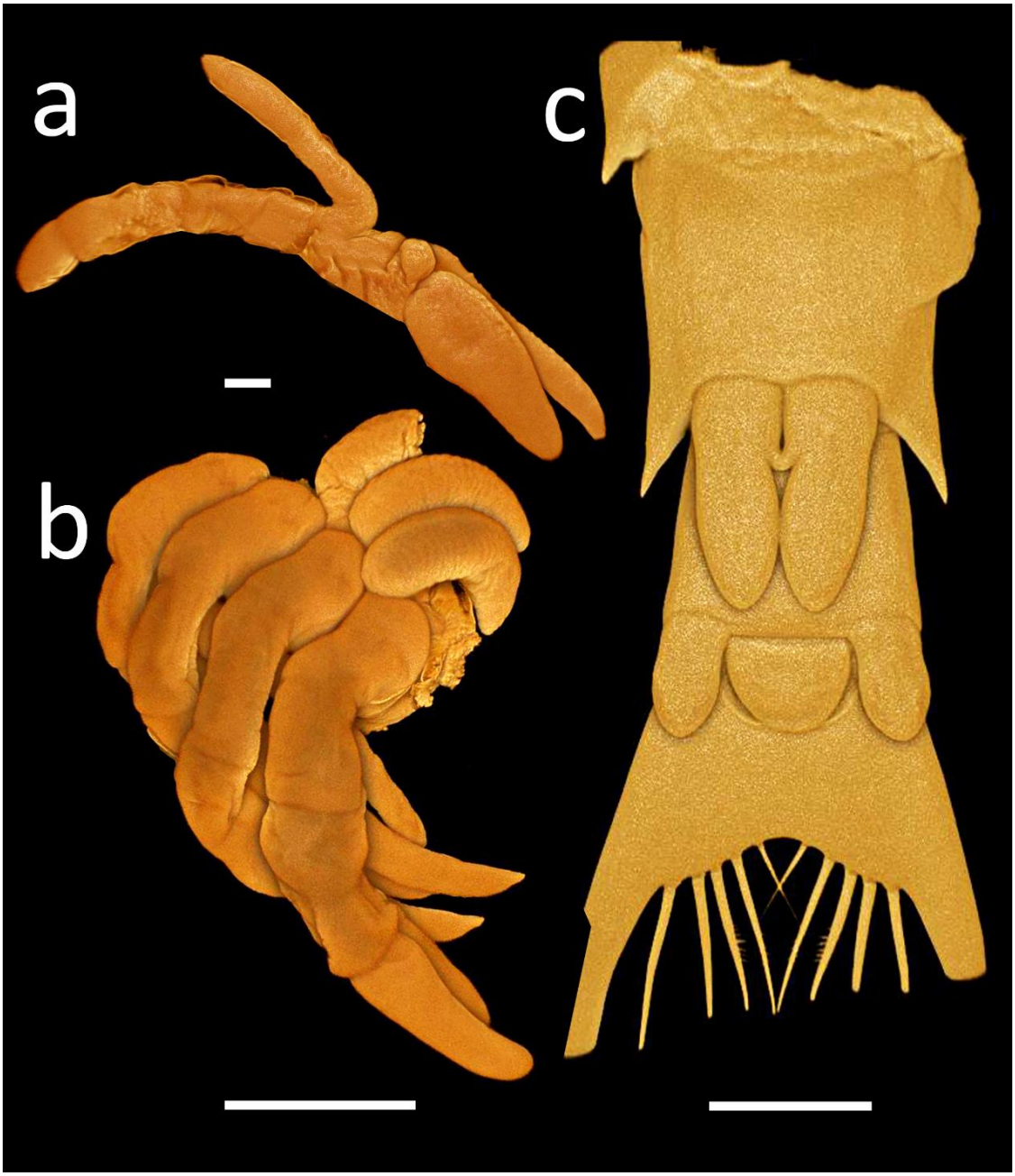

Figure 5.42: *Eriocheir sinensis*, ZV, Nikon A1-Si CLSM with Drishti processing. (a) Third maxilliped, applying "large images" option, scan area of 1×2 fields for image stitching. (b) Pereiopods. (c) Fifth pleopod with endopod and uropod without endopod. Applying "large images" option, scan area of 2×2 fields for image stitching. Objective: 20× dry. Scale bars a = 100 µm; b, c = 500 µm.

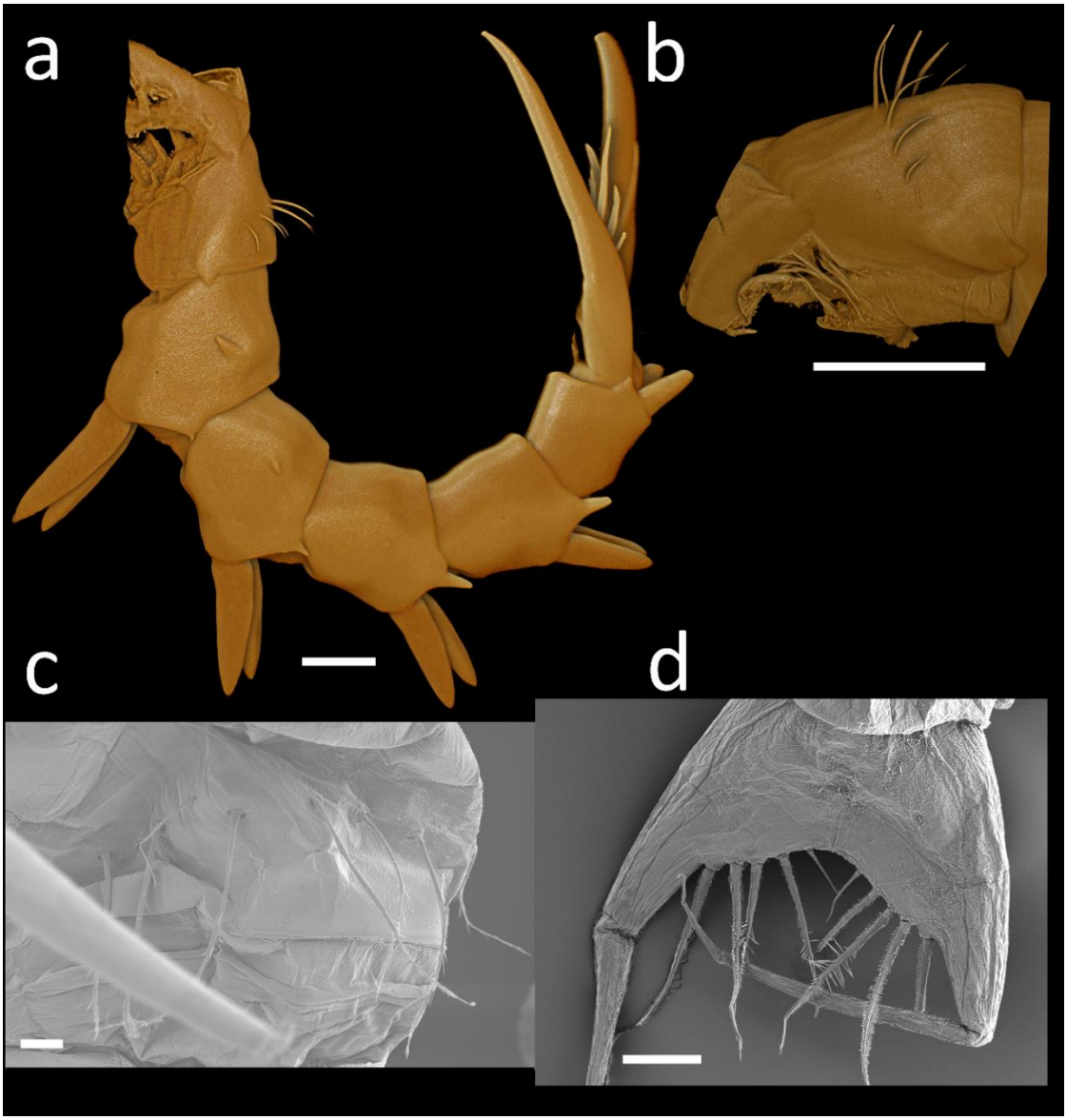

Figure 5.43: *Eriocheir sinensis*, ZV, pleon and telson, Nikon A1-Si CLSM with Drishti processing. (a) Lateral view of pleon and telson, applying "large images" option, scan area of 3×3 fields for image stitching. (b) Somite 1 with 9 medial setae. Zeiss Ultra Plus Field Emission SEM. (c) Somite 1 with 8 medial setae. (d) Ventral margin of telson with 5 pairs of setae. Objective: a = 10× dry; b = 20× dry. Scale bars a = 500 µm; b = 200 µm; c = 20 µm; d = 100 µm.

Zoea VI (Figs 5.44−5.54)

Carapace (Figs 5.44−5.46): Dorsal spine now with 4 pairs of simple setae; now with 9 pairs of anterodorsal highly plumose setae; now 4−5 pairs of sparsely plumose setae on dorsoposterior margin.

Antennule (Fig. 5.47): 5 subterminal long aesthetascs on 1-tie; 5 long aesthetascs on 2-tier and primary flagellum with 6 terminal simple setae; accessory flagellum now more developed but without setae.

Antenna (Fig. 5.48): Endopod now 2-segmented with sign of segmentation and clearly discrete (ca. 75% of whole appendage) with protuberances distally, endopod almost equal with protopod; exopod slightly longer than previous stage, ca. 60% of protopod with 1 distinct seta.

Mandible (Fig. 5.49a): Palp more developed.

Maxillule (Fig. 5.49b-c): 3 epipod long simple setae; coxa now with 3-tiers, 10 armed processes (cuspidate, marginal) setae + 4 plumodenticulate setae + 3 simple setae respectively.

Maxilla (Fig. 5.50): Coxal endite now with 12+6 plumodenticulate setae; basial endite now with 10+11 unequal plumodenticulate setae; endopod unsegmented and bilobed with 2+2 highly plumose setae; exopod (scaphognathite) margin now with 44 highly plumose setae of various length + 1 lateral simple seta.

First Maxilliped (Fig. 5.51): Coxa now with 3 long simple setae 1 short simple setae on developing epipodal bud, 1 epipod with podobranch gill; basis with 12 setae arranged as 2+2+4+1+3 setae; exopod, distal segment now with 14 long terminal plumose natatory setae.

Second Maxilliped (Fig. 5.52): Coxa developing epipodal bud present; exopod now with 13 terminal plumose natatory setae.

Third Maxilliped (Fig. 5.53a): Endopod and exopod more developed.

Pereiopods (Fig. 5.53b): More developed than previous stage and now with four gill buds.

Pleon (Figs 5.53c−5.54): Somite 1 now with 10−11 medial simple setae of various length; pleopods now more developed.

Telson (Fig. 5.54): Unchanged.

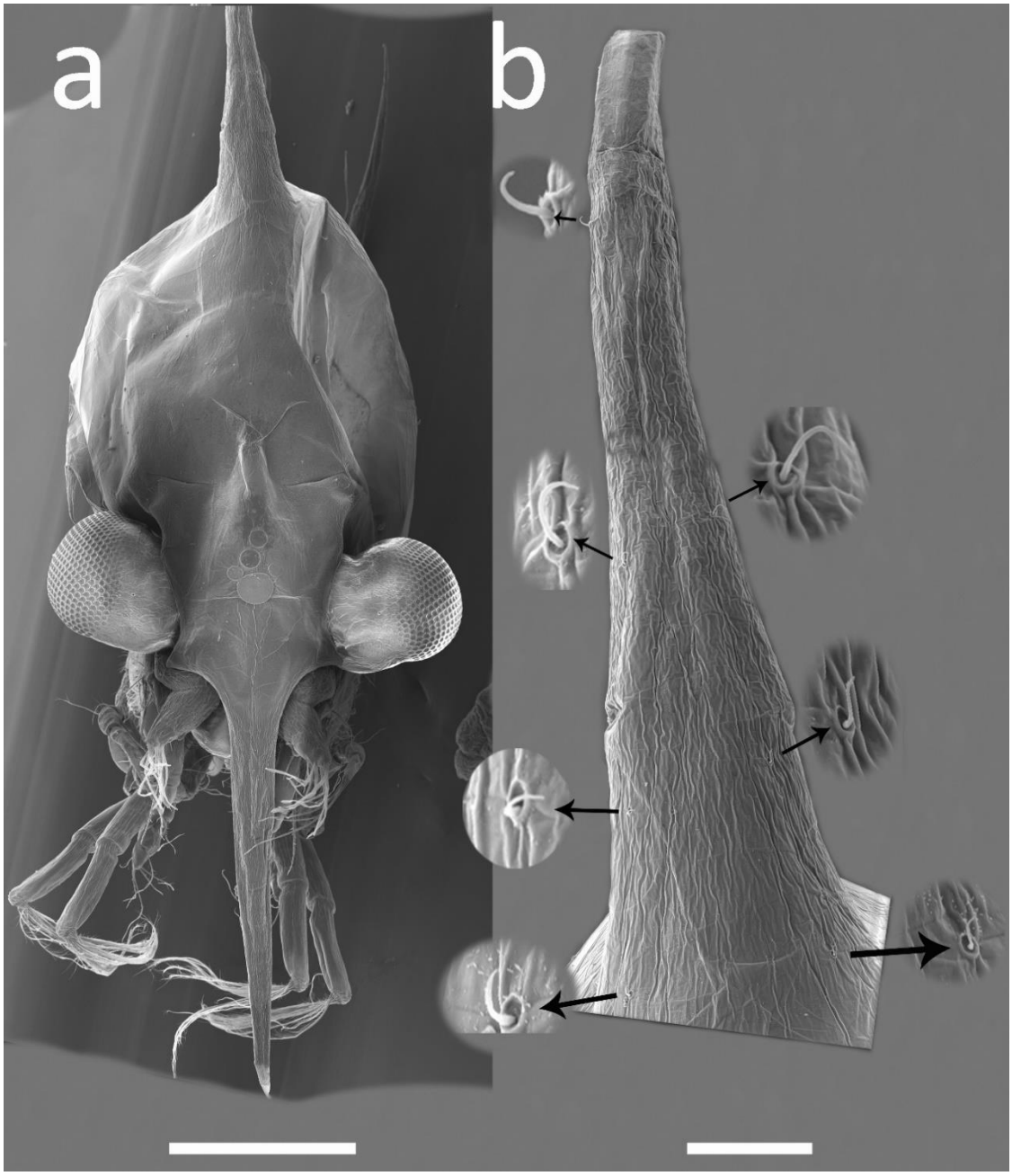

Figure 5.44: *Eriocheir sinensis*, ZVI, dorsal carapace spine, FEI Quanta FEG SEM. (a) Anterior view. (b) 4 pairs of setae on dorsal spine (arrowed). Scale bars a = 500 µm; b = 50 µm.

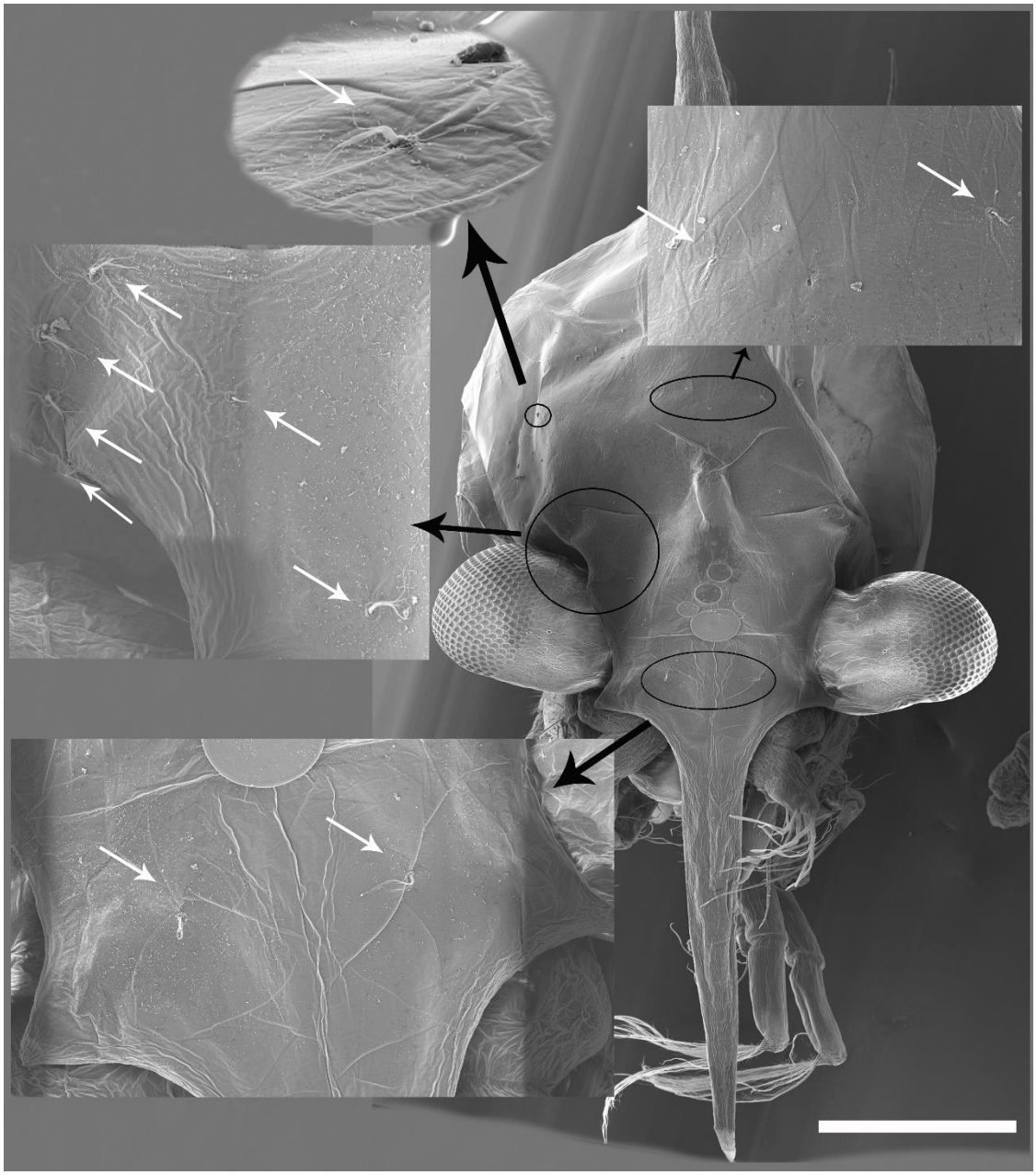

Figure 5.45: *Eriocheir sinensis*, ZV, anterior view of carapace, FEI Quanta FEG SEM. 9 pairs of anterodorsal setae circled and arrowed. Scale bar = 500 µm.

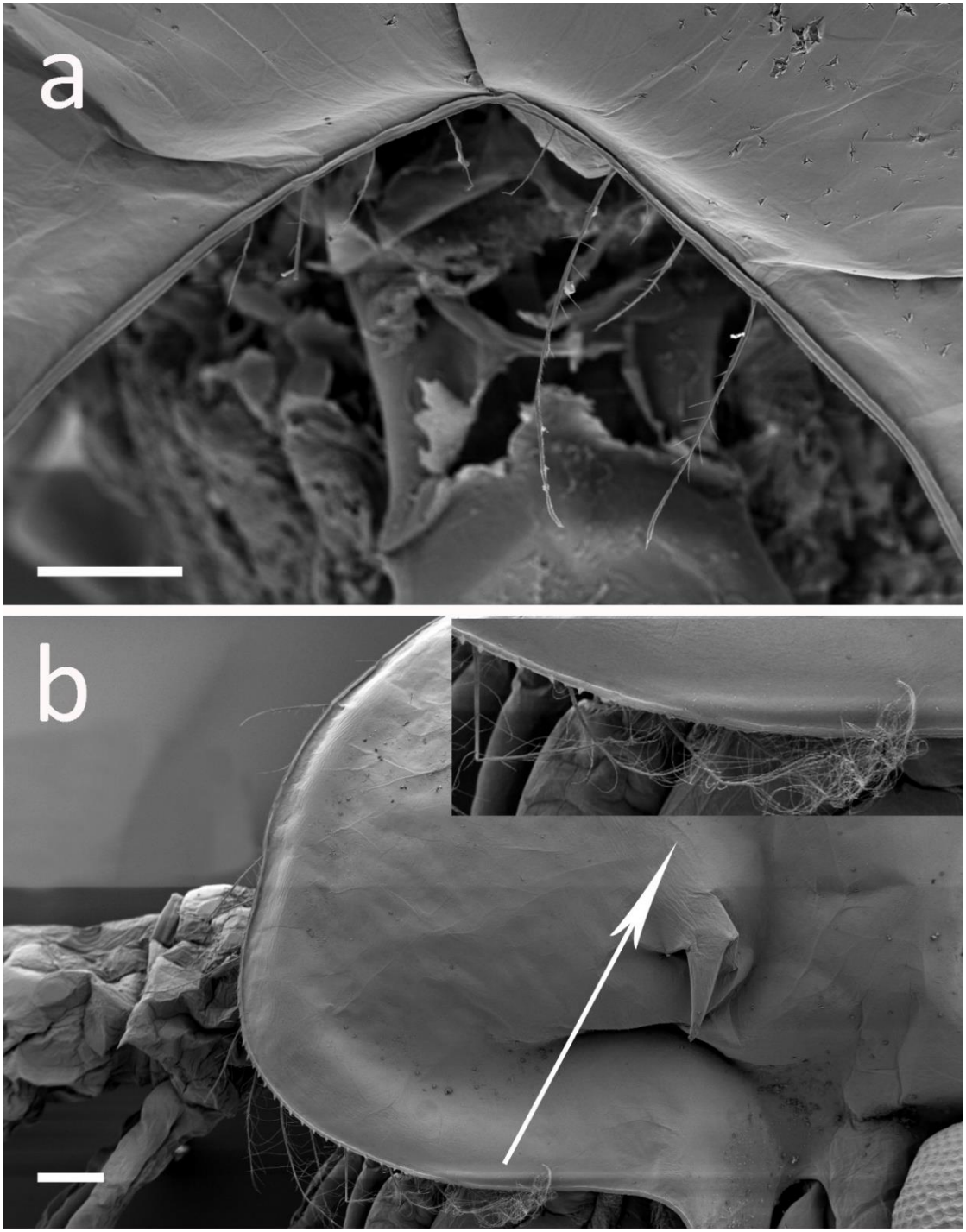

Figure 5.46: *Eriocheir sinensis*, ZVI, carapace, FEI Quanta FEG SEM. (a) 4−5 pairs of setae on dorsoposterior carapace margin. (b) 6−7 anterior plumose setae (arrowed) and 10 posterior setae on ventral carapace margin. Scale bars = 20 µm.

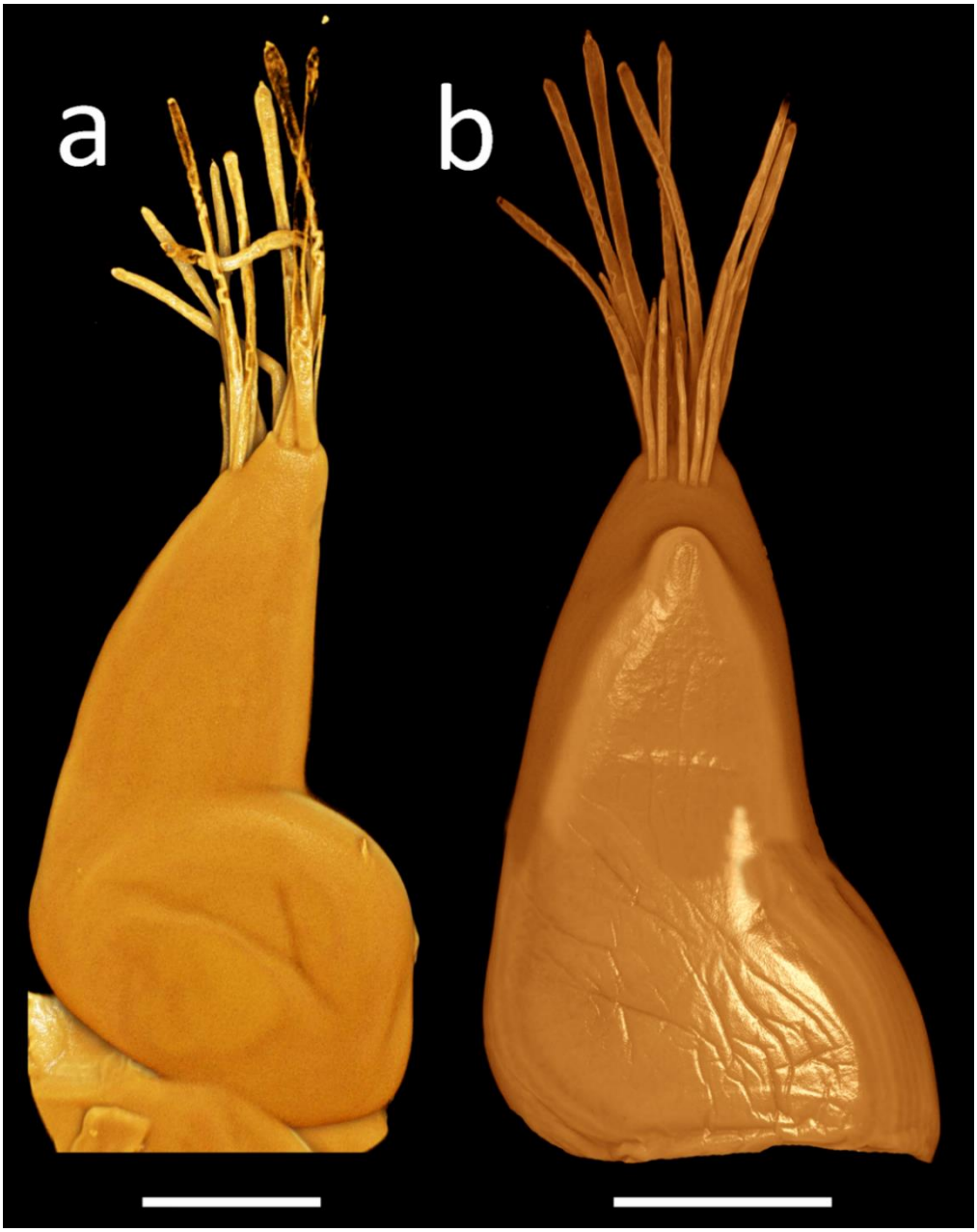

Figure 5.47: *Eriocheir sinensis*, ZVI, antennule, Nikon A1-Si CLSM with Drishti processing. (a) Whole appendage showing small proximal seta, applying "large images" option, scan area of 1×2 fields for image stitching. (b) Antennule rotated to show reverse angle of image a, and the developing accessory bud, image merged using Adobe Photoshop. Objective: a = 20× dry; b = 40× oil immersion. Scale bars = 200 µm. See video 5 for 3D representation of the antennule primary flagellum.

Figure 5.48: *Eriocheir sinensis*, ZVI, antenna, Nikon A1-Si CLSM with Drishti processing. (a) Whole appendage with 2 segmented endopod distal protuberances almost equal to length of protopod, applying "large images" option, scan area of 1×2 fields for image stitching. (b) Whole appendage with endopod slightly shorter than length of protopod, image merged using Adobe Photoshop. Objective: a = 20× dry; b = 40× oil immersion. Scale bars = 200 µm.

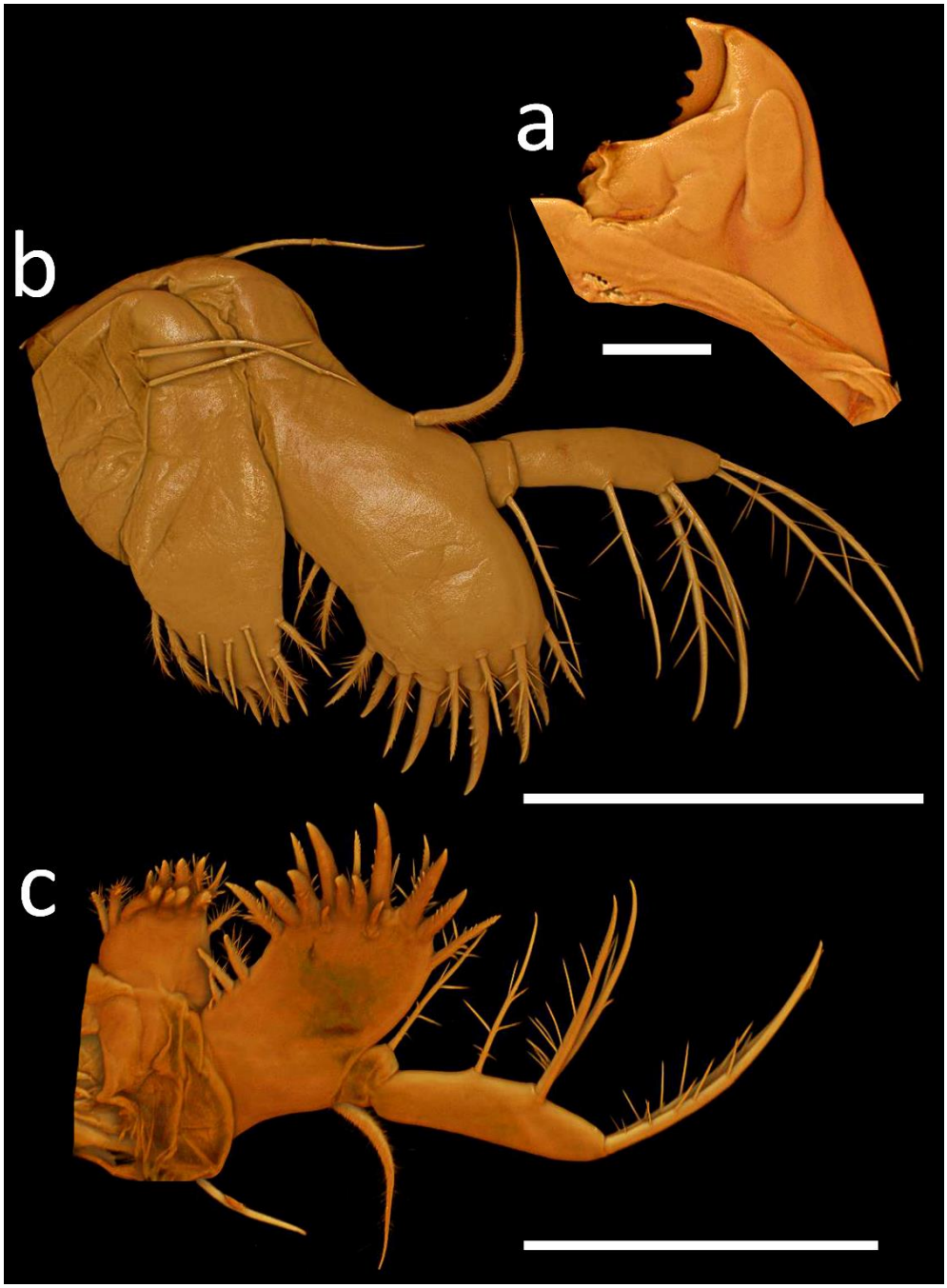

Figure 5.49: *Eriocheir sinensis*, ZVI, Nikon A1-Si CLSM with Drishti processing. a) Mandible. (b) Maxillule, applying "large images" option, scan area of 2×3 fields for image stitching. (c) Maxillule rotated to show from reverse angle of image b, and the setation of the coxal and basial endites. Objective: 40× oil immersion. Scale bars a = 200 µm; b, c = 500 µm. See video 6 for 3D representation of the maxillule.

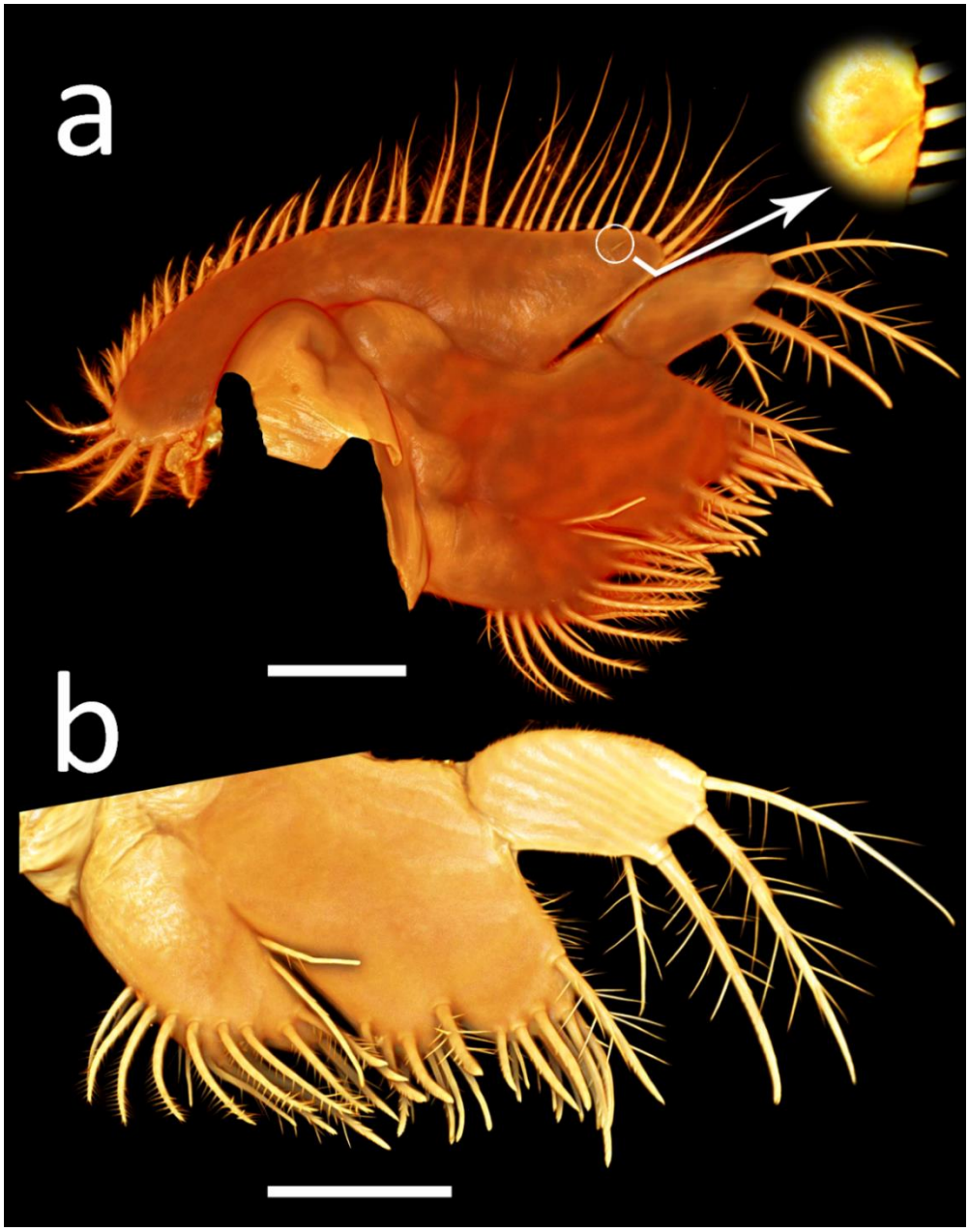

Figure 5.50: *Eriocheir sinensis*, ZVI, maxilla, Nikon A1-Si CLSM with Drishti processing. (a) Whole appendage, applying "large images" option, scan area of 3×3 fields for image stitching, 1 seta on exopod circled and arrowed. (b) Maxilla rotated to show from reverse angle of image a, and the setation of the coxal and basial endites. Objective: 40× oil immersion. Scale bars = 200 µm. See video 7 for 3D representation of the maxilla.

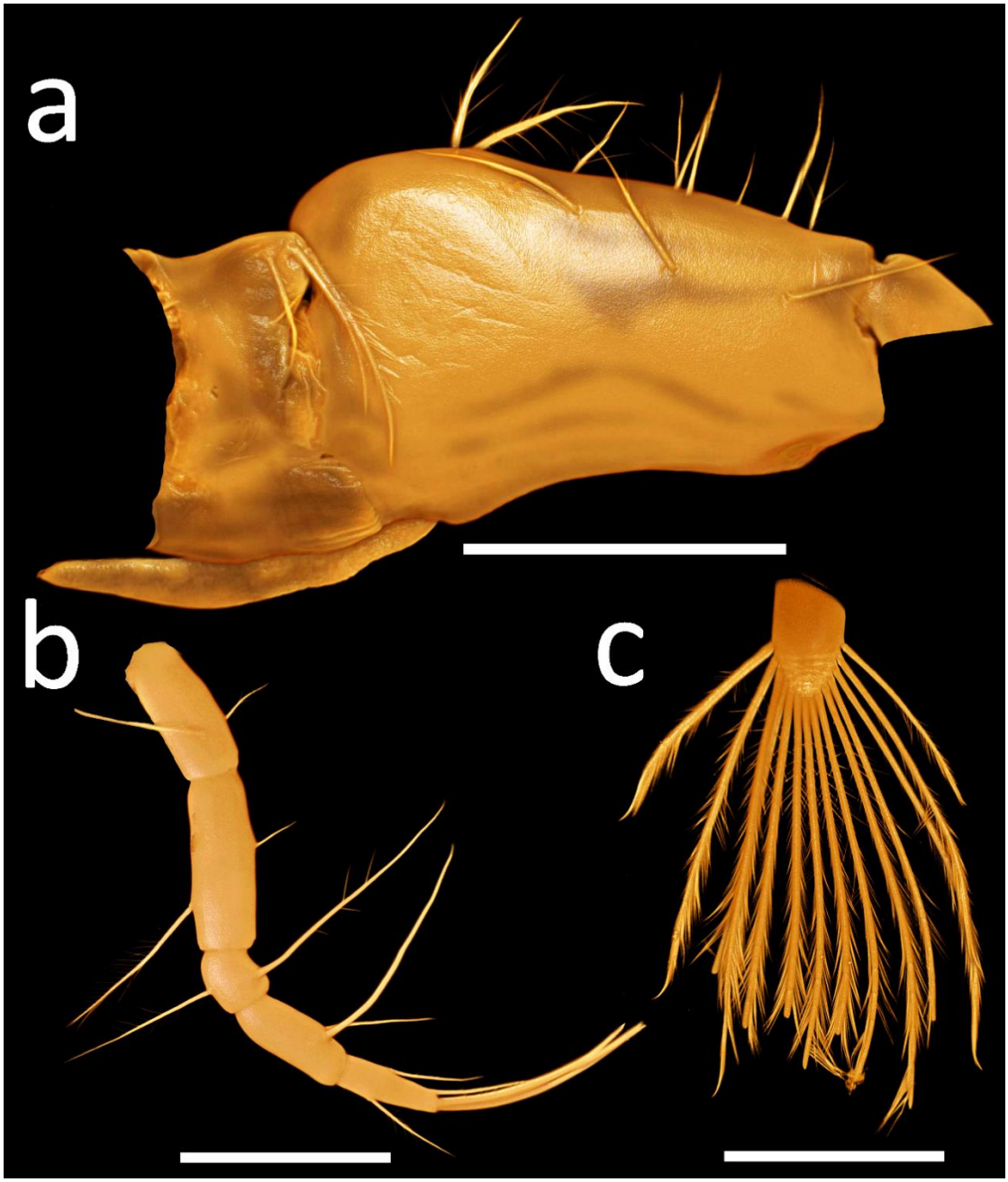

Figure 5.51: *Eriocheir sinensis*, ZVI, first maxilliped, Nikon A1-Si CLSM with Drishti processing. (a) Coxa with 4 +1 setae and basis with 12 setae (b) Endopod. (c) Exopod with 14 natatory setae. All applying "large images" option, scan area of 1×2 fields for image stitching. Objective: 20× dry. Scale bars = 500 µm.

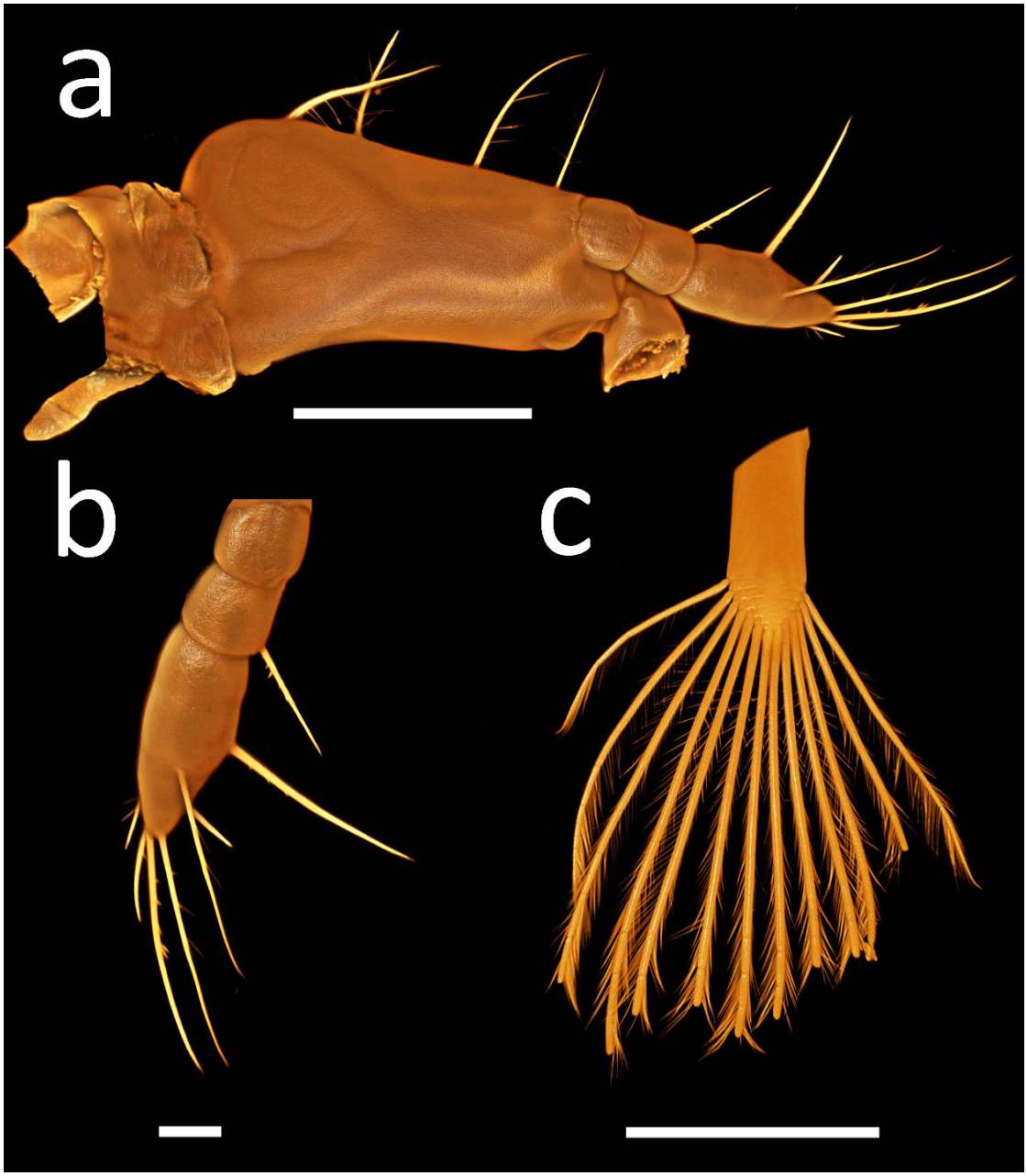

Figure 5.52: *Eriocheir sinensis*, ZVI, second maxilliped, Nikon A1-Si CLSM with Drishti processing. (a) Coxa, basis and endopod, applying "large images" option, scan area of 1×2 fields for image stitching. (b) Endopod with 0+1+7 setae. (c) Exopod with 13 natatory setae. Objective: 20× dry. Scale bars a, c = 500 µm; b = 100 µm.

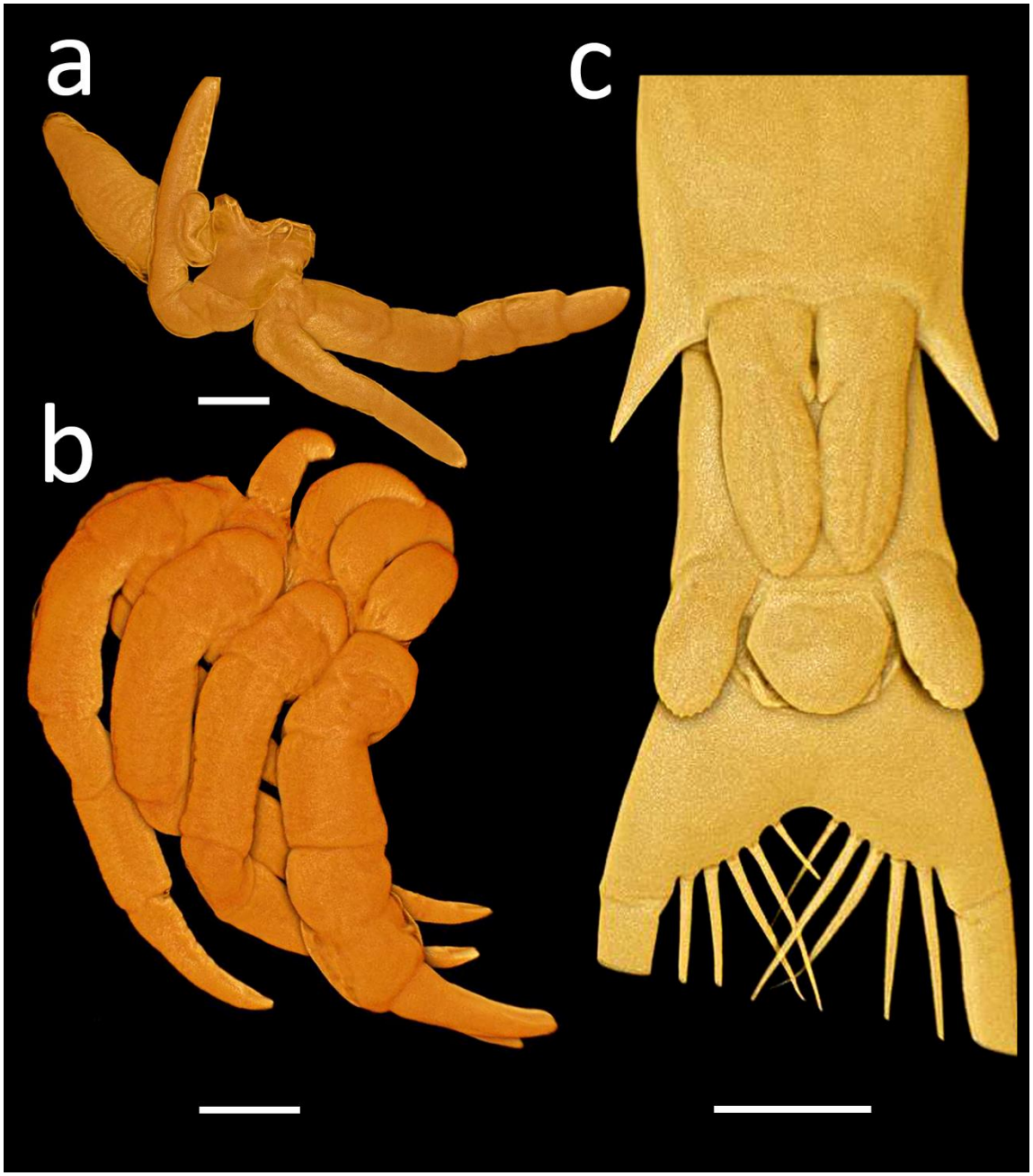

Figure 5.53: *Eriocheir sinensis*, ZVI, Nikon A1-Si CLSM with Drishti processing. (a) Maxilliped three, applying "large images" option, scan area of 1×2 fields for image stitching. (b) Pereiopods. (c) Uropod. Applying "large images" option, scan area of 2×2 fields for image stitching. Objective: 20× dry. Scale bars a = 200 µm; b, c = 500 µm.

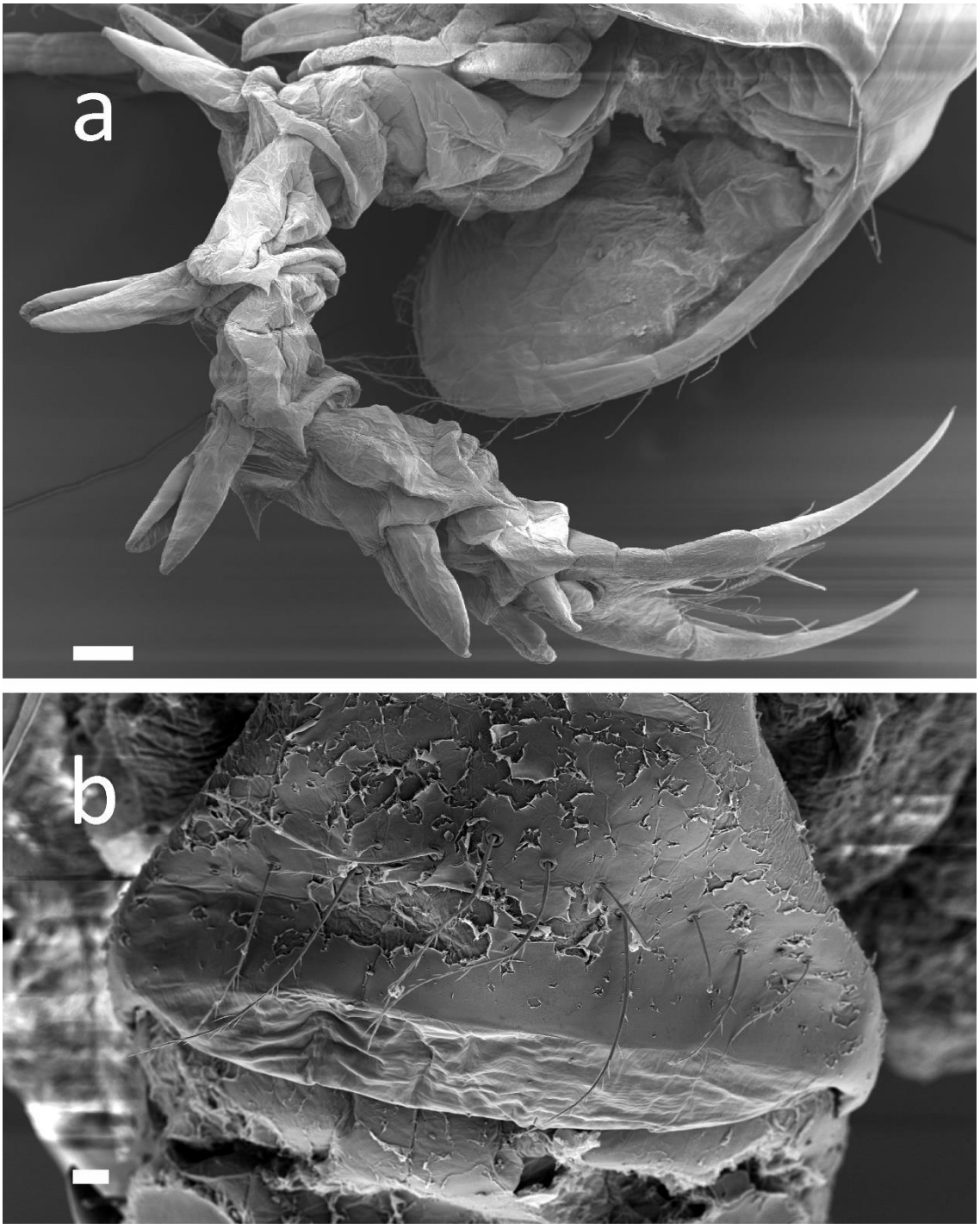

Figure 5.54: *Eriocheir sinensis*, ZVI, pleon and telson, FEI Quanta FEG SEM. (a) Lateral view of pleon and telson. (b) Somite 1 with 10 medial setae. Scale bars a = 100 µm; b = 20 µm.

5.5 Discussion

5.5.1 Zoeal stages measurements

The mitten crab zoeal descriptions of Schnakenbeck (1926, 1933), Hinrichs & Grell (1937), Buhk (1938), Panning (1939) and André (1947) did not provide any measurements in the text or insert scale bars on their illustrations. Many subsequent descriptions of mitten crab zoeal stages did provide detailed size measurements and inserted scale bars on figures.

The most frequently used measurements are the carapace length (C.L.) which was defined as the length "*from the base of the rostrum to the posterior margin*", carapace width (C.W.) described as "*the greatest distance across the cephalothorax*" by Cuesta *et al*. (2011) and the length between the tips of the dorsal and rostral spine named as total length (T.T.; Kim & Hwang, 1995; see Fig. 5.55).

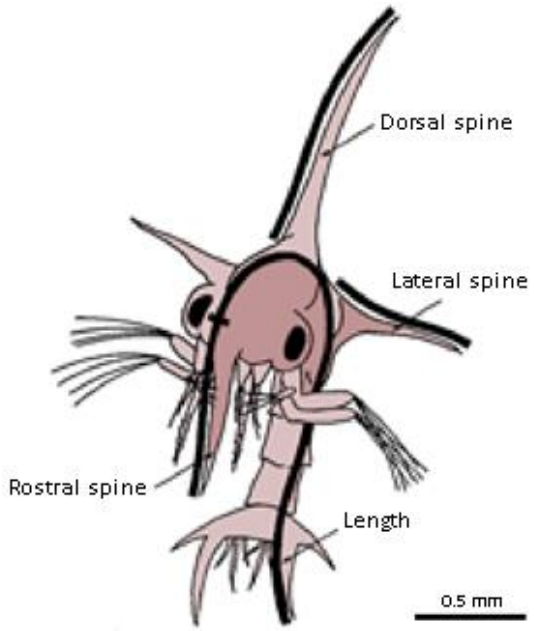

Figure 5.55: An example measurement of dorsal, lateral and rostral spines using a ZI stage of *Cancer magister* (adapted from Shirley *et al.*, 1987).

Liang *et al*. (1974) provided a scale bar for their general images of each zoea stage, while Ingle (1991) used only T.T. for his zoeal stages. Montú *et al*. (1996) provided both C.L. and T.T. lengths for each stage, but Kim & Hwang (1995) provided a wide range of the measurements including C.L., T.T., carapace width (C.W.), dorsal spine length (D.L.) and rostral spine length (R.L.). The spine measurement however can be inconsistent. While the distal measurement, assuming no damage, is stable because the tip is constantly defined, the proximal (base) is variable because it is not clearly delimited.

Comparing some of these measurements taken by various studies is interesting. For example, the T.T. length of zoea I stage was given as 1.15 mm by Ingle (1991), 1.25−1.27 mm by Montú *et al*. (1996) and 1.02 mm by Kim & Hwang (1995) (see related study for detailed standard deviations). Although, a standard deviation was given in the study of Kim & Hwang (1995), these measurements can also show differences according to the shape of the larvae. Therefore, how the zoea is preserved seems to be important for accurate measurements.

When considering the T.T., the pleons in figures 5.56b, 5.56c and 5.56f are all curved dorsally which may be shorter than it being curved ventrally when the somite divisions are extended. Therefore, the present study avoided supplying a general size of carapace spine length and T.T. A 500 μm scale bar, in Figure 5.56, was provided for six zoeal stages to demonstrate the increasing sizes for subsequent zoeal stages.

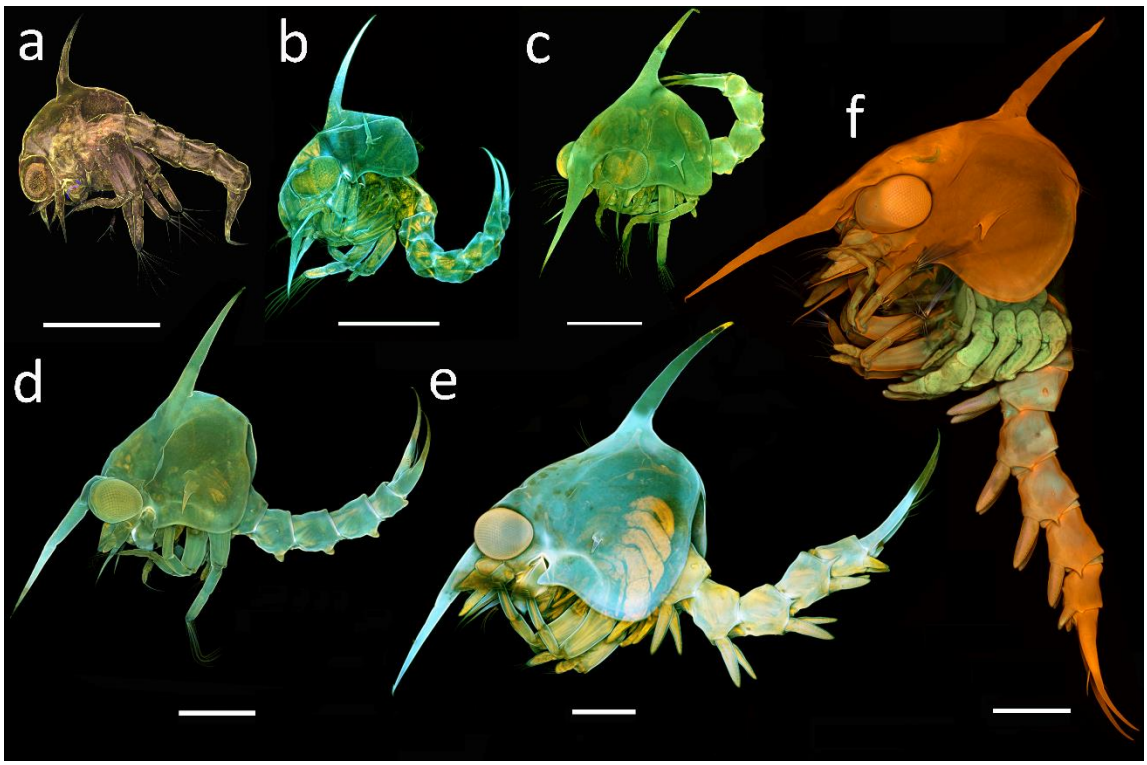

Figure 5.56: Confocal images of *Eriocheir sinensis* zoeal stages. (a) ZI, 10× dry objective. (b) ZII, 10× dry objective applying 'large images' option, scan area of 2×1 fields for image stitching. (c) ZIII, 10× dry objective applying 'large images' option, scan area of 2×2 fields for image stitching. (d) ZIV, 10×dry objective applying 'large images' option, scan area of 3×2 fields for image stitching. (e) ZV, 10×dry objective applying 'large images' option, scan area of 4×3 fields for image stitching. (f) ZVI, 10× dry objective applying 'large images' option, scan area of 4×4 fields for image stitching. Scale bars = 500 μm. CLSM, confocal laser scanning microscopy.

5.5.2 Comparison of the previous descriptions

The earliest descriptions of *E. sinensis* zoeal stages was by Schnakenbeck (1926). The information provided in this incomplete morphological description of ZI was limited. Many differences were found between this early description and the present study (Table 5.1). Dorsal and rostral spines of ZI of Schnakenbeck (1926) were illustrated smooth, whereas small spinules on both spines were clearly shown in the present

description (see Fig. 5.2c). The lateral telson spine was also depicted with less spinules compared with the current study. In addition, no posterodorsal setae were revealed in his description, while one pair of posterodorsal setae was illustrated in the present study. The setation of the mouthpart appendages were also overlooked. Only simple descriptions of the antennule, antenna, first and second maxillipeds were depicted in his basic illustration. Furthermore, the maxillule and maxilla were undescribed. This early illustration used the whole zoea instead of dissecting and figuring individual appendages in detail. Only one aesthetasc and one short seta were shown in his description of antennule, while four terminal aesthetascs (2 broad, 2 slender) and one small seta was illustrated in the present study. Moreover, the formation of the exopod and thereby the setation of the exopod was missed in his antenna drawing. Only the spinulation of the antenna was shown in his research, whereas two (1 short, 1 minute) medial spines on the exopod of the antenna were illustrated in the current study. The maxillule and maxilla were not presented in his description, however, a three-segmented structure could be seen in the figure. Although this was probably the endopod of the maxillule, the endopod of maxilla is two-segmented in all zoeal stages of *E. sinensis*. This appendage was probably drawn from the lateral side, therefore, the main body of maxillule was drawn as the third segment of the whole appendage. If it was assumed as the endopod of maxillule, the setation of the endopod was incorrect. It was drawn as the distal segment with three setae, whereas one seta on the proximal segment and five (1 subterminal, 4 terminal) plumose setae on the distal segment were shown in the present study. Furthermore, no setation of the basis of the first maxilliped was provided. The comparison of the setation of the first maxilliped of both studies is given in detail in Table 5.1 and they are completely different from each other. The remarkable difference is that Schnakenbeck (1926) defined the fourth segment of the endopod with three setae, whereas this was not observed in all six zoea stages in the current examination. The

setation of the basis of the second maxilliped was also overlooked by him (see Table 5.1 for details). No setae were shown in his study of ZI, whereas it has been described with four setae in all six zoeal stages in the present study. Additionally, the setation of the endopod of the second maxilliped was disregarded in his research. It was described as three-segmented with 0,0,6 setae in the current description and this remained the same until the ZV. Lastly, the inner row of the spinules on the telson was shown in his illustration, which was seen in the present study. However, the illustrations of the pleon as well as the denticles on the inner margin of each fork were not figured in detail in his study. The denticles on the inner margin of each fork and inner row of the spinules on the telson were shown in detail in the present study.

Table 5.1: A comparison between the zoea I stage of *Eriocheir sinensis* described by Schnakenbeck (1926) and the present study.

Character	**Schnakenbeck (1926)**	**Present study**
Carapace	**Fig. 1b**	**Figs 5.1−5.2**
Posterodorsal setae	0	1 pair
Ventral margin setation	7−8 serrations	8−9 serrations
Antennule	**Fig. 1b**	**Fig. 5.3a**
Primary flagellum setation	1 aesthetasc+1 seta	4 aesthetascs+1 small seta
Antenna	**Fig. 1b**	**Fig. 5.3b**
Exopod setation	Not figured	1 short+1 minute
Protopod	Spinulate	Distally bilaterally spinulate
Maxillule	**Fig. 1b**	**Fig. 5.4b**
Endopod setation	0,3	1,5
First maxilliped	**Fig. 1b**	**Fig. 5.6**
Basial setation	0	10: 2+2+3+3
Endopod setation	0,2,2,3,5	2,2,1,2,5
Second maxilliped	**Fig. 1b**	**Fig. 5.7**
Basial setation	0	4: 1+1+1+1
Endopod	0,0,4	0,1,6
Pleon	**Fig. 1c**	**Fig. 5.8**
Posterodorsal setae on somite 2−5	0	1 pair each
Dorsolateral processes	A pair directed ventrally on somites 3−5	A pair directed ventrally on somites 3−4

Table 5.1: Continued.

Character	Schnakenbeck (1926)	Present study
Telson	**Fig. 1c**	**Fig. 5.9**
Posterior margin setae	3 pairs	3 stout pairs spinulate
Denticules of inner margin on each fork	0	Double row

Schnakenbeck (1933) produced a second description of the mitten crab first stage zoea and these drawings were in much more detailed than his previous attempt, but only limited appendages such as antennule, antenna and the maxillipeds were detailed. In his description, the undeveloped larva was considered as "pre-zoea" stage. In the present study, the pre-zoea stage was not considered as an actual zoea stage for a proper description. As can be clearly seen in his figures (see Schnakenbeck, 1933: Fig. 46a-b), the setae on the appendages, even the natatory setae on the exopods of the first and second maxillipeds, were not fully developed. The pre-zoea stage was defined as the last embryonic form before moulting to the first zoea by Williamson (1982). According to Clark & Cuesta (2015), the setae and spines are folded or invaginated in the pre-zoea stage and they are non-functional. In addition, they have incomplete setation to make proper descriptions. Furthermore, it was emphasised by Clark & Cuesta (2015) that their survival ability is limited and they mostly die before moulting. Therefore, only the ZI was compared with Schnakenbeck (1933: Figs 47−50) by the present study (see Table 5.2). The posterodorsal setae was overlooked in his previous description of ZI (Schnakenbeck, 1926). The lateral spines were illustrated as smooth, however, it was described in the text that lateral spine present with small spines on the surface in his following description (Schnakenbeck, 1933). Another contradiction was found between his drawings of the antennule and the present study. The antennule was illustrated with one aesthetasc and one seta in their two separate illustrations (see Schnakenbeck, 1933: Figs 47, 49a), whereas the antennule was depicted with three aesthetascs in his Fig. 48.

Nonetheless, these descriptions of the antennule did not match with the present study (see Table 5.2). There was an explicit contradiction of the illustration of the first maxilliped between his and the present study. The different illustrations of the endopod of the maxillipeds at the ZI conducted by Schnakenbeck (1933) did not match with each other. This situation was explained by Montú *et al*. (1996) as deviation. It was referred that "*Schnakenbeck described a somewhat deviating setation for the endopods of zoeal maxillipeds 1 and 2…".* In the present study, no changes occurred in the setation of the endopods of the first and second maxillipeds between ZI-III (see Table 5.2 for detailed comparison). Lastly, there was no considerable alteration between the descriptions of pleon and telson by Schnakenbeck (1926) and Schnakenbeck (1933), therefore the highlighted differences in the previous comparison between his descriptions in both studies and the present study were still valid.

Table 5.2: A comparison between the zoea I stage of *Eriocheir sinensis* described by Schnakenbeck (1933) and the present study.

Character	**Schnakenbeck (1933)**	**Present study**
Carapace	**Figs 47−48**	**Figs 5.1−5.2**
Posterodorsal setae	0	1 pair
Ventral margin serrations	7−8 serrations	8−9 serrations
Antennule	**Figs 47, 48, 49a**	**Fig. 5.3a**
Primary flagellum setation	Figs 47, 49a: 1 aesthetasc+1 seta Fig 48: 3 aesthetascs	4 aesthetascs+1 small seta
Antenna	**Figs 47, 48, 49a**	**Fig. 5.3b**
Exopod setation	Absent	1 short+1 minute
Protopod	Spinulate	Distally bilaterally spinulate
Maxillule	**Fig. 47**	**Fig. 5.4b**
Endopod setation	0,2	1,5
First maxilliped	**Figs 47, 48, 49b-c**	**Fig. 5.6**
Basial setation	0	10: 2+2+3+3
Endopod setation	Fig. 47: 0,2,2,3,5 Fig. 49b: 0,1,2,2,5 Fig. 49c: 0,1,1,2,5	2,2,1,2,5

Table 5.2: Continued.

Character	Schnakenbeck (1933)	Present study
Second maxilliped	**Figs 47, 48, 49b**	**Fig. 5.7**
Basis	0	4: 1+1+1+1
Endopod	Fig 47: 0,1,4 Fig 49b: 0,0,5	0,1,6
Pleon	**Figs 47, 48, 50**	**Fig. 5.8**
Posterodorsal setae on somite 2−5	Absent	1 pair on each
Dorsolateral processes	A pair directed ventrally on somite 3−5	A pair directed ventrally on somite 3−4
Telson	**Figs 47, 48, 50**	**Fig. 5.9**
Posterior margin setae	3 pairs	3 pairs, stout & spinulate
Denticules of inner margin on each fork	0	Double row

Hinrichs & Grell (1937) described only the ZV of *E. sinensis*. There were a few remarkable differences between their ZV description and the present study (Table 5.3). The first difference was the setation of dorsal spine. No setation of the dorsal spine was depicted in their study, whereas the dorsal spine was illustrated with three pairs of setae in the present study. The posterodorsal and the anterodorsal setae were also overlooked by them. In the present study, however, one pair of posterodorsal and seven pairs of setae were shown in detail (Table 5.3). Anterior plumose setae of the ventral carapace margin were completely missed by them and only 6−7 posterior setae were illustrated in their figures. In the present study, 6−7 anterior plumose and 10 posterior setae were depicted on the ventral carapace margin. There was an explicit difference in the description of the antennule between two studies. Although 3-tiers of the antennule were correctly drawn by Hinrichs & Grell (1937), the number of setae was completely incompatible (see Table 5.3 for details). One seta was missed on the exopod of the antenna when comparing their description and the present description. In the case of the first maxilliped, the setation of the coxa was not taken into consideration in their review. In addition, the setation of the basis of the first maxilliped was overlooked by them. Furthermore, the endopod of the first maxilliped was described with 1,3,2,2,6 and

the number of natatory setae on the exopod was given as 12 setae in their detailed drawings. In the present study, variation was observed in the number setae present of the first and second maxillipeds in ZIV-VI. For example, 3+1 setae or 3 setae were separately found on the coxa of the first maxillipeds.

A similar variation was also detected on the basis, endopod and exopod of the first maxillipeds by the present research (see Table 5.3). The basis of the second maxilliped was not completely described in the study of Hinrichs & Grell (1937; see Table 5.3 for correct setation). The setation of the endopod of the second maxilliped was defined as 3-segmented with 0,1,7 in their study. In the present definition, as the variation was observed in zoea V, the setation of the endopod was detected with 0,1,6 and 0,1,7 setae in separate samples within the same zoeal stage. The medial setae on the first somite of the pleon was not described in the text, however, 4−5 setae may be seen in their figure, but this too is not clear. Are these setae present on the posterior margin of the carapace instead of somite 1 of the pleon? Another problem of their description was the drawing of the number of somites of the pleon. The number of somites is increased to 6 in ZIII and a pair of pleopods started to develop on the somites 2−6. In the study of Hinrichs & Grell (1937), pleopods were successfully shown on the somites 2−6, however, somite one was not figured. Consequently, this information could not be accurately interpreted (Table 5.3).

Table 5.3: A comparison between the zoea V stage of *Eriocheir sinensis* described by Hinrichs & Grell (1937) and the present study.

Character	**Hinrichs & Grell (1937)**	**Present study**
Carapace	**Figs 1−2**	**Figs 5.34−5.36**
Dorsal spine setae	0	3 pairs
Anterodorsal setae	0	7 pairs
Posterodorsal setae	0	1 pair
Ventral margin setation	6−7 posterior setae without serrations	6−7 anterior plumose+10 posterior setae with serrations
Posterior carapace margin setation	4	3 pairs
Antennule	**Figs 1, 3a**	**Fig. 5.37a-b**
Accessory flagellum	Absent	Small bud
Primary flagellum setation	3-tiers: 1,1,3 aesthetascs	3-tiers: 4,5, 5+1 aesthetascs
Antenna	**Figs 1, 3a**	**Fig. 5.37c**
Endopod	Developed	Developed
Exopod setation	0	1 simple
Protopod	Spinulate	Distally bilaterally spinulate
First maxilliped	**Figs 1, 3c**	**Fig. 5.40**
Coxal setation	Not figured	Fig. 5.40a: 3 Fig. 5. 40b: 3+1
Basial setation	Not completely figured, 2	Fig. 5.40a: 10: 2+2+3+3 Fig. 5.40b: 12: 2+3+4+3
Endopod setation	1,3,2,2,6	Fig. 5.40c: 1,3,2,2,6 Fig. 5.40d: 2,3,2,2,6
Exopod natatory setation	12 natatory	Fig. 5.40e: 12 Fig. 5.40f: 13
Second maxilliped	**Figs 1, 3d**	**Fig. 5.41**
Basial setation	0	4: 1+1+1+1
Endopod setation	0,1,7	Fig. 5.41a: 0,1,6 Fig. 5.41b: 0,1,7
Exopod natatory setation	12	Fig. 5.41c: 12 Fig. 5.41d: 13
Pleon	**Figs 1−2**	**Figs 5.42c−5.43**
Medial setae on somite 1	4−5?	8−9
Posterodorsal setae on somite 2−5	Absent	1 pair on each
Telson	**Figs 1, 3e**	**Figs 5.43d**
Denticules of inner margin on each fork	One row only	Double row

Buhk (1938, Figs 3, 5a) attempted to describe the ZI of *E. sinensis*. Figure 5a was the same illustration as depicted by Schnakenbeck (1933). Therefore, the ZI description of Buhk (1938) is not compared with the present study. Furthermore, in his study (Buhk,

1938) the zoeal development was described as a pre-zoea and five zoeal stages. In addition, he presented a photograph of the ZIV (Buhk, 1938, Fig. 4). The only detectable characters are the pleopods of the somites of the pleon.

Another zoeal description of *E. sinensis* was by Panning (1939). In his description, the stages were defined with a pre-zoea and four zoeal stages. In his examination, only some appendages at different zoeal stages were illustrated in detail. In his previous description (Panning, 1938), the larval stages were defined without a pre-zoea and stating that eggs developed into the zoea, following by three additional stages. Carapace setae were not shown in these zoeal descriptions (Panning, 1939). The antennule of ZI and ZII were not illustrated, whereas only the figure of the maxillule was depicted in ZI in his study. Similarly, only the illustrations of the maxillule of ZII and ZIII were figured in detail. There was a contradiction between the zoeal stages of the first and second maxillipeds in his research as the natatory setae on the maxillipeds do not match with recent studies. The number of natatory setae of the exopods of the maxillipeds were defined with 4, 6, 8, 10, 12 setae for zoea I, II, III, IV and V respectively in the recent studies (Kim & Hwang, 1995; Montú *et al*., 1996). The exopods of the first and second maxillipeds of ZVI were described by Montú *et al*. (1996) with 14 natatory setae. In the present study, however, the number of natatory setae in the ZV-VI showed variation. The exopod, in the current research, was found to be between 12−14 natatory setae. Apart from that, the number of natatory setae in ZI−IV of the present study matched with the studies of Kim & Hwang (1995) and Montú *et al*. (1996). The number of setae of the exopods is one of the key indicators to identify the zoeal stage of brachyuran crab larvae. Therefore, the zoeal stages of Panning (1939) were completely incompatible with the present study.

In Table 5.4, ZI appendages of *E. sinensis* described by Panning (1939) were compared with the present study. There were slight differences in the illustration of the antenna

between two studies (see Table 5.4). More differences were found in the setation of coxal and basial endite and endopod of the maxillule between two reviews (Table 5.4). Moreover, Panning (1939) described a variation in the setation for the maxillule endopod (2-segmented, 2,6 and 0,5 setae), whereas this was not observed in the present examination. There were no setae depicted on the basis of the first maxilliped in Panning's (1939) description and the endopod of the first maxilliped were not matched within the present study (Table 5.4). Basial setation of the second maxilliped was also not drawn by Panning (1939). In addition, the number of setae of the endopod of the second maxilliped did not match between his and the present study (see Table 5.4 for differences).

Table 5.4: A comparison between the zoea I stage of *Eriocheir sinensis* described by Panning (1939) and the present study.

Character	**Panning (1939)**	**Present study**
Antenna	**Figs 3a**	**Fig. 5.3b**
Exopod setation	2 short	1 short+1 minute
Maxillule	**Fig. 5a-b**	**Fig. 5.4b**
Coxal endite setation	4	5
Basial endite setation	4	5
Endopod setation	Fig. 5a: 2,6 Fig. 5b: 0,5	1,5 (1+4)
First maxilliped	**Fig. 7a-b**	**Fig. 5.6**
Basial setation	0	10: 2+2+3+3
Endopod setation	0,1,0,2,4	2,2,1,2,5
Second maxilliped	**Fig. 8a**	**Fig. 5.7**
Basial setation	0	4: 1+1+1+1
Endopod setation	0,0,5	0,1,6

In ZII (Table 5.5), the antennule was not described by Panning (1939). The description of the antenna, however, was completely incompatible with the present study. In his study, a small bud was depicted on the antenna, whereas the formation of endopod in ZII was not observed neither in the present study nor in the latest descriptions by Kim & Hwang (1995) and Montú *et al*. (1996). The small endopod bud on antenna was

observed on the third zoea stage in the present study. In addition, slight differences were found on the exopod of the antenna between two studies (see Table 5.5). As Panning (1939) described only four zoeal stages for *E. sinensis*, the certain discrepancies between his and the present study were observed across the all zoeal stages. There were certain deficiencies in the description of ZII of the maxilla in his study. The number of setae on coxa, basis, endopod and exopod did not match with the present study (see Table 5.5 for differences). The most remarkable differences were found on the exopod (scaphognathite) of the maxilla. It was illustrated as 7+3 setae by Panning (1939), whereas this was found as 5+3 setae in most of the descriptions (Liang *et al*., 1974; Ingle, 1991; Kim & Hwang, 1995; Montú *et al*., 1996) including the present study. The number of the natatory setae on the exopods of the first and second maxillipeds in ZII description given by Panning (1939) did not match with neither with the present study nor other descriptions. It was obvious that the zoeal stages were not correctly described by him. For example, eight natatory setae were depicted for the ZII in his study, whereas the correct setation for this stage is six natatory setae. It was clear that ZII was confused with ZIII in his research.

Moreover, no setation was conducted on the description of the basis of the first and second maxillipeds by him (see Table 5.5 for the present formula). Lastly, four pairs of posterior margin setae on telson were detected by him in ZII. This was not found in ZII in the current study, however, it was observed in the ZIII. The posterior margin setae and the denticules on each fork of the telson were also not properly demonstrated by him (see Table 5.5 for differences). All in all, it can be concluded that an incorrect description was made between the second and third stages of *E. sinensis* in the study of Panning (1939). This caused to find serious differences between his and the present study.

Table 5.5: A comparison between the zoea II stage of *Eriocheir sinensis* described by Panning (1939) and the present study.

Character	**Panning (1939)**	**Present study**
Antenna	**Fig. 3b**	**Fig. 5.12b**
Endopod	Small bud	Absent
Exopod setation	0	1 short+1 minute
Protopod	Distally bilaterally spinulate	Distally bilaterally spinulate
Maxilla	**Fig. 6a**	**Fig. 5.13**
Coxal endite setation	3	4+3
Basial endite setation	4+4	5+4
Endopod setation	2+2	2+2
Exopod setation	7+3	5+3
First maxilliped	**Fig. 7c**	**Fig. 5.14**
Basial setation	0	10: 2+2+3+3
Endopod setation	0,1,1,1,5	2,2,1,2,5
Exopod setation	8	6 natatory
Second maxilliped	**Fig. 8b**	**Fig. 5.15**
Basial setation	0	4: 1+1+1+1
Endopod setation	0,0,4	0,1,6
Exopod setation	8	6 natatory
Telson	**Fig. 1a**	**Fig. 5.16a**
Posterior margin setae	4 pairs	3 pairs of stout spinulate
Denticules of inner margin on each fork	0	Double row

The description of ZIII was explained by Panning (1939) using only a few appendages and it differs from the present study (Table 5.6). Setal differences in the descriptions of the antennule and antenna are shown in Table 5.6. The distinctive feature of his ZIII antenna was the presence of the small bud (accessory flagellum). His antenna description mostly matched with ZIV description of the present study. An endopod bud on the antenna illustrated by him, however, normally occurs in ZIV. This is consistent in the descriptions by Kim & Hwang (1995) and Montú *et al*. (1996) as well as in the present study.

The description of ZIII of the maxilla was also overlooked by Panning (1939). As emphasised by Kim & Hwang (1995), the larval development of *Eriocheir* (*E.*

leptognathus cf. Lee, 1988, *E. japonicus* cf. Kim & Hwang 1990, *E. sinensis* cf. Kim & Hwang, 1995 and *E. rectus* cf. Shy & Yu, 1992) can easily be distinguished by observing the setation of the antennule and the structures of the pleon in the most zoeal stages. The differences between *E. sinensis* and *E. japonica*, however, exhibit small differences such as the setation of the coxal endites of both maxillule and maxilla in the ZIII (Kim & Hwang, 1995). Therefore, it was important to detect the exact number of setation of such appendages so as to have an accurate description of morphologically similar species. The definition of the maxilla of ZIII exhibited by Panning (1939) was overlooked. The major features of his maxilla description mainly matched with the present ZIV description. The setation of the pleon was given in detail in the early description of *E. sinensis* by Panning (1939). No medial setae on somite one or posterodorsal setae on somites 2−5 as well as dorsolateral processes were illustrated in ZIII description of Panning (1939), whereas more features were observed in the present study (see Table 5.6).

Table 5.6: A comparison between the zoea III stage of *Eriocheir sinensis* described by Panning (1939) and the present study.

Character	**Panning (1939)**	**Present study**
Antennule	**Fig. 2a**	**Fig. 5.19a**
Primary flagellum setation	4 aesthetascs+3 setae	4 aesthetascs+2 setae
Antenna	**Fig. 3c**	**Figs 5.19b-c**
Endopod	More developed bud	Small bud
Exopod setation	0	1 short+1 minute
Protopod	Not spinulate	Distally bilaterally spinulate
Maxilla	**Fig. 6b**	**Fig. 5.20**
Coxal endite setation	6+3	5+3
Basial endite setation	4+4	6+5
Endopod setation	2+2	2+2
Exopod setation	16	9+6 plumose
Pleon	**Fig. 1b**	**Fig. 5.23**
Medial setae on somite 1	0	1
Posterodorsal setae on somite 2−5	0	1 pair on each
Dorsolateral processes	0	A pair directed ventrally on somite 3−4

There were distinct differences in the description of ZIV (zoea IV stage) of the antennule between two studies (Table 5.7). The most remarkable one was the number of tiers of the primary flagellum. It was depicted with two-tiers, whereas 3-tiers were clearly shown in the present study. In addition, the formation of the accessory flagellum on the antennule was illustrated by him, whereas this was not observed in ZIV, but observed in ZV in the present study. The main reason of this contradiction was that only four zoeal stages of *E. sinensis* was described by Panning (1939) and his ZIV description mainly matched with the ZV stage of the present study. It showed that there was confusion in the description of the last zoea stage in his study. Similarly, a developed bud which is almost at the same height of the protopod was shown in his description of the antenna. In the present description of ZIV of the antenna, however, a developing, short endopod bud was illustrated. Additionally, the spinulation of the protopod and the setation of the exopod of the antenna were overlooked as in his ZIII description. As stated before, Kim & Hwang (1995) highlighted the importance of the accurate setation of zoea stages in order to make accurate descriptions of the larval stages of *Eriocheir*. ZIV is also an important stage to detect the differences between *E. sinensis* and *E. japonica*. Kim & Hwang (1995) stated that the endopod of the first maxilliped plays an important role to separate two species (*E. sinensis* and *E. japonica*). Coxal and basial setation of the first maxilliped was overlooked by Panning (1939). The illustration the five-segmented endopod by Panning (1939) did not match with the present study. A variation in the endopod of the first maxilliped was found in the present examination and thereby two different setal formulae were presented (see Table 3.7).

Eleven to 12 natatory setae on the exopods of the first and second maxillipeds were depicted respectively in his study, whereas 10 natatory setae on the exopods in ZIV were shown in the latest (Liang *et al.*, 1974; Kim & Hwang, 1995; Montú *et al.*, 1996)

and the present studies. According to these latest descriptions, demonstrating 12 natatory on the exopods of the first and second maxillipeds proves that the larvae are actually the ZV. Therefore, his ZIV which was described as the "last stage" by Panning (1939) could be considered as ZV. But, in this case, a missing zoea stage would have been obtained. His description of the basis and endopod of the second maxilliped, however, did not match neither the present descriptions for ZIV nor ZV (see Table 5.7).

Table 5.7: A comparison between the zoea IV stage of *Eriocheir sinensis* described by Panning (1939) and the present study.

Character	**Panning (1939)**	**Present study**
Antennule	**Fig. 2b**	**Fig. 5.27a**
Primary flagellum setation	2-tiers: 4,4 aesthetascs	3-tiers: 1,1,4 aesthetascs
Accessory flagellum	Developing	Absent
Antenna	**Fig. 3d**	**Fig. 5.27b**
Endopod	Developed bud	Developing bud
Exopod setation	0	1 short+1 simple
Protopod	Not spinulate	Distally bilaterally spinulate
First maxilliped	**Fig. 7e**	**Fig. 5.30**
Coxal setation	Absent	1
Basial setation	0	10: 2+2+3+3
Endopod setation	0,2,1,2,6	Fig. 5.30b: 2,2,2,2,6 Fig. 5.30c: 2,3,2,2,6
Exopod setation	11	10 natatory
Second maxilliped	**Fig. 8c**	**Fig. 5.31**
Basial setation	3: 1,1,1	4: 1+1+1+1
Endopod setation	0,3,4	0,1,6
Exopod setation	12	10

Andre (1947) described the larval development of Chinese mitten crab with a pre-zoea stage, and after four successful zoeal moults the megalopa stage appeared. The illustration of ZI of Schnakenbeck (1933) was used in his study. Therefore, the comparison of his and the present study was not found to be necessary.

The first profound and detailed description of larval development of *E. sinensis* was by Liang *et al.* (1974). In their description, the larvae have five zoea stages and then it

metamorphoses into the megalopa. The remarkable and different statement in their study was the denotation of the pleon and telson. In the present study and all other previous studies, pleon and telson were named separately. Therefore, it was generally described as pleon with five somites and telson in the first zoea stage and pleon with six somites and telson down from the third zoea stage. However, it was not evaluated as a separate stage by Liang *et al*. (1974). Thus, they described "abdomen" (pleon and telson) as "six-segmented" in the first zoea stage and as "seven-segmented" from the third zoea stage onwards.

In the ZI description (Table 5.8) of Liang *et al*. (1974), the pair of posterodorsal setae was not depicted. In addition, lateral spines were depicted as smooth in their examination, whereas lateral spines were illustrated with small spines in the present study (see Fig. 5.2c).

Table 5.8: A comparison between the zoea I stage of *Eriocheir sinensis* described by Liang *et al*. (1974) and the present study.

Character	**Liang *et al*. (1974)**	**Present study**
Carapace	**Figs 1−2**	**Figs 5.1−5.2**
Posterodorsal setae	0	1 pair
Antennule	**Fig. 4**	**Fig. 5.3a**
Primary flagellum setation	2 aesthetascs+1 seta	4 aesthetascs+1 small seta
Maxillule	**Fig.7**	**Fig. 5.4b**
Coxal endite setation	4	5
Maxilla	**Fig. 1b**	**Fig. 5.5**
Coxal endite setation	4+2	4+3
Basial endite setation	4+4	5+4
Exopod setation	3+1 long distal process	4+1 long distal process
First maxilliped	**Fig. 9**	**Fig. 5.6**
Coxal setation	Not figured	0
Basial setation	6: 2,2,2	10: 2+2+3+3
Second maxilliped	**Fig. 10**	**Fig. 5.7**
Endopod setation	0,1,5	0,1,6
Pleon	**Fig. 3**	**Fig. 5.8**
Posterodorsal setae on somite 2−5	0	1 pair on each

Table 5.8: Continued.

Character	Liang *et al*. (1974)	Present study
Telson	**Fig. 3−3a**	**Fig. 5.9**
Denticules of inner margin on each fork	Fig. 3: Double row Fig. 3a: 0	Double row

In ZII, Liang *et al*. (1974) omitted to describe the carapace setae (see Table 5.9). They had two different setal illustrations for the antennule in their study, neither of which matched with the present study (see Table 5.9). Liang *et al*. (1974) described nine setae on the basis of their second maxilliped, arranged as 3,1,2,2. In the present study, however, 10 setae arranged as 2+2+3+3 were observed for ZI-IV. Similarly, the setation of the endopod of the second maxilliped in the zoea stages of ZI−IV was described by Liang *et al*. (1974) as three-segmented with 0,1,5 setae, whereas 0,1,6 setae were depicted in the mentioned zoea stages in the present research (Table 5.9).

Table 5.9: A comparison between the zoea II stage of *Eriocheir sinensis* described by Liang *et al*. (1974) and the present study.

Character	Liang *et al*. (1974)	Present study
Carapace	**Figs 11−12**	**Figs 5.10−5.11**
Anterodorsal setae	0	2 pairs
Posterodorsal setae	0	1 pair
Ventral margin setation	5 setae	1 anterior plumose+3 posterior setae
Antennule	**Figs 11, 14**	**Fig. 5.12a**
Primary flagellum setation	Fig 11: 2 aesthetascs+1 seta Fig 14: 3 aesthetascs+1 seta	4 broad aesthetascs+2 equal setae
First maxilliped	**Fig. 18**	**Fig. 5.14**
Coxal setation	Not figured	0
Basial setation	9: 3,1,2,2	10: 2+2+3+3
Second maxilliped	**Fig. 19**	**Fig. 5.15**
Endopod setation	0,1,5	0,1,6
Pleon	**Fig. 13**	**Fig. 5.16**
Posterodorsal setae on somite 2−5	0	1 pair on each

In ZIII (Table 5.10), as their previous zoeal stage descriptions, carapace setae were not described in detail in the analysis of Liang *et al*. (1974). There were contradictions between the illustrations and the definitions of the exopods of the first and the second maxillipeds. Liang *et al*. (1974) described 8 natatory setae on the exopods, which is correct for ZIII, however, 6 natatory setae were shown in their detailed drawings. In addition, the coxa in both appendages were not drawn in their report. Furthermore, a pair of small setae on the somites 2−5 of the pleon was overlooked in their study and the medial setae on somite 1 did not match the present studies (Table 5.10).

Table 5.10: A comparison between the zoea III stage of *Eriocheir sinensis* described by Liang *et al*. (1974) and the present study.

Character	**Liang *et al*. (1974)**	**Present study**
Carapace	**Figs 20−21**	**Figs 5.17−5.18**
Anterodorsal setae	0	4 pairs
Posterodorsal setae	0	1 pair
Ventral margin setation	9 setae	2 anterior plumose+6 posterior setae
Maxillule	**Fig. 26**	**Fig. 5.19d**
Epipod setation	1	2
First maxilliped	**Figs 20, 28**	**Fig. 5.21**
Coxal setation	Not figured	0
Exopod natatory setation	Fig. 20: 8 Fig. 28: 6	8
Second maxilliped	**Fig. 29**	**Fig. 5.22**
Coxal setation	Not figured	0
Endopod setation	0,1,5	0,1,6
Pleon	**Fig. 22**	**Fig. 5.23**
Medial setae on somite 1	2	1
Posterodorsal setae on somite 2−5	0	1 pair on each

The ZIV show distinct alternatives, especially on the carapace, namely dorsal spine and anterodorsal setation. In the early descriptions, the complete carapace setation was overlooked (Schnakenbeck, 1926; Schnakenbeck, 1933; Hinrichs & Grell, 1937; Buhk, 1938; Panning, 1939; Andre, 1947; Liang *et al*., 1974). The carapace setation was also

not considered in detail by the later descriptions of Ingle (1991) and Montú *et al*. (1996). The only study depicted full setation of the carapace was conducted by Kim & Hwang (1995).

Carapace setation has been carefully visualised in the present study and shown in Table 5.11. Most of this setation, however, was not depicted by Liang *et al*. (1974). Another considerable difference in ZIV descriptions between the two researches was the setation and the illustrations of the antennule. Number of tiers of the antennule did not match with each other (see Table 5.11). There were slight differences between two studies in the description of the coxal and basial endites of the maxillule in this zoeal stage (see Table 5.11). First and second maxilliped illustrations in two studies were also quite different from each other (Table 5.11). A few considerable variations were found within the ZIV of *E. sinensis* in the current analysis, however, it was not noted by Liang *et al*. (1974).

Telson was described with four posterior margin setae on each fork by Liang *et al*. (1974). The results of the present study demonstrated that there were five pairs of posterior margin setae on each fork in ZIV of *E. sinensis*.

Table 5.11: A comparison between the zoea IV stage of *Eriocheir sinensis* described by Liang *et al*. (1974) and the present study.

Character	**Liang *et al*. (1974)**	**Present study**
Carapace	**Figs 30−31**	**Figs 5.24−5.26**
Dorsal spine setae	0	3 pairs
Anterodorsal setae	0	5 pairs
Posterodorsal setae	0	1 pair
Ventral carapace margin setation	12 setae	4 anterior plumose+7−8 posterior setae
Posterior carapace margin setae	0	3 pairs
Antennule	**Fig. 33**	**Fig. 5.27a**
Primary flagellum setation	2-tiers: 1,4 aesthetascs	3-tiers: 1,1,4 aesthetascs

Table 5.11: Continued.

Character	**Liang *et al*. (1974)**	**Present study**
Maxillule	**Fig. 36**	**Fig. 5.28b-c**
Coxal endite setation	7	7+1 simple
Basial endite setation	10+2	11+2
Maxilla	**Fig. 37**	**Fig. 5.29**
Coxal endite setation	6+3	7+3
Basial endite setation	6+6	8+8
Exopod setation	26	25
First maxilliped	**Fig. 38**	**Fig. 5.30**
Coxal setation	Not figured	1
Basial setation	9: 1,2,3,3	10: 2+2+3+3
Endopod setation	2,2,2,2,6	Fig. 5.30b: 2,2,2,2,6 Fig. 5.30c: 2,3,2,2,6
Second maxilliped	**Fig. 39**	**Fig. 5.31**
Coxal setation	Not figured	0
Endopod setation	0,1,5	0,1,6
Telson	**Fig. 32**	**Fig. 5.33c**
Posterior margin setae	4 pairs	5 pairs

As in the zoea IV, Liang *et al*. (1974) mainly ignored the carapace setation in the description of ZV (Table 5.12). Although, Liang *et al*. (1974) illustrated the primary flagellum of the antennule with 3-tiers in ZV, the number of setae did not match with the current investigation (see Table 5.12 for setation). More differences in the coxal and basial endite setation of the maxillule and maxilla were found between the two studies (see Table 5.12). Coxal and basial endites of the maxillule in ZV thicken and the setae seem like located in 3-tiers in the present study. However, it was drawn as 2-tiers by Liang *et al.* (1974). In addition, the number of setae shown by them does not match with the current investigation (see Table 5.12). This was also the case for the maxilla.

In the present study, the last two zoeal stages (V and VI) showed an unusual setation pattern. This was observed in some segments of the first maxilliped and endopod and the exopod of the second maxilliped. The coxa of the first maxilliped was partly drawn and no setae were presented by Liang *et al*. (1974), whereas three and 3+1 setae were examined separately in the present report. The basis of the first maxilliped was defined

with 10 setae (arranged as 2+2+3+3) by Liang *et al*. (1974). However, two different setation patterns with 10 (2+2+3+3) and 12 (2+3+4+3) setae were demonstrated separately in the present research. A similar difference between two studies (see Table 5.12) was also observed in the endopod and exopod of the first and second maxillipeds.

Table 5.12: A comparison between the zoea V stage of *Eriocheir sinensis* described by Liang *et al*. (1974) and the present study.

Character	**Liang *et al*. (1974)**	**Present study**
Carapace	**Figs 40−41**	**Figs 5.34−5.36**
Dorsal spine setae	0	3 pairs
Anterodorsal setae	0	7 pairs
Posterodorsal setae	0	1 pair
Ventral margin setation	13 setae	6−7 anterior plumose+10 posterior setae
Antennule	**Fig. 43**	**Fig. 5.37a-b**
Primary flagellum setation	3-tiers: 2,4,4 aesthetascs	3-tiers: 4,5,6 aesthetascs
Antenna	**Fig. 44**	**Fig. 5.37c**
Exopod setation	2	1
Maxillule	**Fig. 46**	**Fig. 5.38b-d**
Epipod setation	2	3
Coxal endite setation	2-tiers: 8+4	3-tiers: 9+4+3
Basial endite setation	15+2	16+4
Maxilla	**Fig. 47**	**Fig. 5.39**
Coxal endite setation	13	11+4
Basial endite setation	7+10	10+11
Exopod setation	35	32−33
First maxilliped	**Fig. 48**	**Fig. 5.40**
Coxal setation	0	Fig. 5.40a: 3 Fig. 5.40b: 3+1
Basial setation	10: 2+2+3+3	Fig. 5.40a: 10: 2+2+3+3 Fig. 5.40b: 12: 2+3+4+3
Endopod setation	2,2,2,2,6	Fig. 5.40c: 1,3,2,2,6 Fig. 5.40d: 2,3,2,2,6
Exopod natatory setation	12	Fig. 5.40e: 12 Fig. 5.40f: 13

Table 5.12: Continued.

Character	**Liang *et al*. (1974)**	**Present study**
Second maxilliped	**Fig. 49**	**Fig. 5.41**
Coxal setation	Absent	0
Endopod setation	0,1,6	Fig. 5.41a: 0,1,6 Fig. 5.41b: 0,1,7
Exopod natatory setation	12	Fig. 5.41c: 12 Fig. 5.41d: 13

Another brief description of the Chinese mitten crab larval development was conducted by Ingle (1986). He described *E. sinensis* as possessing five zoeal stages, however, only ZI was illustrated and this was an image re-drawn from Andre (1947). Consequently, a detailed comparison was not required for the current report. Ingle (1991) did, however, make a much more detailed description of *E. sinensis* compared to his previous description. He borrowed the specimens of Buhk (1938) and re-examined them for his study. They were found to be in poor condition and did not allow Ingle (1991) to make a good description. His study was mainly a text description with a few supportive images of some appendages. The only complete illustrations were conducted for the ZI.

There were slight differences when comparing the ZI by Ingle (1991) with the current study (Table 5.13). The antennule was described by Ingle (1991) with five aesthetascs, whereas four aesthetascs (2 broad, 2 slender) and 1 small seta were depicted in the present examination. The coxa of the maxillule was described with four setae, while five setae were revealed in the current investigation. The coxa of the first and second maxillipeds in the description of Ingle (1991) was not discussed in all zoeal stages, therefore, a detailed comparison could not be presented in this study. The other appendages of the ZI matched within the current review.

Table 5.13: A comparison between the zoea I stage of *Eriocheir sinensis* described by Ingle (1991) and the present study.

Character	**Ingle (1991)**	**Present study**
Antennule	**Fig. 2.38a**	**Fig. 5.3a**
Primary flagellum setation	5 aesthetascs	4 aesthetascs+1 small seta
Maxillule	**No fig. only text**	**Fig. 5.4b**
Coxal endite setation	4	5

The ZII description stated by Ingle (1991) was incomplete. It was stated that the anterior-median region was not recorded because of the lack of satisfactory information. He described the setation of the ventral carapace margin (Table 5.14) with two sub-marginal setae, whereas one plumose anterior + three posterior setae were depicted in the present examination. Due to the damaged appendage, there was no data on the setation of the antennule in his description. Although, the number of setae was given as 8 on the exopod of the maxilla in his study, however, Ingle (1991) stated that there could be up to 12. However, it was not successfully viewed because of the damaged specimen. In the present study, 5+3 setae are clearly illustrated; 12 setae were never recorded. There was no description for the first and second maxillipeds in his report.

Table 5.14: A comparison between the zoea II stage of *Eriocheir sinensis* described by Ingle (1991) and the present study.

Character	**Ingle (1991)**	**Present study**
Carapace	**No fig. only text**	**Figs 5.10−5.11**
Anterodorsal setae	Not recorded	2 pairs
Posterodorsal setae	Not recorded	1 pair
Ventral margin setation	2 sub-marginal setae	1 anterior plumose+3 posterior setae
Antennule	**No fig. only text**	**Fig. 5.12a**
Primary flagellum setation	Not recorded	4 broad aesthetascs+2 equal setae
Maxilla	**No fig. only text**	**Fig. 5.13**
Exopod setation	8−12 (damaged)	5+3

A complete carapace description was not provided for the ZIII by Ingle (1991) because the specimens were damaged/unsatisfactory. Therefore, posterodorsal and anterodorsal setation was neglected (Table 5.15). The ventral carapace margin, however, was described with five sub-marginal setae only. Whereas, more setae were described in the current review (see Table 5.15). In addition, there was no information on the epipod of the maxillule in all zoeal stages in the study of Ingle (1991); whereas 2 epipod setae were illustrated in the present research. The descriptions of the coxal and basial endites of the maxillule did not match between two studies. Furthermore, the differences in the description of maxilla are highlighted in Table 5.15.

Table 5.15: A comparison between the zoea III stage of *Eriocheir sinensis* described by Ingle (1991) and the present study.

Character	**Ingle (1991)**	**Present study**
Carapace	**No fig. only text**	**Figs 5.17−5.18**
Anterodorsal setae	Not recorded	4 pairs
Posterodorsal setae	Not recorded	1 pair
Ventral margin setation	5 sub-marginal setae	2 anterior plumose+6 posterior setae
Antennule	**No fig. only text**	**Fig. 5.19a**
Primary flagellum setation	Not recorded	4 broad aesthetascs+2 equal setae
Maxillule	**No fig. only text**	**Fig. 5.19d**
Epipod setation	No info	2
Coxal endite setation	6	5
Basial endite setation	8	7
Maxilla	**No fig. only text**	**Fig. 5.20**
Basial endite setation	5+5	6+5
Exopod setation	16 marginal	9+6 plumose

The carapace description of the ZIV of Ingle (1991) did not include the setation of the dorsal spine; three pairs were present in this study (Table 5.16). The posterodorsal and anterodorsal carapace setation was not recorded by Ingle (1991) because of the damaged specimen. Moreover, the setation of the posterior carapace margin was also ignored in his report. The formation of the tiers on the antennule was not discussed in the study of

Ingle (1991). Although 3-tiers with 1,1,4 aesthetascs were illustrated in the present research, the antennule was described with 8 aesthetascs only by Ingle (1991). There were slight differences between two studies in the description of maxillule and maxilla. However, the pleon and the telson were not recorded in his study. Therefore, a comparison was found to be unnecessary for these appendages in this zoeal stage.

Table 5.16: A comparison between the zoea IV stage of *Eriocheir sinensis* described by Ingle (1991) and the present study.

Character	**Ingle (1991)**	**Present study**
Carapace	**No fig. only text**	**Figs 5.24−5.26**
Dorsal spine setae	Not recorded	3 pairs
Anterodorsal setae	Not recorded	5 pairs
Posterodorsal setae	Not recorded	1 pair
Ventral margin setation	10 setae	4 anterior plumose+7−8 posterior setae
Posterior margin setae	Not recorded	3 pairs
Antennule	**No fig. only text**	**Fig. 5.27a**
Primary flagellum setation	8 aesthetascs	3-tiers: 1,1,4 aesthetascs
Maxillule	**No fig. only text**	**Fig. 5.28b-c**
Epipod setation	No info	2
Coxal endite setation	9	7+1 simple
Basial endite setation	15	11+2
Maxilla	**No fig. only text**	**Fig. 5.29**
Coxal endite setation	Not recorded	7+3
Basial endite setation	Not recorded	8+8
Exopod setation	25	25
Pleon	**No fig. only text**	**Fig. 5.33a-b**
Posterodorsal setae on somites 2−5	Not recorded	1 pair on each somite
Dorsolateral processes	Not recorded	A pair directed ventrally on somite 3−4
Telson	**Fig. 32**	**Fig. 5.33c**
Posterior margin setae	Not recorded	5 pairs

The dorsal carapace setation in the ZV of *E. sinensis* was ignored by Ingle (1991). The antennule was defined with 10 aesthetascs in his study and the formation of the tiers was not referred by Ingle (1991). The epipod setation of the maxillule was not also described in ZV as well as other early zoeal stages in his revision. There were

remarkable differences in the descriptions of the maxillule and maxilla including formation of tiers between two studies (see Table 5.17). Forty-three marginal setae were found on the exopod of the maxilla in the study of Ingle (1991). Only 32−33 setae were observed in the present study. More accurately, 44 highly plumose setae on the exopod of the maxilla was visualised in the ZV in the present study. It is possible that the appendage used in his study could be at ZVI.

Although the definitions of the first and second maxillipeds were not stated in the study of Ingle (1991), the detailed illustrations were provided (see Table 5.17). The endopod of the first maxilliped were depicted as five-segmented with 2,2,1,2,5 by Ingle (1991), whereas two different setation pattern were observed in the current research. These were 1,3,2,2,6 and 2,3,2,2,6 respectively. Moreover, the third segment of the endopod of the first maxilliped were defined with only seta (2,2,**1**,2,5) by Ingle (1991). However, two setae were observed in both different setation patterns (1,3,**2**,2,6 and 2,3,**2**,2,6) of the current study. In addition, 2 setae were observed on the third segment by other researchers (Liang *et al*., 1974; Kim & Hwang, 1995; Montú *et al*., 1996) who revealed detailed descriptions of the ZV of *E. sinensis*. Therefore, this unusual setation pattern can be considered as an incorrect description rather than a variation.

Another essential point is the number of natatory setae of the exopods in the ZV. Twelve natatory setae on the first and the second maxilliped were demonstrated by Ingle (1991). On the other hand, a variation was found in the present review. 12 and 13 natatory setae were observed separately in the current study. Correspondingly, the endopod of the second maxilliped were depicted as three-segmented with 0,1,5 setae in his revision. The similar variation was also observed in this appendage, where 0,1,6 and 0,1,7 setae were depicted separately in the present analysis. This variation was not noticed until the present examination. The endopod of the second maxilliped was defined as three-segmented with 0,1,6 by Kim & Hwang (1995), whereas 0,1,7 were

found in the ZV and ZVI in the study of Montú *et al*. (1996). These results were probably obtained using a single specimen. Therefore, a possible variation was not noticed in the endopod of the second maxilliped. In the current study, more than one specimen was examined and two different results were obtained. 0,1,6 and 0,1,7 setae were demonstrated clearly in the present examination. Therefore, this setation pattern can be considered as variation.

Table 5.17: A comparison between the zoea V stage of *Eriocheir sinensis* described by Ingle (1991) and the present study.

Character	**Ingle (1991)**	**Present study**
Carapace	**Fig. 2.38g−h**	**Figs 5.34−5.36**
Dorsal spine setae	0	3 pairs
Anterodorsal setae	4 pairs of setae	7 pairs
Ventral margin setation	18 setae	6−7 anterior plumose + 10 posterior setae
Posterior margin setae	6 pairs	3 pairs
Antennule	**No fig. only text**	**Fig. 5.37a-b**
Primary flagellum setation	10 aesthetascs	3-tiers: 4,5,6 aesthetascs
Maxillule	**Fig. 1.29f**	**Fig. 5.38b-d**
Epipod setation	Not recorded	3
Coxal endite setation	14	3-tiers: 9,4,3
Basial endite setation	18	16+4
Maxilla	**No fig. only text**	**Fig. 5.39**
Coxal endite setation	11+5	11+4
Basial endite setation	10+9	10+11
Exopod setation	43	32−33
First maxilliped	**Fig. 2.38**	**Fig. 5.40**
Endopod setation	2,2,1,2,5	Fig. 5.40c: 1,3,2,2,6 Fig. 5.40d: 2,3,2,2,6
Exopod natatory setation	12	Fig. 5.40e: Fig. 5.40f:
Second maxilliped	**Fig. 2.38**	**Fig. 5.41**
Endopod setation	0,1,5	Fig. 5.41a: 0,1,6 Fig. 5.41b: 0,1,7
Exopod natatory setation	12	Fig. 5.41c: 12 Fig. 5.41d: 13
Pleon	**Fig. 2.38h**	**Figs 5.42c−5.43**
Medial setae on somite 1	7	8−9

The most accurate description of the *E. sinensis* larval development was by Kim & Hwang (1995). However, the present study and their revision differed from each other in terms of the number of zoeal stages. Five zoeal stages were described by Kim & Hwang (1995), whereas six zoeal stages were identified for the present research and Montú *et al*. (1996).

In ZI description of Kim & Hwang (1995), the lateral spines were depicted with a smooth surface as long with most of the previous studies. The pair of posterodorsal setae was named as anterodorsal setae in the study of Kim & Hwang (1995). In the present study, however, the dorsal carapace setae were separated into two; the anterodorsal setae and posterodorsal (a pair of setae located just behind the dorsal spine; see Table 5.18). The setation of the antennule was described by them with two long and two simple setae, whereas it was depicted as four aesthetascs (2 broad, 2 slender) and 1 simple seta in the current research.

The coxal endite of the maxilla was depicted with 4+2 setae in the review of Kim & Hwang (1995), but was illustrated with 4+3 setae in the present study. In addition, the exopod was described with 4+1 highly plumose setae by them, while four plumose setae and one long distal stout process were illustrated in the current examination.

Table 5.18: A comparison between the zoea I stage of *Eriocheir sinensis* described by Kim & Hwang (1995) and the present study.

Character	**Kim & Hwang (1995)**	**Present study**
Carapace	**Fig. 1a**	**Figs 5.1−5.2**
Posterodorsal setae	0*	1 pair
Anterodorsal setae	1*pair	0
Antennule	**Fig. 1c**	**Fig. 5.3a**
Primary flagellum setation	2 aesthetascs+2 setae	4 aesthetascs+1 small seta
Maxilla	**Fig. 1g**	**Fig. 5.5**
Coxal endite setation	4+2	4+3
Exopod setation	4+1 highly plumose	4 plumose+1 long distal stout process

*Kim & Hwang (1995) did not separate the posterodorsal and anterodorsal carapace setation. They, instead, named this area as “anterodorsal”. Therefore, the information was obtained from their illustrations as well as the text descriptions.

The ZII carapace was described with three pairs of anterodorsal setae by Kim & Hwang (1995). In the present description, it was depicted with two pairs of anterodorsal setae and one pair of posterodorsal setae (Table 5.19). The number of the ventral carapace margin setae were illustrated in the present study however, these details were overlooked in the study of Kim & Hwang (1995; see Table 5.19). Another contradiction between two examinations was the description of the antennule. It was drawn with four aesthetascs + one simple seta in the review of Kim & Hwang (1995). Their description was almost similar with ZI antennule description of the present report, however, the ZII of the antennule description was demonstrated with four broad aesthetascs + two unequal short setae in the present examination.

Table 5.19: A comparison between the zoea II stage of *Eriocheir sinensis* described by Kim & Hwang (1995) and the present study.

Character	**Kim & Hwang (1995)**	**Present study**
Carapace	**Fig. 2a**	**Figs 5.10−5.11**
Anterodorsal setae	3* pairs	2 pairs
Posterodorsal setae	0*	1 pair
Ventral carapace margin	4 plumose	1 anterior plumose+3 posterior
Antennule	**Fig. 2c**	**Fig. 5.12a**
Primary flagellum setation	4 aesthetascs+1 simple seta	4 broad aesthetascs+2 unequal short seta

*Kim & Hwang (1995) did not separate the posterodorsal and anterodorsal carapace setation. They, instead, named this area as “anterodorsal”. Therefore, the information was obtained from their illustrations as well as the text descriptions.

In the ZIII description of Kim & Hwang (1995), the dorsal spine was described with a pair of simple setae, however, no setae were observed in the present study (Table 5.20). Kim & Hwang (1995) did not describe the anterodorsal and posterodorsal setae separately in the third zoea stage (see Table 5.20). In the present research, two plumose anterior and six posterior setae were detected on the ventral carapace margin, however, only two plumose setae were shown on the posterior carapace margin in their report.. In ZIII, three broad aesthetascs and two equal setae were illustrated in the current application. The exopod of the antenna was shown with only one seta in the ZIII description of Kim & Hwang (1995), however, one short and one minute setae were depicted in the current analysis. There were differences found between the two studies in the description of the maxilla and the number of medial setae on somite 1 of the pleon (Table 5.20).

Table 5.20: A comparison between the zoea III stage of *Eriocheir sinensis* described by Kim & Hwang (1995) and the present study.

Character	**Kim & Hwang (1995)**	**Present study**
Carapace	**Fig. 3a**	**Figs 5.17−5.18**
Dorsal spine setae	1 pair	0
Anterodorsal setae	5* pairs	4 pairs
Posterodorsal setae	0*	1 pair
Ventral carapace margin setation	8−10 plumose setae	2 anterior plumose+6 posterior setae
Posterior carapace margin setae	2 plumose	0
Antennule	**Fig. 3c**	**Fig. 5.19a**
Primary flagellum setation	3 aesthetascs+2 unequal setae	4 broad aesthetascs+2 equal setae
Antenna	**Fig. 3d**	**Figs 5.19b-c**
Exopod setation	1 short	1 short + 1 minute
Maxilla	**Fig. 3g**	**Fig. 5.20**
Exopod setation	11+5	9+6
Pleon	**Fig. 3b**	**Fig. 5.23**
Medial setae on somite 1	3 (rarely 1)	1

*Kim & Hwang (1995) did not separate the posterodorsal and anterodorsal carapace setation. They, instead, named this area as “anterodorsal”. Therefore, the information was obtained from their illustrations as well as the text descriptions.

There were a few remarkable differences in the description of the ZIV by Kim & Hwang (1995) and the present study (Table 5.21). The described number of setae on the dorsal spine of their and the current description did not match each other. Two pairs of setae were described by Kim & Hwang (1995), whereas three pairs of setae were visualised and detailed in the present examination. The last difference in the carapace setation between two analyses was observed in the posterior carapace margin (Table 5.21). Two pairs of plumose setae were defined by their analysis, whereas three pairs of plumose setae were illustrated in the current examination. Another considerable difference was observed in the definition of the antennule. The antennule in the ZIV was defined as two-tiers with 1,5 setae by Kim & Hwang (1995). However, the formation of 3-tiers was observed in the antennule with 1,1,4 setae in the current revision. There were also slight differences in the setation of the other appendages i.e. the coxal endite and exopod of the maxilla (see Table 5.21). The endopod of the first maxilliped was defined as five-segmented with 2,**3**,2,2,6 by Kim & Hwang (1995). However, two different setation formula were found for the same appendage in the current analysis. These were 2,**2**,2,2,6 and 2,**3**,2,2,6. The reason for this difference is highly likely that there was a variation in the endopod of the first maxilliped at the ZIV of *E. sinensis* and it was not recognised until now. It was probably because of using a single sample for the examination. On the contrary, a few different samples at the same zoeal stages were observed and this variation was easily understood in the present research.

Table 5.21: A comparison between the zoea IV stage of *Eriocheir sinensis* described by Kim & Hwang (1995) and the present study.

Character	**Kim & Hwang (1995)**	**Present study**
Carapace	**Fig. 4a**	**Figs 5.24−5.26**
Dorsal spine setae	2 pairs	3 pairs
Anterodorsal setae	6* pairs	5 pairs
Posterodorsal setae	0*	1 pair
Ventral carapace margin setation	12−14 plumose setae	4 anterior plumose+7−8 posterior
Posterior carapace margin setae	2 plumose	3 pairs
Antennule	**Fig. 4c**	**Fig. 5.27a**
Primary flagellum setation	2-tiers: 1,5 aesthetascs	3-tiers: 1,1,4 aesthetascs
Maxilla	**Fig. 4g**	**Fig. 5.29**
Coxal endite setation	8+4	7+3+1
Exopod setation	25−27	25
First maxilliped	**Fig. 3b**	**Fig. 5.30b-c**
Endopod setation	2,3,2,2,6	Fig. 5.30b: 2,2,2,2,6 Fig. 5.30: 2,3,2,2,6

*Kim & Hwang (1995) did not separate the posterodorsal and anterodorsal carapace setation. They, instead, named this area as "anterodorsal". Therefore, the information was obtained from their illustrations as well as the text descriptions.

More differences in ZV were observed between two studies (Table 5.22). In total, seven pairs of "antero-dorsal" setae were defined on the carapace in the ZV by Kim & Hwang (1995). However, seven pairs of anterodorsal and one pair of posterodorsal setae were illustrated in detail for the present study. Other differences in the posterior carapace setation are shown in Table 5.22. A significant difference was observed in the description of the antennule in the ZV between two studies. The antennule was described with 2-tiers with five subterminal and 4+1 terminal setae by Kim & Hwang (1995). However, the primary flagellum of the antennule was defined with 3-tiers with four subterminal setae on the third tier, five long aesthetascs on the middle tier and 5+1 terminal setae on the first tier in the current investigation. More differences were also found in the maxillule and maxilla descriptions. It is important to note that the number

of setae on the exopod of the maxilla was described with 38−40 setae in the study of Kim & Hwang (1995). However, only 32−33 setae were found in the present research. In addition, 44 plumose setae were found in the ZVI in the current report. This difference between two studies can be explained by the definition of the number of zoeal stages attributed to the Chinese mitten crab.

The variations in the first and second maxillipeds was overlooked by Kim & Hwang (1995). These differences are listed in Table 5.22. Lastly, seven medial setae were exhibited on somite one of the pleon in their study, while 8−9 medial setae were shown in the current application. The main differences in ZV between two studies occurred in the definition of the number of zoeal stages.

Table 5.22: A comparison between the zoea V stage of *Eriocheir sinensis* described by Kim & Hwang (1995) and the present study.

Character	**Kim & Hwang (1995)**	**Present study**
Carapace	**Fig. 5a**	**Figs 5.34−5.36**
Anterodorsal setae	7* pairs	7 pairs
Posterodorsal setae	0*	1 pair
Posterior margin setation	2 plumose	3 pairs
Antennule	**Fig. 5c**	**Figs 5.37a-b**
Primary flagellum setation	2-tiers: 5,4+1	3-tiers: 4,5, 5+1aesthetascs
Maxillule	**Fig. 5f**	**Fig. 5.38b-d**
Coxal endite setation	11	3-tiers: 9+4+3
Basial endite setation	14+3	16+4
Maxilla	**Fig. 5g**	**Fig. 5.39**
Coxal endite setation	13+6	11+4
Exopod setation	38−40	32−33
First maxilliped	**Fig. 5h**	**Fig. 5.40**
Coxal setation	2	Fig. 5.40a: 3 Fig. 5.40b: 3+1
Basial setation	10: 2+2+3+3	Fig. 5.40a: 10: 2+2+3+3 Fig. 5.40b: 12: 2+3+4+3
Endopod setation	2,3,2,2,6	Fig. 5.40c: 1,3,2,2,6 Fig. 5.40d: 2,3,2,2,6
Exopod natatory setation	12	Fig.5.40e: 12 Fig. 5.40f: 13

Table 5.22: Continued.

Character	Kim & Hwang (1995)	Present study
Second maxilliped	**Fig. 5i**	**Fig. 5.41**
Endopod setation	0,1,6	Fig. 5.41a: 0,1,6 Fig. 5.41b: 0,1,7
Exopod natatory setation	12	Fig. 5.41c: 12 Fig. 5.41d: 13
Pleon	**Fig. 5b**	**Figs 5.42c–5.43**
Medial setae on somite 1	7	8–9

*Kim & Hwang (1995) did not separate the posterodorsal and anterodorsal carapace setation. They, instead, named this area as "anterodorsal". Therefore, the information was obtained from their illustrations as well as the text descriptions.

The most recent description of the *E. sinensis* larval development was conducted by Montú *et al*. (1996). In their study, they followed Anger (1991), and described for the first time the existence of the sixth zoeal stage. The main difference between their and the present study was the contradictions of the setation on many appendages in most of the zoeal stages. Additionally, the anterodorsal setation of the carapace, the dorsal spine setation and the coxa of the first and second maxilliped illustrations in their descriptions were completely omitted for all zoeal stages in Montú *et al*. (1996). A pre-zoea stage was briefly described by Montú *et al*. (1996). However, as emphasised before, this stage was not considered as an actual zoeal stage by the present examination. Therefore, this comparison was omitted for the current study.

In ZI, the carapace description was not completed by Montú *et al*. (1996) with exception of the ventral carapace margin and posterodorsal setae (Table 5.23). Their antenna and maxilla description did not completely match with the present report. The exopod of the maxilla was described with five setae and one long distal process by Montú *et al*. (1996). However, this was described with four setae and one long distal process in the current research. Furthermore, five setae were never observed in all

analysis in the first zoea stage in the present study and other previous descriptions. Therefore, it cannot be assumed as the variation but a misidentification.

The main differences between two studies were observed in the description of the first maxilliped in all zoeal stages. In the ZI, the only six setae arrange as 1,1,2,2 were depicted on the basis by Montú *et al*. (1996), however, 10 setae arranged as 2+2+3+3 were described by the current research. A 5-segmented endopod was described with 1,1,2,2,5 setae in their study, whereas 2,2,1,2,5 setae were illustrated in the current study. The basial setation of the second maxilliped was also overlooked in their research and only 3 setae were illustrated, whereas 4 setae were observed in the present study. Moreover, the number of setae did not change across the all zoeal stages in the present study as it did in their work. There were some contradictions between the text description of Montú *et al*. (1996) and their illustrations. One of them was the description of the endopod of the second maxilliped. The three-segmented endopod was described with 0,1,5 setae in text, but illustrated with 0,1,4 setae in their figure. However, none of them matched the current description. Another contradiction observed in their study was the pleon description. These posterodorsal marginal setae on the somites 3−5 were defined in the text, but were not shown in their figure. This setation, however, found on the somites 2−5 in the current analysis.

Table 5.23: A comparison between the zoea I stage of *Eriocheir sinensis* described by Montú *et al*. (1996) and the present study.

Character	**Montú *et al*. (1996)**	**Present study**
Carapace	**Fig. 1b**	**Figs 5.1−5.2**
Ventral margin setation	6−9 serrations	8−9 serrations
Antenna	**Fig. 4b**	**Fig. 5.3b**
Exopod setation	1 short	1 short+1 minute

Table 5.23: Continued.

Character	**Montú *et al*. (1996)**	**Present study**
Maxilla	**Fig. 8a**	**Fig. 5.5**
Coxal endite setation	3+2	4+3
Basial endite setation	4+4	5+4
Exopod setation	5+1 long distal process	4+1 long distal process
First maxilliped	**Fig. 10a**	**Fig. 5.6**
Basial setation	6: 1,1,2,2	10: 2+2+3+3
Endopod setation	1,1,2,2,5	2,2,1,2,5
Second maxilliped	**Fig. 12a**	**Fig. 5.7**
Basial setation	3: 1,1,1	4: 1+1+1+1
Endopod setation	Text: 0,1,5 Fig 12a: 0,1,4	0,1,6
Pleon	**Fig. 14b**	**Fig. 5.8**
Posterodorsal setae	Text: 2 minute setae on somites 3−5 Fig 14b: none	1 pair on somites 2−5

As stated above, the carapace setation was not described in detail in the study of Montú *et al.* (1996) and this was also an issue in the description of the ZII (Table 5.24). Two pairs of anterodorsal setae were illustrated in the present study. Another difference was the definition of the ventral carapace margin (see Table 5.24). The minute seta on the exopod of the antenna was overlooked in the ZII by Montú *et al*. (1996). A notable mistake in the study of Montú *et al*. (1996) was found in the description of the endopod of the maxillule in zoea II stage. Although, a two-segmented endopod was described correctly in their text, the figure was illustrated as 3-segmented which unusual for this appendage. Slight differences in the maxilla are shown in Table 5.24. Montú *et al*. (1996) described 9 setae arranged as 2,2,3,2 on the basis of the first maxilliped. It was clear that the third fine seta on the distal row was overlooked in their research as no variation on the basis of the second maxilliped at the second zoea stage was stated in all description studies. A 5-segmented endopod was illustrated as 2,**2**,1,2,5 in both studies. However, this was stated as 2,**1**,1,2,5 setae in their text description which can be counted as inconsistency within their study. The 3-segmented endopod of the second

maxilliped was defined with 0,1,5 setae in the study of Montú *et al*. (1996), whereas it does not match with the present research (Table 5.24). Interestingly, the number of the natatory setae of the exopod of the second maxilliped was described with five setae in their research. This was an unusual description for the second zoea stage considering previous studies and the results described here. This was described with 6 natatory setae in the current study as well as the previous reports. Furthermore, 5 setae had never been described in all previous descriptions and the current study. This was probably because of analysing the damaged appendage or it was overlooked in the investigation of Montú *et al*. (1996). Lastly, one medial seta on somite one of the pleon was overlooked in their research.

Table 5.24: A comparison between the zoea II stage of *Eriocheir sinensis* described by Montú *et al*. (1996) and the present study.

Character	**Montú *et al*. (1996)**	**Present study**
Carapace	**Fig. 1c**	**Figs 5.10−5.11**
Anterodorsal setae	0	2
Ventral carapace margin setation	5 setae	1 anterior plumose+3 posterior setae
Antenna	**Fig. 4b**	**Fig. 5.12b**
Exopod setation	1 short	1 short + 1 minute
Maxillule	**Fig. 6b**	**Fig. 5.12c**
Endopod setation	Text: 2-segmented :1,5 (1+4) Fig 6b: 3-segmented 1,0,5 (1+4)	2-segmented: 1,5 (1+4)
Maxilla	**Fig. 8b**	**Fig. 5.13**
Coxal endite setation	4−5+3	4+3
Basial endite setation	6+3	5+4
First maxilliped	**Fig. 10b**	**Fig. 5.14**
Basial setation	9: 2,2,3,2	10: 2+2+3+3
Endopod setation	Text: 2,1,1,2,5 Fig. 10b: 2,2,1,2,5	2,2,1,2,5
Second maxilliped	**Fig. 12b**	**Fig. 5.15**
Endopod setation	0,1,5	0,1,6
Exopod setation	5	6
Pleon	**Fig. 14b**	**Fig. 5.16b-d**
Medial setae on somite 1	0	1

In ZIII (Table 5.25), 4 pairs of anterodorsal setae on the carapace were overlooked by Montú *et al*. (1996) and there were slight differences in the ventral carapace setation between two studies (Table 5.25).

The exopod of the antenna was shown with 1 seta only in the ZIII as well as their ZI and ZII examination. This was described with 1 short and 1 minute setae in ZIII in the current study. More differences in the description of maxillule and the maxilla are shown in Table 5.25. An interesting setae formula was presented on the basis of the first maxilliped in the ZIII by Montú *et al*. (1996). Although it was defined with 9 setae in the ZII by them, this was illustrated with 6−7 setae arranged as 1,1,2,2 setae in the ZIII. Such a decrease in the number of setae on the basis of the first maxilliped was not observed neither in the current research nor previous studies. On the contrary, the number of the setae on the basis remained constant in ZIII in the present study (see Table 5.25). The basis of the second maxilliped was described with 4−5 setae in their examination, however, 4 setae were visualised in all zoeal stages by the current study. The fifth seta has never defined in all other studies as well.

Table 5.25: A comparison between the zoea III stage of *Eriocheir sinensis* described by Montú *et al*. (1996) and the present study.

Character	**Montú *et al*. (1996)**	**Present study**
Carapace	**Fig. 1d**	**Figs 5.17−5.18**
Anterodorsal setae	No info	4 pairs
Ventral margin setation	6−9 plumose setae	2 anterior plumose+6 posterior
Antenna	**Fig. 4c**	**Fig. 5.19b-c**
Exopod setation	1 short	1 short+1 minute
Maxillule	**Fig. 6c**	**Fig. 5.19d**
Epipod setation	1	2 setae
Maxilla	**Fig. 8c**	**Fig. 5.20**
Coxal endite setation	3+3	5+3
Basial endite setation	5+5	6+5
Exopod setation	13	9+6 plumose
First maxilliped	**Fig. 10c**	**Fig. 5.21a**
Basial setation	6−7: 1,1,2,2	10: 2+2+3+3

Table 5.25: Continued.

Character	**Montú *et al*. (1996)**	**Present study**
Second maxilliped	**Fig. 12c**	**Fig. 5.22**
Basial setation	4−5: 1,1,1,2	4: 1+1+1+1

More setal features appear on the carapace in the ZIV (Table 5.26). However, these were not described by Montú *et al*. (1996). For example, 3 pairs of setae on dorsal spine and 5 pairs of anterodorsal setae were overlooked in their revision. A remarkable difference between two studies was observed in the description of the antennule. The primary flagellum of the antennule was depicted as 1-tier with 4+2 setae. However, 3-tiers with 1,1,4 setae were clearly exhibited in the present research (Table 5.26).

Another considerable difference was the basial endite of the maxillule: 8+2 setae were illustrated in their research, whereas 11+2 setae were noted in the current examination. Similarly, the basial endite of the maxilla did not match each other (see Table 5.26). In addition, the illustrations of the coxa of the maxillipeds were overlooked in the study of Montú *et al*. (1996). Therefore, the formation of one seta on the coxa of the first maxilliped in ZIV was overlooked in their examination. In addition, the number of setae on the basis did not match with the current examination. Only 8 setae arranged as 2,1,3,2 on the basis of the first maxilliped were illustrated by Montú *et al*. (1996); it remained as 10 setae (2+2+3+3) in the present description. The definition of 5-segmented endopod by Montú *et al*. (1996) matched that of the Kim & Hwang (1995) study. However, two different setation formulae were found in the present study (see Table 5.26). Like the ZIII description of Montú *et al*. (1996), the basis of the second maxilliped was described with 4−5 setae in their ZIV description. However, the fifth seta was not observed in the present study. An interesting decrease of the number of the setae was defined in the endopod of the second maxilliped by Montú *et al.* (1996). The ZIII description of the endopod of the second maxilliped were defined with 0,1,6 setae

in their study. However, only 0,1,5 setae on the endopod were described in ZIV by Montú *et al.* (1996). This unusual variation was not observed in the current study as well as other studies (Table 5.26).

Table 5.26: A comparison between the zoea IV stage of *Eriocheir sinensis* described by Montú *et al*. (1996) and the present study.

Character	**Montú *et al*. (1996)**	**Present study**
Carapace	**Fig. 1e**	**Figs 5.24−5.26**
Dorsal spine setae	No info	3 pairs
Anterodorsal	No info	5 pairs
Ventral carapace margin setation	15 plumose setae	4 anterior plumose+7−8 posterior setae
Posterior carapace margin setae	No info	3 pairs
Antennule	**Fig. 3d**	**Fig. 5.27a**
Primary flagellum setation	1-tier: 4+2 aesthetascs	3-tiers: 1,1,4 aesthetascs
Maxillule	**Fig. 6d**	**Fig. 5.28b-c**
Epipod setation	1	2
Basial endite setation	8+2	11+2
Maxilla	**Fig. 8d**	**Fig. 5.29**
Basial endite setation	7+6	8+8
First maxilliped	**Fig. 10d**	**Fig. 5.30**
Coxal setation	Absent	1
Basial setation	8: 2,1,3,2	10: 2+2+3+3
Endopod setation	2,3,2,2,6	Fig. 5.30b: 2,2,2,2,6 Fig. 5.30c: 2,3,2,2,6
Second maxilliped	**Fig. 12d**	**Fig. 5.31**
Basial setation	4−5: 1,1,1,2	4: 1+1+1+1
Endopod setation	0,1,5	0,1,6
Pleon	**Fig. 14d**	**Fig. 5.33b**
Medial setae on somite 1	4	5

The ZV description of Montú *et al.* (1996) did not consider the carapace setation in detail (Table 5.27). Three pairs of setae on the dorsal spine, 7 pairs of anterodorsal setae and 1 pair of posterodorsal, which were illustrated in the present study, were not described in their examination. Additionally, the formation of posterior carapace margin setae was overlooked by Montú *et al*. (1996; see Table 5.27). A considerable difference was observed in the description of the ZV antennule. The primary flagellum of the

antennule was illustrated as 2-tiers with 1−2, 5 setae in the study of Montú *et al*. (1996). However, this part was defined with 3-tiers with 4,5, 5+1 setae in the present research. The coxal endite of the maxillule was depicted with 13−15 setae in their research. However, the formation of 3-tiers with 9+4+3 (16 in total) setae on the coxal endite of the maxillule was observed in the present study.

There were additional differences between two studies in the description of the maxilla (see Table 5.27). The exopod of the maxilla was defined with 40 setae in their research, whereas only 32−33 setae were depicted in the current study. Multiple variations were observed on the maxillipeds of in the present application. However, these were not stated in the research of Montú *et al*. (1996). For example, 3+1 setae and three setae were separately depicted on the coxa of the first maxilliped in the current analysis. However, the coxal setation of the first maxilliped was not figured in the examination of Montú *et al*. (1996). Nine setae arranged as 2,0,3,3 on the basis of the first maxilliped were depicted in their research. Although 10 setae arranged as 2+2+3+3 on the basis of the first maxilliped were observed from ZI-VI in the current research, 12 setae arranged as 2+3+4+3 were illustrated here on the basis in the fifth zoea stage. Clearly, variations occur on the first maxilliped in the ZV as it was also observed on the endopod of the first maxilliped. In the current study, two different setation formulae were found on 5-segmented endopod and exopod of the first maxilliped (see Table 5.27).

The basis of the of the second maxilliped was depicted with 4−5 setae in their research, however, as stated before, only four setae were observed across all zoeal stages in the present analysis. Another variation was observed on the endopod of the second maxilliped in the present study. However, this was not stated in the research of Montú *et al*. (1996; see Table 5.27). Additionally, 14 natatory setae on the exopod of the second maxilliped were illustrated in the study of Montú *et al*. (1996). However, this was found with 13 natatory setae in the present examination. The variation of the number of the

natatory setae on the exopods of the first and second maxillipeds was not mentioned in the other studies of the description of the *E. sinensis* larval development. This was partly mentioned in the study of Montú *et al*. (1996) and analysed in detail by the current analysis. Questionably, this kind of variation was not stated in the other descriptions of *E. sinensis* studies, as these studies were all described only five zoeal stages. Last of all, the 10 medial setae on somite one was depicted on the pleon in their analysis, whereas 8−9 medial setae were illustrated in the current application.

Table 5.27: A comparison between the zoea V stage of *Eriocheir sinensis* described by Montú *et al*. (1996) and the present study.

Character	**Montú *et al*. (1996)**	**Present study**
Carapace	**Fig. 2a**	**Figs 5.34−5.36**
Dorsal spine setae	No info	3 pairs
Anterodorsal setae	No info	7 pairs
Posterodorsal setae	0	1 pair
Ventral margin setation	20 plumose setae	6−7 anterior plumose+10 posterior setae with serrations
Posterior margin setae	No info	3 pairs
Antennule	**Fig. 3e**	**Figs 5.37a-b**
Primary flagellum setation	2-tiers: 1−2, 5 aesthetascs	3-tiers: 4,5, 5+1aesthetascs
Maxillule	**Fig. 6e**	**Fig. 5.38b-d**
Coxal endite setation	13−15	3-tiers: 9+4+3 total =16
Basial endite setation	14+2	16+4
Maxilla	**Fig. 8e**	**Fig. 5.39**
Coxal endite setation	12−14+5	11+4
Basial endite setation	9+9	10+11
Exopod	40	32−33
First maxilliped	**Fig. 10e**	**Fig. 5.40**
Coxal setation	Absent	Fig 5.40a: 3 Fig 5.40b: 3 +1
Basial setation	9: 2,0,3,3	Fig. 5.40a: 10: 2+2+3+3 Fig. 5.40b: 12: 2+3+4+3
Endopod setation	Text: 2,3,2,2,6 Fig 10e: 2,2,2,2,6	Fig. 5.40c: 1,3,2,2,6 Fig. 5.40d: 2,3,2,2,6
Exopod natatory setation	12	Fig. 5.40e: 12 Fig. 5.40f: 13

Table 5.27: Continued.

Character	**Montú *et al*. (1996)**	**Present study**
Second maxilliped	**Fig. 12e**	**Fig. 5.41**
Basial setation	4−5: 1,1,1,2	4: 1+1+1+1
Endopod setation	0,1,7	Fig. 5.41a: 0,1,6 Fig. 5.41b: 0,1,7
Exopod natatory setation	14	13
Pleon	**Fig. 14f**	**Fig. 5.42c−5.43**
Medial setae on somite 1	10	8−9

The studies of Montú *et al*. (1996) and present, both describe zoeal VI stage for the zoeal development of the Chinese mitten crab (Table 5.28). There were many differences between two studies in terms of the setation of the appendages of *E. sinensis* in the ZVI. As stated before, many carapace setation features were not considered by Montú *et al*. (1996). On the contrary, these features considerably changed from the ZV to ZVI in the present study. For example, 5 pairs of setae on the dorsal spine were illustrated in the current study. In addition, 9 pairs of anterodorsal setae and 4−5 pairs of setae on the posterior carapace margin were depicted by the present examination (Table 5.28).

Montú *et al*. (1996) stated that the endopod of the antenna was larger than the exopod of the antenna in ZVI. However, two different results were found in the present study. In the first result, the endopod was larger than the exopod as described Montú *et al*. (1996). In the second result, the endopod was found to be shorter than the exopod. This may be considered as a variation. Furthermore, the endopod of the antenna in ZVI were illustrated as 2-segmented in the present application. Montú *et al*. (1996) referred to the primary flagellum of the antennule with 3-tiers in ZVI. On the other hand, the formations of three tiers were stated since ZIV in the present research. 2,4,5 setae on 3-tiers respectively and aesthetascs were defined on the primary flagellum in their study. In the present research, 5,5,6 setae and aesthetascs were illustrated in detail.

There was a contradiction between the text description and the figure of the maxillule in ZVI in their research. The endopod of the maxillule was depicted as 3-segmented, but described as 2-segmented in their study. It was an obvious mistake rather than a possible variation as 3-segmented endopod of the maxillule in any zoea stage has never been found in all other studies and the present study. The coxal and basial endites of the maxilla were demonstrated with 15+4 and 11+11 setae respectively in the study of Montú *et al*. (1996). These were exhibited with 12+4 and 10+11 setae respectively in the present examination. The number of setae on the exopod of the maxilla was given with 46−48 setae and 3 simple setae on the body of the exopod in the study of Montú *et al*. (1996). Forty-four setae and 1 simple seta were illustrated in detail in the current research. Three developed, 2 small developing setae were depicted on the coxa of the first maxilliped for ZVI in the present application. However, the coxa of the first maxilliped was overlooked by Montú *et al*. (1996). Ten to 11 setae arranged as 2,1,3,2,3 on the basis of the first maxilliped were depicted in their study. However, 12 setae arranged as 2,2,4,1,3 setae were clearly demonstrated in the current application. The endopod of the first maxilliped was described as 5-segmented with 2,**3**,2,2,6 setae and figured with 2,2,2,2,6 setae in the study of Montú *et al*. (1996). In the present study, 2,**2**,2,2,6 setae were demonstrated, however, 2,**3**,2,2,6 setae are also possible as this setal formula was also found in ZVI. There was highly likely a variation in ZVI as well. Similarly, another contradiction in the study of Montú *et al*. (1996) was found in the description of the exopod of the first maxilliped. It was defined with 14 natatory setae and figured with 13 setae in their research, whereas it was illustrated with 14 natatory only in the current investigation. The basis of the second maxilliped were demonstrated with 4−5 setae in their study, however, 4 setae was detected in the current study. Fourteen natatory setae on the exopod of the second maxilliped were defined in the study of Montú *et al*. (1996), whereas only 13 natatory setae were visualised in detail in

the present application. There might be 14 natatory setae because of the variation in especially the fifth and the sixth zoeal stage of *E. sinensis*. Lastly, the number of medial setae on somite one of the pleon was demonstrated with 10 setae, whereas 10−11 setae were found in the present examination.

Table 5.28: A comparison between the zoea VI stage of *Eriocheir sinensis* described by Montú *et al*. (1996) and the present study.

Character	**Montú *et al*. (1996)**	**Present study**
Carapace	**Fig. 2b**	**Figs 5.44−5.46**
Dorsal spine setae	No info	4 pairs
Anterodorsal setae	No info	9 pairs
Posterodorsal setae	0	1 pair
Ventral margin setation	21 plumose setae	6−7 anterior plumose+10 posterior setae with serrations
Posterior margin setae	No info	4−5 pairs
Antennule	**Fig. 3f**	**Fig. 5.47**
Primary flagellum setation	3-tiers: 2,4,5 aesthetascs	3-tiers: 5,5,6 aesthetascs
Antenna	**Fig. 1b**	**Fig. 5.48**
Endopod	Larger than exopod	Fig. 5.48a: Larger than exopod Fig. 5.48b: Shorter than exopod
Maxillule	**Fig. 6f**	**Fig. 5.49b-c**
Coxal endite setation	14−15	3-tiers: 10+4+3 total = 17
Basial endite setation	15	16+4
Endopod setation	3-segmented: 1,1,4	2-segmented:1,1+4
Maxilla	**Fig. 8f**	**Fig. 5.50**
Coxal endite	15+4	12+4
Basial endite	11+11	10+11
Exopod	46−48+3	44+1
First maxilliped	**Fig. 10f**	**Fig. 5.51**
Coxal setation	Absent	3+1+1 setae
Basial setation	10−11: 2,1,3,2,3	12: 2+2+4+1+3
Endopod setation	Text: 2,3,2,2,6 Fig 10f: 2,2,2,2,6	2,2,2,2,6

Character	Montú *et al*. (1996)	Present study
First maxilliped	**Fig. 10f**	**Fig. 5.51**
Exopod setation	13−14 natatory	14 natatory
Second maxilliped	**Fig. 12e**	**Fig. 5.52**
Basial setation	4−5: 1,1,1,2	4: 1+1+1+1
Exopod natatory setation	14	13
Pleon	**Fig. 14e**	**Fig. 5.53c−5.54**
Medial setae on somite 1	10	10−11

5.5.3 Mapping setal development

One point of interest regarding the 3D images is that the developing setation of the coxal and basial endites of the maxillule (Figs 5.57−5.59) and maxilla (Figs 5.60−5.62) can be accurately mapped for successive moults (see coloured setae in Figs 5.57−5.62). In Table 5.28, for example, the setation of the coxal endite was reported as 3-tiers: 10+4+3. This terminology may require further consideration, but what it attempted to explain is that after later moults setae are expressed on the periphery of the endite as well sub-terminally anteriorly and posteriorly. For example, with reference to the basial setation of the maxillule; proximal marginal setae are absent in ZI-II (Fig. 5.57), but they are present in ZIII (1 seta; Fig. 5.58), ZIV (2 setae; Fig. 5.58), ZV (4 setae; Fig. 5.59) and without further addition in ZVI (Fig. 5.59). Similar setal mapping can also be seen in the development of the maxilla from ZI to ZVI (see Figs 5.60−5.62). For example, a simple seta on the distal coxal endite of the ZI (see Fig. 5.60) appears as a small spine (bud?), whereas it appears to be developing in ZII (see Fig. 60) and it is now slightly longer. This is seen to be a fully developed seta in ZIII (see Fig. 5.61). Similarly, the development of additional setae can also be mapped after subsequent moults from ZI-ZVI (see Figs 5.60−5.62).

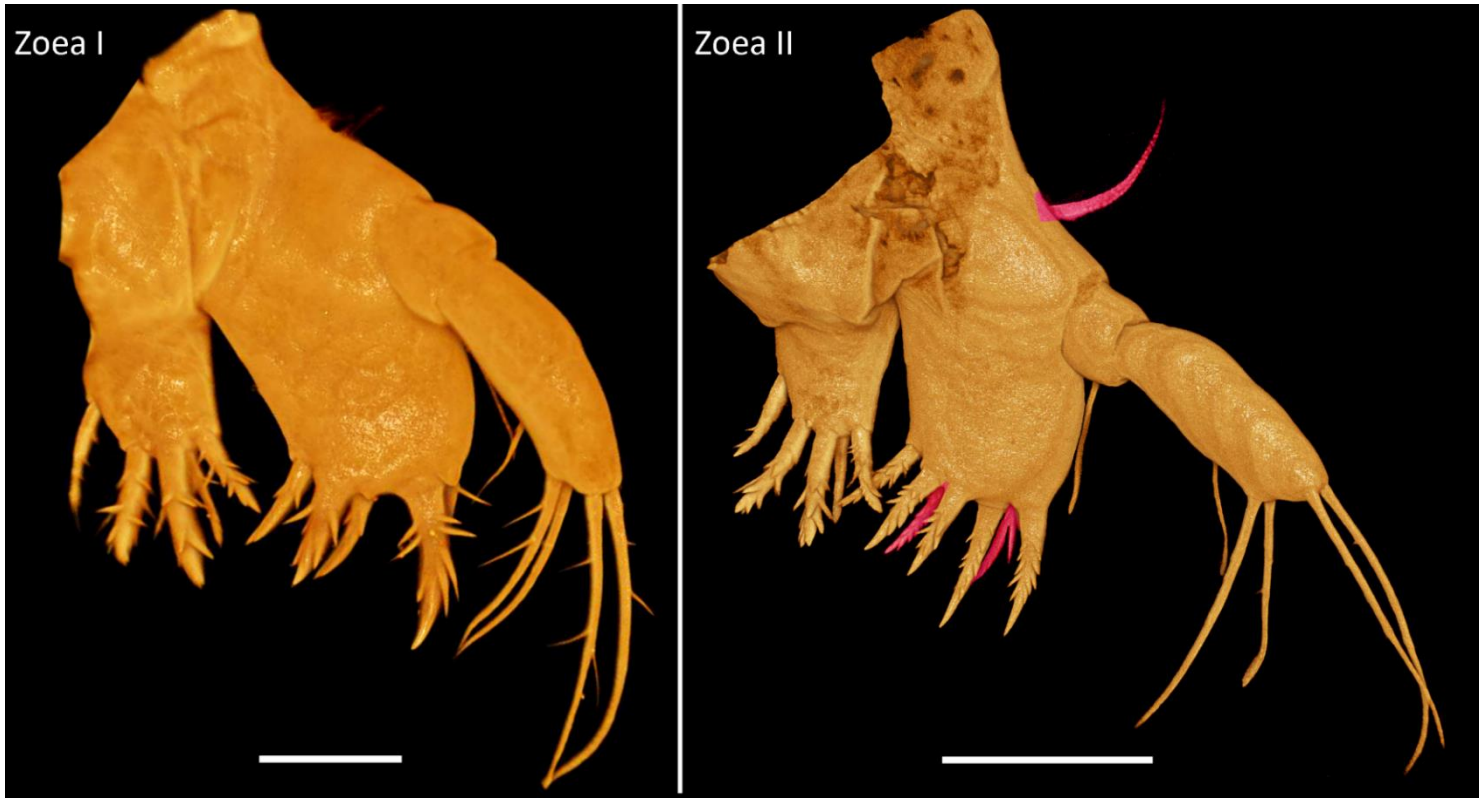

Figure 5.57: *Eriocheir sinensis*, maxillule, setae appearing after moult are coloured. Scale bars zoea I = 50 µm; zoea II = 100 µm.

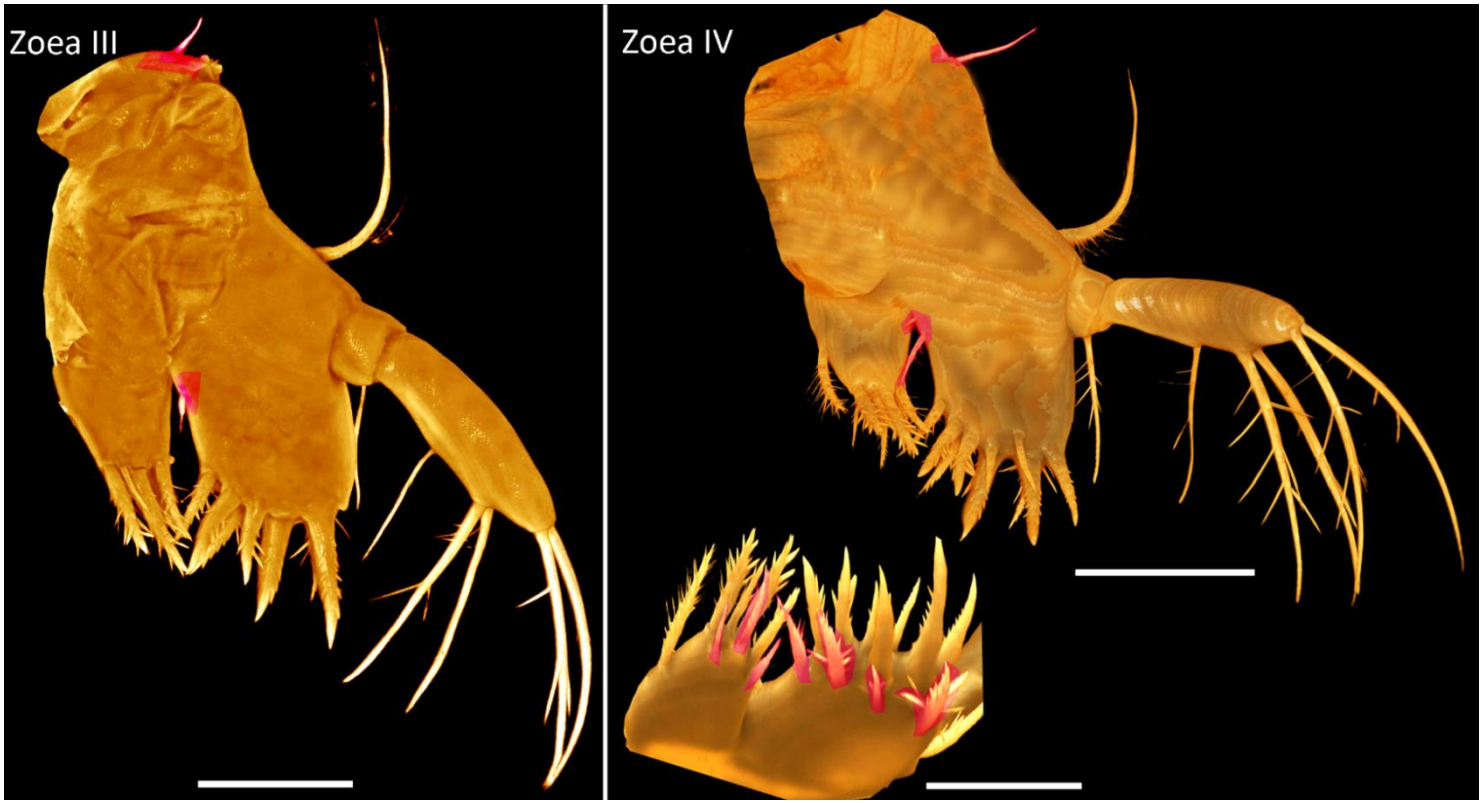

Figure 5.58: *Eriocheir sinensis*, maxillule, setae appearing after moult are coloured. Scale bars zoea III = 100 µm; zoea IV = 200 µm.

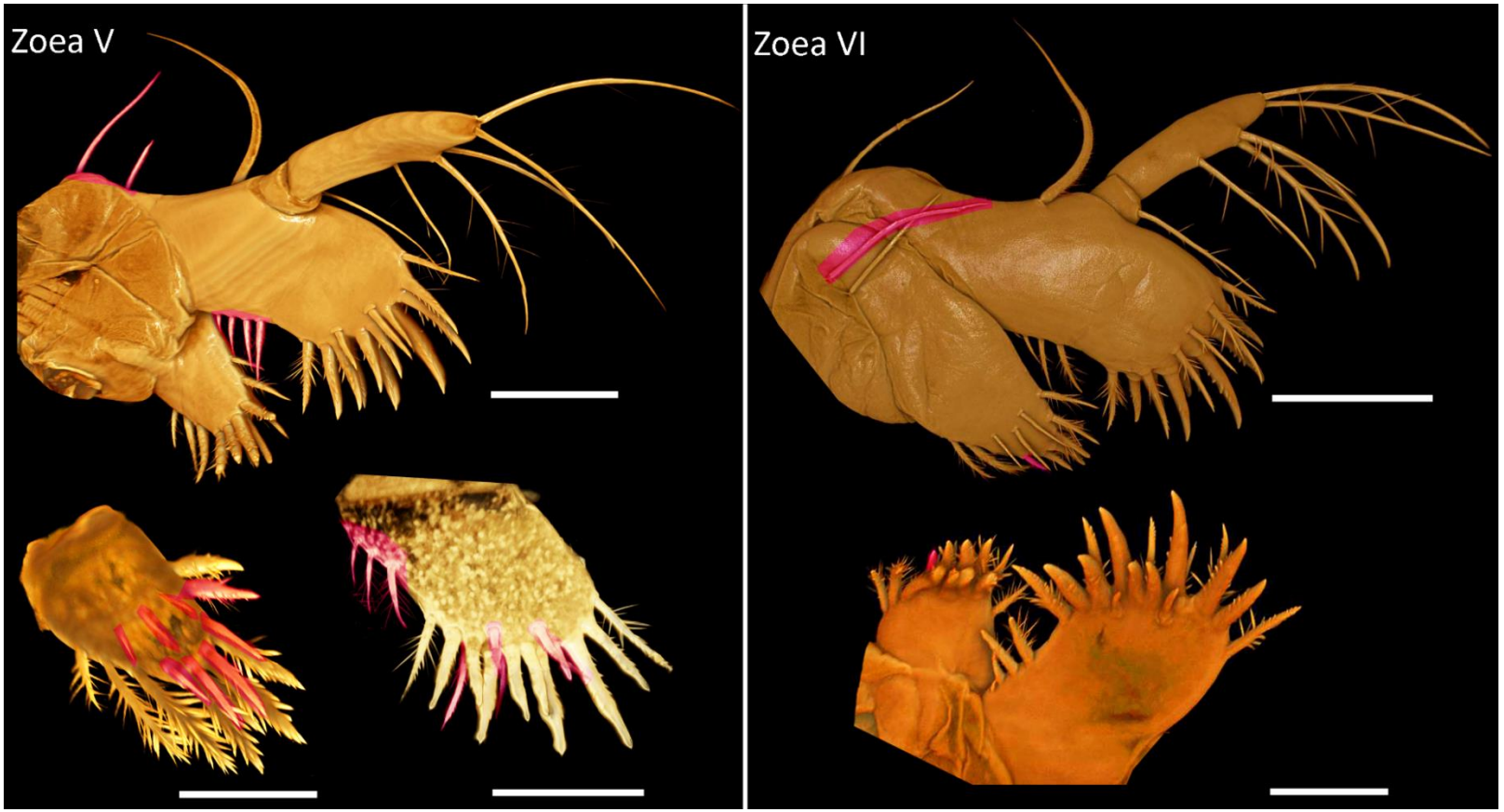

Figure 5.59: *Eriocheir sinensis*, maxillule, setae appearing after moult are coloured. Scale bars = 200 µm.

Figure 5.60: *Eriocheir sinensis*, maxilla, setae appearing after moult are coloured. Scale bars zoea I = 50 µm; zoea II = 100 µm.

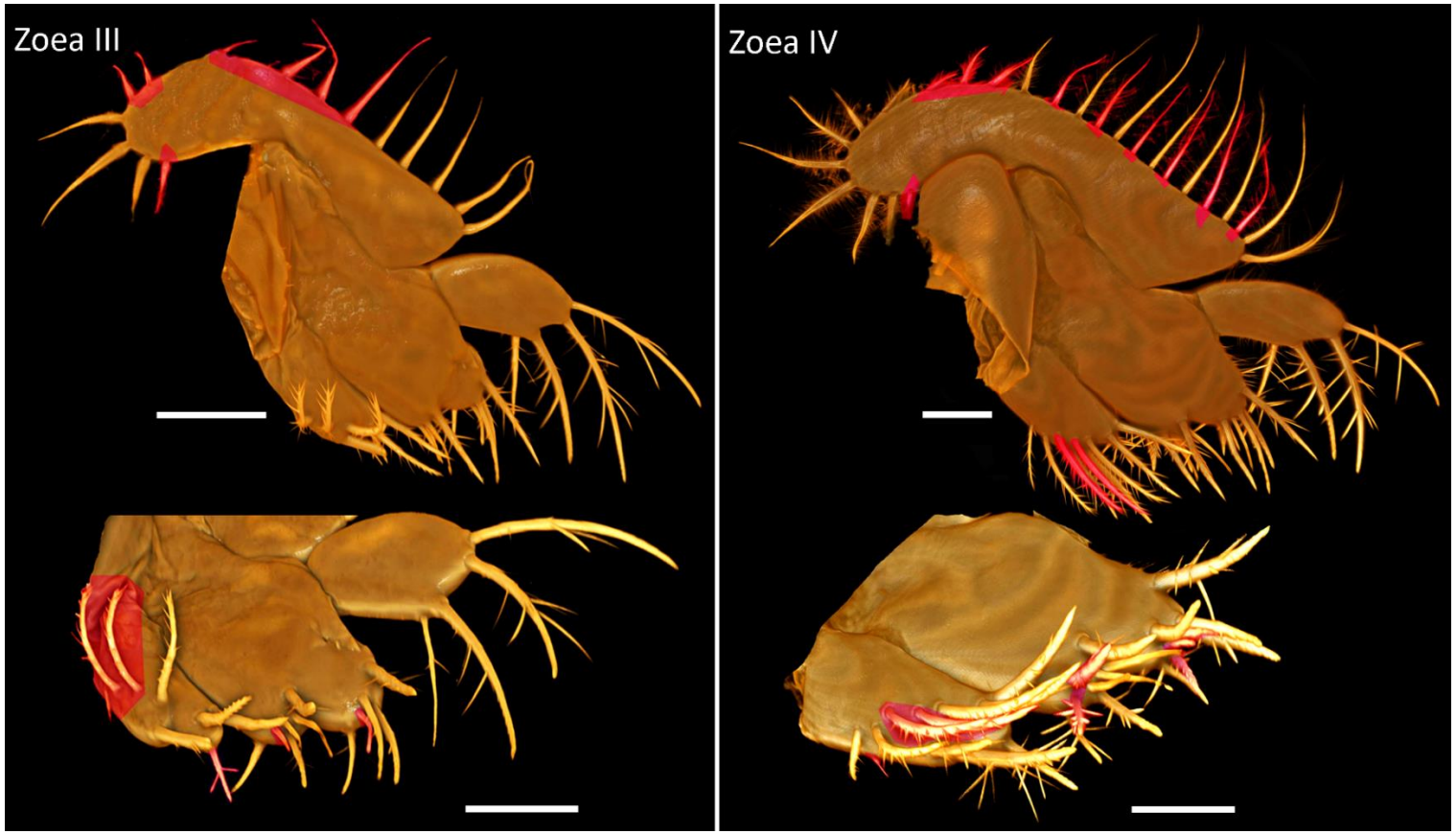

Figure 5.61: *Eriocheir sinensis*, maxilla, setae appearing after moult are coloured. Scale bars zoea III = 100 µm; zoea IV = 200 µm.

Figure 5.62: *Eriocheir sinensis*, maxilla, setae appearing after moult are coloured. Scale bars = 100 µm.

5.6 Conclusions

A common discrepancy between Chinese mitten crab studies is the number of zoeal stages. Panning (1939) stated that *E. sinensis* passed through four zoeal stages, while Schnakenbeck (1933), Hinrichs & Grell (1937), Buhk (1938), Andrea (1947), Liang *et al*. (1974 and Kim & Hwang (1995) stated five zoeal stages. Anger (1991) and Montú *et al*. (1996) highlighted that the larvae have another zoeal stage before metamorphosis into megalop in low salinity waters, therefore, an additional ZVI was identified by them. This was also the case in the present study, and the description of the ZVI was examined in detail. Some of ZVI setation of the current study occasionally matched with the definition of ZIV stage by (Panning, 1939) and other ZV descriptions.

Describing the sixth larval stage of the Chinese mitten crab has the advantage of having a better understanding of the variations between the ZIV-VI (see Tables 5.26−5.28). As discussed above, when the sixth stage is accepted as an actual larval stage, it seems to explain the many differences between the previous studies. In addition, it would give the advantage of making a much more accurate description.

Comparing the previous description of the *E. sinensis* zoeal stage with the present study helped to raise awareness on the variations occurs in the last zoeal stages. The most striking example can be seen in the study of Liang *et al*. (1974) where they described the endopod of the first maxilliped with the setal formula of 2,**2**,2,2,6. On the other hand, Kim & Hwang (1995) and Montú *et al*. (1996) described the same appendage on the same zoea stage with the setal formula of 2,**3**,2,2,6. In the present study, both setal formulae of 2,**2**,2,2,6 and 2,**3**,2,2,6 were found using more than one specimen at the same zoeal stage. The locations of the setae on the endopod described by Liang *et al*. (1974), Kim & Hwang (1995) and Montú *et al*. (1996) were observed in the current study (see Figs 5.40c-d). It appears to indicate that setal variations occur in late zoeal stages of Varuninae species. The similar situation was discussed in the study by Cuesta

et al. (2011), where the variation was found in *Geograpsus lividus* (H. Milde Edwards, 1837) which has one of the longest developmental stages with 8 zoeae. Cuesta *et al.* (2011) have proposed that if the brachyuran species has an additional zoeal stages, the changes in the setation patterns can be observed. Although, their species was assigned to Grapsidae, this similar situation has been observed in the present research using a species from the Varunidae. The reason for this can be that the Chinese mitten crab also has a relatively long zoeal development of six zoeal stages depending on some environmental conditions such as low salinity or food availability. As discussed in detail above, different setation patterns were found especially in the coxa, basis and the endopods of the first maxillipeds in ZV and ZVI. Similar variations were also found in the exopods of the first and the second maxillipeds in these later zoeal stages. Therefore, it is important to use more than one larva while making the descriptions especially in the later zoeal stages. It is important to avoid making wrong descriptions especially comparing the closely related species. As a result, there may be a necessity to re-describe the zoeal staged of other *Eriocheir* species described previously by Lee (1988), Shy & Yu (1992) and Kim & Hwang (1990) in order to consider possible variations and have a better understanding of their development precisely.

CHAPTER 6

EXAMINING GONOPODS OF BRACHYURANS USING CLSM AND MICRO-CT

6.1 Introduction

According to Ernst Mayr (1969) "the diversity of species of animals and plants is astonishing. Millions of species have been described, however, there are more species still undescribed. Each species can exist in various forms such as sexes, seasonal forms, morphs, age classes and classification of the species helps to deal with this enormous diversity".

There is no doubt that many cryptic brachyuran crab species are yet to be discovered, described and classified. The issues with such species are complex and morphological character differences are difficult to define. Consequently, molecular analyses are often required to resolve such controversies (Lai *et al*., 2010). An important diagnostic character for distinguishing closely related species of brachyuran crabs is the distal morphology of the first male gonopod (G1; see Serène, 1984; Galil & Clark, 1994; Castro, 2007, 2009). The G1 is a tubular appendage used during reproduction and is inserted into the female genital opening allowing the transfer of sperm from the male. The second male gonopod (G2) is modified further to push the sperm from the penis (Ng, 1998) along the hollow G1 and into the female (see Fig. 6.1 for a general model). The function is to optimise the sperm transfer during copulation; i.e. transition between external and internal fertilisation and due to carcinization (Türkay, 1975; Becker *et al*., 2012). The term "carcinization", also known as "brachyurization" (McLaughlin & Lemaitre, 1997), was first proposed by Borradaile (1916). This is a hypothesis where a non-crab form evolves into a crab-like form (Blackstone, 1989; McLaughlin & Lemaitre, 2000; Guinot & Quenette, 2005), where the pleon becomes folded under the thorax so that it can be closely pressed by sternum (McLaughlin & Lemaitre, 1997).

The moult of the brachyuran megalop (lobster-like appearance) to first crab stage provides an example of carcinization in that the result of this metamorphosis is that the pleon becomes folded underneath the sternum. The function of the pleon in this position is protection i.e. spawned eggs in females and the G1 in males. The male reproductive system in the true crabs co-evolved with the female genital ducts (Hartnoll, 1979; Sluys, 1992; McLaughlin & Lemaitre, 1997; Guinot & Quenette, 2005; Keiler *et al.*, 2013).

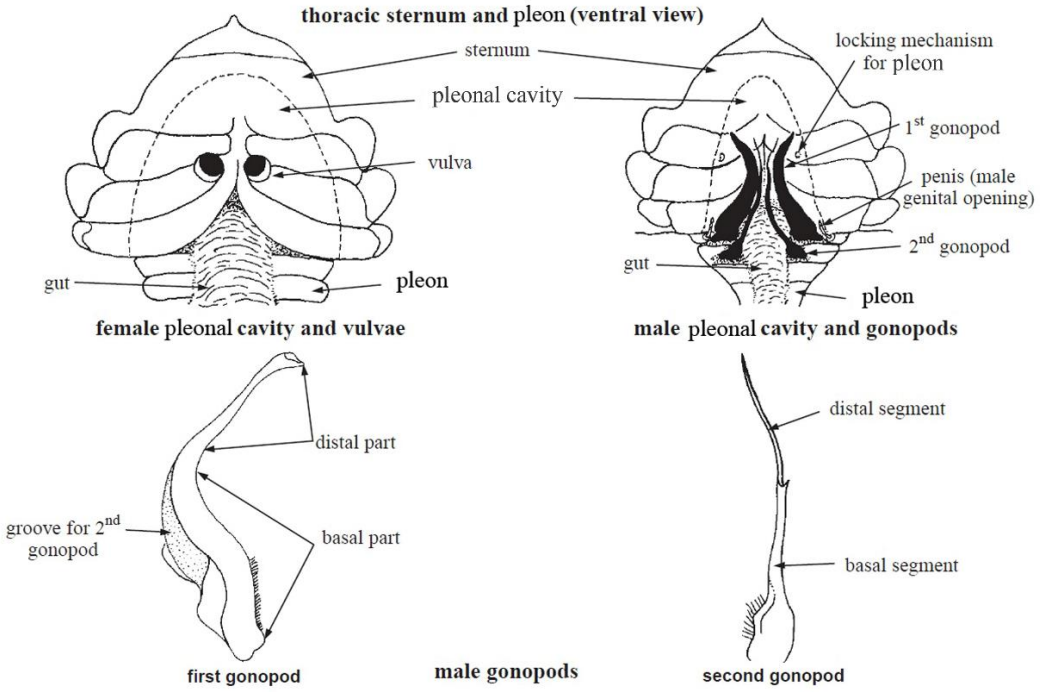

Figure 6.1: An illustration of thoracic sternum of male and female crabs showing the relationship between the pleon and the first (G1) and second (G2) gonopods of adult male crabs (after Ng, 1998; Tavares, 2002).

The distal morphology of the G1 is important, for without the correct morphological structure, the female cannot be penetrated (lock and key principal) by the male and it can take the form of a complex arrangement of setae and hooks (McLay & Becker, 2015). Furthermore, it requires a detailed study of the G1 to distinguish closely related species (Magalhães *et al.*, 2013) as the morphology can be considered to be "species-

specific" (Castro, 2009). These differences in GI and G2 ultimately lead to reproductive isolation of species (McLay & Becker, 2015).

Describing the structure of the male G1 in detail is an effective method to distinguish between closely related species (see Naser *et al*., 2012; Sakai, 2013). Previous studies depended on line drawings, as demonstrated by Serène, (1984) to illustrate G1 distal morphology of xanthoid crabs, however, this drawing technique is not always easy especially if the structure is extremely complex (see Fig. 6.2 for a detailed drawing by Galil & Clark, 1994).

Other techniques, such as scanning electron microscopy, have been used in some previous taxonomic studies of brachyuran crab groups (Apel & Spiridonov, 1998). SEM, however, requires that the G1 is dried and sputter-coated which may not be the preferred solution when dealing with valuable museum type species. CLSM (confocal laser scanning microscopy) was recently used as an alternative to SEM by Becker *et al.* (2012) but the resolution of the G1 images included in their study was somewhat limited. Their image (see Fig. 2 in Becker *et al.*, 2012) required improvement to provide greater morphological detail. This can be achieved by applying some of the methods trialled in the present study.

The aim of the present chapter is to visualise the G1 in selected cryptic species/species complex. This part of the study intends to establish that CLSM imaging techniques can be an alternative method to provide more information on G1 morphology where complex structures are particularly challenging to draw in the traditional way. It also discusses the suitability of methods regarding size of the G1 using CLSM, micro-CT and the supporting 3D software programme. In particular, the present study attempts to clarify some taxonomic controversy with respect to the gonopods of some *Eriocheir* and portunid species used here as case studies.

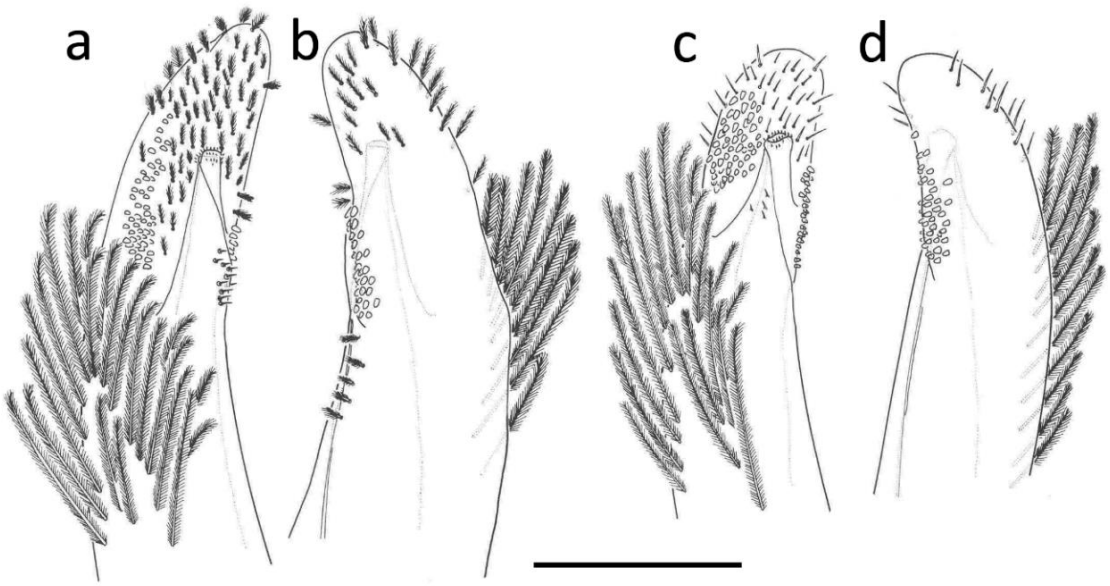

Figure 6.2: Examples of detailed drawings of male G1. (a) Dorsal view of *Ashtoret maculata* Miers, 1877. (b) Ventral view of *A. maculata*. NHM reg. number 1847.21. (c) Dorsal view of *Ashtoret miersii* Henderson, 1887. (d) Ventral view of *A. miersii*. NHM reg. number 1892.7.15.347−356. Scale bar = 1 mm (after Galil & Clark, 1994).

6.2 Visualising the gonopods of species assigned to *Eriocheir*

In order to clarify and corroborate previous studies, the present study investigated the male first gonopods of *E. sinensis*, *E. japonica* and *E. hepuensis* (see Naser *et al*. 2012) using CLSM, CLSM + Drishti and micro-CT techniques.

6.2.1 Gonopod comparison of *E. sinensis*, *E. hepuensis* and *E. japonica*

The taxa assigned to *Eriocheir* De Haan, 1835 is still under debate (see Guo *et al*., 1997; Ng *et al*., 1999; Naser *et al*., 2012; Sakai, 2013). Naser *et al*. (2012) listed six mitten crab species belonging to three genera. These were *E. sinensis* H. Milne Edwards, 1853, *E. japonica* De Haan, 1835, *E. hepuensis* Dai, 1991, *Neoeriocheir leptognatha* (Rathbun, 1913), *E. ogasawaraensis* Komai, Yamasaki, Kobayashi,

Yamamoto and Watanabe, 2006, and *Platyeriocheir formosa* Chan, Hung and Yu, 1995. The study of Naser *et al.* (2012) was based on molecular, morphological and morphometric phylogenetic analysis. Their classification was subsequently revised into four genera and seven species by Sakai (2013) as *Eriocheir* De Haan, 1835 (including *E. japonica* and *E. ogasawaraensis*, *Paraeriocheir* gen. nov. (including *P. hepuensis* and *P. sinensis*), *Platyeriocheir* Ng *et al.* 1999 (*P. formosa* and *P. guangdoga* sp. nov.) and *Neoeriocheir* Tune Sakai, 1983 (only *N. leptognatha* Rathbun, 1913). The study of Sakai (2013) was based solely on morphological characters and G1 morphology.

In contrast to the highly invasive *E. sinensis* (Lowe *et al.*, 2000), its congener *E. japonica* is almost completely restricted to its native range, Japan except for a single captured in the Columbia River, Oregon, USA (Jensen & Armstrong, 2004). *Eriocheir hepuensis*, which was previously considered as an invalid species by Tang *et al*. (2003) and Sun *et al*. (2005) or junior synonym of *E. sinensis* by Chu *et al.* (2003), has also been found outside its native range, being recorded for the first time, from Iraq and Kuwait by Naser *et al.* (2012). The specimen found in Iraq was initially recorded as *E. sinensis* but was later verified by Naser *et al.* (2012) as *E. hepuensis*. Furthermore, Tang *et al.* (2003) suggested that these three species are conspecific and should be classified as subspecies of *E. japonica*. Other studies (Guo *et al.*, 1997; Li & Zheng, 2000, 2001) stated that the Hepu mitten crab should be considered as a separate taxon. The confusion regarding the identities of these three mitten crab species is ongoing. One of the characters given importance by Naser *et al.* (2012) and Sakai (2013) was the morphology of the G1 (see Figs 6.3−6.4). The present study examines this structure by applying CLSM and micro-CT techniques to provide more details for future morphological evaluations.

Descriptions and digital illustrations of gonopods:

Figures 6.5−6.10

Eriocheir sinensis: Guo *et al*., 1997: 449, Fig. 2h; Naser *et al.*, 2012: 75, Fig. 8; Sakai, 2013: 1126, Figs 4c-d.

Eriocheir hepuensis: Guo *et al*., 1997: 459, Fig. 4h; Naser *et al.*, 2012: 75, Fig. 8; Sakai, 2013: 1126, Figs 4a-b.

Eriocheir japonica: Guo *et al*., 1997: 459, Fig. 4h; Naser *et al.*, 2012: 75, Fig. 8; Sakai, 2013: 1114−1145, Figs 2a, 3a-d.

Descriptions:

The G1 descriptions of three species *Eriocheir* were previously conducted by Guo *et al.* (1997) using line drawings. Their G1 description of *E. sinensis* was "*G1 with distal margin truncate, squarish-round when viewed laterally, distal chitinous prominence short, genital pore near distal end, tip reaching suture of sternite III/IV*" (see Fig. 6.3a). Whereas the G1 description of *E. hepuensis* "*G1 with distal margin broadly rounded, ball-like in lateral view, distal chitinous prominence slightly longer. Genital pore near half distal end, tip reaching suture of sternite III/IV*" (see Fig. 6.3b).

The description of the G1 for *E. japonica* was defined by Guo *et al.* (1997) as "*G1 long, slender, distal margin narrowly rounded, slopping shoulder shaped when viewed laterally, short, chitinous prominence, slightly curved dorsally outwards with subdistal lobe, genital opening at 1/3 distally. Tip of G1 reaching suture of sternite Ill/IV*" (see Fig. 6.3a for their drawings of G1).

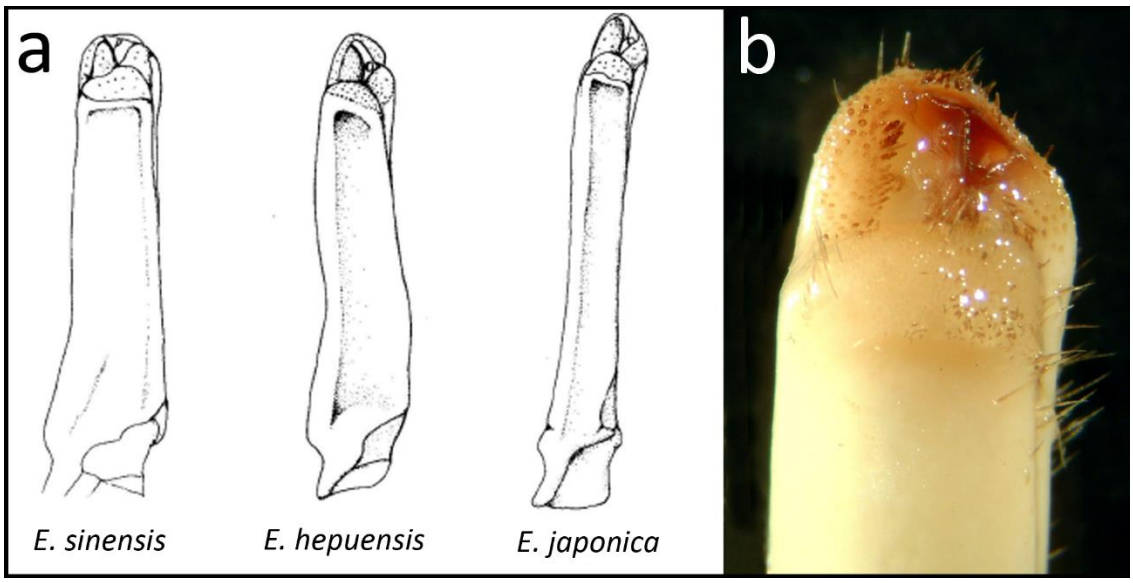

Figure 6.3: The line drawings of adult male gonopods of *Eriocheir* species. (a) First male gonopods of three mitten crab species (Guo *et al.*, 1997). (b) The image of the distal tip, with setae removed, of the first gonopod of *E. hepuensis* from Kuwait photographed by Michael Apel under a light microscope (after Naser *et al.*, 2012) and all viewed in dorsal aspect.

Sakai (2013), on the other hand, claimed that *E. japonica* was so different that the latter two species should be placed in a distinct genus. He also provided detailed descriptions of these species as well as illustrating the distal tip of these complex G1s (see Fig. 6.4).

The description of the G1 of *Paraeriocheir sinensis* (*E. sinensis*) was defined by Sakai (2013) as "*G1 stout and straight; horny endpiece broader than long, distinctly incurved around deep median hollow, and located parallel with thoracic sternites; distomesial half of male G1 broad and flat, and developed distally as high thin lid covering genital opening; distolateral half of male G1 developed as a high bank; genital opening located distomesially* behind horny endpiece*" (see Figs 6.4a, b). Whereas, the G1 of *Paraeriocheir hepuensis* (*E. hepuensis*) was described as "*G1 slender and slightly curved; horny endpiece broader than long, distinctly incurved around deep median*

hollow, and located parallel with thoracic sternites; distomesial half of male G1 broad and convex, developed distally as low thin collar around genital opening; distolateral half of male G1 developed as a high bank; genital opening located distomesially behind horny endpiece*" (see Figs 6.4c, d).

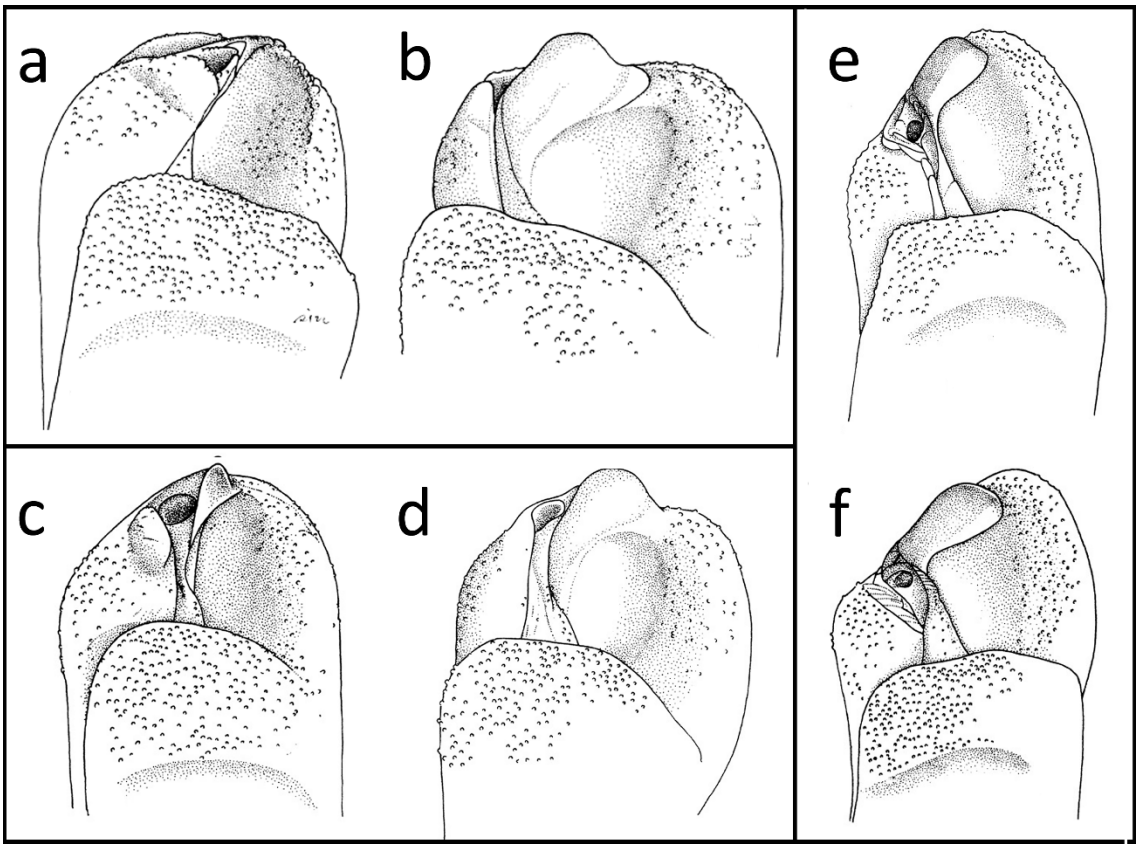

Figure 6.4: The line drawings of the distal tip of adult male gonopods (G1) of *Eriocheir* species from Sakai (2013). (a) Mesial* view of *Paraeriocheir sinensis*. (b) Lateral view of *P. sinensis*. (c) Mesial* view of *P. hepuensis*. (d) Lateral view of *P. hepuensis*. (e) Mesial* view of *E. japonica* from Hokkaido, Japan. (f) Mesial* view of *E. japonica* from Taipei, Taiwan. (after Sakai, 2013). *The term "mesial" used by Sakai (2013) refers "distal dorsal view" in the present study.

Lastly, the G1 of *E. japonica* was described as "*G1 slender and straight; G1 horny endpiece broader than long, slightly incurved around shallow median hollow, and*

located obliquely at 45° to thoracic sternites; distolateral half of male G1 developed as a low bank; distomesial half wide and flat, and developed distally as low, thin collar around genital opening; genital opening located distally at mesial half of horny endpiece" by Sakai (2013; see Figs 6.4e, f).

Describing such complex G1 structures is challenging as characters such as setal details and the locations of genital pores require accurate visualisation. Therefore, the present study provides detailed CLSM images (see Fig. 6.5), CLSM + Drishti (see Fig. 6.6) and micro-CT images (see Figs 6.7−6.9) and short videos (see videos 8−10) in addition to the descriptions of Guo *et al.* (1997) and Sakai (2013). CLSM and CLSM + Drishti images provided high resolution of the distal tips of the G1. The other G1 views i.e. lateral view proved challenging to scan one by one because these gonopods were too large for CLSM. Therefore, micro-CT experiments were used with these gonopods provided 360° images for detailed study.

Digital illustrations: see Figures 6.5−6.10

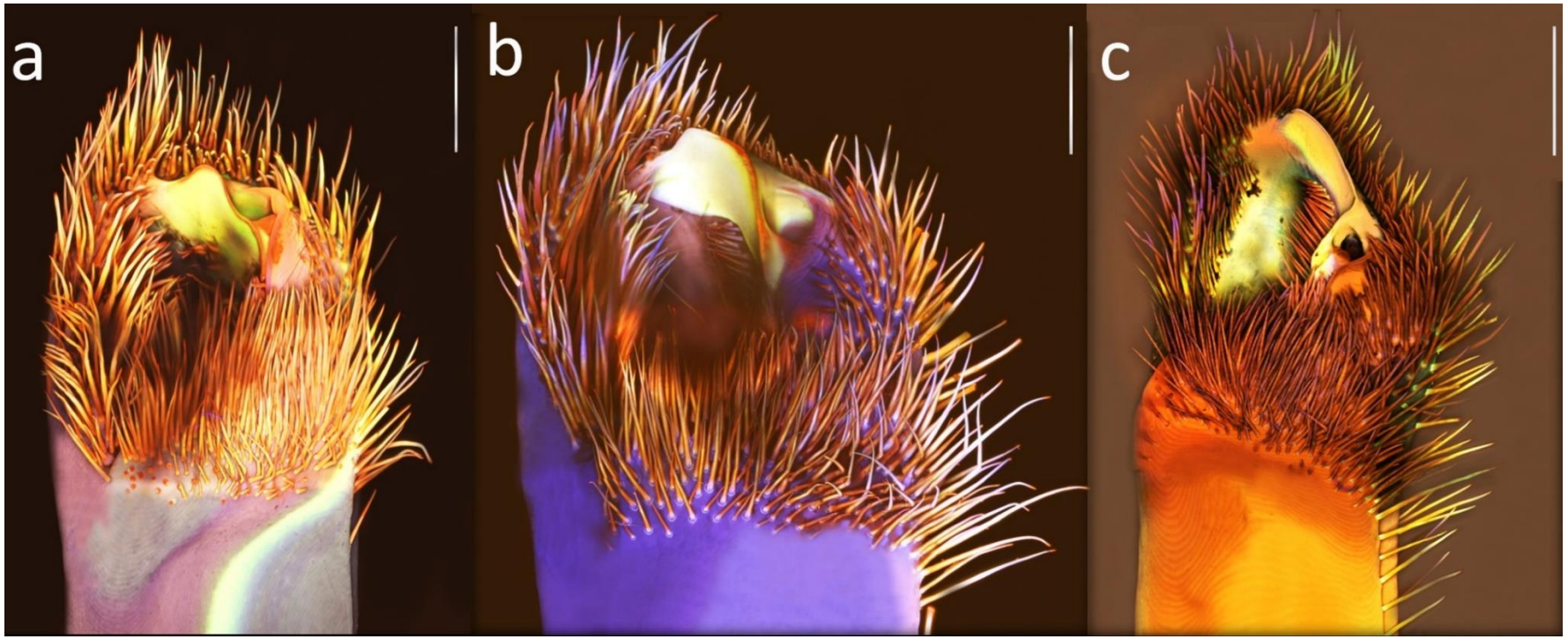

Figure 6.5: CLSM images of three species of *Eriocheir*. Distal dorsal view of: (a) *E. sinensis* from the Thames. (b) *E. hepuensis* from Shatt Al-Basrah Canal, Iraq. (c) *E. japonica* Tsushima, Japan. Images were scanned using 10× dry objective applying 'large images' option, scan area of 4×4 (a) and 4×5 (b, c) fields for image stitching. See Chapter 2 for details. Scale bars = 1000 μm.

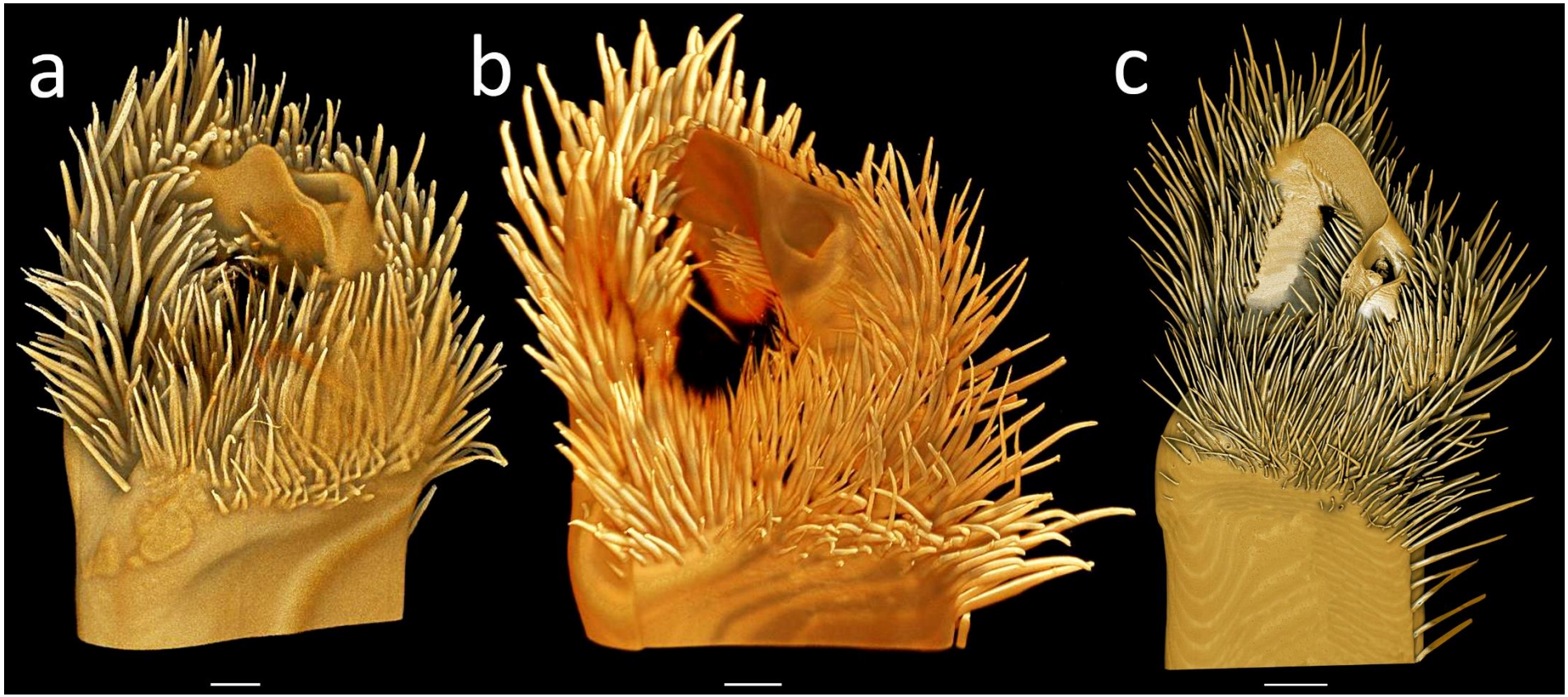

Figure 6.6: Drishti images of three species of *Eriocheir*. Distal dorsal view of: *E. sinensis* from the Thames. (b) *E. hepuensis* from Shatt Al-Basrah Canal, Iraq. (c) *E. japonica* Tsushima, Japan. Scale bars = 1000 μm.

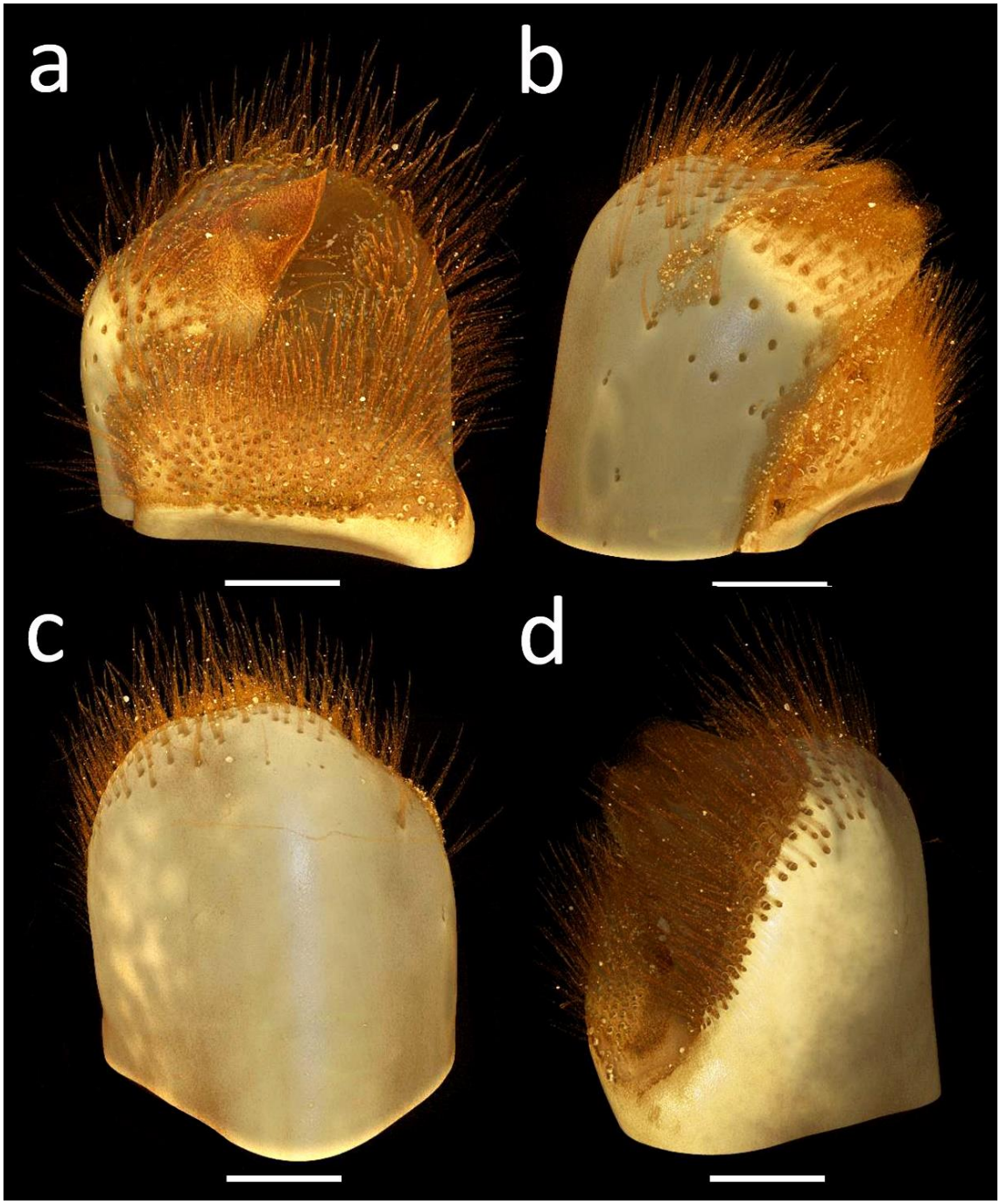

Figure 6.7: Micro-CT image of *E. sinensis*. Image rotated 90° degrees from a to d respectively. (a) Distal dorsal view. (b) Lateral view of left side. (c) Distal ventral view. (d) Lateral view of right side. Scale bars = 1000 μm. See video 8 for detailed view.

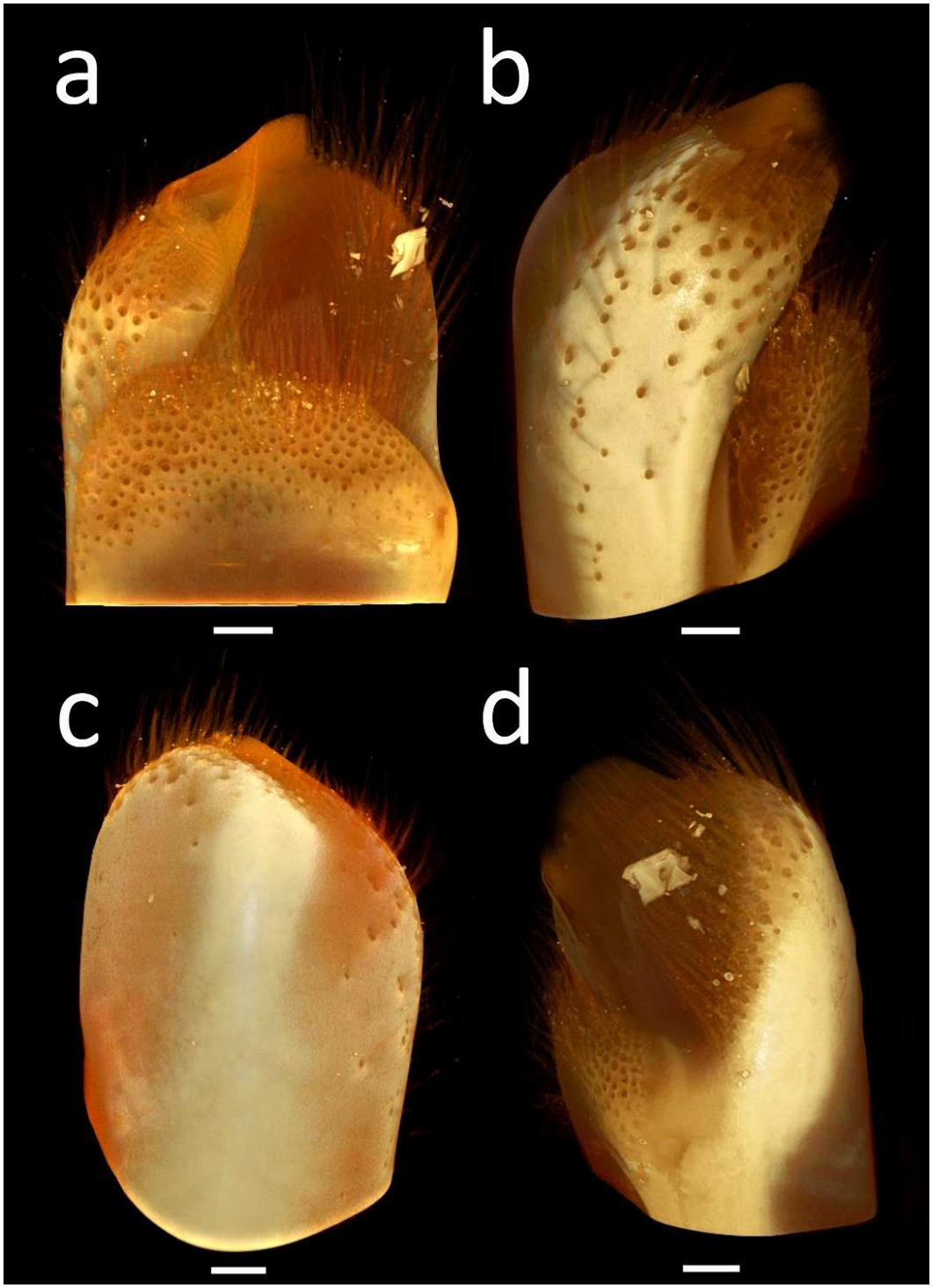

Figure 6.8: Micro-CT image of *E. hepuensis*. Image rotated 90° degrees from a to d respectively. (a) Distal dorsal view. (b) Lateral view of left side. c) Distal ventral view. (d) Lateral view of right side. Scale bars = 500 μm. See video 9 for detailed view.

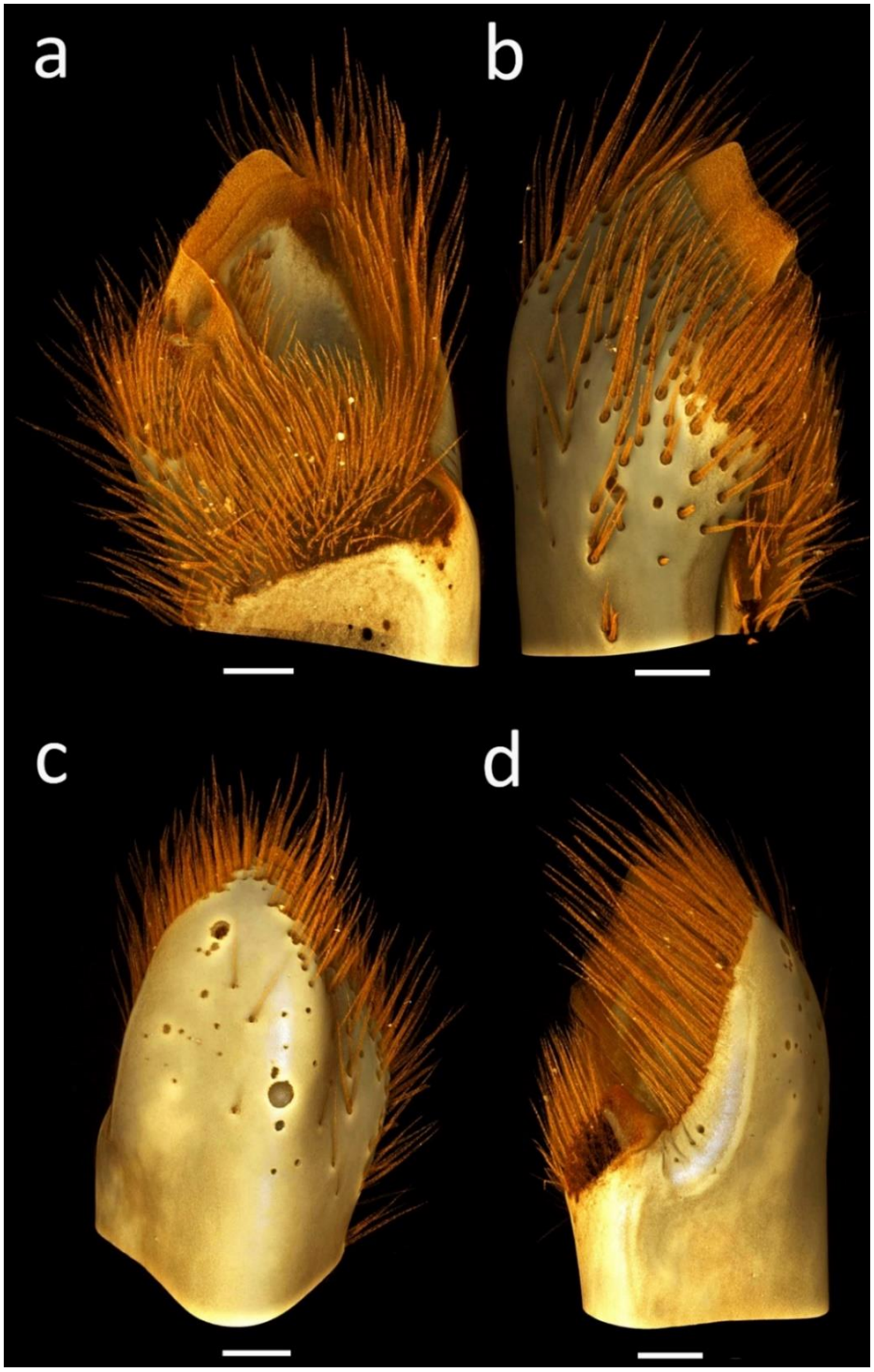

Figure 6.9: Micro-CT image of *E. japonica*. Image rotated 90° degrees from a to d respectively. (a) Distal dorsal view. (b) Lateral view of left side. (c) Distal ventral view. (d) Lateral view of right side. Scale bars = 500 μm. See video 10 for detailed view.

The micro-CT studies provided a view of the exact location of the G1 genital pore openings. The main differences between genital pore openings of the three species described by Guo *et al.* (1997) were summarised as "*genital pore very near distal end for E. sinensis, genital pore 1/2 length from distal end for E. hepuensis and genital pore at 1/3 length from the distal end for E. japonica*". The present study also reveals the exact location of genital pores and tubes of the three-species using micro-CT. The genital pores can also be visualised using CLSM, however, it did not provide sufficient data because of being surrounded by dense setae. Therefore, micro-CT data was processed with Drishti and the genital pores were visualised. The tubes were coloured using Adobe Photoshop to make them distinctive (see Fig. 6.10). The position of the tip of the genital pores visualised in the present study supports the line drawings of Sakai (2013). The genital tubes, however, were not drawn in the previous studies so that a comparison is not possible.

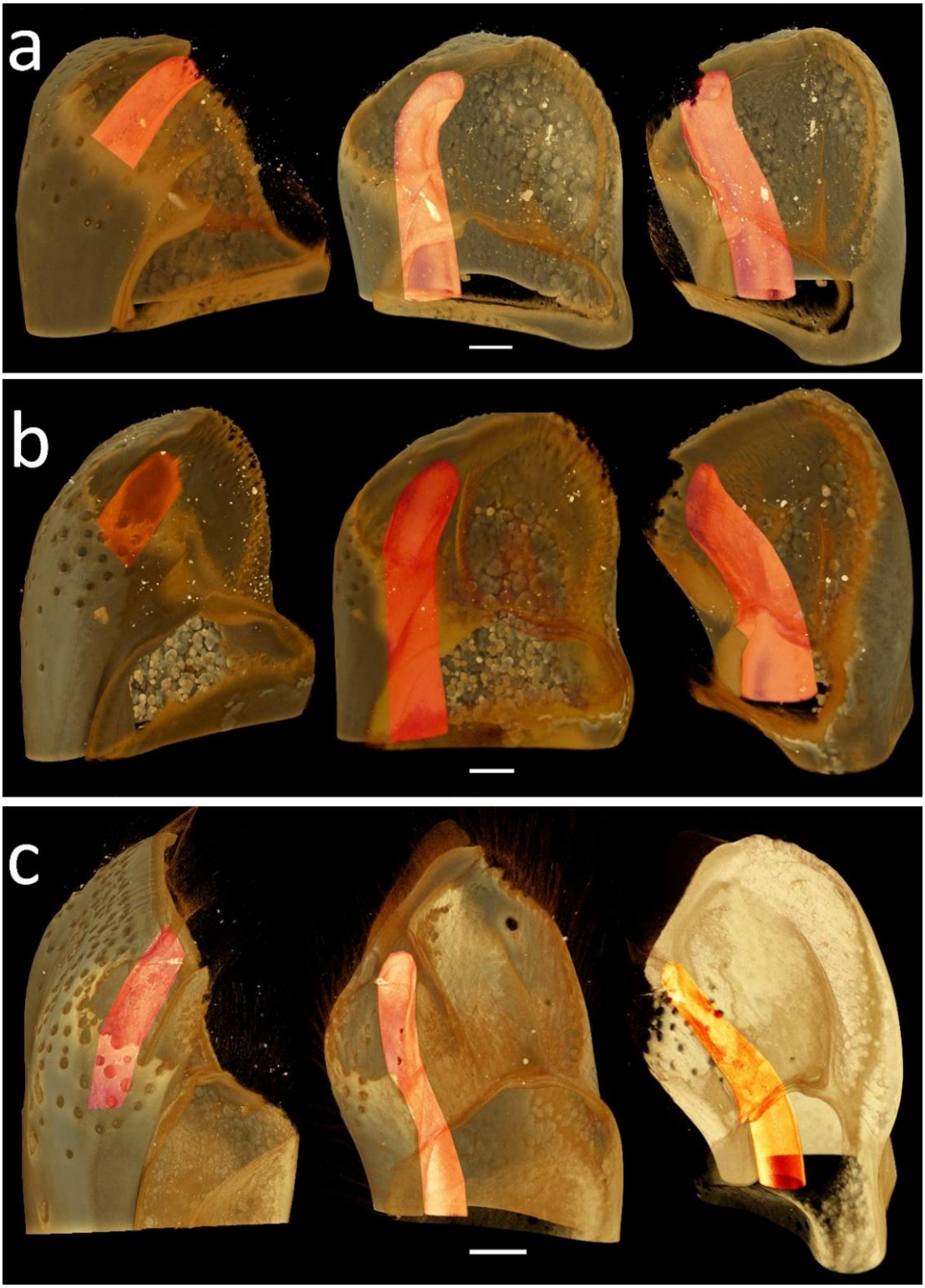

Figure 6.10: The micro-CT image of the male genital pore and tube of *Eriocheir* species from different angles. (a) *E. sinensis*. (b) *E. hepuensis*. (c) *E. japonica*. Scale bars = 500 μm.

6.2.2 Unknown species of *Eriocheir* in Europe

There is an ongoing discussion regarding the forms of *E. sinensis* occurring in Europe. Panning (1933, 1938) and Guo *et al.* (1997) distinguished six different forms of Chinese mitten crabs in German waters and named four of them as "viz. *E. sinensis* form *rostrata* Panning 1933, *E. sinensis* form *rotundifrons* Panning, 1938, *E. sinensis* form *acutifrons* Panning, 1938 and *E. sinensis* form *tribulate* Panning, 1938". Guo *et al.* (1997) questioned if any of these "forms" were *E. hepuensis* or whether there was hybridisation occurring between two *Eriocheir* species in European waters. These four-named species by Panning (1933, 1938), however, were accepted as *E. sinensis* in the study of Guo *et al.* (1997) stating that various forms were damaged samples. The two samples which were not named by Panning (1933, 1938) were, however, referred to as "varieties" by Guo *et al.* (1997) because of their morphological differences. The rate of incidence of these varieties was very low, ca. 0.056% (Guo *et al.*, 1997).

Recently, molecular studies have been undertaken to analysis *E. sinensis* populations occurring in the UK and European waters. The genetic analysis conducted by Hänfling *et al.* (2002) claimed that the Chinese mitten crab populations in Europe are genetically homogenous, whereas Herborg *et al.* (2007) suggested that most of the European populations of the Chinese mitten crab differ from each other as a result of their cluster analysis in different regions by examining genetic differentiation.

The molecular analysis (COI gene) of *E. sinensis* European populations conducted by Palero *et al.* (2016) discussed the origins of UK mitten crabs. Were they related to European populations, or the result of single or multiple invasions? Furthermore, they asked if the European populations of *Eriocheir* were all one species (see Fig. 6.11).

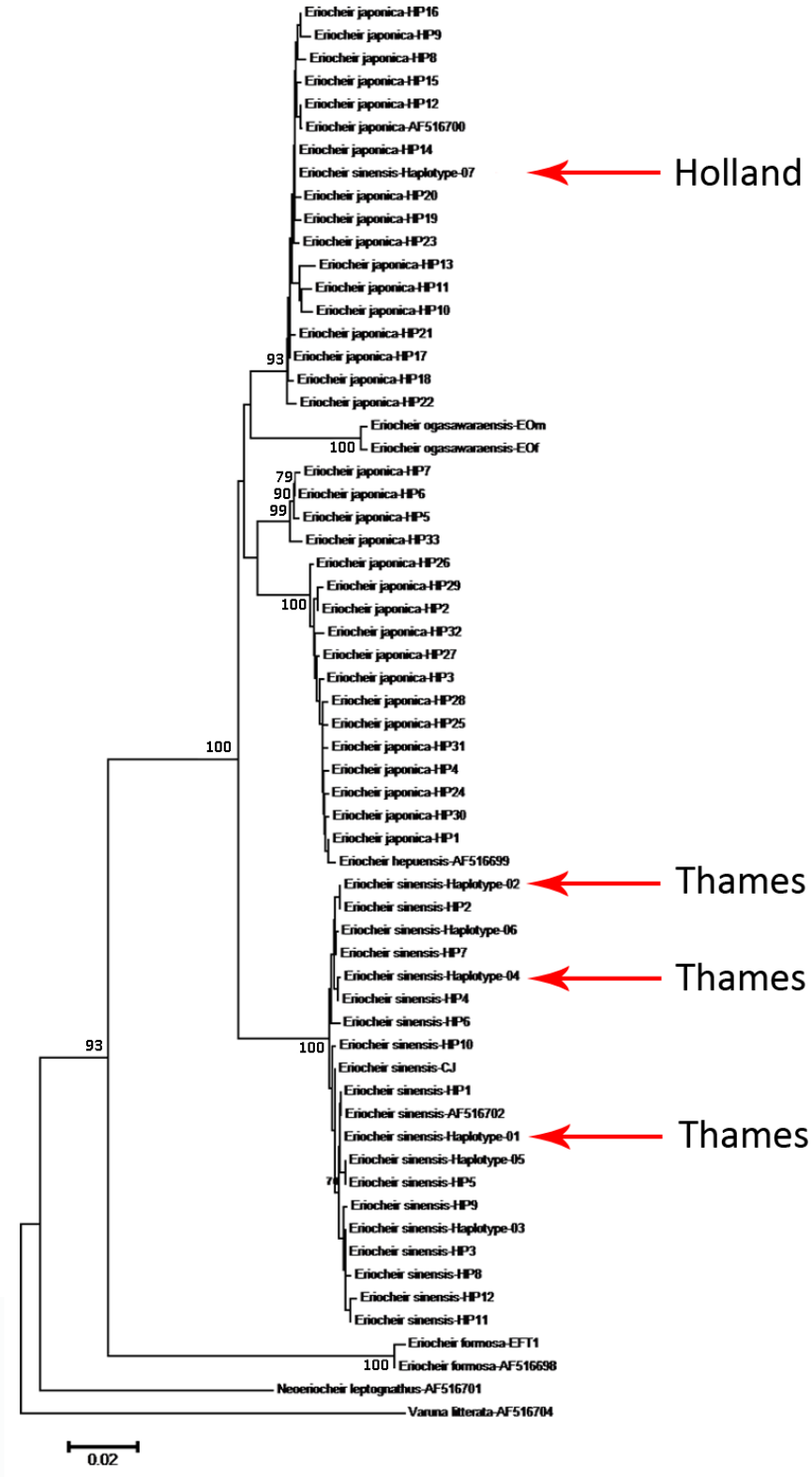

Figure 6.11: Molecular analysis using COI gene only showing evolutionary relationships of European *Eriocheir* taxa. The arrows show the haplotypes of Thames and Dutch *E. sinensis* populations with > 70% support (after Palero *et al.*, 2016).

Palero *et al.* (2016) claimed that the English and Welsh populations of the Chinese mitten crab were probably as a result of independent introductions. Their molecular analysis also showed that there were different DNA sequences of *Eriocheir* in Europe, especially with regard to the populations caught in Hollands Diep and Den Oever, Holland. Furthermore, Palero *et al.* (2016) suggested that the Thames mitten crab population were in fact *E. sinensis* whereas the samples from the Netherlands were a different species of *Eriocheir*.

The left G1 of an adult *E. sinensis* caught in the River Thames and a mitten crab specimen from Den Oever and Hollands Diep, were compared using CLSM and micro-CT. Unfortunately, due to the size of the files, Drishti could not be applied to the Dutch samples.

Digital illustrations of *Eriocheir* G1s:

Figures 6.5−6.10 and 6.12−6.15

Figures 6.5 and 6.6 show the G1 distal morphology of *E. sinensis* (Figs 6.5a, 6.6a), *E. hepuensis* (Figs 6.5b, 6.6b), and *E. japonicus* (Figs 6.5c, 6.6c). The G1s of all three species are distinct and diagnostic.

The molecular study of Palero *et al.* (2016; see Fig. 6.11) showed that the two Thames populations comprised 3 Haplotypes 1, 2, 4 and all of these were referred to *E. sinensis* (see G1 Figs 6.5a, 6.6a, 6.12a). From Palero *et al*. (2016; see Fig. 6.11) the *E. japonica* clade is referred to by nodes HP5-7 and HP33 and its G1 is considered here to be Figures 6.5c, 6.6c. The *E. hepuensis* clade, including many misidentifications of *E. japonica*, is represented by Palero *et al*. (2016; see Fig. 6.11) by specimen AF516699 and G1 Figures 6.5b, 6.6b. The supposed "*E. sinensis*" from the Netherlands (Den

Oever and Hollands Deep) is not clustered within the Thames *E. sinensis*, but appears to be a separate clade as Haplotype 7 together with another group of misidentifications of *E. japonica*. From the examination of G1s from these three populations, the present study indicates that the gonopod morphology supports the results of Palero *et al.* (2016). The G1 morphology of *E. sinensis* from the Thames (Figs 6.5a, 6.12a) differs from the two Dutch examples (Fig. 6.12b, c). The Dutch G1s, although not taken exactly from the same view, appear similar and suggest they are both the same species *Eriocheir*, but not *E. sinensis*. The Dutch *Eriocheir* is either an undescribed species (a cryptic species) or an already described species that has not been recognised and is currently synonymised. The micro-CT investigation of the Dutch specimens were performed and illustrated in Figures 6.13−6.15.

Digital illustrations: see Figures 6.12−6.15

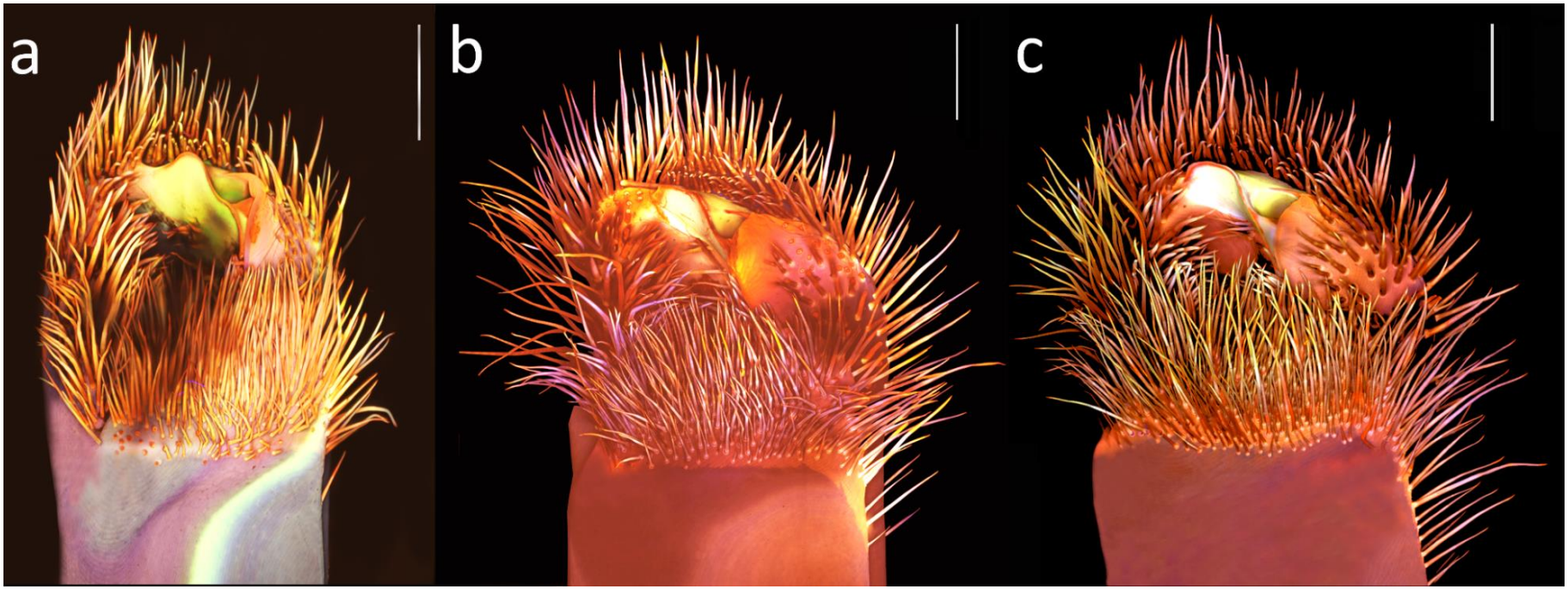

Figure 6.12: CLSM images of three species of *Eriocheir*. Distal dorsal view of: (a) *E. sinensis* from the Thames. (b) Unknown species from Den Oever. (c) Unknown species from Hollands Diep. Images were scanned using 10× dry objective applying 'large images' option, scan area of 4×4 (a) and 5×5 (b, c) fields for image stitching. Scale bars = 1000 µm.

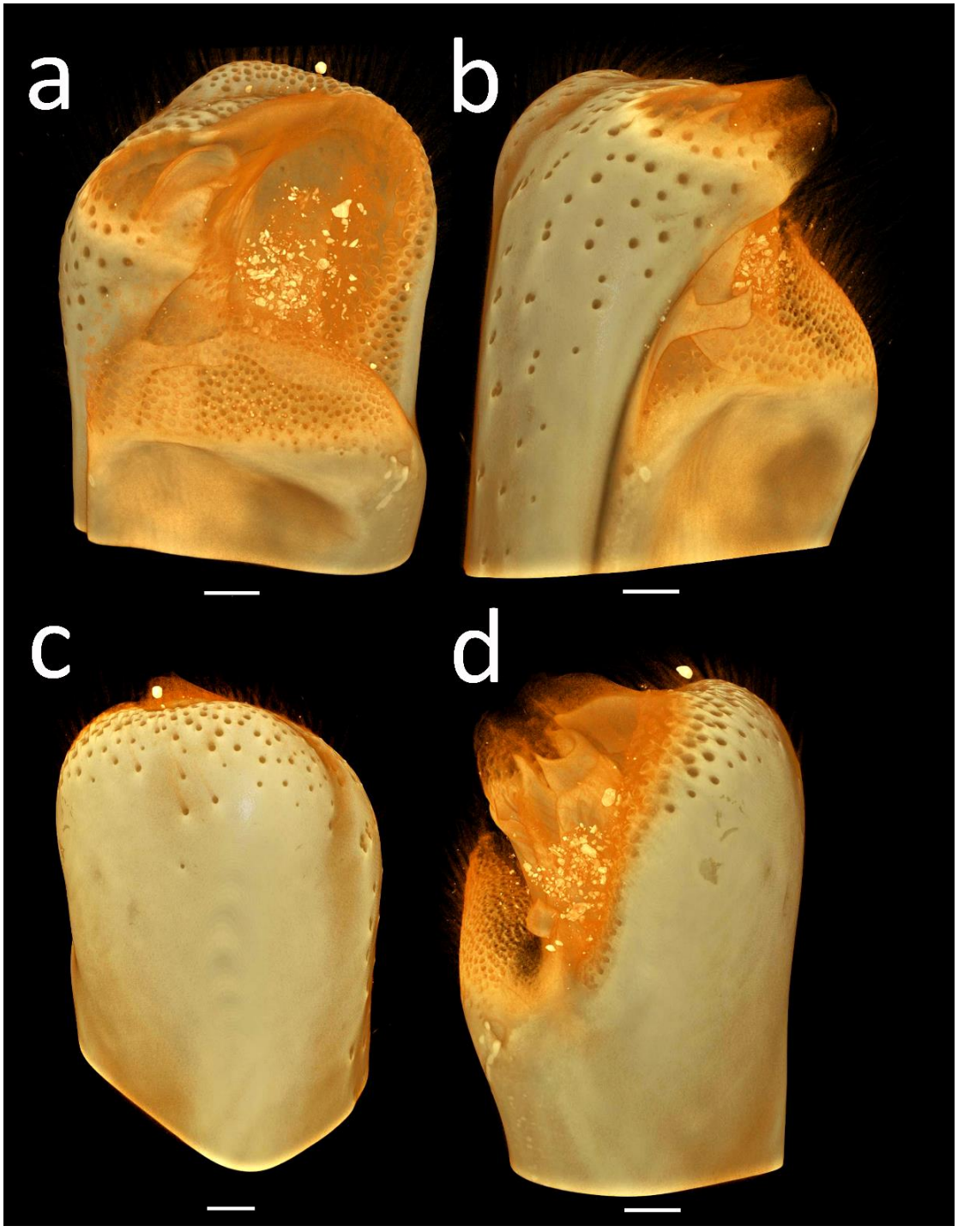

Figure 6.13: Micro-CT image of unknown *Eriocheir* from Den Oever, Holland. Image rotated 90° degrees from a to d respectively. (a) Distal dorsal view. (b) Lateral view of left side. c) Distal ventral view. (d) Lateral view of right side. Scale bars= 500 μm. See video 11 for detailed view.

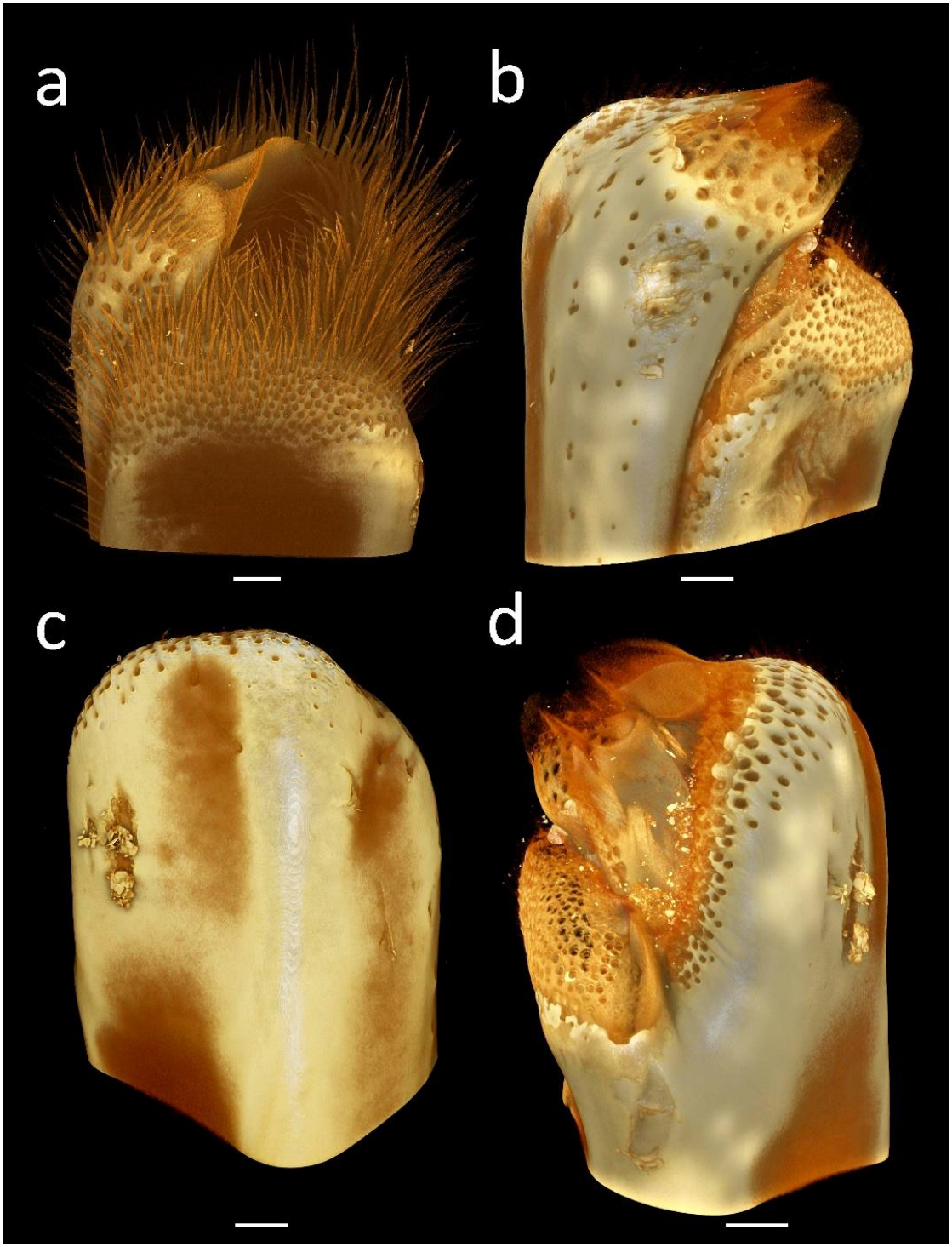

Figure 6.14: Micro-CT image of unknown *Eriocheir* from Hollands Diep, Holland. Image rotated 90° degrees from a to d respectively. (a) Distal dorsal view. (b) Lateral view of left side. (c) Distal ventral view. (d) Lateral view of right side. Scale bars= 500 µm. See video 12 for detailed view.

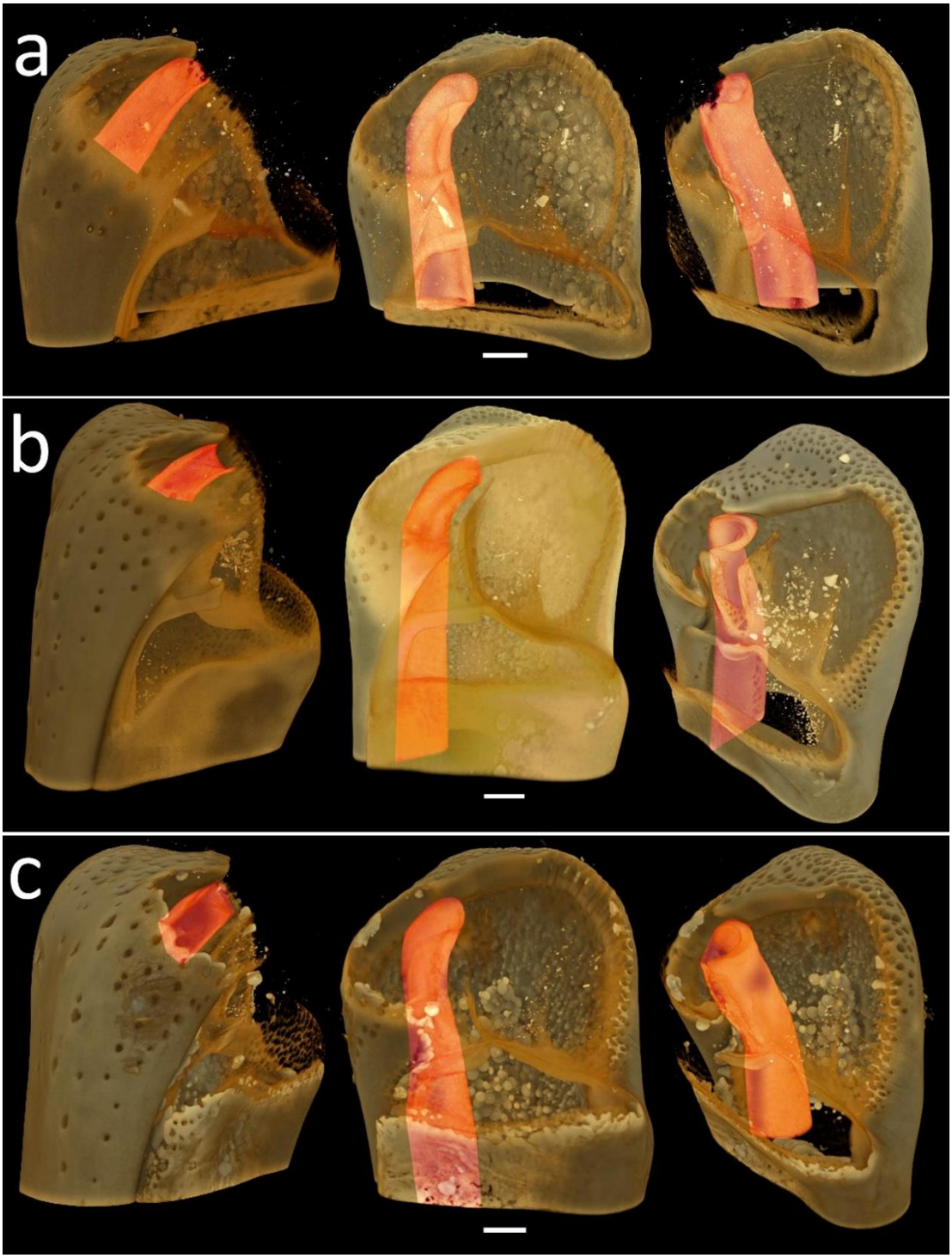

Figure 6.15: The micro-CT image of the genital pore and tube of *Eriocheir* species from different angles. (a) *E. sinensis* from the Thames. (b) Unknown *Eriocheir* from Den Oever, Holland. (c) Unknown *Eriocheir* from Hollands Diep, Holland. Scale bars = 500 μm.

6.3 *Libystes nitidus* A. Milne Edwards, 1867 (Crustacea: Brachyura: Portunidae): A case study of visualising G1s

Relatively small sized gonopods can be scanned using CLSM. The resolution of the confocal microscope and the careful preparation of such samples allow the production of high quality images of gonopods. Indeed, Becker *et al.* (2012) used CLSM and other techniques for their investigation of the male copulatory systems of pea crabs. Using European pea crabs, they showed that the small sized G1 was suitable for confocal imaging, however the resolution of their images, was not of sufficient quality as they only used basic techniques to visualise their materials (see Fig. 6.16).

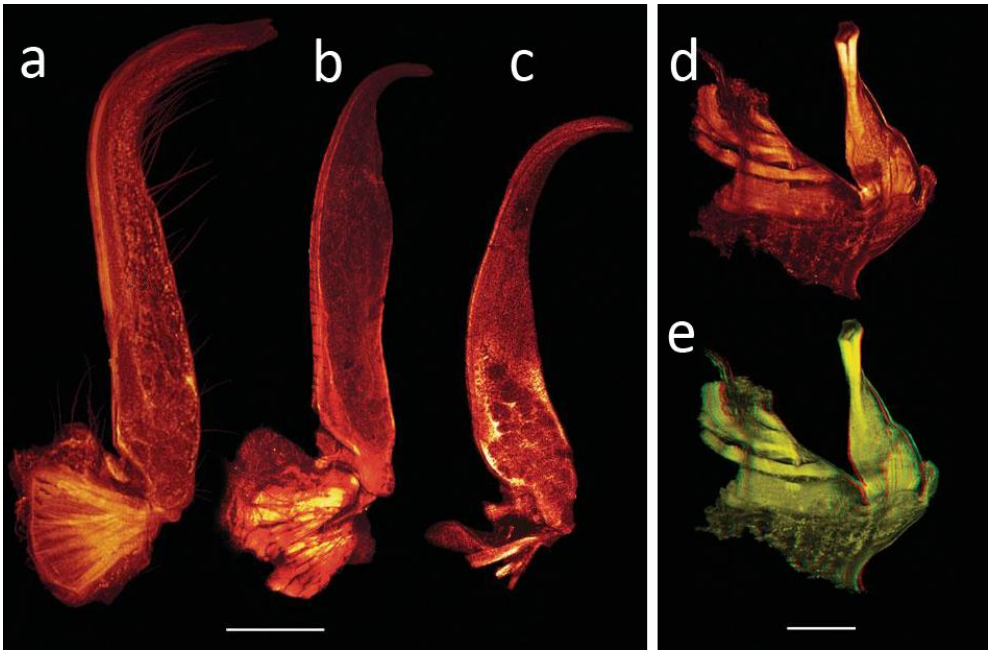

Figure 6.16: Confocal images of the gonopods of European pea crabs. (a) G1 of *Nepinnotheres pinnotheres* Linnaeus, 1758. (b) G1 of *Pinnotheres pisum* Linnaeus, 1767. (c) G1 of *Pinnotheres pectunculi* Hesse, 1872. (d) and (e) G2 of *P. pisum*. Scale bars a-c = 300; d-e = 100 μm (after Becker *et al.*, 2012).

As detailed in the material and methods section of the present study (see Chapter 2), the small sized gonopods can fit into a well which is produced from plastic reinforcement

rings. In addition, staining the G1 also improved imaging quality which helped in adjusting the fluorescent level between the thick and thin structures along the gonopods. The application of 3D reconstruction software, Drishti, produced quality images of G1 morphology.

In the present study, this technique was applied to the G1 of *Libystes nitidus* A. Milne-Edwards, 1867 which was previously illustrated using line drawings (see Crosnier, 1962: 14, Fig. 252; Serène, 1966, Figs 1−6). The locality of the specimens examined by Crosnier (1962) was from Mayotte, Comores, whereas Serène (1966) did not provide any details for his specimens and Apel & Spiridonov (1998, Fig. 6d, e) referred their Arabian Gulf material to *L.* aff. *nitidus*. The G1s of these three studies are reproduced here in Figure 6.17. Crosnier (1962: 148) referred his material from Mayotte, Comores to the type female of *L nitidus* from Zanzibar deposited in the Muséum d'Histoire Naturelle by A. Milne-Edwards (1867). The G1s figured by Serène (1966; Fig. 6.17b-d) were of two distinct forms. One of these (see Fig. 6.17d) was similar to that of Crosnier (1962; Fig. 6.17a). Although Serène (1966) noticed the morphological differences in his samples, he attributed the G1 diversity to having different sized adult specimens. Apel & Spiridonov (1998), however, asserted that the G1 of their specimen from the Arabian Gulf (see Fig. 6.17e) is distinct from those of Crosnier, 1962; Fig. 6.17a and Serène, 1966; see Fig. 6.17b-d). They also noted that their drawings were similar to the specimen that was examined by Serène (1966) and obtained from the Red Sea (see Fig. 6.17b). In the study of Apel & Spiridonov (1998), they explained why Serène (1966) accepted his species from two different localities as being the same (compare Fig. 6.17b, c and 6.17d), i.e. having different sized adult specimens. They emphasised that "*the differences between the two forms are too fundamental to be age dependent*". Therefore, the explanation of Serène (1966) was not accepted by Apel & Spiridonov (1998). They also examined NHM material from the Red Sea (registration number

1934.1.17.114) and Maldives (registration number 1991:156) and they stated that the G1s of the Red Sea and the Arabian Gulf samples were identical and completely different from the crabs from the Maldives. Furthermore, the G1 of Maldives material compared well with that of Crosnier (1962: 14, Fig. 252; Fig. 6.17a) and Serène (1966, Figs 5−6; Fig. 6.17d), whereas the structure of G1 of the Red Sea and Arabian Gulf specimens are almost identical and similar to that of Serène (1966, Figs 1−4; Fig. 6.17c, d). Apel & Spiridonov (1998) referred their Arabian Gulf material to *L.* aff. *nitidus*.

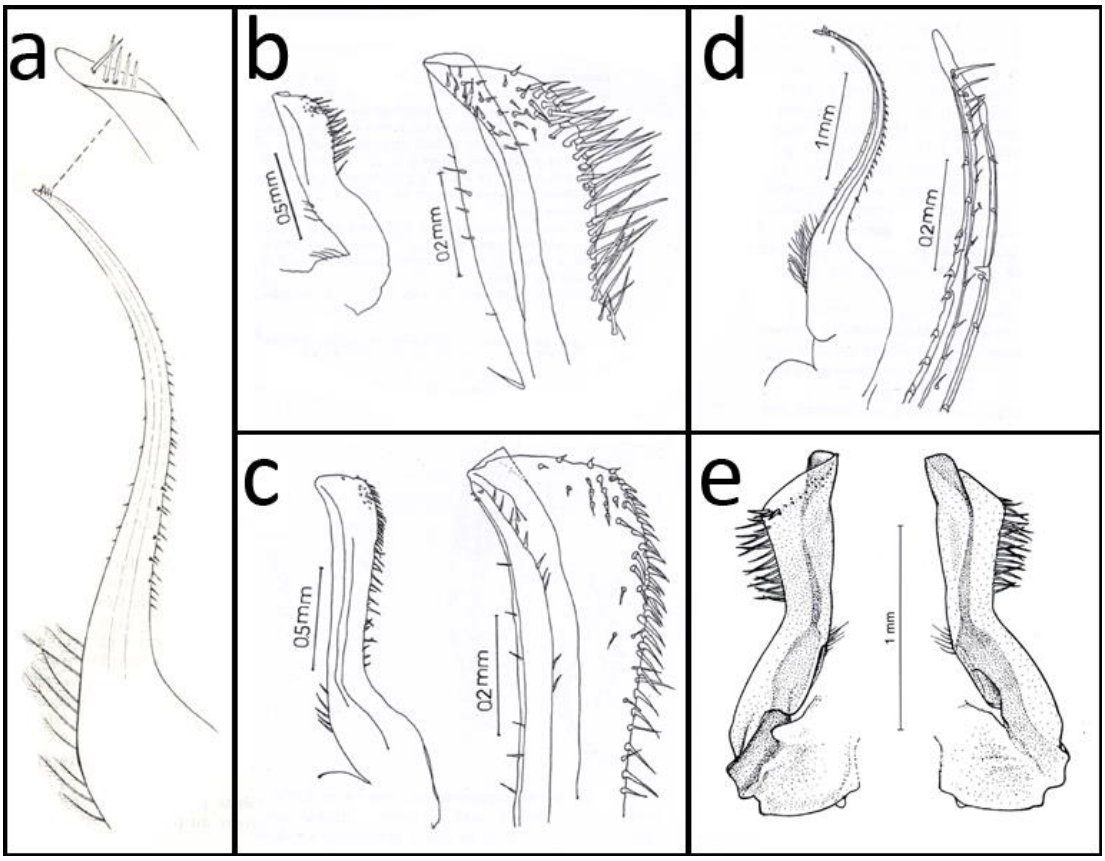

Figure 6.17: The line drawings of the G1 of *Libystes nitidus* A. Milne Edwards, 1867 from different studies and localities. (a) Sample from the Maldives described by Crosnier (1962). (b) Sample from male 5×3 mm by Serène (1966). (c) Sample from male 7×4 mm by Serène (1966). (d) Sample from male 11.5×7 mm by Serène (1966). *L.* aff. *nitidus* (e) Sample from the Arabian Gulf described by Apel & Spiridonov (1998). (Images after Crosnier, 1962; Serène, 1966; Apel & Spiridonov, 1998).

Digital illustrations of *L. nitidus* G1:

In the present study, specimens identified as *L. nitidus* from the Sudanese Red Sea (NHM reg. number: 1934:117.114) and the Maldives (NHM reg. number: 1991:156.1) were re-examined using CLSM + Drishti. After visualising the male gonopods from the two localities, the G1s were found to be completely different (Fig. 6.18). The G1 from the Maldives material compares (Fig. 6.18c, d) well with those figured by Crosnier (1962: 14, Fig. 252; Fig. 6.17a) and Serène (1966, Figs 5−6; Fig. 6.17d) and is considered to be *L. nitidus* A. Milne Edwards, 1867 (confirmed Vassily Spiridonov, pers. comm.). The G1 from the Red Sea (Fig. 6.18a, b) compares well with that of Serène (1966, Figs 1-4; Fig. 6.17d), is different from the of *L. nitidus* and is considered to be an undescribed species of *Libystes* (confirmed Vassily Spiridonov, pers. comm.). The G1 of *L.* aff. *nitidus* figures by Apel & Spiridonov (1998, Fig. 6d, e; Fig. 6.17e) is different from the Red Sea and Indian Ocean material and is probably another undescribed species. But this requires further clarification and CLSM scanning. The G2s of the Red Sea and Maldives specimens appear to be similar if not identical (Fig. 6.19).

Libystes nitidus Crosnier, 1962: 149, Fig. 252; Serène, 1966: 995−996, Figs 5−6; Present study Fig. 6.18a, b.

Libystes n. sp. Red Sea material, NHM reg. 1934:117.114.

Libystes n. sp.? Apel & Spiridonov, 1998: 177, Figs 6d-e.

Digital illustrations: see Figures 6.18−6.19.

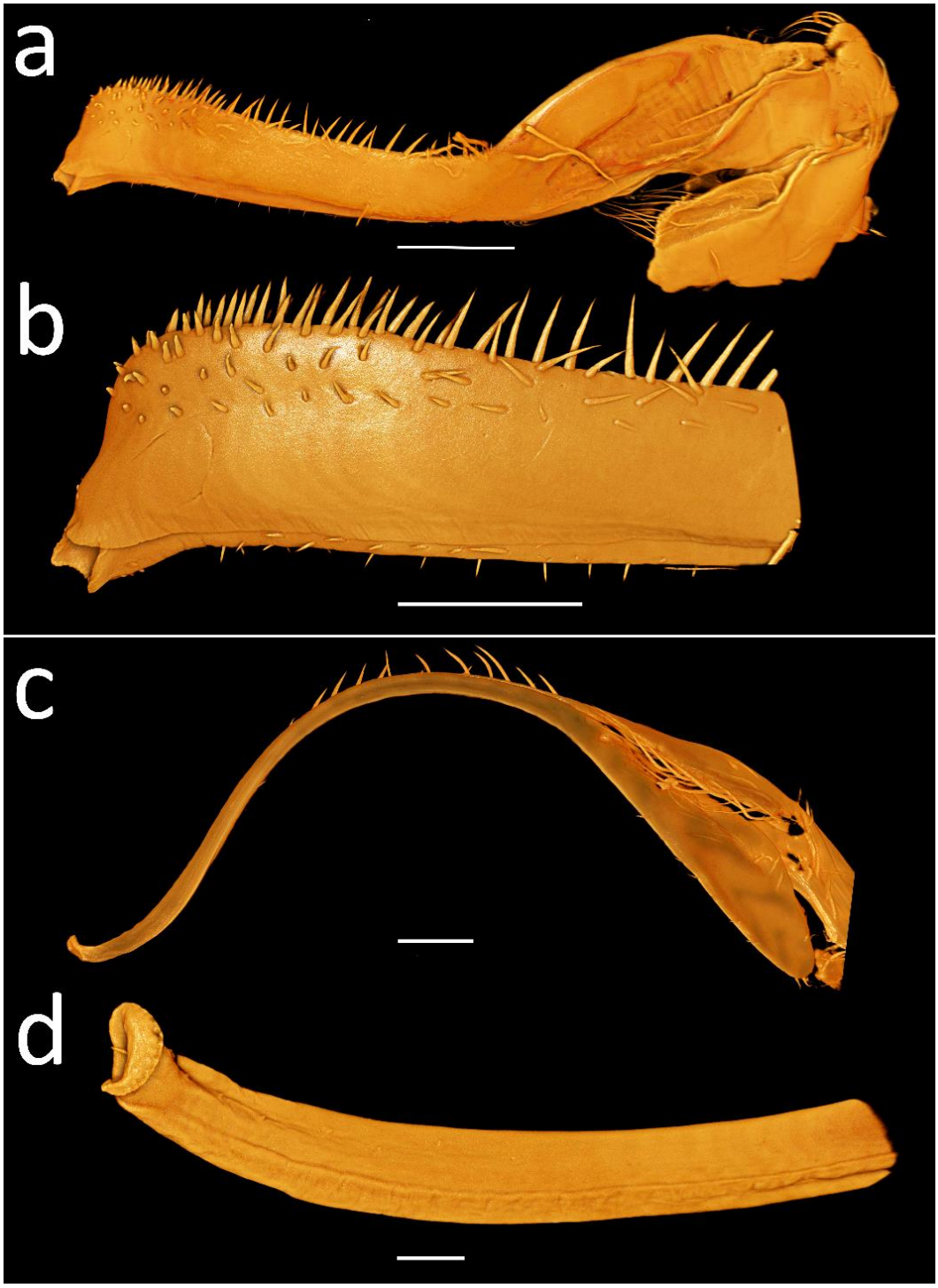

Figure 6.18: Drishti images of G1 of *Libystes nitidus* from different localities. Sudanese Red Sea (a) Whole G1. (b) The tip of the G1 in high resolution. Maldives. (c) Whole G1 (d) The tip of the G1 in high resolution. Scale bars a = 1000 µm; b-c = 500 µm; d = 100 µm.

Figure 6.19: Drishti images of *Libystes nitidus* G2 from different localities. Sudanese Red Sea. (a) Whole G2. (b) The tip of G2 in high resolution. Maldives. (c) Whole G1. (d) The tip of G2 in high resolution. Scale bars a, c = 500 µm; b, d = 100 µm.

6.4 Visualising the G1 of *Monomia argentata* (Crustacea: Brachyura: Portunidae) A. Milne Edwards, 1861

The swimming portunid crab, *Monomia argentata* A. Milne-Edwards, 1861, was originally described from the South China Sea. The species was first described by White (1847) as *Amphitrite argentata* (now assigned to *Monomia*), but the name was considered invalid as no description of the species was provided. Alphonse Milne-Edwards (1861) published and described the material of White (1847) as "*Neptunus argentatus*". The generic name of *Monomia* was established by Gistel (1848) for this species and this was used by Barnard (1950) and Chertoprud *et al.* (2012).

Recent reports stated that *Monomia* includes 12 species (Ng *et al.*, 2008; Koch *et al.*, 2015). The species *M. argentata* was reported to represent 2 or 3 species (Dai & Yang, 1991; Yang *et al.*, 2012; Koch *et al.*, 2017 in press). Therefore, confirmation of the identity of the *M. argentata* as described by A. Milne-Edwards (1861) was "paramount" (Koch *et al.*, 2017, in press) if the species complex of 2 or 3 species was to be resolved. The original specimen described by A. Milne-Edwards (1867) was extant in the Natural History Museum, London, although this male specimen was extremely fragile and dry.

As the male G1 morphology is species specific (Serène, 1984), the aim of the present study was to help clarify the identity of *M. argentata* using a non-destructive method. If the pleon was removed to expose the G1, the whole specimen may have disintegrated. Therefore, it was examined using Micro-CT and Drishti. The scanning and the visualising methods were detailed in the general material and methods section of the present thesis (Chapter 2). Besides providing a unique opportunity to view the hidden G1s, the micro-CT was used to generate a more detailed high-resolution image of the whole specimen. This also helped identify a number of features for the re-description of the species (see Koch *et al.*, 2017, in press for the detailed carapace description using the micro-CT images taken during the present study and see Fig. 6.21a). In addition, a 3D animation of the whole specimen after micro-CT treatment was created to make the material to digitally accessible and is now available online on: https://figshare.com/articles/Monomia_argentata_CT_scan/4836821.

Descriptions and digital illustrations of G1:

Monomia argentata (A. Milne-Edwards, 1861) Figure 6.21

Amphitrite argentata White, 1847: 126 [*nomen nudum*]; *Neptunus argentatus* A. Milne-Edwards, 1861: 332, 339, P1. 31(4); *Portunus* (*Amphitrite*) *argentatus* T. Sakai, 1939:

391, Fig. 5b, P1. 81(1); *Portunus argentatus* (form A) Stephenson & Rees, 1967: 17−18, Fig. 2c; *Portunus* (*Amphitrite*) *argentatus* Dai & Yang, 1991: 222, Fig. 120(1) and Yang *et al.*, 2012: Fig. 44, P1. 8(4).

Description:

The G1 of *M. argentata* was described by Dai & Yang (1991) as "*short and stout, strikingly curved, dilated distally, with a tip bearing a membrane, inner side of the distal part with dense of spiniform bristles*" (see Fig. 6.20).

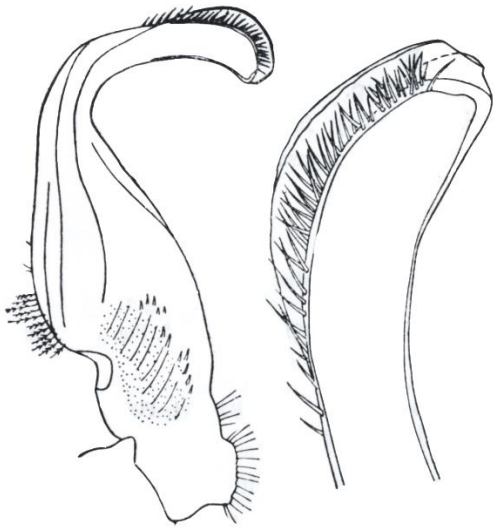

Figure 6.20: Drawings of *Monomia argentata* as *Portunus argentatus* by Dai & Yang (1991).

Digital illustrations:

After scanning the whole crab specimen using Micro-CT (see Fig. 6.21a), the data was digitally dissected to visualise the gonopods (see Fig. 6.21b).

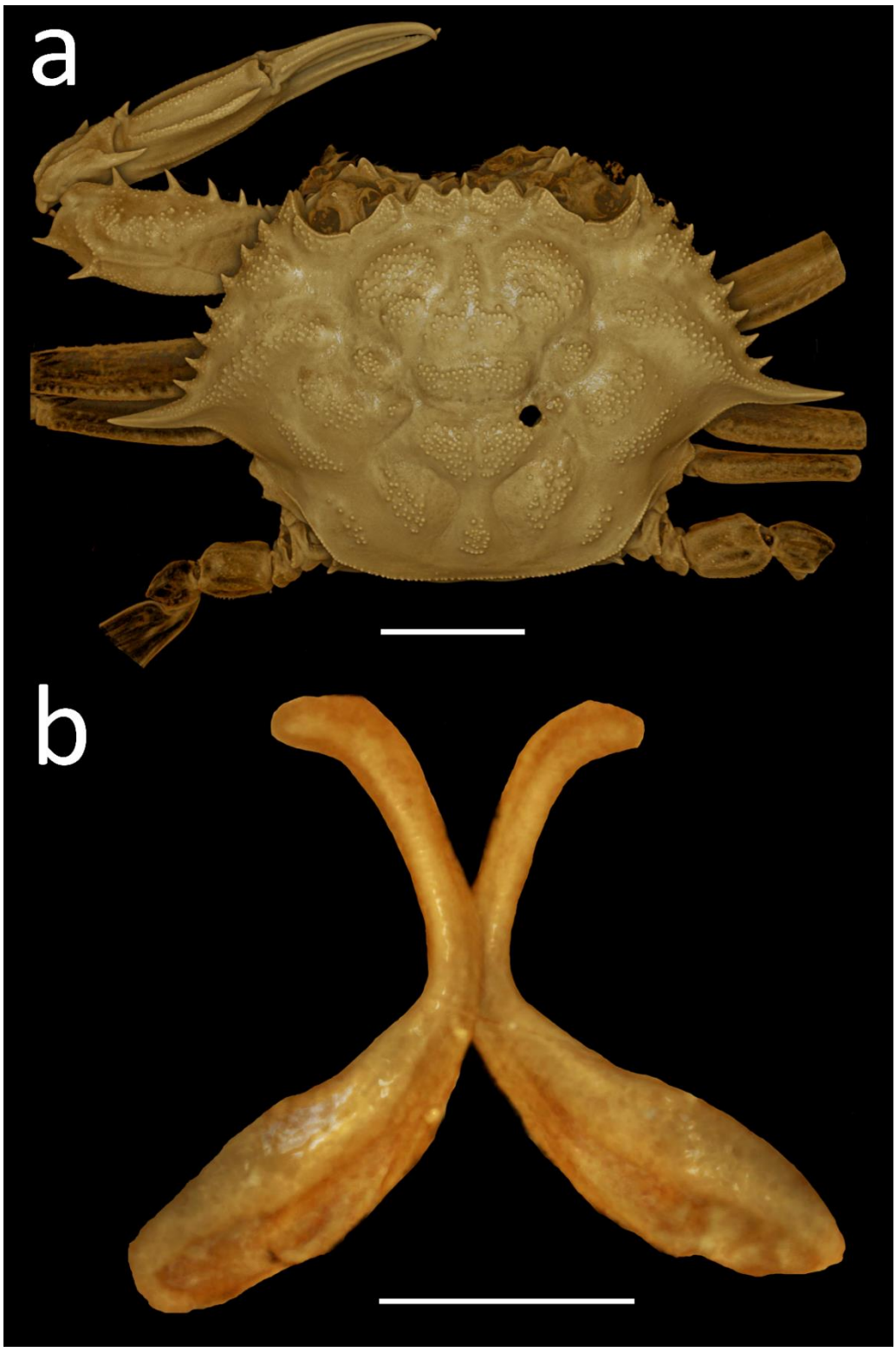

Figure 6.21: Micro-Ct images of *Monomia argentata* A Milne-Edwards, 1861 (NHM reg. number: 1847.21). (a) Dorsal view of whole specimen. (b) Ventral view of the first male gonopods. Scale bars a = 5000 μm; b = 2000 μm. See video 13 for 3D animation of whole specimen.

The CT-scanned figure of the *M. argentata* G1 provided a considerable amount of information and enabled Koch *et al.* (2017, in press) to describe the G1 as "*First male gonopods bent in about 2/3 of its length; the apical part is slightly recurved, distally expanded to reveal a flattened cephalic flange. Apex is rounded slightly curved posteriorly*". Although the general shape of Figure 6.21 compares extremely well with Figure 6.20 by Dai & Yang (1991), the CT-scan was unable to visualise the distal setae of the G1.

6.5 Discussion

The morphology of adult male gonopods can be too complex to draw accurately. Describing the G1 morphology from material scanned using CLSM and Drishti provides additional information and detail about this important species diagnostic character. Furthermore, this treatment does not risk damaging valuable museum specimens. The gonopods have a complex arrangement of setae as well as the overall form of the structure itself which is sometimes extremely challenging to illustrate using traditional techniques. This is especially true if the differences are as subtle as those in the case of the Dutch *Eriocheir* sp. versus Thames *E. sinensis* (Figure 6.12). Previous line drawings illustrated by Guo *et al.* (1997) and Sakai (2013) do not compare well with Figure 6.12, and as a consequence do not provide the detail required to distinguish between closely related species with complex G1 structures. Furthermore, the techniques applied in the present study can be seen as an excellent alternative to line drawings.

Modern techniques such as CLSM and micro-CT have the advantage of providing great detail for these complex structures as well as generating the chance of examining them in three-dimensions when required. Publishing the obtained data as videos in the

supplementary materials is another advantage of these techniques. In addition, unlike SEM, samples used for CLSM and micro-CT preparations can be re-used for further examinations because this is a non-destructive method. It offers a real advantage compared to SEM, especially when the species are vulnerable and valuable, such as the *Monomia argentata* sample from the NHM, London.

Applying these techniques, however, require effort and careful preparation to make the samples suitable for scanning using CLSM and micro-CT.

Does specimen size matter?

The answer in the context of visualising the various sizes of gonopods is "yes". The size of the gonopods used in the present study ranged between 0.6 mm to 2.2 cm. In order to visualise the various size of the image, different techniques were required to obtain high-resolution images. Therefore, preparation techniques as well as scanning methods are important.

The *Eriocheir* G1s were too large for a simple cavity slide. Therefore, a new technique (see Figs 2.51−2.52) was considered to mount and embed such large samples for the present study. Reinforcement rings were, however, adequate for mounting the G1 of smaller specimens such as *Libystes nitidus*. The reason for using a flat cavity slide and reinforcement ring was to obtain sufficient information from the distal tip of the G1 as they are considered to be much more fragile than the main body of the appendage. Otherwise, it can be too challenging to obtain sufficient signal from the tip as in the example of Becker *et al.* (2012; see Fig. 6.16). As the distal tip of the G1 is weaker than the proximal part (see Figs 6.1 and 6.16), staining the gonopod appendages of *L. nitidus* before scanning and applying Drishti, helped enormously to acquire high quality data to produce images in much great detail.

One problem encountered in the imaging of *Eriocheir* G1s was the suitability of the samples for CLSM. A high-resolution image was essential in the case differentiating *Eriocheir* species. Only the distal tips of the gonopods were scanned using CLSM. Although 10× dry objective was used to visualise the distal tips of the G1s, this structure was too large to scan in one attempt. Therefore, the "large images" option of CLSM software was applied by tiling the distal tips into 20 (Fig. 6.5) or 25 (Fig. 6.12b-c). Moreover, the depth of the field (z axis) was also too deep to obtain the required data. For example, it was 1300 μm in the case of *E. japonica* (Fig. 6.5c), whereas a depth of around 2800 μm was scanned for the specimens from Den Oever, Holland (Fig. 6.12c).

As the "large images" option was applied, arranging the saturation for each tile using the same settings was also found to be challenging. It took up to two hours to adjust the settings on such large G1 specimens using CLSM. Moreover, scanning duration ranged between 8 (Fig.6.5c) and 13 (Fig. 6.12c) hours depending of voxel size of the samples. Scanning such large samples also resulted in having extremely large data files for post-processing using Drishti. The final file size of the images in Fig. 6.5 ranged between 13−15 gigabytes (GB), whereas larger samples resulted in having data files of 25−27 GB (see Fig. 6.12b-c). These large data files caused decelerating of the post-processing procedure. Opening such confocal data using ImageJ took up to 20−25 minutes. After processing, these extremely large data files using ImageJ and applying Drishti was also challenging as it slowed down the software. Figures 6.12b-c could not be opened using Drishti because of the size of the file. Despite these problems, CLSM provided high-resolution images of distal morphology. This has contributed significantly to taxonomic studies and has been used to corroborate previous speculations for contentious species descriptions.

CT scanning was also a good alternative for such large sized specimens. It gave the chance to analyse the depth of distal tips. For example, when applying light microscopy or CLSM, it was not possible to visualise the genital pores and tubes of the G1 in detail. Traditional line drawings only showed the opening of genital pores (see Figs 6.3−6.4), whereas micro-CT provided more valuable information of both internal and external structures (see Figs 6.10 and 6.15). Another advantage of micro-CT was the option to rotate and visualise the gonopods in 360°, viewing them laterally and distally (see Figs 6.7, 6.8, 6.9, 6.13 and 6.14). Creating videos by rotating the distal tips of the gonopods gave a unique opportunity to evaluate the morphology of controversial species (see Videos 8−13). Furthermore, the stored data can be post-processed when required and depending on the area of focus such as the complexity of the setae or position of the genital pores. The only disadvantage of micro-CT in the case of scanning large gonopods was poor resolution of the setae. Using higher power objectives restricted the scan area, whereas lower objectives provided relatively less resolution. Therefore, to evaluate the complexity of the setae of gonopods, CLSM could be a better method in such cases.

Micro-CT gave the best result using the dry specimens (see 6.21). The dry specimen used in the present study was also relatively large compared to than other specimens. This proved advantageous and allowed the production of a detailed image. The other samples, however, were preserved in 70% ethanol. Therefore, the resolution was relatively poor compared to that achieved using dry specimens.

6.6 Conclusions

Applying modern-day approaches can contribute to morphological and taxonomic studies in a broad perspective. The detail that was not illustrated using line drawings

and light microscopy has been visualised applying the techniques proposed by the present study. These images can help considerably in distinguishing taxonomically controversial species which need to be examined in detail. The findings of the present study can be applied as an alternative and/or complementary method to the line drawings of male gonopods as the specimens used here provided elaborate images which would be too challenging or impossible to produce using light microscopy and ink penned illustrations. The 3D perspective of G1s can also add a unique contribution for evaluating G1 morphology.

CHAPTER 7

CONCLUSIONS

The purpose of the present study was to develop imaging techniques for studying zoeal and adult brachyuran morphology with an emphasis on the invasive Chinese mitten crab, *Eriocheir sinensis* now established in the River Thames, London. The main focus of the present research was to prepare a workflow which was sufficiently practicable for the study of brachyuran zoeal stages using Confocal Laser Scanning Microscopy (CLSM) and a free 3D software programme to produce detailed images. This procedure was considered in preference to the traditional method of producing line drawings of dissected zoeal appendages. This workflow included both preparation techniques prior to using the CLSM, and post-processing procedures. It was prepared specifically for the requirements of scanning *E. sinensis* zoeae, however, it can be applied to any similar specimens/material in terms of visualising morphology, but is dependent on specimen size. In addition, a component part of the workflow ensured that the data acquired from different CLSM models can be optimised/standardised using additional post-processing software i.e. ImageJ before the application of the freeware software programme, Drishti. Thus, this workflow is applicable to any small specimens and all current CLSM brands.

Another core aim of the present research was to re-describe the zoeal development of the Chinese mitten crab, *E. sinensis*. Various descriptions were proposed by a number of previous studies, but none of proved to be completely compatible. Old descriptions (Schnakenbeck, 1926, 1933; Hinrichs & Grell, 1937; Buhk, 1938; Panning, 1939; André, 1947; Liang *et al*., 1974; Ingle, 1991; Kim & Hwang, 1995; Montú *et al*., 1996) were illustrated using line drawings and did not provide all available detailed appendage information required to comply with modern day standards. Consequently, there was a

requirement to re-describe the zoeal development of *E. sinensis*. This was achieved by applying several techniques developed during the present investigation.

The present research also provided more information on the fecundity of female Chinese mitten crabs in the River Thames, London. This focused on the potential of females to spawn eggs with the emphasis on establishing whether they could produce more than one viable brood after a single mating. Another objective was to examine the male first gonopod in detail with reference to a number of *Eriocheir* species by applying the various techniques established for the study of zoeae. This proved to be really successful when the results were compared with images obtained using traditional methods such as, line drawings. In fact, this part of the study was expanded to examine the male gonopods of a number of other species in order to resolve some complex taxonomic issues. This again develops the general utility of the methods described in this thesis.

7.1 Summary of the chapters

Chapter 1 provided a general introduction to the whole thesis by focusing on the biology on the Chinese mitten crab, *Eriocheir sinensis*, summarising its invasiveness, dispersal, taxonomy, classification, identification of adults, distribution, impacts, life cycle and fecundity. This chapter also addressed the main aims of the present research.

Chapter 2 outlined the material and methods that were applied throughout this study. A protocol was developed for the detailed study of mitten crab zoeae by CLSM (see Fig. 2.3). A number of essential preparation techniques prior to confocal scanning were developed in order to provide maximum detailed data sets for the production of high quality final images. These preparation techniques included removing any debris from the zoeae by using Decon 90 (see Fig. 2.4); finding a process that produced maximum

autofluorescence of specimens, i.e. staining with Congo red and acid fuchsin combined; reducing the interference and background noise caused by internal tissues such as muscle by using a mixture of SDS + DTT (in addition, this digestion of muscles also made appendage dissection of zoeae much easier), using reinforced plastic rings to provide a well of various depth to hold samples horizontally without them being crushed/squashed/deformed by a cover slip and using a non-permeant medium such as diluted glycerine that allowed the sample to be manipulated into an appropriate position for scanning and for it to be retrieved undamaged for additional studies such as DNA analysis or re-scanning. CLSM settings were also used specifically to scan brachyuran zoeae. Applying four lasers at different wavelengths were considered the most effective method of scanning stained material. The optimum format of the images was found to be 1024×1024 pixels. 2048×2048 pixels were found to be too time consuming when considering post-processing. The "Ch (channel) series" option was avoided as it considerably increased CLSM scanning time. Increasing the offset value instead of decreasing it to zero or negative values was specifically applied in order to visualise fine structures such as setules. By applying the "z-intensity correction" option, over/under saturated images were avoided. The "Large images" option of CLSM software was more effective than merging images using post-processing tools in terms of time and having complete images (see Appendix 6 for details). Post-processing tools were found more effective than CLSM provided software to visualise the final images. Two methods were applied for post-processing of confocal data including the use of ImageJ and Drishti (see Appendix 6 for instructions). ImageJ was found to be the most effective method at merging all individual channels. This maximised data sets and helped to produce high quality images when processed afterwards with Drishti. Furthermore, Drishti also enabled digital dissection and the removal of unwanted tissue debris from the image (see Fig. 4.16). The main advantage of using these packages was that

software was free and their results were equivalent those produced by purchasing expensive programmes such as Amira or Avizo (licence ca. £8,600 per year). Such costs may be prohibitively expensive to students, unless a licenced software supplied by their institution.

Chapter 3 provided information on the fecundity of ovigerous mitten crabs in the River Thames, London. *Eriochier sinensis* is catadromous, meaning that mitten crabs spend most of their life in freshwater (as sub-adults), but migrate to estuaries of higher salinities to breed. During this annual autumnal migration, the sexual organs develop and the sub-adults become fully mature adults. Mitten crabs are semelparous, after this mating period the adults do not migrate back upstream into freshwater, but die. Clark (2011, Table 2) reported finding ovigerous crabs from December one year to June the next. He recorded that some ovigerous females trapped June carried a significantly reduced number of eggs. Clark (2011) also suggested that "these were still in the process of hatching or that *Eriocheir sinensis* may hatch off zoeae in batches and not all at once or that mitten crabs can spawn eggs a number of times during the breeding season (see Peters 1933; Panning 1939 for *E. sinensis*; Kobayashi 2001 for *E. japonicus*)". From the fecundity work of the present study one out of the 12 crabs held in the laboratory spawned a huge batch of eggs in its second brood without a mating a second time (see Fig. 3.6b). Some of the crabs held in the laboratory died between hatching zoeae from the first brood without spawning a second. These deaths may have been the result of just the natural mitten crab life cycle, i.e. being semelparous. This chapter concluded that the size of the carapace width is the main indicator of number of eggs spawn by the adult females (see Fig. 3.5). The findings of this chapter also showed that the Chinese mitten crab in the River Thames is highly fecund with a potential of producing more than one brood thus maximising reproductive output during the sole breeding season.

Chapter 4 mainly considered developing and improving CLSM imaging techniques. It justified the necessity to trial and eventually apply a series of successful techniques such as staining samples, submerging whole zoeae in a digesting solution, using a diluted glycerine mounting medium according to zoeal stage of the specimen, using plastic reinforcement rings and plain slides to create a well, and selecting post-processing packages rather than applying the manufactures confocal software programmes. This chapter concluded that these gradually developed processes and their eventual application helped overcome many of the limitations experienced previously in CLSM examinations of small arthropods (see Table 4.2). The main limitation, however, was found to be the size of the specimens and thereby the time spent on scanning. Furthermore, the learning curve required to produce good final images is considerable and could be considered as one of the limitations of the present study. But once learnt, CLSM has many considerable advantages.

Dissecting and mounting specimens without inflecting additional damage is essential and this took time to master. Finding the optimum workflow also took a considerable amount of time. Different combinations of the pre-processing, CLSM scanning and post-processing procedures were trialled until a general framework was developed that could applied repetitively to small brachyuran zoeae. This learning curve also applied to the post-processing tools. It formed some of the most challenging aspects and time-consuming elements of the present study. Converting data using confocal software and applying Drishti for each individual channel were trialled and found not very effective. Processing confocal data applying ImageJ first and afterwards using Drishti was found to be more effective. This, however, required additional time software understanding programme applications. Other software programmes such as Avizo (see Fig. 4.19b), VG-Studio Max (see Fig. 4.12b) and Adobe Photoshop (see Fig. 4.12a) were also required in order to improve the quality of the final image. All individual confocal post-

processing software provided by the manufacturer require slightly different processing procedures. ImageJ and Drishti were effectively used to standardise the confocal data form all brands of CLSM (see Fig. 4.15a). All procedures required a serious amount of study time, however, once learned, this method is faster and probably a more accurate technique than penned line drawings.

Chapter 5 re-described the zoeal stages of *Eriocheir sinensis* that were previously reared in the constant temperature laboratory at the NHM, by applying the techniques that were developed in the previous chapter. Like Anger (1991) and Montú *et al*. (1996), this study described that there is an optional, additional 6th stage in comparison with Schnakenbeck (1926; 1933), Hinrichs & Grell (1937), Buhk (1938), Panning (1939), André (1947), Liang *et al*. (1974), Ingle (1991) and Kim & Hwang (1995), who observed that *E. sinensis* has either 5 zoeal stage or fewer. Missing the sixth zoea could be relatively easy because this stage was remarkably similar zoea V except the third maxilliped, pereiopods and pleopods were more developed; the natatory setae on the first and second maxillipeds, carapace setae, and the setae on the antennule had increased in number; and the endopod of the antenna is equal to or slightly longer than the protopod.

The majority of the previous descriptions were made using traditional methods; a light microscope to produce line drawings. While drawing dissected appendages, the depth of the objective focus needs to be constantly adjusted and the resulting illustrations can represent a misinterpretation of setae. CLSM, however, allowed whole appendage to be visualised in complete focus and thereby reducing the chances of misinterpretation. In addition, unseen structures were visualised in detail by applying 3D software programmes so that the appendage could be rotated through 360°, allowing the confirmation of some characters (see videos 1−7). The main advantage of this scanning technique is confirming the position of accumulative setae that appear between

successive moults. Moreover, some character variations in late zoeal stages that were not described by previous studies were found by the present work. Therefore, two different formulae for the same appendage were observed in the present study, whereas only one setal formula was provided by previous descriptions (see Figs 5.29b-c; 5.38; 5.39c-d). The confocal scanning technique was not entirely successful especially when trying to visualise the anterio-dorsal and carapace margin setation. Although this problem was solved by examining this character under the SEM, this method too was not entirely successfully because of carapace shrinkage (see Fig. 5.16). Also visualising the paired posterodorsal setae on pleonal somites 2−6 proved difficult as scanning it required a considerable amount of time as this structure is relatively large.

Chapter 6 focused on visualising of first male gonopod. The distal morphology of this modified pleopod is a species specific diagnostic character and can be extremely difficult to illustrate using traditional line drawings. The images provided by the present study of closely related *Eriocheir* taxa are of high enough quality to distinguish at the species level (see Figs 6.5−6.10, 6.12−6.15, videos 8−12). In addition, the G1 of small size crab species were also successfully visualised using the current techniques developed for the present study (see Figs 6.18−6.19). Moreover, imaging the G1 outline of one old dry, fragile specimens using micro-CT scanning, 3D imaging and digital dissecting, without damaging it, enable the true identity of *Monomia argentata* to be revealed (see Fig. 6.21; video 13). This was a first in taxonomic studies and demonstrated the significant advantages in using modern day scanning techniques.

7.2. Future work

The present study highlighted a number of subjects that could be further investigated. Scanning the zoeal carapace to resolve the numbers of antero-dorsal setae after

successive moults was found challenging, although the results using SEM preparations was far from satisfactory. The same could be said from the attempt to visualise the pair posterior marginal setae on somites 2−5 of the pleon. A future study would include developing methods to visualise such large structures together with their associated small setal characters. Working on these relatively large characters does not easily fit CLSM imaging options.

The fecundity trials in the present study were undertaken with a total of 42 females spread over a three period; 30 to check eggs size and brood volume/size and only 12 were used to study observe second or third broods in a reproductive season. This could be repeated using a larger number of samples in order to obtain a more statistically robust analysis. Furthermore, a future study could investigate if mitten crabs can actually mate for a second or third time after successive hatchings including calculating the numbers of eggs spawned: does this remain constantly high (higher than spawning without additional mating or is there a natural reduction in clutch size as the reproductive season finishes in mid-summer? If proved to be correct and multiple broods are achieved, then as Clark (2011) stated "during this lengthy period *E. sinensis* larvae must now constitute a significant component of plankton along this part of the Thames estuary".

Before digestion (see Figs 4.3−4.7) of zoeal species was trialled, muscle bands stained by Congo red and acid fuschin produced too much interference to view a number of setal characters. Earlier, Clark *et al*. (1998b) stated that the exopod of the zoeal first maxillipeds the stage is often 2-segmented, but it is also incompletely bi-segmented as in the majoid species of *Hyas* (Christiansen, 1973, Fig. 10a, b; Pohle, 1991, Fig. 3K, L), or unsegmented, as in the pinnotherids *Dissodactylus* and *Clypeaasterophilus* (Pohle 1994, Fig. 1J, K; Marques & Pohle, 1996, Fig. 1J, K).

Recently, Clark & Cuesta (2015) stated that this exopod segmentation "*is a character that needs to be carefully checked because during preservation of live zoeae the animal can absorb the preservative causing the exopod to swell and open the joint giving the impression of incomplete articulation or no articulation at all*". According to (Boxshall, 2004) the intrinsic muscle structure is the distinct character for demonstrating appendage segmentation/articles in arthropods. For certain there appears to be a set of muscle bands in the distal and proximal part of the exopod *E. sinensis* (see Fig. 7.1).

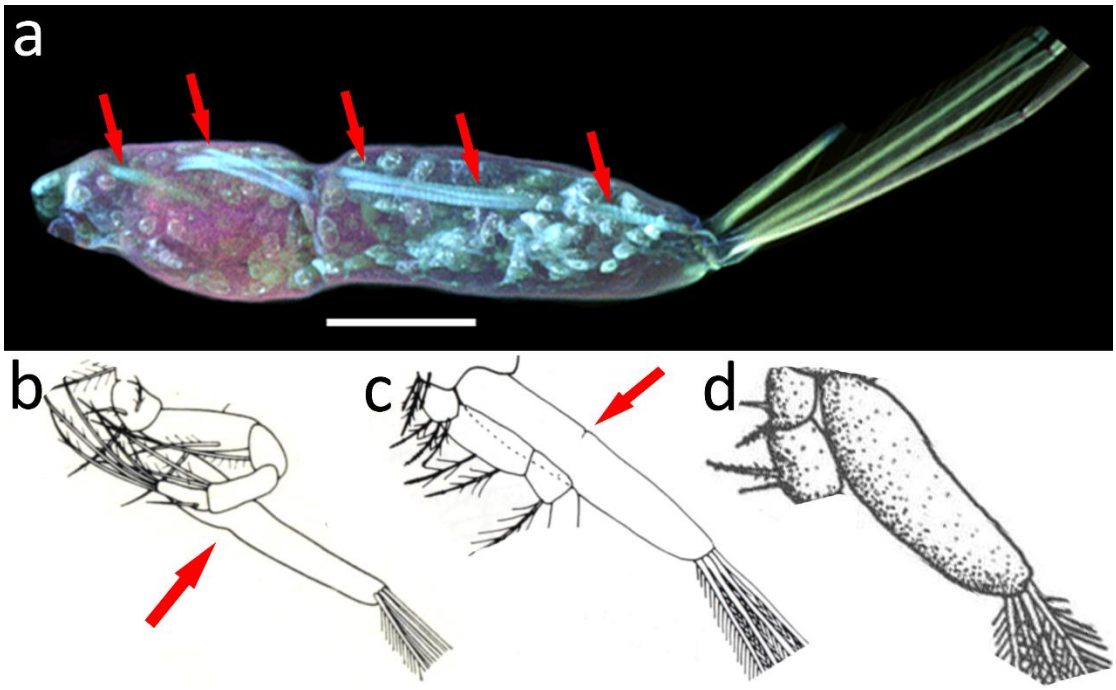

Figure 7.1: Illustrations of ZI stage first maxilliped exopods. (a) Confocal image of muscle bands (arrowed) of *Eriocheir sinensis*; the specimen prepared as undigested and stained with Congo red and acid fuschin. Scale bar = 50 µm. (b) Bi-segmented exopod (arrowed) of *Hyas coarctatus* Leach, 1816 by Christiansen (1973, Fig. 10b). (c) Bi-segmented exopod (arrowed) of *Hyas coarctatus alutaceus* Brandt, 1851 (now Hyas alutaceus J.F. Brandt in Middendorf, 1851) by Pohle (1991, Fig. 3k). (d) Unsegmented exopod of *Clypeasterophilus stebbingi* (Rathbun, 1918) by Marques & Pohle (1996, Fig. 1j).

These were found to be distinct using CLSM to highlight muscle bands (Fig. 7.1a). Consequently, if still extant, a future study could scan the first stage zoeae of Christiansen (1973, Fig. 7.1b), Pohle (1991, Fig. 7.1c) and Marques & Pohle (1996, Fig. 7.1d) and clarify the segmentation of the first maxilliped with respect to muscle structure within the exopods. Although, the muscle bands were visualised successfully using Congo Red and acid fuschin, this study could be extended using internal dyes to specifically stain muscular structures in detail. For example, the phalloidin and DAPI staining (Müller & Worsaae, 2006; Herranz *et al.*, 2014; Kerbl *et al.*, 2015; Altenburger, 2016) maybe be useful for good visualisation.

The research work undertaken here for the visualisation of the first male gonopod and its related commentary further highlights the problems associated with mitten crab taxonomy. The recent studies of Naser *et al*. (2012) and Sakai (2013) are not compatible. Furthermore, the study of Palero *et al.* (2016) suggests two species of mitten crab are present in NE Europe, a fact that is supported by this present study (see Fig. 6.12). Mitten crab taxonomy requires a major revision to included population genetics, morphometrics and CLSM scanning of first male gonopod as so successfully trialled here.

7.3 CLSM as a modern-day technique

CLSM has the advantage of z-axis scanning that enable 3D datasets to be processed using additional re-constructing software. Therefore, CLSM distinctively provides realism to the appendages. Another advantage of CLSM is that once the appendage is scanned, the data can be stored and always re-processed using ImageJ and Drishti. Therefore, a fewer number of samples are required for this application. In addition, the

images can be re-used for comparison by other researches. Moreover, scanned CLSM data provides the opportunity to be re-processed without using the specimen itself.

The disadvantage of CLSM is the speed of scans. The present study attempted to decreased the length of time by the applications shown in the Chapter 4. The expense of purchasing a CLSM could be another problem, however, other scanning equipment such as SEM are also extremely costly, but the price of laser scanning instruments is declining. Applying these techniques by the experts who is familiar with the specimen gives a significant advantage, however, the learning process required to using an CLSM and its additional software programmes is initially considerable. Another disadvantage to CLSM is establishing the most appropriate preparation techniques for the material to be scanned. This requires several trails and again takes time.

SEM was also used in the present research especially for the anterio-dorsal and ventral carapace margin setation of the zoeal carapace. This could not be resolved using CLSM. Actual SEM scanning is extremely quick however, the preparation of the samples takes more time than that required for CLSM. There is an added complication with SEM in that, during preparation, tiny specimens can be damaged and it is almost impossible to scan individual zoeal appendages. As the specimens used in the present study were extremely small and required to be dissected, the application of SEM was almost impossible. After dissecting, the appendages are hard to find/locate during all the procedures required for SEM preparation. Therefore, SEM was not considered practical for zoeal appendage descriptions. It must be noted that some zoeal material was vulnerable during preparation for SEM and destroyed especially after coating. Instead, only whole specimens (i.e. zoeae carapaces) were used in SEM examinations. Furthermore, there is only one chance to mount the specimen it positions prior to SEM scanning. There is no second chance to change position without damaging/destroying the specimens. Another disadvantage of SEM is that after a period of time the samples

prepared for SEM examination are difficult to re-use. Thus, SEM scanning in present study was only used as a last resort.

Micro-CT scanning was found to be extremely successful in a number of applications during the present research. Due to the size restrictions of micro-CT, it could not be used for the zoeal descriptions. It does not supply enough resolution for the smaller specimens and, could also be too expensive to use it for the taxonomic description of the many zoeae stages. It was used to scan the large gonopods of the adult *Eriocheir* species. A successful image was obtained for a dry specimen using micro-CT which would not be possible using other methods. Micro-CT is a perfect non-destructive technique that can be applied to type specimens, - the effects of x-ray radiation on these valuable specimens are unknown. The temperature inside micro-CT which is around 25 °C can also negatively affect these specimens when long scan duration is required.

The potential of CLSM has shown that it is a technique that produces morphological features, such as the male gonopods, in complete focus. The fine setae and setules of zoeal appendages (Figs 6.5 and 6.12) which can be difficult to draw are clearly visible using CLSM. It significantly reduced blurring images so that the setae located in different depth were clearly visualised.

In conclusion, CLSM and micro-CT are non-destructive techniques that can be used for the taxonomic descriptions. Both tools provide three-dimensional datasets that can be processed using 3D software programmes. This will eventually give the advantage of creating perfect images as well as video to make the taxonomic descriptions precisely. CLSM, in particular, is a viable alternative method for the description of zoeal appendages of brachyuran crabs.

REFERENCES

Al-Haj, A.E. & Al-Aidaroos, A.M. (2014) Description of the first zoeal stage of *Geograpsus crinipes* (Dana, 1851) (Decapoda: Brachyura: Grapsidae) from the Red Sea. *African Invertebrates, Pietermaritzburg*. **55**(1), 19–26.

Altenburger, A. (2016) The neuromuscular system of *Pycnophyes kielensis* (Kinorhyncha: Allomalorhagida) investigated by confocal laser scanning microscopy. *EvoDevo*. **7**, 25.

Anosov, S.E. (2000) Keys to the identification of brachyuran larvae of the Black Sea. *Crustaceana*. **73**, 1239–1246.

Andersen, S.O. (1963) Characterization of a new type of cross-linkage in resilin, a rubber-like protein. *Biochimica et Biophysica Acta*. **69**, 249–262.

André, M. (1947) L'envahissement du réseau hydrographique français par le crabe Chinois (*Eriocheir sinensis* H.M. Edw.). *Revue Scientifique, Revue Rosé (Paris)*. **3264**, 33−38.

Anger, K. (1991) Effects of temperature and salinity on the larval development of the Chinese mitten crab *Eriocheir sinensis* (Decapoda: Grapsidae). *Marine Ecology Progress Series*. **72**, 103–110.

Anger, K. (1995) The conquest of freshwater and land by marine crabs: adaptations in life-history patterns and larval bioenergetics. *Journal of Experimental Marine Biology and Ecology*. **193**, 119–145.

Anger, K., Schreiber, D. & Montú, M. (1995) Abbreviated larval development of *Sesarma curacaoense* (Rathbun, 1897) (Decapoda: Grapsidae) reared in the laboratory. *Nauplius*. **3**, 127–154.

Apel, M. & Spiridonov, V.A. (1998) Taxonomy and zoogeography of the portunid crabs (Crustacea: Decapoda: Brachyura: Portunidae) of the Arabian Gulf and adjacent waters. *Fauna of Arabia*. **17**, 159–331.

APEM (2010) Status, distribution and impacts of Chinese mitten crab in the Nene and Ouse Washes. *Stage 1 Report, Natural History Museum, APEM Scientific Report 411010*.

Attrill, J.M. & Thomas, R.M. (1996) Long-term distribution patterns of mobile estuarine invertebrates (Ctenophora, Cnideria, Crustacea: Decapoda) in relation to hydrological parameters. *Marine Ecology Progress Series*. **143**, 25–36.

Ball, A.D., Goral, T. & Kamanli, S.A. (2017a) Confocal microscopy applied to paleontological specimens. *The Paleontological Society Papers*. **22**, 39−55.

Ball, A.D., Job, P.A. & Walker, A.E.L. (2017b) SEM-microphotogrammetry, a new take on an old method for generating high-resolution 3D models from SEM images. *Journal of Microscopy*. **267**, 214–226

Báez, P. (1997) Key to the families of decapod crustacean larvae collected off northern Chile during an EI Nino event. *Investigaciones Marinas Valpariso*. **25**, 167–176.

Barnard, K.H. (1950) Descriptive catalogue of South African decapod Crustacea (crabs and shrimps). *Annals of the South African Museum.* **38**, 1–837.

Becker, C., Brandis, D. & Storch, V. (2011) Morphology of the female reproductive system of European pea crabs (Crustacea, Decapoda, Brachyura, Pinnotheridae). *Journal of Morphology*. **272**, 12–26.

Becker, C., Türkay, M. & Brandis, D. (2012) The male copulatory system of European pea crabs (Crustacea, Brachyura, Pinnotheridae). *Journal of Morphology*. **273**, 1306–1318.

Beckman, E.M., Kawaguchi, T., Chandler, G.T. & Decho, A.W. (2008) Development of a microplate-based fluorescence immunoassay using quantum dot streptavidin conjugates for enumeration of putative marine bacteria, *Alteromonas* sp., associated with a benthic harpacticoid copepod. *Journal of Microbiological Methods*. **75**, 441–444.

Belanger, R., Ren, X., McDowell, K., Chang, S., Moore, P. & Zielinski, B. (2008) Sensory setae on the major chelae of male crayfish, *Orconectes rusticus* (Decapoda: Astacidae) – impact of reproductive state on function and distribution. *Journal of Crustacean Biology*. **28**, 27–36.

Bentley, M.G. (2011) The global spread of the Chinese mitten crab *Eriocheir sinensis*. In Galil, B.S., Clark, P.F. & Carlton, J.T. (Eds), In the wrong place – alien marine crustaceans: distribution, biology and impacts. *Invading Nature – Springer Series in Invasion Ecology, Springer, Dordrecht, The Netherlands*. **6**, 107–127.

Bereiter-Hahn, J. (1976) Dimethylaminostyrylmethylpyridiniumiodine (DASPMI) as a fluorescent probe for mitochondria *in situ*. *Biochimica et Biophysica Acta (BBA)*. **423**, 1–14.

Blackstone, N.W. (1989) Size, shell-living and carcinization in geographic populations of a hermit crab, *Pagurus hirsutiusculus*. *Journal of Zoology*. **217**, 477–490.

Borradaile, L.A. (1916) Crustacea. Part II. Porcellanopagurus: An instance of carcinization. In: British Antarctic ("Terra Nova") Expedition, 1910. Natural History Report. *Zoology*. **3**(3), 111–126.

Bourke, P. (2011) Transferring slice data to Drishti using ImageJ. Retrieved from http://paulbourke.net/miscellaneous/Drishti_intro1/. Accessed 7 October 2016.

Boxshall, G.A. (1990) The skeletomusculature of siphonostomatoid copepods, with an analysis of adaptive radiation in structure of the oral cone. *Philosophical Transactions of the Royal Society of London, Series B, Biological Sciences*. **328**, 167−212.

Boxshall, G.A. (2004) The evolution of arthropod limbs. *Biological Reviews.***79**, 253–300.

Böhm, A., Bartel, D., Szucsich, N.U. & Pass, G. (2011) Confocal imaging of the exo- and endoskeleton of Protura after non-destructive DNA extraction. *Soil Organisms*. **83**(3), 335−345.

Brandt, A., Brix, S., Held, C. & Kihara, T.C. (2014) Molecular differentiation in sympatry despite morphological stasis: deep-sea *Atlantoserolis* Wägele, 1994 and *Glabroserolis* Menzies, 1962 from the south-west Atlantic (Crustacea: Isopoda: Serolidae). *Zoological Journal of the Linnean Society*. **172**, 318−359.

Brady, J. (1965) A simple technique for making very fine, durable dissecting needles by sharpening tungsten wire electrolytically. *Bulletin of the World Health Organization*. **32**, 143–144.

Brix, S., Leese, F., Riehl, T. & Kihara, T.C. (2014) A new genus and new species of Desmosomatidae Sars, 1897 (Isopoda) from the eastern South Atlantic abyss described by means of integrative taxonomy. *Marine Biodiversity*. **45**, 7−61.

Brooker, A.J., Shinn, A.P. & Bron, J.E. (2007) A review of the biology of the parasitic copepod *Lernaeocera branchialis* (L. 1767) (Copepoda: Pennellidae). *Advances in Parasitology*. **65**, 297−341.

Brooker, A.J., Bron, J.E. & Shinn, A.P. (2012a) Description of the free-swimming juvenile stages of *Lernaeocera branchialis* (Pennellidae) using traditional light and confocal microscopy. *Aquatic Biology*. **14**, 153−163.

Brooker, A.J., Shinn, A.P. & Bron, J.E. (2012b) Use of laser scanning confocal microscopy for morphological taxonomy and the potential for digital type specimens (e-types). *Aquatic Biology*. **14**, 165−173.

Buhk, F. (1938) Zu fortpflanzungsbiologie der wollhandkrabbe. *Wochenschrift für Aquarien und Terrarienkunde*. **35**, 776−780.

Bundy, M.H. & Paffenhofer, G.A. (1993) Innervation of copepod antennules investigated using laser scanning confocal microscopy. *Marine Ecology Progress Series*. **102**, 1−14.

Bundy, M.H., Gross, T.F., Vanderploeg, H.A. & Strickler, J.R. (1998) Perception of inert particles by calanoid copepods: behavioural observations and a numerical model. *Journal of Plankton Research*. **20**, 2129−2152.

Bundy, M.H. & Vanderploeg, H.A. (2002) Detection and capture of inert particles by calanoid copepods: the role of the feeding current. *Journal of Plankton Research*. **24**, 215–223.

Butler, A.D., Edgecombe, G.D., Ball, A.D. & Giribet, G. (2010) Resolving the phylogenetic position of enigmatic New Guinea and Seychelles Scutigeromorpha (Chilopoda): a molecular and morphological assessment of Ballonemini. *Invertebrate Systematics.* **24**, 539−559.

Buttino, I., Ianora, A., Carotenuto, Y., Zupo, V.& Miralto, A. (2003) Use of the confocal laser scanning microscope in studies on the developmental biology of marine crustaceans. *Microscopy Research and Technique.* **60**, 458–464.

Buttino, I., do Espirito Santo, M., Ianora, A. & Miralto, A. (2004) Rapid assessment of copepod embryo viability using fluorescent probes. *Marine Biology*. **145**, 393–399.

Buttino, I., De Rosa, G., Carotenuto, Y., Ianora, A., Fontana, A., Quaglia, F., La Rotonda, M.I. & Miralto, A. (2006) Giant liposomes as delivery system for ecophysiological studies in copepods. *The Journal of Experimental Biology*. **209**, 801–809.

Calado, R. & Leal, M.C. (2015) Trophic Ecology of Benthic Marine Invertebrates with Bi-Phasic Life Cycles: What Are We Still Missing? *Advances in Marine Biology*. **71**, 1–70.

Carlton, J.T. (1985) Transoceanic and interoceanic dispersal of coastal marine organisms: the biology of ballast water. *Oceanographic and Marine Biology Annual Review*. **23**, 313–371.

Carlton, J.T. (1996) Pattern, process, and prediction in marine invasion ecology. *Biological Conservation*. **78**, 97–106.

Carlton, J.T. (2003) Community assembly and historical biogeography in the North Atlantic Ocean: the potential role of human-mediated dispersal vectors. *Hydrobiologia*. **503**, 1–8.

Carotenuto, Y. (1999) Morphological analysis of larval stages of *Temora stylifera* (Copepoda, Calanoida) from the Mediterranean Sea. *Journal of Plankton Research*. **21**, 1613–1632.

Carotenuto, Y., Ianora, A., Di Pinto, M., Sarno, D. & Miralto, A. (2006) Annual cycle of early developmental stage survival and recruitment in the copepods *Temora stylifera* and *Centropages typicus*. *Marine Ecology Progress Series*. **314**, 227–238.

Carsen, A.E., Kleinman, S. & Scelzo, M.A. (1996) Fecundity and relative growth of the crab *Platyxanthus patagonicus* (Brachyura: Platyxanthidae) in Patagonia, Argentina. *Journal of Crustacean Biology*. **16**(4), 748−753.

Castro, P. (2007) A reappraisal of the family Goneplacidae Macleay, 1838 (Crustacea, Decapoda, Brachyura) and revision of the subfamily Goneplacinae, with the description of 10 new genera and 18 new species. *Zoosystematics*. **29**, 609−774.

Castro, P. (2009) Two new species of *Carcinoplax* H. Milne Edwards, 1852, and *Pycnoplax* from the western Pacific, and a description of the female of *Thyraplax truncate* (Crustacea, Decapoda, Brachyura, Goneplacidae). *Zoosystematics*. **31**, 949−957.

Chan, T.Y., Hung, M.S. & Yu, H.P. (1995) Identity of *Eriocheir recta* (Stimpson, 1858) (Decapoda: Brachyura), with description of a new crab from Taiwan. *Journal of Crustacean Biology*. **15**(2), 301–308.

Chandler, G.T. & Volz, D.C. (2004) Semiquantitative confocal laser scanning microscopy applied to marine invertebrate ecotoxicology. *Marine Biotechnology (NY)*. **6**, 128–137.

Chertoprud, E.S., Spiridinov, V.A., Ponomarev, S.A. & Mokievsky, V.O. (2012) Commercial crabs (Crustacea Decapoda Brachyura) from Nhatrang Bay (Vietnam). In Britayev, T.A. (Ed.), Benthic fauna of the Nhatrang Bay. *KMK Scientific Press, Moscow, Russia*. **2**, 301–349.

Christiansen, M.E. (1973) The complete larval development of *Hyas araneus* Linnaeus and *Hyas coarctatus* Leach (Decapoda, Brachyura, Majidae) reared in the laboratory. *Norwegian Journal of Zoology*. **21**, 63−89.

Chu, K.H., Ho, H.Y., Li, C.P. & Chan, T.Y. (2003) Molecular phylogenetics of the mitten crab species in *Eriocheir, sensu lato* (Brachyura: Grapsidae). *Journal of Crustacean Biology*. **23**(3), 738–746.

Chung, H.L., Ho, L.Y., Hsu, C.P. & Ts'ao, W.J. (1981) Recent progress in studies of Paragonimus and paragonimiasis control in China. *Chinese Medical Journal*. **94**, 483–494.

Cieluch, U., Anger, K., Charmantier-Daures, M. & Charmantier, G. (2007) Salinity tolerance, osmoregulation, and immunolocalization of Na^+/K^+-ATPase in larval and early juvenile stages of the Chinese mitten crab, *Eriocheir sinensis* (Decapod, Grapsoidea). *Marine Ecology Progress Series*. **329**, 169–178.

Clark, P.F. & Webber, W.R. (1991) A re-description of *Macrocheira kaempferi* (Temminck, 1836) zoeas with a discussion of the classification of the *Majoidea Samouelle*, 1819 (Crustacea: Brachyura). *Journal of Natural History*. **25**, 1259–1279.

Clark, P.F., Rainbow, P.S., Robbins, R.S., Smith, R.B, Yeomans, W.E., Thomas, M. & Dobson, M. (1998a) The Alien Chinese mitten crab *Eriocheir sinensis* (Crustacea: Decapoda: Brachyura), in the Thames catchment. *Journal of the Marine Biological Association of the United Kingdom*. **78**, 1215–1221.

Clark, P.F., Calazans, D. & Pohle, G.W. (1998b) Accuracy and standardization of brachyuran larval descriptions. *Invertebrate Reproduction & Development*. **33**(2–3), 127–144.

Clark, P.F., Abdul-Sahib, I.M. & Al-Asaki, M.S. (2006) The first record of *Eriocheir sinensis* H. Milne Edwards, 1853 (Crustacea: Brachyura: Varunidae) from the Basrah area of southern Iraq. *Aquatic Invasions*. **1**, 51–54.

Clark, P.F. (2007) Xanthoid crab (Crustacea: Decapoda: Brachyura) classification and phylogeny: an appraisal using the chaetotaxy of first stage zoeae. Thesis pp 1–473, Appendix I Larval Descriptions pp 1–227, Appendix II Larval Figures *Acantholobulus bermudensis* to *Lophozozymus Pictor* pp 1–308, Appendix III Larval Figures *Lybia plumose* to *Zozymodes xanthoides* pp 309–590. *PhD dissertation in University Marine Station Millport, University of London*.

Clark, P.F. (2011) The commercial exploitation of the Chinese mitten crab, *Eriocheir sinensis* in the River Thames, London: damned if we don't and damned if we do. In Galil B.S., Clark P.F. & Carlton J.T. (Eds), In the wrong place – alien marine crustaceans: distribution, biology and impacts. *Invading Nature – Springer Series in Invasion Ecology*. **6**, 537–580.

Clark, P.F., Stefanoudis, P.V., Crimmen, O.A., Pearce, D. & Morritt, D. (2013) Commercial exploitation of eels (*Anguilla anguilla*) and Chinese mitten crabs (*Eriocheir sinensis*): fyke net trials. The final report for the Marine Management Organisation and the Environment Agency. For the attention of Philip Lynn, Marine Management Organisation and Heidi Stone and Darryl Clifton-Dey, Environment Agency. pp. 52.

Clark, P.F. & Cuesta, J.A. (2015) Larval Systematics of Brachyura. In Castro, P., Davie, P.J.F., Guinot, D., Schram, F.R. & Von Vaupel Klein, J.C. (Eds), Decapoda: Brachyura, Treatise on Zoology – Anatomy, Taxonomy, Biology. The Crustacea, Complementary to the volumes translated from the French of the Traité de Zoologie [founded by Grassé (†), P.-P.]. *Brill, Leiden and Boston*. Chapter 71–17, 9(CII), pp. 981–1048.

Cohen, E. (1993) Chitin synthesis and degradation as targets for pesticide action. *Archive of Insect Biochemistry and Physiology*. **22**, 245–261.

Cohen, A.N., Carlton, J.T. & Fountain, M.C. (1995) Introduction, dispersal and potential impacts of the green crab *Carcinus maenas* in San Francisco Bay, California. *Marine Biology*. **122**, 225–237.

Cohen, A.N. & Carlton, J.T. (1997) Transoceanic transport mechanisms: introduction of the Chinese mitten crab, *Eriocheir sinensis*, to California. *Pacific Science*. **51**, 1–11.

Cohen, A.N. & Weinstein, A. (2001) The Potential Distribution of Chinese Mitten Crabs (*Eriocheir sinensis*) in selected waters of the Western United States with U.S. Bureau of Reclamation Facilities. *Tracy Fish Collection Facilities Studies*. **21**, 1–61.

Coleman, C.O. (2006) Substituting time-consuming pencil drawings in arthropod taxonomy using stacks of digital photographs. *Zootaxa*. **1360**, 61–68.

Conchello, J.A. & Lichtman, J.W. (2005) Optical sectioning microscopy. *Nature Methods*. **2**, 920–931.

Corey, S. (1987) Interspecific differences in reproductive potential, realized reproduction and actual production in the crayfish *Orconectes propinquus* (Girard 1852) in Ontario. *American Midland Naturalist*. **118**, 424−432.

Corgosinho, P.H.C., Mercado-Salas, N.F., Arbizu, P.M, Silva, E.N.D.S. & Kihara, T.C. (2017) Revision of the *Remaneicaris argentina*-group (Copepoda, Harpacticoida, Parastenocarididae): supplementary description of species, and description of the first semi-terrestrial *Remaneicaris* from the tropical forest of Southeast Mexico. *Zootaxa*. **4238**(4), 499−530.

Crosnier, A. (1962) Crustacés Décapodes Portunidae. *Faune de Madagascar*. **16**, 1−154.

Cuesta, J.A. & Schubart, C.D. (1999) Proposed classification of the Grapsidae and Gecarcinidae (Decapoda, Brachyura) on the basis of larval morphology. *Program and Abstracts, The Crustacean Society 1999 Summer Meeting, Lafayette, Louisiana*. **52**.

Cuesta, J.A., Schuh, M., Diesel, R. & Schubart, C.D. (1999) Abbreviated development of *Armases miersii* (Grapsidae: Sesarminae), a crab that breeds in supralittoral rock pools. *Journal of Crustacean Biology*. **19**(1), 26−41.

Cuesta, J.A., González-Ortegón, E., Drake, P. & Rodríguez, A. (2004) First record of *Palaemon macrodactylus* Rathbun, 1902 (Decapoda, Caridea, Palaemonidae) from European waters. *Crustaceana*. **77**(3), 377–380.

Cuesta, J.A., Guerao, G., Schubart, C.D. & Anger, K. (2011) Morphology and growth of the larval stages of *Geograpsus lividus* (Crustacea, Brachyura), with the descriptions of new larval characters for the Grapsidae and an undescribed setation pattern in extended developments. *Acta Zoologica*. **92**, 225−240.

Cuesta, J.A., Almón, B., Pérez-Dieste, J. & Bañón, R. (2016) Role of ships' hull fouling and tropicalization process on European carcinofauna: new records in Galician waters (NW Spain). *Biological Invasions*. **18**, 619–630.

Dai, A.-Y. (1991) Studies on the subspecies differentiation of the genus *Eriocheir* (Decapoda: Brachyura). In: Zhang, G.X. (Ed.), Scientific Treatise on Systematic Evolution and Zoology. *China Science &. Technology Publication House, Beijing*. **1**, 61–71.

Dai, A.-Y. & Yang, Si-L. (1991) Crabs of the China seas. *Beijing: China Ocean Press, and Berlin: Springer Verlag*. 682 pp. [1991 English reprint of a 1984 Chinese volume].

Dan, Q., Tung, S.X., Weng, Y. Wu, S.C. & Chu, S.C. (1984) The ecological study on the anadramous crab *Eriocheir sinensis* going upstream. *Chinese Journal of Zoology*. **6**, 19–22.

Difato, F., Mazzone, F., Scaglione, S., Fato, M., Beltrame, F., Kubínová, L., Janácek, J., Ramoino, P., Vicidomini, G. & Diaspro, A. (2004) Improvement in volume estimation from confocal sections after image deconvolution. *Microscopy Research and Technique*. **64**, 151–155.

Dittel, A.I. & Epifanio, C.E. (2009) Invasion biology of the Chinese mitten crab *Eriocheir sinensis*: A brief review. *Journal of Experimental Marine Biology and Ecology*. **374**, 79–92.

Doi, W., Lwin, T.T., Yokota, M., Strussmann, C.A. & Watanabe, S. (2007) Maturity and reproduction of goneplacid crab *Carcinoplax vestita* (Decapoda, Brachyura) in Tokyo Bay. *Fisheries Science*. **73**(2), 331−340.

Dreszer, T.B., Raða, T. & Giribet, G. (2015) *Cyphophthalmus solentiensis* sp. nov. (Cyphophthalmi, Sironidae), a new endogean mite harvestman species from Croatia,

with an application of confocal laser microscopy to illustrate genitalia in opiliones. *Bulletin of the Museum of Comparative Zoology*. **543**, 1−15.

Du, N.S. (1998) Congeneric species of Chinese mitten crab and their English names. *Fisheries Science and Technology Information System*. **25**(3), 108–113.

Dutton, C. & Conroy, C. (1998) Effects of burrowing Chinese mitten crabs (*Eriocheir sinensis*) on the Thames tideway. *Environment Agency Report, London*.

Elner, R. & Benninger, G. (1995) Multiple reproductive strategies in snow crab, *Chionoecetes opilio*: physiological pathways and behavioural plasticity. *Journal of Crustacean Biology*. **93**, 93−112.

Emmerson, W.D. (1999) Comparative fecundity and reproduction in seven crab species from Mgazana, a warm temperate southern African mangrove swamp. *Crustacean Issues*. **12**, 499–512.

Epifanio, C. (2007) Biology of larvae. In Kennedy, V.S. & Cronin, L.E. (Eds), The blue crab *Callinectes sapidus*. *Maryland Sea Grant, College Park*. 513–533.

Erdman, R.B., Blake, N.J., Lockhart, F.D., Linberg, W.J., Perry, H.M. & Waller, R.S. (1991) Comparative reproduction of deep-sea crabs *Chaceon fenneri* and *C. quinquedens* (Brachyura, Geryonidae) from the Northeast Gulf of Mexico. *Invertebrate Reproduction and Development*. **19**, 175−184.

Fan, Y., Saito, T. & Isogai, A. (2008) Preparation of chitin nanofibers from squid pen *β*-chitin by simple mechanical treatment under acid conditions. *Biomacromolecules*. **9**(7), 1919–1923.

Felgenhauer, B.E. (1987) Techniques for preparing crustaceans for scanning electron microscopy. *Journal of. Crustacean Biology*. **7**, 71−76.

Fischer, C. & Ahlrichs, W.H. (2011) Revisiting the *Cephalodella trophi* types. *Hydrobiologia*. **662**(1), 205–209.

Floating down the river (n. d.) The River Thames − Its natural history. (Online). http://www.the-river-thames.co.uk/wildlife.htm#twenty. Accessed 28 June 2017.

Floating down the river (n. d.) The River Thames − Its geology, geography and vital statistics from source to sea. (Online). http://www.the-river-thames.co.uk/thames.htm. Accessed 28 June 2017.

Flores, A.A.V. & Negreiros-Fransozo, M.L. (1998) External factors determining seasonal breeding in a subtropical population of the shore crab *Pachygrapsus transversus* (Gibbes, 1850) (Brachyura: Grapsidae). *Invertebrate Reproduction and Development*. **34**, 149–155.

Fukui, Y. (1988) Comparative studies on the life history of the grapsid crabs (Crustacea, Brachyura) inhabiting intertidal cobble and boulder shores. *Publications of the Seto Marine Biological Laboratory*. **33**, 121–162.

Galassi, D.M.P. (1997) The genus *Pseudectinosoma* Kunz, 1935: an update, and description of *Pseudectinosoma kunzi* sp. n. from Italy (Crustacea: Copepoda: Ectinosomatidae). *Archiv für Hydrobiologie*. **139**, 277–287.

Galassi, D.M.P. & De Laurentiis, P. (1997) *Pseudectinosoma reductum*, a new ectinosomatid harpacticoid from springwaters in Italy (Crustacea: Copepoda). *Hydrobiologia*. **356**, 81–86.

Galassi, D.M.P., De Laurentiis, P. & Giammatteo, M. (1998) Integumental morphology in copepods: assessment by confocal laser scanning microscopy (CLSM) (Crustacea, Copepoda). *Fragmenta Entomologica*. **30**, 79–92.

Galil, B.S. & Clark, P.F. (1994) A revision of the genus *Matuta* Weber, 1795 (Crustacea: Brachyura: Calappidae). *Zoologische Verhandelingen, Leiden*. **294**, 1−55.

Garcia-Guerrero, M. & Hendrickx, M.E. (2004) Fecundity traits of seven species of brachyuran crabs (Decapoda: Brachyura) from the Pacific coast of Mexico. *Contributions to the Study of East Pacific Crustaceans*. **3**, 79−87.

Giese, A.C. & Kanatani, H. (1987) Maturation and spawning. In Giese, A.C., Pearse, J.S. & Pearse, V.B. (Eds), Reproduction of marine invertebrates. Palo Alto, CA. *Blackwell Scientific Publications*. 252–313.

Gilbert, M.T.P., Moore, W., Melchior, L. & Worobey, M. (2007) DNA extraction from dry museum beetles without conferring external morphological damage. *PLoS One*. **2**(3), 272.

Gilbey, V., Attrill, M.J. & Coleman, R.A. (2008) Juvenile Chinese mitten crabs (*Eriocheir sinensis*) in the Thames estuary: distribution, movement and possible interactions with the native crab *Carcinus maenas*. *Biological Invasions*. **10**, 67–77.

Gistel, H. (1848) Naturgeschichte des Thierreichs für höhere Schulen bearbeites. (*Scheitlin und Krais: Stutgart, Germany*).

Gollasch, S. & Nehring, S. (2006) National checklist for aquatic alien species in Germany. *Aquatic Invasions*. **1**(4), 245–269.

Gollasch, S. & Rosenthal, H. (2006) The Kiel Canal. In: Gollasch, S., Galil, B.S. & Cohen, A. (Eds), Bridging Divides. *Maritime Canals as Invasion Corridors*. 315 pp.

Gollasch, S. (2011) NOBANIS – Invasive alien species fact sheet – *Eriocheir sinensis.* Online database of the European network on invasive alien species. http://www.nobanis.org. Accessed 14 March 2014.

González-Gordillo, J.I., Dos Santos, A. & Rodriguez, A. (2001) Checklist and annotated bibliography of decapod Crustacea larvae from the Southwestern European coast (Gibraltar Strait area). *Scientia Marina*. **65**, 275–305.

Guinot, D. & Quenette, G. (2005) The spermatheca in podotreme crabs (Crustacea, Decapoda, Brachyura, Podotremata) and its phylogenetic implications. *Zoosystema*. **27**, 267–342.

Guo, J.Y., Ng, N.K., Dai, A.Y. & Ng, P.K.L. (1997) The taxonomy of three commercially important species of mitten crabs of the genus *Eriocheir* de Hann, 1835 (Crustacea: Decapoda: Brachyura: Grapsidae). *Raffles Bulletin of Zoology*. **45**(2), 445–476.

Gurney, R. (1939) Bibliography of the larvae of the decapod Crustacea. *Roy Society, London*. **1**(6), 123.

Hafner, B. (2007) Scanning Electron Microscopy Primer. *University of Minnesota*. Accessed http://www.charfac.umn.edu/instruments/sem_primer.pdf. 10 September 2017.

Hall, N.G., Smith, K.D., de Lestang, S. & Potter, I.C. (2006) Does the largest chela of males of three crab species undergo an allometric change that can be used to determine morphometric maturity? *ICES Journal of Marine Science*. **63**(1), 40–150.

Hammer, Ø., Harper, D.A.T. & Ryan, P.D. (2001) PAST: Paleontological Statistics Software Package for Education and Data Analysis. *Palaeontologia Electronica*. **4**(1), 1–9. https://folk.uio.no/ohammer/past/past3manual.pdf. Accessed 10 September 2017.

Hänfling, B., Carvalho, G. & Brandl, R. (2002) mt-DNA sequences and possible invasion pathways of the Chinese mitten crab. *Marine Ecology Progress Series*. **238**, 307–310.

Haond, C., Flik, G. & Charmantier, G. (1998) Confocal laser scanning and electron microscopical studies on osmoregulatory epithelia in the branchial cavity of the lobster *Homarus gammarus*. *The Journal of Experimental Biology*. **201**, 1817–1833.

Hartnoll, R.G. (1968) Morphology of the genital ducts in female crabs. *Zoological Journal of the Linnean Society*. **47**, 279–300.

Hartnoll, R.G. (1969) Mating in the Brachyura. *Crustaceana*. **16**, 160–181.

Hartnoll, R.G. (1979) The phyletic implications of spermathecal structure in the Raninidae (Decapoda: Brachyura). *Journal of Zoology (London)*. **187**, 75–83.

Hashim, A.A. (2010) Occurrence of the Chinese mitten crab *Eriocheir sinensis* (H. Milne Edwards) in South Iraq. *Mesopotamian Journal of Marine Science*. **25**(2), 31–36.

Haug, C., Mayer, G., Kutschera, V., Waloszek, D., Maas, A. & Haug, J.T. (2011) Imaging and documenting gammarideans. *International Journal of Zoology*. art.380829.

Herborg, L.M., Rushton, S.P., Clare, A.S. & Bentley, M.G. (2003) Spread of the Chinese mitten crab (*Eriocheir sinensis* H. Milne Edwards) in Continental Europe: analysis of a historical data set. *Hydrobiologia*. **503**, 21–28.

Herborg, L.M., Rushton, S.P., Clare, A.S. & Bentley, M.G. (2005) The invasion of the Chinese mitten crab (*Eriocheir sinensis*) in the United Kingdom and its comparison to continental Europe. *Biological Invasions*. **7**, 959–968.

Herborg, L.M., Bentley, M.G., Clare, A.S. & Last, K.S. (2006) Mating behaviour and chemical communication in the invasive Chinese mitten crab *Eriocheir sinensis. Journal of Experimental Marine Biology and* Ecology. **329**, 1−10.

Herborg, L.M., Jerde, C.L., Lodge, D.M., Ruiz, G.M. & MacIsaac, H.J. (2007) Predicting invasion risk using measures of introduction effort and environmental niche models. *Ecological Applications*. **17**, 663–674.

Herranz, M., Boyle, M.J., Pardos, F. & Neves, R.C. (2014) Comparative myoanatomy of *Echinoderes* (Kinorhyncha): a comprehensive investigation by CLSM and 3D reconstruction. *Frontiers in Zoology*. **11**(1), 31.

Hertzler, P.L. (2002) Development of the mesendoderm in the dendrobranchiate shrimp *Sicyonia ingentis*. *Arthropod Structure and Development*. **31**, 33–49.

Hertzler, P.L. (2005) Cleavage and gastrulation in the shrimp *Penaeus* (*Litopenaeus*) *vannamei* (Malacostraca, Decapoda, Dendrobranchiata). *Arthropod Structure and Development*. **34**, 455–469.

Hess, G.S. & Bauer, R.T. (2002) Spermatophore transfer in the hermit crab *Clibanarius vittatus* (Crustacea, Anomura, Diogenidae*). Journal of Morphology*. **253**, 166–175.

Hines, A.H. (1982) Allometric constraints and variables of reproductive effort in brachyuran crabs. *Marine Biology*. **69**, 309–320.

Hines, A.H. (1986) Larval patterns in the life histories of brachyuran crabs (Crustacea, Decapoda, Brachyura). *Bulletin of Marine Science*. **39**, 444–466.

Hines, A.H. (1988) Fecundity and reproductive output in two species of deep sea crabs *Geryon fenneri* and *G. quinquedens* (Decapoda: Brachyura). *Journal of Crustacean Biology*. **8**(4), 557−562.

Hinrichs, V.O. & Grell, K.G. (1937) Entwicklungsstadien von *Eriocheir sinensis* H. Milne-Edwards im Helgolander Plankton. *Zoologischer Anzeiger (Leipzig)*. **119**, 217−221.

Hou, X.L., Mao, Q., Gong, Y.N., Qu, D. & Wang, Q. (2010) Accessory sex gland proteins affect spermatophore digestion rate and spermatozoa acrosin activity in *Eriocheir sinensis*. *Journal of Crustacean Biology*. **30**(3), 435−440.

Huang, J. & Hsueh, P. (1998) New records of two interesting deep-water crabs, *Homolochunia gadaletae* Guinot and Richer de Forges, 1995 (Homolidae) and *Rochinia*

sagamiensis (Gordon, 1931) (Majidae) (Crustacea: Decapoda: Brachyura), from Taiwan. *Zoological Studies*. **37**(3), 222−225.

Hymanson, Z. (1999) The Chinese mitten crab in its native range. *Report presented before the Chinese mitten crab Project Work Team, July 1, Stockton, California*.

Hymanson, Z., Wang, J. & Sasaki, T. (1999) Lessons from the home of the Chinese mitten crab. *IEP Newsletter*. **12**, 25–32.

Ifuku, S., Nogi, M., Abe, K., Yoshioka, M., Morimoto, M., Saimoto, H. & Yano, H. (2009) Preparation of chitin nanofibers with a uniform width as *α*-chitin from crab shells. *Biomacromolecules*. **10**(6), 1584–1588.

Ingle, R.W. (1986) The Chinese Mitten Crab – a contentious immigrant. *London Naturalist* (London). **65**, 101−105.

Ingle, R.W. (1991) [1992] Larval stages of North-eastern Atlantic crabs. An illustrated key. *Natural History Museum Publications*. Chapman & Hall London.

Integrated Taxonomic Information System (ITIS) (2007) Web database application. http://www.itis.gov/servlet/SingleRpt/SingleRpt?search_topic=TSN&search_value=99058. Accessed 20 March 2017.

Jensen, G.C. & Armstrong, D.A. (2004) The occurrence of the Japanese mitten crab, *Eriocheir japonica* (De Haan), on the west coast of North America. *California Fish and Game*. **90**, 94–99.

Jin, G., Xie, P. & Li, Z.J. (2002) The precocious Chinese mitten crab: changes of gonad, survival rate, and life span in a freshwater lake. *Journal of Crustacean Biology*. **22**, 411–415.

Kabata, Z. (1979) Parasitic Copepoda of British fishes. *Ray Society, London*.

Kamanli, S.A., Kihara, T.C., Ball, A.D., Morritt, D. & Clark, P.F. (2017) A 3D imaging and visualisation workflow, using confocal microscopy and advanced image processing for brachyuran crab larvae. *Journal of Microscopy*. **266**, 307–323.

Keiler, J., Richter, S. & Wirkner, C.S. (2013) Evolutionary morphology of the hemolymph vascular system in hermit and king crabs (Crustacea: Decapoda: Anomala). Journal of Morphology. **274**, 759–778.

Kelly, J. & Maguire, C.M. (2009) Chinese Mitten Crab (*Eriocheir sinensis*) Invasive Species Action Plan. *Prepared for NIEA and NPWS as part of Invasive Species Ireland*.

Kerbl, A., Bekkouche, N., Sterrer, W. & Worsaae, K. (2015) Detailed reconstruction of the nervous and muscular system of Lobatocerebridae with an evaluation of its annelid affinity. *BMC Evolutionary Biology*. **15**(1), 277.

Kester, D.R., Duedall, I.W., Connors, D.N. & Pytkowicz, R.M. (1967) Preparation of artificial seawater. *Limnology and Oceanography*. **12**, 176–178.

Kihara, T.C. & Falavigna da Rocha, C.E. (2009) Técnicas para estudo taxonomico de copepodes harpacticoides da meiofauna marinha. *Asterisco, Porto Alegre*. pp. 96.

Kihara, T.C. & Arbizu, P.M. (2012) Three new species of *Cerviniella* Smirnov, 1946 (Copepoda: Harpacticoida) from the Arctic. *Zootaxa*. **3345**, 1−33.

Kim, C.H. & Hwang, S.G. (1990) Complete larval development of *Eriocheir japonicus* De Haan (Crustacea, Brachyura, Grapsidae) reared in the laboratory. *Korean Journal of Zoology*. **33**(4), 411−427.

Kim, C.H. & Hwang, S.G. (1995) The complete larval development of the mitten crab *Eriocheir sinensis* H. Milne Edwards. 1853 (Decapoda, Brachyura, Grapsidae) reared in the laboratory and a key to the known zoeae of the Varuninae. *Crustaceana*. **68**(7), 793−812.

Klaus, A.V., Kulasekera, V.L. & Schawaroch, V. (2003) Three-dimensional visualisation of insect morphology using confocal laser scanning microscopy. *Journal of Microscopy.* **212**(2), 107−121.

Klaus, A.V. & Schawaroch, V. (2006) Novel methodology utilizing confocal laser scanning microscopy for systematic analysis in arthropods (Insecta). *Integrative and Computer Biology.* **46**(2), 207−214.

Klaus, S., Christoph, D., Schubart, C.D. & Brandis, D. (2009) Ultrastructure of spermatozoa and spermatophores of old world freshwater crabs (Brachyura: Potamoidea: Gecarcinucidae, Potamidae, and Potamonautidae). *Journal of Morphology*. **270**, 175–193.

Kleinow, W., Klusemann, J. & Wratil, H. (1990) A gentle method for the preparation of hard parts (trophi) of the mastax of rotifers and scanning electron microscopy of the trophi of *Brachionus plicatilis* (Rotifera). *Zoomorphology*. **109**, 329–336.

Kobayashi, S. & Matsuura, S. (1995) Reproductive ecology of the Japanese mitten crab *Eriocheir japonicus* (De Haan) in its marine phase. *Benthos Re*search. **49**, 15–28.

Kobayashi, S. & Matsuura, S. (1997) Incidence of limb loss and bald chelipeds in the Japanese mitten crab *Eriocheir japonica* (De Haan) in its marine phase. *Benthos Research*. **52**, 61–68.

Kobayashi, S., Kagehira, M., Yoneji, T. & Matsuura, S. (1997) Questionnaire research on the ecology and fishery of the Japanese mitten crab *Eriocheir japonica* (de Haan). *Scientific Bulletin of Faculty of Agriculture, Kyushu University*. **52**, 89–104.

Kobayashi, S. & Matsuura, S. (1999) Reproductive ecology of the Japanese mitten crab *Eriocheir japonica* (De Haan): a review. *Japanese Journal of Benthology*. **54**, 24–35.

Kobayashi, S. (2001) Fecundity of the Japanese mitten crab *Eriocheir japonica* (de Haan), *Benthos Research*. **56**, 1–7.

Kobayashi, S. (2003) Process of growth, migration, and reproduction of middle- and large-sized Japanese mitten crab *Eriocheir japonicus* (De Hann) in a small river and its adjacent sea coast. *Benthos Research*. **58**, 15–28.

Koch, M., Kamanli, S.A., Crimmen, O., Lin, C.W., Clark, P.F. & Ďuriš, Z. (2017 in press) The identity of *Monomia argentata* (Crustacea: Brachyura: Portunidae) resolved by X-ray, CT-scanning and molecular comparisons. *Invertebrate Systematics*.

Komai, T., Yamasaki, I., Kobayashi, S., Yamamoto, T. & Watanabe, S. (2006) *Eriocheir ogasawaraensis* Komai, a new species of mitten crab (Crustacea: Decapoda: Brachyura: Varunidae) from the Ogasawara Islands, Japan, with notes on the systematics of *Eriocheir* De Haan, 1835. *Zootaxa*. **1168**, 1–20.

Korn, O.M., Kornienko, E.S. & Scherbakova, N.V. (2010) Key for the identification of larvae of brachyuran and anomuran crabs in spring plankton of Peter the Great Bay, Sea of Japan. *Russian Journal of Marine Biology*. **36(**5), 373–382.

Kornienko, E.S. & Korn, O.M. (2009) Illustrated key for the identification of brachyuran zoeal stages (Crustacea: Decapoda) in the plankton of Peter the Great Bay (Sea of Japan). *Journal of the Marine Biological Association of the United Kingdom*. **89**(2), 379–386.

Kottmann, J., Kihara, T.C., Glatzel, T. & Veit-Köhler, G. (2013) A new species of *Wellsopsyllus* (Copepoda, Harpacticoida, Paramesochridae) from the deep Southern Ocean and remarks on its biogeography. *Helgoland Marine Research*. **67**, 33–48.

Krouse, J.S. (1980) Distribution and catch composition of Jonah crab, *Cancer borealis*, and rock crab, *Cancer irroratus*, near Boothbay Harbor, Maine. *Fishery Bulletin*. **77**, 685–693.

Kuris, A.M. (1991) A review of patterns and causes of crustacean brood mortality. In Wenner, A. & Kuris, A. (Eds), Crustacean egg production. *Crustacean issues*. **7**, 117–141.

Lai, J.C.Y., Ng, P.T.K. & Davie, P.J.F. (2010) A revision of the Portunus pelagicus (Linnaeus, 1758) species complex (Crustacea: Brachyura: Portunidae), with the recognition of four species. *The Raffles Bulletin of Zoology*. **58**(2), 199–237.

Leasi, F., Rothe, B.H., Schmidt-Rhaesa, A. & Todaro, M.A. (2006) The musculature of three species of gastrotrichs surveyed with Confocal Laser Scanning Microscopy (CLSM). *Acta Zoologica*. **87**, 171–180.

Leasi, F. & Todaro, M.A. (2009) Meiofaunal cryptic species revealed by confocal microscopy: the case of *Xenotrichula intermedia* (Gastrotricha). *Marine Biology*. **156**, 1335−1346.

Lee, H.J. (1988) The larval development of four species of grapsid crabs (Decapoda, Grapsidae) reared in the laboratory. *PhD dissertation in Pusan National University*. 1−78.

Lee, S., Brown, R.L. & Monroe, W. (2009) Use of confocal laser scanning microscopy in systematics of insects with a comparison of fluorescence from different stains. *Systematic Entomology*. **34**, 10−14.

Li, G., Shen, Q. & Xu, Z.X. (1993) Morphometric and biochemical genetic variation of the mitten crab, *Eriocheir*, in Southern China. *Aquaculture*. **111**, 103–115.

Li, M. & Zheng, H. (2000) Study on the morphology of *Eriocheir hepuensis*. *Journal of Zhejiang Ocean University*. **19**, 1–5.

Li, M. & Zheng, H. (2001) The growth and ecological characteristics of *Eriocheir hepuensis*. *Journal of Zhejiang Ocean University*. **21**, 1–5.

Li, S.F. & Zou, S.M. (1999) Phylogenesis of populations of mitten crabs (*Eriocheir sinensis*, *E. japonica*) in six river systems of mainland China: RAPD fingerprinting marker. *Journal of Fish Biology China*. **23**(4), 325– 326.

Liang, X., Yang, S., Cheng, D. & Guo, D. (1974) Larval development of *Eriocheir sinensis* H. Milne Edwards. *Acta Zoologica Sinica*. **20**, 61−71. In: Mariscal Cuesta, J.A. (1999) Morfologia larval de familia Grapsidae (Crustacea, Decapoda, Brachyura). *Ph.D. Dissertation, University of Seville, Seville*.

Limaye, A. (2012) Drishti: a volume exploration and presentation tool. In Stock, S.R. (Ed.), Proceedings of SPIE Vol. 8506 SPIE. *Developments in X-Ray Tomography VIII Bellingham, Washington.*

Litulo, C. (2004) Reproductive aspects of a tropical population of the fiddler crab *Uca annulipes* (H. Milne Edwards, 1837) (Brachyura: Ocypodidae) at Costa do Sol Mangrove, Maputo Bay, southern Mozambique. *Hydrobiologia*. **525**, 167−173.

Llodra, R.E. (2002) Fecundity and life-history strategies in marine invertebrates. *Advances in Marine Biology*. **43**, 87–170.

Low, B.W., Ng, N.K. & Yeo, D.C.J. (2013) First record of the invasive Chinese mitten crab, *Eriocheir sinensis* H. Milne Edwards, 1853 (Crustacea: Brachyura: Varunidae) from Singapore. *Bioinvasions Records*. **2**(1), 73–78.

Lowe, S., Browne, M. & Boudjelas, S. (2000) 100 of the world's worst invasive alien species. A selection from the global invasive species database. Invasive Species

Specialist Group, Auckland, New Zealand. *International Union for Conservation of Nature*. Available at: http://www.issg.org/pdf/publications/worst_100/english_100_worst.pdf. Accessed 17 Oct 2016.

Maas, A. & Waloszek, D. (2001) Larval development of *Euphausia superba* Dana, 1852 and a phylogenetic analysis of the Euphausiacea. *Hydrobiologia*. **448**, 143–169.

Magalhães, C., Campos, M.R. & Türkay, M. (2013) Freshwater crabs from eastern Panamá: a new species of *Potamocarcinus* H. Milne Edwards, 1853, and new records of two little-known species (Crustacea: Decapoda: Pseudothelphusidae, Trichodactylidae). *Zootaxa*. **3702**(4), 348–356.

Manjón-Cabeza, M.E., Cobos, V., García Muñoz, J.E. & García Raso, J.E. (2009) Structure and absolute growth of a population of *Hippolyte inermis* Leach 1815 (Decapoda Caridea) from *Zostera marina* (L.) meadows (Malaga, southern Spain). *Scientia Marina*. **73**(2), 377–386.

Mantelatto, F.L., Reigada, A.L.D., Gatti, A.C.R. & Cuesta, J.A. (2014) Morphology of the first zoeal stages of five species of the portunid genus *Callinectes* (Decapod, Brachyura) hatched at the laboratory. *Anais da Academia Brasileira de Ciencias*. **86**(2), 755–767.

Marco-Herrero, E., Gonzalez-Gordillo, J.I. & Cuesta, J.A. (2014) Morphology of the megalopa of the mud crab, *Rhithropanopeus harrisii* (Gould, 1841) (Decapoda, Brachyura, Panopeidae), identified by DNA barcode. *Helgoland Marine Research*. **68**, 201–208.

Marques, F. & Pohle, G. (1996) Complete larval development of *Clypeasterophilus stebbingi* (Decapoda: Brachyura: Pinnotheridae) and a comparison with other species within the *Dissodactylus* complex. *Bulletin of Marine Science*. **58**, 165−185.

Marques, F. & Pohle, G. (2003) Searching for larval support for majoid families (Crustacea: Brachyura) with particular reference to *Inachoididae* Dana, 1851. *Invertebrate Reproduction and Development*. **43**, 71–82.

Martin, J.W. & Davis, G.E. (2001) An updated classification of the recent Crustacea. *Natural History Museum of Los Angeles County Contributions in Science*. **39**, 1–124.

Maruzzo, D., Minelli, A. & Fusco, G. (2009) Segmental mismatch in crustacean appendages: The naupliar antennal exopod of *Artemia* (Crustacea, Branchiopoda, Anostraca). *Arthropod Structure & Development*. **38**, 163–172.

Matsuoka, H., Yang, H.C., Homma, T., Nemoto, Y., Yamada, S., Sumita, O., Takatori, K. & Kurata, H. (1995) Use of Congo red as a microscopic fluorescence indicator of hyphal growth. *Applied Microbiology and Biotechnology.* **43**, 102–108.

Matsuura, S., Takeshita, K., Fujita, H. & Kawasaki, S. (1972) Reproduction and fecundity of the female king crab, *Paralithodes camtschatica* (Tilesius) in the waters off western Kamchatka. II. Determination of the fecundity based on the counts of the ovarian eggs and of the spawned eggs attached to pleopods. *Bulletin Far Seas Fisheries Research Laboratory*. **8**, 169–190.

Mayr, E. (1969) Principles of systematic zoology. *McGraw-Hill, New York.*

McAllen, R. & Taylor, A. (2001) The effect of salinity changes on the oxygen consumption and swimming activity of the high-shore rockpool copepod *Tigriopus brevicornis. Journal of Experimental Marine Biology and Ecology*. **263**, 227–240.

McLay, C.L. & Becker, C. (2015) Reproduction in Brachyura. In Castro, P., Davie, P.J.F., Guinot, D., Schram, F.R. & Von Vaupel Klein, J.C. (Eds), Decapoda: Brachyura, Treatise on Zoology – Anatomy, Taxonomy, Biology. The Crustacea, Complementary

to the volumes translated from the French of the Traité de Zoologie [founded by Grassé (†), P.-P.]. *Brill, Leiden and Boston*. Chapter 71–17, 9(CII), pp. 185–243.

McLaughin, P.A. & Lemaitre, R. (1997) Carcinization in the Anomura- fact or fiction? I. Evidence from adult morphology. *Contributions to Zoology*. **67**(2), 79−123.

McLaughin, P.A. & Lemaitre, R. (2000) Aspects of evolution in the anomuran superfamily Paguroidea: one larval prospective. Invertebrate Reproduction and Development. **38**(3), 159−169.

Menzel, L. (2011) First descriptions of copepodid stages, sexual dimorphism and intraspecific variability of *Mesocletodes* Sars, 1909 (Copepoda, Harpacticoida, Argestidae), including the description of a new species with broad abyssal distribution. *ZooKeys*. **96**, 39–80.

Meyer, R. & Melzer, R.R. (2004) Scanning EM diagnosis of marine Decapoda larvae: A comparison of preparation techniques. *Crustaceana*. **77**, 883–886.

Meyer, R., Wehrtmann, I.S. & Melzer, R.R. (2006) Morphology of the first zoeal stage of *Portunus acuminatus*, Stimpson, 1871 (Decapoda: Portunidae: Portuninae) reared in the laboratory. *Crustaceana*. **70**(2), 261–270.

Meyer, R., Lehmann, T., Melzer, R.R. & Geiselbrecht, H. (2014) Morphology of the first zoeal stage of the mediterranean bumblebee shrimp *Gnathophyllum elegans* (Risso,1816) studied with light microscopy and scanning EM. *Journal of the Marine Biological Association of the United Kingdom*. **94**(1), 151–158.

Michels, J. (2007) Confocal laser scanning microscopy: using cuticular autofluorescence for high resolution morphological imaging in small crustaceans. *Journal of Microscopy*. **227**(1), 1−7.

Michels, J. & Büntzow, M. (2010) Assessment of Congo red as a fluorescence marker for the exoskeleton of small crustaceans and the cuticle of polychaetes. *Journal of Microscopy*. **238**(2), 95−101.

Michels, J. & Gorb, S.N. (2012) Detailed three dimensional visualisation of resilin in the exoskeleton of arthropods using confocal laser scanning microscopy. *Journal of Microscopy*. **245**(1), 1−16.

Michels, J., Vogt, J. & Gorb, S.N. (2012) Tools for crushing diatoms – opal teeth in copepods feature a rubber-like bearing composed of resilin. *Scientific Reports*. **2**, 465.

Michels, J., Appel, E. & Gorb, S.N. (2016) Functional diversity of resilin in Arthropoda. *Beilstein Journal of Nanotechnology*. **7**, 1241−1259.

Mills, C.D., Clark, P.F. & Morritt, D. (2016) Flexible prey handling, preference and a novel capture technique in invasive, sub-adult Chinese mitten crabs. *Hydrobiologia*. **773**, 135–147.

Mitten Crab Recording Project (n.d.) Acknowledging your sources. Available at: http://mittencrabs.org.uk/. Accessed 20 January 2017.

Montú, M., Anger, K. & de Bakker, C. (1996) Larval development of the Chinese mitten crab *Eriocheir sinensis* H. Milne-Edwards (Decapoda: Grapsidae) reared in the laboratory. Helgoländer Meeresuntersuchungen. **50**, 223−252.

Moriyasu, M. & Benhalima, K. (1998) Snow crabs, *Chionoecetes opilio* (O. Fabricius, 1788) (Crustacea: Majidae) have two types of spermatophore: hypotheses on the mechanism of fertilization and population reproductive dynamics in the southern Gulf of St. Lawrence, Canada. *Journal of Natural History*. **32**(10–11), 1651–1665.

Morritt, D., Mills, H., Hind, K., Clifton-Dey, D. & Clark, P.F. (2013) Monitoring downstream migrations of *Eriocheir sinensis* H. Milne Edwards, 1853 (Crustacea:

Brachyura: Grapsoidea: Varunidae) in the River Thames using capture data from a water abstraction intake. *Management of Biological Invasions*. **4**, 139–147.

Moussian, B., Tång, E., Tonning, A., Helms, S., Schwarz, H., Nüsslein-Volhard, C. & Uv, A.E. (2006) Drosophila Knickkopf and Retroactive are needed for epithelial tube growth and cuticle differentiation through their specific requirement for chitin filament organization. *Development*. **133**, 163−171.

Müller, M.C.M. & Worsaae, K. (2006) CLSM analysis of the phalloidin-stained muscle system in *Nerilla antennata*, *Nerillidium* sp. and *Trochonerilla mobilis* (Polychaeta, Nerillidae). *Journal of Morphology*. **267**, 885–896.

Naser, M.D., Page, T.J., Ng, N.K., Apel, M., Yasser, A.G., Bishop, J.M., Ng, P.K.L. & Clark, P.F. (2012) Invasive records of *Eriocheir hepuensis* Dai, 1991 (Crustacea: Brachyura: Grapsoidea: Varunidae): implications and taxonomic considerations. *BioInvasions Records*. **1**(1), 71–86.

Nepszy, S.J. & Leach, J.H. (1973) First Records of the Chinese Mitten Crab, *Eriocheir sinensis*, (Crustacea: Brachyura) from North America. *Journal of the Fisheries Research Board of Canada*. **30**(12), 1909–1910.

Ng, P.K.L. (1998) Crabs. In: Carpenter, K.E. & Niem, V.H. (Eds), FAO species identification guide for fishery purposes. The living marine resources of the Western-Central Pacific. Vol 2: Cephalopods, crustaceans, holothurians and sharks. *Food and Agriculture Organization of the United Nations, Rome*. **2**, 1045–1155.

Ng, N.K., Guo, J. & Ng, P.K.L. (1999) Generic affinities of *Eriocheir leptognatha* and *E. formosa* with description of a new genus (Brachyura: Grapsidae: Varuninae). *Journal of Crustacean Biology*. **19**(1), 154–170.

Ng, P.K.L., Guinot, D. & Davie, P.J.F. (2008) Systema Brachyurorum: Part I. An annotated checklist of extant brachyuran crabs of the world. *Raffles Bulletin of Zoology, Supplement*. **17**, 1–286.

Ng, P. (2014) *Monomia argentata* (White & Milne Edwards, 1861). Online: World Register of Marine Species at http://www.marinespecies.org/aphia.php?p=taxdetails&id=210294. Accessed 31 July 2017.

NNSS, GB non-native species secretariat (2017) Chinese mitten crab. Online. www.nonnativespecies.org. Accessed 8 June 2017.

Oatley, C.W., Nixon, W.C. & Pease, R.F. W. (1965) Scanning electron microscopy. *Advances in Electronics and Electron Physics*. **21**, 181−247.

Okazaki, R.K. & Wehrtmann, I.S. (2014) Preliminary survey of a nemertean crab egg predator, *Carcinonemertes*, on its host crab, *Callinectes arcuatus* (Decapoda, Portunidae) from Golfo de Nicoya, Pacific Costa Rica. *ZooKeys*. **457**, 367−375.

Otto, T. & Brandis, D. (2011) First evidence of *Eriocheir sinensis* reproduction from Schleswig-Holstein, northern Germany, western Baltic Sea. *Aquatic Invasions*. **6**, 65–69.

Otto, T. (2012) Reproduction biology and population genetics of the alien Chinese mitten crab (*Eriocheir sinensis*) in Schleswig-Holstein. *PhD dissertation in Mathematisch-Naturwissenschaftlichen Fakultät der Christian-Albrechts-Universität zu Kiel*.

Packard, D.S., Cox, C. & Poole, T.J. (2000) Improved techniques for avian embryo culture, somite cell culture, and microsurgery. *Methods in Molecular Biology*. **137**, 185–199.

Palero, F., Ferrer Mateu, I., Wray, B., Hughes, R., Morritt, D., Lepage, M., Van Der Meer, M., Tate, M. & Clark, P.F. (2016) Pathways of invasion: the genetic structure of the Chinese mitten crab in Europe. XIX Simposio Ibérico de Biología Marina Porto (Portugal), 5 – 9 Sep 2016. Frontiers in Marine Science. Conference Abstract. DOI: 10.3389/conf.FMARS.2016.05.00183.

Panning, A. (1938) The Chinese mitten crab. *Annual report of the Board of the Smithsonian Institution*. 361−375.

Panning, A. (1939) Die Larven von *Eriocheir sinensis* H. M.-Edw. *Zoologischer Anzeiger*. **125**, 273−283.

Paula, J. (1998) Larval retention and dynamics of the prawns *Palaemon longirostris* H. Milne Edwards and *Crangon crangon* Linnaeus (Decapoda, Caridea) in the Mira estuary, Portugal. *Invertebrate Reproduction & Development*. **33**, 221–228.

Pawley, J. (1995) Handbook of biological confocal microscopy. *New York: Plenum Press*.

Peters, N. (1938) Ausbreitung und Verbreitung der chinesischen Wollhandkrabbe (*Eriocheir sinensis* H. M.-Edw.) in Europa in den Jahren 1933 bis 1935. In: Neue Untersuchungen über die chin. Wollhandkrabbe in Europa. *Mitteilungen aus dem Hamburger Zoologischen Museum und Institut*. **47**, 1–31.

Pessani, D., Burri, R. & Salton, L. (1998) A key for the identification of the known larval stages of the Mediterranean Brachyura. *Invertebrate Reproduction and Development*. **33**, 191–199.

Pfeiffer, I., Volkel, I., Taubert, H. & Brenig, B. (2004) Forensic DNA-typing of dog hair: DNA-extraction and PCR amplification. *Forensic Science International*. **141**, 149–151.

Pinheiro, M.A.A. & Fransozo, A. (2002) Reproduction of the speckled swimming crab *Arenaeus Cribrarius* (Brachyura: Portunidae) on the Brazilian coast near 23°30′S. *Journal of Crustacean Biology*. **22**, 416–428.

Pohle, G. & Telford, M. (1981) Morphology and classification of decapod crustacean larval setae: a scanning electron microscope study of *Dissodactylus crinitichelis* Moreira, 1901 (Brachyura: Pinnotheridae). *Bulletin of Marine Science*. **31**, 736−752.

Pohle, G.W. (1991) Larval development of Canadian Atlantic oregoniid crabs (Brachyura: Majiidae), with emphasis on *Hyas coarctatus alutaceus* Brandt, 1851, and a comparison with Atlantic and Pacific conspecifics. *Canadian Journal of Zoology*. **69**, 2717−2737.

Pointner, K., Kihara, T.C., Glatzel, T. & Veit-Köhler, G. (2013) Two new closely related deep-sea species of Paramesochridae (Copepoda, Harpacticoida) with extremely differing geographical range sizes. *Marine Biodiversity*. **43**, 293−319.

Przemyslaw, C. & Marcello, D.G. (2013) Realized fecundity in the first brood and size of eggs of Chinese mitten crab (*Eriocheir sinensis*) – Laboratory Studies. *International Resarch Journal of Biological Sciences*. **2**(1), 1−6.

Puls, A.L. (2001) Arthropoda: Decapoda. In Shanks, A.L. (Ed.), A guide to the identification of the larval invertebrates of the Pacific Northwest. Oregon. *Oregon State University Press*. pp. 179–250.

Rabalais, N.N. & Cameron, J.N. (1985) Abbreviated development of *Uca subcylindrica* (Stimpson, 1859) (Crustacea, Decapoda, Ocypodidae) reared in the laboratory. *Journal of Crustacean Biology*. **3**, 519–541.

Rainbow, P., Roni, R. & Clark, P.F. (2003) Alien invaders: Chinese mitten crabs in the Thames and spreading. *Biologist*. **50**(5), 227−230.

Rebolledo, A.P., Wehrtmann, I.S. & Cuesta, J.A. (2015) Morphological and morphometric comparison of the first zoeal stage of mangrove crabs of the genus *Aratus* H. Milne Edwards, 1853 (Decapoda; Sesarmidae). *Zootaxa*. **3949**(2), 217–228.

Rice, A.L. (1979) Improved standards in crab zoeal descriptions. *Crustaceana*. **37**, 213–218.

Rice, A.L. (1980) Crab zoeal morphology and its bearing on the classification of the Brachyura. *Transactions of the Zoological Society of London*. **35**, 271–424.

Rice, A. & Tsukimura, B. (2007) A key to the identification of brachyuran zoeae of the San Francisco Bay estuary. *Journal of Crustacean Biology*. **27**, 74–79.

Robbins, R.S., Clark, P. & Rainbow, P. (2003) Alien invaders: Chinese mitten crabs in the Thames and spreading. *Biologist*. **50**(5), 227–230.

Robbins, R.S., Sakari, M., Nezami Baluchi, S. & Clark, P.F. (2006) The occurrence of *Eriocheir sinensis* H. Milne Edwards, 1853 (Crustacea: Brachyura: Varunidae) from the Caspian Sea region, Iran. *Aquatic Invasions*. **1**, 32–34.

Robbins, R.S., Clark P.F. & Rainbow, P. (2007) Mitten Crabs: Oriental Invaders of the River Thames (Online). http://www.nhm.ac.uk/nature-online/life/other-invertebrates/chinese-mitten-crabs/chinese-mitten-crabs.html.

Roy, L., Dowling, A.P.G., Chauve, C.M. & Buronfosse, T. (2009) Delimiting species boundaries within *Dermanyssus* Dugès, 1834 (Acari: Dermanyssidae) using a total evidence approach. *Molecular Phylogenetics and Evolution*. **50**, 446–470.

Rudnick, D.A., Halat, K.M. & Resh, V.H. (2000) Distribution, ecology and potential impacts of the Chinese mitten crab (*Eriocheir sinensis*) in San Francisco Bay. *Water Resources Center, Contribution #206, University of California Water Resources Center, Berkeley, CA.*

Rudnick, D.A., Hieb, K., Grimmer, K.F. & Resh, V.H. (2003) Patterns and processes of biological invasion: The Chinese mitten crab in San Francisco Bay. *Basic Applied Ecology*. **4**, 249–262.

Rudnick, D.A., Veldhuizen, T., Tullis, R., Culver, C., Hieb, K. & Tsukimura, B. (2005) A life history model for the San Francisco Estuary population of the Chinese mitten crab, *Eriocheir sinensis* (Decapoda: Grapsoidea). *Biological Invasions*. **7**, 333–350.

Sakai, K. (2013) A review of the genus *Eriocheir* De Haan, 1835 and related genera, with the description of a new genus and a new species (Brachyura, Grapsoidea, Varunidae). *Crustaceana*. **86**(9), 1103–1138.

Santana, W., Marques, F.P.L., Fransozo, A. & Bertini, G. (2006) Larval development of *Notolopas brasiliensis* Miers, 1886 (Brachyura: Majoidea: Pisidae) described from laboratory reared material and a reappraisal of the characters of Pisidae. *Papeis Avulsos de Zoologia, Museu de Zoologia da Universidade de Sao Paulo*. **46**(19), 219–232.

Santos, A.D. & González-Gordillo, J.I. (2004) Illustrated key for the identification of the Pleocyemata (Crustacea: Decapoda) zoeal stages, from the coastal region of south-western Europe. *Journal of the Marine Biological Association of the United Kingdom*. **84**, 205–227.

Santos, A.D. (2014) Chinese mitten crab (*Eriocheir sinensis*). *Aquatic Invasion Ecology*. **423**, 1−12. Available at: http://depts.washington.edu/oldenlab/wordpress/wp-content/uploads/2015/09/Eriocheir_sinensis_DelosSantos_2014.pdf. Accessed 16 June 2017.

Sarda, F. (1991) Reproduction and moult synchronism in *Nephrops norvegicus* (L.) (Decapoda, Nephropidae) in the Western Mediterranean. Is spawning annual or biennial? *Crustaceana*. **60**, 186–199.

Schawaroch, V., Grimaldi, D. & Klaus, A.V. (2005) Focusing on morphology: Applications and implications of confocal laser scanning microscopy (Diptera: Campichoetidae, Camillidae, Drosophilidae). *Proceedings of the Entomological Society of Washington*. **107**, 323–335.

Schawaroch, V. & Li, S.C. (2007) Testing mounting media to eliminate background noise in confocal microscope 3-D images of insect genitalia. *Scanning*. **29**(4), 117–184.

Schnakenbeck, W. (1926) Neue Beobachtugen über die Wollhandkrabbe (*Eriocheir sinensis* Milne-Edw.). *Der Naturforscher (Berlin)*. **3**, 352−355.

Schnakenbeck, W. (1933) Larven und erste Bodenformen (pp. 157−170). In: Peters, N. & Panning, A. *Die Chinesische Wolhandkrabbe* (*Eriocheir sinensis* H. Milne-Edwards) in Deutschland. *Zoologischer Anzeiger (Leipzig)*. **104**, i−viii + 180 pp.

Schneider, C.A., Rasband, W.S. & Eliceiri, K.W. (2012) NIH Image to ImageJ: 25 years of image analysis. *Nature Methods*. **9**(7), 671−675.

Schroeder, W., Martin, K. & Lorensen, B. (1998) The visualization toolkit. *Prentice Hall, Upper Saddle River, New Jersey, USA*.

Schubart, C.D., Cuesta, J.A., Diesel, R. & Felder D.L. (2000) Molecular phylogeny, taxonomy, and evolution of nonmarine lineages within the American grapsoid crabs (Crustacea: Brachyura). *Molecular Phylogenetics and Evolution*. **15**, 179–190.

Schubart, C.D., Cuesta, J.A. & Felder, D.L. (2002) Glyptograpsidae, a new brachyuran family from Central America: larval and adult morphology, and a molecular phylogeny of the Grapsoidea. *Journal of Crustacean Biology*. **22**, 28–44.

Schubart, C.D. & Reuschel, S. (2009) A proposal for a new classification of Portunoidea and Cancroidea (Brachyura: Heterotremata) based on two independent molecular phylogenies. In Martin, J.W., Crandal, K.A. & Felder, D.L. (Eds), Decapod crustacean

phylogenetics. *Crustacean Issues, CRC Press, Taylor & Francis Group: Boca Raton, London, New York*. **18**, 533−549.

Schuh, M. & Diesel, R. (1995) Breeding in a rock pool: larvae of the semi terrestrial crab *Armases (= Sesarma) miersii* (Decapoda: Grapsidae) develop in a highly variable environment. Journal of *Experimental Marine Biology and Ecology*. **185**, 109−129.

Sepahvand, V., Rastegar-Pouyani, N. & Kihara, T.C. (2017) Two new species of *Clausidium* copepods (Crustacea, Poecilostomatoida) associated with ghost shrimps from Iran. *Journal of Marine Association of the United Kingdom*. 1−9.

Serène, R. (1966) Note sur les genres Catoptrus et Libystes et les Catoptrinae. *Bulletin du Muséum national d'Histoire naturelle (2).* **37**(6), 989–1000.

Serène, R. (1984) Crustaces Decapodes Brachyoures de l'Ocean Indien et de la Mer Rouge. Xanthoidea: Xanthidae et Trapeziidae. Editions Orstom. Collection. *Faune Tropicale*. **24**, 1–400.

Severino-Rodrigues, E., Fernandes, J.M., Moura, A.A.S., Branco, G.M.P. & Canéo, V.O.C. (2013) Fecundity, reproductive seasonality and maturation size of *Callinectes sapidus* females (Decapoda: Portunidae) in the Southeast coast of Brazil. *Reviasta de Biologia Tropical*. **61**(2), 595–602.

Sewell, K.B. & Cannon, L.R.G. (1995) A scanning electron microscope study of *Craspedella* sp. from the branchial chamber of red claw crayfish, *Cherax quadricarinatus*, from Queensland, Australia. *Hydrobiologia*. **305**, 151–158.

Shirley, S.M., Shirley, T.C. & Rice, S.D. (1987) Latitudinal variation in the Dungeness crab, *Cancer magister*: zoeal morphology explained by incubation temperature. *Marine Biology*. **95**, 371–376.

Shy, J.Y. & Yu, H.P. (1992) Complete larval development of mitten crab *Eriocheir rectus* Stimpson, 1858 (Decapoda, Brachyura, Grapsidae) reared in the laboratory. *Crustaceana*. **66**(3), 277−290.

Škraba, D., Tošić, A., Miličić, D., Nikolić, V. & Simonović, P. (2013) Invasiveness assessment of the Chinese mitten crab *Eriocheir sinensis* (H. Milne Edwards, 1853) in the Serbian section of the River Danube. *Archives of Biological Sciences*. **65**(1), 353–358.

Sluys, R. (1992) Evolutionary side-steps *Bijdragen tot de Dierkunde*. **62**(2), 121–126.

Solovyeva, A. & Bailey, K. (2017) *Eriocheir sinensis*, Chinese mitten crab (Online). http://animaldiversity.org/accounts/Eriocheir_sinensis/. Accessed 25 May 2017.

Soltanpour-Gargari, A., Engelmann, R. & Wellershaus, S. (1989) Development and rearing of zoea larvae in Brachyura (Crustacea Decapoda): A bibliography. *Crustaceana Supplement*. **14**, 1–173.

Sousa, G.L., Lenz, P.H., Hartline, D.K. & Christie, A.E. (2008) Distribution of pigment dispersing hormone- and tachykinin-related peptides in the central nervous system of the copepod crustacean *Calanus finmarchicus*. *General and Comparative Endocrinology*. **156**, 454–459.

Spiridonov, V.A., Neretina, T.V. & Schepetov, D. (2014) Morphological characterisation and molecular phylogeny of Portunoidea Rafinesque, 1815 (Crustacea Brachyura): Implications for understanding evolution of swimming capacity and revision of the family-level classification. *Zoologischer Anzeiger*. **253**, 404–429.

Spivak, E.D. & Cuesta, J.A. (2000) Larval development of *Cyrtograpsus affinis* (Dana) (Decapoda, Brachyura, Varunidae) from Rio de la Plata estuary, reared in the laboratory. *Scientia Marina*. **64**, 29–47.

Stechey, D.P.M. & Somers, K.M. (1995) Potential, realized and actual fecundity in the crayfish *Orconectes immunis* from southwestern Ontario. *Canadian Journal of Zoology*. **73**, 672−677.

Stella, V.S., Lopez, L.S. & Rodriguez, E.M. (1996) Fecundity and brood biomass investment in the estuarine crab *Chasmagnathus granulatus* Dana, 1851 (Decapoda, Brachyura, Grapsidae). *Crustaceana*. **69**(3), 306−312.

Stentiford, G.D. (2005) Survey of Chinese mitten crab (*Eriocheir sinensis*) from the Thames estuary to investigate their potential as vectors for the metacercarial stage of the human lung fluke (*Paragonimus westermani*). *Report by the Centre for Environment, Fisheries and Aquaculture Science (CEFAS), Barrack Road, The Nothe, Weymouth, Dorset UK for London Port Health Authority (LPHA), Corporation of London*.

Sternberg, R.V. & Cumberlidge, N. (2000) Taxic relationships within the Grapsidae MacLeay, 1838 (Crustacea: Decapoda: Brachyura). *Journal of Comparative Biology*. **3**, 115–136.

Sudha, K. & Anilkumar, G. (1996) Seasonal growth and reproduction in a highly fecund brachyuran crab, *Metopograpsus messor* (Forskal) (Grapsidae). *Hydrobiologia*. **319**, 15−21.

Sun, H., Wang, G., Zhan, D. & Zhou, K. (2005) Mitochondrial DNA sequence variation in two geographical subspecies of the mitten crab, *Eriocheir japonica. Acta Zoologica Sinica*. **51**, 862−866.

Swetha, C.H., Girish, B.P. & Reddy, P.S. (2015) Reproductive cycle and fecundity in natural population of edible freshwater crab, *Oziothelphusa senex senex* (Fabricius, 1798) (Decapoda: Brachyura). *Journal of Aquaculture Research & Development*. **6**(7), 349.

Tallack, S.M.L. (2007) Size–fecundity relationships for *Cancer pagurus* and *Necora puber* in the Shetland Islands, Scotland: how is reproductive capacity facilitated? *Journal of the Marine Biological Association of the United Kingdom*. **87**(2), 507−515.

Tamura, H., Landreira, J.M. & Goshima, S. (2017) Morphological and morphometric variability in the zoea I larvae of *Pugettia quadridens* (De Haan, 1839): looking for reliable characters for taxonomic studies on the genus *Pugettia* Dana, 1851 (Majoidea: Epialtidae). *Zootaxa*. **4226**(2), 264−272.

Tang, B., Zhou, K., Song, D., Yang, G. & Dai, A. (2003) Molecular systematics of the Asian mitten crabs, genus *Eriocheir* (Crustacea: Brachyura). *Molecular Phylogenetics and Evolution, Academic Press*. **29**, 309−316.

Tavares, M. (2002) True crabs. In: Carpenter, K.E. (Ed.), The living marine resources of the Western Central Atlantic. Vol 1: Introduction, molluscs, crustaceans, hagfishes, sharks, batoid fishes, and chimaeras. FAO Species. *Identification Guide for Fishery Purposes and American Society of Ichthyologists and Herpetologists. FAO, Rome. Special Publication*. **5**, 1–600.

The W.M. Keck Microscopy Center (n.d.) Acknowledging your sources. Retrieved from http://depts.washington.edu/keck/leica/pinhole.htm. Accessed 5 September 2017.

Thorn, K (n.d.) Acknowledging your sources. Retrieved from http://slideplayer.com/slide/10417592/. Accessed 5 September 2017.

Thurman, C.L. (1985) Reproductive biology and population structure of the fiddler crab *Uca subcylindrica* (Stimpson). *Biology Bulletin*. **169**, 215–229.

Tonning, A., Hemphala, J., Tång, E., Nannmark, U., Samakovlis, C. & Uv, A. (2005) A transient luminal chitinous matrix is required to model epithelial tube diameter in the *Drosophila* trachea. *Developmental Cell*. **3**, 423–430.

Torres, P., Penha-Lopes, G., Narciso, L., Macia, A. & Paula, J. (2009) Fecundity and brood loss in four species of fiddler crabs, genus Uca (Brachyura: Ocypodidae), in the mangroves of Inhaca Island, Mozambique. *Journal of the Marine Biological Association of the United Kingdom*. **89**(2), 371–378.

Turra, A. & Leite, F.P.P. (2001) Fecundity of three sympatric populations of hermit crabs (Decapoda, Anomura, Diogenidae). *Crustaceana*.**74**(10), 1019–1027.

Tuset, V.M., Espinosa, D.I., Garcia-Mederos, A., Santana, J.I. & Gonzalez, J.A. (2011) Egg development and fecundity estimation in deep-sea red crab, *Chaceon affinis* (Geryonidae), off the Canary Islands (NE Atlantic). *Fisheries Research*. **109**, (373−378).

Türkay, M. (1975) Statement: Die Bedeutung des Gonopodenaufbaus für die Aufklärung von Verwandtschaftsverhältnissen bei dekapoden Crustaceen. *Aufsaetze und Reden der Senckenbergischen naturforschenden Gesellschaft*. **27**, 114–115.

Uttieri, M., Brown, E.R., Boxshall, G.A. & Mazzocchi, M.G. (2008) Morphology of antennular sensors in *Clausocalanus furcatus* (Copepoda: Calanoida). *Journal of the Marine Biological Association of the UK*. **88**, 535–541.

Vakati, V., Kihara, T.C. & Lee, W. (2016) A new species of the genus *Nannopus* (Copepoda, Harpacticoida, Nannopodidae) from the mudflat of Ganghwa Island, Korea. *Proceedings of the Biological Society of Washington*. **129**, 212–233.

Valdecasas, A.G. (2008) Confocal microscopy applied to water mite taxonomy with the description of a new genus of Axonopsinae (Acari, Parasitengona, Hydrachnidia) from Central America. *Zootaxa*. **1820**, 41−48.

Valdecasas, A.G. & Abad, A. (2011) Morphological confocal microscopy in Arthropods and the enhancement of autofluorescence after proteinase K extraction. *Microscopy and Microanalysis*. **17**, 109–113.

Vehof, J., van der Meij, S.E.T., Türkay, M. & Becker, C. (2016). Female reproductive morphology of coral-inhabiting gall crabs (Crustacea: Decapoda: Brachyura: Cryptochiridae). *Acta Zoologica*. **97**, 117−126.

Veilleux, E. & de Lafontaine, Y. (2007) Biological synopsis of the Chinese mitten crab (*Eriocheir sinensis*). *Canadian Manuscript Report of Fisheries and Aquatic Sciences*. **2812**, vi + 45p.

Vela, M.J. & Gonzalez-Gordillo, J.I. (2016) Larval descriptions of the family Porcellanidae: A worldwide annotated compilation of the literature (Crustacea, Decapoda). *ZooKeys* **564**, 47–70.

Veldhuizen, T.C. & Stanish, S. (1999) Overview of the life history, distribution, abundance, and impact of the Chinese mitten crab, *Eriocheir sinensis*. *California Department of Water Resources. Environmental Services Office*.

Veldhuizen, T.C. (2001) Life history, distribution and impacts of the Chinese mitten crab, *Eriocheir sinensis. Aquatic Invaders*. **12**, 1–9.

Verísimo, P., Bernárdez, C., González-Gurriarán, E., Freire, J., Muiño, R. & Fernández, L. (2011) Changes between consecutive broods in the fecundity of the spider crab, *Maja brachydactyla*. *ICES Journal of Marine Science*. **68**, 472–478.

Vernet-Corxubert, G. (1958) Recherches sur la sexualite du crabe *Puchygrapsus ntarmwatus* (Fabricius). *Archives de zoologie expérimentale et générale*.**96**, 104−274.

Wang, C., Li, C. & Li, S. (2008) Mitochondrial DNA-inferred population structure and demographic history of the mitten crab (*Eriocheir sensu stricto*) found along the coast of mainland China. *Molecular* Ecology. **17**, 3515–3527

Wear, R.G. (1985) Checklist and annotated bibliography of New Zealand decapod crustacean larvae (Natantia, Macrura Reptantia, and Anomura). *Zoology Publications from Victoria University of Wellington*. **79**, 1–15.

Webster, J.M., Clark, P.F. & Morritt, D. (2015) Laboratory based feeding behaviour of the Chinese mitten crab, *Eriocheir sinensis* (Crustacea: Decapoda: Brachyura: Varunidae): fish egg consumption. *Aquatic Invasions*. **10**(3), 313−326.

White, A. (1847) List of the specimens in the collection of the British Museum. *British Museum, London, UK*.

White, R., Mefford, B. & Liston, C. (2000) Evaluation of the mitten crab exclusion technology during 1999 at the Tracy Fish Collection Facility, California, Sacramento (CA). *Bureau of Reclamation, Tracy Fish Collection Facility Studies*. **14**, 43 pp.

Wilkommen, J., Michels, J. & Gorb, S.N. (2015) Functional morphology of the male caudal appendages of the damselfly *Ischnura elegans* (Zygoptera: Coenagrionidae). *Arthropod Structure & Development*. **44**, 289−300.

Williamson, D.I. (1982) Larval morphology and diversity. In Abele, L.G. (Ed.), The biology of Crustacea. *Academic Press, New York*. **2**, 43−110.

Williams-Howze, J. (1996) The biology and morphology of the marine harpacticoid copepod *Heteropsyllus nunni* Coull, during encystment diapause. *Hydrobiologia*. **320**, 179–189.

Wójcik, D. & Normant, M. (2014) Gonad maturity in female Chinese mitten crab *Eriocheir sinensis* from the southern Baltic Sea – the first description of ovigerous females and the embryo developmental stage. *Oceanologia*. **56**(4), 779–787.

Wolf, M. (2010) The reproductive ecology of a northeastern Pacific nudibranch, *Janolus fuscus*, with an examination of its endoparasitic copepod, *Ismaila belciki*. *Ph.D. Dissertation, University of Oregon, Eugene, Oregon*. Retrieved from https://scholarsbank.uoregon.edu/xmlui/handle/1794/11057.

WoRMS: World Register of Marine Species (2017) *Eriocheir sinensis* H. Milne Edwards, 1853. Available at: http://www.marinespecies.org/aphia.php?p=taxdetails&id=107451. Accesses 31 August 2017.

Xiao, Y. & Kumar, M. (2004) Sex ratio and probability of sexual maturity of females at size, of the blue swimmer crab, *Portunus pelagicus* (Linnaeus) off southern Australia. *Fisheries Research*. **68**(1–3), 271–282.

Yang, S.L., Chen, H.L. & Dai, A.Y. (2012) Fauna Sinica: Invertebrata. Vol. 49, (Crustacea: Decapoda: Portunidae). *Science Press: Beijing, R.O.C.*

Yeo, D.C.J., Ahyong, S.T., Lodge, D.M., Ng, P.K.L., Naruse, T. & Lane, D.J.W. (2010) Semisubmersible oil platforms: understudied and potentially major vectors of biofouling-mediated invasions. *Biofouling*. **26**, 179–186.

Zhang, T., Li, Z. & Cui, Y. (2001) Survival, growth, sex ratio, and maturity of the Chinese mitten crab (*Eriocheir sinensis*) reared in a Chinese pond. *Journal of Freshwater Ecology*. **16**(4), 633–640.

Zhao, A.N. (1999) Ecology and aquaculture of the Chinese mitten crab in its native habitat. *Report presented before the Chinese mitten crab Project Work Team of the Interagency Ecological Project, Richmond, California*.

Zill, S., Frazier, S.F., Neef, D., Quimby, L., Carney, M., Dicaprio, R., Thuma, J. & Norton, M. (2000) Three-dimensional graphic reconstruction of the insect exoskeleton through confocal imaging of endogenous fluorescence. *Microscopy and Research Technique.* **48**, 367–384.

Zucco, C. (1999) Burrow distribution of the Chinese mitten crab (*Eriocheir sinensis*) at Syon park flood meadow (SSSI). *M.Sc. dissertation in Conservation, University College London.*

Zupo, V. & Buttino (2001) Larval development of decapod crustaceans investigated by confocal microscopy: an application to *Hippolyte inermis* (Natantia). *Marine Biology*. **138**, 965−973.

APPENDICES

Appendix 1: Table App. 8.1: A list of biological specimens used to conduct the present study.

Species name	#	Locality	Collector	Collection date	Institution	Experiment name
Eriocheir sinensis H. Milne Edwards, 1853	30 adult ovigerous females	Tilbury, River Thames	David Morritt	21.11.2013 & 05.12.2013 (see Table 3.1)	Marine aquarium of RHUL	Fecundity of Chinese mitten crab in the River Thames (Chapter 3)
Eriocheir sinensis H. Milne Edwards, 1853	12 adult ovigerous females	Tilbury, River Thames	David Morritt	05.11.2013, 21.11.2013, 18.11.2014 & 12.11.2015 (see Table 3.3)	Marine aquarium of RHUL	Observation of more than one brood without mating (Chapter 3)
Eriocheir sinensis H. Milne Edwards, 1853	Numerous ZI larvae hatched 14−16 April 1999	Tilbury, River Thames	Roni Robbins	16.03.1999	NHM reg. number: 2002.791	Materials & methods (Chapter 2) and developing of imaging techniques for the study of brachyuran larvae (Chapter 4)
Eriocheir sinensis H. Milne Edwards, 1853	Numerous ZI larvae hatched 2013−2015 terms	Tilbury, River Thames	David Morritt	December 2013-February 2015 (See Tables 3.4 and 3.5 for details)	RHUL	General material & methods (Chapter 2) and Developing of imaging techniques for the study of brachyuran larvae (Chapter 4)

Table App. 8.1: Continued.

Species name	#	Locality	Collector	Collection date	Institution	Experiment name
Eriocheir sinensis H. Milne Edwards, 1853	2 megalopa stage	Tilbury, River Thames	Roni Robbins	28.05.1999	NHM	Developing of imaging techniques for the study of brachyuran larvae (Chapter 4)
Eriocheir sinensis H. Milne Edwards, 1853	One crab I stage	Tilbury, River Thames	Roni Robbins	22.06.1999	NHM	Developing of imaging techniques for the study of brachyuran larvae (Chapter 4)
Sesarma curacaoense De Man, 1892	Larvae obtained from an ovigerous female	Coastal mangrove swamp near Mangrove Point, Trelawny, northern Jamaica	See Anger *et al.* (1995)	March 1993	NHM	Developing of imaging techniques for the study of brachyuran larvae (Chapter 4)
Armases miersii Rathbun, 1897	Larvae obtained from an ovigerous female	Devil's Cook Room, Trelawny, Jamaica	Schuh & Diesel (see Cuesta *et al.*, 1999)	March-July 1996	NHM	Developing of imaging techniques for the study of brachyuran larvae (Chapter 4)

Table App. 8.1: Continued.

Species name	#	Locality	Collector	Collection date	Institution	Experiment name
Eriocheir sinensis H. Milne Edwards, 1853	10 for each zoea stage (ZI−VI) larvae obtained from ovigerous female	Tilbury, River Thames	Roni Robbins	April-May 1999	NHM reg. number: 2002.791	Re-description of the zoeal development of the Chinese mitten crab (Chapter 5)
Eriocheir sinensis H. Milne Edwards, 1853	One adult male	Bam Elms reservoir, Barnes, London	Martin Honey	02.10.1991	NHM reg. number: 1992.36.1	Examining gonopods of brachyurans using CLSM and micro-CT (Chapter 6)
Eriocheir sinensis? Undescribed species	One adult male	Den Oever, Holland: Lat. 52°56'0.6.1" N 005°01' 43" E	Michiel Kotterman	2015	NHM	Examining gonopods of brachyurans using CLSM and micro-CT (Chapter 6)
Eriocheir sinensis? Undescribed species	One adult male	Hollands Diep, Holland: Lat. 51°42'0.19.2" N 004°32' 42.5" E	Michiel Kotterman	2015	NHM	Examining gonopods of brachyurans using CLSM and micro-CT (Chapter 6)
Eriocheir japonica De Haan, 1835	One adult male	From a stream at Sasuna near tsol of Tsushima, Japan	Presented by Duke of Bedford	1907	NHM reg. number: 1907: 12.9.1	Examining gonopods of brachyurans using CLSM and micro-CT (Chapter 6)

Table App. 8.1: Continued.

Species name	#	Locality	Collector	Collection date	Institution	Experiment name
Eriocheir hepuensis Dai, 1991	One adult male	Shatt Al-Basrah Canal, Iraq near the dam at 30°24' 33.75" N 047°46' 32.32" E	Murtada Naser	30.11.2010	NHM reg. number: 2011.8035−8037	Examining gonopods of brachyurans using CLSM and micro-CT (Chapter 6)
Libystes nitidus A. Milne Edwards, 1867	One adult male	Station 142: Lat. 5°23'12" S 73°37' 06" E	Determined by Michael Türkay in "John Murray Expedition"	1991	NHM reg. number: 1991: 156.1	Examining gonopods of brachyurans using CLSM and micro-CT (Chapter 6)
Libystes nitidus? Undescribed species	One adult male	Sudanese Red Sea, station VI: Mersa Ar-rakiya, among coral in 1 fathom. 20°15' N	Presented by Miss Herdman	1934	NHM reg. number: 1934: 117.114	Examining gonopods of brachyurans using CLSM and micro-CT (Chapter 6)
Monomia argentata A. Milne Edwards, 1861	One adult male	Mouth of Lundu River Borneo	Collected by Arthur Adams Esq, presented by Captain Sir E. Belcher during voyage of HMS Samarang	_____	NHM reg. number: 1847.21.	Examining gonopods of brachyurans using CLSM and micro-CT (Chapter 6)

Appendix 2: List of equipment, instruments and material used for the present study

Studies into mitten crab fecundity

Sea salt

Water tanks.

Incubator (18 °C) available at RHUL.

Air diffuser for water aeration.

Preparation of fine dissecting needles

Needle-nose pliers/wire cutters.

Tungsten wire; 0.2−0.36 mm diameter thickness (Clark *et al*., 1998b).

Metal needle holder with adjustable chuck. Overall length 16−22 cm.

Aqueous KOH (potassium hydroxide) at 10%.

Small glass vial.

Power supply (10 V).

Flexible electric wire.

Crocodile clips.

Cleaning reagents

Surface cleaning agent Decon 90 was purchased from Decon Ltd. Decon 90 and stored at room temperature (ca. 20 °C) in a glass vial.

Stock solution of SDS (sodium dodecyl sulphate) and ammonium hydrogen carbonate (NH_4HCO_3) and the reducing agent DTT (1,4-dithio-DL-threitol) were used to clean and digest the Chinese mitten crab larvae (Fisher & Ahlrichs, 2011). Stock solution of SDS was kept in a 250 ml Erlenmeyer flask and stored in a fridge (ca. 4 °C) with the reducing agent DTT.

Stains

Congo red powder was obtained from Fisher Scientific Ltd., Loughborough, England.

Acid fuschin powder was obtained from Sigma-Aldrich Co. Ltd., Irvine, England.

Stock solutions of Congo red and acid fuschin powders were prepared to stain larval specimens/ appendages and adult male first and second gonopods.

A syringe filter, Filtropur 0.2 μm, was used to filter the stock solutions.

Deionised water was used to prepare stock solutions.

The stains were stored in a cupboard at room temperature (ca. 20 °C) in dark glass vials and covered with aluminium foil to protect them from the light which causes bleaching.

Slides and cover slips

Standard 25 mm microscope slides and cavity slides were used to mount the all stages of the mitten crab larvae before using the confocal laser scanning microscope (CLSM) and macro confocal image acquisition.

Self- adhesive white vinyl reinforcement rings were obtained from Ryman Ltd. The rings are made of plastic (vinyl) as the paper rings soak the mounting medium and caused leakage of the mountant.

0.17 mm thick circle and square coverslips (No. 1.5−0.16 to 0.19 mm thick) were used to seal off specimens for CLSM. The coverslips were cleaned both sides with tissue before use.

Mounting mediums

Diluted glycerine with distilled water at different concentrations was used as a mounting medium.

Diluted polyvinyle lactophenol diluted with 70% ethanol at different concentrations was used as an alternative method for the preparation of microscope slides.

Thin glass pipettes were used to transfer mounting medium onto the microscope slides.

A colourless nail varnish was used to seal the cover slips.

Appendix 3: Model of microscopes used during the present study

A Carl Zeiss, BL 2612 microscope was at the RHUL and used to measure the egg diameter of Chinese mitten crab and for observations of the first zoeal stage.

The larvae were dissected under a Leica MZ 16 stereomicroscope and was available in the Life Science Department (LS), NHM.

An automated upright microscope system, Leica DM5000 B was used to check the mounted appendages/species available in the LS, NHM.

Zoeal specimens and gonopods of the adult Chinese mitten crabs were scanned using a Nikon A1-Si confocal microscope fitted to a Nikon Eclipse upright microscope which is available at the Imaging and Analysis Department, NHM.

Zoeal appendages of *Eriocheir sinensis* were also scanned using the Olympus Fluoview FV1000 IX81 inverted microscope available at the School of Biological Sciences, RHUL and Zeiss LSM 880 airy scan upright confocal microscope available at the Bioimaging Hub within the School of Biosciences of Cardiff University.

Zoeal appendages of the *Sesarma curacaoense* and *Armases miersii* were scanned using Leica TCS SP5 equipped with a Leica DM5000 B (upright microscope) available at German Centre for Marine Biodiversity Research (DZMB).

Zoeal stages of *Eriocheir sinensis* were also investigated using a Zeiss Ultra Plus Field Emission SEM and a FEI Quanta 650 FEG SEM in variable pressure mode (15−20 Pa chamber pressure) at different kV from 5 kV to 20 kV. For debris analysis, a LEO 1455 VP SEM which was available in the Imaging and Analysis Department, NHM.

An AZ-C1 macro confocal system was also trialled in order to scan larger specimens/ appendages.

Zeiss Axio zoom V16 stereo zoom microscope for large fields were also used to visualise the megalopa and crab I stage of Chinese mitten crab.

Micro-computed tomography (CT) used for the present study

A micro-CT scanner, Nikon Metrology HXM ST 225, available at the Imaging and Analysis Department, NHM was used to scan the megalopa stage Chinese mitten crabs.

An x-ray microtomography, X Radia 520 versa, available at the Imaging and Analysis Department, NHM was used to scan the pleopods of adult Chinese mitten crabs.

Appendix 4: Preparation of artificial sea water

The salinity dilutions used for brooding Chinese mitten crabs suggested by Anger (1991) was 25‰. This is 25 grams per litre of solution. The appropriate amount of salt was weighted using a top loading balance and transferred in an appropriate container (a demijohn was used when needed for more than a crab). Then, the appropriate volume of tap water was added to produce the final dilution (Kester *et al*., 1967). The mixture was shaken vigorously and aerated for overnight to ensure thorough the dissolution of the salt. The salinity of the water was then checked using the Atago hand- held refractometer (calibrated against distilled water at 20 °C). The salinity was further adjusted by adding salt/tap water as required.

Appendix 5: Preparation of tungsten wires used for the present study

The tungsten wire (0.2−0.36 mm diameter thickness) was cut into pieces approximately 2 cm length using a needle-nose pliers. At least four needles with different types and thicknesses were required to perform different tasks such as transferring the larvae from glass laboratory dish, dissecting and mounting. Each piece of tungsten wire was then inserted into an aluminium needle holder with an adjustable chuck using forceps. The method for the preparation of the power source to sharpen the needles electrolytically is diagrammatically illustrated in Figure App. 8.1.

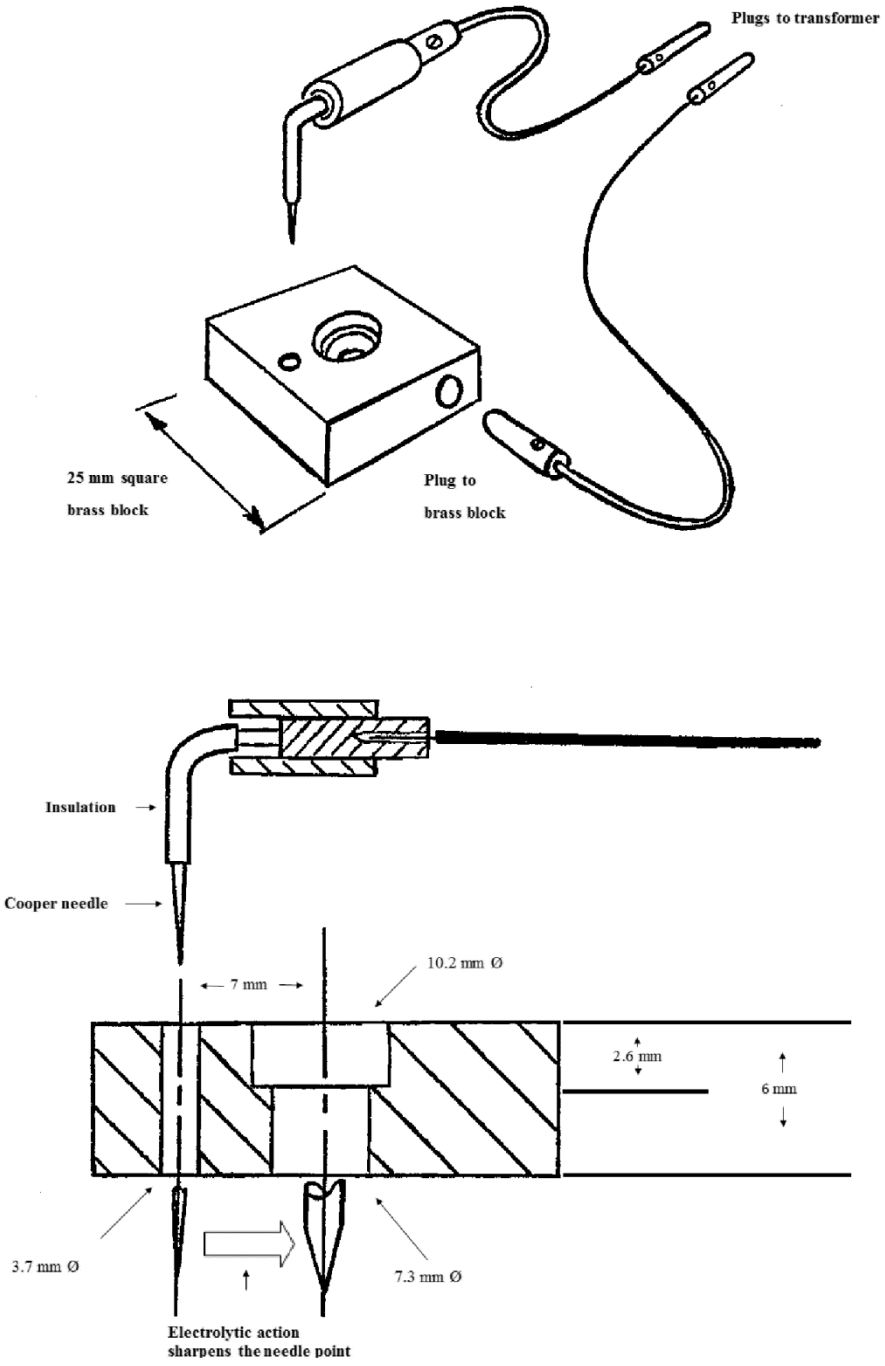

Figure App. 8.1: Diagrammatic illustration of designed apparatus to sharpen tungsten wire needles electrolytically. Two side of output terminal of the flexible wires were plugged to transformer (12 V power supply) with the connection in parallel. One tip of the wire was attached to brass block and the other tip was plugged to cooper needle and inserted in the brass block using the small hole on the surface (Clark, 2007).

Using a 10 V power supply transformer, the 25-mm brass block with cooper needle and electrode was placed into the aqueous KOH solution in the small glass vial as shown in Fig. App. 8.2. After applying the electrical voltage, the tip of tungsten wire was immersed into the solution. 2−5 mm of the wires was usually immersed in the solution and was held vertically until the wire is eroded by electrolysis. The needle was held against the brass block for the best electrolysis result.

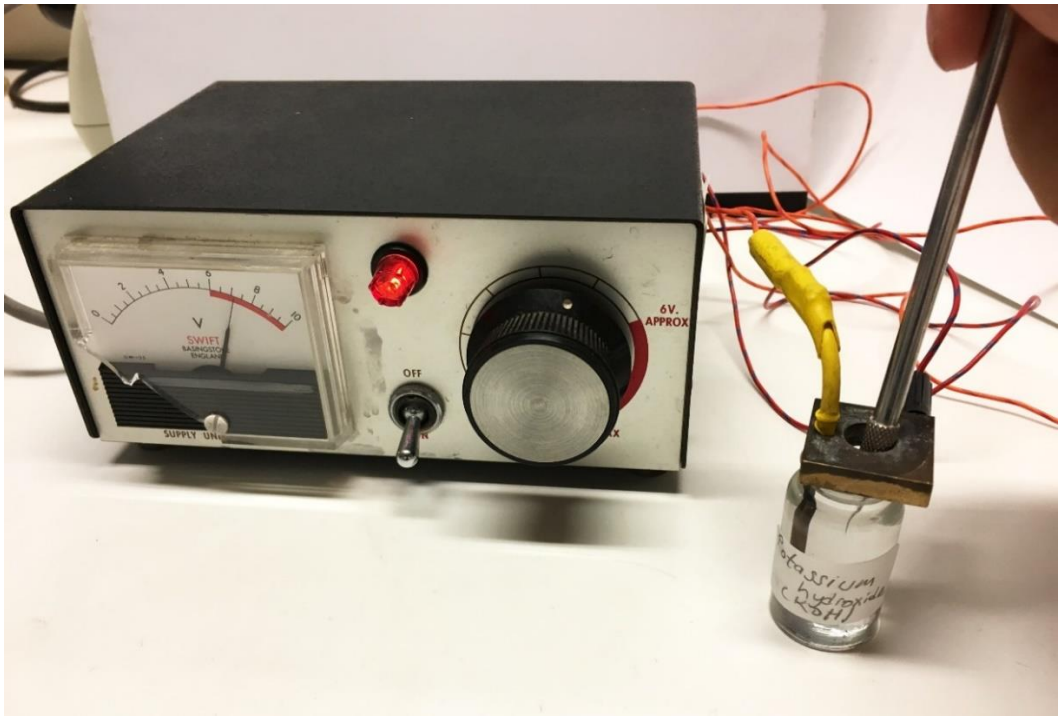

Figure App. 8.2: Application of sharpening tungsten wire needles electrolytically with a 10 V power source.

Sharpening can take 4 to 6 minutes depending on the desired needle thickness and voltage supply. 5−8 V power were applied to sharpen the needles used for this study. The needle tip was checked for needle sharpness periodically using a stereomicroscope. For this study, four types of needles with different shape and thicknesses and with a length of 16−22 cm metal holder (Fig. App. 8.3a) were prepared (Fig. App. 8.3b). Very fine and fine needles (Fig. App. 8.3b1 and 8.3b2 respectively) were prepared for the

dissection. A Fine needle (Fig. App. 8.3b2) was used to keep the zoea still while very fine needles was used to dissect zoeal appendages (Fig. App. 8.3b1). The needle with the hook (Fig. App. 8.3b3) was mostly used to transfer the zoeal appendages for the mounting in the slide well. The thick needle (Fig. App. 8.3b4) was used to move and arrange the cover. When the task was complete, the needle was washed thoroughly in deionised water.

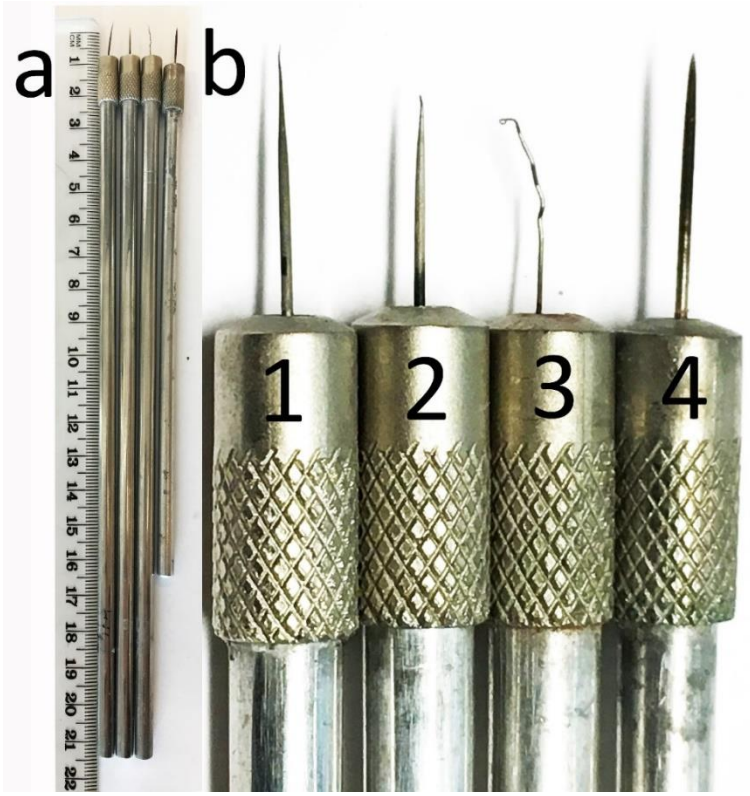

Figure App. 8.3: Preparation of tungsten wire needles. (a) The length of the aluminium metal holder according the type of the needles; (b) Type of the needles used; (b1) very fine needle to dissect zoeal appendages dissection; (b2) fine needle to hold the larvae/main body during the dissection; (b3) the needle with hook was used to transfer zoeal appendages or whole specimens after dissection, staining, cleaning etc.; (b4) Thick needle to move the cover slip slightly and arrange in the correct position.

The needles which lost their sharpness or were damaged re-sharpened using the same method by applying shorter immersion time. The KOH solution can be re-used for several times and stored in room temperature (ca. 20 °C) in a glass vial. When sharpened needles were moved to other laboratories, to avoid damage to the tips, the needles were removed from the metal needle holder and stored in a small box separately.

Appendix 6: CLSM and 3D software instructions

Obtaining confocal images

After deactivating the "Eye Port" in order to send the light to the confocal detectors, "remove interlock" was clicked (Fig. App. 8.4). "DU4" option was selected to use 4 detectors. "Pixel dwell" was set to 2.4 (µs/pixel) for all images (Fig. App. 8.4). A higher pixel dwell can increase the acquisition and photo-bleaching time. "Image size" was set to 1024 pixels to scan the samples.

"Channel (Ch) series" option was not applied advertently in the present study (Fig. App. 8.4). When Ch series was applied during the scanning procedure, the microscope scans the sample 4 times using each channel in every round, then stitches the channels together at the end of the scanning. Therefore, it was time-consuming.

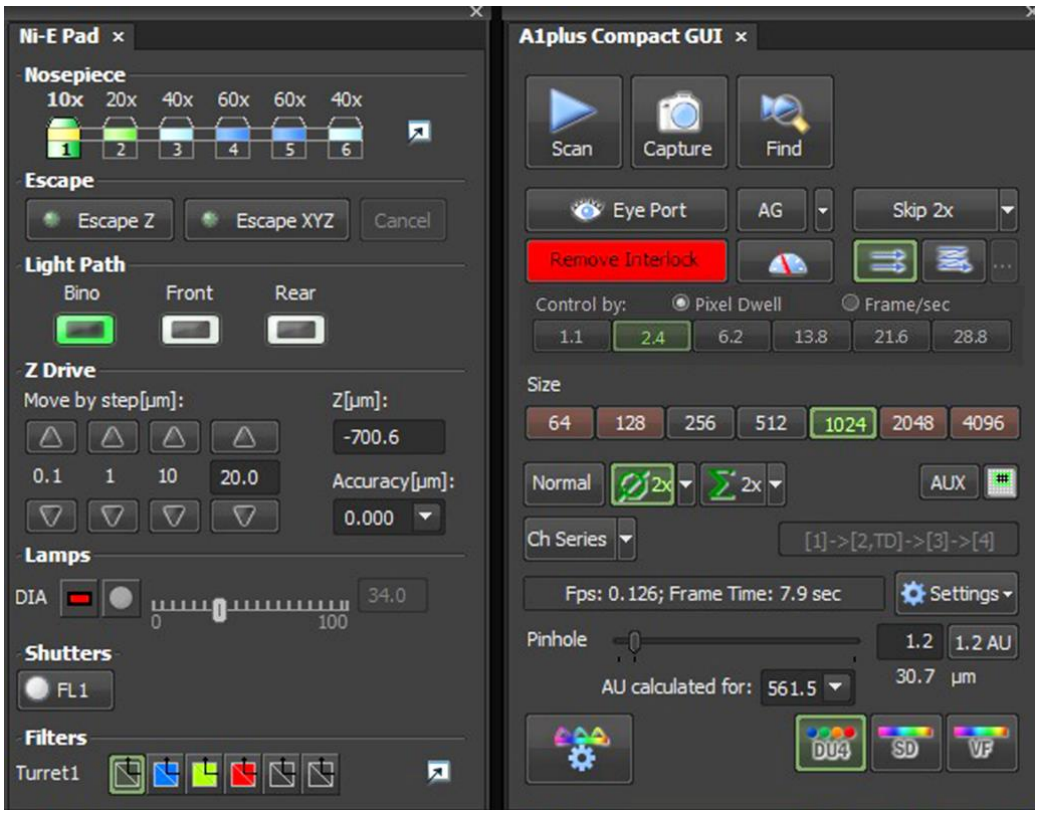

Figure App. 8.4: Graphical User Interface (GUI) showing the settings applied in the present study.

Channel settings and Image acquisitions

"HV" and "offset" were manually adjusted to the optimum settings (Fig. App. 8.5a). HV is the detector sensitivity, while the offset controls the baseline intensity of the image. A recommended start setting is 100 for all channels and this can be either increased or decreased depending on the sample. Offset should ideally start at "0" and can be decreased to negative values to decrease the background signal/ background noise. Therefore, detector gain and amplitude offset were manually adjusted to deliver a black background in the present study.

(Fig. App. 8.5c). After using the Z-intensity option the option of "Run Z Corr" (Run Z Correction) instead of "Run now" was selected to apply the Z- correction settings.

Optimisation of the number of Z-frames scanned was also required. 3D reconstruction required more Z-frames than 2D images, so the number of frames needed to be selected to match the final use case.

“Order of experiment” should be carefully selected when using the “large images” option (Fig. App. 8.5d). ‘Large images (Lambda (Z series))’ order was the preferable choice in the present study (Fig. App. 8.5d).

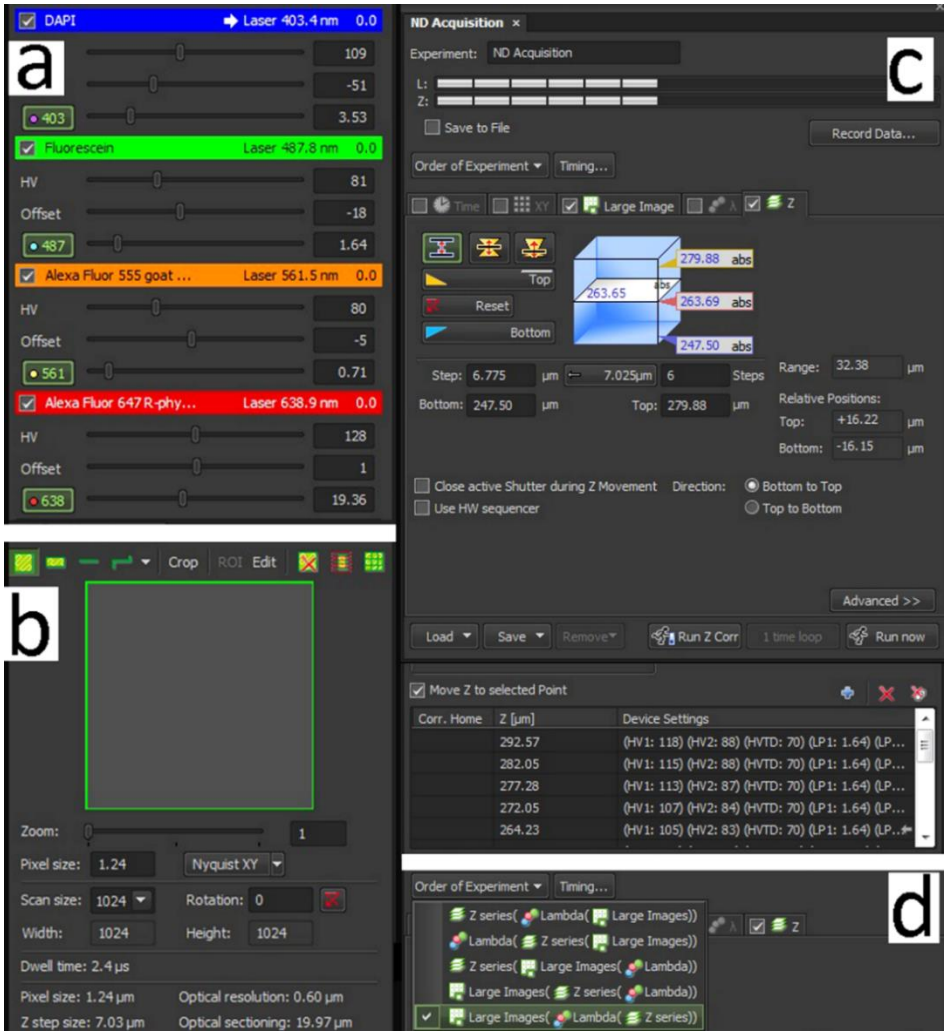

Figure App. 8.5: General settings applied in the present study. (a) Adjusting channel settings with a focus on “HV” and “offset”. (b) A1 scan area window to zoom, and rotate. (c) Applying Z- intensity correction function (d) “Order of the experiment” for the “large images” option of confocal microscopy software.

Exporting stack data as TIFF images using Nikon confocal microscopy software

Nikon's NIS elements viewer (version 4.20) (Nikon) software is shown in the present study. The other software could also be trialled by following the similar method. Typically, only a single channel was selected for 3D modelling. For this application, the orange channel (561nm) was chosen which provided the optimal fluorescence signal for Congo red and acid fuchsin stains between other channels. All stack images in one channel were then selected and transferred to a new folder (e.g. "Orange channel"). Image properties (voxel size) were noted for later reference in order to produce a scale bar in Drishti (see Figs App. 8.6−8.10).

For the Nikon system, NIS-Elements viewer was used. This is a free programme to view images and confocal microscopy datasets. However, it requires a dongle from the company to use its full features. Software was downloaded from http://www.nikoninstruments.com/en_GB/Products/Software/NIS-Elements-Advanced-Research/NIS-Elements-Viewer. Images were initially opened using the software that allows the user to view and image selection modes as the NIS-Elements core packages (Fig. App. 8.6). Once the programme was set up, nd2 files were either (a) dragged into the NIS-Elements viewer or (b) opened by going to File>open> your nd2 file.

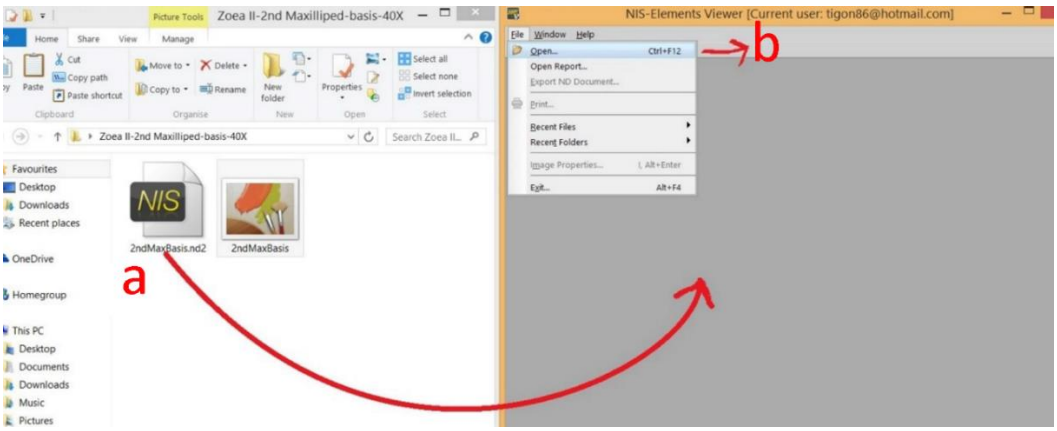

Figure App. 8.6: Viewing the confocal data using confocal software, in this case Nikon software, NIS- Elements (version 4.20) was used. (a) Dragging and dropping the confocal data into the software. (b) An alternative way to open the confocal data by going to File>open> your nd2 file.

Then, a new folder was created (a) to export nd2 files (b) as TIFF images (Fig. App. 8.7).

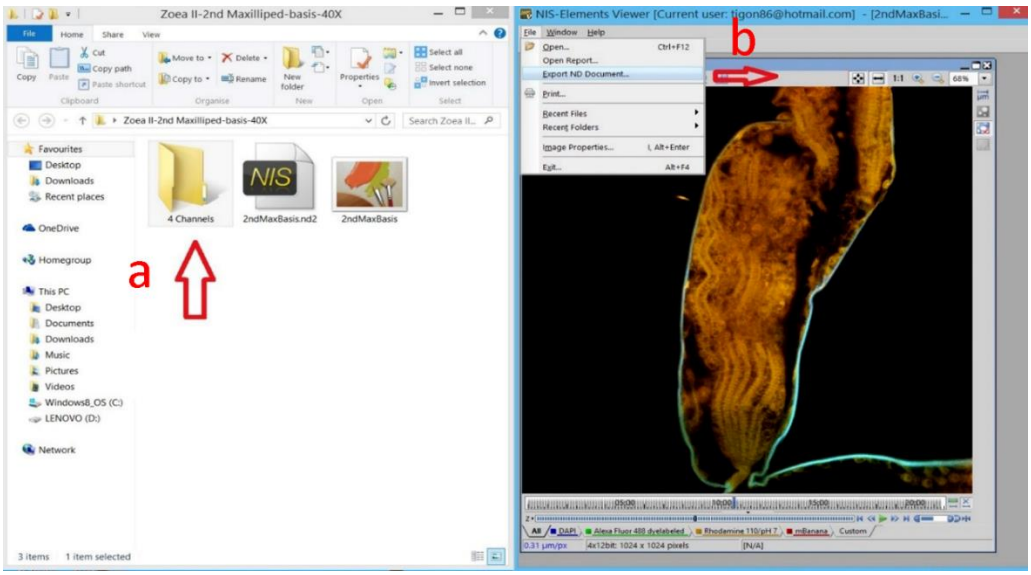

Figure App. 8.7: Exporting ***.nd2 files as TIFF images using confocal software. (a) Create a new folder for the exported TIFF images. (b) Go to File>Export ND document and click.

Next, the options of mono image for each channel (a), scale 12 bit to 16 bit (b) were selected. By clicking on browse (c), the folder which the images will be exported was chosen and the data was exported by pressing “Export” (d) (Fig. App. 8.8).

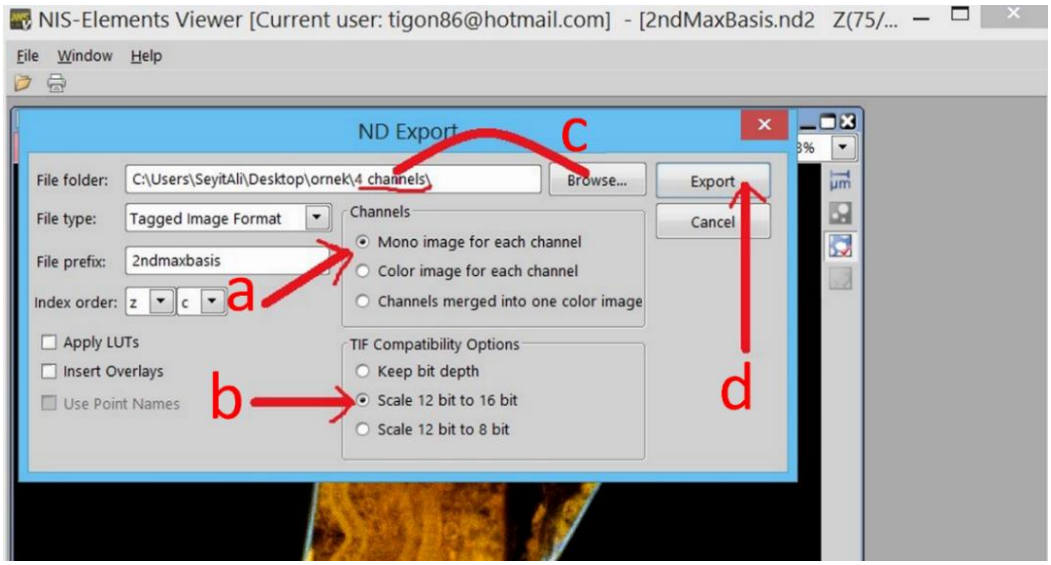

Figure App. 8.8: Options of exporting the confocal data as TIFF images. (a) Select the option of “Mono image of each channel”. (b) Select “Scale 12 bit to 16 bit”. (c) Click “Browse” to locate images (in our example, it is 4 channels). (d) Click “Export”.

Nikon elements software (free download from Nikon) was used to export the data as 16-bit mono tiff images. The Nikon software creates a folder containing a tiff image for each channel at each focal plane. In the export process, the files were grouped with a single folder for each channel, containing all the focal planes c1-n, c2-n, and c3-n; c4-n where c represents the channel and n is the frame number. If the experiment is making use of autofluorescence in a single channel, then it is only necessary to import the relevant channel into the reconstruction software. If the experiment uses multi-channel fluorescence, then each channel needs to be imported separately.

If the option of “View> large icons” is selected, and the size of folder can be adjusted suitably so that each channel c1, c2, c3, c4 would be rowed one under the other. This made it easier to select only targeted images from top to bottom. For this example, c3 channel was selected. Once all c3 images were selected, a new folder called “orange channel” was created and images were pasted in this folder (Fig. App. 8.9).

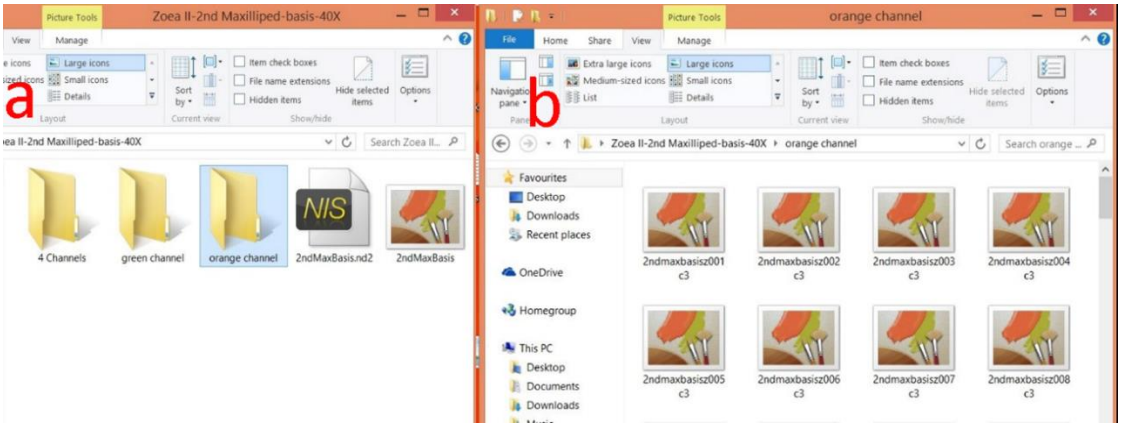

Figure App. 8.9: Example of using single channel to import. (a) Creating folder for single channels, in the example “Orange channel” was used. (b) Representation of orange channel’s TIFF images.

By right clicking on the image on the image using NIS-Elements viewer, and clicking on “image properties” (Fig. App. 8.10). Once clicked, x and y calibrations can be found in “image fields” (Fig. App. 8.10b). Whereas z value can be found in “experiment data” (Fig. App. 8.10c). In this example, x and y calibrations are 0.31 nm, whereas z- step value is 0.7 nm.

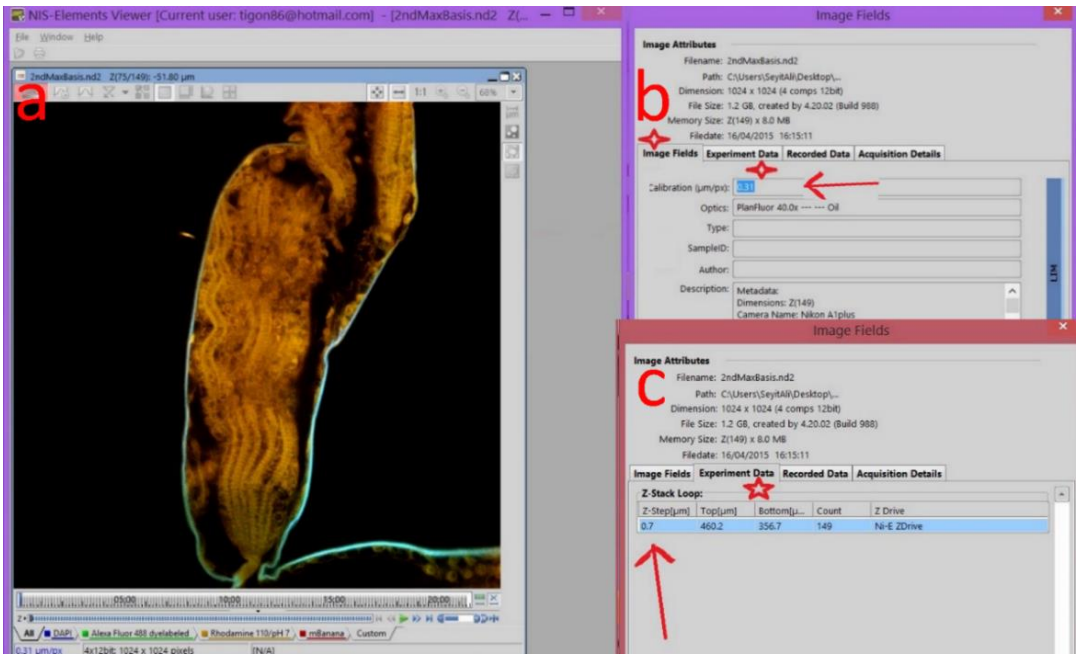

Figure App. 8.10: Viewing image properties. (a) Right click on image using NIS Element viewer. (b) Click "Image Fields" to view x and y calibrations. (c) Click "Experiment Data" to view z-step value.

Exporting stack data using ImageJ

The method using ImageJ for any confocal data follows as: (see Figs App. 8.11−8.21).

Any confocal stack data file can be opened using ImageJ. Opening ImageJ software programme (Fig. App. 8.11), go to File> Open> click on data; click open (Fig. App. 8.12).

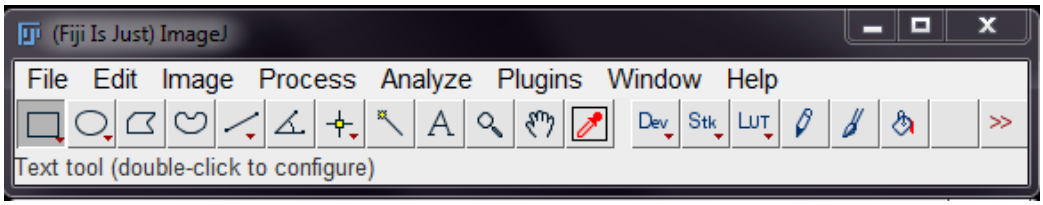

Figure App. 8.11: The menu bar for ImageJ.

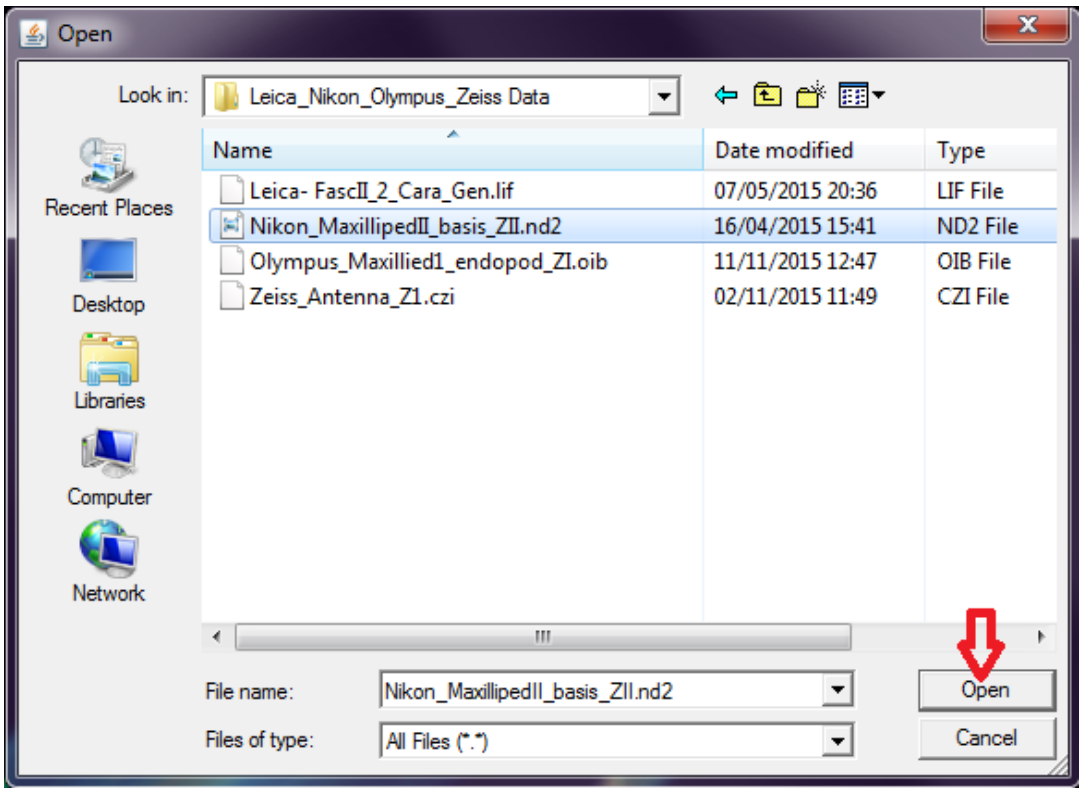

Figure App. 8.12: Opening stack data in ImageJ, e.g. Nikon_MaxillipedII_basis_ZII.nd2 has been selected.

Open stack data; select "Grayscale" from dropdown menu and select options "Autoscale" and "Split channels"; click OK (Fig. App. 8.13).

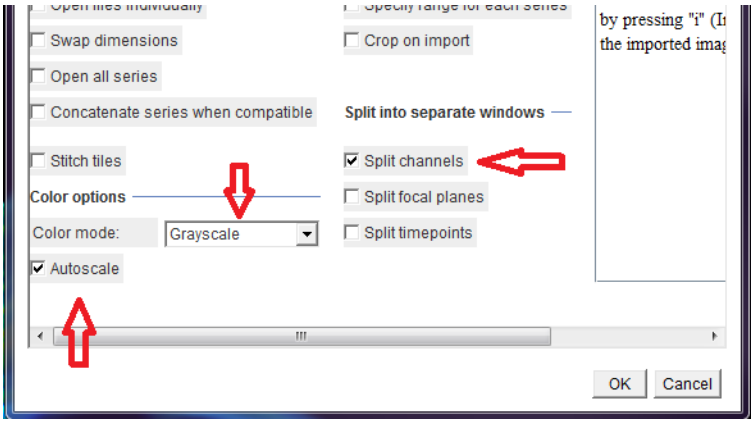

Figure App. 8.13: Import options for stack data.

The stack data will split into the number of channels scanned, in this example 4 (see Fig. App. 8.14); go to Image> Properties; note image properties (voxel size), this information was required for the reconstruction of an accurate scale bar in the final images. In this example, pixel width represents X, pixel height represents Y and voxel depth represents Z in microns. Record image properties, e.g. x = 0.31, y = 0.31 and z = 0.7 microns; click OK (Fig. App. 8.14).

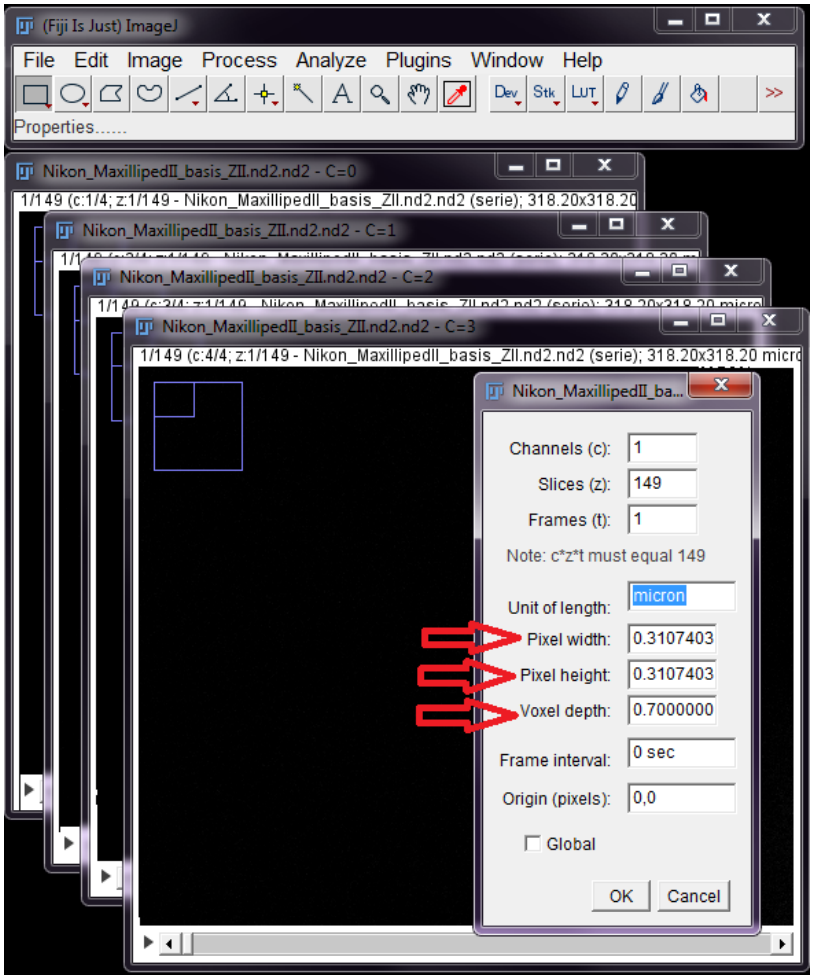

Figure App. 8.14: Record image properties (voxel size) for later use, e.g. x = 0.31, y = 0.31 and z = 0.7 microns.

Then, scanned image quality of each channel was checked: click ► to play image stacks; any channel not providing full information, e.g. corrupted scans, oversaturated

images, or high level of background noise, these channels should not be selected when merging channels (Fig. App. 8.15).

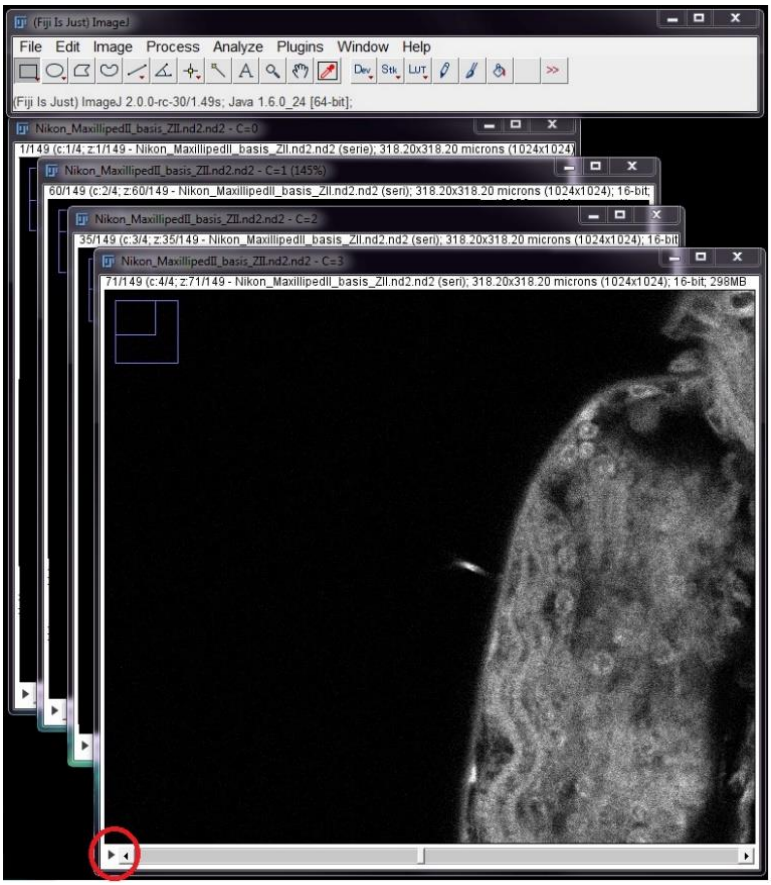

Figure App. 8.15: Click on ► to check image quality for each channel.

Go to Image> Color> Merge Channels… and click (Fig. App. 8.16).

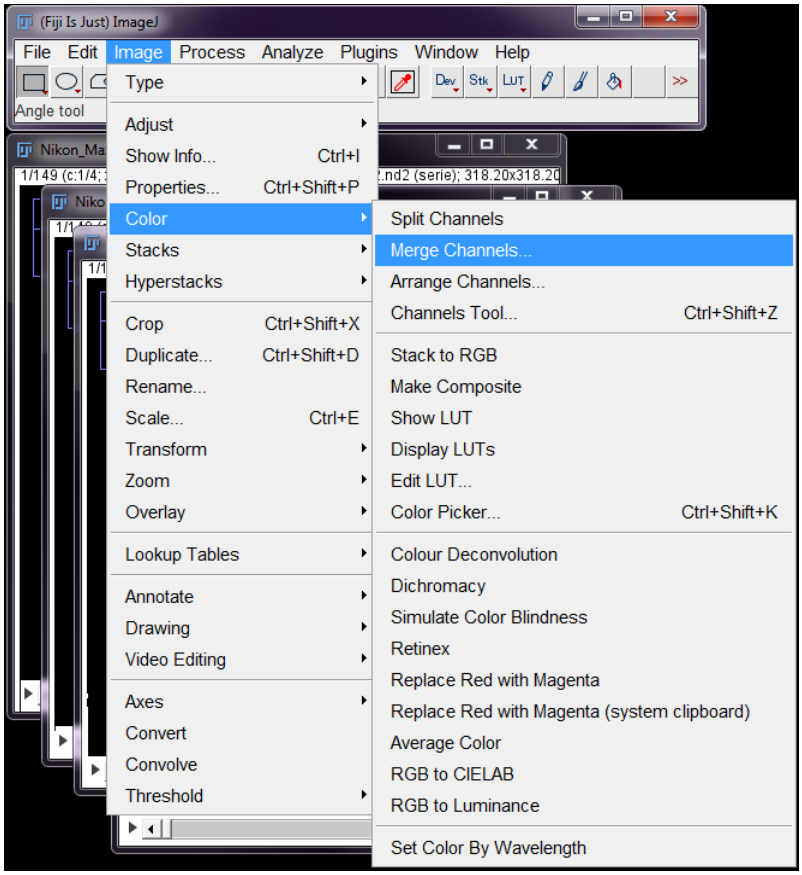

Figure App. 8.16: Merging selected channels in ImageJ.

Channels to be merged were selected by clicking ▼; any channels not selected due to poor quality will not be merged; after selecting channels, click option "Create composite"; click OK (Fig. App. 8.17).

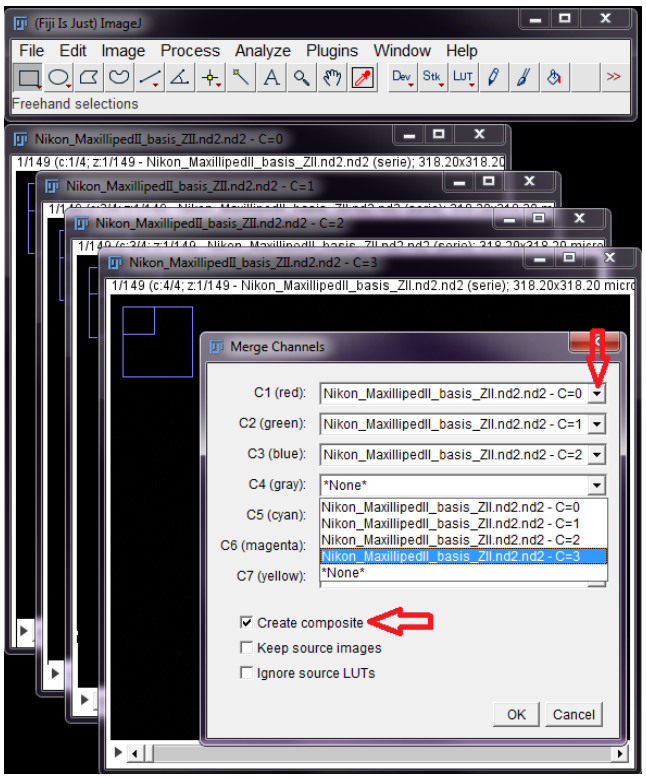

Figure App. 8.17 Selecting channels to be merged.

Next, go to Image> Color> Channels Tool…, click; More> Convert to RGB (Fig. App. 8.18).

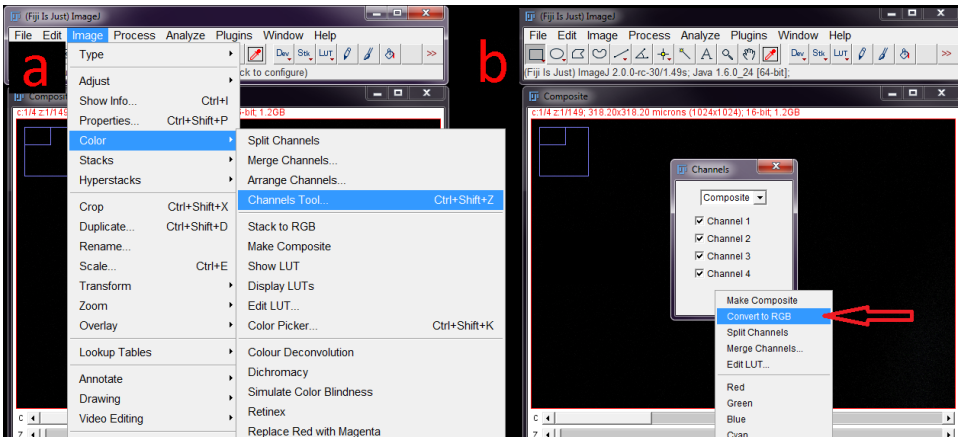

Figure App. 8.18: Image J instructions for exporting confocal data. (a) Go to Image> Color> Channels Tool…. (b) Convert to RGB.

After clicking OK (Fig. App. 8.19a), single channel was converted from RGB colour to 8-bit image; go to Image> Type and click 8-bit (Fig. App. 8.19b).

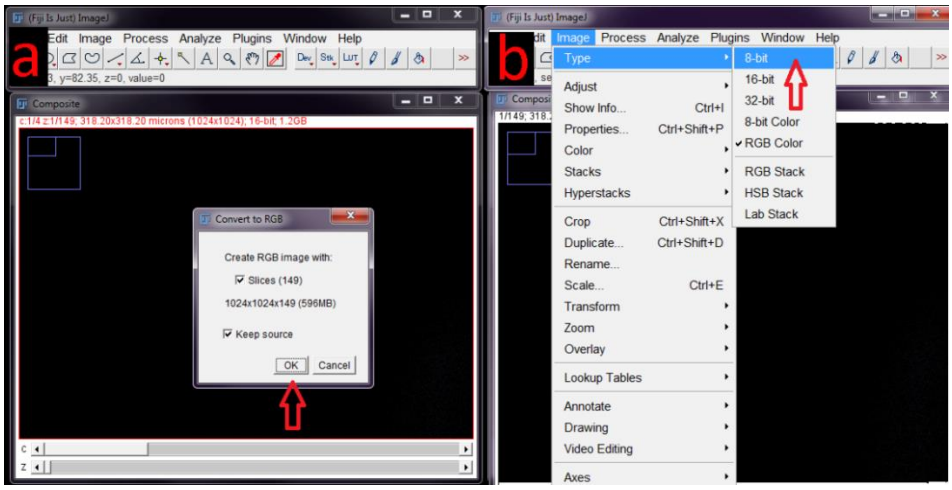

Figure App. 8.19: Image J instructions for exporting confocal data. (a) Click OK for the following processes. (b) Changing image from RGB color to 8-bit in ImageJ.

Then, the data was saved as Image sequence; go to File> Save as > Image Sequence… (Fig. App. 8.20a) and click; then OK in TIFF format (Fig. App. 8.20b).

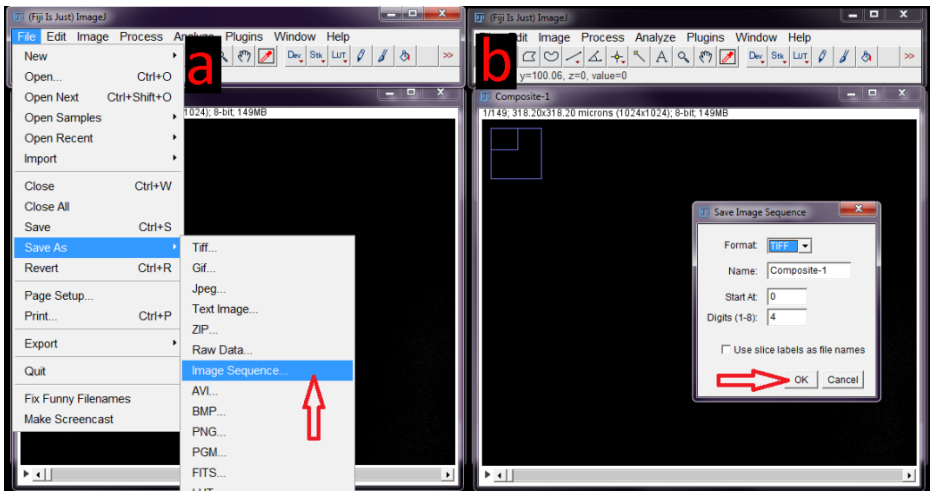

Figure App. 8.20: Following ImageJ instructions. (a) Save merged channel image stacks as image sequence. (b) Save merged channel image stacks to TIFF format; click OK.

After creating and naming a new folder; save image stacks to folder; click save (Fig. App. 8.21).

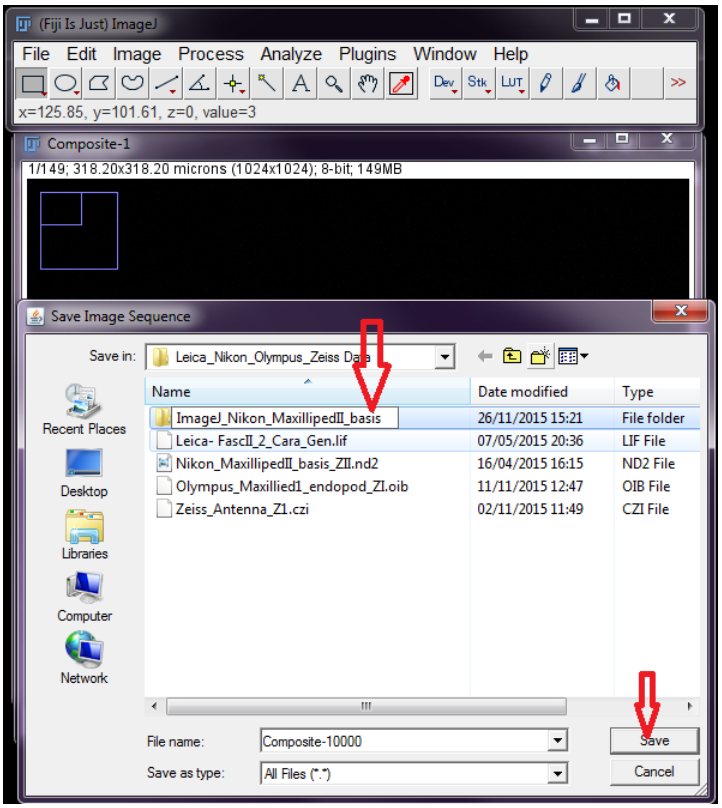

Figure App. 8.21: Save merged image stacks to new folder, e.g. ImageJ_Nikon_Maxilliped II_basis.

Application of Drishti

The processing method of either single or multi-channel data using Drishtiimport is as follows (see Figs App. 8.22−8.30):

Drishti was downloaded from the website (http://sf.anu.edu.au/Vizlab/drishti/). After downloading “drishtiimport - Shortcut” icon was used (Fig. App. 8.22).

Figure App. 8.22: Shortcut icon for "drishtiimport".

After clicking on "drishti - Shortcut" icon, a blank window appears. From post-processing (3D Modelling) treatment, either a new folder from the standard option (e.g. "Orange channel") (Fig. App. 8.23a) or ImageJ (e.g. "ImageJ_Nikon_Maxilliped II_basis") was dragged and dropped into the "drishtiimport" window (Fig. App. 8.23b). Next, "Select Directory Type" window was automatically opened and the 6th option "Grayscale TIFF Image Directory" was selected (Fig. App. 8.23).

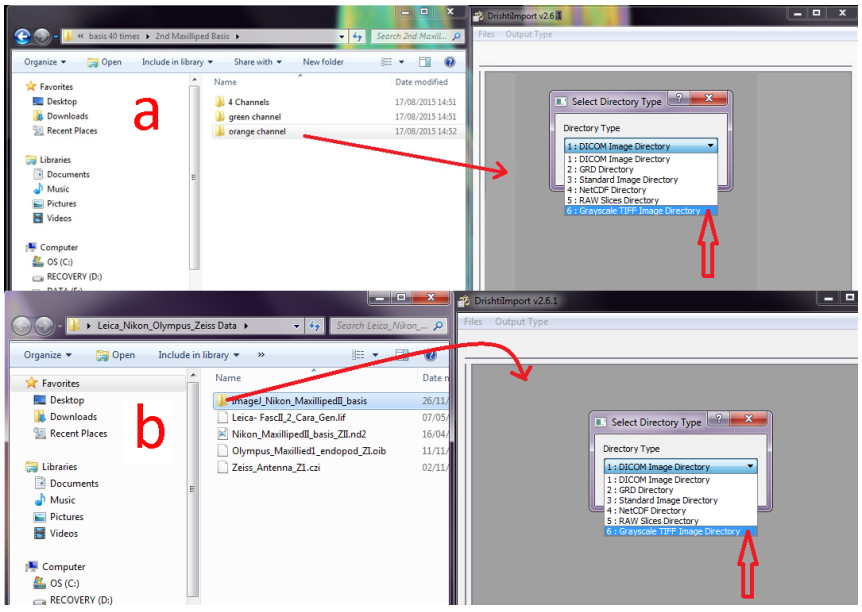

Figure App. 8.23: Importing processed data into Drishtiimport. (a) Importing single channel data processed using confocal data. (b) Importing multi-channel processed using ImageJ.

Then, “Select Voxel Type” window appeared and OK was clicked (Fig. App. 8.24).

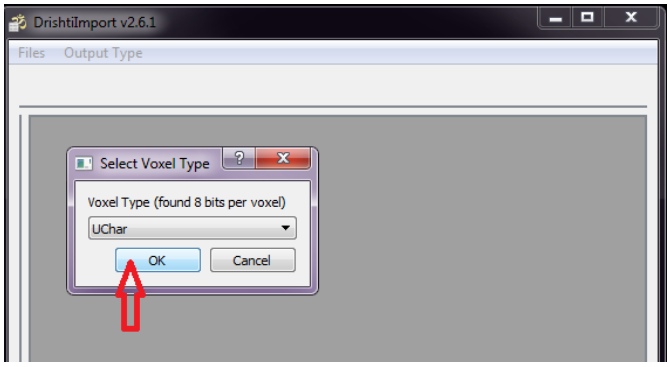

Figure App. 8.24: Following instructions for importing the data to Drishti.

Then, followed as File> Save as (S) and name new file ***.pvl.nc which are referred to as volumes in Drishti, e.g. “MaxillipedII_basis_Drishti_import.pvl.nc”; click save (Fig. App. 8.25).

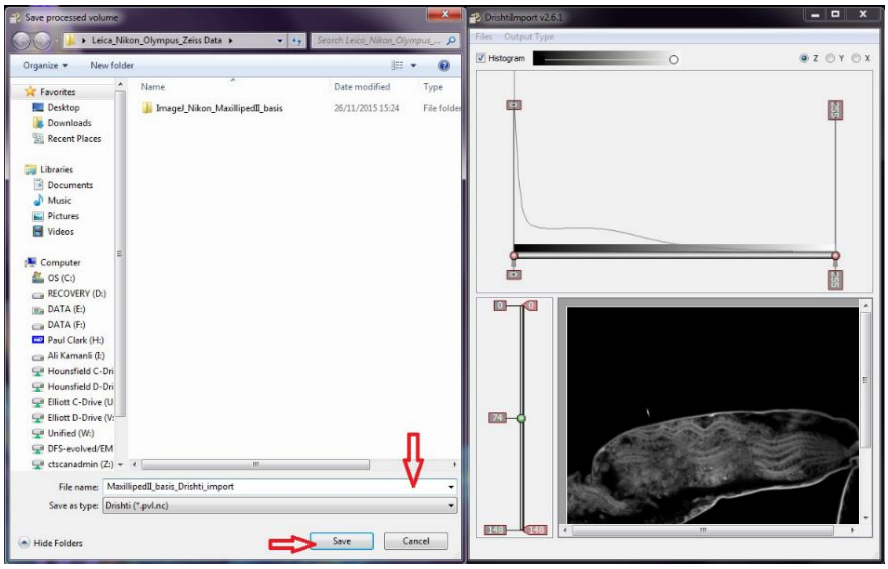

Figure App. 8.25: Save to ***.pvl.nc file which are referred to as volumes in Drishti.

When, a series of 5 windows appeared respectively; OK was clicked (Fig. App. 8.26a-e).

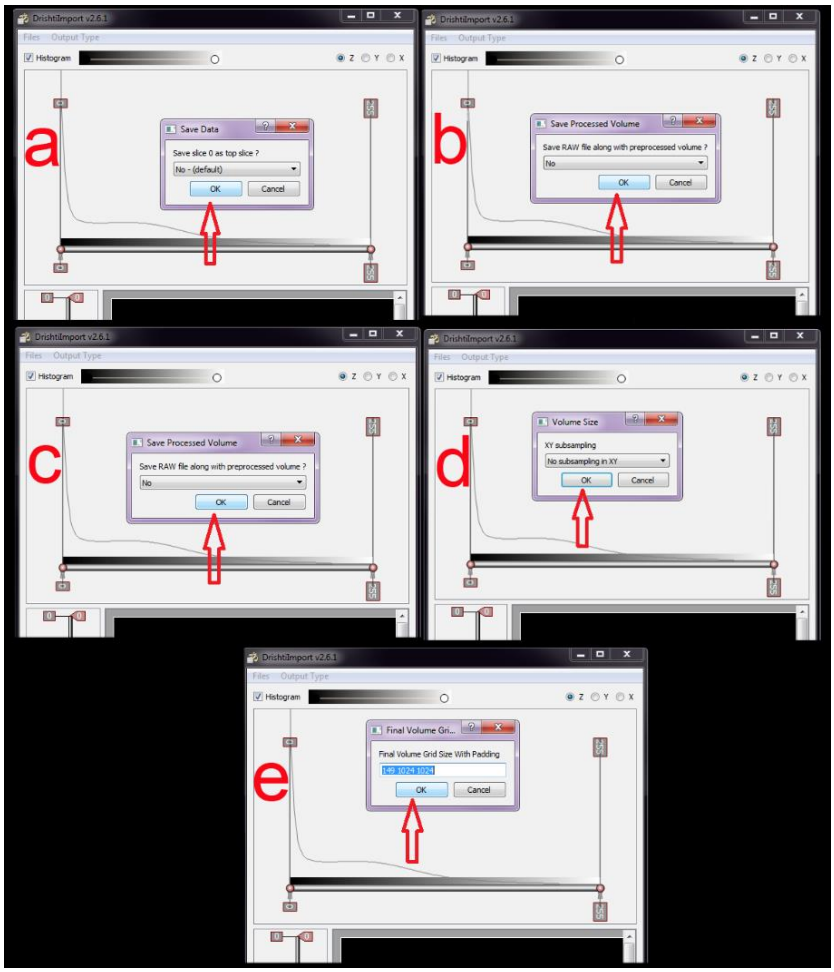

Figure App. 8.26: Following save, a series of 5 windows will open; for each click OK.

The "Additional Information" window appears, noted "image properties" (voxel size) recorded from the standard manufacturers package (Fig. App. 8.10) or ImageJ (Fig. App. 8.14) was entered. The data was written manually by leaving one-character space between, x, y, and z values e.g. 0.31 nm, 0.31 nm and 0.7 nm; click OK (Fig. App. 8.27).

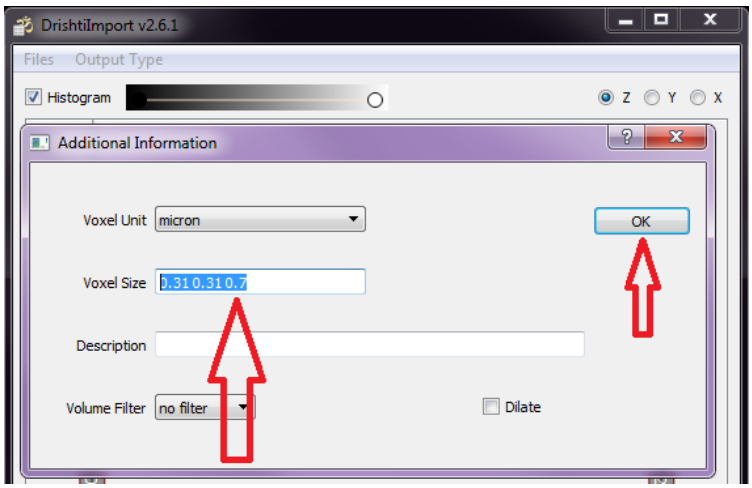

Figure App. 8.27: Entering "image properties" (voxel size); x, y and z values.

When "Done" appeared, OK was clicked to save the files in "***.pvl.nc" and "***.pvl.nc001" (Fig. App. 8.28).

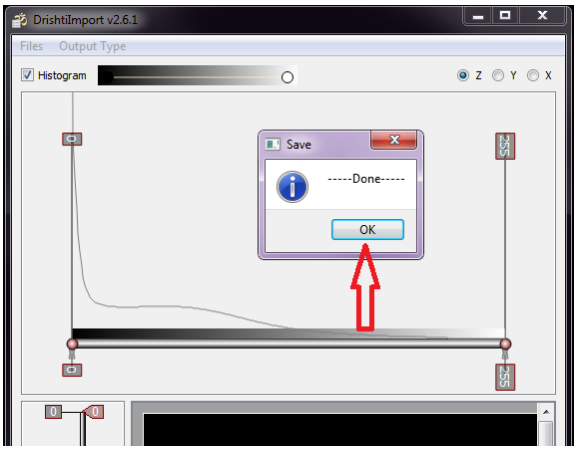

Figure App. 8.28: Saving the data for the use of Drishti.

Visualisation of data using Drishti (3D Visualisation)

The instructions were followed the method below:

"Drishti" was opened (Fig. App. 8.29) and the ***.pvl.nc file created using "Drishtiimport" was either dragged and dropped or opened by going to File> Load

volume> Load one volume and selecting the ***.pvl.nc file, e.g. “MaxillipedII_basis_Drishti_import.pvl.nc” (Fig. App. 8.30).

Figure App. 8.29: Shortcut icon for “Drishti”.

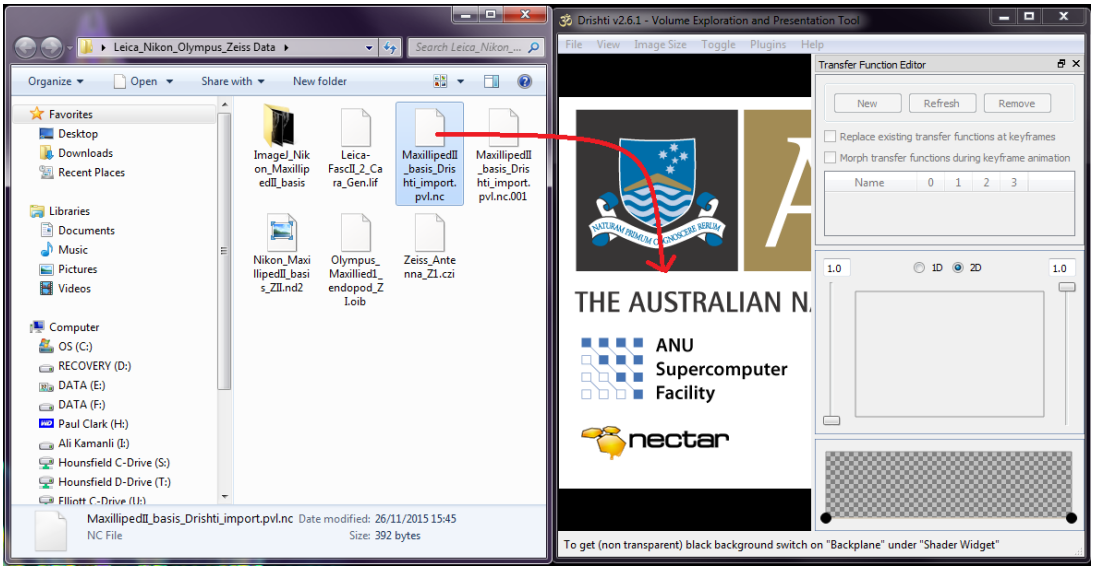

Figure App. 8.30: Loading ***.pvl.nc file, e.g. “MaxillipedII_basis_Drishti_import.pvl.nc” into Drishti.

After loading the volume, a 3D representation of the file was viewed. Then, the initial volume was cropped to fit the scanned image; left click and drag the crossed square when the red line appears (Fig. App. 8.31).

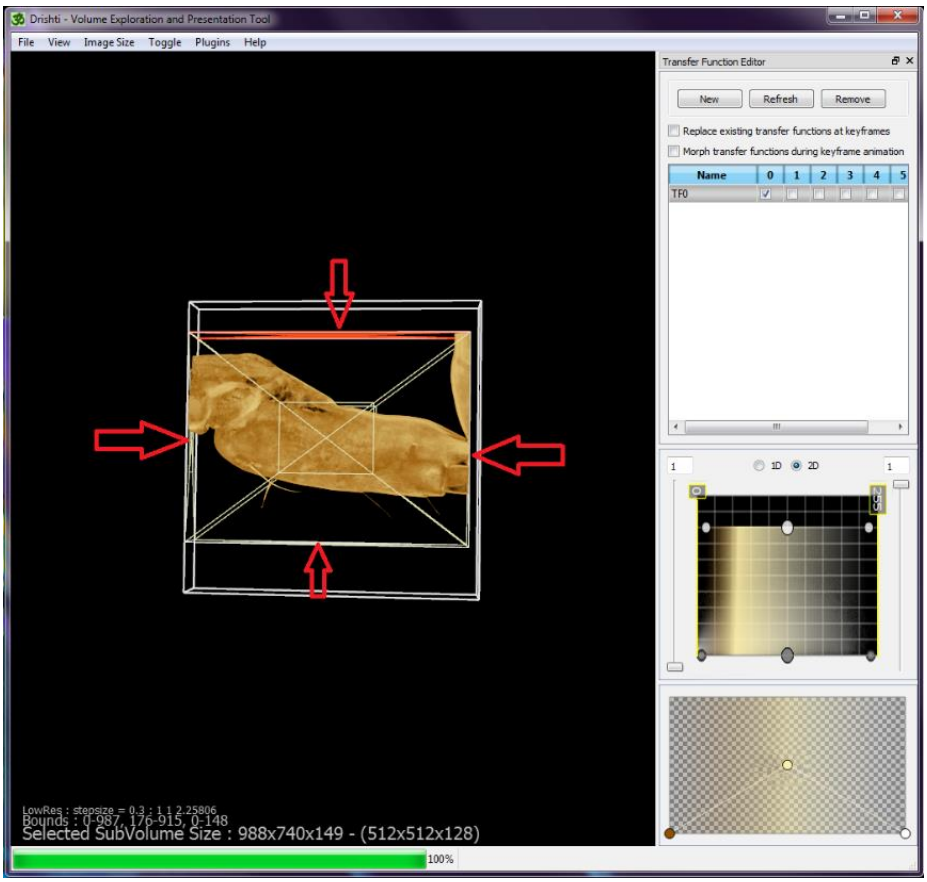

Figure App. 8.31: Viewing 3D representation of the volumes and cropping the initial scanned volume.

F2 was used to toggle between high resolution and standard mode. 1 was used to toggle the lighting. B was used to toggle between box frames present or absent. To zoom in/out the mouse wheel was used. Image quality and background colour can be adjusted, go to View> Preferences (see arrows on left of main window). To adjust offset and intensity of image use buttons in right window (Fig. App. 8.32).

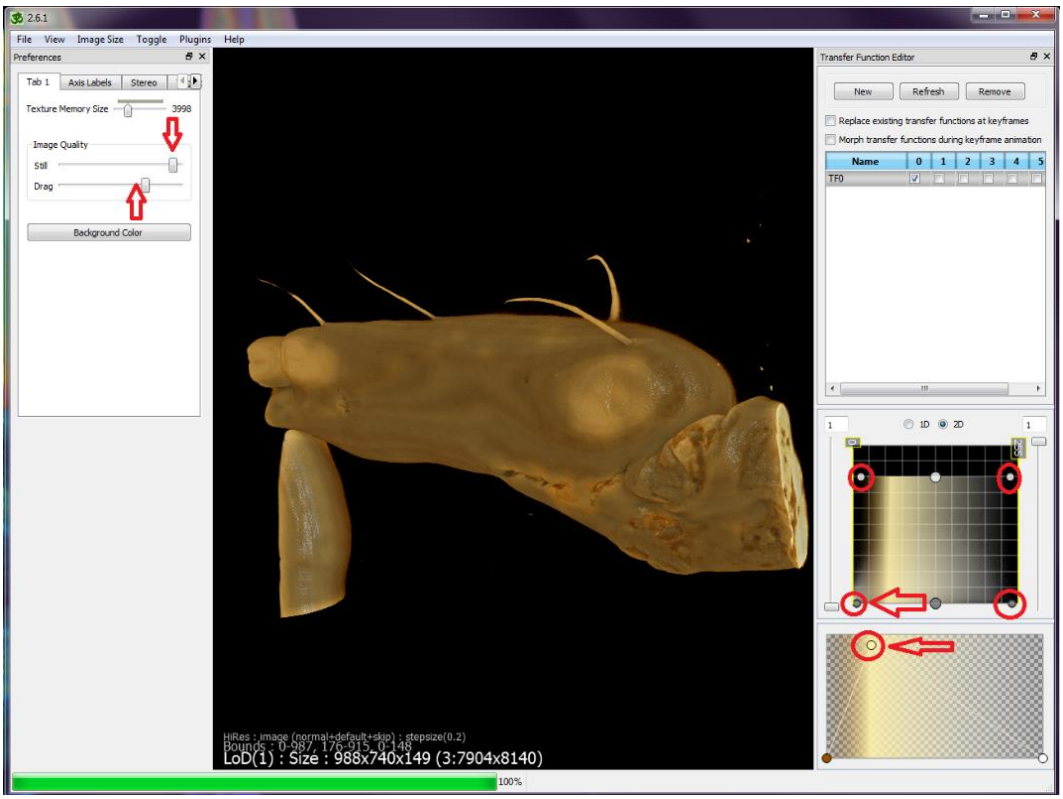

Figure App. 8.32: Getting high resolution images and some useful tools for Drishti.

To add a scale bar, after opening the command help window by pressing the space bar, the command “scalebar 100” was entered, this applied a 100 µm scale bar to the image (Fig. App. 8.33). To change the location of the scale bar, click and drag it to the correct position.

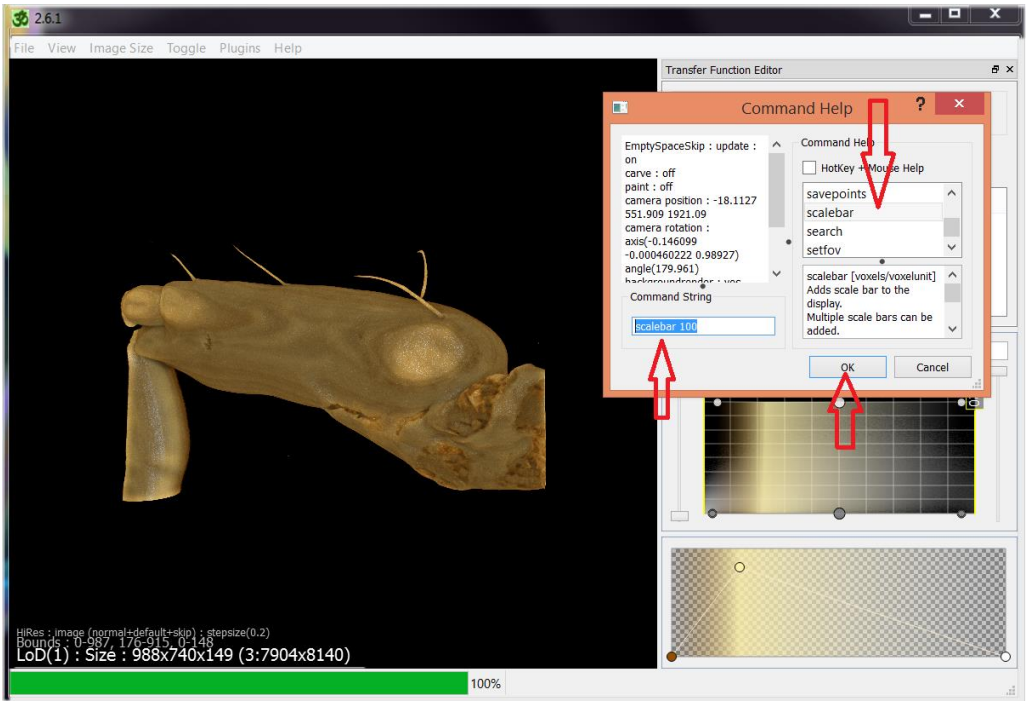

Figure App. 8.33: Adding a scale bar in Drishti.

The, the image was saved by clicking File> Save image (Alt + S) and image size was select; click OK (Fig. App. 8.34).

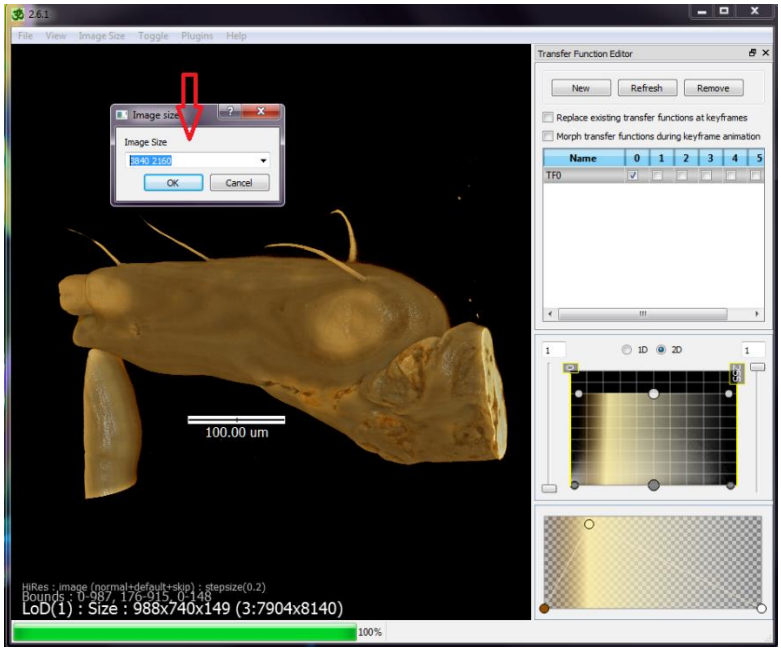

Figure App. 8.34: Saving the image and selecting image size.

Snap shots were saved by naming the file in ***.jpg format (Fig. App. 8.35).

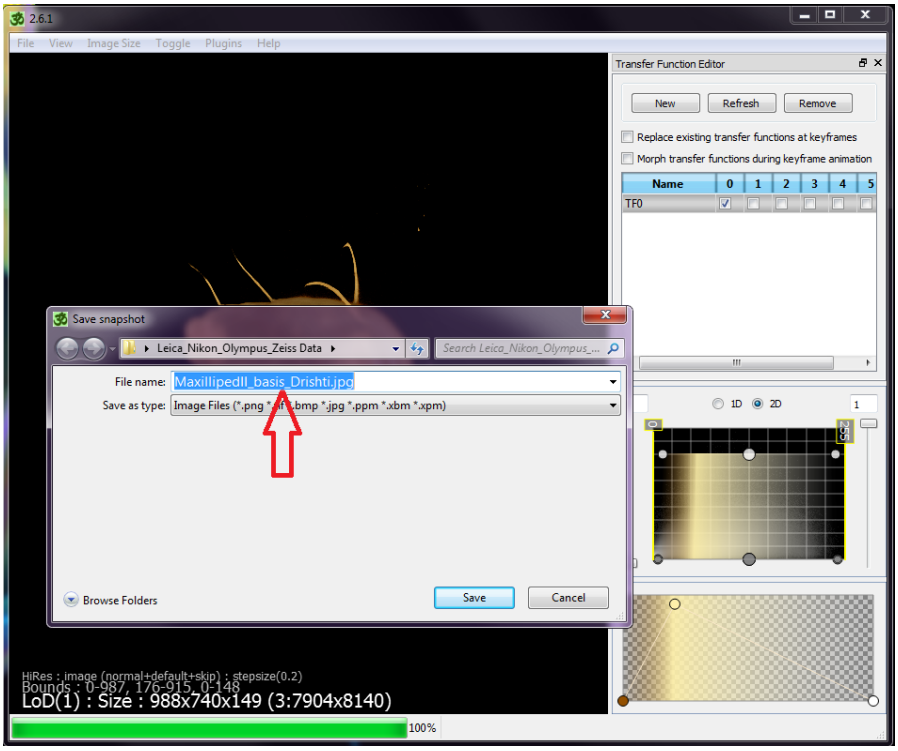

Figure App. 8.35: Naming image and saving in ***.jpg format.

"Mono Image" option in drop down box was selected and OK was clicked. The snapshot was saved as an image in ***.jpg format (Fig. App. 8.36). The snap shot window will remain open and, the volume can be repositioned and a new snapshot saved.

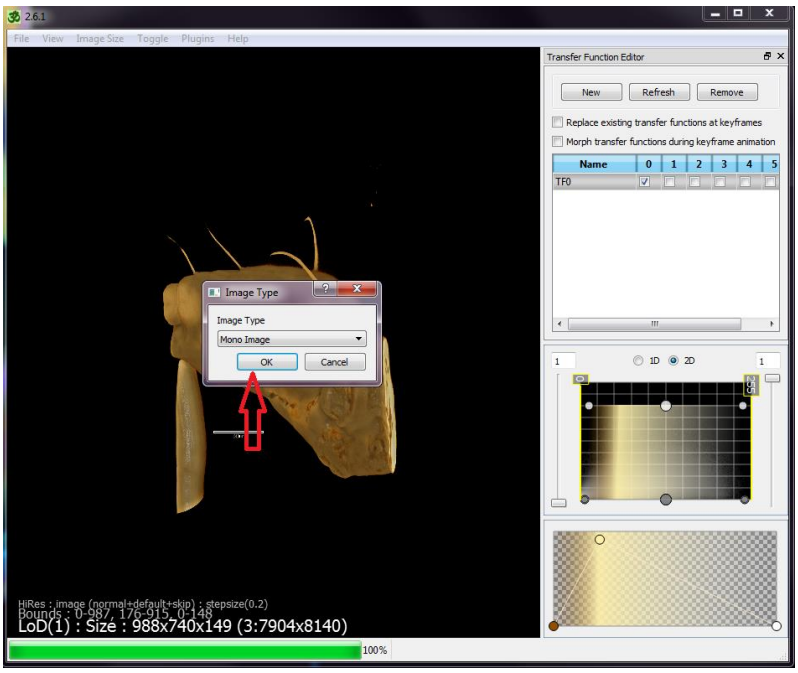

Figure App. 8.36: Taking a snapshot by selecting Mono Image and saving image.

Digital dissection (segmentation) instructions

The instructions below were followed for the digital dissection / segmentation.

First of all, segmentation was undertaken in high resolution via the F2 key and commenced by depressing "spacebar" on keyboard. When the "Command Help" box appeared, "mop update off" command was typed in Command String box and OK was clicked (Fig. App. 8.37).

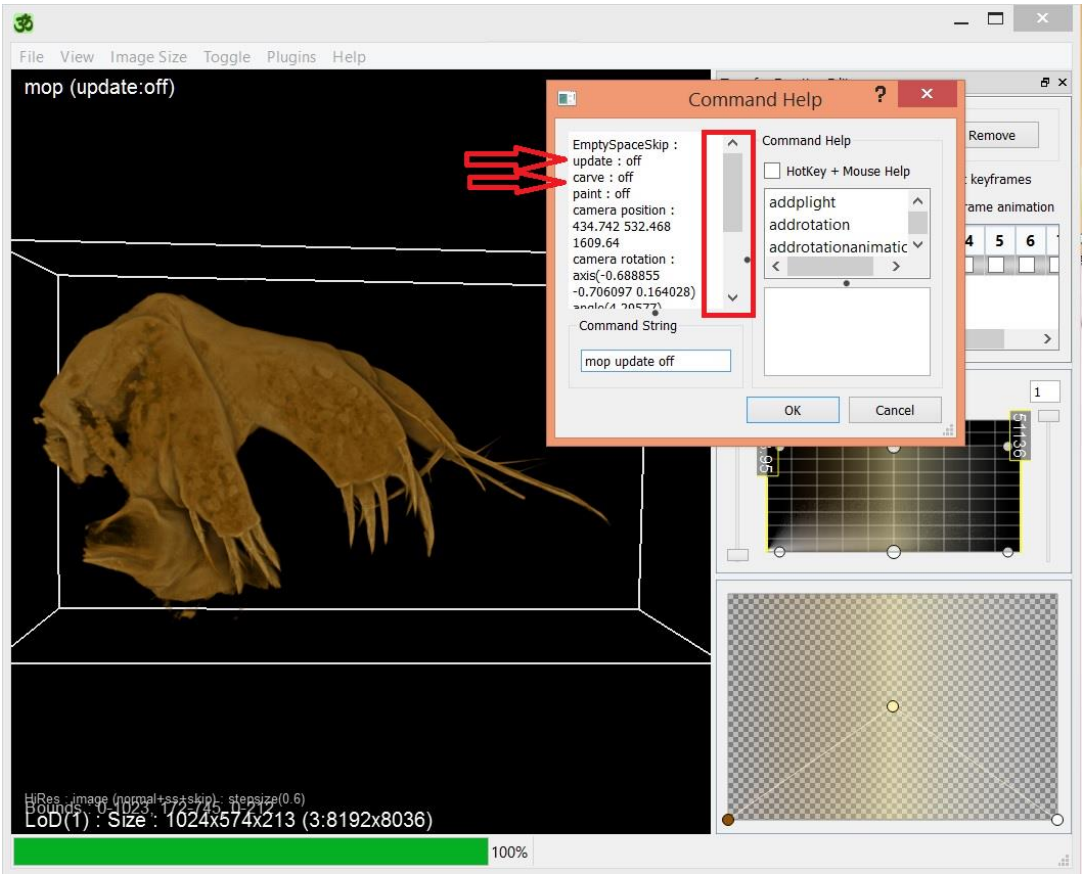

Figure App. 8.37: Segmentation: selecting mop update off for 3D data using Drishti.

The space bar was once again depressed and “mop carve” command was typed in appeared box and OK was clicked. Fragments to be removed/deleted were rotated and cleaned by pressing shift + left click (Fig. App. 8.38). After editing, the procedure was completed by pressing the space bar again and entering the command “mop carve off”; clicking OK.

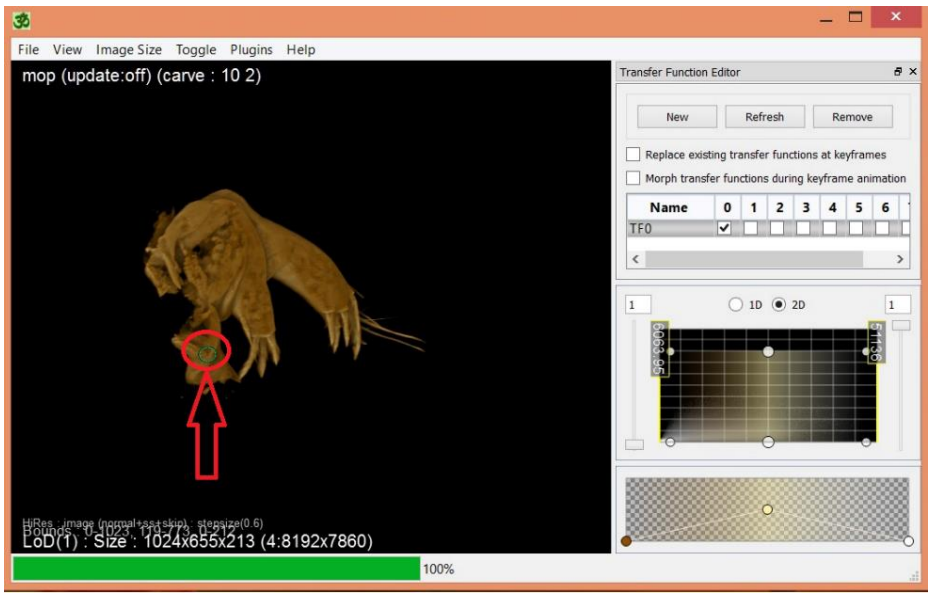

Figure App. 8.38: Rotating and removal of unwanted fragments in 3D images using Drishti.

Lastly, the opacity and colour interface was adjusted by manipulating the dots (Fig. App. 8.39).

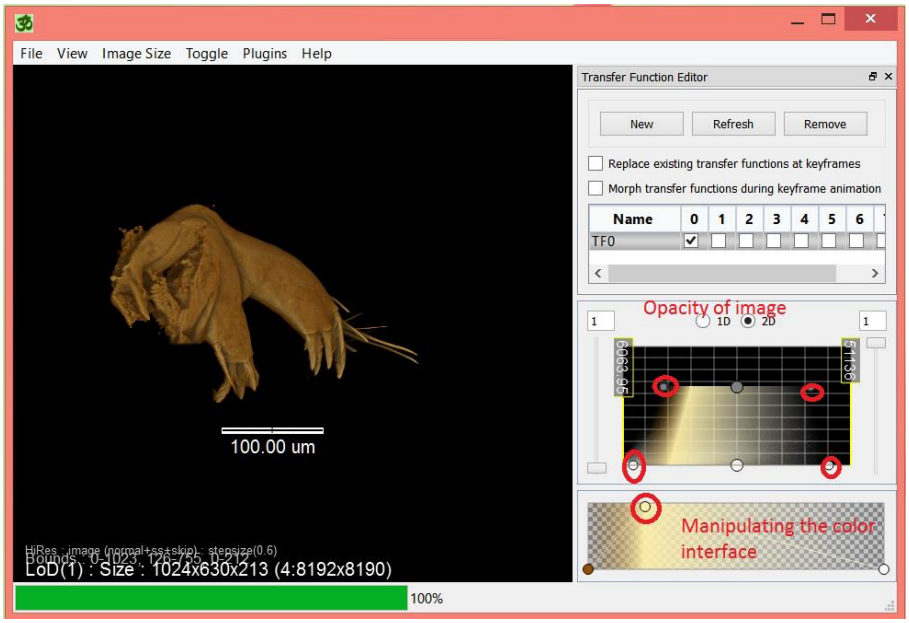

Figure App. 8.39: Adjusting opacity and colour of the image by manipulating interface.

After the editing process, the image can be saved as “Mono Image” by clicking File> Save image as. If the image is saved as ***.jpg, the background will be black, if ***.tiff the background is white.

Preparing videos using Drishti

All single and multi-channel data obtained from confocal microscopes can be converted into video format after processing the data using Drishti. In order to make the videos, after applying all the defined processes, the command of “addrotatioanimation” was commenced by depressing “spacebar” on keyboard. When the “Command Help” box appeared, “addrotationanimation x 360” command was typed in Command String Box and OK was clicked. This applied a 360° rotation in the x axis. This, depending on the position of the sample, can be rotated in y and z axis as well. In that case, this can be shifted changing the command. After converting any confocal data following the specific instructions into Drishti format, the videos can be created after having snapshots as a final step. The basic instructions and tutorial videos are available on YouTube (https://www.youtube.com/watch?v=BKnb_ayRVI&index=3&list=PLC511E6135E402898).

Appendix 7: Ball, A.D., Goral, T. & Kamanli, S.A. (2017) Confocal microscopy applied to paleontological specimens. *The Paleontological Society Papers*. **22**, 39−55.

The Paleontological Society Papers, 22, 2017, p. 39–55

1089-3326/17/2399-7575
doi: 10.1017/scs.2017.7

CONFOCAL MICROSCOPY APPLIED TO PALEONTOLOGICAL SPECIMENS

Alexander D. Ball[1], Tomasz Goral[1], and Seyit A. Kamanli[2]

[1]Imaging and Analysis Centre, Core Research Laboratories, The Natural History Museum, London, UK, ⟨a.ball@nhm.ac.uk⟩, ⟨t.goral@nhm.ac.uk⟩
[2]School of Biological Sciences, Royal Holloway University of London, Egham, Surrey, UK, ⟨Seyit.Kamanli.2013@live.rhul.ac.uk⟩

ABSTRACT.—Confocal laser scanning microscopy is a well-established optical technique allowing for three-dimensional (3-D) visualization of fluorescent specimens with a resolution close to the diffraction limit of light. Thanks to the availability of a wide range of fluorescent dyes and selective staining using antibodies, the technique is commonly used in life sciences as a powerful tool for studying different biological processes, often at the level of single molecules. However, this type of approach is often not applicable for specimens that are preserved in historical slide collections, embedded in amber, or are fossilized, and cannot be exposed to any form of selective staining or other form of destructive treatment. This usually narrows the number of microscopic techniques that can be used to study such specimens to traditional light microscopy or scanning electron microscopy. However, these techniques have their own limitations and cannot fully reveal 3-D structures within such barely accessible samples. Can confocal microscopy be of any help? The answer is positive, and it is due to the fact that many paleontological specimens exhibit a strong inherent autofluorescence that can serve as an excellent source of emitted photons for confocal microscopy visualizations either through reconstruction of the induced autoflourescent signal from the sample, or through reconstruction of the reflected signal from the sample surface. Here, we describe the workflow and methodology involved in acquiring confocal data from a sample and reprocessing the resulting image stack using the image-processing program imageJ before reconstructing the data using the open-source 3-D rendering program, Drishti. This approach opens new possibilities for using confocal microscopy in a nondestructive manner for visualizing complex paleontological material that has never previously been considered as suitable for this type of microscopic technique.

INTRODUCTION

Paleontologists are increasingly interested in three-dimensional (3-D) visualizations of fossils to study morphology and better describe, identify, and understand the paleobiology and evolution of ancient organisms. This can be done by means of different imaging techniques including optical tomography, which covers a range of modern light-based image capture approaches yielding slice data (i.e., a dataset of two-dimensional [2-D] cross-sectional images through the sample that can then be used as the basis for creating a 3-D digital model). These methods include: Optical Projection Tomography (OPT), Optical Coherence Tomography (OCT), Single Plane Illumination Microscopy (SPIM), Light Sheet Microscopy, Structured Light Microscopy, Confocal Laser Scanning Microscopy (CLSM), and a variety of closely related techniques. Of these, only confocal laser scanning microscopy (hereafter called confocal microscopy) will be discussed in this paper. Although the other techniques are widely documented online (see Haisch, 2012, for a recent review), their applications are predominantly in the field of bioimaging,

typically using fluorescently labeled tissue samples (Sharpe et al., 2002; Huisken and Stainier, 2009; Marschall et al., 2011). Unlike confocal microscopy, OPT, SPIM, and light sheet microscopy are not currently used for paleontological imaging applications, although some could have limited relevance (structured light microscopy and OCT in particular).

Confocal microscopy can be used to image samples that are autofluorescent, i.e., they naturally emit light at specific wavelengths after they have absorbed a packet of light energy. Because there are a range of biomolecules that retain fluorescent properties even after very extended periods of time (e.g., cuticle or chlorophyll and kerogens), confocal microscopy has been used very effectively in a paleoimaging context (Shi et al., 2013; Andersen et al., 2015; Strullu-Derrien et al., 2015; Hickman-Lewis et al., 2016), and is a widely available technique with well-understood strengths, but perhaps less well-described weaknesses. The following discussion is an attempt to summarize approaches that have been applied to a range of different sample types, whether paleontological or closely related, including some approaches that we have not been able to implement successfully. It should be noted that there are several applications using confocal microscopes in reflection mode to describe surface topographic features at high resolution. Evans et al. (2001) discussed the limitations of conventional confocal microscopy for imaging teeth or similar, translucent and reflective specimens by reflection mode confocal microscopy and described a method for confocal analysis of the topography of casts of bat teeth. In particular, they concluded that it outperformed laser scanning mainly due to the higher resolution datasets that were generated. Another powerful method for characterizing the morphology of paleontological specimens is high-resolution X-ray computed microtomography (micro-CT). Optical techniques will usually be suboptimal for applications involving transparent, translucent, reflective, or highly specular materials, whereas X-ray or electron-beam imaging techniques are entirely insensitive to the optical properties of materials. SEM imaging combined with tilt series reconstruction (i.e., Alicona's MeX software application; http://www.alicona.com/produkte/mex/) can describe surface features accurately at high resolution, but like confocal microscopy and optical-focus stepping techniques, has limitations when steep-sided and undercut features are encountered. X-ray micro-CT, provided it can offer sufficient resolution in the sample under investigation, offers many advantages over other volumetric analytical applications, but high performance instruments are extremely expensive and still relatively difficult to access. Furthermore, X-ray micro-CT does not work well for distinguishing sample phases that provide insufficient X-ray attenuation contrast, or insufficient differences in contrast between the specimen and the matrix, even if they are optically distinct.

In such cases, optical techniques (e.g., confocal microscopy) can provide a very effective way to characterize the sample. Confocal microscopy offers a technique that can provide excellent 2-D images of 3-D specimens (Fig. 1A, B; 2A, B) and under appropriate conditions, can deliver high-resolution 3-D reconstructions of suitable specimens.

HOW DOES A CONFOCAL MICROSCOPE WORK?

Detailed descriptions of the function of confocal microscopes are given in a number of books (e.g., Sheppard and Shotton, 1997) and on manufacturer websites (e.g., Zeiss Microscopy Online Campus, http://zeiss-campus.magnet.fsu.edu/index.html; Nikon Microscopy, http://www.microscopyu.com/; Leica Science Lab, https://www.leica-microsystems.com/science-lab/; Olympus Microscopy Resource Center, http://www.olympusmicro.com/). Online resources have the advantage that they are specific to the microscope described, and in some cases, include detailed, instrument-specific technological information, applications, and workflows.

Confocal microscope systems are packaged into a number of discrete components (Fig. 3): 1) the microscope, usually a standard light microscope; 2) the scanning stage, normally a standard XY stage coupled to a high precision galvanometer-driven Z stage; 3) the laser bed, where the lasers are housed (in modern systems, most commonly solid state lasers); and 4) the scan head, which includes the scanning system (typically galvanically controlled mirrors), pinholes, dichroic mirrors, and detector system. The whole instrument is coordinated by a system controller and connected to a PC that drives the microscope and acts as a local data store.

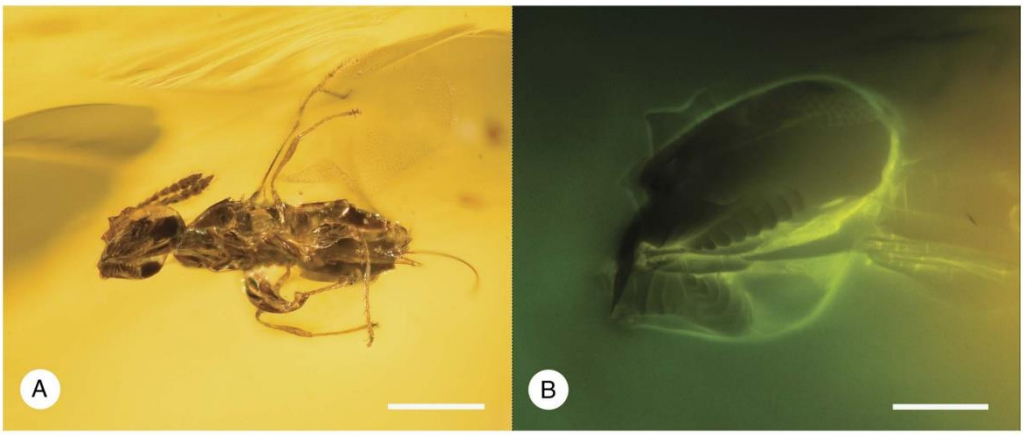

FIGURE 1.—(A) Macrophotograph of a fig wasp (*Pegoscapus*) preserved in Dominican amber; (B) confocal microscope image of the underside of the head of the same specimen; Scale bars = 250 µm (A) and 25 µm (B).

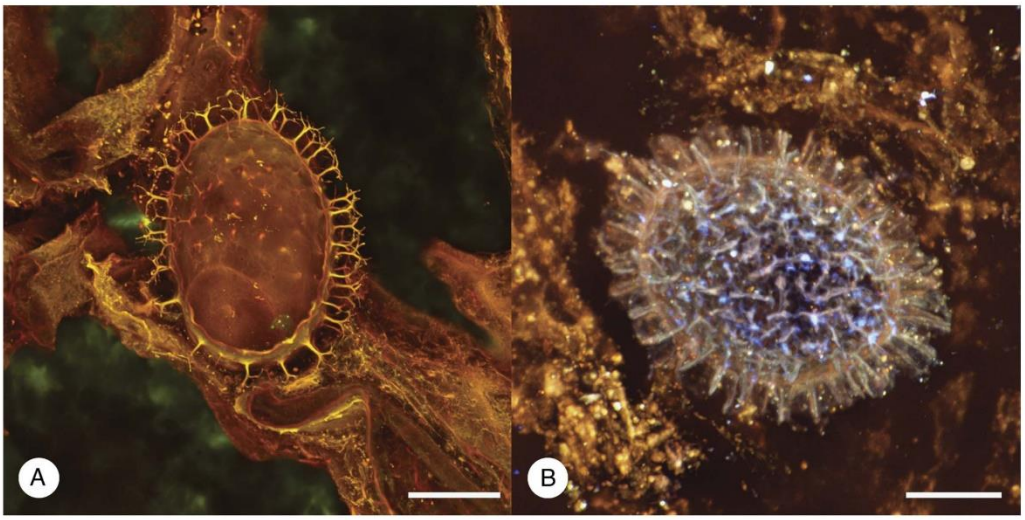

FIGURE 2.—Confocal microscope images of microorganism (fungus/fungus-like microorganism/green alga?) under investigation; (A) slide 162.628/01 (Coll. Norwegian Museum of Natural History, Oslo); (B) slide 114038 (Coll. Hunterian Museum, Glasgow); Scale bars = 30 µm (A); 10 µm (B).

In its simplest terms (and in most commercial systems), the confocal microscope scans a laser spot across the sample to excite fluorescence from the sample. The emitted fluorescent light passes from the specimen back through the optical train (i.e., the optical and mechanical components of the microscope) and through a pinhole, sized to allow only focused light rays to reach the detector. As a result, each image frame represents a single focal plane. By moving the stage in the Z plane, additional focal planes are collected, with the end-result being a stack of slices forming a registered 3-D dataset that can subsequently be reconstructed and rendered for visualization from different orientations.

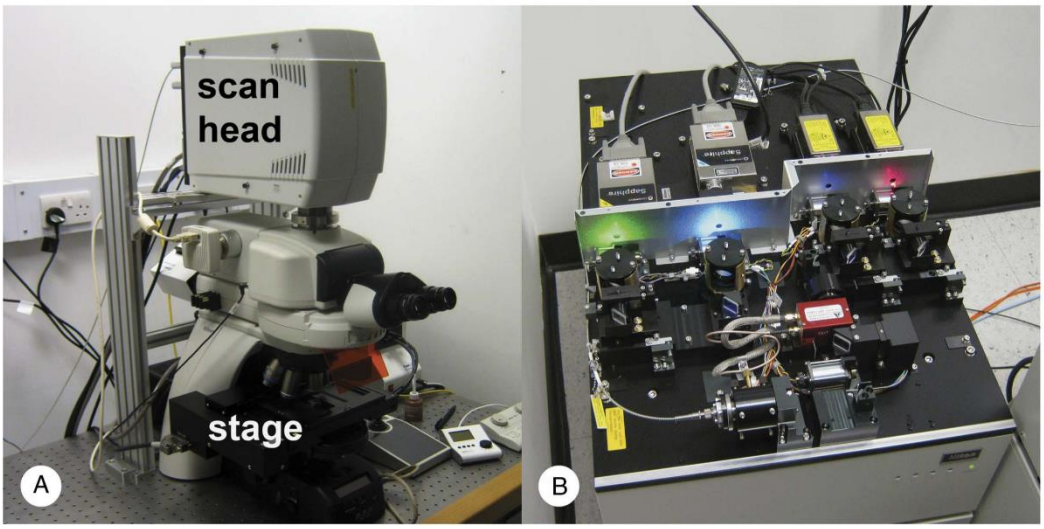

FIGURE 3.—Major components of a confocal microscope: (A) microscope, incorporating the scan head and stage; (B) laser bed showing the four solid state lasers; not shown: PMT and spectral detectors (these are sealed), and computer.

The output format from a confocal microscope is a stack of aligned image frames. Each frame reflects a single optical plane and image channel (i.e., representing a portion of the emitted signal within a specific wavelength range), and the dataset is typically grouped by channel and image plane. Thus, a stack of 50 slices in three channels would be packaged as 150 frames in three groups of 50.

A typical confocal microscope has several lasers of different wavelengths. For example, at ~400 nm for near-UV excitation, in the range 450–500 nm for blue light, 500–550 nm for green light, 550–570 nm for yellow light, 600–630 nm for orange, and >640 nm for red light excitation, a typical, four-laser setup might include 405, 488, 561, and 640 nm. In tandem, there will be a series of detectors, usually based around photomultiplier devices, which allow for the simultaneous collection of signals at different wavelengths. The excitation beam from the laser and the response from the sample (the emission signal) share the same light path, but are separated using a dichroic mirror that is transparent to certain wavelengths, but reflects selected wavebands. Dichroic mirrors are selected to match the lasers installed in the microscope and might be single, double, or multiple dichroics (i.e., allow the transmission of a single, double, or three or more wavelengths of laser light, but are reflective to all other wavelengths). Confocal microscopes also allow for the emission signal to be scanned across a series of different wavelengths by using either a prism or diffraction grating to split the signal into a spectrum, which is then detected in narrow wavebands or passed to a multichannel detector.

The theoretical resolution of a confocal microscope is defined by: 1) the numerical aperture of the lens (i.e., a measure of its ability to gather light and resolve fine-specimen detail at a fixed object distance); 2) the wavelength of the excitatory light (i.e., the wavelength generated by the laser used for fluorescence excitation); and 3) the refractive index of the medium under examination, measured as the change in the speed of light as it passes from a vacuum (or air as an approximation) into that medium. This normally equates to a spatial resolution in the X/Y plane of approximately half the illumination wavelength (i.e., for green excitatory light of ~550 nm, the resolution would be expected to be in the range of 200–300 nm). However, in the Z plane, the resolution is considerably reduced, and therefore is typically two to three times worse than the lateral resolution. Confocal datasets thus have nonisotropic voxels. This has implications for 3-D reconstruction and for morphometric analysis. In practical terms,

the greatest factors in the ability to resolve features of interest are the topography of the specimen (which can prevent the use of high-resolution, high-numerical-aperture lenses), the strength of the emitted fluorescent signal (balancing the signal-to-noise ratio), and the opacity of the specimen medium (which can scatter the laser and reduce signal strength).

THE OPTICAL TRAIN AND ITS EFFECT ON 3-D RECONSTRUCTION

Confocal microscopes are typically designed around compound light microscopes of two basic types: upright and inverted. Inverted microscopes are more common and widely used in cell biology because they are ideal for examining both slide-mounted samples and samples mounted in micro-well plates. However, because the objective lenses are positioned beneath the stage, they are not well suited for the examination of the majority of paleontological samples. Even slide-mounted samples can prove challenging. For the types of samples typically encountered by paleontologists, an upright microscope is essential. Less common are stereomicroscopes with either confocal scan heads or structured light-scanning systems. These macroconfocal microscopes offer advantages, including a large field of view (in the range of 1–2 cm rather than ~1 mm in standard confocal systems), a large working space under the final lens, and relatively low cost. However, in the experience of the authors, tested against a variety of fossil and modern samples including macroinvertebrates, the performance was not comparable to a conventional confocal microscope, particularly with regard to resolution.

In typical bioimaging applications, both upright and inverted confocal microscopes are used to examine samples mounted on slides fitted with coverslips. For the best resolution, a high numerical aperture lens is used in conjunction with immersion oil. The coverslip and immersion oil allow light exiting the specimen to enter the lens with the least amount of change in refractive index. This delivers higher contrast and minimizes distortion in the final image. However, the microscope is designed for optimum performance when the sample is close to the underside of the coverslip (within 10–20 μm). This does not allow for high-resolution imaging or reconstruction of an object of appreciable size. When the sample is farther away from the coverslip and deeper penetration of the focal plane is attempted, the image suffers increasingly from distortion along the axial plane as the image is increasingly distorted by refraction.

Some lenses have insufficient focal working distance to be able to focus on the sample at all. This effect is magnified by any mismatch between the refractive indices of the sample and the optical train (see Hell et al., 1993, for experimental validation and a detailed explanation of this effect). For example, a biological sample in saline (Refractive Index [RI] of 1.3–1.35) has a different refractive index from that of an oil immersion lens and standard glass coverslip (RI ~1.5) and this can lead to appreciable distortion in the image if the sample is significantly below the coverslip. Hydrated biological samples can also be mounted in glycerol, which has a refractive index of 1.47, intermediate between oil and saline and thus a good compromise. To optimize for samples in glycerol, immersion lenses specifically for use with glycerol are available and are corrected for a quartz glass coverslip (RI = 1.46). These lenses also perform well for samples close to the coverslip. However, for longer working distances, water-immersion lenses have been shown to outperform oil or glycerol-immersion lenses because there is less refractive index variation between saline and distilled water. Thus, the lens can be designed to have a longer focal working distance. The increase in interest in live-cell imaging has led to extensive developments in high-performance water-immersion lenses to address these issues.

PRACTICAL APPLICATIONS

From a paleontological imaging perspective, slide-mounted samples with coverslips are the easiest samples to handle because these are closest to the conventional biomedical samples for which these kinds of microscopes were designed. These samples allow the full range of objective lenses to be utilized, and the instrument can be used at, or close to, its optimum settings. In this application, confocal microscopes have been used for the examination of a variety of microfossils, including dinoflagellate cysts (Feist-Burkhardt and Pross, 1999), pollen (Hochuli and Feist-Burkhardt, 2013), plant material

(Strullu-Derrien et al., 2015), and microorganisms (see Shi et al., 2013, for a review of the history and limitations of confocal microscopy in this context).

If the specimen is a flat section (e.g., a polished geological sample or acetate peel) with no coverslip, an immersion lens normally cannot be used. The immersion lens needs to be optically coupled via the coverslip to the sample, and the coverslip helps to protect the lens against damage. However, because nonimmersion lenses have significantly lower resolution than immersion lenses in all dimensions, if high-resolution imaging is required and an immersion lens can be used, it is worth fitting a coverslip to the sample, even temporarily. Coverslips can be fitted temporarily using immersion oil, glycerol, or water, provided that a matching immersion objective lens is used. Note, however, that an unsecured coverslip will move between the lens and the sample as the sample is scanned. Using a longer coverslip (e.g., 22 × 64 mm) allows one end to be temporarily attached to the sample to prevent movement.

DATA ACQUISITION WORKFLOW

In practice, many paleontological slides are far from ideal in terms of their preservation and mounting (Fig. 4A). For example, historical slides or acetate peels can be of unusual sizes and thicknesses, the thickness of the coverslip might be nonstandard or unknown, or bulk samples might be highly irregular in shape or barely fitting on the microscope stage (Fig. 4B, C). Almost all of the published research relating to confocal microscopy is focused on biological applications, and its use in paleontological imaging is highly atypical. From that perspective, well-established biological protocols might not work with paleontological samples, and in many cases, novel approaches and methodologies are required for best results. As the first step in analyzing the sample, the fluorescence response from the sample must be analyzed and the microscope tuned to optimize the signal.

FLUORESCENCE MICROSCOPY

The basic principles of confocal microscopy, as outlined above, typically rely on an autofluorescent component in the sample generating a signal strong enough to detect and reconstruct. Screening samples to determine their suitability for confocal microscopy is easily accomplished using a wide-field fluorescence microscope. Indeed, laser-induced fluorescence imaging for revealing hidden details in fossils has recently been promoted as a new technique (Kaye et al., 2015), although a similar approach was earlier described by Haug et al. (2011), who applied fluorescence imaging to comparative morphology using a range of excitation wavelengths to induce autofluorescence in modern and fossil specimens. The majority of modern and fossil specimens fluoresce in the yellow to red wavelengths, and are excited by an emission source in the blue to green wavelength range. This falls within the typical FITC/TRITC (Fluorescein IsoThioCyanate/Tetramethyl Rhodamine IsoThioCyanate) dyes, which were commonly utilized in fluorescence and confocal microscopy prior to being replaced by more stable molecules with similar excitation and emission profiles. A legacy of usage of these dyes is that almost all fluorescence microscopes are fitted with compatible illumination and filter systems, which also work well for assessing the autofluorescence of samples by direct observation.

A simple workflow for confocal microscopy of paleontological samples is outlined below.

Screening step

Is autofluorescence readily detectable optically using an epifluorescence microscope (or a confocal microscope) in either the FITC or TRITC channel?

If yes, then the sample will likely be suitable for confocal microscopy.

If no, and the sample is of great interest, it is worth checking the sample using a confocal microscope with a detector system that offers greater sensitivity than a wide-field epifluorescence microscope. If the sample shows no sign of fluorescence, it might not be suitable for confocal microscopy.

Fluorescence optimization

Typically, a confocal microscope includes the capacity to carry out a lambda or wavelength scan. This uses a single laser wavelength as the excitatory source, then a range of wavelengths and sampling intervals is selected for the detection window (e.g., with a 405 nm laser, the detection window might be set between 420 and 700 nm in 10 nm steps, collecting 28 data points).

FIGURE 4.—Examples of 'difficult' samples that still might be amenable to confocal microscopy: (A) irregular slide-mounted materials; (B) amber with inclusions; (C) moldic fossil of an insect (fig wasp '*Ponera*') showing excellent 3-D preservation and some remnant cuticle preservation; Scale bars = 2 mm (B), 250 µm (C).

A similar experiment is set up for each available excitatory wavelength (laser line), starting at a suitable interval away from the excitation line (because the emission will always be at longer wavelengths than the excitation wavelength). These experiments yield a series of graphs, each showing the peak emission for any given excitation wavelength (Fig. 5A, B). Setting up the lasers requires an estimate of the fluorescence characteristics of the sample, hence, the prescreening step in epifluorescence.

More recently, instruments have been developed that dramatically reduce the time required for this lambda scanning step by fitting multichannel spectral detectors that can simultaneously collect the entire

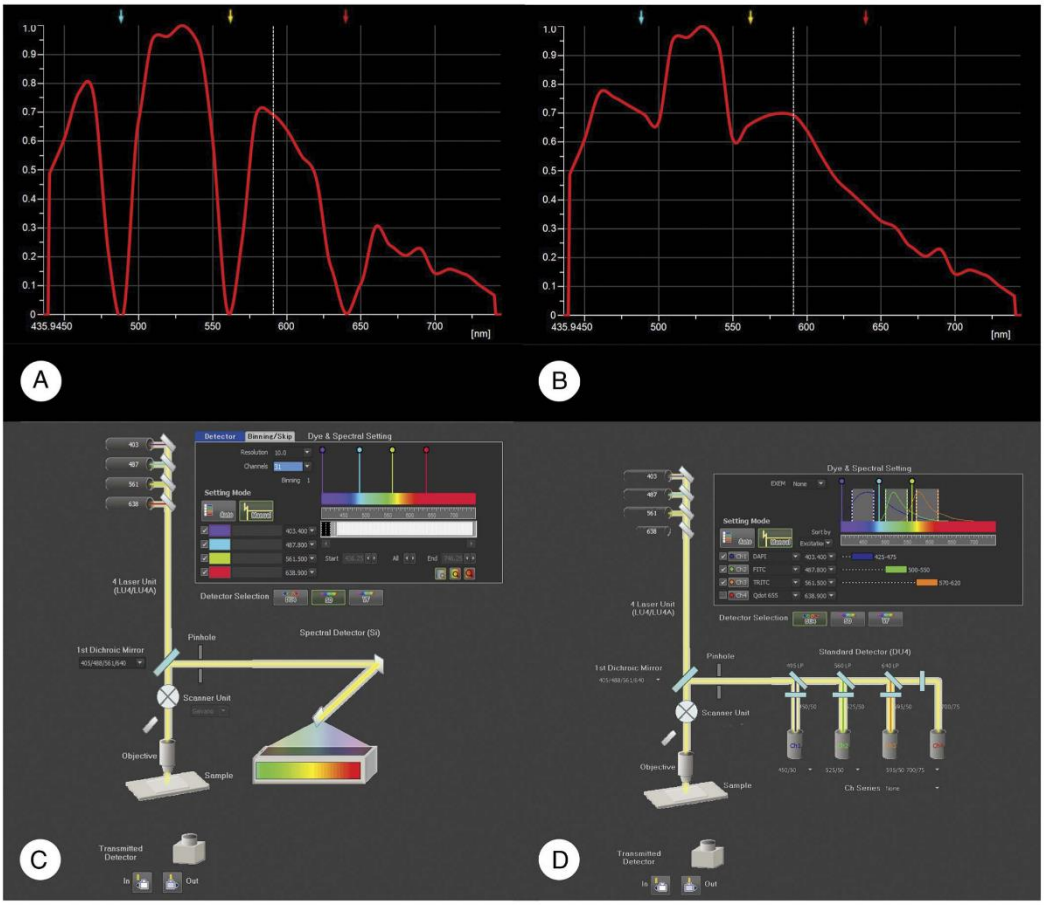

FIGURE 5.—Spectral analysis and image capture setup on a Nikon A1 confocal system: (A) spectral analysis of a region of interest collected from the emission signal excited by 403, 487, 561, and 638 nm lasers; the sharp dips are the 'blocking fingers' that prevent detection of the reflection signal from the lasers; (B) 'smoothed' spectral analysis, with blocking fingers removed, showing that the sample is strongly fluorescent between 500 and 600 nm with a smaller emission peak at 470 nm; (C) diagrammatic light path for the 32-channel spectral detector showing the use of a single quadruple dichroic mirror and a spectral resolution of 10 nm; (D) diagrammatic light path for quadruple PMT detection; the same dichroic is used, together with three further single dichroic mirrors, to divert the signal to four individual PMTs detecting bandwidths of 425–475, 500–550, 570–620, and >638 nm.

dispersed signal across a detector array consisting of 30 or more multianode, photomultiplier detectors (Fig. 5C). These have the advantages of: 1) speed, because the lambda scan for each wavelength is collected in a single frame, and 2) displaying a 'true-color' fluorescence image of the sample. Filters can be tuned by changing the portion of the spectrum projected onto the detector array; from an initial experiment dispersing the spectrum from blue to red onto 32 channels, the detection sensitivity can be retuned so that a narrower band (e.g., a signal corresponding to orange to red fluorescence) can be spread onto the detector to refine the spectral fingerprint collected. When photomultiplier tubes (PMTs) are in use, the signal is passed through a series of dichroic mirrors to the appropriate PMT (Fig. 5D).

Brightness and contrast settings

Once the lambda or spectral scan is complete, the combination of detectors and channels is determined along with the gain and offset in the image set; the latter is determined by the final use-case for the dataset. For example, the image setup conditions are different for an image stack that will be compressed down to form a single 2-D image, and a dataset that is acquired to generate a 3-D volume for reorientation or 3-D modeling. The settings will also differ if parts of the sample are highly fluorescent compared to the general sample background.

Two-dimensional projections from confocal image stacks are typically achieved by creating a projection image that either displays the average pixel value through Z at every XY position (Average Intensity Projection), or the brightest pixel through the Z plane at every XY position (Maximum Intensity Projection). Some experimentation might be required to determine which projection best represents the visualization of the data, and which combination of settings best achieves this aim. For example, oversaturation of a series of image planes containing a very strongly fluorescent feature within the volume of the image stack can render the final 2-D projection image unusable, whereas setting the brightness and contrast to match the most fluorescent feature can result in undersaturation of the remainder of the dataset. This is a known problem in confocal microscopy and manufacturers typically supply some form of adaptive brightness control that allows gain and offset to be set to different intensities at different points in the Z stack (Fig. 6).

Finally, the signal-to-noise ratio needs to be optimized. This can be through a combination of scan speed settings or scan averaging. A simple way to set up the scan-averaging parameter is to set a high value from frame averaging (e.g., 16 frames) and observe the image as it accumulates on screen. At the point (number of frames) when changes in the images are no longer observed (e.g., if after four frames, the noise in the image has disappeared and no longer appears to change with each new frame), then this value can be reliably used for frame averaging. Data required for 2-D output can be acquired at lower slice intervals than data required for 3-D reconstruction, which should always include as many Z planes as required at the highest practical resolution.

Determining the best setting could require iterative low-resolution scans. If the sample is subject to photobleaching (destroying fluorophores so that they can no longer emit a signal) or fluorescence depletion, this can leave scan marks in the specimen. In such cases, if possible, the reactivity of the sample to confocal microscopy should first be determined in a region of low scientific value.

Data acquisition for later 3-D reconstruction is subject to a variety of additional factors. Ideally, the final dataset should include all of the features required in the final 3-D visualization. For example, setting the gain and offset to capture structures such as fine setae can compromise other aspects of the specimen, or might require high magnification or the use of a high-resolution objective lens. The net effect of these choices might require image tiling to capture the total field of view and the acquisition of a very large number of slices, both of which can lead to very long acquisition times (~4–8 h). An additional, related consideration is whether the sample is robust enough to cope with this treatment. Long acquisition times can result in the loss of fluorescence (photobleaching).

Capturing focal planes in a sample that scatters the laser and its return signal could require the combined use of adaptive brightness in the laser. This maximizes the signal being delivered to the deeper parts of the sample by increasing power to the lower slices in the dataset and reducing it at the surface layers, and adaptive signal processing in the detection system to reduce gain closer to the sample surface and enhance it further from the surface. Use of the XZ- or YZ-scanning orientation (Fig. 6B) can help with instrument setup as can selecting a tall, thin rectangular region of interest for the XZ/YZ scan because this will average the signal in the XY plane, thus giving a clearer picture of the sample in the Z plane (if the instrument supports adaptable regions of interest for scanning).

IMAGING FOR OPTIMUM 3-D DATA CAPTURE

In general, capturing 3-D volumes requires the highest resolution lens available to deliver the best compromise between focal working distance (the ability to project the laser into the sample and retrieve the focal plane) and resolution (defined by the numerical aperture of the lens). However, a higher numerical aperture or oil-immersion lens might not deliver the best result for slide-mounted specimens.

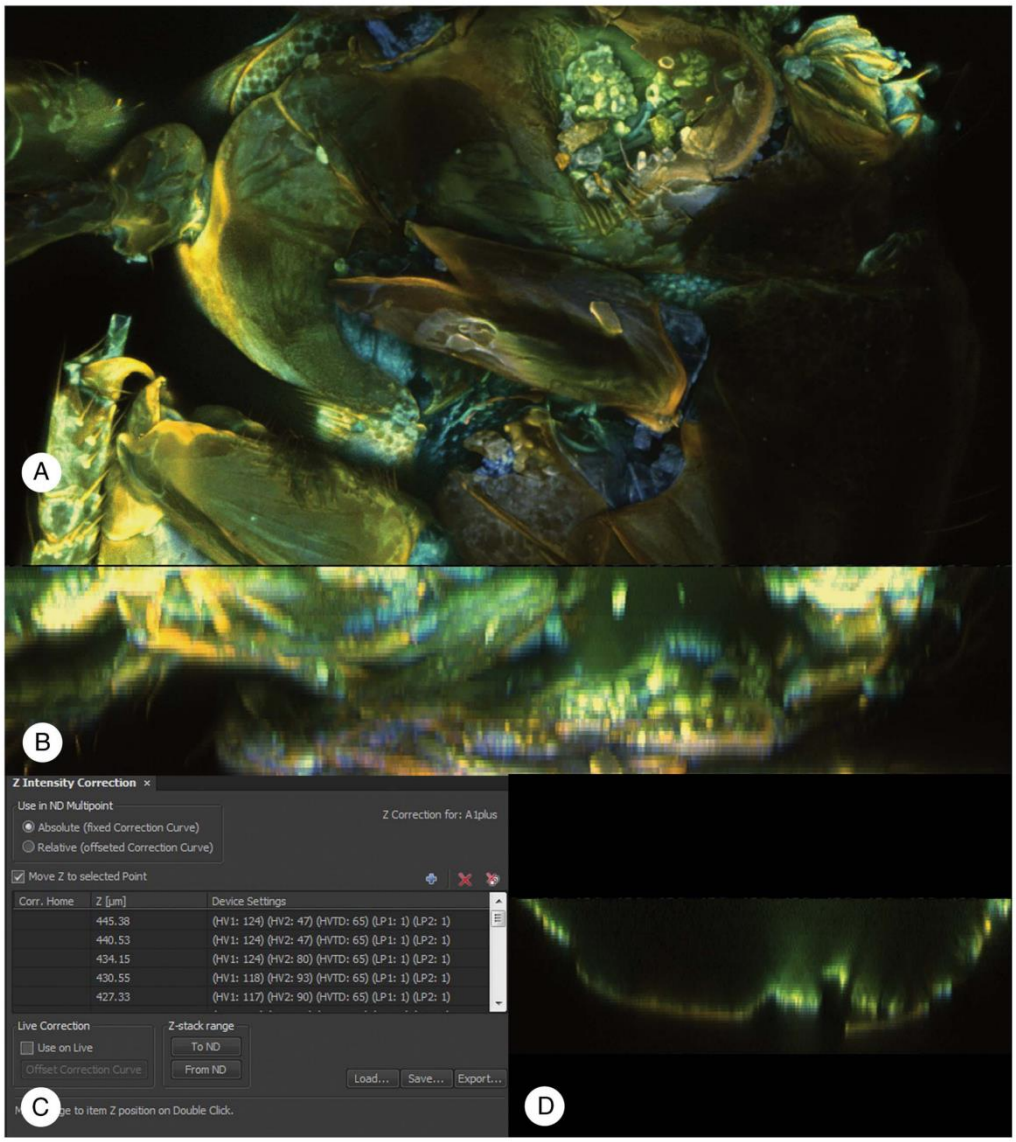

FIGURE 6.—Depth compensation in a data stack; the sample is from a modern fig wasp (*Liporrhopalum*); (A) maximum intensity projection image captured with depth compensation enabled; (B) orthogonal section through (A) showing that the brightness throughout the sample has been maintained; (C) table of correction factors applied; at each focal step, the gain and offset in the detectors has been adjusted to maximize the signal collected at each focal depth; (D) same dataset, but collected without depth compensation; the gain and offset were set to match the signal at the sample surface.

Three-dimensional image capture can be divided into two broad categories: 1) capture for surface features (roughly equivalent to trying to generate an SEM-like image); and 2) capture for volume. By default, the microscope will capture and render a volume dataset in which the content of every slice is

rendered into the final visualization. This makes sense because this is what confocal microscopes were designed to do—reproduce, contextually, the 3-D organization of tissues by showing the spatial arrangement of the various components (nucleus, cytoskeleton, stained cell components, etc.). However, if the specimen under examination is a fossil, then the most useful information might be the surface features (Andersen et al., 2015).

If the final images will be reproduced in the same orientation as the specimen, e.g., the confocal microscope will use fluorescent data to create what is essentially an extended depth-of-field image, then the microscope can be optimized to give the best resolution in X and Y by selecting a lens that gives the appropriate resolution at the required magnification, then acquiring sufficient focal steps to produce a good quality 2-D image. When the sample cannot be oriented to deliver an acceptable view of the features of interest, or a larger field of view is needed and the low magnification lenses do not give the required resolution, or when a 3-D dataset is required, then the highest practical magnification and resolution lens should be used. All modern confocal microscopes allow for image tiling in X, Y, and Z image planes, and this can be used to acquire sufficient data to generate a good 3-D reconstruction, or to acquire a large field of view. However, large data sets can take many hours to acquire, so the sample needs to be stable and not subject to fluorescence photobleaching. In practice, there is no advantage to oversampling in the Z plane. For example, Figure 7 shows the effect of capturing a dataset with a 10×0.3 n.a. Plan Fluor lens using the recommended step size of 8 µm (Fig. 7A, C) or the oversampled step size of 2 µm (Fig. 7B, D). The figures clearly show that there is no gain in the 2-D maximum intensity projection (Fig. 7A, C), nor in the 3-D reconstruction (Fig. 7B, D). However, using a 20×0.5 n.a. Plan Fluor lens gives a clear gain in both axial resolution (Fig. 8A) in the 2-D maximum intensity projection and in the 3-D reconstruction (Fig. 8B).

3-D SURFACE RENDERING

Most confocal microscopes include a basic 3-D reconstruction and visualization program as part of their core functionality, but the lighting models and capability in these programs are very poor compared to those that are commercially available. However, there are open source alternatives that work very well. The workflow described here, which has been tested with data from four main manufacturers, allows a confocal dataset to be imported into the widely used micro-CT visualization program Drishti (Limaye, 2012), requiring a short conversion step in ImageJ (Schneider et al., 2012) or Fiji (Schindelin et al., 2012). Drishti is a powerful package for applying surface rendering, lighting, or for reorientation and editing of 3-D datasets to remove spurious or obscuring data.

METHODOLOGY FOR IMPORTING CONFOCAL SLICE DATA TO DRISHTI

For this method, it is assumed that the user has some familiarity with ImageJ, Drishti (tutorials and explanatory videos are available on the Drishti website, https://sf.anu.edu.au/Vizlab/drishti/), and the basic Drishti import tool.

ImageJ or Fiji can directly open an image stack from Leica (.LIF), Zeiss (.CZI), Nikon (.ND2), and Olympus (.OIB) confocal microscopes using the standard Bio-Formats import dialogue box in the file menu (open data option). At this point, the user should ensure that the 'Autoscale' option is selected, that the data are imported in grayscale, and that the option 'Split Channels' is selected. This will separate each color channel into a single image stack. The image stacks should be reviewed for bad data (saturation, etc.), to determine whether all channels will be used or if selected channels will be excluded from the final dataset.

Before creating the final dataset, the user needs to open the Image Properties dialogue box and note the pixel dimensions in X, Y, and Z (these will be needed for Drishti). Once these have been recorded, then the channels can be merged using the Image > Color > Merge Channels… option, selecting the required channels, and creating a composite in the Image menu. Next, using the Image > Color > Channels Tool… option, click More > Convert to RGB. The slices need to be converted to 8 bit RGB format and saved as a TIFF Image Sequence (File > Save As > Image Sequence).

Once saved, the image stack can be imported into Drishti as a grayscale TIFF image directory, with 8-bit voxel type UChar. The resulting .PVL.NC file

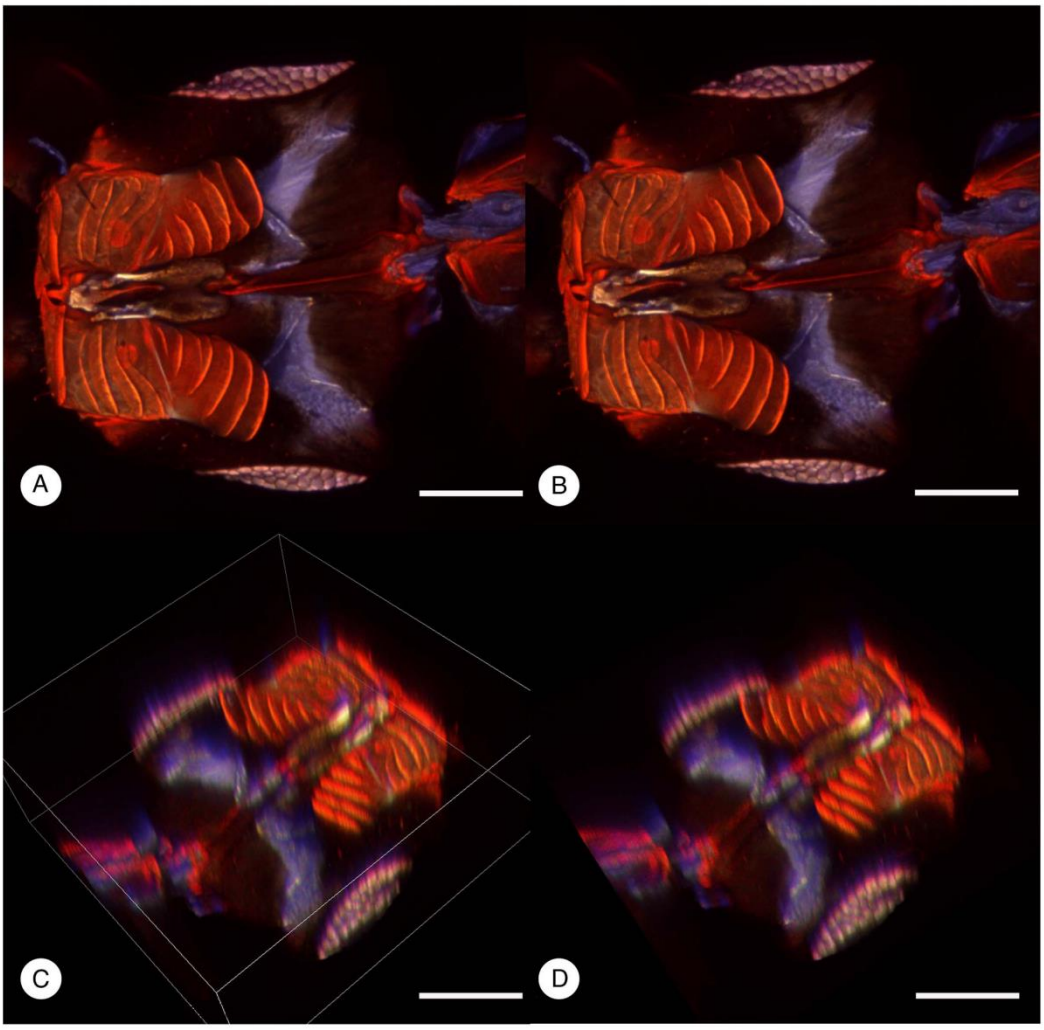

FIGURE 7.—Comparisons between step size with the same objective lens using a modern fig wasp (*Liporrhopalum*): images collected at (A) 8 µm step intervals and (B) 2 µm step intervals; both images are maximum intensity projections; (C) reorientated image from the 8.65 µm step-size dataset; (D) reorientated image from the 2.65 µm step size dataset; both 8 µm and 2 µm datasets captured with a Nikon 10×0.3 n.a. Plan Fluor objective lens; Scale bars = 100 µm.

can be saved with the default values. Finally, the voxel size needs to be entered into the 'Additional information' dialogue box (e.g., X, Y, and Z values of 200, 200, and 400 nm would be entered as 0.2, 0.2, and 0.4 with the Voxel unit selected as 'Micron').

From this point, data can be manipulated as a conventional Drishti volume. The advantages of Drishti over conventional volume-rendering programs utilized for confocal microscopy is that Drishti has far more powerful surface rendering, opacity, color, and lighting tools, and also allows for reorientation of the volume (Fig. 9).

The segmentation tools in Drishti allow for cropping and removal of obscuring features. For example, adhered detritus can be removed by reorienting the volume so that the detritus is above

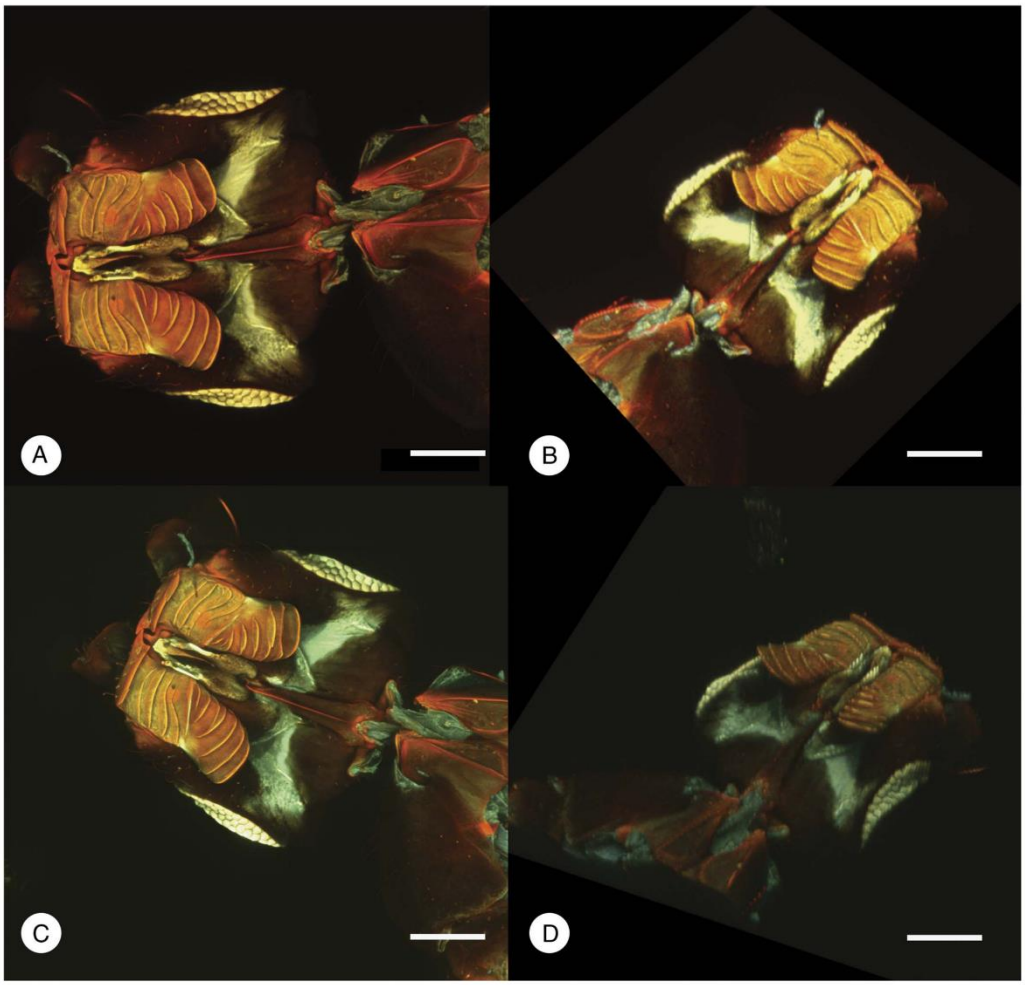

FIGURE 8.—Performance gain with high resolution lenses: (A) image collected at 2.65 µm step intervals, maximum intensity projection; (B) reorientated image from the dataset shown in (A); (A, B) collected using 20 × Plan Fluor 0.5 n.a. lens; (C) image collected at 1 µm step intervals, maximum intensity projection; D. reorientated image from the dataset shown in (C); (C, D) collected using 40 × Plan Fluor 0.75 n.a. lens and stitched from 512 × 512 pixel tiles (total image size 1267 × 1267 pixels); Scale bars = 100 µm.

the plane of the sample, then using the 'Mop Carve' tool in Drishti to delete it from the volume, which does not alter the original specimen data. This is arguably a more 'ethical' way to manipulate the image because the underlying data are unaffected, unlike, for example, digital manipulation on a 2-D image using eraser or cloning tools.

DISCUSSION

Not all samples are suitable for confocal microscopy (Fig. 10) and the technique requires some experimentation. However, when successful, the results can be both informative and visually stunning. Outlined below are a few observations of the authors'

FIGURE 9.—Datasets re-rendered in Drishti using 512 × 512 pixel stitched datasets acquired with a 40 × 0.75 n.a. lens at 1 µm step intervals: (A) showing the render with the 'lighting' enabled; (B) showing the render effect with 'lighting' disabled different features are highlighted and considerably greater control of shadow and surface texture is possible; Scale bars = 100 µm.

experiences with a small range of samples that have been encountered in our laboratory. A typical microscope setup used for capturing the datasets listed below involves using all available laser lines (405, 488, 561, and 640 nm) to maximize autofluorescence emission, and a range of different objectives depending on the type of the investigated material. For example, for amber inclusions, we used 10× or 20× nonimmersion lenses (numerical apertures of 0.3 or 0.5, respectively), and for the slide-mounted Rhynie Chert thin sections, we used an oil-immersion 40× lens (numerical aperture of 1.3) with a coverslip.

Amber inclusions

Amber-embedded specimens can be difficult to image for a number of reasons: 1) the size of the amber block might not be suitable for confocal microscopy, 2) the orientation of the specimen might be disadvantageous; 3) the sample might be too deeply embedded in the block, 4) the light path to the specimen might be impeded by other inclusions, and 5) the level of background signal and amount of scattering might be problematic. For example, after acquiring good data from a fig wasp preserved in Dominican amber (Compton et al., 2010; Fig. 1) and a midge preserved in Rovno amber (Andersen et al., 2015), examination and testing of subsequent samples proved to be less successful, with none of the specimens tested being sufficiently fluorescent to allow data acquisition (Fig. 10A). Similar mixed results were experienced with a variety of different amber and specimen types. In some cases, the amber was highly fluorescent, but the specimen appeared darker, so that the image appeared to be inverted rather than fluorescent (Fig. 10A). This could be due to differences in the degree of pigmentation in the specimen. Experience with modern insects and arthropods has shown that pigmented cuticle is much less fluorescent than unpigmented or 'untanned' cuticle, so much so that for studies of extant arthropods, it is typical to stain the cuticle to improve the fluorescent response (Lee et al., 2009).

Pollen grains, cuticle remnants, and microfossils

Confocal microscopy works well with slide-mounted, fluorescent materials of small size. These samples are

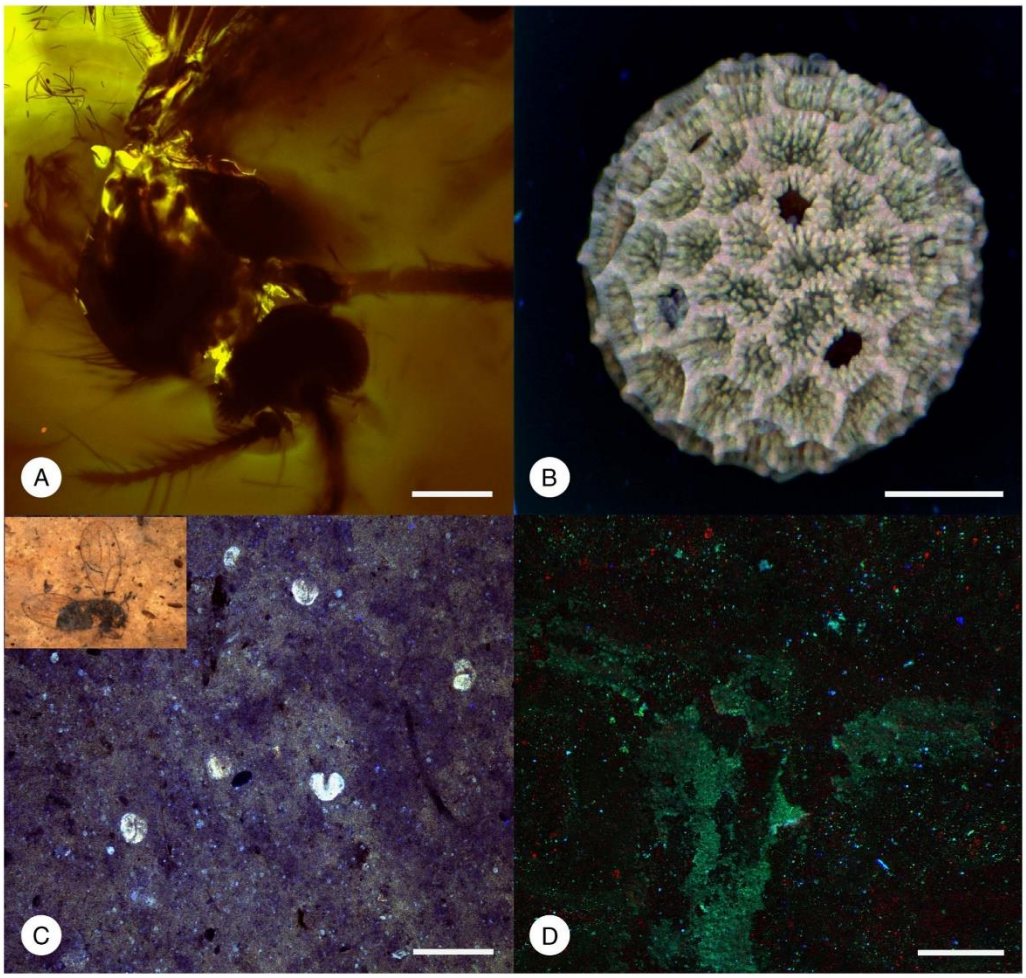

FIGURE 10.—(A) Dorsal view of head and thorax of a midge (species unknown) embedded in Lebanese Cretaceous amber (120–135 Mya); the image appears inverted due to a lack of fluorescence in the specimen compared to the background amber; (B) Redshank pollen grain (*Persicaria*) recovered from sediment within a bone tool (ca. 400,000 years old), Clacton, UK; (C) fossil insect from the Kishenehn Formation (northwestern Montana, USA; ca. 46 Mya); no fluorescence signal detected from the fossil compared to the background; inset image showing the specimen viewed under light microscopy (total body length ~2 mm); (D) fossil arthropod (*Marella*) from the Burgess Shale (ca. 508 Mya) showing weak and unusable fluorescence signal from both the background and the fossil; Scale bars = 1 mm (D), 200 µm (A, C), and 10 µm (B).

typically well suited to confocal microscopic examination and reconstruction (Fig. 10B).

Moldic fossils

The authors have successfully imaged fluorescent fragments of insect cuticle from Bembridge Marls, Isle of White, UK (Compton et al., 2010; Fig. 4C). Conversely, we have failed with much older fossilized material (ca. 100 Mya) in which the background fluorescence was very high, whereas the fossil itself exhibited almost no fluorescence (Fig. 10C), and with Burgess Shale fauna, in which both the fossil and

background exhibited a poor fluorescence response (Fig. 10D). It is also possible to use the confocal microscope in reflection mode to generate 3-D models of the sample. However, this only works well with relatively shallow samples. Steep sides and overhangs are not accurately rendered using this technique.

Rhynie Chert

Specimens from the Rhyne Chert have been successfully imaged as polished sections fitted with coverslips, revealing plant, fungal, and arthropod remains (Strullu-Derrien et al., 2015; personal observation). This investigation was one of the first attempts to apply confocal microscopy to visualize such complex and old (407 Mya) fossilized material in three dimensions using historical slide collections. A detailed discussion on the advantages of using confocal technique over traditional microscopy for those fossils was provided by Strullu-Derrien et al. (2015).

CONCLUSIONS

Acquiring images of paleontological samples requires more experimentation than for biological samples. In particular, sample mounting can be critical to the success or failure of the endeavor, i.e., flat, polished sections or slide-mounted specimens are generally more successful than thick, irregular, bulky samples. Confocal microscopy offers a high-resolution option for retrieving data from slide-mounted samples and from some types of amber inclusions. It is perhaps less useful than SEM on 3-D fossils, but can reveal data at higher resolution than micro-CT on appropriate samples. The use of micro-CT rendering packages to enhance surface features can be a particularly powerful technique for visualization and allows for direct comparison between SEM surface data, micro-CT rendered datasets, and data acquired through confocal microscopy.

ACKNOWLEDGMENTS

The authors would like to thank the Paleontological Society for financial support to allow TG to attend the short course meeting, and to M. Lewis, C. Strullu-Derrien, and P. Kenrick for permission to use their data in the figures. We would also like to acknowledge the loan of material in Figure 2 from the collections of the Norwegian Museum of Natural History, Oslo and the Hunterian Museum, Glasgow.

REFERENCES

Andersen, T., Baranov, V., Goral, T., Langton, P., Perkovsky, E., and Sykes, D., 2015, First record of a Chironomidae pupa in amber: Geobios, v. 48, p. 281–286.

Compton, S.G., Ball, A.D., Collinson, M.E., Hayes, P., Rasnitsyn, A.P., and Ross, A.J., 2010, Ancient fig wasps indicate at least 34 Myr of stasis in their mutualism with fig trees: Biology Letters, v. 6, p. 838–842, DOI:10.1098/rsbl.2010.0389.

Evans, A.R., Harper, I.S., and Sanson, G.D., 2001, Confocal imaging, visualization and 3-D surface measurement of small mammalian teeth: Journal of Microscopy, v. 204, p. 108–119.

Feist-Burkhardt, S., and Pross., J., 1999, Morphological analysis and description of Middle Jurassic dinoflagellate cyst marker species using confocal laser scanning microscopy, digital optical microscopy and conventional light microscopy: Bulletin du Centre de Recherché Elf Exploration Production, v. 22, p. 103–145.

Haisch, C., 2012, Optical tomography: Annual Review of Analytical Chemistry, v. 5, p. 57–77.

Haug, J.T., Haug, C., Kutschera, V., Mayer, G., Maas, A., Liebau, S., Castellani, C., Wolfram, U., Clarkson, E.N.K., and Waloszek, D., 2011, Autofluorescence imaging: An excellent tool for comparative morphology: Journal of Microscopy, v. 224, p. 259–272.

Hell, S., Reiner, G., Cremer, C., and Stelzer, E.H.K., 1993, Aberrations in confocal fluorescence microscopy induced by mismatches in refractive index: Journal of Microscopy, v. 169, p. 391–405.

Hickman-Lewis, K., Garwood, R.J., Brasier, M.D., Goral, T., Jiang, H., McLoughlin, N., and Wacey, D., 2016, Carbonaceous microstructures from sedimentary laminated chert within the 3.46 Ga Apex Basalt, Chinaman Creek locality, Pilbara, Western Australia: Precambrian Research, v. 278, p. 161–178.

Hochuli, P.A., and Feist-Burkhardt, S., 2013, Angiosperm-like pollen and *Afropollis* from the Middle Triassic (Anisian) of the Germanic Basin (northern Switzerland): Frontiers in Plant Science, v. 4, p. 344 DOI: 10.3389/fpls.2013.00344.

Husiken, J., and Stainier, D.Y.R., 2009, Selective plane illumination microscopy techniques in developmental biology: Development, v. 136, p. 1963–1975.

Kaye, T.G., Falk, A.R., Pittman, M., Sereno, P.C., Martin, L.D., Burnham, D.A., Gong, E., Xu, X., and

Wang, Y., 2015, Laser-stimulated fluorescence in paleontology: PLoS ONE, v. 10, p. e0125923 DOI: 10.1371/journal.pone.0125923.

Lee, S., Brown, R.L., and Monroe, W., 2009, Use of confocal laser scanning microscopy in systematics of insects with a comparison of fluorescence from different stains: Systematic Entomology, v. 34, p. 10–14.

Limaye, A., 2012, Drishti: a volume exploration and presentation tool, *in* Stock, S.R., ed., Proceedings of SPIE Volume 8506, Developments in X-Ray Tomography VIII: San Diego, California, August 12, 2012, p. 85060X, DOI: 10.1117/12.935640.

Marschall, S., Sander, B., Mogensen, M., Jørgensen, T. M., and Andersen, P. E., 2011, Optical coherence tomography—Current technology and applications in clinical and biomedical research: Analytical and Bioanalytical Chemistry, v. 400, p. 2699–2720.

Schindelin, J., Arganda-Carreras, I., Frise, E., Kaynig, V., Longair, M., Pietzsch, T., Preibisch, S., Rueden, C., Saalfeld, S., Schmid, B., Tinevez, J.-Y., White, D.J., Hartenstein, V., Eliceiri, K., Tomancak, P., and Cardona, A., 2012, Fiji: an open-source platform for biological-image analysis: Nature Methods, v. 9, p. 676–682.

Schneider, C.A., Rasband, W.S., and Eliceiri, K.W., 2012, NIH Image to ImageJ: 25 years of image analysis: Nature Methods, v. 9, p. 671–675.

Sharpe, J., Ahlgren, U., Perry, P., Hill, B., Ross, A., Hecksher-Sørensen, J., Baldock, R., and Davidson, D., 2002, Optical projection tomography as a tool for 3D microscopy and gene expression studies: Science, v. 296, p. 541–545.

Sheppard, C., and Shotton, D., 1997, Confocal Laser Scanning Microscopy: Oxford, UK, BIOS, 106 p.

Shi, C.S., Schopf, J.W., and Kudryavtsev, A.B., 2013, Characterization of the stem anatomy of the Eocene fern *Dennstaedtiopsis aerenchymata* (Dennstaedtiaceae) by use of confocal laser scanning microscopy: American Journal of Botany, v. 100, p. 1626–1640.

Strullu-Derrien, C., Wawrzyniak, Z., Goral, T., and Kenrick, P., 2015, Fungal colonization of the rooting system of the early land plant *Asteroxylon mackiei* from the 407-Myr-old Rhynie Chert (Scotland, UK): Botanical Journal of the Linnean Society, v. 179, p. 201–213.

Appendix 8: Kamanli, S.A., Kihara, T.C., Ball, A.D., Morritt, D. & Clark, P.F. (2017) A 3D imaging and visualisation workflow, using confocal microscopy and advanced image processing for brachyuran crab larvae. *Journal of Microscopy*. **266**, 307–323.

Journal of Microscopy

Journal of Microscopy, Vol. 266, Issue 3 2017, pp. 307–323 doi: 10.1111/jmi.12540
Received 19 April 2016; accepted 25 January 2017

A 3D imaging and visualization workflow, using confocal microscopy and advanced image processing for brachyuran crab larvae

S.A. KAMANLI*,†,‡, T.C. KIHARA§, A.D. BALL†, D. MORRITT* & P.F. CLARK‡
*School of Biological Sciences, Royal Holloway University of London, Egham, Surrey, UK
†Imaging and Analysis Centre, Core Research Laboratories, The Natural History Museum, London, UK
‡Department of Life Sciences, The Natural History Museum, London, UK
§German Centre for Marine Biodiversity Research, Senckenberg am Meer, Wilhelmshaven, Germany

Key words. Brachyuran crab larvae, confocal laser scanning microscopy, Drishti, ImageJ, visualization, 3D imaging.

Summary

Confocal laser scanning microscopy is an excellent tool for nondestructive imaging of arthropods and can provide detailed information on morphology including fine surface detail. A methodology is presented here for the visualization by confocal microscopy of arthropods, using brachyuran crab zoeal stages as examples and postprocessing techniques derived from micro-CT protocols to improve the final images. This protocol is divided into description of the preprocessing steps (cleaning, staining, digesting and mounting), confocal laser scanning microscopy and data visualization using open-source, freeware programs ImageJ and Drishti. The advantages of using ImageJ to standardize stack data and Drishti for surface rendering are discussed. The methodology has been comprehensively tested using data acquired from all four brands of confocal microscope (Leica, Nikon, Olympus and Zeiss).

Introduction

Confocal laser scanning microscopy (CLSM) offers an excellent option for nondestructive imaging of brachyuran crab larvae and other macro-invertebrates (Butler *et al.*, 2010). The images obtained are comparable in quality to scanning electron microscopy (SEM) at the same magnifications, and the technique offers a 3D data set. In addition, the sample preparation routine for CLSM is simpler than that for SEM. Applying SEM protocols to individual larval appendages (which may be only a few hundred microns in length and tens of microns in diameter) can be difficult (Wolf, 2010) and often results in them being damaged (Michels, 2007) or even lost during the preparation steps due to the fact that they are so small. Finding a suitable SEM dehydration protocol that does not result in distortion of the cuticle, particularly in larval specimens, has proven to be extremely challenging (Wolf, 2010), whereas samples are examined in a hydrated state for CLSM. This allows the appendages to be manipulated within the mounting medium to offer views of the specimen from multiple angles, which can be problematical to achieve using SEM since some viewpoints may be inaccessible due to the way that the specimen is mounted and the tilt limitations in the SEM (e.g. Fig. 1A). Since CLSM is an optical technique, the transparency of the sample allows the origins of spines/setae and internal anatomy (musculature, digestive or nervous system) to be viewed/recorded and specimens held in historical slide collections to be examined/compared with recently collected material. CLSM illustrations can include much finer details than the traditional line drawings (e.g. Figs. 1B, C) for morphological descriptions, which are incredibly time consuming (Coleman, 2006) and figuring dense concentrations of setae can be challenging. Furthermore, CSLM samples can be recovered after imaging and used for DNA extractions.

Previous studies have described a number of different techniques for applying CLSM to macro-invertebrates including the use of a variety of stains, mounting media and cleaning protocols (Table 1). However, one issue with CLSM visualization is that the software is optimized for generating images of transparent, fluorescent volumes rather than for rendering and lighting surfaces. Commercial software capable of producing this type of visualization tends to be expensive. Workflows can be developed to allow the use of the open-source freeware program 'Drishti' (http://sf.anu.edu.au/Vizlab/drishti/; Limaye, 2012) to visualize CLSM data (e.g. Fig. 1D).

Correspondence to: Seyit Ali Kamanli, Department of Life Sciences, The Natural History Museum, Cromwell Road, London SW7 5BD, UK. Tel: +44 (0) 2079425564; fax: +44 (0) 2079425054; e-mail: Seyit.Kamanli.2013@live.rhul.ac.uk

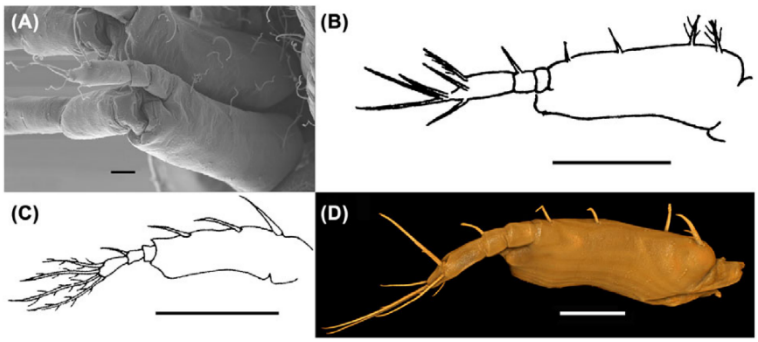

Fig. 1. *Eriocheir sinensis*, zoea I, second maxilliped. A comparison of (A) SEM image obtained using Zeiss Ultra Plus Field Emission; (B) line drawing from Kim & Hwang (1995); (C) line drawing from Montu *et al.* (1996); (D) Drishti image obtained using Nikon A1-Si CLSM. Scale bars: (A) = 20 μm; (B)–(D) = 100 μm. SEM, scanning electron microscopy. CLSM, confocal laser scanning microscopy.

The purpose of this study is to demonstrate a workflow for the 3D imaging of arthropods using CLSM and visualization using a combination of ImageJ and Drishti to process the resulting data. The first stage of the workflow, as detailed in the preprocessing section of this paper, is the application of improved cleaning, staining, digestion and mounting protocols to the specimen prior to scanning. The second stage is scanning of the specimens using a Nikon A1-Si confocal microscope. The third stage is a specific method for processing the resulting image stacks using the open source software programmes ImageJ and finally apply Drishti for 3D visualization. The data presented here were obtained using a Nikon CLSM, however, the third stage of the workflow was also tested using comparable data sets obtained using confocal microscopes from Leica, Olympus and Zeiss. A common workflow for preparing data from different brands of confocal microscope for 3D visualization has been created using ImageJ (http://imagej.nih.gov/ij/; Schneider *et al.*, 2012) and the results were found to be consistent across all instruments tested. This method is detailed in the postprocessing (3D modelling) section of this paper.

Material and methods

Source of larvae

Eriocheir sinensis H. Milne Edwards, 1853; ovigerous female; Tilbury, River Thames, England; collected by Roni Robbins, 16 March 1999; hatched 14–16 April 1999; Natural History Museum, London (NHM) registration number 2002.791.

Sesarma curacaoense De Man, 1892; ovigerous female; coastal mangrove swamp near Mangrove Point, Trelawny, northern Jamaica; collected March 1993 (see Anger *et al.*, 1995).

Armases miersii (Rathbun, 1897); ovigerous female; Devil's Cook Room, Trelawny, Jamaica; collected Schuh & Diesel, March–July 1996 (see Cuesta *et al.*, 1999).

Larvae

Preprocessing

Protocol. A number of protocols were applied to the larval specimens during the preparation of the slides, namely cleaning, staining, protein digestion and mounting. Specimens were scanned using a Nikon A1-Si confocal microscope (Nikon Corporation, Tokyo, Japan) fitted to a Nikon Eclipse upright microscope. Generation of the 3D images was conducted using the open source software program Drishti (version 2.6.1; Limaye, 2012). Other brands of confocal microscopes including the Olympus Fluoview FV1000 IX81 inverted microscope (Olympus Corporation, Tokyo, Japan), Zeiss LSM 880 airy scan upright confocal microscope (Carl Zeiss, Jena, Germany) and Leica TCS SP5 (Leica Microsystems, Wetzlar, Germany) equipped with a Leica DM5000 B (upright microscope) were also tested using a protocol with the aim of finding a consistent workflow. In order to apply the same instructions to the different types of confocal image data, ImageJ was used before the application of Drishti (Fig. 2).

Cleaning. For this study, laboratory hatched larval (zoeal) stages of the Chinese mitten crab (*E. sinensis*), previously fixed in 70% ethanol and deposited in the crustacean collections of the NHM, were scanned using CLSM. Numerous zoeae were contaminated with deposits that had adhered to the exoskeleton. The specimens were cleaned (see Sewell & Cannon, 1995; McAllen & Taylor, 2001) using Decon 90 (Decon Ltd., Sussex, England). Two or three drops of Decon 90 were added to 100 mL of 70% ethanol and specimens were left in this solution for 3–4 h. This solution was gently agitated occasionally by hand during the cleaning process. The sonication methodology as proposed by Felgenhauer (1987) and the use of a tumbler were also trialled. After cleaning, the specimens were pipetted into deionized water for 5 min and washed thoroughly including three changes of 5 min each. The chemistry of the

Table 1. List of reviewed papers that used CLSM in the study of macro-invertebrates with information on studied material, stain, mounting medium, confocal microscope, visualisation and performance observed.

References	Species	Stain	Mounting medium	CLSM	Visualisation[a]	Performance
Bundy and Paffenhöfer (1993)	*Labidocera aestiva*l, *Eucalanus pileatus*, *Centropages velificatus* (Copepoda)	DiI (Dioctadecyl-tetramethylindocarbocyanine perchlorate)	Seawater	Biorad MRC600	VoxelView	Optical cross-sections of the specimens can be animated and rotated in 3D.
Galassi *et al.* (1998)	*Moraria poppei*, *Parastenocaris vicesimal* (Copepoda)	Autofluorescence	Polyvinyl lactophenol	Sarastro 2000	Maximum intensity projection (MIP)	CLSM provides better understanding of 3D structure of copepods.
Carotenuto (1999)	*Temora stylifera* (Copepoda)	Autofluorescence	Seawater	Zeiss 410	MIP	A non-destructive and fast method to distinguish transparent copepod stages.
Buttino *et al.* (2003)	*Calanus helgolandicus* (Copepoda, Calanoida) *Hippolyte inermis* (Decapoda)	DiI (Dioctadecyl-tetramethylindocarbocyanine perchlorate)	Seawater	Zeiss 410	Zeiss and Crisel instruments software packages MetaVue	Using bright-field microscopy is time consuming, however. CLSM is an effective method for visualising copepod morphology.
Klaus *et al.* (2003)	*Culex tarsalis*, *Drosophila melanogaster* (Insecta)	Autofluorescence	Euparal, Glycerine jelly	Zeiss 510	MIP, volume rendering and isosurface rendering	MIP images can be ambiguous. Volume rendered models enhance surface features.
Klaus & Schawaroch (2006)	*Drosophila melanogaster*, *Culex tarsalis*, *Cladocheata inversa* (Insecta)	Autofluorescence	Euparal, Glycerine jelly	Zeiss 510	Zeiss LSM image browser for MIP and Imaris	Using spacer between coverslips protects 3D structure of the specimens. MIP images are good, but Imaris provides more satisfactory visualisation.
Michels (2007)	*Acanthocyclops mirnyi*, *Heterorhabdus* sp., *Alteutha potter* (Copepoda)	Autofluorescence	Euparal, Glycerine jelly	Leica TCS SP5	Amira 3D software	Euparal produces red autofluorescence at excitation wavelength of 488nm or less. Glycerine jelly is a favourable embedding medium to visualise tiny structures of crustaceans.
Schawaroch & Li (2007)	*Drosophila melanogaster* (Insecta)	Autofluorescence	Glycerine jelly (mixture of mountants)	Zeiss 510	Zeiss LSM image browser for MIP and Imaris	Using agarose with glycerine jelly decreases background noise. Using 3D image re-construction removes low level of background noise.
Valdecasas (2008)	Water mites; *Vagabundia sci* (Axonopsinae (Acari,Parasitengona, Hydrachnidia)	Autofluorescence	Glycerine jelly	Leica TCS SP2	ImageJ	CLSM provides more efficient results than bright field microscope results.
Lee *et al.* (2009)	*Carpatolechtia* (Insecta)	Autofluorescence, Mercurochrome, Safranine, Chlorazol black E, Eosin Y, Eosin Y + Chlorazol black E, Orange G	Euparal	Zeiss LSM 510	MIP	Autofluorescence level of chitin was low. The best results were obtained using eosin Y, safranine and mercurochrome respectively. Poor images were obtained using orange-G and eosin Y + chlorazol black E.
Maruzzo *et al.* (2009)	*Artemia* (Crustacea, Branchiopoda, Anostraca)	Evans Blue	Glycerol	Nikon Eclipse E600	MIP	Specimens digested in KOH and stained with Evans Blue provided better results.
Butler *et al.* (2010)	*Ballomena gracilipes* (Chilopoda)	Autofluorescence	Canada balsam	Leica TCS SP1	MIP	Non-destructive imaging for historical museum material. Resolution is comparable to SEM. Canada balsam makes specimens more fluorescent for CLSM visualisation.

(*Continued*)

Table 1. Continued.

References	Species	Stain	Mounting medium	CLSM	Visualisation[a]	Performance
Michels & Büntzow (2010)	Small crustaceans and polychaetes	Autofluorescence, Congo red	Glycerine	Leica TCS SP5	Leica LAS software for MIPs	Congo red stains exoskeleton effectively, but internal tissues and proteins were not stained so successfully.
Böhm *et al.* (2011)	*Ionescuellum carpaticum* (Protura, Entognatha Artrophoda)	Autofluorescence, Congo red	Polyvinyl lactophenol (unstained), Euparal (Congo red)	Leica TCS SP 2	MIP, Fiji, OsiriX	Congo red fades in polyvinyl lactophenol, any mountant such as Euparal can be used so long as it is not strongly autofluorescent. Autofluorescence of unsclerotised cuticle is low. Stained regions with Congo red was effective.
Menzel (2011)	*Mesocletodes elmari* sp. (Copepoda, Harpacticoida, Argestidae)	Congo red	Glycerol	Leica TCS SP5	MIP	Successful visualisation.
Valdecasas & Abad (2011)	Aquatic mites (Acari, Hydrachnidia)	Autofluorescence	Glycerine jelly	Leica SPE	ImageJ to obtain MIPs, Gamma correction with Photoshop CS3	Using proteinase K does not affect the external morphology of mites.
Brooker *et al.* (2012a)	*Lernaeocera branchialis* (Copepoda)	Blankophor, Gomori's trichrome	Distilled water	Leica TCS SP2	Leica Confocal Software (MIP), Photoshop CS3	Successful visualisation.
Brooker *et al.* (2012b)	*Lernaeocera branchialis* (Copepoda)	Blankophor, Gomori's trichrome	Distilled water	Leica TCS SP2	LCSM composite images in Photoshop CS3	Using 3D CLSM stack data to draw specimens digitally provides accurate data.
Kihara & Martínez Arbizu (2012)	*Cervinella danae*, sp. nov., *Cervinella arctica* sp. nov., *Cervinella hitoshi* sp. nov. (Copepoda, Harpacticoida)	Congo red	Glycerine	Leica TCS SP5	LAS AF 2.2.1. for MIPs and CLSM illustrations, Adobe Photoshop CS4	For the taxonomic study of new species, CLSM is used to visualise the details of the appendages of the specimens.
Michels & Gorb (2012)	*Locustamigratoria*, *Sympetrum striolatum*, *Eristalis tenax* and so on (Insecta) *Temora longicornis* (Copepoda)	Autofluorescence, Congo red	Glycerine	Zeiss LSM 700	ZEN software	CLSM is a good tool to visualise resilin in arthropods. It is also effective to detect the differences in the material composition.
Michels *et al.* (2012)	*Centropages hamatus* (Copepoda)	Congo red, Fluorescein isothiocyanate	Glycerine	Zeiss LSM 700	Nikon Capture NX 2, Adobe Photoshop CS4	Successful visualisation.
Brandt *et al.* (2014)	*Atlantoserolis vemae* (Isopoda: Serolidae)	Congo red and acid fuchsin	Glycerine	Leica TCS SPV	LAS AF 2.2.1. for MIPs and CLSM illustrations, Adobe Photoshop CS4	Stained whole specimen and the dissected parts (e.g. mouthparts and legs) were visualised using CLSM.
Kaji *et al.* (2014)	Clam shrimp (Crustacea, Branchiopoda)	Rhodamine, Phalloidin	Vectashield	Leica TCS SP5 II	Imaris	The cuticle surface is smooth and fine setae are present using Imaris.
Dreszer *et al.* (2015)	*Cyphophthalmus solentiensis* sp. nov. (Arachnida)	Autofluorescence	Glycerine	Zeiss Elyra	Carl Zeiss Zen software	Successful visualisation by taking advantage of the autofluorescence of the arthropod cuticle.
Wilkommen *et al.* (2015)	*Ischnura elegans* (Insecta)	Autofluorescence	Glycerine	Zeiss LSM 700	ZEN 2009 for MIPs	Successful visualisation.

[a]Some of the papers did not provide detailed information on visualization. SEM, scanning electron microscopy; CLSM, confocal laser scanning microscopy.

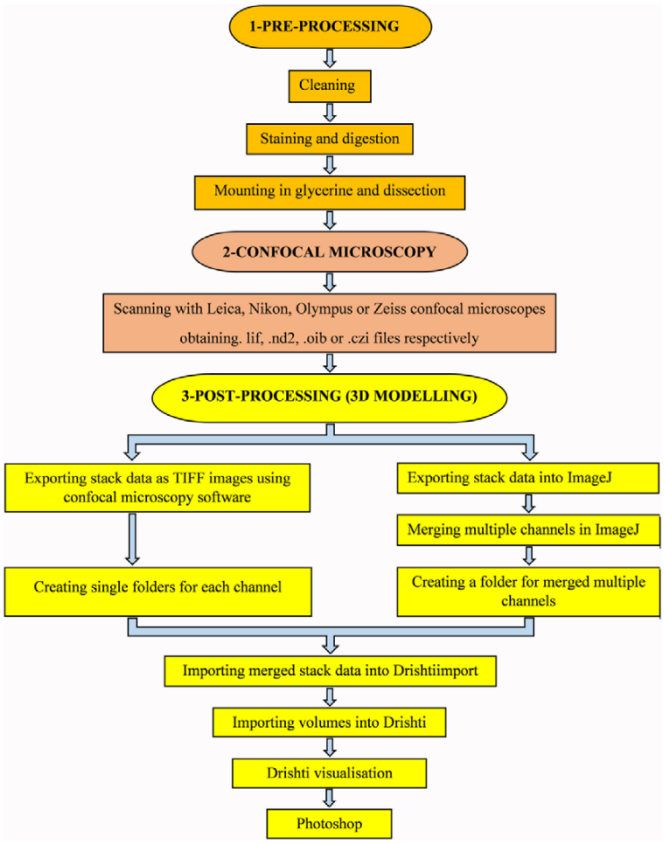

Fig. 2. A flowchart for visualization and 3D imaging of brachyuran crab larvae.

deposits was also investigated using X-ray spectroscopy using an LEO 1455VP SEM (Carl Zeiss, Jena, Germany) fitted with an Oxford Instruments X-Max 80 EDX (Oxford Instruments, Oxford, England) detector (see Supporting Information 1; SEM preparation). The SEM was operated in variable pressure mode (15 Pa chamber pressure) at 20 kV and the samples examined qualitatively in spot mode using internal standards.

Staining and digestion. The larvae were stained using a 1:1 mixture of Congo red (Fisher Scientific Ltd., Loughborough, England) and acid fuchsin (Sigma-Aldrich Co. Ltd., Irvine, England). These stains were available in powder form and each made into a stock solution by dissolving 0.5 mg of stain in 100 mL of deionized water. Stock solutions were filtered (Filtropur 0.2 μm) to remove unwanted particles. The stains were stored in a cupboard at room temperature (ca. 20°C) in dark glass vials and covered with aluminium foil to protect them from the light, which causes bleaching. Before staining the specimens, Congo red and acid fuchsin stock solutions were mixed 1:1 in a glass dish using separate plastic pipettes for each stain. Using mounted needles, the larvae were carefully lifted into the mixed stain, covered with a glass lid to prevent evaporation and left in a covered box for 24 h at room temperature. The larvae were next transferred into a solution of sodium dodecyl sulfate SDS [5.2 g (0.18M) SDS and 0.24 g (0.03M) NH_4HCO_3 (ammonium hydrogen carbonate) in 100 mL deionized water] + DTT (0.1 g 1, 4 dithio-DL-threitol in 5 mL stock solution of SDS) to be digested (see Supporting Information 2; Preparation of SDS + DTT solution; Fischer & Ahlrichs, 2011). A few drops of the SDS + DTT solution (depending of the size and number of specimens) were dropped into a cavity slide. The stained specimen was placed into the solution and left until the muscles within the larvae were digested. For zoea I (ZI) larvae (Fig. 3A), this was achieved in 75 min. As the size increased in subsequent zoeal stages (ZII–ZVI), the duration of immersion

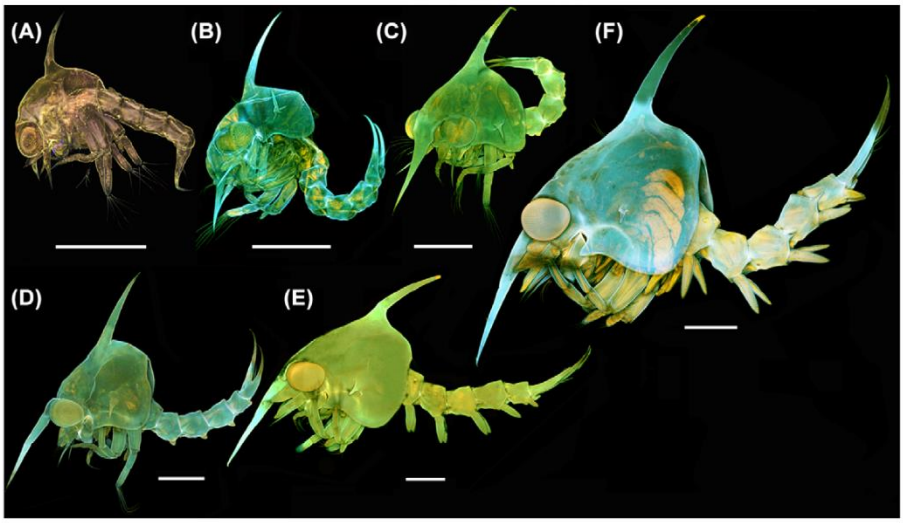

Fig. 3. *Eriocheir sinensis* zoeal stages using Nikon A1-Si CLSM. Confocal images. (A) ZI, 10× dry objective. (B) ZII, 10× dry objective applying 'large images' option, scan area of 2 × 1 fields for image stitching. (C) ZIII, 10× dry objective applying 'large images' option, scan area of 2 × 2 fields for image stitching. (D) ZIV, 10× dry objective applying 'large images' option, scan area of 3 × 2 fields for image stitching. (E) ZV, 10× dry objective applying 'large images' option, scan area of 4 × 3 fields for image stitching. (F) ZVI, 10× dry objective applying 'large images' option, scan area of 4 × 4 fields for image stitching. Scale bars = 500 μm. CLSM, confocal laser scanning microscopy.

Fig. 4. Preparation of slide using reinforcement rings.

in the SDS + DTT solution was increased depending on the stage of development, for example, ZII (Fig. 3B) = 2–3 h, ZIII (Fig. 3C) = 4–5 h, ZIV (Fig. 3D) = 6–8 h, ZV (Fig. 3E) = 10 h, ZVI (Fig. 3F) = more than 10 h. When digestion was complete, the larvae were rinsed three times in deionized water (each rinse lasting 5 min). Digested specimens were then transferred back into the mixture of Congo red and acid fuchsin where they remained for a further 24 h in a box, at room temperature, for a final staining.

Mounting in glycerine and specimen dissection. The use of a suitable mounting medium was essential in order to deliver optimum images using CLSM and for 3D re-construction purposes. The larvae (ZI and ZII) were removed from the stain and transferred into a solution of 10% glycerine and 90% deionized water. This solution avoided shrinkage problems when transferring the larvae from the stain to glycerine for dissection, but this solution concentration was varied according to the stage and size of the larvae, for example, 25% glycerine and 75% deionized water was used for ZIII and ZIV, and 50% glycerine and 50% deionized water was used for ZV and ZVI. Before dissection, glass slides were prepared using self-adhesive reinforcement rings (Fig. 4) glued to the surface as described by Kihara & Falavigna da Rocha (2009). Reinforcement rings raised the cover slip above the slide and allowed more space for the dissected appendages to lie naturally in the cavity without

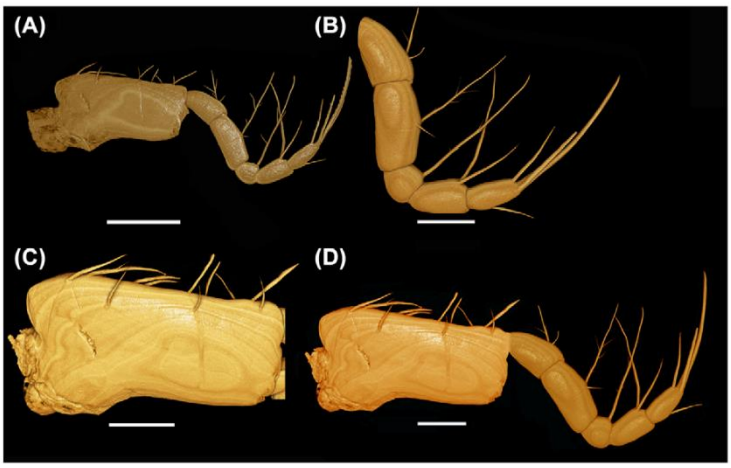

Fig. 5. *Eriocheir sinensis*, zoea II, Drishti images of first maxilliped using Nikon A1-Si CLSM. (A) Basis and endopod, scan area of 1 × 2 fields for image stitching, 20× dry immersion objective applying 'large images' option. (B) Endopod. (C) Basis. Both using 40× oil immersion objective. (D) Basis and endopod merged from two images using Adobe Photoshop, after applying ImageJ and Drishti. Scale bars: (A) = 300 μm; (B)–(D) = 100 μm. CLSM, confocal laser scanning microscopy.

being crushed and flattened. Two to three droplets of glycerine solution were pipetted into the cavity formed by the reinforced rings.

The larvae were dissected under a Leica MZ 16 stereomicroscope (Leica Microsystems, Wetzlar, Germany) using tungsten wire needles (Clark & Cuesta, 2015). After dissection, the appendages were individually transferred into the prepared cavities of the glass slides. This ensured that the slide had a clean, debris-free background for confocal microscopy. For the pleon and larger appendages, the number of self-adhesive reinforcement rings used was increased (Michels & Büntzow, 2010). After the appendages had been placed into the cavities, they were carefully covered using 0.17-mm-thick cover slip. After dissection and mounting, slides were kept in a dark area at room temperature prior to scanning as Congo red and acid fuchsin are affected by light.

Confocal laser scanning microscopy

The larval appendages were scanned using a Nikon A1-Si confocal microscope. Four lasers were available, 405 nm, 488 nm, 561 nm and 640 nm. Although an excitation wavelength of 561 nm was recommended by Michels & Büntzow (2010) to match the optimal fluorescence of Congo red, a wavelength of 640 nm also proved effective. During scanning, all available wavelengths were used so that no data were missed. For each preparation, the most appropriate objectives were chosen to match the size of the appendages.

For larger appendages, such as the pleon, a 20× dry objective with a numerical aperture (N.A.) of 0.75 was used to obtain a general image before scanning at a higher magnification. Oil immersion objectives were used to increase resolving power of the microscope for scanning at 40× with N.A. of 1.30 and 60× with N.A. of 1.4 to produce higher resolution images of smaller larval appendages. Detector gain and amplitude offset were manually adjusted to deliver a black background. Setules (fine structures with a relatively low signal level) of the appendages, proved challenging to scan. To specifically visualize the setules, the offset was increased in order to make them apparent; this would also apply to any similar fine arthropod feature (fine setae, scales, etc.). For image setting, the Z-intensity correction function was used to avoid oversaturating images. This function provided an opportunity to make colour adjustments between oversaturated or under saturated layers. Optimization of the number of Z-frames scanned was also required. 3D reconstruction required more Z-frames than 2D images, so the number of frames needed to be selected to match the final use case. Acquisition times were manually adjusted to deliver an acceptable background noise level and slides were typically scanned with 2× frame averaging. The format of all images is 1024 × 1024 pixels and these were viewed using maximum intensity projections as 2D image stacks.

Two options can be applied to scan large appendages at higher magnification using CLSM. The first method uses the 'large images' software option of the microscope and scans the sample in discrete areas known as tiles. The large images software option automatically stiches the tile together (Fig. 5A). Scanning duration, however, increases when applying this method and the resulting data sets can be extremely large. Manipulating such data sets may present problems

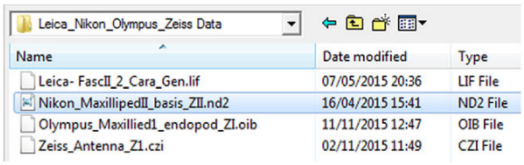

Fig. 6. File formats of different confocal microscopes. Leica uses ***.lif files. Nikon uses ***.nd2 files. Olympus uses ***.oib files. Zeiss uses ***.czi files.

during postprocessing unless a powerful computer is made accessible. A second option is to scan the sample in sections (i.e. basis and endopod separately; Figs. 5B, C) and then, after applying ImageJ and Drishti, merge these using Photoshop (Fig. 5D).

Nikon confocal microscopes store the data stacks as ***.nd2 file; Leica as ***.lif; ***.oib files for Olympus and ***.czi files for Zeiss (Fig. 6). Each manufacturer provides its own software package to visualize the image and to create maximum intensity projections. FV 10−ASW 4.2 software was developed by Olympus; ZEN lite imaging software for Zeiss; LAS AF 2.2.1 software is used by Leica and NIS elements viewer (version 4.20) by Nikon.

Postprocessing using ImageJ and Drishtiimport

The first method for importing image stacks into Drishtiimport involves the use of ImageJ. Instead of using the confocal manufacturer software packages, the image stacks are opened directly in ImageJ which splits the stack data into channels which can be viewed independently. At this point, the image properties (voxel size) should be noted in order to produce a scale bar later in Drishti. Any channels considered to be of insufficient quality can be ignored and the remaining channels merged. The advantage of using ImageJ is that merged channels can be converted to 8-bit composite images creating one common workflow for data from any brands of confocal microscope. The merged images can then be exported into Drishtiimport. Multichannel data can be easily manipulated by Drishti and produce images of much greater quality (see Supporting Information 3 & 4; Exporting stack data into ImageJ and Importing stack data into Drishtiimport, respectively).

As an alternative method, the stack data files can be exported as TIFF images by separating the chosen excitation wave lengths (channels) using the software packages provided by the manufacturers to deliver a single image stack for each channel. Typically, only a single channel was selected for 3D modelling (Bourke, 2011). For this application, the orange channel (561 nm) provided the optimal fluorescence signal for Congo red and acid fuchsin stains. All stack images in one channel were then selected and transferred to a new folder (e.g. 'Orange channel'). Image properties (voxel size) were noted for later reference in order to produce a scale bar in Drishti.

Whichever workflow was chosen, the new folder was then imported into Drishtiimport which standardizes the data and creates a ***.pvl.nc file called 'volumes.pvl.nc' (see Supporting Information 4; Importing stack data into Drishtiimport). The user has the option to individually import all the channels into Drishtiimport to be saved as volumes. Although Drishti does provide an option to load more than one volume, the size of the files can be extremely large and may prevent the program from operating. Furthermore, any resulting images tended to be over saturated.

Visualization of data using Drishti (3D Visualization)

After opening Drishti (Lovett, 2013), the volume files (***.pvl.nc) created in Drishtiimport were imported, processed and visualized in three dimensions. The processing capabilities of Drishti were used as follows. Before visualizing the volumes in high resolution in three dimensions, the images were cropped to fit the scanned image or area of interest on the appendages. Adjusting the lighting option helped to visualize the setae on the appendages. Adding a scale bar and increasing the image quality was possible using the program. As well as visualizing the surface characters on the appendages in detail, Drishti allowed the 3D specimen data set to be reoriented and more than one snapshot of the same appendage to be taken from different angles. Consequently, the exact number of setae and other details could be accurately determined. One of the most helpful options of the program was the ability to edit pictures by removing debris or unwanted tissues on the images in three dimensions. Opening the 'command help' box gave a number of different options for processing the volumes, for example, making videos. The images can be adjusted and improved (see Supporting Information 5; Drishti visualization instructions). Final images were adjusted in Adobe Photoshop. Adjustments included modifying the brightness and contrast, changing the image and canvas size, improving the quality and consistency of the Drishti scale bars, standardizing the background, deleting any remaining debris and saving as a final image for publication.

'Digital dissection'. This may also be referred to as 'data cleansing' and/or 'segmentation'. Unprocessed CLSM data sets frequently contained fragments of dissected debris and additional tissue which appeared to 'float' in the 3D volume or which were attached to appendages. This unwanted data can be removed (cleaned) using Adobe Photoshop, but this option only affects the final 2D viewpoint of the 3D volume. Such editing may pose ethical issues with regard to alteration of the image since areas 'behind' the fragment would also be removed and need to be 'cloned' back into the image. A much better option was to remove the unwanted scanned fragments directly from the 3D volume using Drishti by rotating the specimen. From examination of the rotated specimen, the viewer can determine whether the fragment was a part

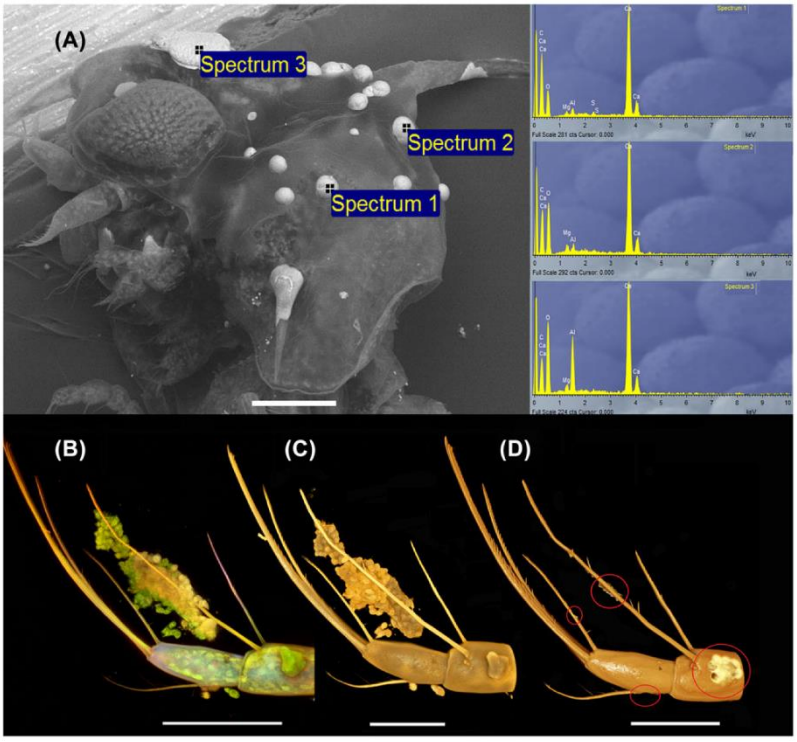

Fig. 7. *Eriocheir sinensis*, zoeae with debris adhered to the exoskeleton. (A) ZI showing calcium carbonate using SEM LEO 1455 VP analysis. (B) ZII, confocal image of endopod using Nikon A1-Si CLSM, 60× oil immersion objective. (C) ZII, Drishti image of endopod. (D) ZII, attempt at debris removal using Drishti and Photoshop was not always successful, see circled areas. Scale bars: (A) = 300 μm; (B)–(D) = 100 μm. CLSM, confocal laser scanning microscopy.

of the specimen. If not, it can be removed to allow for an improved visualization of the specimen. Three-dimensional volume manipulation, therefore, allowed for the specimen to be digitally dissected in postprocessing and this was considered to be a much more powerful technique than simple 2D image manipulation (see Supporting Information 6; Segmentation instructions). After the 3D manipulation process, a 2D image was saved and edited in Photoshop.

Results and discussion

Cleaning and digesting

Cleaning the specimens with Decon 90 proved to be an effective method of removing debris that had adhered to the exoskeleton (compare Figs. 3 with 7A). The sonication methodology proposed by Felgenhauer (1987) for cleaning aquatic arthropods, proved ineffective as it often resulted in the natatory setae of the maxillipeds of the zoeae becoming tangled. A similar problem was encountered when using a tumbler.

The results of the SEM-EDX analysis showed that debris found on limbs was composed of calcium carbonate (see Fig. 7A). These items of debris were effectively removed using the surface-active cleaning agent, Decon 90.

Digesting the muscle within specimens using a mixture of SDS + DTT (Fischer & Ahlrichs, 2011) was an effective method of clearing the appendages, making them more transparent and fluorescent for CLSM imaging. This clearing of internal tissue also helped the visualization of setae that were otherwise masked behind the muscles on the distal side of the appendage. Furthermore, dissection of zoeae became much easier after the specimen had been placed in the digesting solution. Another advantage of using the digestion mixture was to balance the acquisition settings of the microscope to avoid having over/under saturated images. As the setae provided a weaker signal than the main part of the exoskeleton, the settings of the channels needed to be increased to visualize these smaller structures. If the settings were increased, however, the main exoskeleton had a tendency to become oversaturated because it yielded a stronger signal (Fig. 8A). This problem was

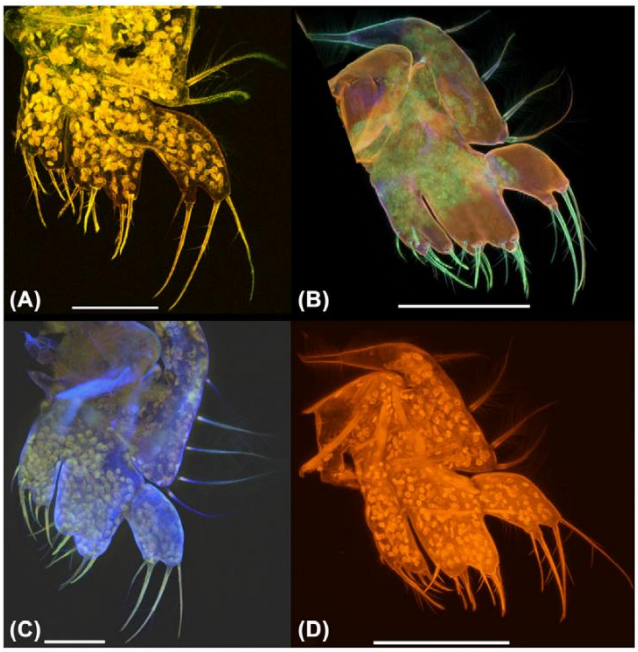

Fig. 8. Advantages of staining and digesting appendages. *Eriocheir sinensis*, zoea I, scanned images of the maxilla using Nikon A1-Si CLSM. (A) Undigested and unstained, 60× oil immersion objective. (B) Digested and stained with Congo red and acid fuchsin, 40× oil immersion objective. (C) Undigested and stained using only Congo red, 60× oil immersion objective. (D) Undigested and stained using the mixture of Congo red and acid fuchsin, 40× oil immersion objectives. Scale bars: (A) and (C) = 50 μm; (B) and (D) = 100 μm. CLSM, confocal laser scanning microscopy.

resolved by digestion since its relative signal strength was reduced compared to that of the setae (Fig. 8B).

If the appendage was not digested, however, some of the minute exoskeletal structures were 'masked' (Fig. 9A) by the signal from basial musculature of the second maxilliped and did not appear when ImageJ and Drishti was applied to the confocal stack data (Fig. 9B). But after digestion of the basial muscles (Fig. 9C), these tiny structures could be visualized when fully processed (Fig. 9D).

Comparing methods to eliminate oversaturation after staining

Congo red has been a commonly used external stain for crustaceans and polychaetes (Michels & Büntzow, 2010; Michels & Gorb, 2012) prior to CLSM. Although the present study demonstrated good results using Congo red alone for CLSM, some appendages were not completely saturated by the stain (Fig. 8C). This problem of patchy staining was mentioned by Michels & Büntzow (2010) and Böhm *et al.* (2011) who were attempting to stain small crustaceans, the cuticle of polychaetes and the tarsal sensilla of Protura. Michels & Büntzow (2010) clarified that Congo red stained the exoskeleton effectively, but was not so successful for internal tissues and proteins. Böhm *et al.* (2011) attributed this to the embedding medium and compensated for this by changing acquisition settings during CLSM imaging. In order to overcome this problem in the present study, Congo red was mixed with acid fuchsin, which is another effective stain of arthropod exoskeletons. The combination of Congo red and acid fuchsin greatly improved the overall saturation of staining and proved a more effective way to balance the acquisition settings compared to using Congo red alone (Fig. 8D).

In addition, Michels & Büntzow (2010) suggested that after staining, specimens should be washed several times until the Congo red was no longer present prior to dissection. This was not found to be an issue in the present study because the specimens were removed from the stain and placed in a solution of diluted glycerine and then the appendages were dissected. The dissected appendages were then individually transferred to slides containing a fresh solution of dilute glycerine to be scanned; the specimens were, thus, effectively isolated from the Congo red.

Comparison of mounting media

Two types of mounting medium were initially trialled, polyvinyl lactophenol (permanent) and diluted glycerine (non-permanent). Polyvinyl lactophenol was placed on a glass slide,

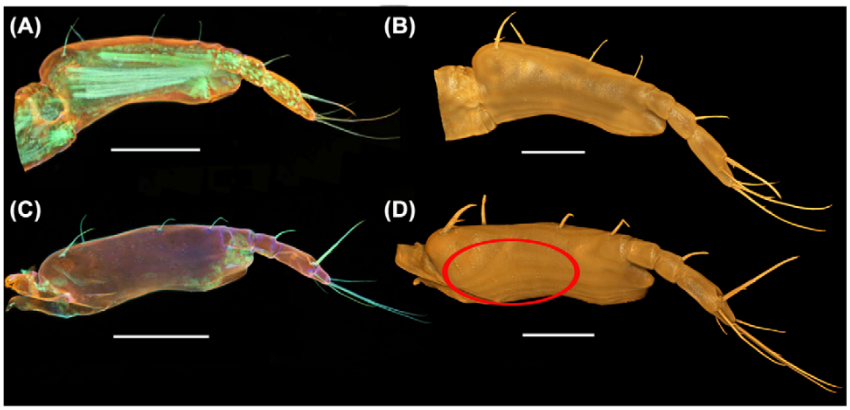

Fig. 9. Advantages of digesting appendages. *Eriocheir sinensis*, zoea I, images of second maxilliped using Nikon A1-Si CLSM. (A) Confocal image of nondigested appendage showing basial musculature. (B) Drishti image of nondigested appendage. (C) Confocal image of digested basial muscles. (D) Drishti image of digested appendage (tiny structures are circled). All 40× oil immersion objective, applying 'large images' option, scan area of 1 × 2 fields for image stitching. Scale bars = 100 μm. CLSM, confocal laser scanning microscopy.

stained larvae were transferred directly into it, dissected and a cover slip applied. Polyvinyl lactophenol proved to be extremely viscous and hard when set, consequently manipulation of the appendages into an improved position for CLSM was almost impossible. An advantage of a hard setting mount was that during scanning, the heat caused by the laser did not change the position of the specimen. It was not possible, however, to reposition the specimen or to use it for DNA extractions after scanning. In addition, during dissection, much debris was produced and these fragments adhered to the appendages (Figs. 7B, C) causing background noise. Furthermore, removing the debris from the appendage or background using Drishti or Photoshop proved extremely time consuming and was not always successful (see circled areas, Fig. 7D). The background noise could be compensated for by increasing averaging times. But this could increase the duration of scanning (scan time doubled with 4 times averaging, tripled with 8 times averaging and quadrupled with 16 times averaging). Consequently, a clean background reduced the duration of scanning and helped to avoid bleaching of the stain. Another issue with polyvinyl lactophenol was it caused immediate shrinkage of the specimens that were transferred to the medium. The mountant could be diluted with alcohol to avoid specimen shrinkage, however, both polyvinyl lactophenol and alcohol, individually and together, did in time bleach the stained specimens.

Glycerine was therefore the preferred mounting medium for CLSM studies. Shrinking specimens placed in diluted glycerine could be recovered with the addition of more deionized water and, furthermore, could be easily manipulated for repositioning. A disadvantage of this medium, especially when diluted, was that it could be heated by the lasers during scanning. There was a tendency for it to liquefy, which caused movement of the specimen. Another problem was the formation of air bubbles. Their expansion during scanning caused the specimen to move and the production of a blurred final image. Air bubbles also tended to form over time and appeared overnight between mounting the specimen and scanning. This was possibly because the initial volume of fluid was insufficient or evaporation had taken place overnight. It was, therefore, better to scan directly after the sample had been mounted. Furthermore, samples could also lose their stain if allowed to remain in glycerine over long periods of time.

Scanning procedures

The use of reinforced rings to create adequate space under the cover slip (Fig. 4) proved to be effective in preventing samples from being crushed and distorted. Once the sample was correctly positioned, the confocal microscope was able to obtain extremely high-quality image data. For larger specimens, it proved necessary to tile the sample (collect data as series of overlapping fields of view in X and Y and also Z; Fig. 10), which led to long acquisition times, with consequent risk of specimen movement. The resulting data files were also exceptionally large and processing these data using Drishti required an extremely powerful computer. This problem was also solved by scanning the appendage in separate sections and merging these at the end of the scanning procedure using Photoshop (Fig. 11), however, this protocol was somewhat time consuming.

For smaller larval appendages, 40× and 60× oil immersion objective lenses were used to produce higher resolution

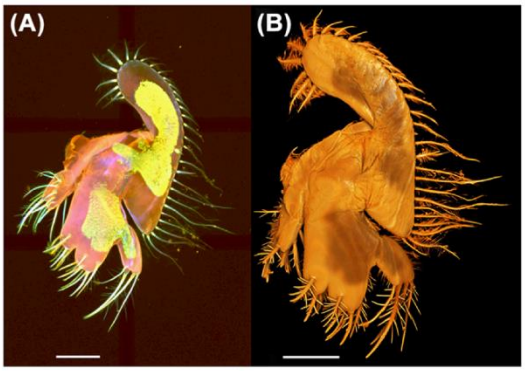

Fig. 10. 'Tiling' appendages when scanning at higher magnification. *Eriocheir sinensis*, zoea V, image of maxilla using Nikon A1-Si CLSM. (A) Confocal image showing tiled areas. (B) Drishti image. 40× oil immersion objective, applying 'large images' option, scan area of 2 × 3 fields for image stitching. Scale bars: (A) = 100 μm; (B) = 200 μm. CLSM, confocal laser scanning microscopy.

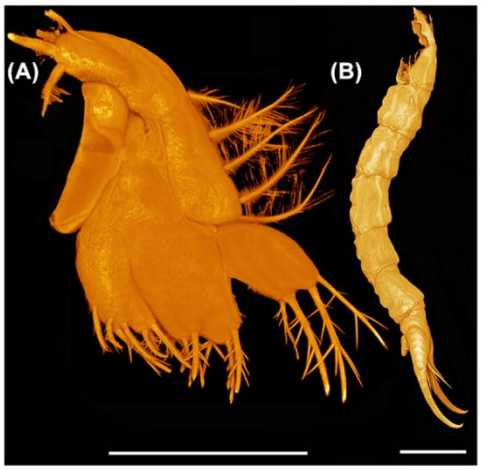

Fig. 11. Merging Drishti images using Adobe Photoshop. *Eriocheir sinensis* zoeal appendages using Nikon A1-Si CLSM. (A) ZII, maxilla, 40× oil immersion objective. (B) ZI, lateral view of pleon, 20× dry immersion objective. Scale bars: (A) = 200 μm; (B) = 300 μm. CLSM, confocal laser scanning microscopy.

images. Using a lower magnification objective lens to obtain a larger field of view was ineffective since the lower magnification lens did not provide adequate resolution to resolve fine setae (e.g. dorsal setae on somite of the pleon are not resolved with lower magnification lenses; Fig. 12). Lower magnification lenses also reduced resolution along the Z-axis and were thus not capable of obtaining sufficiently fine image slices for effective 3D reconstruction in Drishti. The requirement to obtain large numbers of Z slices and for image tiling meant that confocal microscope data acquisition was relatively slow and could take several hours, hence the need to optimize the stability of the sample in the mounting medium.

Fig. 12. Visualization of fine setae. *Eriocheir sinensis*, zoea I. Image of dorsal view of pleon using Nikon A1-Si CLSM, 40× oil immersion objective, applying 'large images' option, scan area of 2 × 6 fields for image stitching. Scale bar = 200 μm. CLSM, confocal laser scanning microscopy.

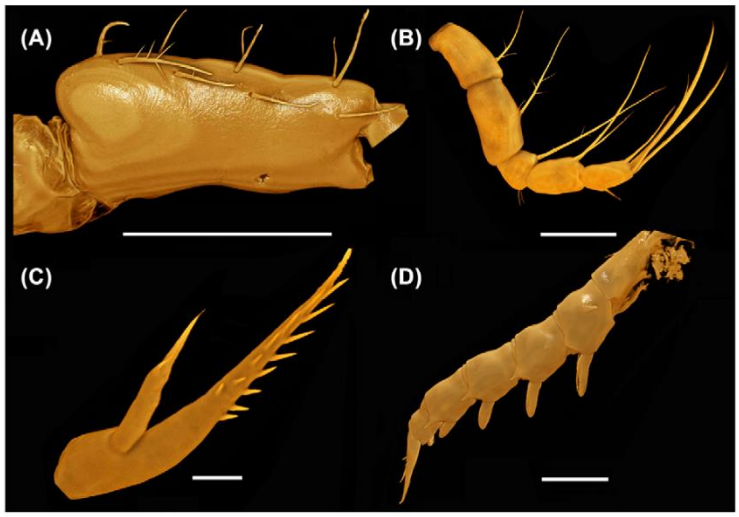

Fig. 13. Scanned brachyuran crab larvae using different brands of CLSM processed in Drishti. *Eriocheir sinensis*, zoea I, first maxilliped. (A) Basis, Nikon A1-Si CLSM. (B) Endopod, Olympus Fluoview FV1000 IX8. (C) Antenna, Zeiss LSM 880 airy scan. All 40× oil immersion objective. (D) *Sesarma curacaoense*, ZIV, lateral view of pleon, Leica TCS SP5, 10× dry objective. Scale bars: (A) and (B) = 100 μm; (C) = 50 μm; (D) = 500 μm. CLSM, confocal laser scanning microscopy.

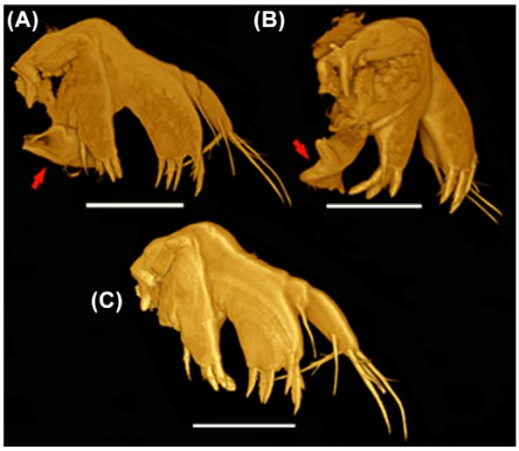

Fig. 14. Digital dissection. *Eriocheir sinensis*, zoea I, image of maxillule using Nikon A1-Si CLSM and processed using Drishti. (A) Unwanted tissue arrowed; (B) repositioning of appendage to allow the removal of unwanted tissue (arrowed); (C) after digital dissection of tissue (compare A with C), 40× oil immersion objective. Scale bars = 100 μm. CLSM, confocal laser scanning microscopy.

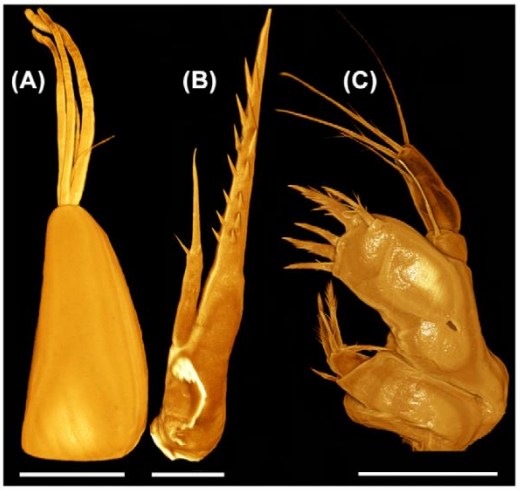

Fig. 15. Drishti images of *Eriocheir sinensis* zoeal appendages using Nikon A1-Si CLSM: (A) ZII, antennule, 40× oil immersion objective; (B) ZI, antenna, 60× oil immersion objective; (C) ZI, maxillule, 40× oil immersion objective. Scale bars: (A) and (C) = 100 μm; (B) = 50 μm. CLSM, confocal laser scanning microscopy.

ImageJ and Drishti

The methodology and data processing workflow (Fig. 2) described here was successfully tested on confocal microscopes manufactured by Olympus, Zeiss, Nikon and Leica. The method for handling the data was the same and the ImageJ and Drishti import process was identical for each file format

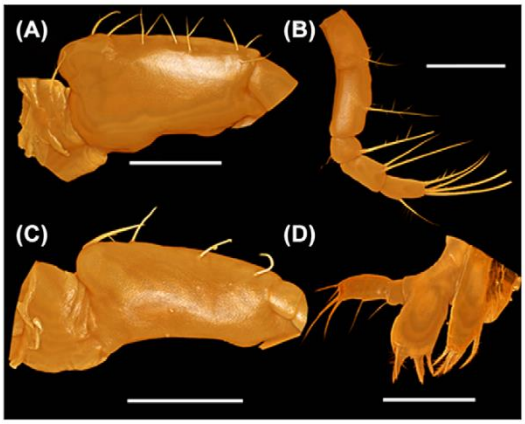

Fig. 16. Drishti images of *Sesarma curacaoense*, zoea I appendages using Leica TCS SP5. First maxilliped. (A) Coxa and basis. (B) Endopod. (C) Coxa and basis of second maxilliped. (D) Maxillule. All 40× oil immersion objective. Scale bars: (A) and (B) = 50 μm; (C) and (D) = 100 μm.

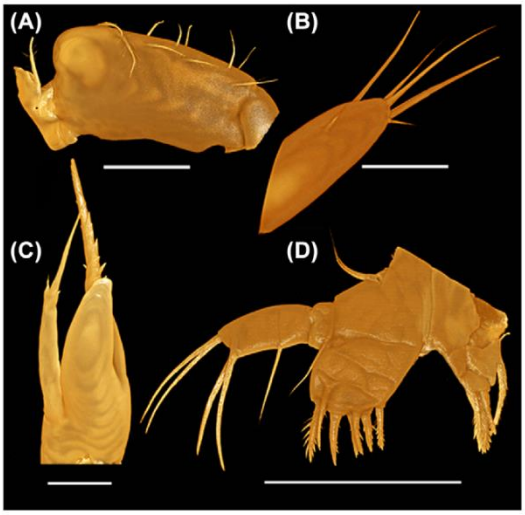

Fig. 17. Drishti images of *Armases miersii*, zoea IV appendages using Leica TCS SP5. (A) Coxa and basis of first maxilliped. (B) Endopod of second maxilliped. Both using 40× oil immersion objective. (C) Antenna. (D) Maxillule. Both using 20× dry objective. Scale bars: (A) and (D) = 200 μm; (B) and (C) = 100 μm.

(Fig. 13). The final quality of merged channels images combining ImageJ and Drishti appeared to be an improvement compared to importing a single channel into Drishti (using the manufacturers' own programs to extract each channel). Merged channel images provided more information, especially with regard to the visualization of setae. Drishti provided an added advantage in being able to reconstruct stack data and manipulation of images.

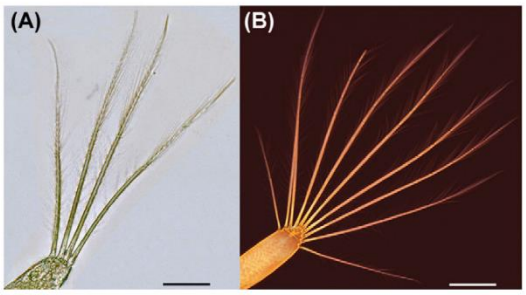

Fig. 18. Comparing bright field and confocal images. *Eriocheir sinensis* zoea, images of second maxilliped using Nikon A1-Si CLSM. (A) ZI, bright field image of exopod, 20× dry objective. (B) ZIV, confocal image of exopod, 20× dry objective applying 'large images' option, scan area of 1 × 2 fields for image stitching. Scale bars: (A) = 50 μm; (B) = 100 μm. CLSM, confocal laser scanning microscopy.

Once 3D data sets had been acquired, Drishti proved to be a powerful tool in reconstructing the specimen from different viewpoints (Fig. 14) and also offered the advantage of allowing the user to remove parts of the specimen from the foreground to reveal features which would otherwise be obscured (a useful form of digital dissection; Fig. 14C). Various images of brachyuran crab larvae from different species (*E. sinensis*, *S. curacaoense*, *A. miersii*) were scanned using CLSM and processed with ImageJ, Drishti and Photoshop (see Figs. 15–17).

Additionally, Drishti is a freeware software program whereas other comparable surface rendering packages are extremely expensive. The visualization packages produced by Nikon, Leica, Olympus and Zeiss are limited and not cross compatible, whereas ImageJ and Drishti are universal across all brands.

Conclusions

Conventional observation of fine features, as seen in brachyuran larvae, normally relies on light microscopy often using techniques such as DIC (differential interference contrast) or phase contrast (Fig. 18). Furthermore, dissected appendages are challenging to mount as they can move while trying to fix them in an appropriate position. The narrow focal depth of compound microscopes may also make some direct observations difficult, as a result features can be overlooked. Consequently, many line drawings tend to simplify and codify the essential features for diagnostic illustrations. For specimens with complex topography and setation, however, this approach can be subjective and makes comparison difficult (Figs. 1B, C). In addition, traditional 2D photography, even with the addition of focal stacking, may not accurately record

the 3D complexity of limbs and larval appendages or the position of setae. In comparison, high-quality CLSM image data can be further enhanced by the use of Drishti. For example, in previous studies, the number of setae on the basis of the first maxilliped especially in the small early zoea stages, such as ZI and ZII (for correct setation see Figs. 13A and 16A) and the fine second seta on the first and second segments of the first maxilliped endopod were overlooked (for correct setation see Figs. 13B and 16B). In addition, one seta can mask another if it lies along the same image path, but on a different focal plane. The masked setae can be visualized by rotating the appendage using Drishti (see Figs. 9B, D, 17B). Another advantage of Drishti is the application of digital dissection and the removal of unwanted fragments (see Figs. 11A, 14, 15C).

The methodologies described here the combination of improved cleaning, digestion and preparation methods, allowing for reduced transfer of contaminants into the final slide mounts, the confocal data processing protocols and the possibility of postacquisition removal of artefacts using free software have been shown to overcome all the previous limitations in the use of confocal microscopy for the examination of small arthropods. Furthermore, the methodologies described for the use of Drishti to postprocess samples have also been successfully applied to other confocal data sets and even been used for the production of 3D prints from the data.

The main limitation now remains the speed of the confocal microscope and its ability to handle and image larger specimens. 'Macro confocal microscopes' have been assessed, but found to have inadequate resolution for this application. The use of high-resolution micro-CT is currently being investigated as a complementary technique to provide further contextual 3D information on macro-invertebrates.

Acknowledgements

We acknowledge the two anonymous reviewers for their time, considerations and comments which improved this paper. We would like to thank Dr. Tomasz Goral for the support obtaining images from the A1-Si confocal microscope and Dr. Farah Ahmed, Dan Sykes and Rebecca Summerfield for assistance in training on Drishti (all staff in the Imaging and Analysis Centre, Natural History Museum, London). We also like to thank Dr. Anthony J. Hayes and Dr. Peter Watson (Bio imaging Unit, Cardiff School of Biosciences, Cardiff University) for making Zeiss LSM 880 airy scan upright confocal microscope available, Dr. Christopher Wilkinson (School of Biological Science, Royal Holloway University of London) for providing access to the Olympus FV1000 IX81 inverted confocal microscope. This project was supported financially by the Republic of Turkey Ministry of National Education. Terue Kihara acknowledges funding from NHM departmental investment fund to run Confocal Microscopy workshop in February 2015 at the Natural History Museum, London. Part of the project was supported by SYNTHESYS: DE-TAF-4692 for Paul Clark to study with Terue Kihara in the German Centre for Marine Biodiversity Research, Senckenberg am Meer, Wilhelmshaven.

References

Anger, K., Schreiber, D. & Montú, M. (1995) Abbreviated larval development of *Sesarma curacaoense* (Rathbun, 1897) (Decapoda: Grapsidae) reared in the laboratory. *Nauplius*. **3**, 127–154.

Bourke, P. (2011) Transferring slice data to Drishti using ImageJ. Retrieved from http://paulbourke.net/miscellaneous/Drishti_intro1/. Accessed 7 Oct 2016.

Böhm, A., Bartel, D., Szucsich, N.U. & Pass, G. (2011) Confocal imaging of the exo- and endoskeleton of Protura after non-destructive DNA extraction. *Soil Org.* **83**(3), 335–345.

Brandt, A., Brix, S., Held, C. & Kihara, T.C. (2014) Molecular differentiation in sympatry despite morphological stasis: deep-sea *Atlantoserolis* Wägele, 1994 and *Glabroserolis* Menzies, 1962 from the south-west Atlantic (Crustacea: Isopoda: Serolidae). *Zool. J. Linn. Soc.* **172**, 318–359. doi: 10.1111/zoj.12178

Brooker, A.J., Bron, J.E. & Shinn, A.P. (2012a) Description of the free-swimming juvenile stages of *Lernaeocera branchialis* (Pennellidae), using traditional light and confocal microscopy. *Aquat. Biol.* **14**, 153–163. doi: 10.3354/ab00388

Brooker, A.J., Shinn, A.P. & Bron, J.E. (2012b) Use of laser scanning confocal microscopy for morphological taxonomy and the potential for digital type specimens (e-types). *Aquat. Biol.* **14**, 165–173. doi: 10.3354/ab00389

Bundy, M.H. & Paffenhöfer, G.A. (1993) Innervation of copepod antennules investigated using laser scanning confocal microscopy. *Mar. Ecol. Prog. Ser.* **102**, 1–14.

Butler, A.D., Edgecombe, G.D., Ball, A.D. & Giribet, G. (2010) Resolving the phylogenetic position of enigmatic New Guinea and Seychelles Scutigeromorpha (Chilopoda): a molecular and morphological assessment of Ballonemini. *Invertebr. Syst.* **24**, 539–559.

Buttino, I., Ianora, A., Carotenuto, Y., Zupo, V. & Miralto, A. (2003) Use of the confocal laser scanning microscope in studies on the developmental biology of marine crustaceans. *Microsc. Res. Tech.* **60**, 458–464.

Carotenuto, Y. (1999) Morphological analysis of larval stages of *Temora stylifera* (Copepoda, Calanoida) from the Mediterranean Sea. *J. Plankton. Res.* **21**(9), 1632–1632.

Clark, P.F. & Cuesta, J.A. (2015) Larval Systematics of Brachyura. *Decapoda: Brachyura, Treatise on Zoology – Anatomy, Taxonomy, Biology. The Crustacea, Complementary to the volumes translated from the French of the Traité de Zoologie [founded by P.-P. Grassé (†)]*. (ed. by P. Castro, P.J.F. Davie, D. Guinot, F.R. Schram & J.C. Von Vaupel Klein), Chapter 71–17, 9(CII), pp. 981–1048. Brill, Leiden and Boston.

Coleman, C.O. (2006) Substituting time-consuming pencil drawings in arthropod taxonomy using stacks of digital photographs. *Zootaxa*. **1360**, 61–68.

Cuesta, J.A., Schuh, M., Diesel, R. & Schubart, C.D. (1999) Abbreviated development of *Armases miersii* (Grapsidae: Sesarminae), a crab that breeds in supralittoral rock pools. *J. Crust. Biol.* **19**(1), 26–41.

Dreszer, T.B., Raða, T. & Giribet, G. (2015) *Cyphophthalmus solentiensis* sp. nov. (Cyphophthalmi, Sironidae), a new endogean mite harvestman species from Croatia, with an application of confocal laser microscopy to illustrate genitalia in opiliones. *Bull. Mus. Comp. Zool.* **543**, 1–15. doi: http://dx.doi.org/10.3099/MCZ18.1

Felgenhauer, B.E. (1987) Techniques for preparing crustaceans for scanning electron microscopy. *J. Crust. Biol.* **7**, 71–76.

Fischer, C. & Ahlrichs, W.H. (2011) Revisiting the *Cephalodella trophi* types. *Hydrobiologia*. **662**(1), 205–209.

Galassi, D.M.P., Laurentiis, P.D. & Giammatteo, M. (1998) Integumental morphology in copepods: assessment by confocal laser scanning microscopy (CLSM) (Crustacea, Copepoda). *Fragm. Entomol.* **30**(1), 79–92.

Kaji, T., Fritsch, M., Schwentner, M., Olesen, J. & Richter, S. (2014) Male claspers in clam shrimps (Crustacea, Branchiopoda) in the light of evolution: a case study on homology versus analogy. *J. Exp. Zool. (Mol. Dev. Evol.)*. **9999**, 1–12.

Kihara, T.C. & Falavigna da Rocha, C.E. (2009) Técnicas para estudo taxonomico de copepodes harpacticoides da meiofauna marinha. *Asterisco, Porto Alegre*. pp. 96.

Kihara, T.C. & Martinez Arbizu, P. (2012) Three new species of *Cerviniella* Smirnov, 1946 (Copepoda: Harpacticoida) from the Arctic. *Zootaxa*. **3345**, 1–33.

Kim, C.H. & Hwang S.G (1995) The complete larval development of the mitten crab *Eriocheir sinensis* H. Milne Edwards. 1853 (Decapoda, Brachyuran, Grapsidae) reared in the laboratory and a key to the known zoeae of the Varuninae. *Crustaceana*. **68**(7), 793–812.

Klaus, A.V., Kulasekera, V.L. & Schawaroch, V. (2003) Three-dimensional visualisation of insect morphology using confocal laser scanning microscopy. *J. Microsc.* **212**(2), 107–121.

Klaus, A.V. & Schawaroch, V. (2006) Novel methodology utilizing confocal laser scanning microscopy for systematic analysis in arthropods (Insecta). *Integr. Comp. Biol.* **46**(2), 207–214.

Lee, S., Brown, R.L. & Monroe, W. (2009) Use of confocal laser scanning microscopy in systematics of insects with a comparison of fluorescence from different stains. *Syst. Entomol.* **34**, 10–14.

Limaye, A. (2012) Drishti: a volume exploration and presentation tool. In *Proceedings of SPIE Vol. 8506 SPIE, Developments in X-Ray Tomography VIII Bellingham*, Stock, S.R. (ed.), WA. doi: 10.1117/12.935640.

Lovett, B. (2013) The basics of Drishti. *Australian National University Internal Paper*. 1–37. Retrieved from http://www.scribd.com/doc/191007517/The-Basics-of-Drishti-A-Free-To-Download-Volume-Exploration-Presentation-Tool.

Maruzzo, D., Minelli, A. & Fusco, G. (2009) Segmental mismatch in crustacean appendages: the naupliar antennal exopod of *Artemia* (Crustacea, Branchiopoda, Anostraca). *Arthropod. Struct. Dev.* **38**, 163–172.

McAllen, R. & Taylor, A. (2001) The effect of salinity change on the oxygen consumption and swimming activity of the high-shore rockpool copepod *Tigriopus brevicornis*. *J. Exp. Mar. Biol. Ecol.* **263**, 227–240.

Menzel, L. (2011) First descriptions of copepodid stages, sexual dimorphism and intraspecific variability of *Mesocletodes* Sars, 1909 (Copepoda, Harpacticoida, Argestidae), including the description of a new species with broad abyssal distribution. *ZooKeys*. **96**, 39–80. doi: 10.3897/zookeys.96.1496

Michels, J. (2007) Confocal laser scanning microscopy: using cuticular autofluorescence for high resolution morphological imaging in small crustaceans. *J. Microsc.* **227**(1), 1–7.

Michels, J. & Büntzow, M. (2010) Assessment of Congo red as a fluorescence marker for the exoskeleton of small crustaceans and the cuticle of polychaetes. *J. Microsc.* **238**(2), 95–101. doi: 10.1111/j.1365–2818.2009.03360

Michels, J. & Gorb, S.N. (2012) Detailed three-dimensional visualisation of resilin in the exoskeleton of arthropods using confocal laser scanning microscopy. *J. Microsc.* **245**(1), 1–16.

Michels, J., Vogt, J. & Gorb, S.N. (2012) Tools for crushing diatoms: opal teeth in copepods feature a rubber-like bearing composed of resilin. *Sci. Rep.* **2**, 465. doi: 10.1038/srep00465

Montu, M., Anger, K. & de Bakker, C. (1996) Larval development of the Chinese mitten crab *Eriocheir sinensis* H. Milne-Edwards (Decapoda: Grapsidae) reared in the laboratory. *Helgol. Meeresunters.* **50**, 223–252.

Schawaroch, V. & Li, S.C. (2007) Testing mounting media to eliminate background noise in confocal microscope 3-D images of insect genitalia. *Scanning*. **29**(4), 117–184.

Schneider, C.A., Rasband, W.S. & Eliceiri, K.W. (2012) NIH Image to ImageJ: 25 years of image analysis. *Nat. Methods*. **9**(7), 671–675.

Sewell, K.B. & Cannon, L.R.G. (1995) A scanning electron microscope study of *Craspedella* sp. from the branchial chamber of redclaw crayfish, *Cherax quadricarinatus*, from Queensland, Australia. *Hydrobiologia*. **305**, 151–158.

Valdecasas, A.G. (2008) Confocal microscopy applied to water mite taxonomy with the description of a new genus of Axonopsinae (Acari, Parasitengona, Hydrachnidia) from Central America. *Zootaxa*. **1820**, 41–48.

Valdecasas, A.G. & Abad, A. (2011) Morphological confocal microscopy in Arthropods and the enhancement of autofluorescence after proteinase K extraction. *Microsc. Microanal.* **17**, 109–113. doi: 10.1017/S1431927610094213

Wilkommen, J., Michels, J. & Gorb, S.N. (2015) Functional morphology of the male caudal appendages of the damselfly *Ischnura elegans* (Zygoptera: Coenagrionidae). *Arthropod. Struct. Dev.* **44**, 289–300.

Wolf, M. (2010) *The reproductive ecology of a northeastern Pacific nudibranch, Janolus fuscus, with an examination of its endoparasitic copepod, Ismaila belciki*. PhD Dissertation, University of Oregon, Eugene, Oregon. Retrieved from https://scholarsbank.uoregon.edu/xmlui/handle/1794/11057.

Supporting Information

Additional Supporting information may be found in the online version of this article at the publisher's website:

Fig. S1. The menu bar for ImageJ.
Fig. S2. Opening stack data in ImageJ, e.g. Nikon_MaxillipedII_basis_ZII.nd2 has been selected.
Fig. S3. Import options for stack data.
Fig. S4. Record image properties (voxel size) for later use, e.g. x = 0.31, y = 0.31 and z = 0.7 microns.
Fig. S5. Click on ► to check image quality for each channel.
Fig. S6. Merging selected channels in ImageJ.
Fig. S7. Selecting channels to be merged.
Fig. S8. Go to Image> Color> Channels Tool . . . .
Fig. S9. Convert to RGB.
Fig. S10. Following ImageJ instructions.
Fig. S11. Changing image from RGB color to 8-bit in ImageJ.
Fig. S12. Save merged channel image stacks as image sequence.
Fig. S13. Save merged channel image stacks to TIFF format; click OK.
Fig. S14. Save merged image stacks to new folder, e.g. ImageJ_Nikon_Maxilliped II_basis.

Fig. S15. Shortcut icon for 'drishtiimport'.
Fig. S16. Importing postprocessing data into Drishtiimport.
Fig. S17. Following instruction for importing the data to Drishti.
Fig. S18. Save to ***.pvl.nc file which are referred to as volumes in Drishti.
Fig. S19. Following save, a series of 5 windows will open; for each click OK.
Fig. S20. Entering 'image properties' (voxel size); x, y and z values.
Fig. S21. Saving the data to use in Drishti.
Fig. S22. Shortcut icon for 'Drishti'.
Fig. S23. Load ***.pvl.nc file, e.g. 'MaxillipedII_basis_Drishti_import.pvl.nc' into Drishti.
Fig. S24. Cropping the initial scanned volume.
Fig. S25. Getting high resolution images and some useful tools for Drishti.
Fig. S26. Adding a scale bar in Drishti.
Fig. S27. Saving the image and selecting image size.
Fig. S28. Naming image and saving in ***.jpg format.
Fig. S29. Taking a snapshot by selecting Mono Image and saving image.
Fig. S30. Segmentation: selecting mop update off for 3D data using Drishti.
Fig. S31. Rotating and removal of unwanted fragments in 3D images using Drishti.
Fig. S32. Adjusting opacity and colour of the image by manipulating interface.

Appendix 9: All figures and videos are supplied on DVD inside the rear cover.